The HANDBOOK of SIDESCAN SONAR

Philippe Blondel

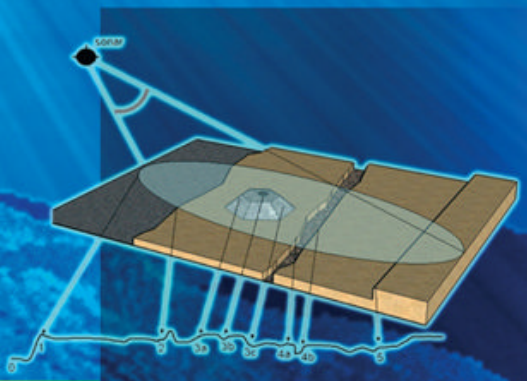

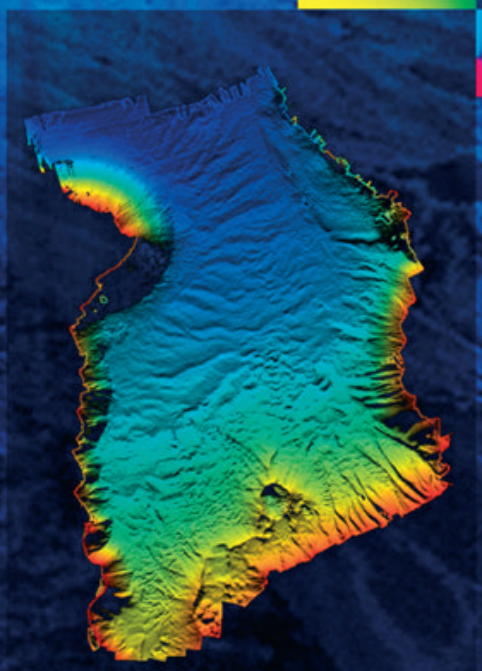

Springer

PRAXIS

The Handbook of Sidescan Sonar

Philippe Blondel

The Handbook of Sidescan Sonar

Springer

Published in association with
Praxis Publishing
Chichester, UK

PRAXIS

Dr Philippe Blondel, C.Geol., F.G.S., Ph.D., M.Sc.
Senior Scientist
Department of Physics
University of Bath
Bath
UK

SPRINGER–PRAXIS BOOKS IN GEOPHYSICAL SCIENCES
SUBJECT *ADVISORY EDITOR*: Philippe Blondel, C.Geol., F.G.S., Ph.D., M.Sc., Senior Scientist, Department of Physics, University of Bath, Bath, UK

ISBN 978-3-540-42641-7 Springer Berlin Heidelberg New York

Springer is part of Springer-Science + Business Media (springer.com)

Library of Congress Control Number: 2008924629

Cover design: Jim Wilkie
Project management: OPS Ltd, Gt Yarmouth, Norfolk, UK

Printed in Germany on acid-free paper

Contents

Preface

Sonar instruments are the only ones capable of accurately mapping large areas of the seabed and any water-covered area, because of the much lower attenuation in water of acoustic radiation compared with, for example, electromagnetic radiation. Sonars are therefore used all around the world, often in areas not mapped before. This meant there was a clear need for a reference book for new users, or users confronted with new features. This was first addressed by the *Handbook of Seafloor Sonar Imagery*, which I wrote in 1997 with the help of my colleagues Bramley J. Murton, D. Milkert and V. Hühnerbach whilst still at the Southampton Oceanography Centre (UK). Since then, we have had the pleasure of seeing this book used as a reference by many colleagues, in academic circles and in industry, during surveying or during processing and interpretation on land. Some university courses have adopted it as their main textbook and some survey companies have used it as the main learning support for their new engineers.

As time passed, and as the last edition went out of print, friends and colleagues everywhere started to press for a new edition. In the meantime, I had moved to the Department of Physics, University of Bath and my research interests (and publications) covered a broader range than just seabed mapping. Looking at other underwater instruments (e.g., bistatic sonars, bio-inspired sonars, passive sensors) has helped broaden the outlook of this book and put sidescan sonar applications in perspective. Continued research in planetary remote sensing also helped better seeing the general aspects of image interpretation, especially when confronted with strange, new environments. These changes are reflected in this *Handbook of Sidescan Sonar*, and in the way the different themes have been approached. After a brief introduction (Chapter 1), this book is divided into three main sections: the acquisition of sonar imagery (Chapters 2–4), covering all technological and scientific aspects of relevance to the sonar user; examples from the different environments (Chapters 5–9), including the increasing presence of man-made objects at all depths on the seabed; and techniques of advanced interpretation (Chapters 10–11), with their latest developments

but also an assessment of how far they can be used reliably. I have aimed at making this book widely accessible by pitching it at a scientific graduate level, and reducing the equations to the bare minimum. Wherever necessary, references are available for the reader wanting to go further, essential ones at the end of each chapter and a full reference list at the end of the book.

Reference to commercial products, processes, or services by tradename, trademark, manufacturer, or otherwise does not constitute or imply its endorsement by the author or his institution. Similarly, the presence or absence of particular articles or results does not imply any judgment value, but merely the need to present the basics of sidescan sonar processing and interpretation in a finite space and writing time, focusing on the most representative and readily available examples.

Acknowledgments

This book has used my own research and activities, but has benefited from the influence of working and meeting many people throughout the world. Early on, as a Lavoisier Fellow, I was fortunate enough to work with Jean-Christophe Sempéré, Véronique Robigou, and John R. Delaney at the School of Oceanography, University of Washington, and they gave me the taste for mapping the seabed and discovering new areas on the Earth (closer than Venus, my previous field, but much easier to ground-check and map). I came back to Europe at the Institute of Oceanographic Sciences, Deacon Laboratory (U.K.), which relocated to the Southampton Oceanography Centre in 1995. In both places, I had the pleasure of working with other friends and experts of seabed mapping, including Lindsay Parson, Bramley J. Murton, Peter Hunter, Doug Masson, Neil Kenyon, Tim LeBas, and many others too numerous to mention. The 1997 *Handbook of Seafloor Sonar Imagery* also mentioned (in no particular order) Mike Somers, Roger Searle, Neil Mitchell, R.A. Jablonski, Fran-Jo Hollender, Dave Coller, Martin Critchley, Eric Pouliquen, F. Werner, A. Kuijpers, R. Köster, Graham Westbrook, Rick Hagen, V. Purnachandra Rao, M. Veerayya, Valerie Paskevich, Joe Cann, Sandy Shor, Susan Humphris, Marty Kleinrock, Ken Stewart, Keith Pickering, Bill Schwab, Patty Fryer, Tim LeBas, B. Bader, H.G. Schröder, K. Schwarzer, P. Schäfer, K.W. Tietze, and A. Wehrmann. It is my pleasure to thank them again for their help and input, in whatever form. By their critical reviews of the 1997 book, esteemed friends and colleagues like Rachel Cave, Olga Gómez Sichi, and Veerle Huvenne have made sure that some mistakes or omissions would be corrected in any subsequent work. I am sure they will point out the new ones in this new book ... A special mention should be made of Doris Milkert and Veit Hühnerbach, who have now moved to different institutions (FWG and National Oceanography Centre, respectively) and have been a constant source of encouragement during the writing of this book. Over the 12 years it took to research (and write) the *Handbook of Sidescan Sonar*, I have strongly benefited from interaction with the Woods Hole Deep-Submergence Group (Dan Fornari, Bob Ballard,

Andy Bowen, John Howland, Steve Lerner, Dana Yoerger, and others), with colleagues from the BRIDGE (British Mid-Ocean Ridge Initiative), ECUA (European Conferences on Underwater Acoustics), and InterRidge communities (including Andrea Caiti and all our SITAR partners, Alan Evans, Eulalia Grácia, Thierry Garlan, Chris German, Jean-Pierre Henriet, Tony Laughton, Yves LeGall, Xavier Lurton, Raímon Pallas, François Parthiot, Jean-Pierre Sessarego, Vera van Lancker, Claudia Wienberg, Benoît Zerr, to name but a few), with different researchers from the NATO Undersea Research Centre (past and present, including Gaetano Canepa, Tony Lyons, Lucie Pautet, Alessandra Tesei), with Jaroslaw Tegowski and Aleksandra Kruss from Poland, and with my acoustics-minded colleagues at Bath, including Mario Cosci (now at EMC Projects), Peter Dobbins (now at SEA Ltd.), Cathy Dyer, Victor Humphrey (now at ISVR Southampton), Nisabha Jayasundere (now at the University or Ruhuna, Sri Lanka), William Megill, Nick Pace, etc. These regular interactions often meant going to sea or doing experiments or writing publications and proposals together. This huge list, and the fact I am sure I have forgotten many people I would have liked to include in these acknowledgments, show how much this book has benefited from the research and experience of other scientists around the world, and how much I hope it will profit sonar users internationally.

Last but not least, these acknowledgments should recognize the important role played by Clive Horwood of Praxis Publishing. Numerous unforeseen delays, and others that could have been planned better, have affected the writing of this book. Throughout it all, Clive and his small but dedicated team helped, pushed, and encouraged to make sure this book could be delivered to its end-users, the sonar mapping community. Another steady source of encouragement came from Neil Shuttlewood (OPS Ltd.), whose scientific knowledge also came in handy in the thorough editing of this book. Thank you both very much.

Bath, April 2009

Figures

Tables

Abbreviations and acronyms

AGDS	Acoustic Ground Discrimination Systems
AI	Artificial Intelligence
ANN	Artificial Neural Network
APL-UW	Applied Physics Laboratory, University of Washington
AR	Auto-Regressive model
ARC/INFO	Geographic Information System produced by ESRI Inc. (*http://www.esri.com/software/arcgis/arcinfo/index.html*)
ARMA	Auto-Regressive Moving Average model
ART	Adaptive Resonance Theory
ASA	Acoustical Society of America
ASW	AntiSubmarine Warfare
ATR	Automatic Target Recognition
AUV	Autonomous Underwater Vehicle
AVG	Angle-Varying Gain
AVR	Axial Volcanic Ridge
AWI	Alfred-Wegener Institut (Germany)
BIO	Buque de Investigación Oceanográfica (Oceanographic Research Vessel) (Spain)
BORIS	Bottom Response from Inhomogeneities and Surface
BP	Back-Propagation; Before Present
BP networks	Back-Propagation networks
BRIDGE	BRitish mID-ocean RidGE initiative
CA	Coarse Acquisition (code)
CAC	Computer-Aided Classification
CAD	Computer-Aided Detection
CAR	Circular Auto-Regressive model
CARIS	Series of commercial geomatics software products (*http://www.caris.com/*)

CS3	Combined Survey System (as in the GIMS/CS3 towed survey system)
CSEM	Controlled Source ElectroMagnetic
CTD	Conductivity–Temperature–Depth
CW	Continuous Wave
DCE-GESMA	Laboratory of the Groupe d'Études Sous-Marines de l'Atlantique (France)
DGPS	Differential Global Positioning System
DSL	Deep Submergence Laboratory, WHOI (U.S.A.)
DSS	Decision Support System
ECUA	European Conferences in Underwater Acoustics
EEZ	Exclusive Economic Zone
EPR	East Pacific Rise
ERDAS	Commercial remote-sensing software from ERDAS Inc. (*http://www.ermapper.com/*)
ETOPO5	Earth TOPOgraphy 5′-resolution
ETP-SRTM30	Earth Topography–Shuttle Radar Topography Mission 30′-resolution dataset (*http://www2.jpl.nasa.gov/srtm/*)
EXCAPI	EXpérimentation de Capteurs Acoustiques pour repérer le Pétrole Immergé
GCP	Ground Control Point
GIB	GPS Intelligent Buoy
GIMS	Gamma Isotope Mapping System
GIS	Geographic Information System
GLCM	Gray-Level Co-occurrence Matrix
GLORIA	Geological LOng-Range Inclined Asdic
GLORIA-B	GLORIA with Bathymetry
GPI	Geological and Paleontological Institute (Germany)
GPS	Global Positioning System
HDF	Hierarchical Data Format
HMR-1	A shallow-towed sonar
ICES	International Council for the Exploration of the Sea
IEEE	Institute of Electrical and Electronics Engineers
IET	Institution of Engineering and Technology
IFREMER	Institut FRançais pour l'Exploitation de la MER
IHO-S44	Bathymetry processing standard explained in the Fourth Edition of the International Oganisation Special Publication No. 44
ILSBL	Integrated Long and Short Baseline
INS	Inertial Navigation Systems
IOA	Institute Of Acoustics
ISA	International Seabed Authority
ISODATA	Iterative Self-Organizing Data Analysis Techniques
ISSAMS	*In Situ* Sediment Geoacoustic Measurement System
iUSBL	inverted USBL

IZANAGI	A shallow-towed sonar
JPL	Jet Propulsion Laboratory (U.S.A.)
LBL	Long BaseLine
LOS	Law of the Sea
LUSBL	Long USBL (*see* USBL)
MAK-1	A Russian sonar
MAR	Mid-Atlantic Ridge
MARFLUX/ATJ	Mid-Atlantic Ridge FLUXes/Azores Triple Junction
MARPOL	MARine POLlution
MCM	Mine Counter-Measure
MEDINAUT	Large French/Dutch program on the occurrence of mud volcanoes in the eastern Mediterranean Sea (MEDINAUT, MEDINETH)
MEDINETH	Large French/Dutch program on the occurrence of mud volcanoes in the eastern Mediterranean Sea (MEDINAUT, MEDINETH)
MEDUSA	Multi-Element Detector system for Underwater Sediment Activity
MIT	Massachusetts Institute of Technology (U.S.A.)
MLO	Mine-Like Object
MOR	Mid-Oceanic Ridge
MSG	Measurement Space–Guided clustering
NASA	National Aeronautics and Space Administration (U.S.A.)
NERC	Natural Environment Research Council (U.K.)
NetCDF	Network Common Data Form
NGDC	National Geophysical Data Center (U.S.A.)
NOC	National Oceanography Centre (U.K.) (previously Southampton Oceanography Centre, SOC)
OASES	Ocean Acoustics and Seismic Exploration Synthesis (MIT software)
ORETECH	A sidescan sonar
P	Precision (code)
p.s.u.	practical salinity unit
pixel	picture element
PRF	Pulse Repetition Frequency
PRISM	Processing of Remotely sensed Imagery for Seafloor Mapping
PSAS	Parametric Synthetic Aperture Sidescan
PVDF	PolyVinylidene DiFluoride
PZT	lead–zirconate–titanate alloy
QTC	Quester Tangent Company (Canada)
RIDGE	Mid-Ocean RIDGE Initiative (U.S.A.)
ROV	Remotely Operated Vehicle
RRS	Royal Research Ship
RTK	Real-Time Kinematic (GPS)

RV	Research Vessel
SA	Selective Availability
SAR	Système Acoustique Remorqué (Towed Acoustic System)
SAS	Synthetic Aperture Sonar
SBL	Short BaseLine
SCICEX	Scientific Ice Expeditions (U.S. research pogram)
SeaMARC	Sea Mapping And Remote Characterization
SEG-Y	One of several standards developed by the U.S. Society of Exploration Geophysicists
SHOALS	Commercial airborne lidar bathymetry measurement system, originating from the Scanning Hydrographic Operational Airborne Lidar Survey
SIO	Scripps Institution of Oceanography (U.S.A.)
SITAR	European Union research program on "Seafloor Imaging and Toxicity: Assessment of Risk Caused by Buried Waste"
SMS	Seafloor Massive Sulfide
SMS-960	A sidescan sonar
SOC	Southampton Oceanography Centre (U.K.)
SONAR	SOund Navigation And Ranging
TAG	Trans-Atlantic Geotraverse
TOBI	Towed Ocean-Bottom Instrument
TOPAS	Series of high-resolution bottom profilers developed by Kongsberg
TRANSIT	U.S. Navy satellite navigation system
TVG	Time-Varying Gain
UNESCO	U.N. Education, Scientific and Cultural Organization
USBL	Ultra-Short BaseLine
USGS	United States Geological Survey
UTM	Universal Transverse Mercator
UUV	Unmanned Underwater Vehicle
UW	University of Washington (U.S.A.)
WHIPS	Woods Hole Image Processing Software
WHOI	Woods Hole Oceanographic Institution
WWW	World Wide Web
XBP	eXpendable Bottom Probe
XBT	eXpendable Bathy-Thermograph
XTF	eXtended Triton Format

1

Introduction

1.1 BOOK OVERVIEW

Knowledge of the Earth and its evolving environment is proving increasingly crucial. Scientific, economic, political, and social decisions all depend at some time or another on this knowledge, and we like to think that we know all there is to know about our planet. One may be justified in doing so today, in the 21st century, by looking back at those maps with white unexplored regions that were still prevalent at the beginning of the 20th century. Yet, in many respects, we know more about the solid surface of other planets than about our own Earth. Rovers driving on Mars for years on end, landers on far-away Titan, and now the international missions to the Moon cannot mask the fact that ocean bottom landscapes only a few kilometers from our shores are still completely unknown.

More than half of the world's population live within 100 km of the sea. Thirteen of the 15 largest cities in the world are now located on or near the coast. The effects of denser population and accelerating climate change include the disappearance of ecosystems, coastal erosion, over-fishing, marine pollution, and higher vulnerability to marine disasters such as tsunami or volcanic activity. But the oceans cover more than two-thirds of the Earth's surface, and are not accessible to direct observation. It is only in the last 20 to 30 years that technological advances have allowed us to discover and map the Earth's seafloor, mostly through acoustic remote sensing.

Why only—some would say "primordially"—acoustic remote sensing? Why not use our most intuitive sense, vision, and the plethora of Earth observation satellites in orbit? We are used to seeing satellite-derived topography for the entire Earth, from one pole to the other (e.g., the ETP-SRTM30 dataset, at kilometric resolution). But it is derived from average gravity measurements and even when supplemented with actual bathymetry measurements, it cannot account for evolution over time, and is easily subject to confusion with gravity anomalies. Conversely, more accurate mapping systems (e.g., SHOALS, using airborne lasers) have shown it possible to

map coastal areas in great detail. But even lasers can only penetrate through a few tens of meters in very clear water. Diving with submersibles is limited too, because only a handful of submersibles in the world are capable of diving below 3,000 m (thus limiting us to 46% of the planet's surface) and further because their field of view is limited. Most of the light travelling into water is absorbed and converted into heat, and in the visible wavebands, the path length in pure sea water is still limited to a few tens of meters towards the blue part of the spectrum (Figure 1.1). Vision is therefore of limited use under water.

Acoustic waves, by contrast, can travel over long distances without attenuating too much (see Chapter 2 for more details). They can reach all depths in the ocean, from the deepest (>11 km in the Marianas Trench) to the most common ($\sim$ 4 km) and

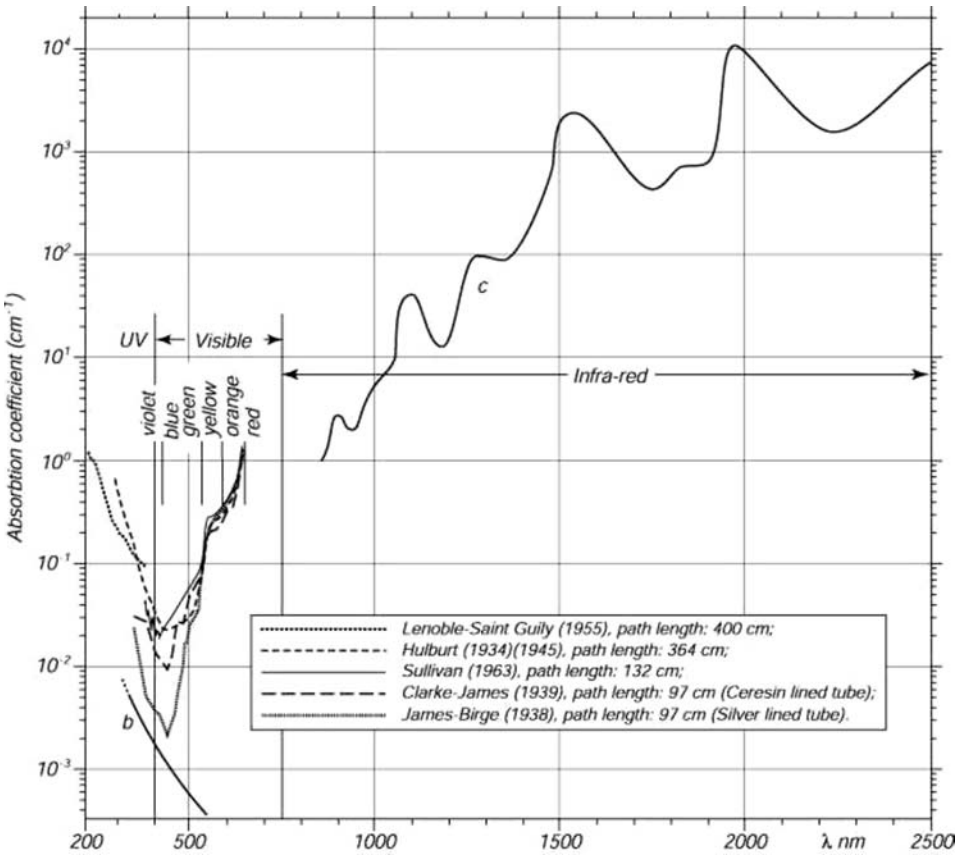

Figure 1.1. Light attenuation in pure water, as measured in different experiments (from *http://oceanworld.tamu.edu/resources/ocng_textbook/chapter06/chapter06_10.htm*). An absorption coefficient of 1 cm^{-1} (coefficient *c*) means that in a single centimeter, light intensity will be divided by *e*. Blue light is absorbed least, and red light attenuates very quickly. Seawater contains salt and many heterogeneities (e.g., plankton), increasing the attenuation even more.

the shallowest (a few centimeters). Acoustic echoes inform us about the range travelled (i.e., the depth) and about how they were reflected (i.e., the type of seabed or obstacle). Complex processing can reveal information at very small scales, down to a few centimeters in some cases. They are used in instruments called sonars (for sound navigation and ranging). The images and maps produced by these sensors are not easy to interpret, because of their nature and because of the complex processes at play during their propagation and reflection. There are different types of sonars, mostly single-beam echo-sounders (looking directly beneath the supporting vessel), multibeam echo-sounders (looking on both sides of the vessel, providing mainly bathymetry and sometimes imagery), and sidescan sonars (usually flown closer to the seafloor, providing mainly imagery and sometimes bathymetry). They are all presented in Chapter 2, but because the emphasis of the book is on imagery and its interpretation, it will concentrate on sidescan sonars, whose imagery is much more detailed, complex, and varied. Interpretation of multibeam imagery follows the same principles and does not warrant separate treatment. Following in the footsteps of the first (and then only) work on the subject (Belderson *et al.*, 1972), the *Handbook of Seafloor Sonar Imagery* (Blondel and Murton, 1997) was the first modern and comprehensive book explaining the different steps of sidescan sonar imagery interpretation. It proved a success, and the latest edition is now out of print. Ten years on, it was felt necessary to update this book and expand its scope to the new domains of sidescan sonar remote sensing.

The *Handbook of Sidescan Sonar* is more than just a new edition of the *Handbook of Seafloor Sonar Imagery*, with a few updates and corrections. It has been in fact substantially remodelled, redressing the undue bias toward mid-ocean ridges of the previous version (explained by the domain in which both authors worked) and taking into account more of the wider underwater world. This book has also been substantially affected by many important developments of the last 10 years.

— The democratization of sonars. Once only used by powerful companies and institutions, sonar sales and rentals have greatly increased every year (24% in 1997 alone).
— The emergence of new platforms. Sidescan sonars can still be towed behind ships, but Unmanned Underwater Vehicles (UUVs), whether autonomous (AUV: Autonomous Underwater Vehicles) or tethered (ROV: Remotely Operated Vehicles) have become increasingly common and regularly use sidescan sonar as their main mapping tool.
— The introduction of new manufacturing technologies. Innovative materials and production techniques, and their fast transfer from research to commercial products (e.g., the blazed array technology, patented in 1999 and first commercialized in 2002), have led to advances in the capabilities of sidescan sonars and to a greater portability (some shallow-water applications have even used kayaks).
— The introduction of new transducer configurations, or their easier implementation. This has led in particular to the development of interferometric sonars (providing bathymetry at the same scale as imagery).

— Advances in sonar processing have been made possible by developments in computer technology and processing power. CPU speed has increased more than ten-fold since 1997, and the price of data storage decreased roughly a hundred-fold: Moore's law means this trend is likely to follow for the next 10–20 years.
— Advances in sensor merging. Driven by the advances in processing means that different sonars can be considered together for interpretation, rendering a richer picture of the actual processes on the seabed. Information from other sensors (e.g., attitude and navigation) is also better integrated, making for more accurate maps.
— Developments in navigation and processing techniques. More accurate navigation, or even micro-navigation at scales of millimeters or centimeters, have made possible the development of Synthetic-Aperture Sonars, whose performance does not degrade with range (see Chapter 2).
— The spread of the Internet, even at sea. The ease with which information can now be retrieved, from anywhere in the world, has made redundant long lists of technical specifications in books, as they can be accessed more timely and more completely at the click of a mouse (coupled with the sheer variety of sonars now available on the market, this is the reason the list of sonars and their characteristics has been greatly reduced in this book, to show only the most representative or interesting).
— New advances in knowledge of the seabed. In the last 10 years, our knowledge of the oceans has tremendously increased, because of the wider availability of sonars and because of the wider types of surveys done. Many readers of the *Handbook of Seafloor Sonar Imagery* contributed to these developments themselves, and the present book will try to do justice to their endeavors by showing some of the latest examples of new features.

This long list of developments in the field means that a single book is not enough to describe everything and acknowledge everybody in a varied, rich, and interdisciplinary field, merging research, development, and straight applications. The *Handbook of Sidescan Sonar* does not pretend to be an exhaustive list of everything; it does not aim either at being a "coffee table" book with pretty images of every feature under the sea. And it does not aim to recognize all past research or activities. Rather, we have aimed at making it a convenient book for researchers and practitioners wanting a concrete answer to their questions. Users of the previous *Handbook* have encouraged us in this way by telling us how they used it, often at sea, and what they liked and disliked in it, and we are grateful for their comments. Students new to the field of sidescan sonar have used the book as a base for further learning (starting with the "Further reading" sections at the end of each chapter). Engineers have used it to think about new products. Surveyors have used it to check intriguing images or double-check their analyses. And researchers have used it to think about new ways of processing or analysing the data, as well as to better understand specific images. Such widespread use, by so many experienced users, has led us to bolster the sections on

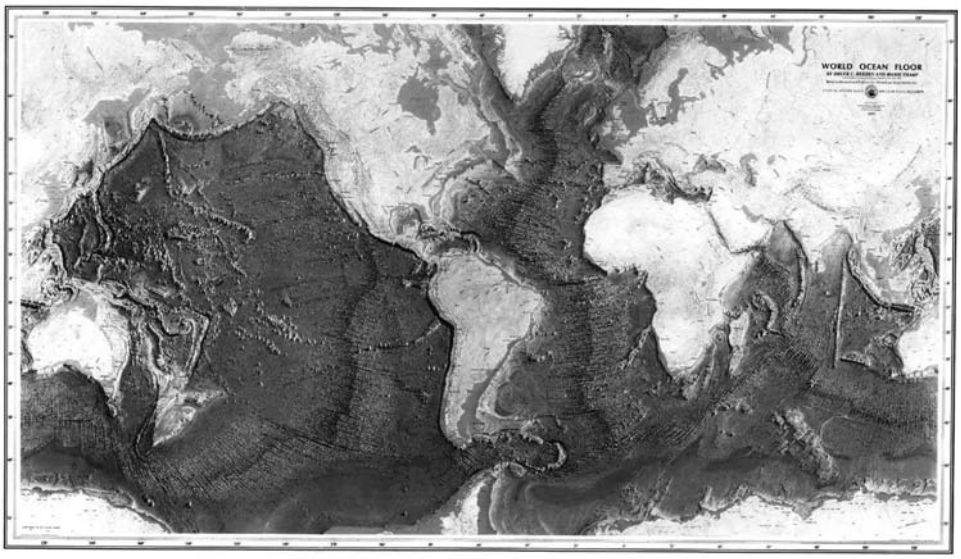

Figure 1.2. The famous map of the seabed, compiled by Mary Tharp and Bruce Heezen during the 1960s, was the first to show so dramatically the variety of the seabed. It is now superseded by more accurate sea-based surveys and satellite measurements, but its scientific and artistic qualities remain.

new techniques, currently on the market or still a few years away, and the sections on computer-assisted interpretation.

This book is divided into chapters that deal first with the stages of sonar data acquisition and processing and then (roughly) to the different regions of the seabed (Figure 1.2). Chapter 2 (''Acoustics for sidescan sonars'') presents the basics of acoustics needed to successfully process and interpret sidescan sonar imagery. It also introduces some of the new tools which are currently emerging or will transition from prototypes to finished products in the coming decade. Finally, it synthesizes the performance of sonars: how to choose the one most adapted to the survey in mind, and how to compare different instruments, sometimes widely different. Chapter 3 (''Imagery and bathymetry'') presents the acquisition of bathymetric data, either from sidescan sonars or from other sources, and how it can be successfully merged with imagery. Chapter 4 (''Sidescan sonar data processing'') explains in detail the different steps to create a true and accurate map of the seabed, finishing with examples of a handful of successful systems (commercial and academic). Chapter 5 (''Spreading and subduction'') presents the manifestations of plate tectonics on the seabed, and its varied examples on different types of mid-ocean ridges and subduction environments. Chapter 6 (''Abyssal basins and polar seas'') presents sidescan sonar images from poorly known environments, often accessed with great difficulty but nonetheless acoustically rich and scientifically important. Chapter 7 (''Continental margins'') summarizes the wide variety of structures—sedimentary, tectonic, and

volcanic—visible in these regions of highly varying depths. Chapter 8 (''Shallow-water environments'') moves closer to shore, presenting features that can also be found in lakes and rivers. Wherever possible, the detailed examples of specific features and processes shown in Chapters 5 to 8 are followed by regional imagery showing a variety of structures as they might appear in a full survey. Chapter 9 (''Synthetic structures'') acknowledges both the move of sonars to increasingly shallower environments and the pros and cons of the growing influence of human population on the seabed. It will therefore include examples of planned activities (e.g., pipelines, mineral exploitation) and ''accidental'' discoveries (e.g., shipwrecks, marine pollution, and the effects of trawl-fishing). This chapter will also present examples of problems posed by mines and more peaceful applications to underwater archaeology. Chapter 10 (''Anomalies and artefacts'') assesses what can go wrong in the acquisition of a sonar image, in its processing, and in its interpretation, drawing on real examples from all over the world. Chapter 11 (''Computer-assisted interpretation'') presents the different techniques now available to assist (or sometimes replace) the interpreter, from traditional Computer-Aided Detection/Computer-Aided Classification (CAD/CAC) techniques to ATR (Automatic Target Recognition) and the potential of Artificial Intelligence (AI) techniques. All chapters end with a small section suggesting ''Further reading''. The ''Bibliography'' chapter at the end of the book bolsters these suggestions with more references. Chapter 12 (''Conclusion'') aims at putting these distinct topics in a coherent framework, showing the few differences and great similarities in the interpretation of sonar imagery in all environments, as well as thoughts about the evolution of the field in the next decade.

This book is an ambitious project, trying to form a single source of easy reference covering all the stages of data acquisition, processing, and interpretation. It covers all environments found on Earth, from the deepest to the shallowest. It draws on first-hand personal experience, at sea (from 44°S to 79°N) and in the laboratory, of the complexity of acoustic scattering processes. But it would not have been possible without the combined experience of all our colleagues, who opened their ''treasure chests'' of images for this book, as they did for its predecessor back in 1997. As in the first book, we have endeavoured to give credit where credit is due (i.e., for each image, to mention who acquired it, with which instrument, and if possible to mention the reference publication). Any mistake or omission should be notified to the author or publisher, who will correct it for the next edition. Commercial systems are presented throughout this book, and it should go without saying that their mention does not present any form of endorsement by the author or the publisher.

Finally, ''last but not least'', this introduction should acknowledge the important role played by Clive Horwood, director of Praxis Publishing Ltd. and his colleagues at Praxis and Springer. Numerous changes to the scope of this project, and (numerous) delays in the writing of this book have taxed patience and nerves, but the unfailing assistance of Clive and his team, combined with the expert support of Neil Shuttlewood, mean that this book is now completed and ready to join the older *Handbook of Seafloor Sonar Imagery* on the bookshelves of colleagues around the world, on land and at sea, with hopefully the same success.

2

Acoustic signals and data acquisition

2.1 SONAR MAPPING SYSTEMS

Acoustics is the best and often the only means to investigate the water column and seabed efficiently and accurately. There is a large variety of instruments now available, and sonar mapping systems can be roughly divided into three categories: single-beam echo-sounders, multibeam echo-sounders, and sidescan sonars (Figure 2.1).

Single-beam, down-looking echo-sounders have long been the tool of choice for mapping, because they are simple to use and widespread on nearly all vessels. They transmit a single beam, oriented toward the ship's nadir. They generally use low-frequency signals ($<$20 kHz) transmitted in short pulses ($<$2 ms) from a single transducer. The first return from the seabed corresponds to points closest to the ship, and farther as the cone spreads. Sub-surface penetration is often an issue in sedimentary areas. Echosounders are not always calibrated, but often give a very good estimate of the depth and type of seabed. The shape of the echo can be analysed quantitatively (e.g., Pouliquen and Lurton, 1992; Tegowski and Lubniewski, 2000) to derive more information about the local habitat. Innovative techniques were also developed to extract more information from the echoes of the secondary lobes (e.g., Heald and Pace, 1996). However, single-beam echo-sounders only provide information on the seabed immediately below the surveying vessel. The footprint on the seabed varies in size, depending on the water depth and the local slopes, but is generally large. Seafloor coverage will therefore be variable and rather small.

This led to the design of multibeam echo-sounders. Becoming more accessible in the late 1980s, these instruments transmit several beams (up to 120 for some instruments), covering a wide swath on each side of the ship's track (up to 20 times the water depth in some cases). These beams are narrower than single beams, and are produced with transducer arrays (made of identical transducer elements equally spaced). These systems principally acquire bathymetry measurements for each beam,

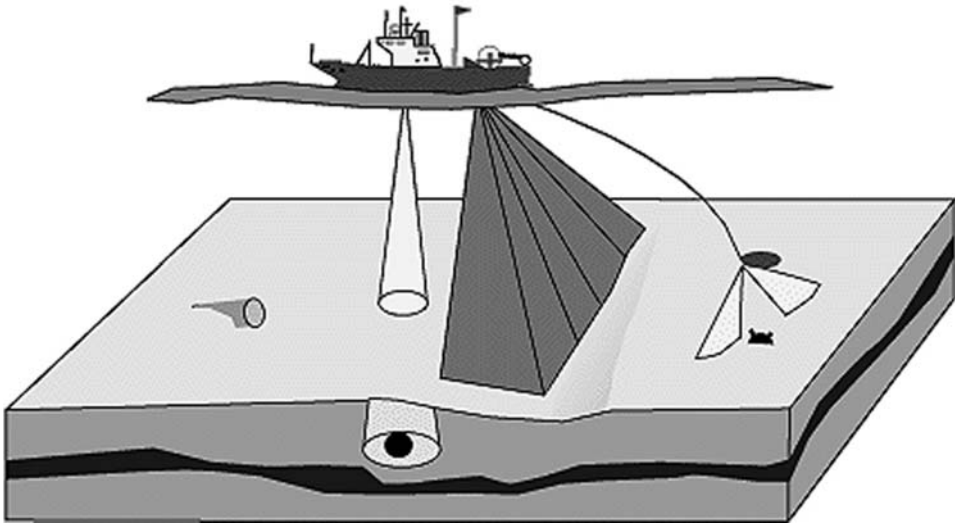

Figure 2.1. The main sonar mapping systems are (from left to right) the single-beam echosounder, aiming straight below the surveying vessel and imaging a wide portion of seabed (and sub-seabed) at once; the multibeam echosounder, made of narrower beams and mapping a wide swath of seabed across the track of the surveying vessel; and the sidescan sonar, often towed separately and close to the seabed, imaging at grazing angles (adapted from the EC-ISACS project *http://www.ntnu.no/ISACS/*).

but, increasingly, backscatter strengths can also be derived. Targets smaller than the footprint can now be resolved by some systems, using the "split aperture" method (e.g., Lurton, 2000). Multibeam echo-sounders are particularly attractive for the mapping of Exclusive Economic Zones, and their processing is well standardized, following high standards of calibration and accuracy (e.g., IHO-S44 for bathymetry). Knowledge of the local bathymetry, at each point where backscatter has been acquired, can be used to correct the imagery and represent it using the exact local incidence angles. Its interpretation is not too different from that of sidescan sonar imagery.

But the tool of choice for high-resolution seabed mapping remains the sidescan sonar. This instrument covers a much larger portion of the seabed away from the surveying vessel, from a few tens of meters to 60 km or more. This coverage is attained by transmitting one beam on each side (broad in the vertical plane and narrow in the horizontal plane). Using different frequencies (from 6.5 kHz to 1 MHz), sidescan sonars achieve resolutions of 60 m down to 1 cm. The processing steps are less standardized, depending on the manufacturer, despite the consensus on the types of corrections desirable (see Chapter 4).

Whenever possible, these instruments are used in combination. The imagery can be draped over the bathymetry, producing 3-D views of the seabed, and the bathymetry can be used to further refine the processing of the imagery (see Chapter 4). Sonars, and in particular sidescan sonars, can provide stunning images, similar in

quality and extent to satellite images. But they cannot be interpreted in the same way, because of the high differences in the physical processes leading to their creation. Considering the sonar as a "black box" merely producing an image is severely limiting potential analyses, and it is necessary to understand the basic acoustic processes leading to the formation of an image, and impacting on its quality.

2.2 ACOUSTIC THEORY; BASICS

2.2.1 Acoustic waves

Acoustic waves consist in the propagation of a pressure wave in the water and/or targets (e.g., seabed). This wave is characterized by its intensity, often measured in decibels (dB) relative to the source, its frequency (or wavelength), and the type and length of the pulse (as sidescan sonars usually transmit finite pulses in the water).

The intensity is related to the changes in acoustic pressure, as measured by the hydrophone arrays on the sonar system, and can easily span several orders of magnitude (hence the logarithmic scaling in decibels).

The frequency f of the wave is related to the wavelength λ (the spatial distance between two points in the propagation medium with the same pressure):

$$f = \frac{c}{\lambda}, \tag{2.1}$$

where c is the velocity of sound in the medium. It ranges between 1,450 m/s and 1,550 m/s in seawater, depending on salinity, pressure, and temperature (see Section 2.2.2).

Frequencies typically used with sidescan sonars range from 1 kHz to 1 MHz (Figure 2.2). For an average sound speed of 1,500 m/s in seawater, the associated wavelengths will therefore range from 1.5 m at 1 kHz down to 1.5 mm at 1 MHz. The wavelength dictates the scale of features that can be detected on the seabed; for example, through micro-scale roughness (see Section 2.2.3). This is an important factor in the interpretation of sonar imagery and (at an earlier stage) in the choice of the most appropriate sidescan sonar (see Section 2.6).

Other important parameters are the type and length of the pulse transmitted into the water. An important body of literature exists on the subject, and the reader is referred to Burdic (1990), Medwin and Clay (1998), and Lurton (2002) for in-depth discussions of the merits of each signal, in terms of resolution on the ground and ease of processing. For some of the most modern sonars, it is possible to change the type of signal transmitted, or at least its frequency and duration. Typical signals used with sidescan sonars include bursts and chirps (Figure 2.3). Bursts are narrowband pulses (i.e., continuous wave, CW, pulses). They are formed by a sine wave, of fixed frequency, transmitted during a limited time T (typically 0.1 ms to 10 ms). The duration directly impacts on the resolution: two CW pulses of duration T can only be distinguished if they are separated by a time of at least T. After reflection from a target, this corresponds to a spatial resolution of $cT/2$ (0.75 m for a 1 ms pulse). Less

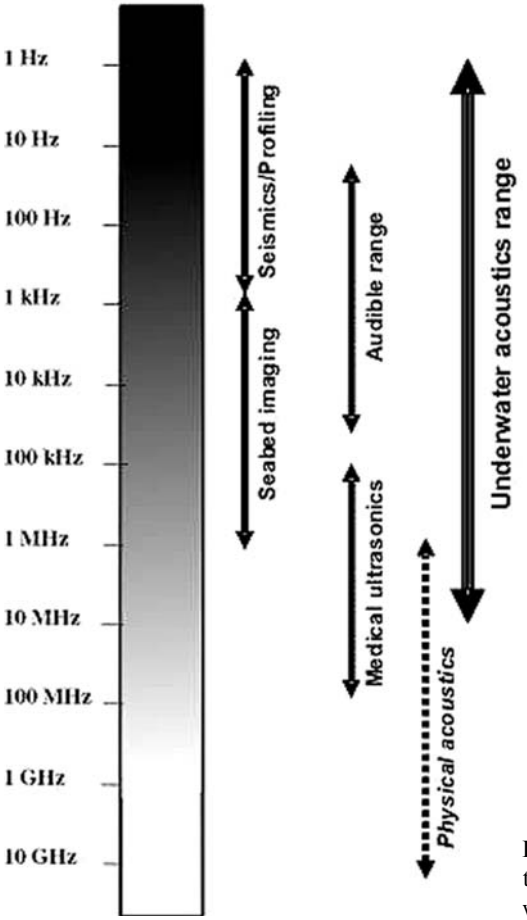

Figure 2.2. Comparison of frequencies typically used in underwater acoustics with other domains of acoustics.

common, chirp signals are linear swept-frequency cosines, also of limited duration. They are more advantageous than bursts in noisy environments; for example, to compensate for the very strong attenuation of the signal during propagation inside the seabed, at the detriment of more complex processing. Ricker signals are much less common. They consist in a single pulse (similar to the second derivative of a Gaussian pulse) and have interesting signal-processing properties: they are mostly used for the detection of small targets or for high-resolution sediment profiling (e.g., in the TOPAS system).

2.2.2 Acoustic propagation

Acoustic waves will be affected during their propagation in the water column, either on their way to the target/seabed or on their way back to the sonar. As the acoustic

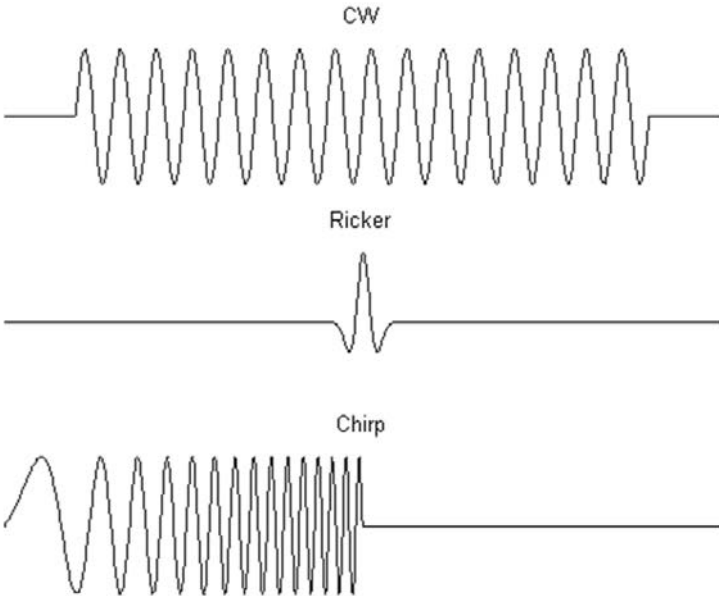

Figure 2.3. The type (and length) of acoustic pulse selected depends on the application, as it governs the range and resolution achievable. The amplitudes of the signals shown here are plotted as a function of time.

waves move away from the transmitter they will spread over a larger volume. After a certain distance (far field), they can be approximated as plane waves, and their intensity will decrease in $1/R^2$, where R is the distance travelled from the source to the point of measurement (for a sonar imaging the seabed, this will be the straight distance to the seabed and back, the slant range).

Another factor contributing to the attenuation is the dissipation of the acoustic energy viscosity and chemical reactions in the medium. In seawater, the main processes leading to attenuation with distance are the viscosity of pure water, the relaxation of boric acid ($B(OH)_3$) molecules at frequencies above 1 kHz, and that of magnesium sulphate ($MgSO_4$) molecules above 100 kHz (e.g., Lurton, 2002). These variations have been well studied theoretically and experimentally, and the sonar user now benefits from several reliable models, such as that of Francois–Garrison:

$$\alpha = A_1 P_1 \frac{f_1 f^2}{f_1^2 + f^2} + A_2 P_2 \frac{f_2 f^2}{f_2^2 + f^2} + A_3 P_3 f^2. \tag{2.2}$$

This model gives the attenuation coefficient α in dB/km. This is on a logarithmic scale: a 1 dB difference corresponds to around 10% in acoustic pressure. Noting z the water depth (in meters), S the salinity (in practical salinity units, p.s.u.), T the temperature of the water (in °C), pH its pH, and f the frequency of the propagating wave, the terms of this equation can be decomposed into the contribution of pure water (last term) and the additional constituents of $MgSO_4$ and $B(OH)_3$. The

contribution of boric acid reads

$$\left.\begin{aligned} A_1 &= \frac{8.86}{c}10^{(0.78pH-5)} \\ P_1 &= 1 \\ f_1 &= 2.8\sqrt{\frac{S}{35}}10^{\left(4-\frac{1{,}245}{T+273}\right)} \\ c &= 1{,}412 + 3.21T + 1.19S + 0.0167z. \end{aligned}\right\} \tag{2.3}$$

The contribution of magnesium sulphate reads

$$\left.\begin{aligned} A_2 &= 21.44\frac{S}{c}(1 + 0.025T) \\ P_2 &= 1 - 1.37 \cdot 10^{-4}z + 6.2 \cdot 10^{-9}z^2 \\ f_2 &= \frac{8.17 \cdot 10^{\left(8-\frac{1{,}990}{T+273}\right)}}{1 + 0.0018(S-35).} \end{aligned}\right\} \tag{2.4}$$

And the contribution of the viscosity of pure water is

$$\left.\begin{aligned} P_3 &= 1 - 3.83 \cdot 10^{-5}z + 4.9 \cdot 10^{-10}z^2 \\ t < 20^{\circ}\mathrm{C} &\Rightarrow A_3 = 4.937 \cdot 10^{-4} - 2.59 \cdot 10^{-5}T + 9.11 \cdot 10^{-7}T^2 - 1.5 \cdot 10^{-8}T^3 \\ t > 20^{\circ}\mathrm{C} &\Rightarrow A_3 = 3.964 \cdot 10^{-4} - 1.146 \cdot 10^{-5}T + 1.45 \cdot 10^{-7}T^2 - 6.5 \cdot 10^{-10}T^3. \end{aligned}\right\} \tag{2.5}$$

The Francois–Garrison model is widely used and accurate. For an average depth of 100 m, an acoustic wave would experience an attenuation of 0.95 dB/km if transmitted at 10 kHz, compared with 124 dB/km at 500 kHz. This effect cannot be neglected, and should be part of both the choice of the optimal sonar configuration (see Section 2.6) and the interpretation of far-range data.

The velocity at which the acoustic waves travel will also vary with the temperature of the water, its salinity, and whether it contains heterogeneities (e.g., bubbles or suspended sediments). Because it is generally difficult to measure local sound velocity, it is most often derived from proxy measurements of temperature, salinity, and depth, using tools such as XBT (expendable bathy-thermograph) or CTD (conductivity–temperature–depth). When even these measurements are not possible, approximate values can be derived from compilations such as the Levitus Database (*http://ingrid.ldgo.columbia.edu/SOURCES/.LEVITUS94/*). Again, there are many models of sound velocity in the literature (e.g., Medwin and Clay, 1998; Lurton, 2002). A quick approximation, limited to 1,000 m deep, was proposed by Medwin (1975,

in Medwin and Clay, 1998):

$$\begin{aligned} c = {} & 1{,}449.2 + 4.6T - 0.055T^2 + 0.00029T^3 \\ & + (1.34 - 0.01T)(S - 35) + 0.016Z \end{aligned} \tag{2.6}$$

where T is the local temperature (in °C), Z is the depth (in m), and S is the salinity in parts per thousand (‰) (equal to the modern unit of practical salinity unit, or p.s.u.).

A more complex but more accurate equation is available for all depths in the ocean. The Chen–Millero–Li equation reads:

$$c_{TSP} = c_w(T,P) - c_c(T,P) + A(T,P) \times S + B(T,P) \times S^{3/2} + D(P) \times S^2,$$

where

$$\left.\begin{aligned} c_w(T,P) = {} & 1{,}402.388 + 5.03711T - 5.80852 \cdot 10^{-2}T^2 \\ & + 3.3420 \cdot 10^{-4}T^3 - 1.4780 \cdot 10^{-6}T^4 + 3.1464 \cdot 10^{-9}T^5 \\ & + P\begin{pmatrix} 0.153563 + 6.8982 \cdot 10^{-4}T - 8.1788 \cdot 10^{-6}T^2 \\ +1.3621 \cdot 10^{-7}T^3 - 6.1185 \cdot 10^{-10}T^4 \end{pmatrix} \\ & + P^2\begin{pmatrix} 3.1260 \cdot 10^{-5} - 1.7107 \cdot 10^{-6}T + 2.5974 \cdot 10^{-8}T^2 \\ -2.5335 \cdot 10^{-10}T^3 + 1.0405 \cdot 10^{-12}T^4 \end{pmatrix} \\ & + P^3(-9.7729 \cdot 10^{-9} + 3.8504 \cdot 10^{-10}T - 2.3643 \cdot 10^{-12}T^2) \\ c_c(T,P) = {} & P(0.0029 - 2.19 \cdot 10^{-4}T + 1.4 \cdot 10^{-5}T^2) \\ & + P^2(-4.76 \cdot 10^{-6} + 3.47 \cdot 10^{-7}T - 2.59 \cdot 10^{-8}T^2) \\ & + 2.68 \cdot 10^{-9}P^3 \\ A(T,P) = {} & 1.389 - 1.262 \cdot 10^{-2}T + 7.164 \cdot 10^{-5}T^2 \\ & + 2.006 \cdot 10^{-6}T^3 - 3.21 \cdot 10^{-8}T^4 \\ & + P\begin{pmatrix} 9.4742 \cdot 10^{-5} - 1.2580 \cdot 10^{-5}T - 6.4885 \cdot 10^{-8}T^2 \\ +1.0507 \cdot 10^{-8}T^3 - 2.0122 \cdot 10^{-10}T^4 \end{pmatrix} \\ & + P^2\begin{pmatrix} -3.9064 \cdot 10^{-7} + 9.1041 \cdot 10^{-9}T \\ -1.6002 \cdot 10^{-10}T^2 + 7.988 \cdot 10^{-12}T^3 \end{pmatrix} \\ & + P^3(1.100 \cdot 10^{-10} + 6.649 \cdot 10^{-12}T - 3.389 \cdot 10^{-13}T^2) \\ B(T,P) = {} & -1.922 \cdot 10^{-2} - 4.42 \cdot 10^{-5}T + P(7.3637 \cdot 10^{-5} + 1.7945 \cdot 10^{-7}T) \\ D(P) = {} & 1.727 \cdot 10^{-3} - 7.9836 \cdot 10^{-6}P. \end{aligned}\right\} \tag{2.7}$$

The temperature T (in °C) can range between 0°C and 40°C. The salinity S (in p.s.u.) can vary between 0 and 40 (typical values are around 35 p.s.u. in the deep ocean,

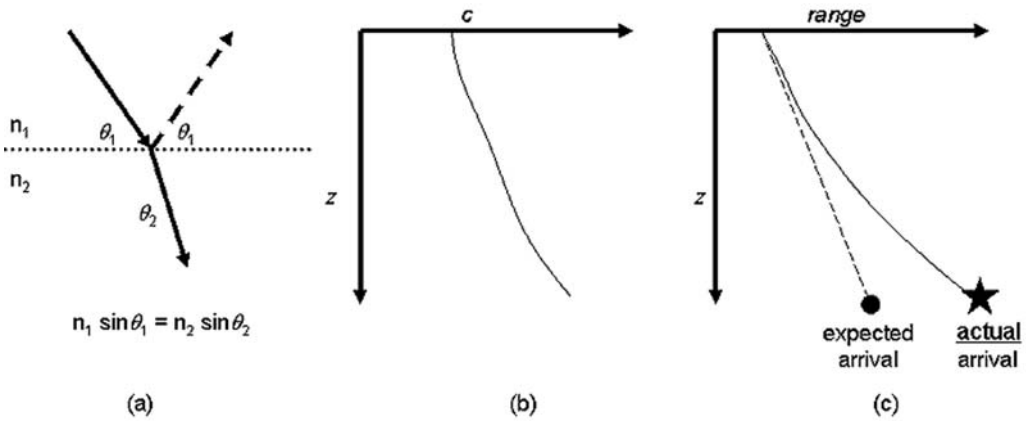

Figure 2.4. Refraction at the interface between two water layers (a) with distinct properties will correspond to variations in sound velocity (b). The actual arrival of the acoustic wave on the seabed can therefore be much farther than expected (c).

14 p.s.u. in fresher waters like the Baltic). The pressure P (in bar) ranges between 0 bar and 1,000 bar (i.e., depths down to 10,200 m, covering most of the world's water bodies). $c_w(T, P)$ is the sound speed of pure water. The uncertainty of this equation is claimed to be ± 0.07 m/s, which is extremely accurate.

The influence of attenuation on sonar imagery is immediately perceived: as the range increases, the acoustic returns will become weaker and they will often need amplifying (see Section 4.3). The influence of sound velocity is more subtle but just as important. Like electromagnetic waves, acoustic waves follow Snell–Descartes' laws of reflection and refraction at interfaces. Two layers of water with distinct sound velocities will act as an interface, and the path of the acoustic waves will bend one way or the other (Figure 2.4). This means that in most circumstances the points on the seabed will be farther than expected. This also shows the danger of using a constant sound velocity, or a velocity constantly increasing with depth, rather than actual measurements. This is important in deep water, if the imaging sonar is near the surface and the acoustic wave travels through distinct water layers. It is also important in shallow water, because of the effects of radiative forcing from the Sun or the winds on water temperature.

Acoustic waves can also travel in the seabed, although for much shorter distances. The attenuation is much more important, and will depend on the type of seabed (orders of magnitude of 100 dB/m are common at high frequencies). The sound speed will vary widely, with values of 1,500 m/s to 2,000 m/s for some sediments. Most common values are tabulated in articles (e.g., Hamilton and Bachman, 1982) and in technical reports (e.g., APL-UW, 1995), but they correspond to "pure" seabeds. The values for "mixed" seabeds (e.g., basalt with a thin sedimentary cover) will vary with each case and the amount of mixing. *Ad hoc* values can sometimes be determined by geoacoustic inversion and numerous techniques are available in the literature (e.g., Taroudakis and Makrakis, 2001; Caiti *et al.*, 2006).

2.2.3 Acoustic scattering; theory

A sidescan sonar will transmit two beams, one on each side (Figure 2.5). These beams are narrow along-track to get a high resolution, and wide across-track to cover as much range as possible (the swath width corresponds to the range on both sides of the sonar). The distance from the sonar to a point on the seabed is called the slant range. It should not be confused with the ground range, between this point and the sonar's nadir (the point immediately below the sonar). The angle of incidence of the incoming acoustic wave is a key factor in understanding how it will scatter. Most of the energy is reflected in the specular direction (like shining a pencil beam on a mirror). Some will be reflected along other angles (scattering angles, distributed along the main reflection angle). Depending on the terrain, some energy will be lost in the seabed. Only a very small portion (several orders of magnitude lower) might be reflected back toward the imaging sonar (backscatter).

Once recorded, the backscattered energy will provide different types of information. The time offset between the transmission (initial "ping") and the reception is directly proportional to the slant range. From the sonar's height above the seabed, we can deduce the ground range to the echo. The frequency shift indicates the speed of the target relative to the sensor (Doppler effect). Phase shifts are used to deduce the

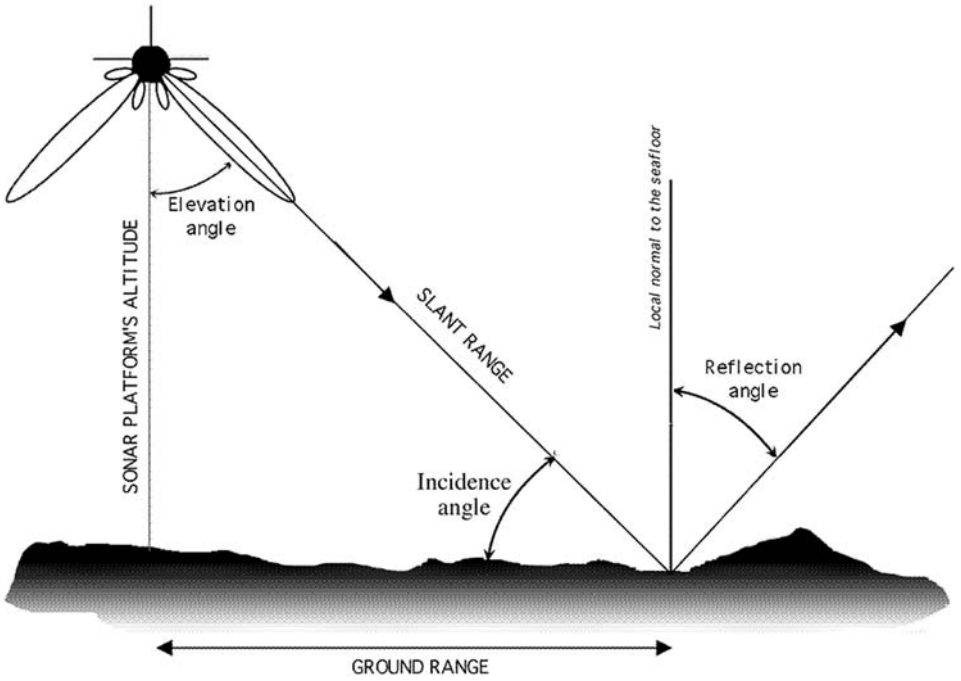

Figure 2.5. Definitions of some parameters (see text for details). The actual acoustic scattering will be distributed around the reflection angle: only the portion scattered back toward the sonar (backscatter) is used in sidescan sonars (from Blondel and Lurton, 1997).

arrival angle of the beam. Some systems also extract bathymetry from the phase difference between neighbouring transducers. The amplitude of the echo will give some information about the nature of the point imaged (seabed or target).

Backscattering is affected, in decreasing order of importance, by

- the geometry of the sensor–target system (local angle of incidence of the sonar beam, local slope, etc.);
- the physical characteristics of the surface (micro-scale roughness, density, sound speed, etc.);
- the intrinsic nature of the surface (composition, density, relative importance of volume vs. surface scattering for the selected frequency and imaging configuration).

These effects are shown in Figure 2.6. Slopes facing toward the sonar will produce more backscatter, whereas slopes facing away from the sonar will show reduced backscatter or (in some conditions) no backscatter. This is why fault scarps will be acoustically brighter on a sidescan sonar image if they are facing "the right

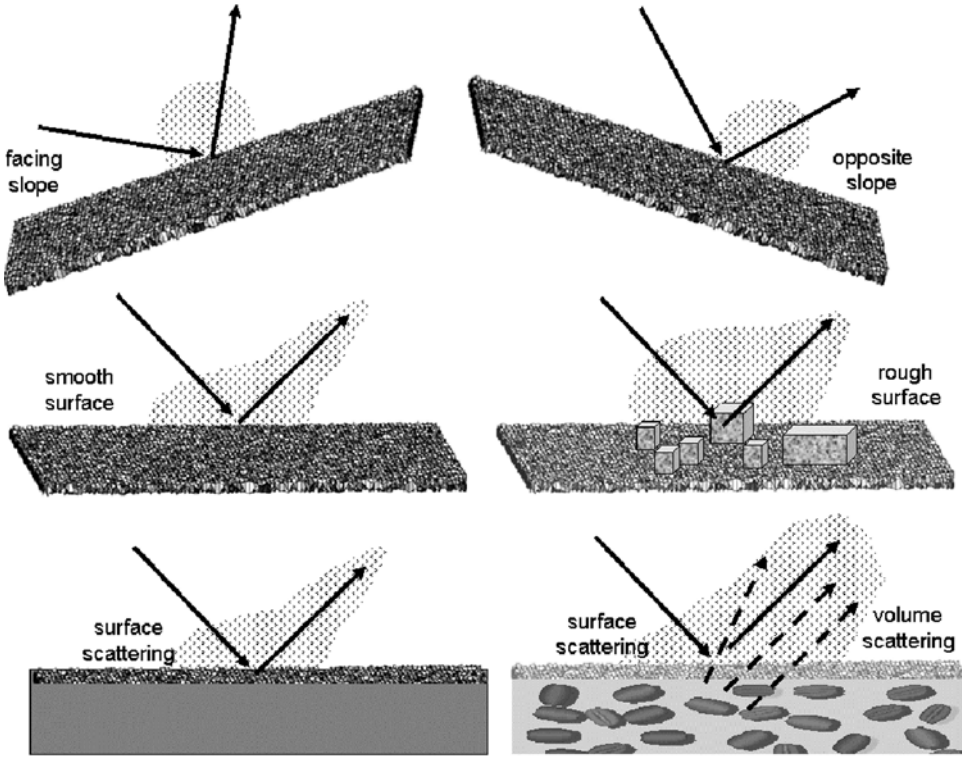

Figure 2.6. Backscattering from the seafloor is influenced by three factors (from top to bottom): local geometry of ensonification, roughness of the seafloor at scales comparable with the sonar's wavelength, intrinsic properties of the seafloor (e.g., rocks vs. sediments).

way'' and can be missed if facing ''the wrong way''. This is also why some terrains might appear acoustically brighter, although they are just on a different slope. These possible effects should be kept in mind during interpretation (see Chapters 10 and 11). Similarly, a surface smooth at the scale of the acoustic wavelength (e.g., 5 cm for a 30 kHz frequency) will scatter mostly along the specular direction, and the backscatter will be very low (this explains why abyssal plains are acoustically darker). But a rougher surface will be more likely to have small facets facing toward the sonar, thus increasing the backscatter (and scattering in other directions). Gravel patches will appear acoustically brighter than mud patches, for example. Last but not least, the effect of volume scattering should not be neglected. It will be increased by the type of seabed and the possibility of acoustic penetration at the frequency used: some seabeds will appear smooth at one wavelength, because they are flat, and rough at another wavelength, because of buried objects or bioturbation.

Understanding the respective roles of each configuration, and how they contribute to the overall backscatter recorded, is the object of very active research in underwater acoustics (e.g., Medwin and Clay, 1998; Lurton, 2002). The simplest

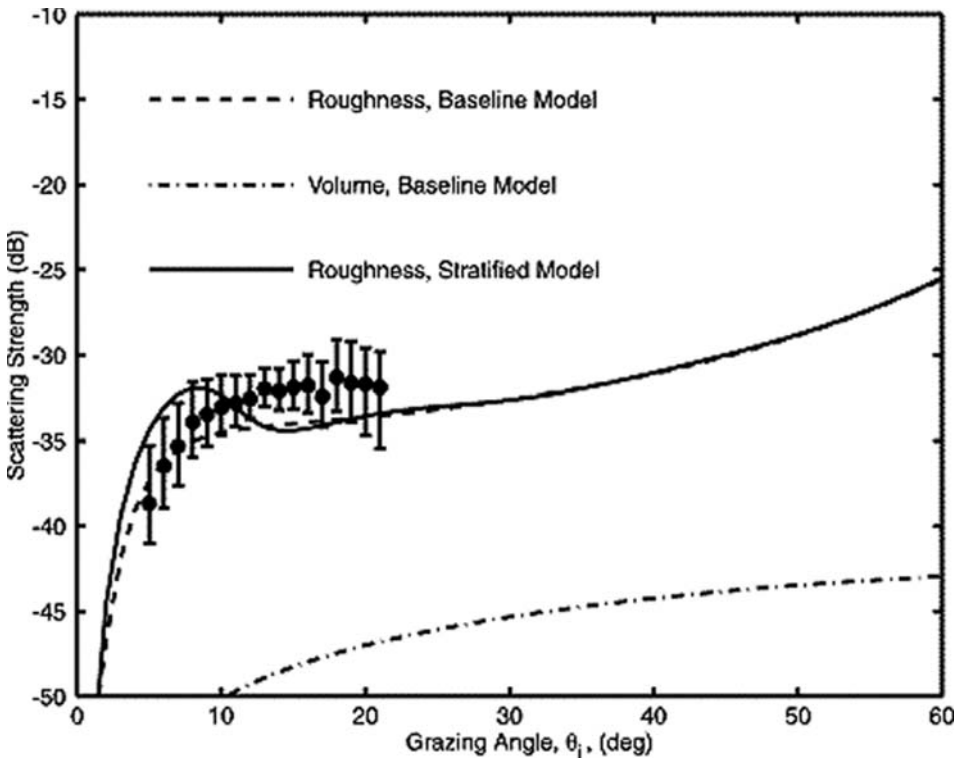

Figure 2.7. Some of the latest backscatter models compare rather well with experimental measurements, especially if they take into account contributions from the surface of the seabed and from its volume (i.e., the immediate sub-seabed) (from Briggs *et al.*, 2002).

model is Lambert's law (e.g., Lurton, 2002), approximating backscatter as a linear function of the square cosine of the incidence angle. Its simplicity makes it attractive, but it does not account for complex surfaces or local variations. More complex approaches use the Helmholtz–Kirchhoff theory for surface contributions, using the r.m.s. roughness of the seabed, its geoacoustic properties (porosity, density, etc.) and correlation lengths (Figure 2.7). They usually complement the surface contributions with a detailed calculation of likely volume contributions. These models can run relatively fast, and the sidescan sonar applications of the last years have singled out a few converging models such as the Jackson/Williams model (APL-UW, 1995), the BORIS model (Pouliquen, Bergem, and Pace, 1999), and the OASES model (Schmidt, 2000). They work best in the frequency range of 10 kHz to 100 kHz, although some can be safely used at higher frequencies. A discussion of their relative merits would go far beyond the scope of the present handbook, especially as they are always restricted to certain ranges of frequencies and seafloor types (mainly sedimentary areas). It is also possible to model the backscattering from individual objects, and theoretical "form functions" can be found in the literature for simple shapes (spheres, cylinders, etc.) of various sizes and contents. The backscattering from more complex shapes (e.g., submarine hull, target clusters) is another topic of very active research. Regularly, journals such as the *Journal of the Acoustical Society of America*, its Russian counterpart *Acoustical Physics*, or the European *Acustica* publish new models and their comparisons with experimental data (obtained at sea or in the laboratory).

2.3 SIGNAL GENERATION AND DATA ACQUISITION

2.3.1 Acoustic projectors

Electro-acoustic transducers are the most common in underwater acoustics, and they are essential to the transmission and reception of acoustic waves (Lurton, 2002). They use piezoelectric ceramics (or composite ceramics at the highest frequencies), converting electricity into acoustic pressure (for transmitters) and *vice versa* (for receivers). This is the same principle as in air, with loudspeakers producing the sound and microphones measuring it. Underwater acoustic sources are called projectors, and receivers hydrophones. Rows of transducers make up antennas, or arrays. For the high frequencies used in sidescan sonar applications, blocks of piezo-electric ceramics, driven by surface electrodes, are built in different shapes (rods, parallelepipeds, rings, etc.). With suitable backing (to limit undesired backward radiation), they are moulded into elastomer matrices or acoustically transparent fluid-filled housings (Figure 2.8). Projectors are characterized by their nominal frequency, their directivity, the source level, and the type of signals transmitted.

They work best at their nominal frequency, close to the resonance frequency of the material. Narrow-band transducers will transmit at one particular interval of frequencies, for which they are most suited and for which they have an optimal

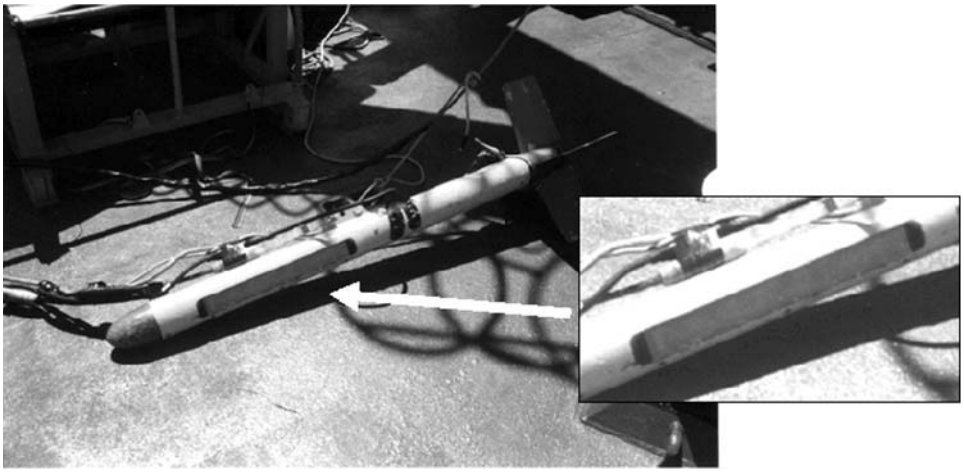

Figure 2.8. Detail of the transducer array of a Klein 5500 sidescan sonar mounted on a towfish (photo: Author).

directivity (see below for explanations). They could in theory still transmit at other frequencies, but to the detriment of their quality. Narrow-band transducers are most suited to sidescan sonar imaging. There exist also broadband transducers, which can transmit over a larger frequency range. They might have different characteristics in each frequency regime, and the acoustic returns need complex processing. This type of projector is therefore not often used in sonar imaging.

The directivity of a projector is usually measured in the laboratory or, more rarely, during deployment (e.g., calibration with targets of known scattering characteristics, such as metal spheres). Theoretical directivity patterns can be calculated for simple shapes (e.g., linear arrays), but the design and manufacturing of the transducers means that they deviate from theoretical expectations. The acoustic power radiated at a fixed distance from the source is measured in the horizontal plane and (often) in the vertical plane. The directivity pattern usually shows a main lobe, characterized by the 3 dB drop of the peak signal transmitted. It expresses the angular resolution of the antenna. Sidelobes are on each side of this main lobe, and not always symmetrical: they reduce the quality of the instrument, and should be kept in mind during interpretation if they are large enough. They can also contribute to some unwanted effects, like reflections from the sea surface or strong reflectors along their direction. Figure 2.9 shows the example of TOBI (Towed Ocean Bottom Instrument), designed and operated by the U.K.'s National Oceanography Centre in Southampton. Its directivity pattern was measured in the vertical direction (i.e., across-track and vertically). The projectors on each side operate at slightly different frequencies (respectively, 30.37 kHz and 32.15 kHz), to avoid interference. The resulting directivity patterns are broadly similar: they cover a large portion of the seabed across-track (to get as much range as possible). The directivity pattern in the orthogonal plane would be very narrow, corresponding

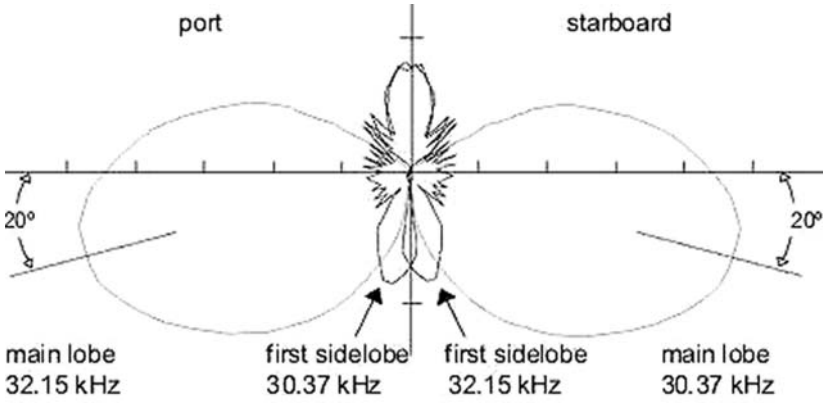

Figure 2.9. Example of a vertical beam pattern for TOBI, a typical sidescan sonar with a nominal frequency of 30 kHz (data from National Oceanography Centre, Southampton, U.K.).

to a much smaller portion of the seabed along-track (to avoid or minimize overlap between successive pings). Typically, a sidescan acoustic beam is very narrow in the horizontal dimension ($\sim 0.1^\circ$) and much wider (40°–60°) in the vertical dimension.

The source levels quantify the acoustic power radiated. It is usually measured at a fixed distance from the projector, and extrapolated to 1 m for easier reference. Source levels are expressed in dB re 1 μPa/1 m, often (abusively) abbreviated to dB. They are an essential component of the calibration of a sidescan sonar. Their value (and any change) should be part of the description of any survey, especially as it can be input into the comparison of the measurements with some of the backscatter models available (see Section 2.2.3).

The signals transmitted by the projectors can have different types, as shown in Section 2.2.1 and Figure 2.3. Because of resonances within the transducer, the signals recorded are not always exact replicas of the signals input into the transducer (e.g., short pulses might exhibit some "ringing" with additional, shorter, and smaller pulses). The transmitted signals are associated with a PRF (pulse repetition frequency), indicating how much time there is between two transmissions. This time should be short enough that successive pings cover the entire seabed along the track of the sonar: it will therefore be influenced by the maximum survey speed available with the supporting platform. And this time should be long enough to cover the travel of the acoustic wave to the farthest range and back, to avoid mixing between echoes associated to different pings. Strong acoustic reflectors out of the nominal range can sometimes be detected as echoes from the previous pings, if the PRF is not adapted for this particular application (see Chapter 10). The signal type and PRF are usually fixed before deployment, although some of the most modern sonars can now switch between signal types during deployment. This is of particular interest for some missions using AUVs (Autonomous Underwater Vehicles), mapping the seabed and then homing in on specific targets (e.g., mines): the sonar can go from a long-

range, lower resolution mode to image the entire area, switching to a short-range, high-resolution mode when close to targets of interest.

The acoustic waves transmitted by a projector are first oscillating with distance, in a short region called the near field (or Fresnel zone). After a certain distance, called the Fresnel distance (e.g., Lurton, 2002), the interference between different points on the face of the transducer decreases enough that the wave intensity decreases continuously with distance. This region is called the far field, or Fraunhofer zone. All sidescan sonar surveys are conducted in the far field, defined as:

$$R \geq \frac{L^2}{4\lambda}, \tag{2.8}$$

where R is the range, L the length of the array, and λ the wavelength of the signal transmitted.

2.3.2 Hydrophones and arrays

Acoustic receivers, or hydrophones, are also characterized by their frequency range and their directivity pattern. They are generally organized as arrays. Narrow-band transducers can only detect a small range of frequencies, limiting the imaging to non-moving targets, or those with no significant Doppler shift. Broadband transducers can detect a wide range of frequencies: those not associated with acoustic backscattering from the seabed can be filtered out during acquisition and/or processing (see Section 2.3.3).

The directivity patterns of the arrays should at least match the directivity patterns of the projectors, so that they receive all the returns from the points that have been imaged, and as few returns as possible from points not directly ensonified. In many sonar systems, and particularly sidescan, the same transducer is used for transmission and reception.

Even in the absence of an acoustic signal, receiving arrays still record some very small pressure variations: this self-noise is made of the internal noise of the receiver and the noise of any attached amplifier electronics. The sensitivity of receiving arrays to any incoming acoustic radiation is expressed as the sensitivity. It is measured in dB re 1 V/1 μPa, often abbreviated to dB. For the same reason as the source level of the projector, this calibration should be part of the description of any survey.

Individual hydrophones and complete arrays are piezoelectric devices too; most often made of PZT (lead–zirconate–titanate alloy), characterized by their good sensitivity and low self-noise. Other materials such as lithium sulphate, PVDF (polyvinylidene difluoride), and piezo-composite materials can also be used in a few of the most modern sonars.

2.3.3 Signal conditioning

Backscattered signals are often very weak, because of attenuation with distance, and very noisy, because of the perturbations within the water column on the way from the

sonar to the target and on the way back. Additional noise can come from the transducers themselves (self-noise) or from neighbouring instruments (e.g., other acoustic sensors working at the same time). Signal conditioning covers all the instruments and techniques that can "improve" the signal as much as possible before it is used in the formation of the sidescan sonar image itself (see Chapter 3).

In most sidescan sonar applications, the arrays have the adequate geometry to yield the expected directivity (Lurton, 2002). In some cases, however, particularly for the highest frequencies and narrowest beams, array focusing should be applied before transmission. This consists in delaying the different elements in the array, to compensate for the differences in phase (or time) of the wave centered on the target. Techniques like array focusing and dynamic focusing are discussed in greater detail in several textbooks, including Burdic (1990), Medwin and Clay (1998), and Lurton (2002). The input signal to the projector(s) sometimes needs to have a high voltage; this is achieved using a power amplifier (and associated band-pass filters if it creates some noise before inputting the signal into the transducer).

In terms of reception, the first operations needed are equalization or at least compensation of the received echo level (because of attenuation with range, echoes can show differences of 20 dB or more between near range and far range); demodulation and filtering; analog-to-digital conversion of the signal; non-coherent reception processing (band-pass filtering, to focus on signals with frequencies close to the frequency transmitted, and envelope detection); processing gain compensation; and data storage. All these steps are performed with dedicated electronic circuits, often shared with the transmission stage. They need to be accurately synchronized, with an internal or external clock, to ensure the transmitted signal has ample time to be received before the next pulse. Figure 2.10 shows the organization of a generic sidescan sonar.

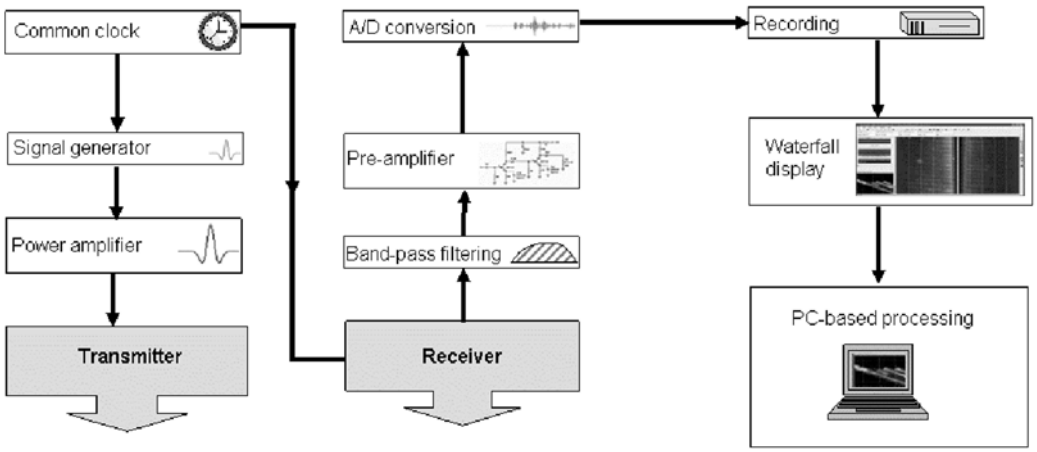

Figure 2.10. Block diagram of a generic sonar system. Some of the components (e.g., pre-amplifier and band-pass filter) might not always be in the same order (although it makes sense to filter out the noise before amplifying the signal).

2.4 NEW CONCEPTS; NEW TOOLS

2.4.1 Higher frequencies; higher resolutions

Chapter 1 (Introduction) hinted at the many advances in sidescan sonar imaging during the last decade, in particular on the technological side. The first maps of the seabed were mainly concerned with general areas (e.g., the mapping of Exclusive Economic Zones). Covering large areas required large sonar coverage (i.e., low frequencies), little attenuated over the distances involved. Sidescan sonars like GLORIA (6.5 kHz imaging frequency) proved ideal, yielding swath widths of 60 km with a resolution of 60 m after processing. Increasingly demanding applications drove the need for higher resolutions, and this was achieved by using higher frequencies. To use a common analogy, whereas a 6.5 kHz sonar could distinguish objects the size of a football field, a 30 kHz sonar (e.g., TOBI, with 6 m resolution after processing) can detect objects the size of a goal, a 120 kHz sonar (e.g., DSL-120, with 0.6 m resolution) follows the individual players, and a 455 kHz sonar (e.g., the Klein-5500, with 0.1 m resolution) can track the football itself.

The use of higher frequencies comes with a cost, though. The first challenge is technological, with the need for faster data acquisition systems and faster processing speeds. Solutions like heterodyning (e.g., Burdic, 1990; Medwin and Clay, 1998) can alleviate the need for high-frequency sampling of the backscatter echoes, but only to some degree. The second challenge is acoustic: higher frequencies do not propagate as far, and the swath widths achievable decrease quite rapidly (e.g., 6 km for TOBI). The third challenge is physical. Figure 2.11 shows the same mud volcano, imaged at decreasing frequencies. As the frequency decreases, the acoustic wavelength increases, and the resolution of each pixel degrades visibly. The fourth and most important challenge lies in the interpretation of these very different images, understanding which factor is predominant in the backscattering from the seabed, for each specific wavelength (cf. Figure 2.6). Do backscatter variations correspond to roughness or slopes with different wavelengths? Or, because the volume penetration of

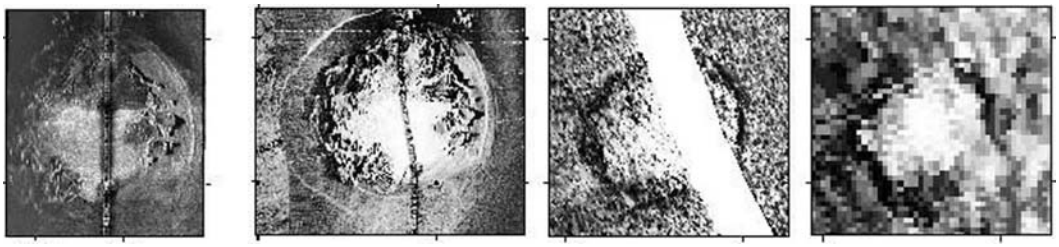

Figure 2.11. Compiled by the U.S. Naval Research Laboratory for its Global Ocean Mapping Project, this image shows the Håkon Mosby mud volcano (Barents Sea) imaged at decreasing frequencies: 100 kHz, 30 kHz, 12 kHz, and 6 kHz (left to right). High backscatter levels are bright, and the middle bands in the first three images correspond to the nadir of the sonar. The volcano is nearly 1 km in diameter. Both its size and its details get obscured as the frequency (and therefore the spatial resolution) decrease (adapted from an NRL 7420 graphic; Vogt and Gardner, 2001).

acoustic waves into the seabed varies with the frequency (notion of skin depth: see Section 3.4 for details), do these variations reflect different depths below the seabed? The answer is usually far from straightforward, but can be partially reached by using appropriate backscattering models (see Section 2.2.3).

Multi-frequency systems are now available on the market. They can generally be switched from one frequency to another before deployment or, more rarely, during deployment. Two examples among many include the Klein-3000 dual-frequency sonar (working at 132 kHz and 446 kHz) and the Imagenex 881A (tunable from 280 kHz to 1.1 MHz by 5 kHz steps). Complete multi-frequency systems, working at all frequencies at the same time and akin to the multispectral imagers used in optical ranges, do not exist yet. But current systems can already address several types of complementary measurements, at distinct ranges, resolutions, and (in some cases) penetration depths.

2.4.2 Multistatic sonars

The acoustic energy scattered by a typical seabed, or a target, covers a wide range of angles and only a small portion is scattered back toward the receiver (Figure 2.6). Measuring this acoustic energy at other angles can therefore add to the identification of the objects imaged by sonar. The recent and ongoing development of AUVs (autonomous underwater vehicles) and UUVs (unmanned underwater vehicles) has been instrumental in driving the investigation of other geometries, where the transmitter can be physically decoupled from the receiver(s). These geometries are known as bistatic (for one receiver), or multistatic (for several receivers), and backscattering is but one particular case of all the configurations achievable.

Bistatic sonars usually work with one transmitter (e.g., on an underwater vehicle) and several receivers (e.g., on a hydrophone chain, Figure 2.12, left). The receivers can also be placed on another moving vehicle, for greater flexibility. Accurate

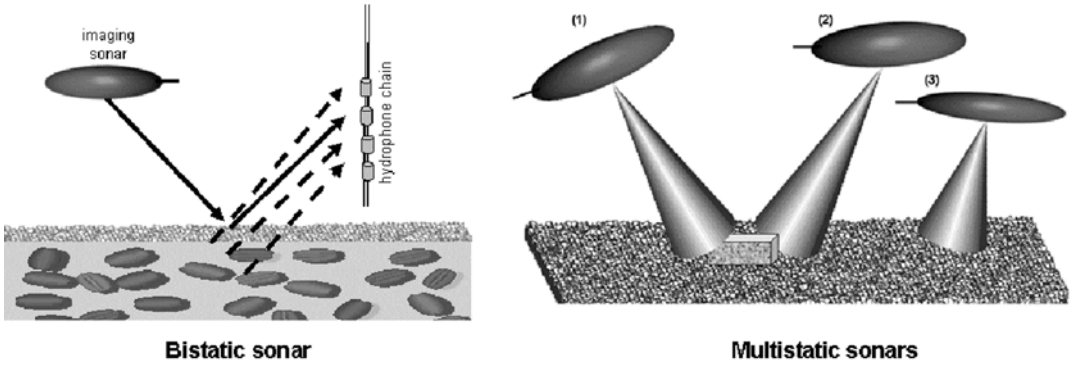

Figure 2.12. Left: in bistatic sonars, the imaging sonar is physically decoupled from the receiver(s), giving access to a wider range of scattering processes. Right: multistatic sonars (three in this case) can image targets from several angles and work in swarms, adapting their mapping strategy to the environment and to the mission.

positioning of receivers relative to the imaging sonar is important, as it conditions interpretation of the measurements. Bistatic images can be represented in a variety of ways, including as range–angle diagrams of scattering strengths (i.e., a cross-section along the scattering plane), but their interpretation is not always evident. Because of the difficulties in deployment, and in mapping large areas, bistatic sonars are still restricted to specific shallow-water applications such as mine-hunting (e.g., Lucifredi and Schmidt *et al.*, 2006[1]) and buried waste identification (e.g., Blondel and Caiti, 2007). They can, for example, be used to complement traditional sidescan sonar mapping, refining the acoustic information available on specific features already detected.

Multistatic sonars work with one or several transmitters, generally on AUVs, and several receivers, separate or on the same vehicles (Figure 2.12, right). They can sometimes use "traditional" sidescan sonars, imaging targets of interest from several angles ("multi-look" studies). Several research groups around the world are now investigating the optimal ways to fly multiple instruments in swarms, capable of self-organizing in response to the environment and the constraints originally dictated by the mission profile. These vehicles need to communicate with each other (exchanging information about their relative positions and targets of interest, for example), and they need to communicate with a baseline or reference station (checking the accurate positioning of all members of the swarm, or sending back information about specific features). Again, because of the difficulties of deployment and, often, the costs associated with both instruments and logistics, there have been very few studies to date, mostly in shallow water. And the merging of the sonar images taken by the different instruments leads to interesting interpretation problems (mainly due to the large variations in grazing angles and directions of ensonification).

2.4.3 Synthetic aperture sonar

The resolution of a sidescan sonar decreases with range away from the sensor. It can be increased by using a higher frequency (subject to much higher attenuation in water) or by using a longer imaging array, often far greater than physically feasible. The same problem occurs with radar imaging (e.g., Lillebrand *et al.*, 2004), where it was solved by replacing the large antenna needed with a shorter one, integrating successive measurements along the line of flight (Figure 2.13). The first patents for sonar synthetic aperture processing date back to the late 1960s and the first research articles were published in the 1970s (e.g., Cutrona, 1975, 1977), but synthetic aperture sonar (SAS) imagery really matured only in the last 5 years or so. It is, however, producing impressive results.

[1] This reference is only one of many on bistatic scattering and mine-hunting, but it shows different images that can be used for direct interpretation, in the same way that traditional sonar images are open to direct, visual interpretation.

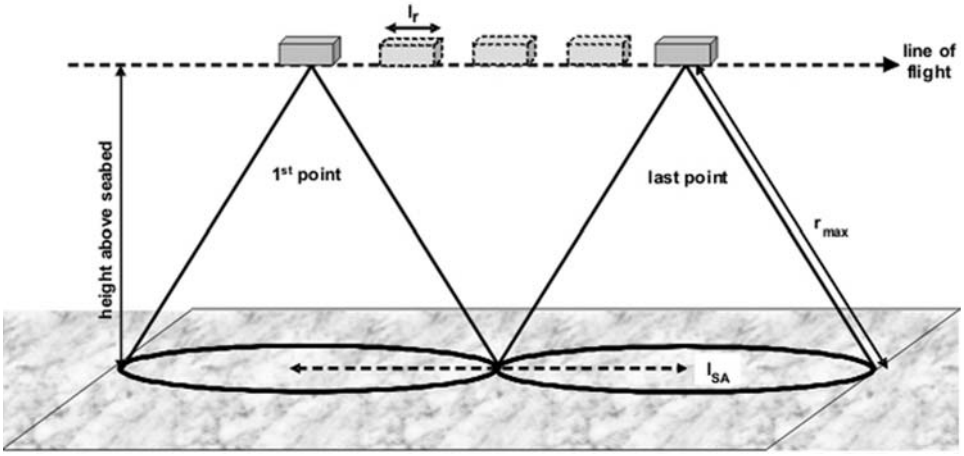

Figure 2.13. Principles of synthetic aperture processing: an array of size l_{SA} is synthesized by processing successive returns from a much smaller array of size l_r. See text for details.

The equivalent length l_{eq} of a real array yielding the same resolution as the synthetic array formed by processing N_{SA} measurements made with an array or real length l_r reads (e.g., Amate *et al.*, 2007):

$$l_{eq} = 2l_{SA} = 2(N_{SA} - 1)\frac{v}{PRF} + l_r, \tag{2.9}$$

where v is the speed of the platform, and PRF is the pulse repetition frequency. The distance l_{SA} is measured between the first and last points immediately below the positions of the sonar used in the synthetic aperture processing scheme (Figure 2.13). This means that the along-track resolution does not depend on the range across-track—but on the physical length of the transducer array. The shorter the physical array, the better the resolution. This also means that lower frequencies can be used to yield similar resolutions, with less attenuation throughout the water column. Typical resolutions are of the order of 10 cm–15 cm, constant to ranges up to 300 m (e.g., Jean, 2006; Amate *et al.*, 2007). The current challenge to synthetic aperture processing lies mainly in the stability of the supporting platform and the accuracy of its navigation. The distance between two measurements along the line of flight should not exceed half the length of the physical array. For synthetic aperture radar imaging, this never proved much of a problem, because of the high velocity of the platforms (usually orbiting satellites) and the extremely high speed of light. But the much lower velocity of sonar platforms in water (usually less than 10 knots) and the low velocity of sound in water mean that deviations from the ideal, linear trajectory need to be much smaller, of the order of a few centimeters (of the order of 1/8th of the imaging wavelength). Figure 2.14 shows how even small movements will need to be compensated to perform accurate processing.

Deeper discussions of the physics of SAS processing are presented in Lurton (2002) *inter alia* and an extensive review of the field is available in Pinto (2006).

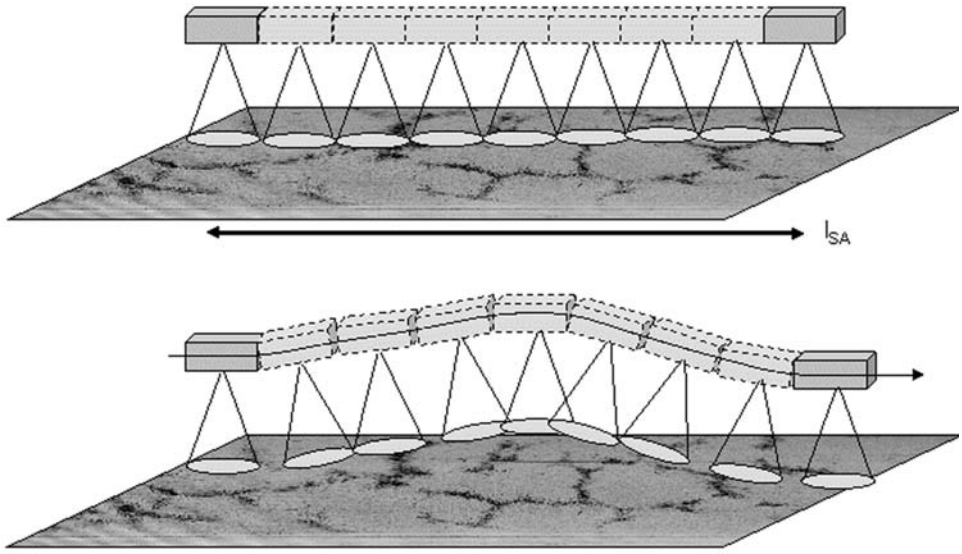

Figure 2.14. Influence of the exact movements of the imaging sonar in synthetic aperture processing. The synthetic array is formed using successive positions from a much smaller array. But, because of the dynamics of the vehicle (roll, yaw, pitch, heave) and the influence from the ocean (e.g., variable currents), even if the vehicle's navigation were perfectly accurate, the linear assumption behind traditional synthetic aperture is rarely met. Several techniques have been designed to address this challenge.

Overall, SAS has greatly progressed and could well prove the tool of the future, even if traditional sidescan sonars are still the tool of choice because of their wider accessibility and easier deployment. Once processed, SAS images are visually indistinguishable from conventional sidescan sonar images acquired at higher resolution (e.g., Figure 2.15), apart from the absence of some artefacts like beam spreading (see Chapter 10). The interpretation of SAS imagery will therefore be similar to that of sonar imagery.

2.4.4 Parametric sidescan sonar

Conventional sonar systems are based on linear acoustics: the acoustic signal transmitted into the water is linearly proportional to the electric input into the transducer, it has the same frequency content, and its beamwidth is primarily related to the dimensions of the transducer array. To increase the spatial resolution of these systems, the beamwidth should be minimized and the bandwidth maximized. New materials and designs can now yield higher bandwidth transducers. Section 2.4.3 showed how synthetic aperture processing could also increase the resolution without unduly increasing the size of the transducers. An interesting development was

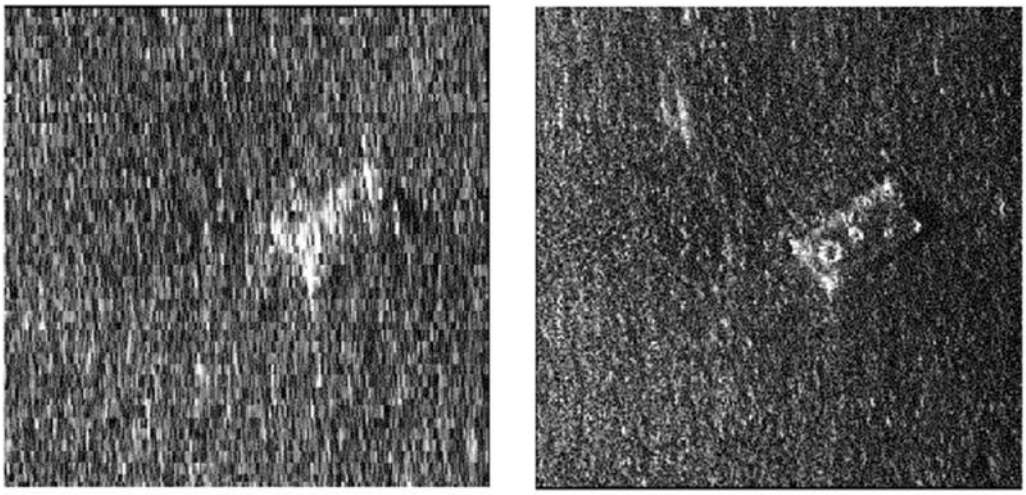

Figure 2.15. The importance of synthetic aperture processing, when it can be achieved, is brought home by these data acquired by DCE-GESMA (France): (left) traditional sidescan sonar image of a 2 m × 1 m target; (right) sonar image after synthetic array formation and auto-focusing (from Lurton, 2002).

proposed by Zakharia and Dybedal (2007), using a parametric array, whose data were then processed using synthetic aperture.

Parametric arrays use non-linear acoustics (e.g., Westervelt, 1963): high-intensity acoustic pulses with slightly different frequencies (noted f_1 and f_2) will interfere in the water column and create harmonic waves of varying frequencies, $2f_1$, $2f_2$, $f_1 \pm f_2$, etc. The most interesting frequency to be used in sub-bottom profiling is the difference frequency, $|f_1 - f_2|$, also called the secondary frequency. Typically, less than 1% of the energy is converted into the secondary frequency waveform. However, this is sufficient to achieve very good performance for the parametric sonar. The secondary beamwidth may be relatively close to the beamwidth of the primary frequency signal. Zakharia and Dybedal (2007) designed a parametric array with a frequency range of 2 kHz–20 kHz and a secondary frequency of 20 kHz, doubling up as a conventional sidescan sonar with a primary frequency of 100 kHz. The beamwidths achieved were impressive: 0.7° along-track for the primary signal, and 1.4° for the secondary signal. SAS processing of primary and secondary frequencies led to three images of the seabed, with comparable resolutions and revealing details at different penetration depths (Figure 2.16). Tests at sea (presented in Blondel and Caiti, 2007) showed it was possible to detect small buried objects, and often the approximate depth at which they were buried. A single, conventional sonar image would instead have just revealed the presence of an object, if reflective enough or within the penetration depth of the sonar. These impressive achievements must however be tempered by the very important computational power required to process the data, and the fact that real-time imaging is not yet achievable.

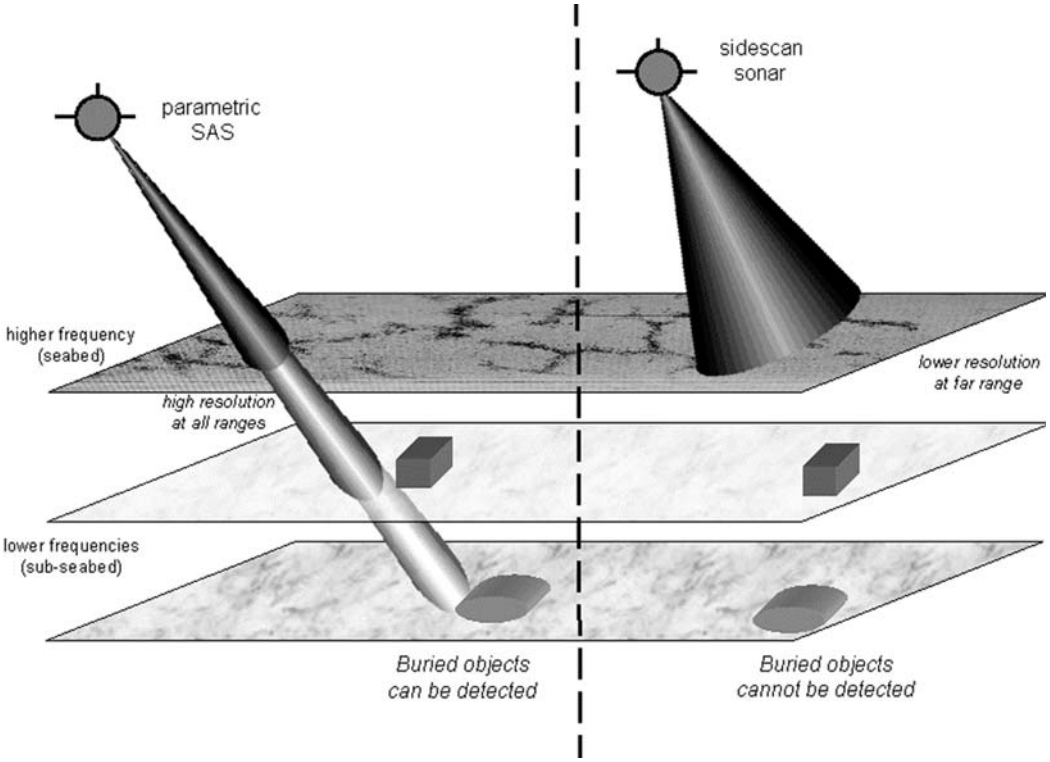

Figure 2.16. The concept of Parametric Synthetic Aperture Sidescan (PSAS) sonar imaging.

2.4.5 Biomimetics

Biomimetics is an emerging field of science, aiming at transferring to systems or concepts the techniques used in the natural world. This rapidly progressing field spans the domains of biology, engineering, and artificial intelligence. Typical applications relevant to underwater acoustics and seabed mapping include

— the optimization of transducer shapes or configurations for specific applications (e.g., mimicking the acoustic receiving structures of whales or dolphins);
— the study of biosonars, such as used by dolphins or whales, for the transmission of signals into the water, their reception, or the types of signals which will propagate best depending on the environment and the application (e.g., Dobbins, 2008);
— the design of new types of vehicles (e.g., ''swimming'' platforms, copying the undulating movements of fish, or ''streamlined'' hulls, copying the skin of sharks for smoother displacement under water);
— new ways to look at the navigation of underwater platforms (either for the processing of the navigation data, or for synchronizing and regulating the movements of ''swarms'' of vehicles);

— object recognition (e.g., using neural networks inspired by dolphins' capabilities for distinguishing metallic objects).

The field of biomimetics is active and attracts much interest, in particular among the media. The images produced by future biomimetic sonars are bound to be very similar to the images produced by existing sonar systems, and can therefore be interpreted and analysed in the same way.

2.5 SONAR PERFORMANCE

The performance of a sonar is broadly defined as its ability to detect and locate objects of interest on the seabed, to a specific range and at a specific rate. It is affected by the generation of the acoustic wave by the sonar transducer, its propagation throughout the water column, its scattering on the seabed (or any other targets, even in the water column or in the immediate sub-surface), its propagation back to the transducer, and its subsequent processing. The limiting factors were presented throughout Chapter 2, and some will become clear in the applications presented in the next chapters.

The role of the imaging frequency is, for example, extremely important, as it defines both the maximum range achievable (because of the attenuation of sound with distance) and the resolution attainable (see Section 2.4.1). Low frequencies (e.g., 6.5 kHz for GLORIA) will travel large distances (e.g., 30 km on each side of the sonar) but give worse resolution (e.g., 60 m after processing) than high-frequency sonars (e.g., 120 kHz for the DSL-120) covering a smaller swath (e.g., 1 km). Taking into account the speed of the imaging platform, lower frequency sonars can be used to map large areas of the seabed in a relatively short time (e.g., GLORIA was used to map Exclusive Economic Zones and large portions of continental margins around the world), whereas high-frequency sonars will be more suited to detailed studies of smaller areas (e.g., DSL-120 being used for mapping hydrothermal fields).

The directivity of the sonar will be a function of the shape and dimensions of the transducer array, as well as the frequency used (e.g., Lurton, 2002). The beam pattern (see Section 2.3.1) needs to be narrow along-track and wide across-track. Sidelobes are generally inevitable, but use of the right frequency, or the right technology, should minimize their importance, or ensure they are pointing in directions from which reflections are unlikely to be recorded. This can be modified by adapting the height of the sonar above the seabed (influencing the minimum and maximum ranges of the resulting image).

The spatial resolution of a sidescan sonar will be the main limiting factor in its performance. The nominal resolution corresponds to the minimum distance between two objects that can still be distinguished on the sonar image (Figure 2.17). It is usually quoted for optimal conditions and can be very different in practice (e.g., in turbid water or in rough terrains). It combines the along-track and across-track resolutions, which are different.

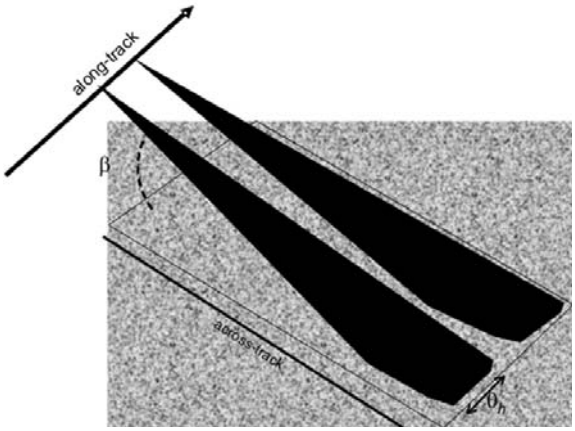

Figure 2.17. The resolution of a sidescan sonar combines two quantities: the along-track resolution (function of the horizontal beamwidth θ_h of the sonar) and the across-track resolution (function of the pulse length and the local grazing angle β). The resolution decreases with range in conventional sidescan sonars but can be improved if synthetic aperture processing is usable.

The along-track resolution Δx is the smallest of the distance travelled over ground during the reception interval, and the width of the beam on the ground. The latter is a function of the range R and the horizontal beamwidth θ_h:

$$\Delta x = R \times \sin \theta_h. \tag{2.10}$$

The across-track resolution, or range resolution, Δy is a function of the effective pulse length τ of the sonar transmitter, the speed of sound c in water, and the local grazing angle β (it is often unknown, and β is then replaced either with 0 or with the value expected for a flat seabed)

$$\Delta y = \frac{c\tau}{2} \times \frac{1}{\cos \beta}. \tag{2.11}$$

The merging of successive profiles across-track into an image requires the computation of square picture elements (pixels). The pixel size can actually be anything; some early applications, for example, reduced the size of each swath to 1,024 pixels, because of limitations in data storage and computing speed, actually greatly underestimating the achievable resolution. If the pixel size is greater than the distance between measurements, the different backscatter values are averaged (smoothing and loss of small-scale details). Conversely, if the pixel size is smaller, interpolation will be needed, and is likely to produce errors by creating new data or distorting existing features. The optimal pixel size should in fact combine the most common values of along-track and across-track ranges, often presented as "pixel resolution" or just "resolution". Single features may indeed be detected on the basis of 1 pixel only (and therefore the resolving power is the same as the pixel size). But this is not totally true, as this pixel could be influenced by one small portion of the area ensonified or by electronic noise, and confident interpretation usually requires groups of several pixels. The separation of two distinct features will likewise require several pixels.

One important point to keep in mind is that the performance of sidescan sonars should not be reduced to the spatial resolution of the system. Many other aspects

intervene, such as transmitting power and frequency (see above), pulse repetition frequency (and how flexible it is), height/speed combinations available, etc. All these aspects should be taken into consideration when planning a survey or comparing datasets acquired over the same area. For example, laying an offshore cable or pipeline would require a large swath survey, with co-registered bathymetry and imagery, to locate the possible route and then another survey with a high-resolution sonar to identify possible hazards at a metric scale. The search for a shipwreck would require a first survey with a larger swath width to locate the approximate wreck site, and then a higher resolution survey with a smaller swath width, concentrating on the shipwreck itself and the small details (e.g., the general layout and possible loss scenario, or the disposition of potential obstructions to submersible investigation). A dual-frequency sidescan sonar would be perfectly suited for these tasks. Of course, not all applications require several surveys. Exploration of mid-oceanic ridges or the mapping of continental margins can be, and have been, perfectly achieved using single systems (e.g., GLORIA for the U.S. Exclusive Economic Zone, TOBI or DSL-120 for the Mid-Atlantic Ridge). Mapping of harbours or inland waterways is also perfectly achievable using single systems (e.g., the SWATHplus range of sonars). Table 2.1 gives the technical characteristics of a handful of sonars, mostly sidescan, to provide some elements of comparison with the many other sonar systems currently available. These systems have been selected mainly because they cover most of the range of acoustic frequencies available, and users are strongly encouraged to search around for the system most suited to their particular needs.

2.6 CONCLUSION

This chapter has aimed at presenting the basics of acoustics necessary to successfully process and interpret sidescan sonar imagery. First, it presented the generation of a generic acoustic wave, its propagation through the underwater environment, its scattering on/in the seabed, and its propagation through water on the way back to the sonar receiver. This summary was followed with a description of the actual instruments: the acoustic projector, hydrophones and arrays (keeping in mind that in most sidescan systems the same transducer acts as transmitter and receiver), and the different instruments conditioning the raw sonar signal to be fit for visualization and processing. This chapter also introduces some of the new tools which are currently emerging (e.g., synthetic aperture sonars) or will transition from prototypes to finished products in the coming decade. Finally, it synthesizes the performance of sonars: how to choose the one most adapted to the survey in mind, and how to compare different instruments, sometimes widely different.

This chapter is not a summary of all acoustic theory to date, nor does it intend to be. The main reason is that acoustics, in general, and underwater acoustics, in particular, are fast-moving fields of physics. This is evident from the growing number of theoretical and experimental articles regularly published in high-ranking international journals such as the *Journal of the Acoustical Society of America*, the *IEEE Journal of Oceanic Engineering*, *Acoustical Physics*, and many others. Excellent

Table 2.1. Examples of a few sidescan sonars and their technical specifications. The typical daily coverage is calculated using the recommended operating speed and the maximum range: it will of course vary with the application. The footprint size depends on many parameters (including the range setting) and is usually modified during processing to produce a constant, square footprint.

	GLORIA Mk II	*TOBI*	*DSL-120*	*Klein System 3000*
Operator	NERC, USGS (now out of commission)	NERC	WHOI	L-3 Klein Associates Inc.
Type	Shallow-towed	Deep-towed	Deep-towed	Deep-towed
Swath width	$\leq$60 km	6 km	$\leq$1 km	0.9 km and 0.3 km
Typical daily coverage	20,000 km^2	470 km^2	90 km^2	$<$200 km^2
Frequency (wavelength)	6.3 kHz–6.7 kHz (23.8 cm–22.4 cm)	30 kHz–32 kHz (5 cm–4.7 cm)	120 kHz (1.25 cm)	132 and 445 kHz (1.14 cm and 0.33 cm)
Footprint size (along/across-track)	175×45 m to 657×45 m	8×3.5 m to 43×2.1 m	3.3×0.33 m to 13.7×0.15 m	Metric to sub-metric. Depends on range setting
Product	Imagery (bathymetry for GLORIA-B)	Imagery Bathymetry in some applications	Imagery Bathymetry	Imagery

textbooks on underwater acoustics and its sonar applications can be found, such as Medwin and Clay (1998) and Lurton (2002), giving much more detail than could be achieved in a limited space. Instead, the present chapter aimed at presenting end-users with a selection of what is needed to extract the most from sidescan sonar measurements, for their own applications. The next chapters will now present typical raw measurements and the extraction of sonar backscatter (Chapter 3) and their processing into complete images (Chapter 4).

2.7 FURTHER READING (*see also* References at end of book)

About underwater acoustics in general

Burdic, W.S. (1990). *Underwater Acoustic System Analysis*, Second Edition. Prentice-Hall, Englewood Cliffs, NJ, 466 pp.

Lurton, X. (2002). *An Introduction to Underwater Acoustics*. Springer/Praxis, Heidelberg, Germany/Chichester, U.K., 380 pp.
Medwin, H.; and C.S. Clay (1998). *Fundamentals of Acoustical Oceanography*. Academic Press, London, 712 pp.
Urick, R.J. (1996). *Principles of Underwater Sound*, Third Edition. Peninsula Publishing, Los Altos, CA, 444 pp.

About different approaches to acoustic scattering

Jackson, D.R.; and M. D. Richardson (2006). *High-frequency Seafloor Acoustics*. Springer-Verlag, New York, 616 pp.
Jackson, D.R.; K.B. Briggs; K.L. Williams; and M.D. Richardson (1996). Test of models for high-frequency seafloor backscatter. *IEEE J. Oceanic Eng.*, **21**(4), 458–470.
Pouliquen, E.; O. Bergem; and N.G. Pace (1999) Time-evolution modeling of seafloor scatter, I: Concept, *J. Acoust. Soc. Am.*, **105**(6), 3136–3141.
Schmidt, H.; and W.A. Kuperman (1995). Spectral representation of rough interface reverberation in stratified ocean waveguides. *J. Acoust. Soc. Am.*, **97**, 2199–2209.

About the latest developments in sonar systems

Conference Proceedings: *Synthetic-Aperture Sonar and Synthetic Aperture Radar*, Institute of Acoustics (U.K.), Publication No. 2050 (2006).
General IEEE search engine: *http://ieeexplore.ieee.org/Xplore/dynhome.jsp*

3

Imagery and bathymetry

3.1 PROCESSING ACOUSTIC MEASUREMENTS

The previous chapter (Chapter 2) presented basic acoustic theory, from the generation of a sound wave to its scattering on/in the seabed and its reception by the sonar platform. Acoustic pressures are used to quantify the response of the seabed at the particular frequency used. These backscatter measurements are combined across-track to create a swath, and successive swaths are combined to form an image of backscatter variations. If the sonar is calibrated, these variations can provide generic measurements, called backscatter strengths, comparable with results from other surveys (with the same sonar at the same settings, or not). These processes are detailed in Section 3.2. Sidescan sonar imagery can be usefully compared and merged with bathymetry measurements. The newest generation of sidescan sonars can now produce imagery and bathymetry at the same time, using interferometry (explained in Section 3.3). These measurements of the seafloor topography are at the same resolution and co-registered with the measurements of the acoustic response of the seafloor. The large majority of sidescan sonars currently in use do not have interferometric capabilities though, so bathymetry is derived from other sources, like multibeam sonars. These measurements usually do not have the same ground resolution (e.g., 100 m multibeam bathymetry and 6 m sonar imagery), and rarely benefit from the same exact geographic registration requiring the use of techniques like rubbersheeting (presented in Chapter 4). The problem is compounded by the fact that new multibeam systems also provide some forms of imagery, calculated by analysing each beam or only portions centered on the first seabed return. The resulting images can be interpreted in the same way as sidescan sonar images, keeping in mind the differences in acquisition (i.e., grazing angle variations) and in processing.

Typical raw pressures are shown in Figure 3.1: they correspond to backscatter from a silt tray, imaged in the laboratory, and a small target placed on top of the silt. The pressure waves are received as a function of time, and measured (at the receiver)

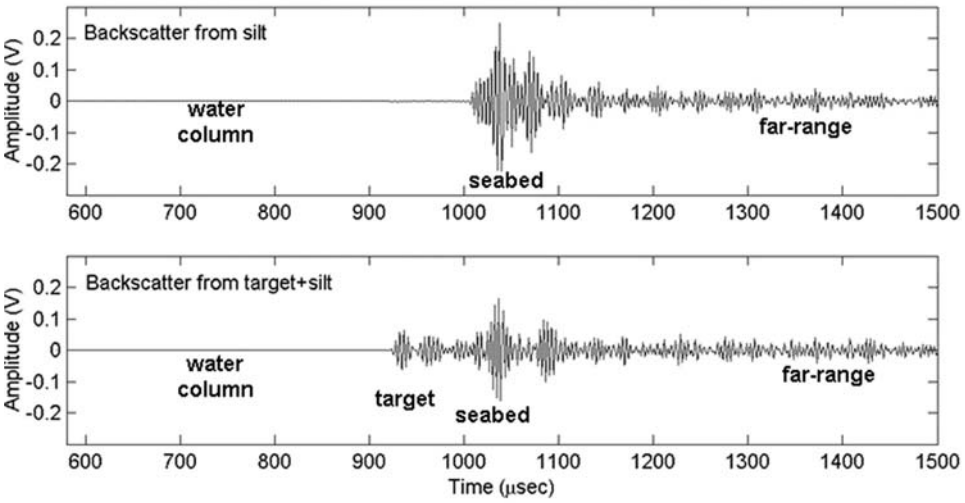

Figure 3.1. Acoustic backscatter from a raw seabed (top) and the same seabed with a surface target (bottom). The receiving transducer converts the pressure into a voltage; its variation with time corresponds to points at increasing ranges. Note that, in this particular case, the immediate sub-surface also contributes to the backscatter.

as voltages. These voltages can then be converted into dB values, using the sensitivity of the receiver if known (see Section 2.3). They can also be referenced to a value common to all signals received, giving unitless numbers. Both plots in Figure 3.1 show that nothing was recorded early on: these measurements correspond to the time the signal is propagating back from the seabed and is in the water column. Backscatter from the raw silt seabed (relatively flat at the wavelength considered) clearly preserves the structure of the waveform originally transmitted by the sonar. There are small echoes, corresponding to parts of the seabed farther in range, whose signals take longer to come back to the receiver. As the time of reception increases, the far-range signals become increasingly smaller. For full-scale surveying (not for laboratory experiments like this one), this would correspond to attenuation with range. Backscatter from the target, placed proud on the silt seabed, exhibits the same structure. Early returns are associated with the target being, say, higher than its surroundings (i.e., closer to the sonar). Backscatter from the seabed, immediately after the target, is made more complex by the reflections within the target and between the target and seabed. This will not be the case for acoustically hard targets, such as lava flows or debris deposits, where the interactions with the surrounding seabed are negligible.

Pressure waves correspond to successive compressions and rarefactions (i.e., positive and negative variations of pressure). The positive envelope of the signal is obtained by using tools like the Hilbert transform (e.g., Burdic, 1984). Additional tools, such as band-pass filters, might be needed to remove unwanted frequency components. Some processing schemes also remove the influence of the type of signal transmitted (e.g., chirp vs. pulse) through deconvolution. Figure 3.2 shows the

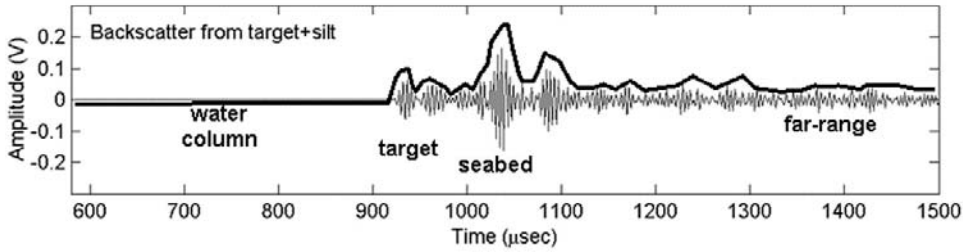

Figure 3.2. The envelope (thick black line) of the raw backscatter signal is obtained using tools like the Hilbert transform.

envelope of the signal backscattered from a target placed on a silt background. The average acoustic energy scattered by each object is clearly visible. The sampling frequency (i.e., the time interval between two successive measurements of the acoustic energy) determines the spatial resolution of the signal along the line of sight.

For some sonars, particularly those working over large ranges, the attenuation of the signal with distance traveled (to the seabed and back to the sonar) is already compensated. For example, TOBI uses a time-varied gain of the form $40 \log R + 2\alpha R$ (where R is the two-way distance and $\alpha = 3.65\,\text{dB/km}$) to compensate for these attenuation losses (Flewellen *et al.*, 1993). Even if this gain is applied, the sonar signals might still need further processing to fully compensate for this attenuation (see Section 4.3 "Radiometric corrections"). The signals received after each successive ping, as the sonar moves past targets, are stacked to produce an image of the seabed and its structures (Figure 3.3). The signals are recorded during a finite time window: one of the two dimensions in the image therefore corresponds to the two-way travel time (i.e., the slant range). Each successive signal is recorded after a specific interval, governed by the Pulse Repetition Frequency and the range desired (see Section 2.3 "Signal generation and data acquisition"): the resulting dimension will therefore correspond to the distance along the sonar track. For a sonar moving at constant speed and altitude over a flat terrain, these two dimensions will correspond to the ground dimensions. But, in most—if not all—cases, the conversion to ground coordinates needs to be done during processing.

3.2 SIDESCAN SONAR IMAGERY

3.2.1 Slant range and ground range

In each successive ping, the time t at which a measurement is recorded corresponds to the two-way travel between the sonar, the target, and back (Figure 3.4). The corresponding distance r is called the slant range. Using the sound speed c, we can deduce:

$$r = \frac{c \times t}{2}. \tag{3.1}$$

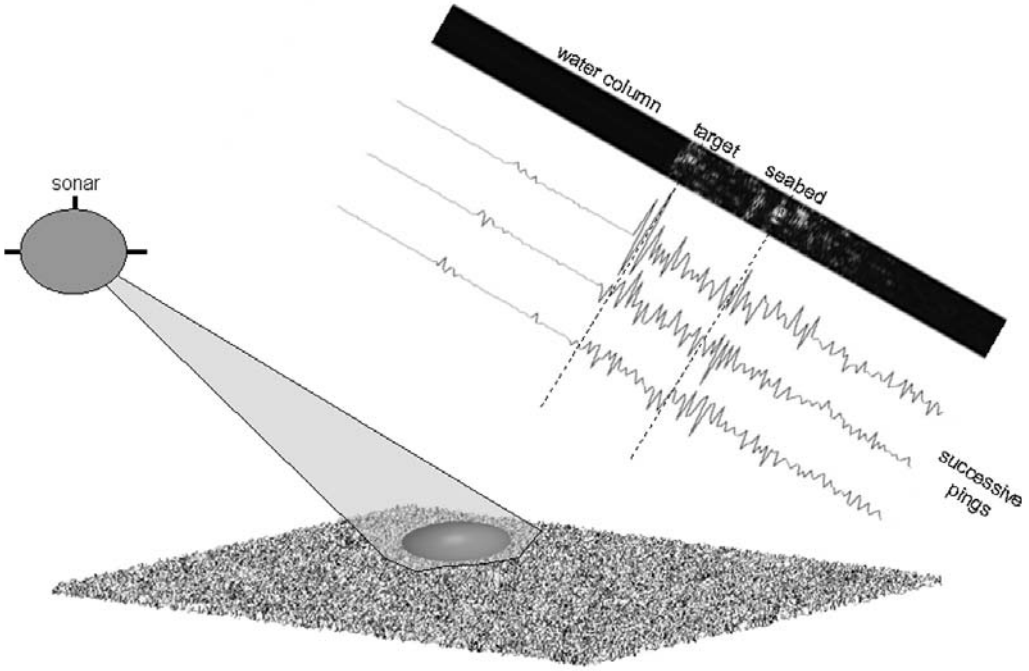

Figure 3.3. Successive pings are used to form an image. As the sonar flies past a proud target, it records successive backscattered signals (only three are shown here). They are stacked to form an image, whose dimensions respectively correspond to the time of arrival (i.e., the slant range) and the time of recording (i.e., distance along the sonar track). To compensate for attenuation with distance, it might be necessary to apply some range-dependent compensation (see text for details).

Assuming flat ground, and knowing the height h of the sonar at the time of acquisition, we can calculate the distance from the nadir of the sonar to the object of interest (ground range d):

$$d = \sqrt{\left(\frac{c \times t}{2}\right)^2 - h^2}. \tag{3.2}$$

If the flat-ground assumption is not justified, distortions in the imagery will increase as the topography becomes more rugged or the overall slope becomes more important (see Chapter 10 "Detection of anomalies and artefacts"). At lower frequencies ($<$10 kHz) or in water-saturated sediments, bottom penetration might induce other distortions, as backscatter will correspond to returns from the surface of the sediments at some angles, and from the sub-surface at other angles.

3.2.2 Backscatter strength

Figure 3.2 showed extraction of the envelope of the raw signal. This gives us a backscatter value for each point in the swath. It is already possible to combine successive swaths to get an image (cf. Figure 3.3). But these values are relative: they

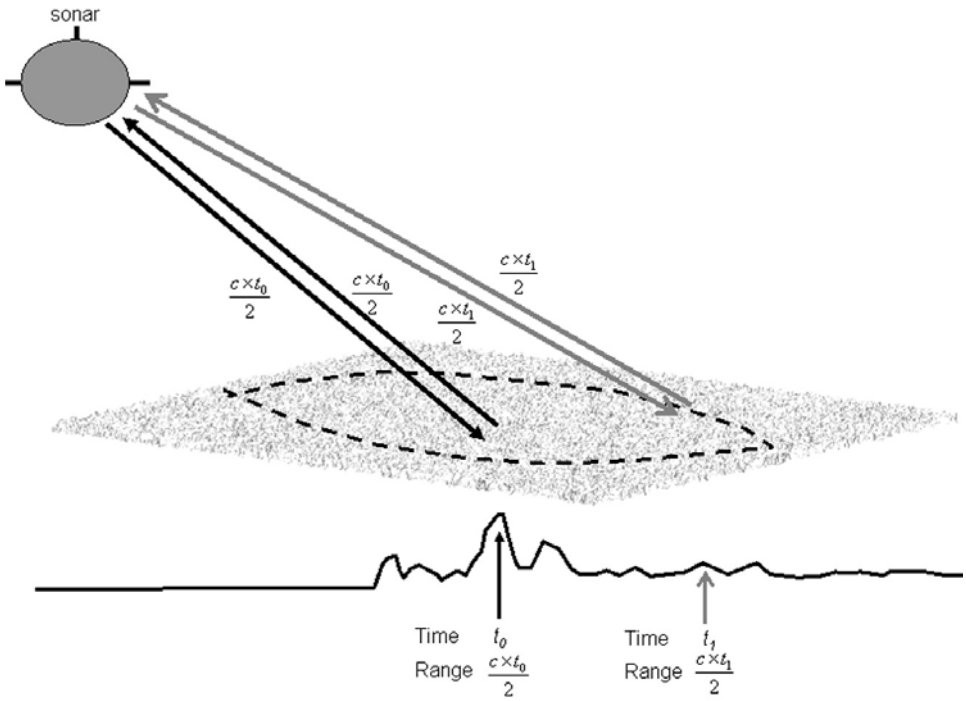

Figure 3.4. The conversion from time to slant range is straightforward; the backscatter of any point in the sonar footprint (dashed line on the seabed) will be recorded at a time proportional to the distance traveled by the acoustic wave from the sonar to the seabed and back.

need to be modulated by the source level and the gain of the receiver(s). Indeed, increasing the power of the imaging sonar will increase the response from the seabed (i.e., its relative backscatter). Keeping the source level constant, but mapping the same terrain twice with different receiving gains, we would measure different backscatter amplitudes, despite it being the same terrain. This is why it is important to use a calibrated source and account for the actual receiving gains, which should have been recorded accurately during the sonar survey. The sonar equation, explained in detail in most acoustic textbooks (e.g., Lurton, 2002) translates these relative backscatter values into backscatter strengths, expressed in dB. Then, and only then, can results from different surveys be meaningfully compared. This is particularly important as repeat surveys have often been used to demonstrate specific processes for the first time (e.g., Chadwick *et al.*, 1991, looking at repeat volcanic eruptions at a spreading center, or Hagen and Vogt, 1999, quantifying the seasonal variability of gas emissions underwater). Repeat sidescan surveys are now increasingly used for geo-hazard monitoring (e.g., small landslides in near-shore areas), resource monitoring (e.g., habitat mapping or control of gravel extraction).

Backscatter strengths describe the response of the seafloor at the frequency used and for specific conditions of ensonification (mostly the grazing angle). If calibrated

and expressed in dB, they can also be compared with acoustic backscatter models (see Section 2.2.3 ''Acoustic scattering: Theory''), providing more insights into seafloor processes. Full knowledge of the processing chain, and accuracy of the calibrated backscatter strength of a particular pixel on the seabed, allows the interpreter to assess whether surface or volume processes (e.g., penetration) predominate, and compare the geotechnical properties of this portion of the seabed with known quantities (i.e., is it more likely to be silt, or sand, or rock?).

3.3 ADDING BATHYMETRY

3.3.1 Sidescan bathymetry and interferometry

The time of arrival of an echo gives a slant range, theoretically corresponding to a portion of a sphere, centered on the sonar and limited to its directivity pattern. The intersection with a uniformly flat seabed would yield the angle of arrival, and therefore the exact position on the seabed. But this assumption is usually false in most real conditions. Interferometric sonars can however calculate the exact angle of arrival by comparing the time-domain signals between several receivers.

Also called bathymetric sonars, they use one transmitter array (also called a stave) and several receiver arrays (usually two to four). These receivers are parallel to the transmitter array, closely spaced, and slightly inclined, meaning that the backscatter signal will arrive at slightly different times (Figure 3.5). All arrays should have similar directivity patterns, narrow along-track and wide across-track. The time difference between the signal received at each stave, and its relative phase variations, can be used to calculate the angle between the direction of the acoustic signal and the transmitter array. Combining angle and slant range makes it possible to determine the exact location of each scatterer.

The phase difference $\Delta\varphi$ between A and B corresponds to the difference in acoustic paths scattering back from point M on the seabed (Figure 3.5):

$$\Delta\varphi = \frac{2\pi}{\lambda} \times \Delta R = \frac{2\pi}{\lambda} \times a \times \sin\theta. \tag{3.3}$$

The phase difference corresponds to the number of additional wavelengths the backscattered signal travels before it reaches the farthest transducer (point A in Figure 3.6). It is used to deduce the angle θ of arrival from the target:

$$\theta = \arcsin\left(\frac{\Delta\varphi}{\frac{2\pi}{\lambda}a}\right). \tag{3.4}$$

The calculation of the angle of arrival includes an ambiguity as soon as the spacing a between staves is larger than $\lambda/2$, as the phase is measured modulo 2π (e.g., Lurton, 2002). Phase difference ambiguities increase as receiving staves are farther apart, and can also be affected by environmental noise. This leads to the problem of ''phase wrapping'' (Figure 3.6). Techniques commonly used to remove ambiguities include

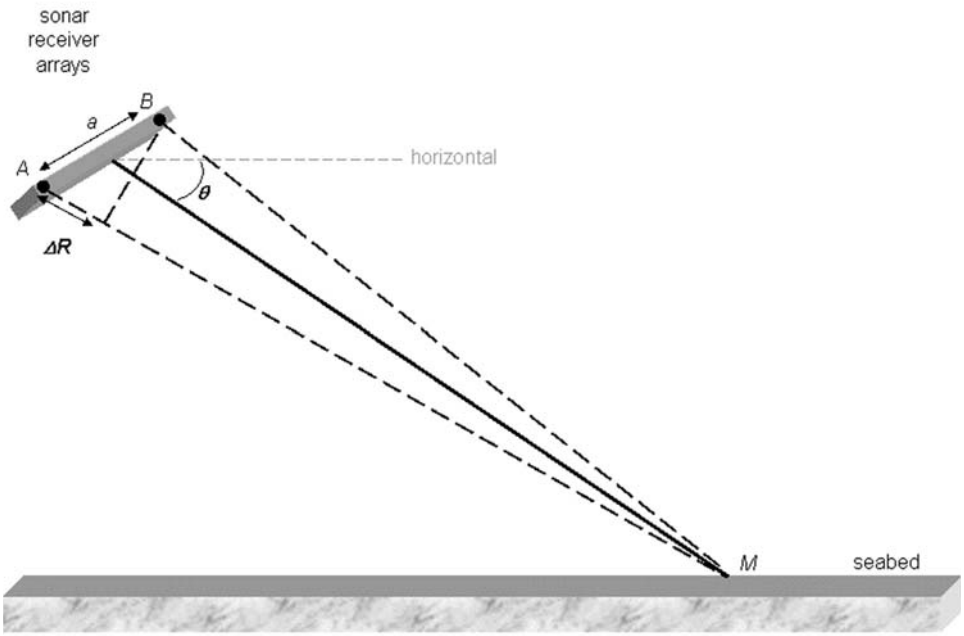

Figure 3.5. Interferometry principle. The signal backscattered from point M on the seabed is received at two different points A and B (corresponding to different receiver arrays). The difference in acoustic paths between the two is ΔR, related to the direction θ of the seabed return. See text for details.

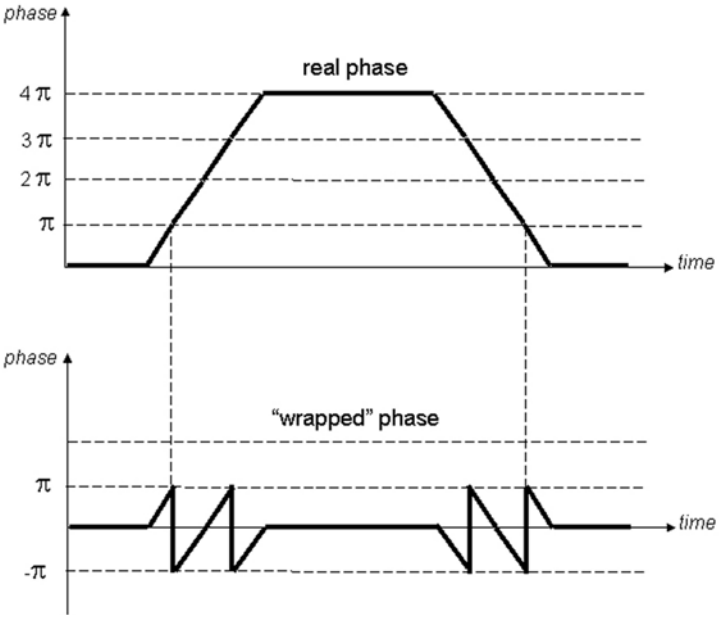

Figure 3.6. Example of phase wrapping. The phase variations are sawtooth-shaped. The arctangent of the function real phase (top graph) yields measurements between $-\pi$ and $+\pi$. Jumps of 2π in phase are clearly visible. The unambiguous phase must be unwrapped to produce a graph like the top one.

the placement of receivers at distances smaller than $\lambda/2$ (yielding low angular accuracy), the use of several receivers with different spacings (vernier methods), and phase unwrapping.

The "vernier" technique was first introduced at the University of Bath, U.K. (Cloet *et al.*, 1982) with the use of two widely spaced pairs of receivers, 13 λ and 14 λ apart, and then quickly adopted for many other sidescan sonars (e.g., SeaMARC-II). Detailed in Denbigh (1989), the vernier technique consists in using a first pair of receivers to measure the phase, and a second pair of receivers with a different spacing, therefore introducing a different ambiguity in phase measurements. The combination of the two outputs (similar to the bottom graph of Figure 3.6, but offset in time) corresponds to one angle only. If the difference in the separation of the two pairs of receivers is small, the subtraction of the two phase outputs gives a coarse but unambiguous measurement used to fix ambiguous measurements from one pair only.

Phase unwrapping can be achieved simply, using its local changes. The bottom graph of Figure 3.6 shows "wrapped" phase measurements, between $-\pi$ and $+\pi$. The first derivative of the phase is used to correct all values greater than $+\pi$ or smaller than $-\pi$ by adding or subtracting an integer multiple of 2π and integrating the phase derivative. The main obstacles to this technique can be low signal-to-noise ratios, baseline decorrelation (possible non-coherence of the sum of individual scatterers within each footprint), "shifting" footprint effects (degradation of phase measurements with range) and complex bottom topography, with the presence of acoustic shadows in the phase data and/or high numbers of phase wraps (typically eight for TOBI phase bathymetry). Research into the phase unwrapping of sidescan sonar measurements is an active field, in line with current research in radar interferometry, and recent articles have shown how Kalman filters, 2-D unwrapping (e.g., Banks *et al.*, 2000), quadrature-matched filtering (e.g., Shippey, 1997), genetic algorithms (e.g., Avgerinos, 2003), and other techniques could be used with success.

Like any physical measurement, and whatever the technique used to unwrap the phase, bathymetry derived by interferometric sonars is still subject to errors. Observations by Babb (1989) showed bathymetric errors in the range of 1 m–100 m for GLORIA bathymetry (60 m resolution, 60 km swath width, towed close to the sea surface). These errors depended strongly on the wind speed and in some cases the combination of water depth and swath width (e.g., ranges much smaller than water depth). More systematic calculations of expected errors can be found in Lurton (2000) and Bird and Mullins (2005). Interferometric sonars are nonetheless extremely useful, and in optimal conditions they could achieve swath widths many times larger than the water depth with high accuracies. Modern interferometric sonars like SwathPlus cover swaths 10–15 times wider than the water depth (up to 30 m: Geen, 2007), providing bathymetric measurements with a vertical accuracy of approximately 1% of water depth (Barnhardt *et al.*, 2005). Other sonars like the DSL-120 achieve swath widths commensurate with the imagery and roughly ten times the depth below the sonar (Scheirer *et al.*, 2000). As hardware and processing techniques improve, interferometric sonars are proving increasingly reliable and accurate.

3.3.2 Multibeam bathymetry

Not all sidescan sonars can provide interferometric bathymetry, though. Many past and current applications are therefore relying on multibeam bathymetry. Multibeam systems can be mounted on the surveying platform (e.g., ship or AUV), in which case their measurements will be geographically co-registered with sidescan sonar imagery (see Chapter 4 "Sidescan sonar data processing"). Bathymetry measurements can also be provided by other surveys, in which case the accuracy of their navigation should be checked. It is possible to accurately relocate both datasets to the same geographical reference frame by using Ground Control Points (GCPs) and techniques such as rubbersheeting (explained in Chapter 4).

Multibeam systems will not be detailed in this book, and the interested reader is recommended de Moustier (1988) and Lurton (2002) for full descriptions. Presented in Chapter 2 (and Figure 2.1), these instruments transmit several beams (up to 120 for some instruments), covering a wide swath on each side of the ship's track (up to 20 times the water depth in some cases). They estimate jointly the time of propagation and angle of arrival at each beam, resulting in data processing quickly becoming complex (e.g., Lurton, 2002). Multibeam systems provide fewer depth measurements across-track than interferometric sonars, as they only look at each individual beam. More complex to set up and install, they are also usually much more expensive, restricting the number of applications. But, because they are generally calibrated to very high standards (e.g., IHO-S44), they have proven excellent and multibeam bathymetry is routinely used to compare sidescan sonar measurements and/or process them further.

3.4 MERGING IMAGERY AND BATHYMETRY

All sidescan sonars provide images of the seabed and some also provide concurrent bathymetry, at the same resolution and at the same geographical positions. Combining the two types of information greatly improves the interpretation of acoustic measurements, as shown in Figure 3.7. Acquired with the HMR-1 swath sonar operated by the Hawaii Mapping Research Group, these images show a cluster of volcanoes of different sizes (Figure 3.7a) and elongated structures in the abyssal plains (Figure 3.7b). Although the volcanoes are very close and do not project shadows, their heights (and therefore volumes) and modes of emplacement can clearly be seen on the bathymetry. In the abyssal plain, the very low reliefs help identify the rough textures at the top of the imagery as lava deposits. The continuity of the abyssal hills is more clearly visible in the bathymetry than in the concurrent imagery, where it presents different aspects from the imaging sonar.

Bathymetry can also be used to refine the processing of the imagery, for example, by improving the slant-range to ground-range corrections (see Chapter 4 "Sidescan sonar data processing"). For a calibrated sonar, where acoustic measurements can be related to a value in dB (see Chapter 2), calculation of the exact angle of incidence allows comparing the acoustic reflectivity measured to the backscatter expected from

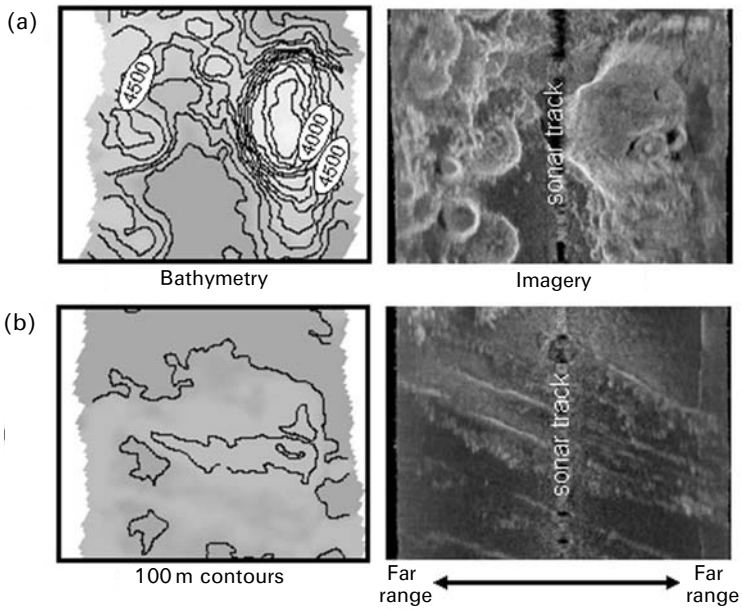

Figure 3.7. Example of co-registered sidescan bathymetry and imagery (HMR-1 sonar data, swath width 20 km): (a) clustered volcanoes; (b) abyssal hills in the Northern Pacific (original data source: *http://www.soest.hawaii.edu/HMRG/MR1*).

a model, and deduce useful parameters like sub-pixel roughness or the amount of volume scattering.

Side-by-side comparison of bathymetry and imagery can be lengthy and labor-intensive, and 3-D maps speed up the interpretation time by providing a synoptic view. Figure 3.8 (color section) shows the 3-D bathymetry acquired with the swath sonar IMI-30 between the islands of Maui and Hawaii, in perspective (top, in color). Sidescan sonar imagery, acquired with the same sonar and at the same metric resolution, can then be draped over the bathymetry (bottom). Similarly, Figure 3.9 shows TOBI sidescan sonar imagery (6 m resolution) of the Mid-Atlantic Ridge draped over EM-12 multibeam bathymetry (100 m resolution). Although the two datasets do not have the same resolution, individual structures (small volcanoes, fault scarps, etc.) are clearly visible.

Seductive as they are, 3-D perspective views of sonar datasets should however be interpreted by keeping in mind how they were produced. Vertical exaggeration should be clearly stated. On small scales, a vertical exaggeration of 1 often limits the visibility of distinct features, but greater vertical exaggerations might over-amplify small features (“making a mountain out of a molehill”, to use a common expression). The perspective used can also be misleading (Figure 3.10), and it should be explicitly stated. Azimuth variations can mask smaller features, whereas elevation variations can decrease the apparent differences between neighbouring structures. Even if a particular 3-D image is preferred because of its dramatic visual impact, it is useful to show the same 3-D image with a different perspective (or even the 2-D projection of the same area, with different colours and transparency levels for bathymetric contours). This shows the importance of “fly-by” presentations:

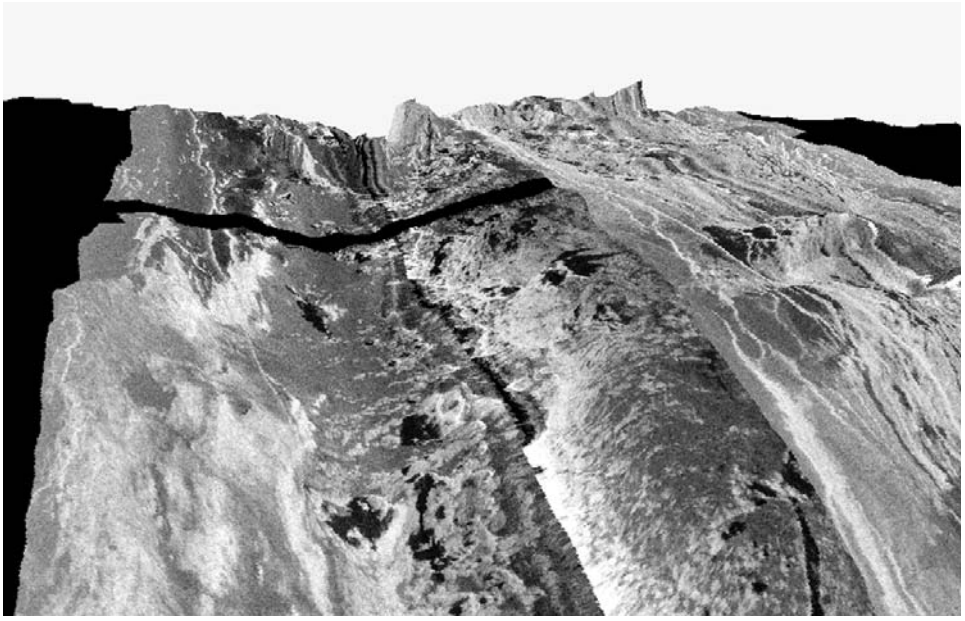

Figure 3.9. TOBI sidescan imagery from the Mid-Atlantic Ridge, draped over EM-12 multibeam bathymetry. Areas in black correspond to gaps in the TOBI imagery (from Blondel and Lurton, 1997).

although they usually focus on specific structures, they can provide important information on their exact relation with their surroundings. Finally, although it should go without saying, the types (and resolutions) of the original data should be explicitly stated. For example, in Figure 3.9 the resolution of the TOBI imagery is nearly an order of magnitude smaller than that of the EM-12 bathymetry: 1 bathymetry pixel

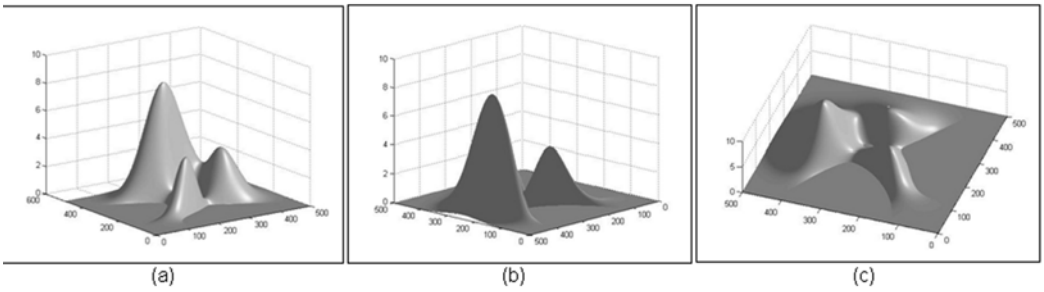

Figure 3.10. These three perspective views of the same synthetic bathymetry show the need to look at 3-D images from several angles, clearly explaining the parameters used: (a) three Gaussian-shaped hills on a flat background, with different heights and widths; (b) a view from a different azimuth, masking one of the hills and exaggerating the thinness of the biggest hill; (c) a view from a different azimuth and elevation, making the relative heights of the hills more similar, and increasing their apparent surfaces.

covers 16 imagery pixels. Problems of geographic co-registration (see Chapter 4 "Sidescan sonar data processing") notwithstanding, how would we interpret an acoustically complex structure in an apparently flat terrain? Is this structure complex because of its characteristics (e.g., roughness, reflectivity) or because of small-scale changes in its local slope? Both bathymetry and imagery datasets usually display some missing data (e.g., Figure 3.9, where a few swaths were not recovered due to a minor electronic problem). If the missing data need to be masked or replaced, the level and type of interpolation should also be clearly explained.

3.5 CONCLUSION

Acoustic measurements collected by sidescan sonar mostly consist in backscattering amplitudes of points on the seabed and in the water column, translated into imagery. These images are still the main product of sidescan sonars, although more recent (interferometric) sonars are using combinations of transducer arrays to collect bathymetry, at the same resolution and in the same locations as the imagery. This chapter aimed at presenting raw acoustic measurements, and how they were translated into imagery and, when using phase differences, into bathymetry. The actual processing (via hardware and software) of the raw data into usable backscatter values is not fully explained, as the purpose of this book is mostly to look at the interpretation of sidescan sonar datasets, but the references in the text and in the Further reading section can be used if necessary. The merging of imagery and bathymetry is a powerful aid to sonar data interpretation, as shown in the examples provided in this chapter.

But the ultimate limit to sonar performance is the quality of the processing. It depends on the accuracy of the data provided (acoustic measurements, but also in large part the navigation, the acquisition log, etc.) as much as on the thoroughness of compensating for everything that has affected the acoustic wave from transmission to backscattering to reception. Chapter 4 ("Sidescan sonar data processing") will therefore explain in detail the different steps necessary to create a true and accurate map of the seabed.

3.6 FURTHER READING (*see also* References at end of book)

About the transformation of raw acoustic measurements into sidescan sonar imagery

Burdic, W.S. (1990). *Underwater Acoustic System Analysis*, Second Edition. Prentice Hall, Englewood Cliffs, NJ, 466 pp.

Medwin, H.; and C.S. Clay (1998). *Fundamentals of Acoustical Oceanography*. Academic Press, London, 712 pp.

About sidescan sonar bathymetry processing

Denbigh, P.N. (1989). Swath bathymetry: Principles of operation and an analysis of errors. *IEEE Journal of Oceanic Engineering*, **14**(4), 289–298, October.

Jin, G.; and D. Tang (1996). Uncertainties of differential phase estimation associated with interferometric sonars. *IEEE J. Oceanic Eng.*, **21**(1), 53–63.

Lurton, X. (2000). Swath bathymetry using phase difference: Theoretical analysis of acoustical measurement precision. *IEEE J. Oceanic Eng.*, **25**(3), 351–363.

Bird, J.S.; and G.K. Mullins (2005). Analysis of swath bathymetry sonar accuracy. *IEEE J. Oceanic Engineering*, **30**(2), 372–390.

About multibeam bathymetry

de Moustier, C. (1988). State of the art in swath bathymetric survey systems. *Int. Hydrogr. Rev.*, **65**(2), 25–54.

Lurton, X. (2002). *An Introduction to Underwater Acoustics*. Springer/Praxis, Heidelberg, Germany/Chichester, U.K., 380 pp.

4

Sidescan sonar data processing

4.1 BACKSCATTER PROFILES

As they follow each other, backscatter profiles build up a fuller picture of the seabed. As time of reception (i.e., range from the sonar) increases, each profile will show typical variations (Figure 4.1, see color section). First, there are very low returns, due to background noise and reverberation as the signal still propagates in the water column. The first seabed returns (from small rubble, in this example) mark a strong difference, as the transmission loss is minimal. As it propagates with time, the acoustic signal will then image areas farther away from the sonar track, and subject to increasingly higher transmission losses. Using the terrain of Figure 4.1 as an example, the first topographic change (fault scarp close to the sonar track) is marked by a sharp peak in reflectivity, from slopes directly facing the imaging sonar. The small volcano will be clearly visible, as its sonar-facing slope will be more reflective, the caldera at the top will show lower backscatter, and its slope facing away from the sonar will be less reflective. The fissure on the ground will also be marked by a strong decrease in reflectivity, especially if it is deep enough and large enough that some portions of it are in the acoustic shadow zone. Backscatter levels return to normal on the other side of the fissure. Far-range fault scarps will still be associated with increased reflectivities, but subdued because of the higher ranges (and attenuation).

The accuracy of the combination of these individual backscatter profiles is important, as it is used for interpretation: seabed structures should be accurately located, not distorted, and their acoustic variations should be affected by artifacts. These processes are explained in Sections 4.2–4.8. Only once the sonar measurements have been processed to the best available extent can one make meaningful, quantitative measurements. For the interpretation of sonar images one needs to keep in mind the limits induced by the imaging geometry and the processing, and this will be detailed in Section 4.9.

4.2 NAVIGATION AND ATTITUDE

To accurately locate the different sonar echoes on the seabed, one needs to know where the sonar is located (navigation), in which direction it is imaging (attitude), and therefore which area of the seafloor it is ensonifying. This information is given by the combination of position information (latitude, longitude, altitude above a reference datum), heading, speed, and attitude information (heave, roll, pitch, and yaw). The following subsections will detail the techniques currently used for measuring the position of the survey vessel (i.e., at the sea surface), the position of the sonar platform if not attached to the survey vessel (i.e., below the sea surface), and their relative variations in attitude.

4.2.1 Navigation of surface vehicles

The earlier navigation methods were of course the sextant and, for near-shore surveys, triangulation with artificial or natural landmarks on-shore. Navigation was only known in sparse points, with a limited accuracy depending on the user's experience. Starting from a fixed, accurately located base station, the movements of a surface vehicle can be measured through the combination of heading and speed. They are usually accessed with 3-D accelerometers, one integration of acceleration giving speed and the next integration giving displacement. The speed can also be measured with hull-mounted Doppler velocimeters. Accuracies are usually good, although varying from one instrument to the other, and subject to local weather conditions (i.e., sea state). But small, relative offsets quickly add up to larger errors, especially with distance from the reference station.

Operations occurring further off-shore or requiring a better precision can make use of radionavigation. The first type of radionavigation aids used the travel time between the ship and a shore station (e.g., radar, shoran, and the range–range mode of Loran-C). More complex systems measured the difference in travel time (or phase) of signals coming from several stations (e.g., Raydist, Lorac, Decca, Toran, Loran, and Omega), or combined distance and direction measurements through microwaves. Systems like shoran were effective up to 80 km from the shore stations (250 km with more specific equipment), giving location accuracies of 20 m to 40 m. This precision depended on the number of stations available and their angles respective to the receiver.

The last few decades saw the spreading of satellite-based navigation systems. The TRANSIT system, like its Russian counterpart Cicada, is based on a constellation of satellites revolving around the Earth on polar orbits (Figure 4.2). They transmit continuous waves at 150 MHz and 400 MHz. The measurements of Doppler shifts during the time of observation of each satellite (around 18 minutes) are combined with the speed and heading of the receiving vessel and yield information about the ship's position. Up to 20 observations are possible each day with accuracies of 30 meters. Between these fixes, position is usually computed by dead-reckoning (close estimates of the current positions from the ship's speed and heading), thus

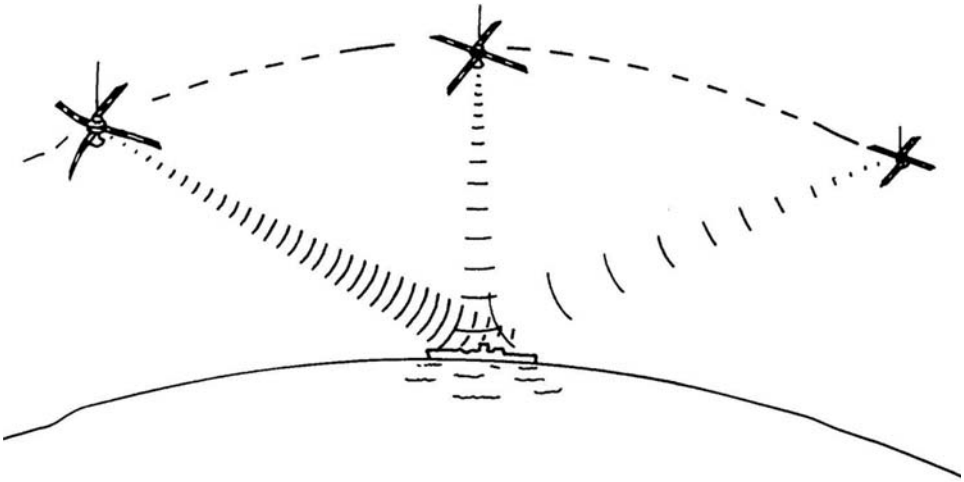

Figure 4.2. Basic principle of satellite navigation systems (from Telford *et al.*, 1990).

degrading the accuracy to a few hundred meters or more. Other similar satellite-based systems are available (e.g., DORIS, GLONASS).

These navigation systems have all been superseded by the Global Positioning System (GPS), commercially released in 1993 and now ubiquitous. GPS consists in a constellation of satellites[1] in synchronous orbits (Figure 4.3), associated ground stations, and user equipment. Each satellite transmits two codes, the P (precision) code and the CA (coarse acquisition) code. With the CA code, precision is in the order of 15 meters. To gain access to the full precision of the system, a user will need knowledge of the P code, usually inaccessible to commercial users. This P-code yields positioning accuracies of around 30 cm worldwide. Several satellites are visible at any moment, which allows near-continuous measurements of 3-D position (latitude, longitude, altitude above the geoid) as well as horizontal and vertical velocities and time (through the satellite's atomic clock). To limit unauthorized military applications, GPS signals can be severely degraded (down to 100 m accuracy) at very short notice. This mode, called selective availability (SA), is currently disabled. But the possibility of its use means that other systems have been explored (e.g., the GALILEO system being set up by the European Union). Modern surveys now rely heavily on GPS but still use the other systems as a back-up and in order to cross-verify the location accuracies.

The (already good) resolution of GPS can be enhanced by comparing measurements from several GPS receivers; the most popular schemes are differential GPS (DGPS) and real-time kinematic (RTK) GPS. DGPS uses GPS receivers placed at fixed, known locations and compares information from each satellite in the constella-

[1] Thirty-two main satellites as of June 2008 (*http://tycho.usno.navy.mil/gpscurr.html*). These satellites are replaced and updated as necessary to maintain the worldwide performance of the positioning system.

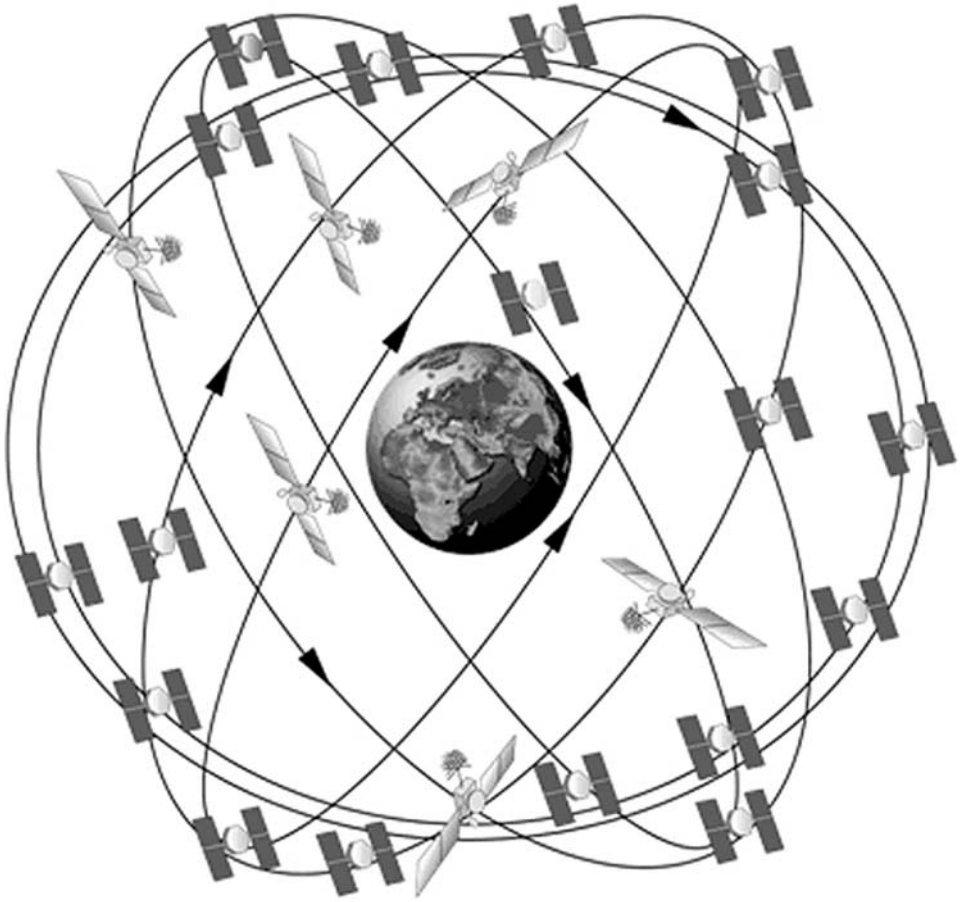

Figure 4.3. Constellation of satellites making up the Global Positioning System (from *pnt.gov*).

tion. RTK GPS uses several receivers, one of which remains stationary and has been located with very high accuracy. These comparisons can be done in real time, or refined through post-processing after the survey. Resulting accuracies improve to less than 10 meters (and often 1 m to 5 m) for vehicles above water.

4.2.2 Navigation of underwater vehicles

Ship positioning techniques have drastically changed in ease and accuracy since the "GPS revolution" in the early 1990s. But the situation is more complex for underwater vehicles. In many applications, the sonar platform is towed by the ship, sometimes only a few hundred meters above the seafloor (deep-tow). The platform, or towfish, may be positioned accurately by calculating how far back it lies behind and below the ship, or by using acoustic ranging techniques.

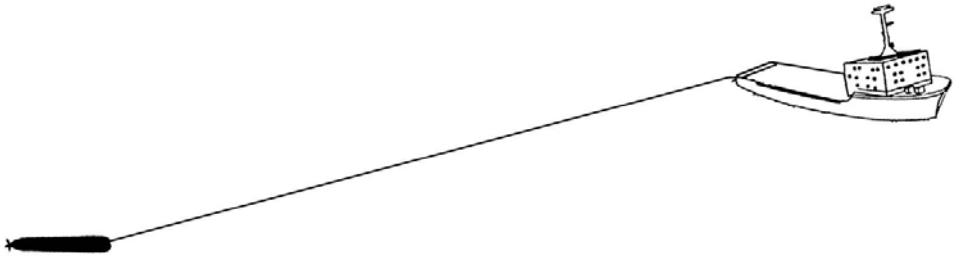

Figure 4.4. Layback of the towfish. A depressor weight can sometimes decouple the sonar platform from small-amplitude movements of the towing vessel. The cable is assumed straight, although this is not the case when changing speed (the towfish going up or down) and/or heading (the towfish tending to move around its axis).

The layback of the towfish is computed from the length of cable out and simple trigonometric relations assuming the cable is straight (Figure 4.4). The absolute position of the towfish can be estimated with a precision of a few hundred meters for cable lengths of 4 km and more. This technique is obviously inaccurate for long cable lengths or when the ship is changing speed or heading (and the cable becomes slack). This is, however, the easiest and cheapest of the positioning methods. Its inaccuracies can be mitigated by a precise recording of the length of cable out and, when possible, successive runs over the target area or comparison with known reference points (e.g., underwater landmarks, or matching depth readings with other sources like ship bathymetry). Because of its limitations, the layback method is most suited to large-scale surveys and surveys along linear routes.

An increasing number of survey platforms are now separate from the surface vehicle, either because they are tethered but can move anywhere in the water column (remotely operated vehicles, ROVs) or because they are completely independent (autonomous underwater vehicles: AUVs). They can all be located using acoustic ranging systems. These are based on two main types of configuration (Figure 4.5): short baseline (SBL), long baseline (LBL), and variants thereof.

SBL systems consist in acoustic transducers placed on the hull of the ship as a net, and receiving signals from a transponder on the towfish. The time delays are converted to distances and the relative position of the towfish can be computed with accuracies of 1% for distances out to 2,500 meters. Once installed, SBL systems can be used throughout a survey. Working on a similar principle, ultra-short baseline (USBL) systems calculate position by combining acoustic range and bearing data from a vessel transducer with attitude, heading, and GPS sensor information. Other possible configurations include the iUSBL (inverted USBL, where the transmitters are on the underwater vehicle instead of the surface vessel), and the integrated long and short baseline (ILSBL). For very precise positioning, multiple vessels may also be used (this is still rather uncommon). USBL errors have recently decreased to 2 m–6 m at 500 m depth, and 2 m–10 m at 1,800 m depth, depending on the type and the accuracy of other attitude and heading sensors used in combination. These errors will of course depend on the application, the time spent

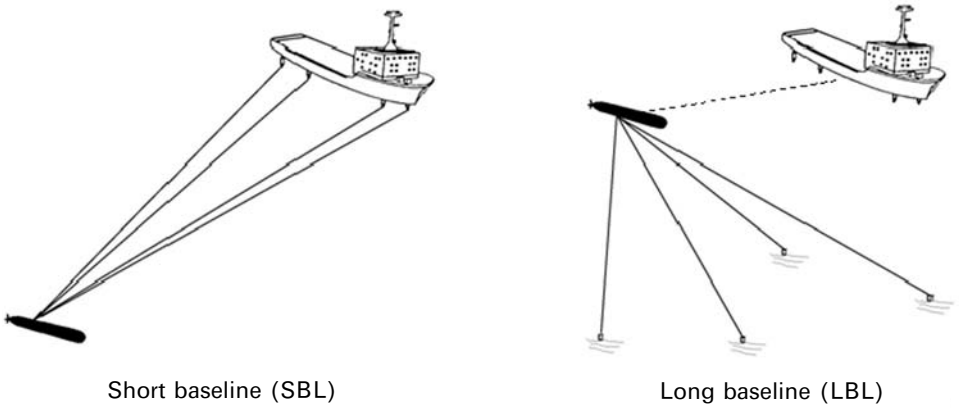

Figure 4.5. Acoustic ranging systems used to locate underwater vehicles use two basic concepts: reference to a surface vessel (SBL) or to a transponder net on the seabed (LBL), with possible connection to the surface vessel.

on post-processing the navigation measurements, and the local conditions during the survey.

Conversely, LBL systems rely on acoustic transponders emplaced on the seafloor and accurately positioned. A transponder on the towfish interrogates acoustically the different elements of the net and computes the towfish position by triangulation. The minimum number of seabed beacons required for unambiguous navigation is three, but additional beacons will provide more redundancy and improve quality checks. A main advantage of LBL systems is that the (often sub-metric) accuracy of positioning is independent of depth. The maximum range between transducers in the net is about 3,000 meters. Their accurate positioning and calibration can take a long time, increasing with depth, and the limited range of the complete net means this type of positioning system is only useful for fixed applications (e.g., mapping of a shipwreck or part of a pipeline—not a route survey).

When several systems are used in the same area, there is always a risk of interference. The use of wideband techniques (transmitting at several frequencies) reduces this risk, and can also be used when the water column becomes more complex (i.e., variable sound velocity profiles). Some systems (e.g., LUSBL) can also merge the two approaches (USBL and LBL). Finally, and increasingly, the sensors aboard the sonar platform itself are used in refining the positioning data.

GPS positioning can also be extended underwater, using different techniques (e.g., Thomas, 1994, 1998). The simplest is to have a buoy with a GPS receiver on the surface, towed by the surveying platform or extending up from it via a rigid pole. This technique is limited to use in shallow water. In deeper water, the buoy can be towed well behind (and to the side) of the vehicle, yielding inaccuracies of tens of meters. In shallow water, the presence of a rigid pole couples it with the surface waves and can induce undesirable vibrations in the surveying platform. This technique can be extended by having several buoys (with their own GPS receivers) communicating

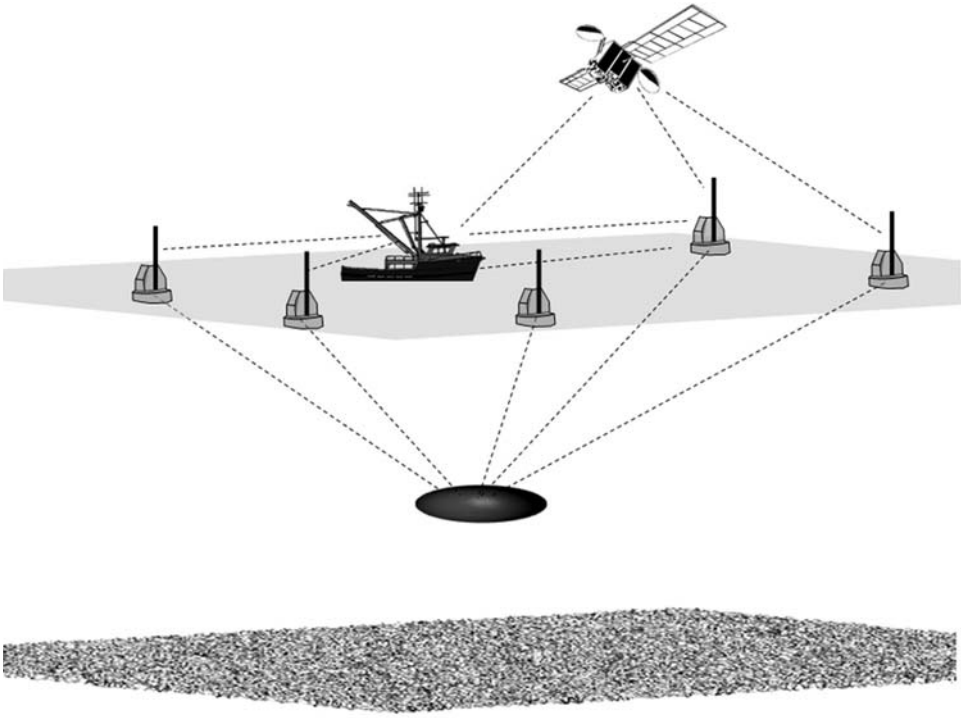

Figure 4.6. GIB underwater positioning works like an underwater LBL system, with added GPS differential correction. The transponder net on the seabed is replaced with a series of GPS-instrumented buoys on the sea surface.

via acoustic waves with the surveying platform underwater. This system has been developed in several patents, the earliest one dating back to 1992.

Very similar, the GIB (GPS intelligent buoys) technology includes acoustic communication from the platform to the buoys, and not only from the buoys to the platform (e.g., Alcocer *et al.*, 2007). Single-buoy GIB positioning combines the information from dead-reckoning of the platform's navigation systems (inertial navigation unit and Doppler velocimeter, if available) with the positions of the buoy and its successive ranges to the vehicle. ''Direct'' navigation is computed aboard the vehicle, whereas ''reverse'' navigation is computed on the topside station. Typical GIB systems consist in four buoys with DGPS receivers and hydrophones (Figure 4.6). Each hydrophone receives acoustic pulses transmitted periodically by a pinger onboard the surveying platform (these pulses usually include depth). The buoys communicate by radio with a central station (support vessel or shore station) where the exact position of the surveying platform is computed. The maximum distance between two buoys is $\sim$1.5 km, giving similar access to LBL systems but with an easier (re)deployment of the transponder net. Current GIB systems can provide accuracies of 1 m–3 m underwater.

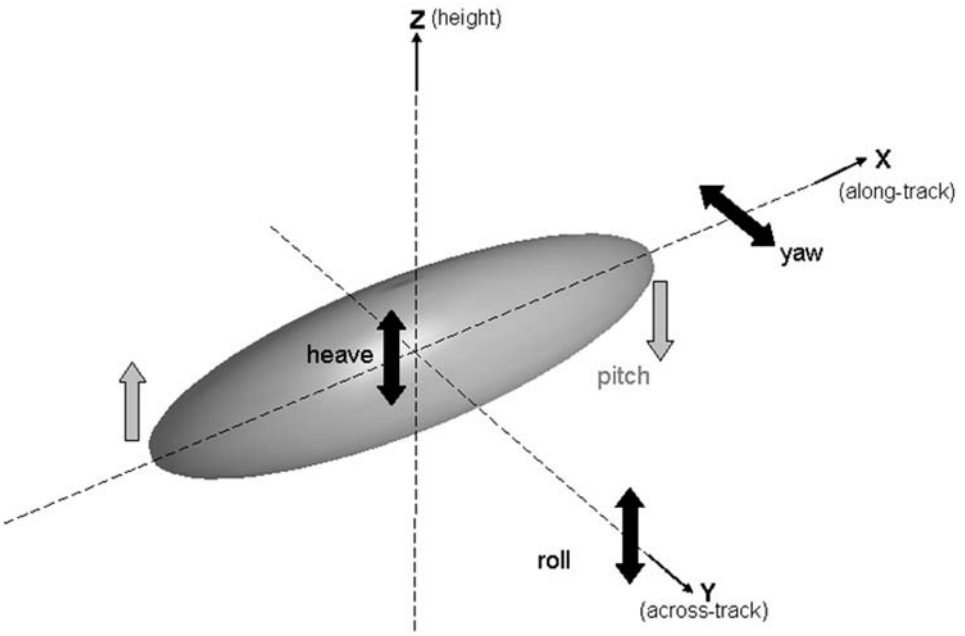

Figure 4.7. The attitude variations of the surveying platform (and sonar) are combinations of variations around the axes: roll, pitch, yaw, and heave.

4.2.3 Attitude information

The other important question (''Which area of the seafloor is the sonar ensonifying?'') is answered by looking at the attitude of the ship or sonar platform. Four types of movements are recognized: yaw, pitch, roll, and heave (Figure 4.7). Heave corresponds to the small-scale variations in altitude of the sonar platform (in the YZ plane). Roll is a lateral movement of the towfish around its longitudinal axis (in the YZ plane). Pitch is a side-to-side movement of the nose and tail of the towfish around its horizontal axis (in the XZ plane). And yaw is a side-to-side movement of the towfish around its vertical axis (in the XY plane). The movements experienced by the ship will not always be copied by the platform underwater, because they are offset in time when propagating through the tether, or because they are attenuated (e.g., through a neutrally buoyant decoupler between the sonar and the towing vessel). These parameters need to be explicitly recorded for the sonar platform. They are usually measured through gyrocompasses with accuracies of a few degrees to a few tens of degrees. Inertial Navigation Systems (INSs) merge the outputs of gyroscopes and accelerometers (usually three, one for each perpendicular axis), improving the accuracy of navigation (e.g., from acoustic ranging systems). The influence of attitude variations on sonar images is presented later in this chapter, as well as in Chapter 10 (''Anomalies and artifacts'').

4.3 PRE-PROCESSING

4.3.1 Definitions

To avoid confusion and misinterpretation, we have decided to follow the methodology presented in Blondel and Parson (1994) and Blondel and Murton (1997), dividing into three distinct stages the transformation of raw sonar data into usable images:

- *pre-processing*, preparation of the raw sonar data for processing. This includes, but is not limited to, the cleaning of the navigation and sensor's attitude files and the conversion between formats.
- *processing*, transformation of the raw swath data to usable images or grids, radiometrically and geometrically correct representations of the seafloor. This includes grid interpolation and mosaicking.
- *post-processing*, all operations not necessary for a correct interpretation but which constitute a definite plus. This includes the computation of statistics, cosmetic operations (e.g., contrast enhancement), the removal of survey-scale noise, and multiple reflections. More advanced image analysis techniques are detailed in Chapter 11 (''Computer-assisted interpretation'').

4.3.2 Data formats

Raw sonar data come in a very large variety of formats, most of them tied to the type of sonar used. These specific formats are necessary because of the hardware used and the diversity of measurements taken. The decisions made when building the hardware are in particular related to how much information can be transmitted topside (to the acquisition stage) and at what rate. The other measurements necessary to process sonar data (e.g., navigation, attitude) are associated with other formats, generally different. The preparation of raw sonar data for processing often includes the conversion between the format(s) delivered by the acquisition system and the format of the processing software, and the merging of these disparate files into a consistent dataset. These formats must contain as much as possible of the information needed for processing. Even if it has now become less common to encounter widely different computer platforms (e.g., Vax/Sun/IBM), format conversion can be a frustratingly slow and cumbersome task.

Starting from the principle that sonar imagery formats should be translatable easily from one computer type to the other, and record as much information as possible, several solutions have been proposed. Blondel and Murton (1997) showed the emergence in international research efforts of HDF (Hierarchical Data Format, a public domain service from the National Center for Supercomputer Applications, U.S.A.) and its simplified offspring NetCDF.[2] NetCDF (Network Common Data Form) is a machine-independent, self-describing, binary data format. Being self-

[2] Freely accessible at *http://www.unidata.ucar.edu/downloads/netcdf/index.jsp*

describing, it means the header of the file describes the layout of the rest, in particular data arrays and any additional metadata. Being platform-independent, it avoids the problems that plague data transfer between Windows, Mac and Unix/Linux systems (e.g., the differences between big-endian and little-endian floating-point values,[3] a common source of grief when transferring between systems or re-processing legacy sonar measurements). Because of its efficient subsetting, this format lends itself to pyramidal presentation of the data, enabling quick access to increasingly accurate portions of the entire dataset. Another standard format, called SEG-Y, is one of several standards developed by the U.S. Society of Exploration Geophysicists. Designed originally for the seismic community and in widespread use since its beginning in 1975, this standard is adapted to acoustic profiler data but might not always be adapted to sidescan sonar measurements.

Several industrial formats have aimed at solving this problem for sonar records. Amongst many, one can cite XTF (''Extended Triton Format'', created by Triton Elics). This open-source format[4] allows saving different types of sonar, navigation, telemetry, and bathymetry measurements in one single file, rather than a collection of individual files. Like NetCDF, this format can easily be adapted to include any type of future data. During real-time data acquisition, data can come from the variety of instruments associated with the sidescan sonar, and it does not always come synchronously. Sidescan measurements might be gathered every second, whereas navigation might be logged every 0.1 second, and the sonar platform's roll every 0.8 second. With XTF, the data is recorded as it comes, without the need for synchronization between data packets (Figure 4.8). Each packet of independent data comes with its own header. During processing, the software can then easily detect and ignore irrelevant data packets. XTF is but one of the sonar formats available, but seems to be gaining a strong foothold amongst sonar manufacturers.

There are several other successful formats in sonar imagery (ISIS, Q-MIPS, and many others). These formats are increasingly relying on open-source freeware, whose developments/improvements implicate a wider community than just a single academic institution or company. The success of these formats will depend on their accessibility, their versatility, and the range of processing tools accommodating them.

4.3.3 Navigation pre-processing

Section 4.2 presented the acquisition of navigation and attitude data: 3-D positions, heading, speed, heave, roll, pitch, and yaw. Their changes are usually quite smooth, although some spurious values may be introduced during their recording. If undetected or unaccounted for, these variations can induce important errors during the geometric rectification of the image (see also Chapter 9, ''Anomalies and

[3] This problem, also called ''endianness'', is related to the order in which individual bits are stored to make floating-point values, usually on 4 bytes, based on a sign, a mantissa and an exponent.

[4] Downloadable at *http://www.tritonimaginginc.com/site/content/public/downloads/FileFormatInfo/*

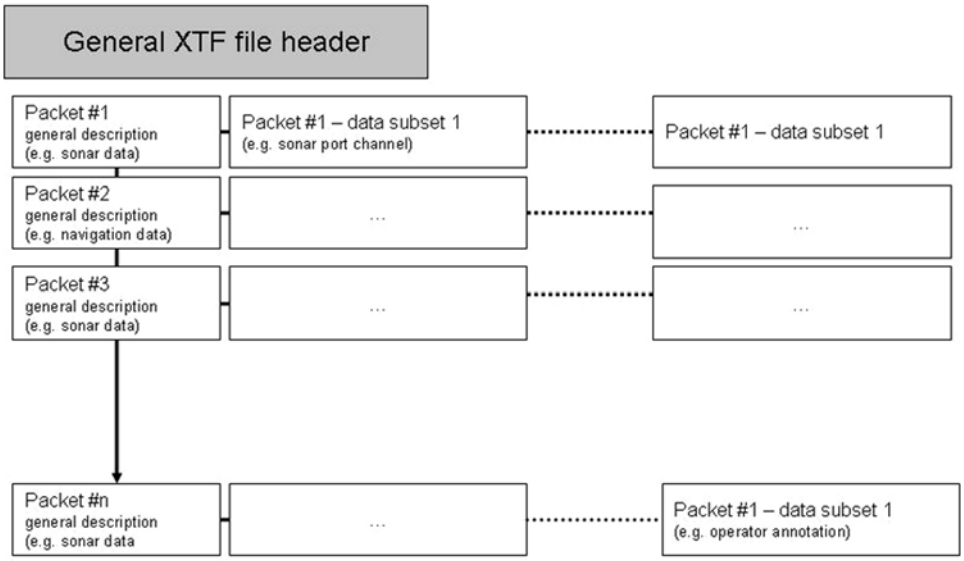

Figure 4.8. Example of a self-describing data format: XTF general structure.

artifacts''). Practical and theoretical studies show that features on the seafloor can be arbitrarily merged, distorted, or truncated if navigation and attitude are not correctly processed.

Depending on the navigation system used, ship and towfish positions can be inaccurate because of large time intervals between position fixes (e.g., when no satellite is in view) and when the measurements are excessively noisy (e.g., bad weather conditions, ionospheric perturbations, receiver problems). With the advent of GPS positioning, these inaccuracies are less important than with other systems. They can usually be processed with local averaging to remove the spikes. The accuracies need comparing with the overall scales of the survey (e.g., Figure 4.9). Will a 2 m jump in a few positions be important for a 500 km survey line? Will a systematic offset of a few meters per day be important when measuring a small harbour?

Towfish positioning has other limitations coming from the techniques used underwater. Acoustic ranging systems measure depth and range, and this estimation might be influenced by sound propagation in the water column (hence the need for regular sound velocity profiles). These variations will be more visible as the horizontal and vertical distances increase, because the likelihood of encountering water layers with sufficiently distinct properties increases. SBL and USBL positioning will also need to integrate the motion of the supporting vessel (i.e., from the attitude sensors). Again, a sense of proportion must be kept. Will a difference in roll of 0.2° make a noticeable difference 100 m away, depending on whether the sonar is flying 20 m or 300 m above the seabed?

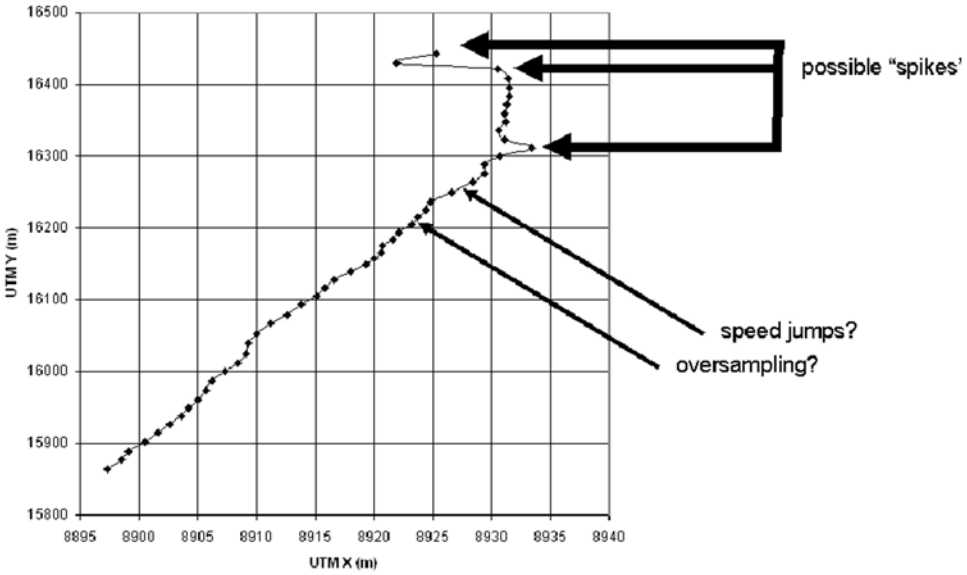

Figure 4.9. Typical navigation data (in this case, corresponding to the location of a deep-tow sonar, measured every 27 seconds) can exhibit different types of unexpected variation. The role of processing is to determine which of these variations are real, and which ones can be safely removed.

When the only control on the position of the towfish is the length of cable out, the situation becomes more complex. Most sonar platforms now have a depth meter or profiler, and simple trigonometry can be used to derive the distance d behind the ship (Figure 4.10):

$$d = \sqrt{L^2 - (H - h)^2} \tag{4.1}$$

where L is the length of cable out; and H and h are the depths below the ship and the

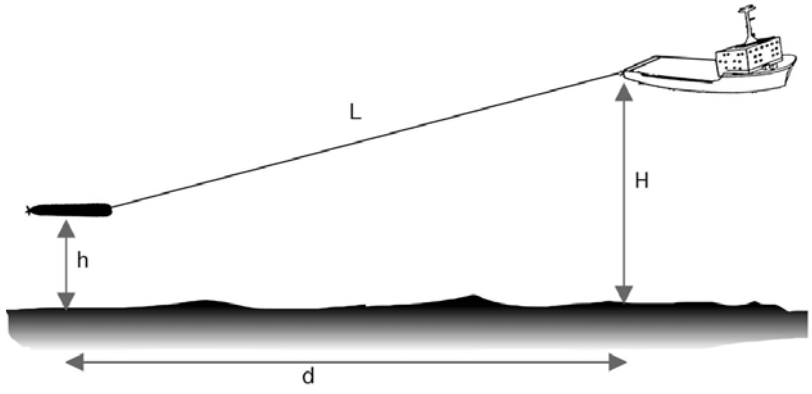

Figure 4.10. Relation between the respective positions of the survey vessel and the towfish (from Blondel and Murton, 1997).

sonar platform, respectively. This distance lies in fact on an arc circle behind the ship. Only once the ship has been on the same heading for a long time does it lie on the same line, and across-track displacements become important during turns and some time afterwards. "Geophysical" techniques aim at matching measurements made on the towfish (e.g., bathymetry, magnetic field, gravity) with general maps of the area (e.g., Leonard *et al.*, 1998). A more accurate approach was proposed by LeBas *et al.* (1995), matching the profiles from the altimeter aboard the sonar platform and the ship's vertical bathymetry measurements. Again, profile-matching works best for sub-linear tracks. During turns, the towfish is deported away and its depth profile needs to be matched with the multibeam bathymetry away from the ship's track. Because all possible combinations must be tested, this proves very computationally intensive.

4.3.4 Attitude pre-processing

For the same reasons (hardware problems), attitude information is also prone to noise and outliers. Along-track profiles typical from a deep-sea survey are shown in Figure 4.11. The towfish's altitude varies regularly, but some spikes of nearly 100 meters are visible here and there. These improbable values are due to the loss of the bottom by the platform's altimeter. The platform's pitch and roll exhibit important variations at the same moments. The pitch variations correspond to changes in

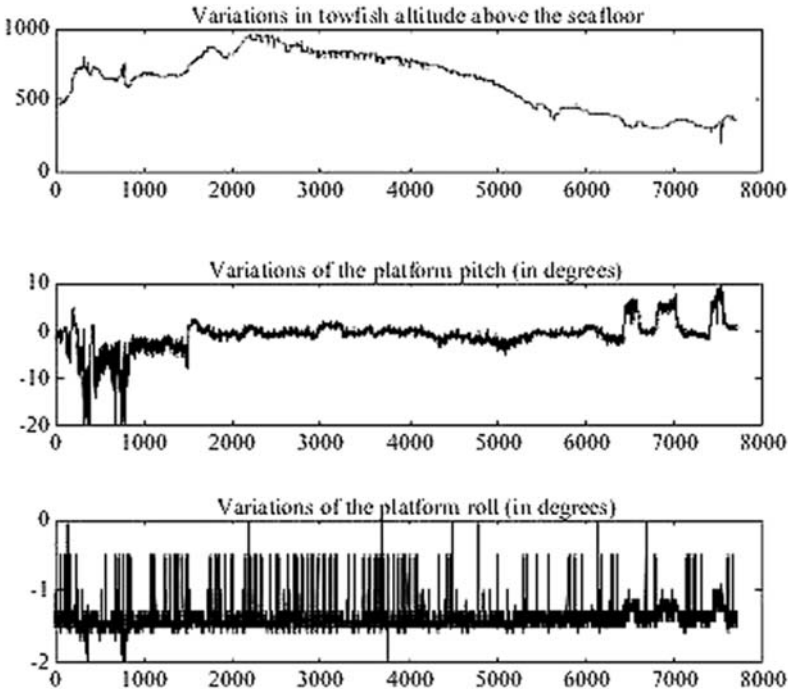

Figure 4.11. Along-track variations of attitude during an actual survey (from Blondel and Murton, 1997).

altitude, as the sonar platform moves up or down and then stabilizes again to the position it was trimmed for (nominal pitch of 0°). The roll variations are less important, but have a poor signal-to-noise ratio. If left unfiltered, these variations would create positioning inaccuracies of a few tens of meters on the seafloor (for an initial footprint close to 1 m).

Several techniques can be used for the detection and removal of outliers and spikes. Apart from manual selection, they usually rely on smoothing filters (moving average, Kalman filters, etc.) and interpolation with polynomial or spline functions. These pre-processing operations are essential to the formation of correct maps of the seafloor. Often, when thorough processing of sonar imagery fails to produce the expected results, another good look at the navigation and attitude helps enhance the images.

4.4 RADIOMETRIC CORRECTIONS

This section assumes that the sonar signal is already processed to amplitude and/or bathymetry measurements, and will not delve into the processing of I/Q values or hardware operations (the interested reader will be able to find more in Medwin and Clay, 1998 and Lurton, 2002, as well as in the technical literature). The first stage of processing is usually to recalibrate individual sonar backscatter measurements, first individually (requantization), second as successive profiles (across-track), and finally on the entire image thus formed (along-track).

4.4.1 Requantization

Most sonar processing packages now use measurements of backscatter scaled between 0 and 255 (8-bit quantization) or 0 and 32,767 (16-bit quantization). The output from the sonar hardware does not always follow the same quantization schemes (i.e., it could have been sampled with an 11-bit or a 64-bit system) and it may be necessary to resample the data. If not performed correctly, this operation will irretrievably lose the dynamic range of the original backscatter. In extreme cases, the return signals may be saturated or under-saturated for complete regions of the seafloor, thus rendering their analysis impossible. One technique commonly used is the Bell μ-law. Its expression is:

$$new\_value = C \times \ln\left(1 + \frac{2^n \times raw\_value}{2^m}\right) \tag{4.2}$$

where C is a user-defined constant; m is the original number of bits; n is the new number of bits (i.e., $n = 8$ for a range 0–255). This logarithmic condensing of the data is most useful in low-backscatter areas (abyssal plains, sedimentary fans), because it creates more contrast. In areas already highly contrasted (e.g., mid-oceanic ridges), requantization through simple division by 2^{m-n} is more adequate. Another advantage of requantization is that it can lessen the costs of further computation and storage. Ideally, backscatter measurements from a calibrated sidescan sonar would be in

decibels (relative to a reference power level), but many sidescans are still uncalibrated, and the backscatter values should be fully traceable (knowing the gains used during acquisition, etc.). In the absence of this information, many sidescan sonar images are very interesting, but as they represent relative backscatter levels, they cannot be compared with other maps from the same area, using the same sonar in a different setting, or completely different sonars (cf. Figure 2.11 and Section 3.2.2).

In the past, sidescan sonar imagery was output on electrical line scan paper recorders in which high voltages (high signal values) were represented as black. However, the human eye intuitively interprets dark areas as shadows, and bright areas as illuminated. For this reason, sidescan sonar images in this book are represented with highest backscatter values as white and lowest backscatter values as black. This is consistent with the representation scheme used in other domains of remote sensing such as optical and radar imagery.

4.4.2 Across-track corrections

Backscattered signals are orders of magnitude lower than the signal transmitted because of attenuation with distance and other effects. Identical targets placed at different positions across-track will therefore have increasingly lower backscatter (see Figure 4.12). Time-varying gains (TVGs) are corrections designed to compensate for this effect. A fixed correction is usually built in the sonar hardware, correcting for known effects (e.g., from range or beam pattern only). These corrections can be used directly, sometimes giving step-wise variations with groups of grazing angles which need to be smoothed and reapplied to the relevant points. TVG corrections can also be computed as a single *ad hoc* function accounting for the local surveying conditions, known from *in situ* probes such as XBTs (expendable bathy-thermographs) or hull-mounted velocimeters, extended down to the seafloor if necessary by using environmental databases.[5]

4.4.3 Along-track corrections

Systematic radiometric variations are often visible on the sonar images once they have been processed (Figure 4.13). Uniformly black lines (dropout lines) sometimes occur across-track. They are attributable to acquisition problems within the transducer, or loss of data during the transmission between the sonar and the ship. Lines with anomalously low values (across-track striping) may occur due to vehicle motion or various system errors. Some lines may also be shifted across-track, part of the line being black. This last effect is usually attributable to the sonar's altimeter losing the bottom and subsequently timing the backscattered returns inaccurately. Across-track striping is removable through a filtering process which detects low-amplitude lines and replaces the values using the averaged values of adjacent lines.

[5] For example, the Levitus database, regularly updated: *ftp://ftp.ldeo.columbia.edu/pub/MB-System/annual.gz*

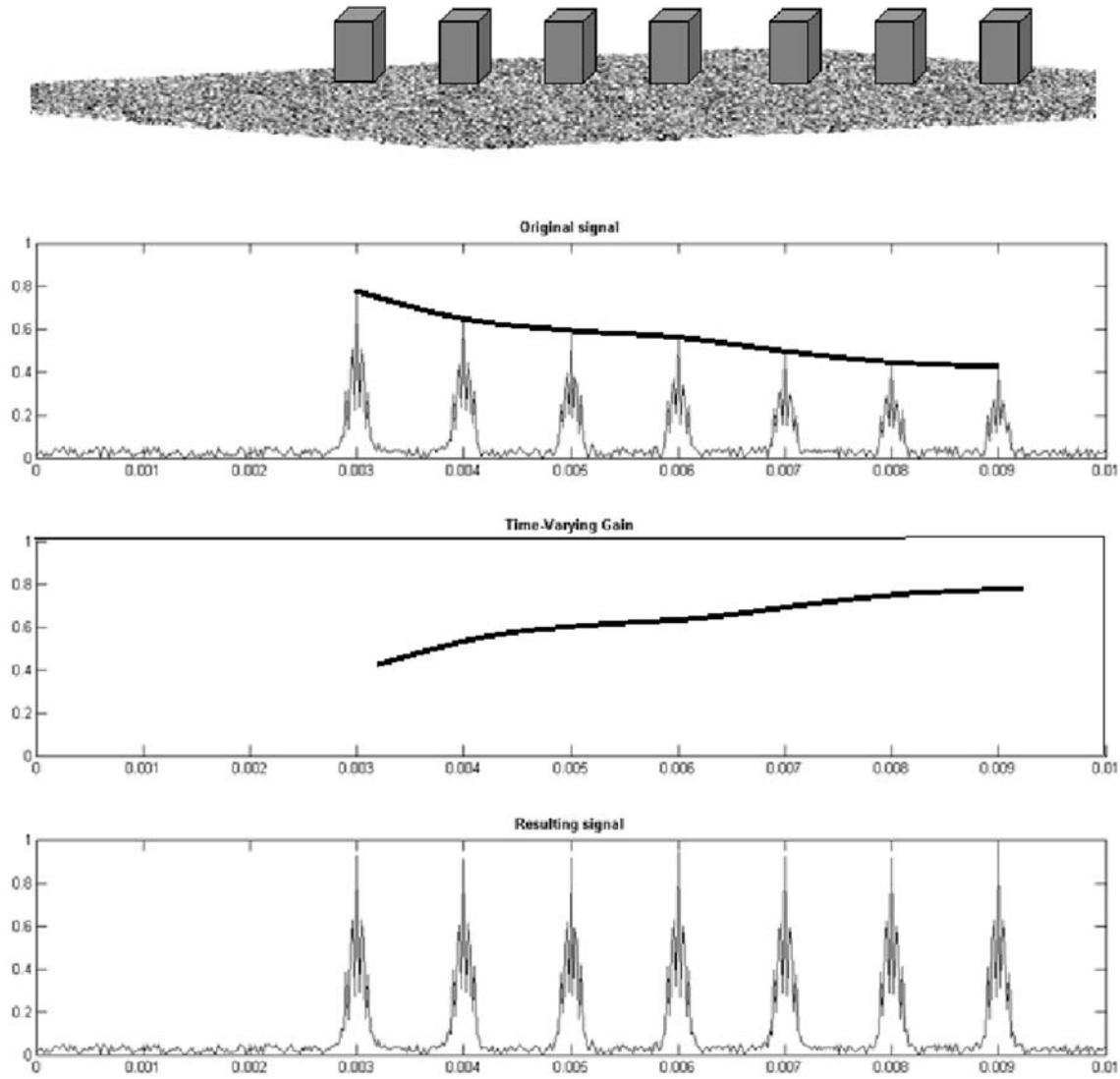

Figure 4.12. Principle of time-varying gain (TVG), shown with a series of identical targets (e.g., concrete blocks placed at regular intervals). The backscatter would decrease with increasing range (top plot) and needs to be compensated with a time-varying gain (middle plot). The resulting signal (bottom plot) should show identical backscatter for each target.

Variations in backscatter conditions may result in intensity patterns which are not completely compensated for by the TVG corrections, and "fine-tuning" might be required. This usually manifests itself as systematic along-track variations (along-track striping). They are corrected by reassessing the time-varying gains or, more

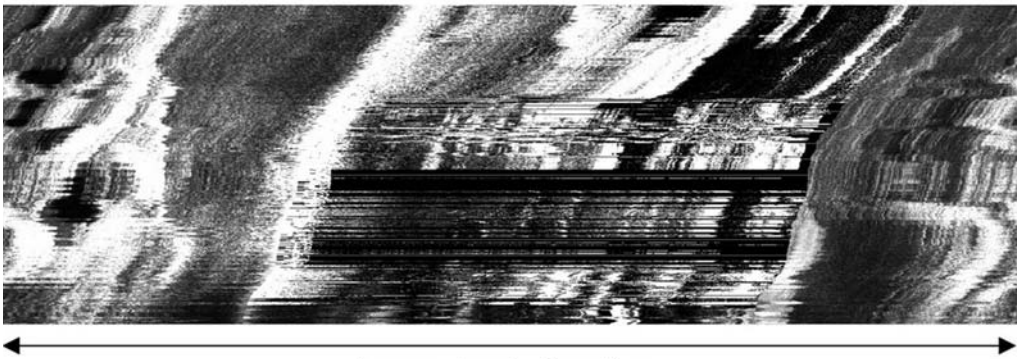

Figure 4.13. Examples of along-track and across-track striping in 30 kHz TOBI imagery.

easily, by averaging with the along-track profiles computed for each angular bin. This empiric correction can be planned for by surveying a flat, featureless portion of the seafloor (e.g., abyssal plain or mud flat). The resulting tables are used to apply an angle-varying gain (AVG) to amplify each backscattered return according to its arrival time.

4.5 GEOMETRIC CORRECTIONS

4.5.1 Slant range correction

Raw sidescan sonar imagery also presents important across-track geometric distortions, known as slant range distortions. They occur because sonar systems actually measure the time for a transmitted pulse to travel from the transducer to the target and back to the transducer. Figure 4.14 shows the slant range distortion: two targets close to the nadir (D_1 and D_2) will have nearly identical slant ranges R_1 and R_2. Conversely, two targets at far ranges (D_3 and D_4), at the same distance from each other, will be associated with very different slant ranges R_3 and R_4 and therefore placed further apart. Without slant range correction, near-range areas are more compressed than far-range areas. Some specific applications do not use slant range correction because they need to keep the information just below the sonar's track: fisheries and some target search surveys, but these uncorrected images are definitely not accurate representations of the seafloor.

Slant range correction is a remapping of pixels from their apparent position to the true one and is computed from the elapsed receiving time and the sonar platform's height. It should take into account the variation of sound velocity and depth at the point of interest. In practice, neither is done because only the pixels within one or two water depths are remapped by much more than one pixel dimension and in this region the error involved in assuming rectilinear propagation is small. At further ranges the

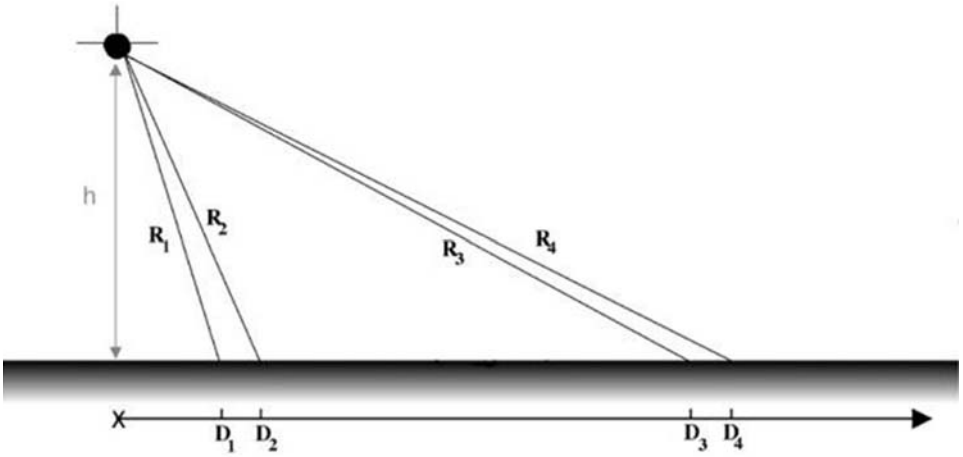

Figure 4.14. Slant range distortion: pairs of targets at the same distance from each other will appear much closer than they are at near ranges (e.g., targets D_1 and D_2) and much farther at far ranges (e.g., targets D_3 and D_4).

remapping is too small to show the error. Therefore, assuming a flat seafloor, the correct distance on the ground is:

$$D_i = \sqrt{\left(\frac{cT_i}{2}\right)^2 - h^2} \tag{4.3}$$

where $R_i = cT_i/2$ is the slant range distance of pixel i at time T_i; c is the local sound speed; and h is the local height of the sonar platform above the seabed.

Slant range correction assumes a flat seafloor across-track. This can be a problem in areas of high relief, creating two sorts of artifacts: layover and foreshortening (see Chapter 10, ''Anomalies and artifacts''). When bathymetry is available, this should be included in the later stages of processing. More complex expressions of Equation (4.3) could also include variations in sound speed, although vertical variations would mostly be important in very shallow water and horizontal variations in complex oceanographic settings (e.g., cold or hot seeps, or in harbours).

4.5.2 Anamorphosis

After slant range correction, the sonar image is geometrically correct across-track, or as close as it can be. The along-track correction accounts for the variations in platform speed (Figure 4.15). This process, called anamorphosis, produces an image in which the inter-pixel spacing is the same across-track and along-track. The nominal along-track spacing is determined by either the width of the horizontal beam on the ground or the distance travelled by the transducer during the reception interval, whichever is smallest. Successive lines are replicated if the local speed produces a smaller along-track resolution (higher speed), and sub-sampled if the

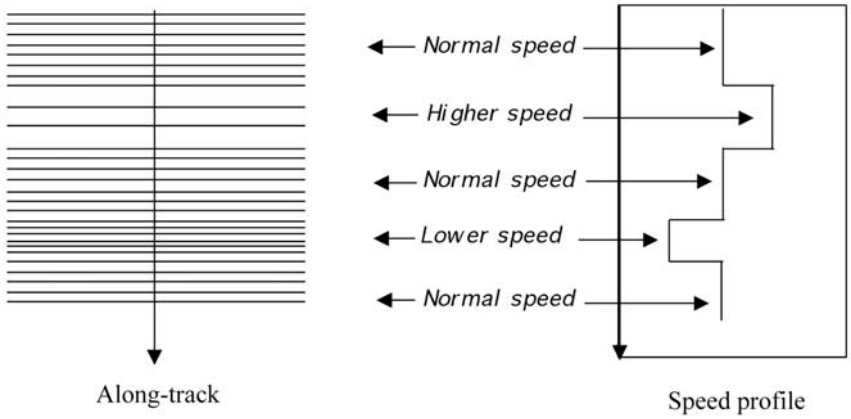

Figure 4.15. Variations in the survey speed create distortions in the along-track footprint. These distortions are corrected through anamorphosis.

speed is lower. The anamorphic correction aims at producing an image with a 1:1 aspect ratio, in which ground features are correctly represented with the right aspect ratio.

4.6 BATHYMETRY PROCESSING

Section 3.3 showed how bathymetry could be "unwrapped" from raw phase measurements, whereas Section 3.4 showed how any type of bathymetry (e.g., from a multibeam sonar or from a base map) could be used in conjunction with the sidescan sonar imagery. Sidescan sonar bathymetry can be geometrically corrected using the same steps as sidescan sonar imagery (Section 4.5), as this ensures all measurements are placed on their correct positions on the ground.

A strong advantage of sidescan sonar bathymetry is that it is exactly co-registered with the sidescan sonar imagery and can be used to refine its processing. But an inconvenient is that it is by nature more noisy, and in practice final maps may have a slightly lower resolution. Looking at the statistical errors and measures, such as total propagated error, some modern multibeam tools (e.g., CARIS) provide maps of the weighted bathymetric uncertainty to rapidly identify areas where processing should be refined.

Other corrections, akin to the radiometric corrections of sidescan sonar imagery, are necessary when the bathymetry shows obvious artifacts or does not correspond with expectations. On a larger scale, systematic deviations along-track and across-track can be explained by the use of incorrect sound velocity profiles or, in some areas, the absence of appropriate tidal corrections. Systematic variations across-track, repeated line after line, can come from incorrect unwrapping of the phase or inherent uncertainties (e.g., close to acoustic shadows). Local noise in the bathymetry is mainly represented by spurious values and line dropouts. Spurious values

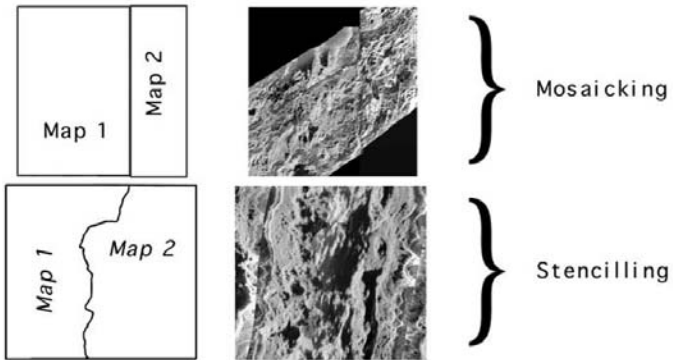

Figure 4.16. Overlapping images can be merged by mosaicking or stenciling.

can easily be median-filtered. Line dropouts, as well as small gaps in the acquisition or between individual swaths, are dealt with during interpolation. Bathymetry is usually interpolated in three or four stages, with increasing resolution. At each stage, the original bathymetry can be appended to the interpolated one, in order to ensure convergence.

4.7 MAP PRODUCTION

4.7.1 Mosaicking/Stenciling

The processed sidescan sonar imagery is composed of picture elements (pixels) organized into one or several images. These pixels are located by relative coordinates, usually respective to the upper left corner of the image. Georeferencing, also known as geocoding, is the transformation of these relative coordinates into absolute coordinates such as latitude and longitude. It is the first step toward the merging of images and the production of maps. Georeferencing also includes rectification of the image(s) to a particular map projection (Mercator, UTM, Lambert–Gauss, etc.)

The merging of different images can be decomposed into two parts: stenciling and mosaicking (Figure 4.16). When the boundary between two overlapping images is linear, or when overlapping pixels values can be averaged, mosaicking merges them into a single dataset. But, when the border between these images is more complex or when averaging of pixel values is to be avoided, the boundary is defined by hand. This is stenciling. Stenciling is particularly useful when two sidescan swaths imaged with opposed directions are overlapping (Figure 4.16).

4.7.2 Interpolation/Rubbersheeting

Several interpolation schemes exist. The simple ones average overlapping pixels with the mean or median values. More complex interpolation methods are available, such as krigeing, polynomial or spline-fitting, or finite element techniques. The accuracy of the interpolation will depend on the original spacing and trends of the

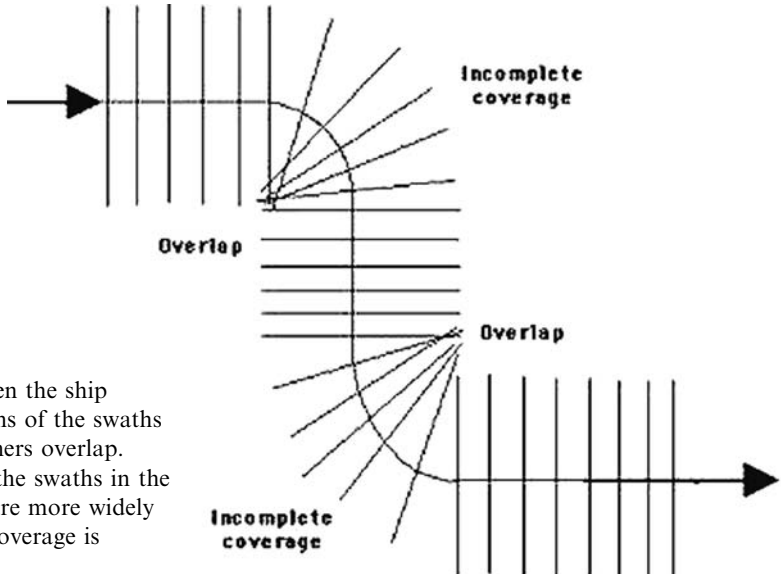

Figure 4.17. When the ship turns, the portions of the swaths in the inside corners overlap. The portions of the swaths in the outside corners are more widely spaced and the coverage is incomplete.

points. Discussion of their respective merits are given in reviews such as Lancaster and Salkaukas (1986) or Smith and Wessel (1990). Although they are more needed during bathymetric data processing, interpolation algorithms are very useful when successive swaths are overlapping (Figure 4.17) or when additional geometric corrections are needed.

The most elaborate interpolation schemes are used to "tie" an image with inaccurate or imprecise positioning to another precisely located image or series of points. This last process, called rubbersheeting, is most often used to co-register a sidescan image to a bathymetric map. For example, if sidescan data are imprecisely located because of the errors on the length of cable out (especially during a ship's turns), recognizable features (e.g., seamounts) are located on the imagery and on the (more accurately positioned) bathymetry. They serve as control points to modify the geometry of the sonar imagery so that the control points have the same coordinates. Obviously, the number of control points need to be large enough to provide a reasonable accuracy in the maps thus produced.

4.8 POST-PROCESSING

4.8.1 Image statistics

Post-processing is limited here to operations which constitute a definite plus for a correct interpretation, but do not alter significantly the quantitative information in the processed data. Other, more complex operations, which affect the measurements, will be described in Chapter 11 ("Computer-assisted interpretation").

The easiest way to measure the information in the image uses first-order statistics (i.e., the relative frequencies of appearance of different grey levels). The distribution of these frequencies is plotted through histograms (see Figure 4.18). Its shape helps define the data statistics: unimodal (a single peak) or multimodal (several peaks), smooth or irregular, compressed or well spread, etc. From its limits, the minimum grey level $I_{\min}$ and maximum $I_{\max}$ found in the whole image define the dynamic range D:

$$D = I_{\max} - I_{\min} \tag{4.4}$$

The contrast C measures the separation of pixel values within the histogram:

$$C = \frac{I_{\max} - I_{\min}}{I_{\max} + I_{\min}} \tag{4.5}$$

If grey levels are grouped around a single peak, the image will have a low contrast. Conversely, if the grey levels are spread evenly throughout the histogram, the contrast will be higher. If the image is uniform and only presents one grey level, the contrast is minimal. Associated measures of grey level distribution are the mean, the median (most frequently occurring grey level), the standard deviation, and other statistical moments such as skewness or kurtosis.

Their repartition is shown on the TOBI image in Figure 4.18 (from Blondel and Murton, 1997). This image is coded on 8 bits (i.e., 256 grey levels between 0 and 255). The minimum grey level is $I_{\min} = 54$, the maximum $I_{\max} = 251$. The dynamic range is quite important, $D = 197$ (i.e., 77% of the available dynamic range), as is the contrast ($C = 0.64$). The mean value is 122, the median value 116, and the grey levels are grouped around the mean with a standard deviation of 52. The two principal regions visible in the histogram are the peak of low grey levels corresponding to the shadows (in darker tones in the image), and the smooth central region of freshly erupted basalts.

4.8.2 Histogram manipulations

The "quality" of an image is very subjective, even with the numerical descriptors presented in Section 4.8.1: Is a higher contrast necessarily better? What would be the optimal contrast? Therefore, image enhancement is not aiming at increasing the "quality" of the sidescan sonar image, but at increasing the separation between different regions deemed interesting by the interpreter. Most enhancement operations are mathematical manipulations of the grey levels. Histogram-sliding consists in adding (or subtracting) a fixed value to all pixels in the image, hence "sliding" or shifting the histogram from one side of the dynamic range to the other. If the offset is too large, the histogram will be truncated: some grey levels will be forced to the minimum of the range (under-saturation) or to the maximum (saturation).

Similar to histogram-sliding, histogram-stretching redistributes the pixel values in order to increase the contrast and dynamic range, by multiplication by a constant

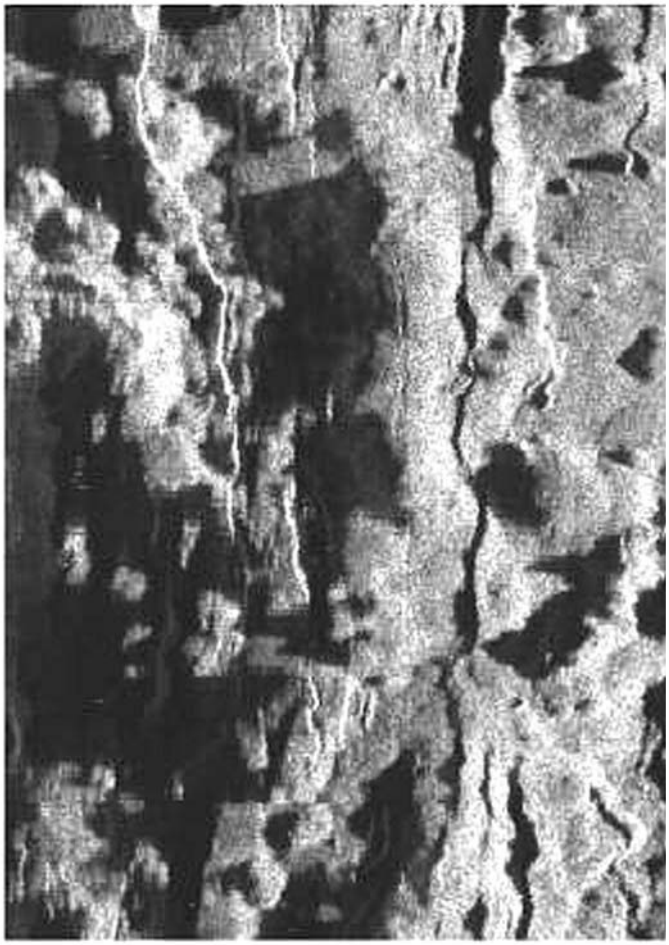

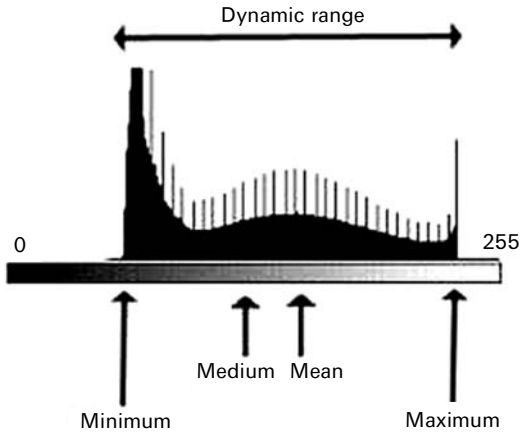

Figure 4.18. The aspect of an image can be described by its histogram and the resulting statistics. See text for additional explanations.

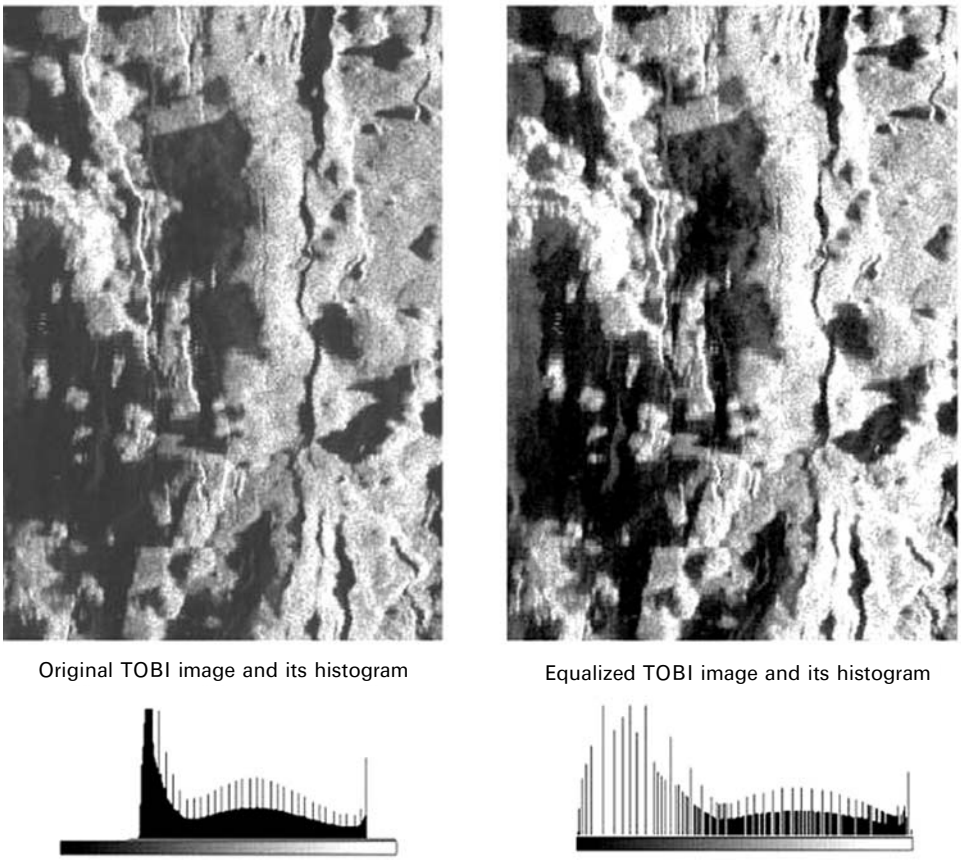

Figure 4.19. Example of histogram equalization. The original TOBI image (left) shows a histogram with a high number of dark pixels. The histogram of the equalized image (right) shows increasing contrasts for most common grey levels, and decreasing contrasts for the others (from Blondel and Murton, 1997).

and rescaling. For an image quantized on n bits, each new grey level will be given by:

$$I_{\text{new}} = \frac{I_{\text{old}} - I_{\max}}{I_{\max} + I_{\min}} \times (2^n - 1) \tag{4.6}$$

Histogram-stretching can also produce grey levels outside the range available. Its main advantage is to usually improve the appearance of poorly contrasted images with a small dynamic range.

These two operations, sliding and stretching, are usually combined into "histogram equalization" (Figure 4.19). The idea is to adjust the new pixel assignments to specific grey levels so that there are an equal number of pixels with each new amplitude value. For example, if 64,000 pixels are to be displayed along 64 grey levels, histogram equalization will partition the range of values in 64 intervals with

around 1,000 pixels each. The effect of equalization is to expand the contrast between grey levels that occur frequently and to decrease the contrast between those pixel amplitudes that occur infrequently, using the limited amount of available image contrast where it is most effective. To further enhance details in specific regions, other histogram manipulations are available: piecewise stretching to stretch independently different portions of the histogram, linear stretching, stretching according to predetermined histogram shapes, etc. These mathematical operations necessary to enhance basic images are described in standard image-processing textbooks (e.g., Watt and Policarpo, 1998; Mather, 2004; and many others).

4.8.3 Speckle removal

Speckle is a high-frequency noise commonly observed in sidescan sonar imagery (Figure 4.20). It is in fact common to all types of remote sensing using coherent radiations as a source of illumination (i.e., radar as well). After interaction with the seafloor, the acoustic waves are no longer in phase. And positive or destructive interferences may occur, producing anomalously high or low returns. Because speckle is difficult to distinguish from real signals at the limit of resolution of the sonar, it proves hard to remove without affecting significantly the image. Numerous algorithms are available in the literature, from the "quick and dirty" (the mean filter, which averages the speckle in the data but lowers the resolution) to the most elaborate (using simulated annealing algorithms). Common techniques use the local statistics computed on several images, a process known as "multilooking". Local distributions of grey levels are approximated by Gaussian or gamma statistics. Mean and variance are computed on small moving windows, and pixels with mean and variance too far from the image mean are considered as speckle and averaged. The results vary from one sensor and one wavelength to another, and no generic despeckling algorithm has yet been found. Moreover, certain applications (e.g., target searches) are looking at the limit of resolution of the sonar, and despeckling can lose valuable data.

Figure 4.20. Example of speckle (high-frequency noise) in a sonar image.

4.8.4 Sea surface reflection removal

When the swathwidth is less than the water depth, sidescan sonar imagery might be affected by reflections from the sea surface. The first reflection is formed when the sonar beam reflects once from the seafloor and once from the sea surface (Figure 4.21). It manifests itself as bright lines parallel to the sonar track, at a distance from the sonar track roughly equivalent to the water depth. If the swath is wide enough, subsequent multiples will also be present as equidistant bright lines parallel to the first reflections. They occur principally in sedimentary areas where the seafloor is flat and smooth. Traditional methods attempt to remove multiple reflections by spatial or frequency filtering. Crosby and Cobb (2005) use binary morphology on threshold-limited regions, looking for hourglass templates typical of surface reflections and unprocessed altitude variations. Working with processed imagery, LeBas *et al.* (1995)

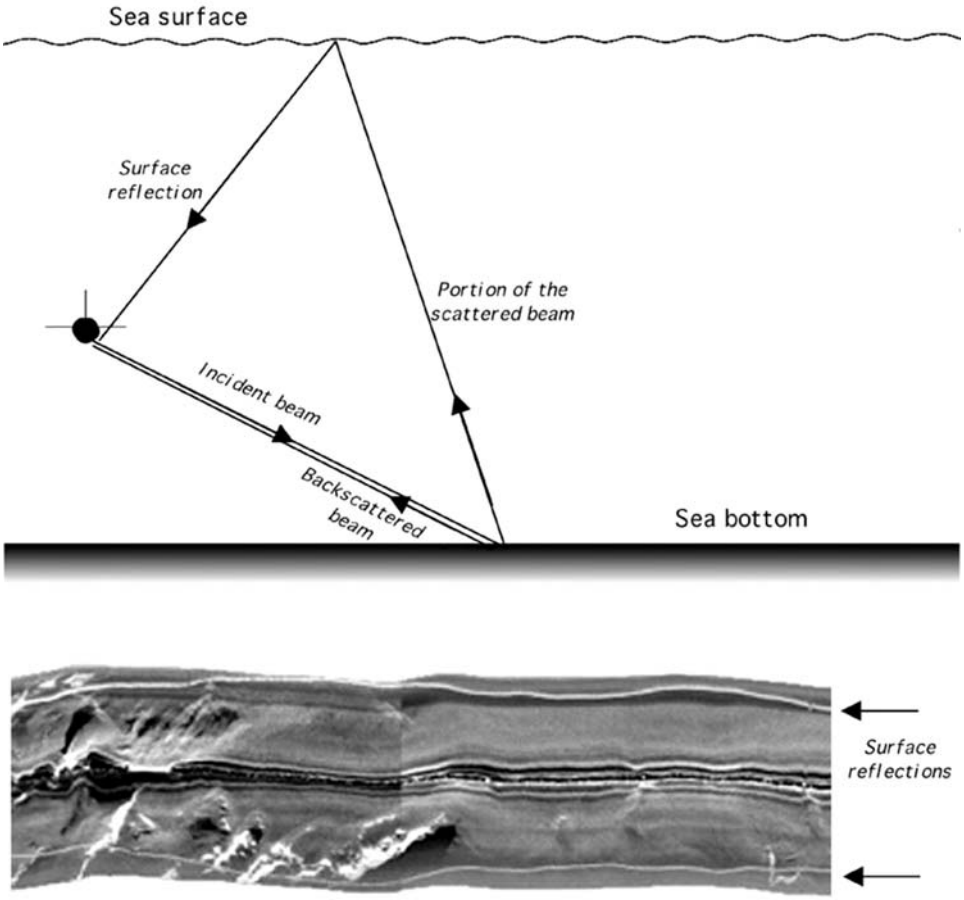

Figure 4.21. Multiple reflections on the sea surface may affect sonar images acquired in shallow waters. The continuous white lines at the far range of this TOBI image are typical examples.

identify the multiples explicitly, by looking at intervals centered on across-track distances where multiple reflections are most likely to occur; that is $(n+1)$ times the water depth, minus the towfish depth. Searching is conducted within range intervals typically one-tenth of the depth. Pixel values flagged as surface reflections are replaced by linear interpolation, and random noise added to avoid an overly smooth appearance. Tried and tested on numerous datasets, this method has proved its robustness.

4.9 OPERATIONAL EXAMPLES

The increased availability of sidescan sonars, and the important advances in both computing power and data storage, mean there are now many software packages available to process sidescan sonar measurements. Some are vendor-specific, often coming with the instrument when it is bought/rented, and others have been derived from local efforts at institutions or laboratories. These software packages are increasingly able to cope not only with sidescan sonar data in different formats, but also to add additional data (e.g., sub-bottom profiler or multibeam bathymetry) and produce highly accurate maps. Listing the large number of software packages available on the market, their constant evolution, and comparison of their relative capabilities is beyond the scope of this book. Instead, this section will focus on two distinct applications, experienced at first hand by the author.

The academic software package PRISM (processing of remotely sensed imagery for seafloor mapping) is command-based and was developed at the National Oceanography Centre, Southampton, U.K. to deal with many types of sidescan and bathymetric datasets (e.g., Searle *et al.*, 1990; LeBas *et al.*, 1995; LeBas and Hühnerbach, 2000). Originally building on the Woods Hole image-processing software (Chavez *et al.*, 1986), PRISM has steadily developed into a standalone academic software package now favoured by many institutions (it is free for *bona fide* academic researchers). As a base for image processing and Geographic Information Systems, ERDAS^{TM} Imagine is used in conjunction with PRISM to produce final maps and any post-processing. Combined with 3-D visualization software like Fledermaus^{TM}, it is a versatile and straightforward example of thorough sonar processing. It accepts many input formats, and its open-source configuration allows in principle checking all the operations done during the processing (i.e., no "black box"). Figure 4.22 shows typical output from PRISM.

The following example comes from the author's direct experience with PRISM; however, the rapidly evolving nature of the system means it can only provide a broad picture. In this application, TOBI sidescan sonar imagery was acquired on a mid-ocean ridge, and supplemented with multibeam bathymetry (at a scale ten times larger). The first step consisted in estimating the position of the TOBI platform, towed a fair distance behind the vessel. This was achieved by smoothing the ship's track and using simple trigonometry, using the length of cable deployed and the altitude of the platform above the seabed. Vehicle altitude data were also filtered, using a 280-second median filter. Occasionally, transmit and receive systems would

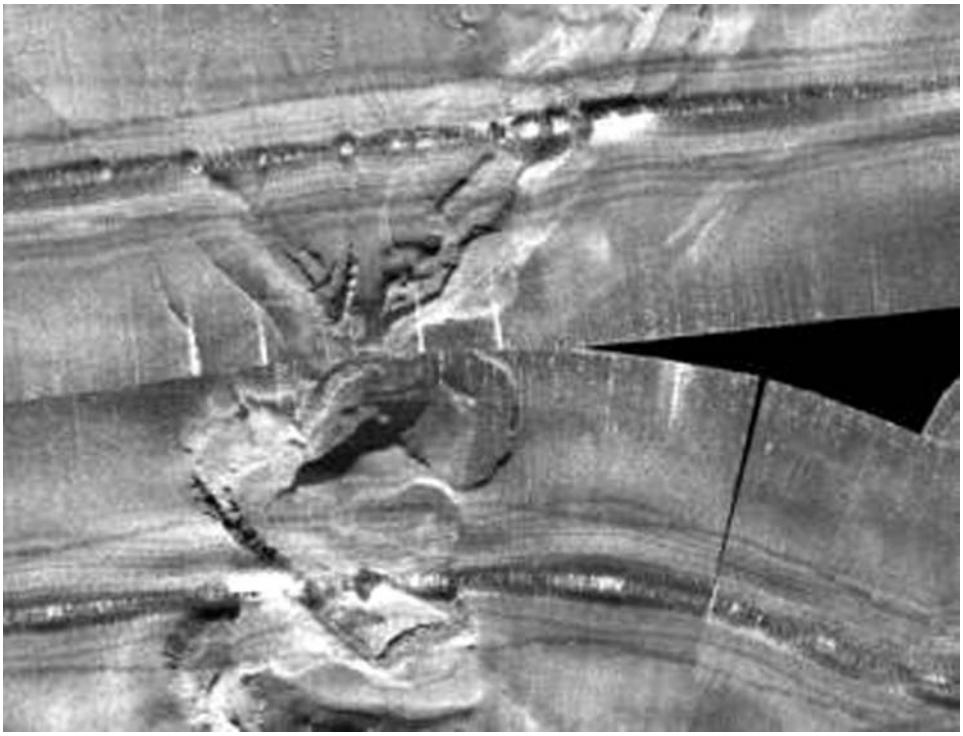

Figure 4.22. Mosaic of TOBI sidescan sonar imagery from the Andarax Canyon (Spain), calculated with PRISM onboard BIO *Hesperides* (HITS-2001 cruise, chief scientist E. Grácia). Note how stencilling retains details associated with imaging structures from different angles, and how curved swaths nicely abut each other once navigation has been fully processed.

become asynchronous and miss an entire swath of data, leaving it unrecorded. A dummy line (replicated from the previous line) was then added to the image to maintain its geometry. As the TOBI data were acquired, a time-varying gain was applied within the hardware, accounting for attenuation of the signal with increasing range. For a uniformly grey across-track return, this creates small steps in the contouring of the recorded imagery. To correct this, a smooth graph of the TVG was created and compared with the quantized TVG, and then applied to the relevant pixels. Geometric corrections included the slant range to ground range correction, using the smoothed altitude of the vehicle. After these corrections, each pixel is 6 meters across-track. For anamorphosis, variations in the ship's speed were accounted for and swath lines replicated or removed accordingly. The final image had a pixel size of 6 meters. Noise present in the imagery fell into three categories: sharp, single-pixel peaks (removed by median filtering); partial swath lines with anomalously low intensities; and partial dropouts (replaced through nearest-neighbour interpolation). Sea surface reflection, clearly visible in some swath lines, could be easily removed. In the last stage, TOBI imagery is projected on a geographic

map. Adjacent or overlapping swaths are colour-coded differently and added successively to the final mosaic, using either pre-defined trimming masks or, preferentially, user input (as this is the best way to ensure that important features are ensonified from the correct angle and not masked or blurred). Checking against raw mosaics produced onboard allows identifying the artifacts or (more generally) the enhancements brought by digital processing. The final sonar mosaics can then be imported into ERDAS, for co-registration with bathymetry (using rubbersheeting if necessary), fusion with other data layers, and production of 3-D views for interpretation.

Coming from a different perspective, MosaicBasic™ is the latest processing tool from Triton Imaging Inc., using files already processed by Isis® SS-Logger™. With functionality similar to PRISM, SS-Logger provides access to most if not all the operations outlined in this chapter. Windows-based, this stand-alone software can accept most major sonar data formats. MosaicBasic can accept individual survey lines, which can be moved relative to one another and displayed in either "cover-up" or "shine-through" mode (but they cannot be stencilled, contrary to PRISM). Processed mosaics can then be exported as GeoTiff files to tools like Triton Perspective™ for further interpretation and presentation. Figure 4.23 shows a mosaic processed by the author from the demonstration sonar dataset.

These rapid examples are limited in scope: they merely intend to show how the reality of sonar processing has progressed in the last 10 years. Many other software packages though not presented here are still definitely of interest; for example, Xsonar (Danford, 1997) and commercial products such as Coda GeoSurvey (*www.codaoctopus.com*), GeoTexture (*www.geoacoustics.com*), SwathPlus (*www.sea.co.uk*).

4.10 INTERPRETATION OF SONAR IMAGES

The sidescan sonar images created by these systems are visually attractive, especially when complemented with bathymetry or presented in 3-D, and look like visual pictures of the seabed. But, as presented here and in the previous chapters, they are the result of more complex physical processes and cannot be interpreted as easily. Before attempting any interpretation of sidescan sonar imagery, it is important to know a number of details about the acquisition system, the survey method, and the way the data were processed. When trying to identify specific features within sonar images, it is important to know a number of key parameters: resolution of system, range of targets, depth beneath the sonar, geological context (i.e., deep-ocean, continental shelf, etc.). Furthermore, at frequencies used by sidescan sonars (roughly from 5 kHz to 1 MHz), the backscattering from the seabed can generally be separated into surface and volume contributions (Figure 4.24). Part of the energy is scattered by the surface itself: sub-horizontal facets, close to normal incidence, or micro-scale roughness, at increased grazing angles. Another part penetrates the seabed and is backscattered by volume heterogeneities. The relative importance of each process (surface or volume) will vary with the angle, the acoustic wavelength relative to the spatial wavelengths of structures on/in the seabed, and the geotechnical properties of

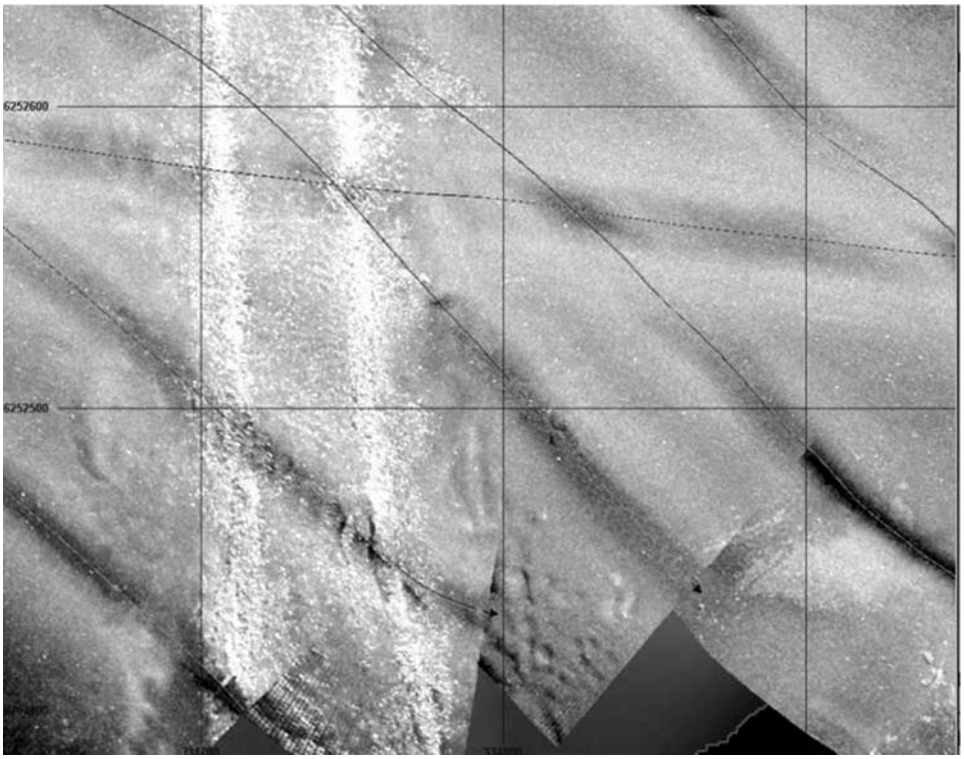

Figure 4.23. Mosaic of demonstration sidescan sonar imagery from Sidney Harbour (Australia) as obtained with MosaicBasic^{TM}. Oblique lines correspond to the survey lines. Individual structures are clearly defined, even though the merging of overlapping swaths loses details associated with the different imaging angles (from Triton Imaging Inc.).

the seabed. They can be predicted quantitatively using the acoustic models presented in Section 2.2.3, but only if the sonars are accurately calibrated.

For experienced interpreters of sidescan sonar imagery, these parameters are automatically taken into consideration. However, to aid the processes of interpretation, or at least an understanding of how to make an interpretation, we have compiled a checklist of parameters that need to be considered (Figure 4.25). By repeatedly referring to this checklist when confronted with new sidescan sonar images, the methodology behind the interpretations should become clear, and users will gain confidence in making their own interpretations.

- *How?* How was the image acquired? Most important is the type of sonar, and the frequency it transmits and receives. As emphasized in previous chapters, the response of the seafloor will differ with frequency. A surface smooth at low frequency (i.e., long wavelength) may appear rougher at a higher frequency (i.e., shorter wavelength). Equally important is knowledge of the configuration in which the sonar was used. Was it hull-mounted or deep-towed? How high was

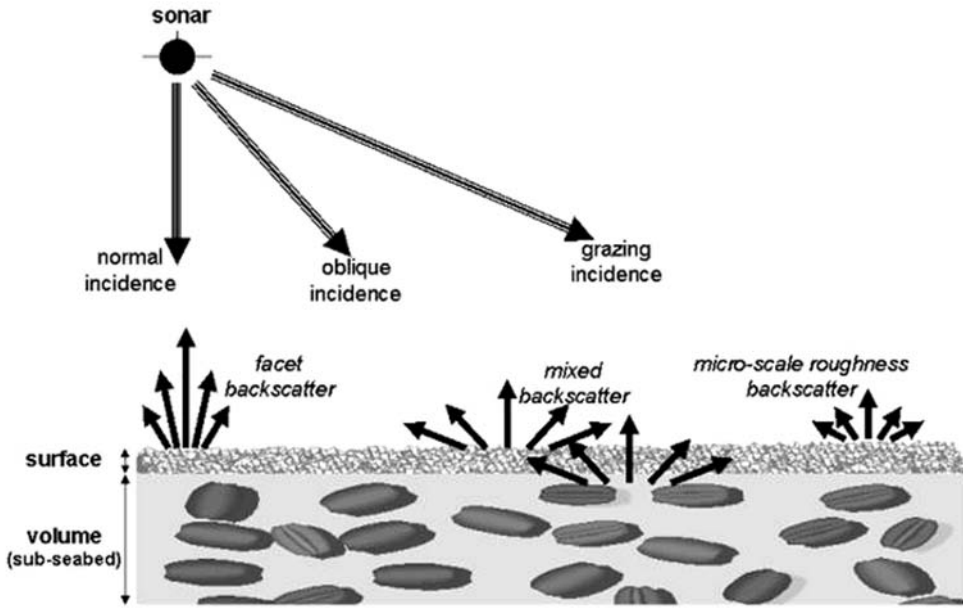

Figure 4.24. Depending on the local angle of incidence, different physical processes will be predominant. They will involve surface and (in some cases) volume contributions from the seabed (adapted from Lurton, 2002).

it above the seafloor? Information about the beamwidth(s) and swathwidth will prove most useful when looking at the ground resolution. Whatever the sonar platform is, one must also know precisely its heading and speed variations. Were there any sudden accelerations? Was the platform zigzagging or going straight? Variations in attitude (roll, pitch, and yaw) also need to be known. As mentioned in Section 4.3.4, unprocessed variations in attitude have been shown to drastically change the shape of objects on the seafloor, or even separate them into what appears to be distinct pieces.

- *How?* How was the image processed? Was the image we are looking at processed in an analogue fashion, or digitally? The potential application of time-varying gains (TVGs) yields varying backscatter levels for the same types of objects or processes along the survey line. Conversely, angle-varying gains (AVGs) would create across-track variations of backscatter. Another crucial point to consider is the presence or absence of slant range correction and anamorphosis, because they influence the shapes of each identifiable object and how close they are to reality.
- *What?* What are the characteristics of each of the regions of interest inside the image? Primarily, what was the imaging geometry? Each morphological region or object will appear differently whether it was imaged at near range or far range, with a sub-perpendicular sonar beam or at low grazing angle, or if both ranges and angles are varying across the region.

- *What?* What does the acoustic backscatter look like for the region of interest? Are the values relatively low or high, homogeneous or heterogeneous, contrasted or not? What is the texture of the target (smooth or grainy or mixed)? Are there any organized patterns inside the region, or is the texture random?
- *What?* What is the relation of the region/object with its surroundings? This concerns not only the dimensions of the region, but also includes connection with the regions/objects around it, and extraction of its 3-D aspect from the 2-D sonar image.

The last point of the checklist in Figure 4.25 reminds us of the need to keep an open mind in interpreting an image. Plausible alternatives should be considered. The author remembers a high-resolution survey from an abyssal plain, where smooth and featureless terrain showed a long, linear, and very reflective line of rough reflectors. Based on its size, and on his willingness to find shipwrecks, an interpreter decided it was a shipwreck, and could even identify with great certainty it was a Japanese tanker from the 1960s (based on lengths, variable widths, and proximity to Japan). Based on this forceful interpretation, a submersible was lowered down, and after several hours revealed the object in question was in fact a series of pillow lavas on a ridge (confirming a more detailed analysis of the sonar imagery and bathymetry). Chapter 10 (''Anomalies and artifacts'') will present other examples where interpretation should be made with caution, and where its limits should be kept in mind.

By answering these questions one by one, the interpreter should be able to restrict the hypotheses to only a few, and correctly identify the different features in the sonar image. A reasonable knowledge of the region surveyed, its context, and of what to expect is of course helpful to the final interpretation. The following chapters will show the application of these principles to sonar imagery taken in all marine environments with as wide a range of instruments as possible.

Like imagery, bathymetry on its own can be interpreted in the same way. For each identifiable region, imaging geometry and range should not influence topography measurements, unless part of the region is imaged at very far range with an interferometric sonar. In general, the interpretation of bathymetry, alone or in conjunction with imagery, should make a clear distinction between co-registered bathymetry at the same scale (e.g., from the same or another interferometric sidescan) and bathymetry at another scale or from another sonar (e.g., from multibeam, possibly not exactly co-registered; control points should then be used to control the interpretation).

Because of their low grazing angles at far ranges, sidescan sonars are more prone to shadows (Figure 4.26). These shadows have very low or non-existent acoustic returns, and can also create artifacts when unwrapping phase bathymetry (e.g., Lurton, 2002).They can however contribute to the interpretation. Shadows will be related to the grazing angle and the height of the masking object, and they can be analysed to derive estimates of the shape and size of this structure. The height h of the object in Figure 4.26 can be calculated using the length ΔR of its shadow zone, its

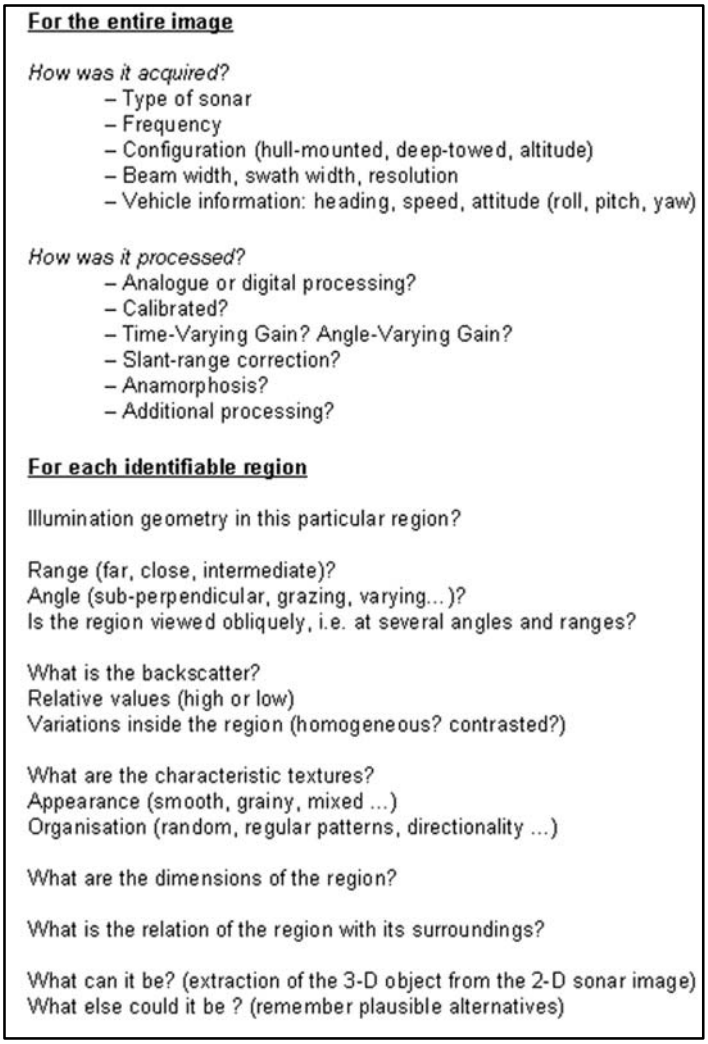

Figure 4.25. Interpretation checklist (see text for details).

maximum range R, and the height H of the imaging sonar above the seabed. From trigonometric considerations, one deduces:

$$\frac{H}{R} = \frac{h}{\Delta R} \quad \Leftrightarrow \quad h = \Delta R \times \frac{H}{R} \tag{4.7}$$

As sidescan sonars are designed to ensonify the seabed at grazing incidence, the slightest height variation on the seabed will create acoustic shadows much larger than the object being ensonified. These shadows are often very helpful in identifying objects. Figure 4.27 shows, for example, a 1,200 kHz image of a sunken bicycle. The high acoustic reflectivity shows there is an object on the seabed, and its regular

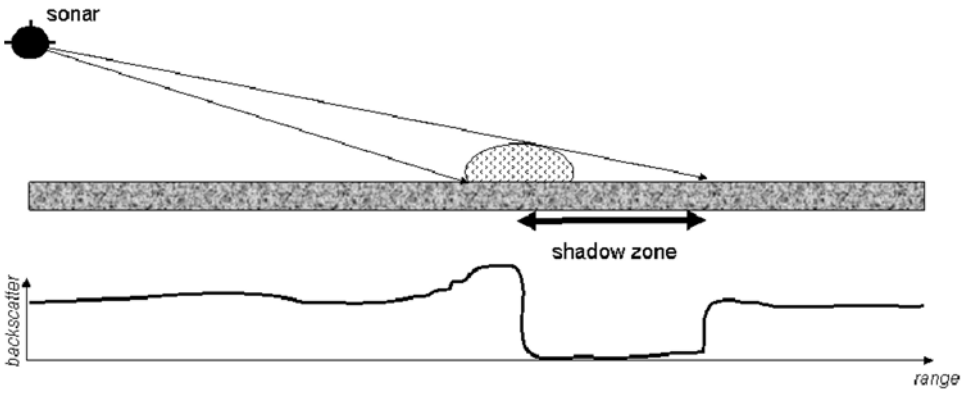

Figure 4.26. Formation of acoustic shadows.

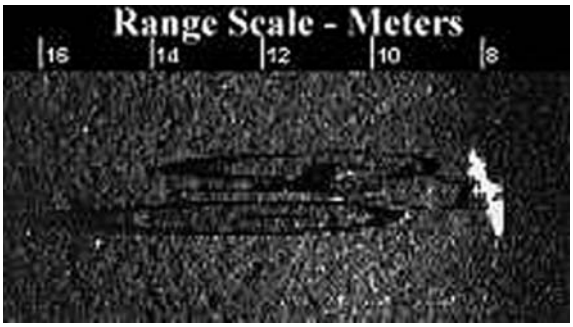

Figure 4.27. Sidescan sonar image of a racing bicycle, imaged at 1,200 kHz (courtesy Pete Wilcox, Marine Sonar Technology, 1997). The pattern of high acoustic returns clearly shows this is a man-made object, but it is the acoustic shadows alone that reveal the true nature of the object (and the fact it is lying upside down). Note also the exaggeration of the shadows, brought about by the imaging geometry (© Marine Sonar Technology, 2003).

shape shows it is most likely man-made. But most of the information in this case comes from the shadows, using which one can make out many small-scale details, including the drive chain and front forks. One can also see the bicycle is resting upside down. But the shadows are greatly exaggerated (8 m long in this case), and the imaging geometry should be kept in mind (cf. Figure 4.26).

4.11 CONCLUSION

In the course of this chapter, we have endeavoured to present all stages of a comprehensive processing of sidescan sonar imagery. This processing has been broken down into its logical order (Figure 4.28): pre-processing of navigation and attitude data, radiometric corrections, geometric corrections, etc. All these stages are desirable, but some are not always achievable. At the time the *Handbook of Seafloor Sonar Imagery* was written (1997), this was because of the computing power needed,

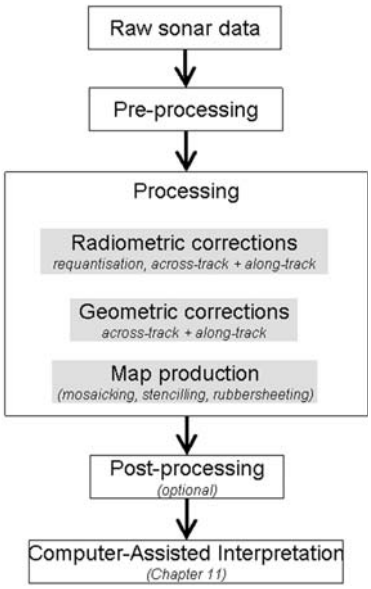

Figure 4.28. Typical data-processing chain. All stages are desirable, but some will not be achievable, due to operational circumstances or lack of input data. Several iterations might be necessary (e.g., if processing reveals systematic navigation offsets).

or because of the lack of available software (at this time, only PRISM could satisfactorily process turns in the surveys). Progress on both fronts means it is generally not a problem now. Restrictions now are more likely to stem from operational circumstances or the lack of input data of the desired quality (e.g., navigation recorded at the right rate, or attitude sensors on the sonar transducer). The interpretation checklist (Figure 4.25) shows how this can all be accounted for when analysing the image products. The following chapters will be devoted to representative examples of the different environments.

4.12 FURTHER READING (*see also* References at end of book)

About navigation (above and under water)

Alcocer, A.; P. Oliveira; and A. Pascoal (2007). Study and implementation of an EKF GIB-based underwater positioning system. *Control Eng. Practice*, **15**, 689–701.

Lancaster, P.; and K. Salkaukas (1986). *Curve and Surface Fitting: An Introduction*. Academic Press, London, 280 pp.

Leonard, J.; A. Bennett; C. Smith; and H. Feder (1998). *Autonomous Underwater Vehicle Navigation*, Tech. Memo. 98-1. MIT Marine Robotics Laboratory. Available at *http://cml.mit.edu/~jleonard/pubs/tech_report981.pdf*

Robertson, K.G. (1990). Deep sea navigation techniques. *Marine Geophysical Researches*, **12**, 3–8.

Thomas, H.G. (1994). New advanced underwater navigation techniques based on surface relay buoys. *Proc. IEEE-OCEANS '94, Brest*.

Thomas, H.G. (1998). GIB buoys: An interface between space and depths of the oceans. *Proc. IEEE AUV, Cambridge, MA*, pp. 181–184.

About image processing

Mather, P.M. (2004). *Computer Processing of Remotely-sensed Images: An Introduction*, Third Edition. Wiley, Chichester, U.K., 324 pp.

Watt, A.; and F. Policarpo (1998). *The Computer Image*, Addison Wesley, 784 pp.

About the sonar-processing software presented here

PRISM (developed by Dr. T.P. LeBas at the National Oceanography Centre, Southampton, U.K.). Available at *http://www.noc.soton.ac.uk/gg/facilities/software.php*

Triton sonar products. Available at *http://www.tritonimaginginc.com*

5

Spreading and subduction

5.1 PLATE TECTONICS AND THE SEAFLOOR

Morphologically, mid-ocean ridges are the most complex and geologically active terrains on the seabed. They are now recognized as the places where the Earth's oceanic crust is constructed (starting with the seminal paper of Vine and Matthews, 1963). Characterized by high topographic relief, the mid-ocean ridges are dominated by volcanic and tectonic processes. Globally, over 60,000 km of mid-ocean ridges produce $\sim$35 km^3 of new volcanic crust every year. This new crust is welded to the retreating edges of the older crust as the Earth's plates move apart. Some of these plates will collide, one plate sliding below another (a process known as subduction). This oceanic crust is destroyed in deep-ocean trenches, characterized by extreme topographic relief and dominated by tectonic and sedimentary processes. Spreading and subduction are the two extreme stages of the evolution of oceanic crust, corresponding to its creation and its recycling. Since the recognition of plate tectonics in the late 1960s, there has been much theoretical and practical work on their respective mechanisms. This chapter aims at presenting the main structures that can be observed on the seabed, and how they can be related to specific volcanic, tectonic, or sedimentary processes.

Much of our knowledge of mid-ocean ridges and subduction areas has been gained using multibeam bathymetry (e.g., Wille, 2002), because of its prevalence on most survey vessels and its wide angular coverage. Figure 5.1 (see color section) shows two examples of mid-ocean ridges: the slow-spreading (1–5 cm/year) Mid-Atlantic Ridge (Figure 5.1a) and the fast-spreading ($\sim$14 cm/year) East Pacific Rise (Figure 5.1b). The morphology of a mid-ocean ridge is clearly influenced by the spreading rate. Slower spreading will result in large (several kilometers) and deep axial valleys, with central volcanic constructs and high (several hundreds of meters) valley walls, on each side of which the bathymetry will decrease to the level of the surrounding abyssal plains. Tectonic activity results in elevated topography

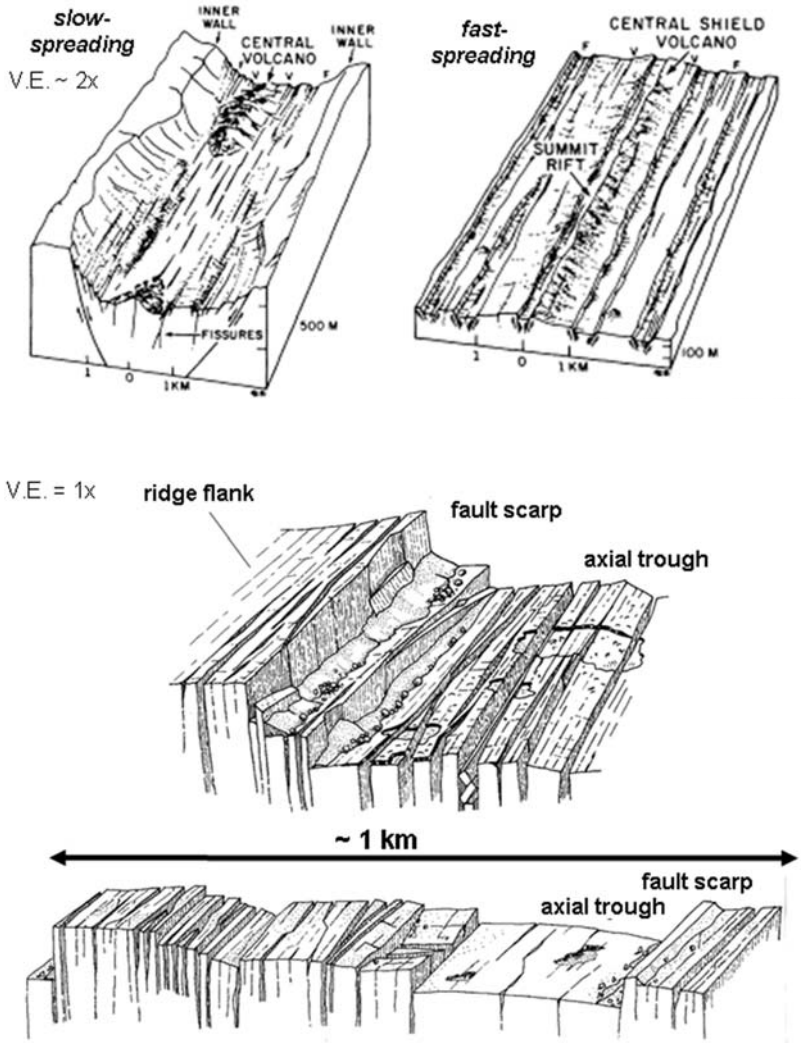

Figure 5.2. (Top) Contrasting morphologies of a slow-spreading ridge like the Mid-Atlantic Ridge and a fast-spreading ridge like the East Pacific Rise (adapted from MacDonald, 1982). Volcanism and tectonics are the main processes at play. (Bottom) Details of the typical seafloor morphology, based on sonar surveys and submersible dives (adapted from Lagabrielle, 2005).

dominated by steep and high inward-facing fault scarps bounding a central axial valley. For faster spreading rates, the ridge axis becomes a central plateau or broad dome, with an axial trough <100 m wide and 10 m to 20 m deep. They are characterized by point source seamount volcanoes and sheet flows. Their tectonic activity results in a dense population of small-throw fault scarps parallel to the ridge axis. Based on submersible dives and high-resolution observations of mid-ocean ridges around the world, Figure 5.2 shows their contrasting morphologies and the relative contributions of volcanism and tectonics. All types of ridges have now been shown to have hydrothermalism, either as isolated constructions or as complex and large groups of structures. New examples are regularly being discovered, including in places where theory was not expecting them.

Unsurprisingly, the destruction of old oceanic crust at subduction zones creates completely different seafloor morphologies (Figure 5.3, see color section). As the oceanic crust generated at mid-ocean ridges moves away, it becomes covered in a thick blanket of pelagic sediments. The oldest crust (e.g., around the northern and western rims of the Pacific Ocean) can be so dense that it sinks under its own weight. In other places, like the eastern rim of the Pacific Ocean, it is pushed under the overthrusting plate (Figure 5.4). These movements result in deep trenches, running along the length of the plate margins. A famous example is the Challenger Deep (~11,000 m) in the Marianas Trench. Faults on the sides of the trenches are often associated with landslides. In some places, old volcanoes and other structures on the subducting crust are carried into the trench, being first uplifted, then slumping into large accumulations on the inner trench wall and creating accretion prisms. Reaching several kilometers thick, these piles of wet sediments are compressed under their own weight, forcing pressurized water and mud to the surface as mud volcanoes (e.g., Dickinson and Seely, 1979). When the subducted plate begins to melt (~110 km deep), the rising material forms volcanic chains, called island arcs. Many sport hydrothermal systems. Another form of volcano, formed in the trench, is unique to the subduction zones. These are "cold" volcanoes, erupting a mineral mud called serpentine. Formed when seawater penetrates through the cracks in the walls of the trenches and reacts with the mantle rock deep within the Earth's interior, the serpentine expands and forces its way to the surface (Fryer and Fryer, 1977). It pours onto the seafloor like lava, building up the flanks of serpentinite seamounts. Fluids then deposit minerals on the seafloor as chimneys (e.g., Fryer *et al.*, 1990), similar to the black smokers of mid-ocean ridges.

Spreading centers and subduction zones are rather different, geologically and morphologically, but similar constructs can be found in both types of regions. Sections 5.2 to 5.6 examine the features that are the basic units of construction, modification, and destruction of the oceanic crust. They start by looking at the role of tectonic activity, and the obvious structures that are fissures and faults, and follow with the main types of volcanic structures, from the simplest to the most complex. The role of sedimentation and the edifices associated with hydrothermalism are then presented, before focusing on the structures typical of subduction. Section 5.7 presents regional imagery from typical sections of the slow-spreading Mid-Atlantic Ridge and the deepest segment of the Mariana Trench subduction zone.

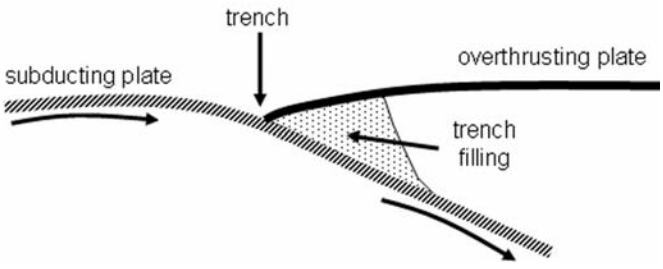

Figure 5.4. Simplistic sketch of subduction processes.

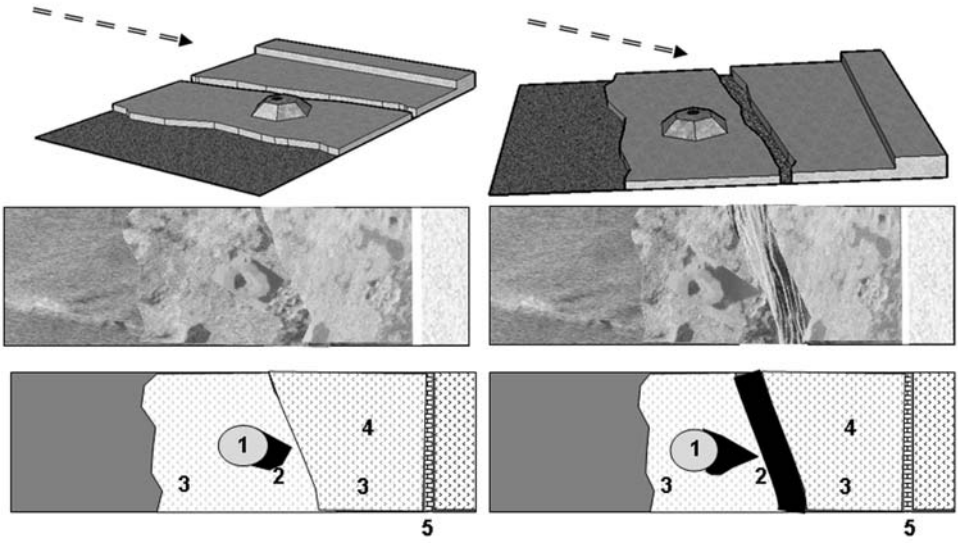

Figure 5.5. Imaging the same terrain (top) from different angles (or heights) will affect the sonar image (middle) and change the interpretation (bottom). Using a composite of typical MOR terrains for illustration, we see that (1) volcanoes and targets in general can be distorted; (2) different shadows make it more difficult to estimate their heights; (3) the boundaries and extent of different terrains might be exaggerated; (4) small fissures might not be visible any more; (5) fault scarps might appear thinner or lower.

The geological aspect of all these environments is visible with sidescan sonar, as the examples in this chapter (and the next ones) show clearly. The degree to which details can be seen depends on the type and frequency of the imaging sonar (lower frequency generally meaning lower resolution but larger coverage), on its navigation (deep-towed or not, going at a rate matching its imaging rate or not), and on the local imaging geometry. Figure 5.5 shows the generic example of a stepped terrain imaged by the same sonar from two different directions and heights. The pictures on the left correspond to a terrain imaged obliquely relative to the direction of the steps, and from a higher altitude. The pictures on the right correspond to the same terrain, imaged perpendicularly to the steps and from a lower altitude. Smooth and rough terrains will appear with similar textures, as the imaging configurations are not that different (*cf.* Figure 4.24). Volcanoes and any type of edifice on a flat seabed will be distorted, and their shadows might be shortened or extended, making it more difficult to accurately estimate their heights (cf. Figure 4.26). The boundaries of sloped terrains will also vary slightly. Small fissures might disappear altogether if imaged from the wrong direction or at the wrong angle, whereas topographic changes (the steps, here) might appear thinner or lower. All these difficulties do not prevent the generally accurate understanding of the different regions on the seabed; they just mean that any interpretation needs to incorporate all the information available (following the "interpretation checklist" of Figure 4.25). They also explain why

seabed surveying with a sidescan sonar generally follows similar configurations (e.g., flying above the center of the axial valley to image ridge-parallel faults at the optimal angles).

5.2 TECTONIC STRUCTURES

Although the seabed is formed at spreading centers by volcanic processes (cf. Section 5.3), tectonic structures are presented first, because they are easier to recognize and because they exist (with some variations) in all types of seafloor environments. At mid-ocean ridges, faults and fissures are caused by the forces stretching the ridge and pulling the global tectonic plates apart, cutting into the newly formed crust and acting through brittle extension and shear. Extensional tectonics can be perpendicular to the direction of plate extension (usually within the axial valley/crest) or parallel to the plate boundary (farther away). On slow-spreading ridges, faults can displace the crust by several kilometers, exposing the underlying mantle (e.g., at megamullions). At faster spreading ridges, the faults are less important, but, like their slower counterparts, they mainly step down and up away from the rift axis. Shearing is more important at transform faults (lateral offsets in the axes of mid-ocean ridges). Overall, tectonic structures play a dominant part in controlling the surface manifestations of volcanism and hydrothermalism.

Figure 5.6 shows the general morphology of faults and fissures. The latter are usually narrow and their two sides are at the same level. The former are defined in geology dictionaries as "fracture surfaces or zones along which appreciable displacement has taken place." Fault scarps vary in height, from a few tens of meters (at fast-spreading ridges) to hundreds of meters (at slow-spreading ridges). They are often organized in several steps, corresponding to different stages of ridge activity, and their morphologies vary with their age. The most common scarps in the inner floor are simple fault scarps, which vary in height from less than a meter to several hundred meters. Except for a few exceptions when they cut lithified sediments, the rock unit exposed in all these scarps is a vertical section of truncated pillow lava (e.g., Ballard and Moore, 1977). The "freshest" fault scarps are characterized by an exposition of the original fault surface (Figure 5.6, "immature" stage). Small talus fans develop at the base of the fault scarps, and on terraces at different levels. The base of the fault is sharp and linear, whereas small erosive scars and debris chutes usually dissect the original upper surface (Allerton *et al.*, 1996). In a later, "mature" stage, the fault scarp gets covered by thick sediments, produced by the gravitational collapse of the unstable, steeper slope. The sediment-free upper surface erodes deeply, and its morphology is typified by rock buttresses and gullies. The debris slope is less inclined, typically 30°–40°. The base of the slope is cuspate, marking the growth of individual fans. In the final stage (Figure 5.6, "drape" stage), the fault scarp is nearly entirely covered by sediments and only a small section is still exposed. Pelagic sedimentation is more rapid than continued erosion and debris deposition. Faults often link together or, especially for larger faults, terminate in complex splays. Some fault systems might have been resubmitted to tectonic activity, with more, smaller

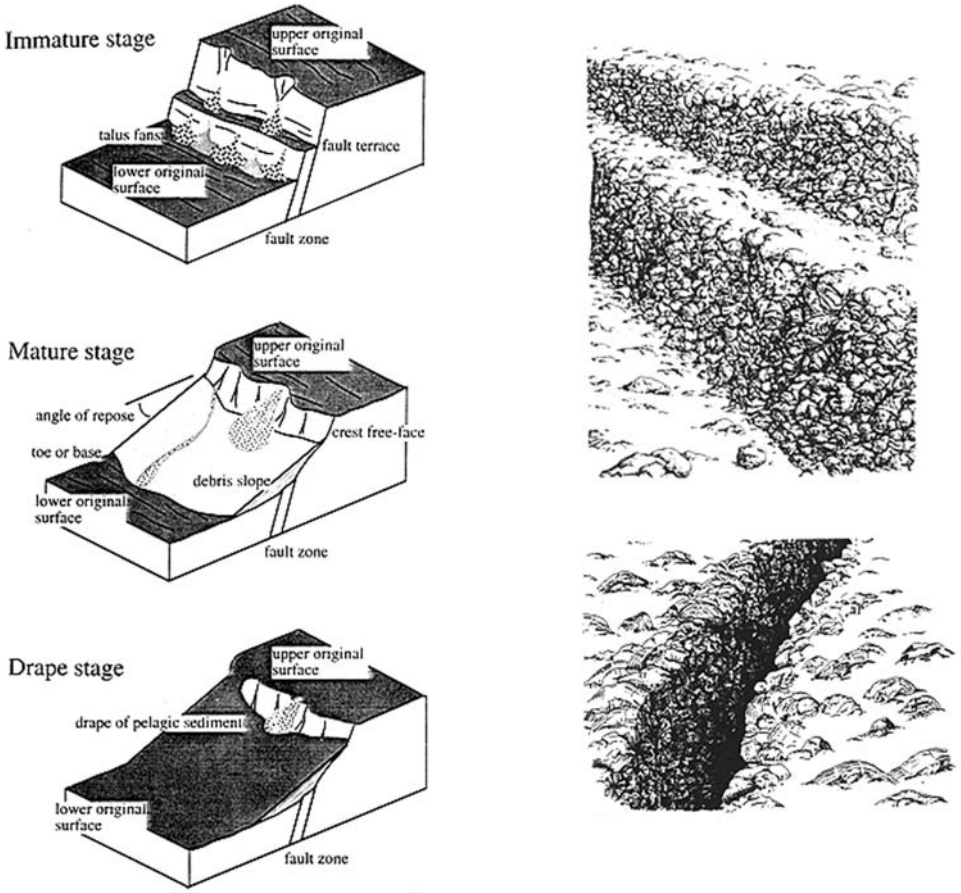

Figure 5.6. Tectonic components of a mid-ocean ridge. (Left) Different stages of evolution of a fault scarp (from Allerton *et al.*, 1996). (Right) Sketches of a fault and a fissure (adapted from Ballard and van Andel, 1977).

faults and fissures. Others might also be overlain by volcanic flows or sediments. How will these stages be translated on sidescan sonar images?

Morphologically, fissures are mainly a small-scale disruption in the underlying terrain. Their widths can vary from a few centimeters to several meters. Ballard and Moore (1977) observed that in many cases, there were still pillow forms out over the edges of the fissure. On sidescan sonar images, the fissures will appear as linear discontinuities in the backscatter, sometimes with a rougher texture along their edges if the sonar resolution matches the size of the pillows on the edges. If the ground resolution or the angle of incidence are large enough, it may be possible to detect the sides of the fissures facing toward and away from the sonar, respectively bright and dark. The fissures and cracks parallel to the sonar track are more visible, as they are more susceptible of reflecting acoustic energy. Fissures sub-perpendicular to the sonar track will be much more difficult to detect.

Fault scarps facing the sonar will be acoustically more reflective, the more so as the local angle of incidence is higher. Fault scarps facing away from the sonar will be less reflective, or not reflect any energy. Back-tilting will have the same effect. Because of their homogeneous nature, scarps will appear as large bright regions, with a fine-grained texture and a generally elongate shape. If they are overlaid with sediments, their textures on sidescan sonar imagery will become smoother and less bright. Scree and talus fans have smaller slopes than the scarps, but are composed of many small blocks with randomly oriented facets, some of which will reflect most of the acoustic energy back to the instrument. They will therefore appear as very reflective, bright areas with more mottled textures, covering more restricted areas on the seafloor. Occasionally, the over-steepened crest-free face can be observed at the top of the scarp as a bright line on the sidescan image (Allerton *et al*., 1996). The boundaries of these surfaces are irregular and gradational, but still relatively bright. Individual gullies and erosion scars will not always be visible, depending on the ground resolution of the imaging sonar. Their acoustic appearance may range from small groups of pixels of varying levels, showing a mottled texture, to larger regions whose textures will be akin to fault scarps, but slightly brighter (if the separate elements are rougher) or slightly darker (if the elements are smoother but with a lower angle respective to the imaging sonar). When interpreting mosaicked images, it is important to also account for the direction of ensonification. Fault scarps facing the sonar in one swath, and thus appearing bright, might show mostly as shadows in the adjacent swath. Therefore, a feature can alternate between bright and dark reflections as it crosses the mosaic, without changing the direction of its slope.

Figure 5.7 shows simple examples of faults and fissures at the Mid-Atlantic Ridge on a background of sheet flows. The sidescan image (on the left) was acquired with TOBI (30 kHz, 6 m resolution after processing). The nadir zone is clearly visible, diagonally across the right of the image (cf. interpretation at right). It means that structures on the left of the nadir will be imaged from the right, and conversely structures on the right of the nadir will be imaged from the left. The leftmost portion of the TOBI image is several kilometers wide, close to the TOBI half–swath width of 3 km. This can be seen by the far-range attenuation of backscatter close to the extreme left of the image. This means that imaging angles will vary significantly from the nadir outwards. The shadows of the individual, small volcanic constructs indeed lengthen with distance from the nadir. The individual fissures appear as black (i.e., poorly reflective) lines, with thicknesses matching their apparent widths. They are more important on the right, toward the center of the axial valley. Fault scarps appear as larger, distinctive, and highly reflective (i.e., bright) elongated marks. The more recognizable ones have been marked with hashed patterns on the interpretation. They are increasingly wider (i.e., higher) farther away from nadir. A long line, toward the top left of the nadir, is similar in morphology to the fault scarp marked nearby, but the constant series of shadows immediately behind it show it is made of individual constructs, most likely of volcanic origin, and is not a fault scarp at all. Smaller fault scarps, also visible as bright lines, and smaller fissures, also visible as dark lines, have not been noted to avoid cluttering Figure 5.7, but they should of course be part of any full interpretation of the local geology.

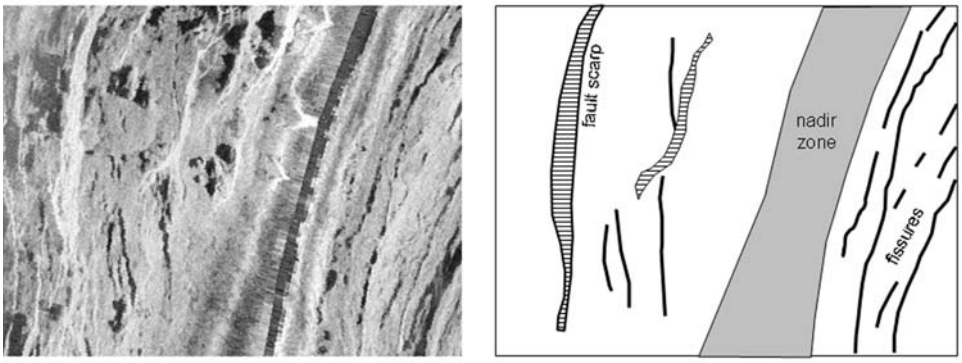

Figure 5.7. TOBI image (approximately 3.1 km wide, 6 m/pixel) of fissures and fault scarps at the Mid-Atlantic Ridge. Although they are imaged from different directions on each side of the nadir zone, the fissures still have the same appearance.

Figure 5.8 has also been acquired with TOBI and processed to the same resolution. The nadir area widens as the relative altitude of the TOBI platform increases (meaning that either the seabed below it deepens or the platform flies higher). The fault scarps are imaged from the left; the variations in acoustic back-scatter indicate therefore that the heights increase from left to right. Only a small portion of the image (upper-left corner) was imaged from the right. The two main

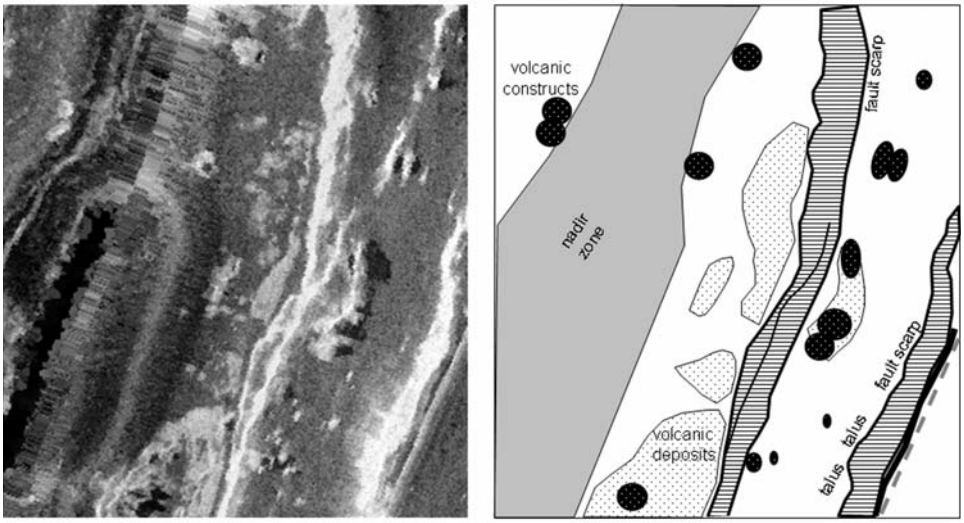

Figure 5.8. Typical fault scarps are shown in this TOBI image of the Mid-Atlantic Ridge (left: 6 m/pixel, approximately 2 km wide). (Right) Summary interpretation of the most visible structures. Volcanic edifices are marked as black circles and volcanic deposits as mottled patterns. The fault scarps themselves are hashed, approximately in the direction of the throw. The dashed line (bottom right) is an image artifact. See text for more details.

fault scarps (horizontal hatch patterns) vary in width and their throws are nearly perpendicular to the survey track. The left scarp is divided into two levels (black line), with a small terrace. The right scarp has a prominent shadow (thick black line), unfortunately cut during mosaicking by the sea surface reflection from the neighboring swath (hashed gray line). The underlying terrain is smooth and much less reflective; it can therefore be tentatively interpreted as sedimented sheet flows (this is supported by independent information, from distance to the ridge axis and from dredges and dives). The smaller width of this image means that the range of incidence angles is smaller, and this is shown by the absence of systematic across-track variations in the shadows of the volcanic constructs scattered throughout the image. Note that, as in Figure 5.7, some series of volcanic constructs show on the sonar image as bright lines with a series of round, individual shadows. In this case, their textures are also much more ''fuzzy'', helping to clearly distinguish them from the genuine fault scarps.

Recent surveys have shown that, in some cases, tectonic features can be restricted to large topographic highs and all follow the same direction (perpendicular to the ridge axis). These structures, called megamullions, were first identified on sidescan sonar images by Cann *et al.* (1997), using 30 kHz TOBI imagery from the Mid-Atlantic Ridge. Since this first paper, more megamullions have been identified, mostly at slow-spreading ridges (e.g., Tucholke *et al.*, 1998) but also in back-arc basins (e.g., Ohara *et al.*, 2000). Geophysical surveys (using multibeam bathymetry as the primary tool) reveal that megamullions are typically 0.5 km to 1.5 km high and 5 km to 15 km in diameter, although Ohara *et al.* (2000) report at least one structure an order of magnitude larger. The structures (mullions) on the surface of megamullions can have low heights (a few tens of meters) with wavelengths up to several hundred meters; they can also be higher (up to several hundreds of metres), 1 km to 2 km wide, more isolated and peaked. Because of their amplitudes, sometimes at the limit of resolution, these striations are often difficult to detect in 3-D images (e.g., from an interferometric sonar, or from sidescan sonar imagery draped onto multibeam bathymetry), except with low-angle imaging or shading. Megamullions are thought to expose deep cross-sections of the ocean crust and uppermost mantle, making them uniquely accessible to direct study. Rather than pillow basalts, surface samples have so far consisted in gabbros and serpentinized peridotites, likely to produce slightly different textures when imaged at very high resolutions (e.g., submetric). Figure 5.9a shows a typical, fully formed megamullion, ensonified from the northwest. Bright stripes are interpreted as linear outcrops of bare rock, separated by darker (i.e., less reflective) stripes likely to be sediment-filled grooves between the rock outcrops. The area immediately right of the megamullion is affected by a continuous linear artifact due to sea surface reflection. As the sea is a bit less than 2 km deep in this area, and the TOBI half–swath width is 3 km, this means that the megamullion is imaged at mid-range, in ideal conditions. Its large and irregular shadow can be used to infer its relative height. The lower right part of the image also shows some typical fault scarps amid volcanic terrain. This sonar image can be compared with the conceptual sketch of a typical megamullion (Figure 5.9b), based on thorough analyses of multibeam bathymetry, gravity, and *in situ* sampling (Tucholke *et al.*, 1998). Megamullions are

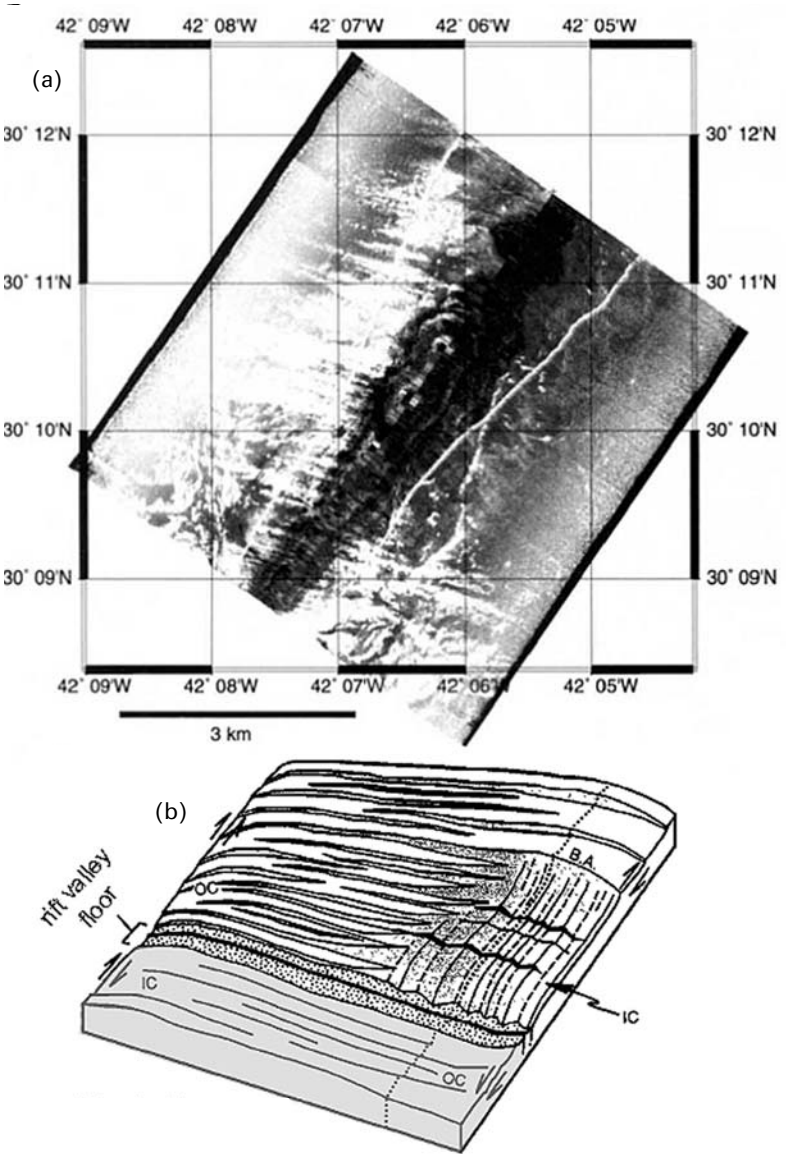

Figure 5.9. Megamullions consist in large domes with typical corrugations extending along the direction of plate spreading: (a) the first high-resolution sidescan sonar image (from Cann *et al.*, 1997), taken with TOBI (30 kHz, 6 m resolution); (b) conceptual sketch of a typical megamullion (adapted from Tucholke *et al.*, 1998). IC = inside corner; OC = outside corner; B.A. = break-away zone.

usually found at the intersection of a spreading ridge and a transform zone, and the breakaway zone (noted as B.A. in Figure 5.9b) corresponds to where the fault began.

5.3 VOLCANIC STRUCTURES

Volcanism is the main form of construction at mid-oceanic ridges. Erupted lava will have different morphologies, depending on characteristics such as magma composi-

tion, original viscosity, eruption depth and rate, and therefore the mechanisms of interaction of magma with water (e.g., Gregg and Fink, 1995; Fouquet *et al.*, 1998). More viscous lavas will be smoother, resulting in sheet flows blanketing large portions of the seafloor. High acoustic reflectivities will be combined with smooth textures and shapes generally following the topographic contours. Pillow basalts are the predominant building blocks of volcanic structures underwater. With bulbous shapes, they can be stacked or individual (as shown in the sketches of Figure 5.6, right, drawn after repeated dives). Also having high acoustic reflectivities, they will create mottled acoustic textures, varying with the imaging resolution and the distribution of individual pillows. More rarely, volcaniclastic deposits result from submarine explosive fragmentation. Present research estimates their maximum depth to vary from $\sim$200 m to several thousand meters depending on local geological history (Fouquet *et al.*, 1998). Although they have not been documented with sidescan sonar alone, because their physical evidence on the seabed is generally submetric, they are likely to occur in several settings (e.g., shallower portions of mid-oceanic ridges) and can actually be detected visually (still/video observations, dredging). Extrapolation from dive data (by Fouquet *et al.*, 1998) shows that volcaniclastic deposits would have a specific acoustic signature, and be gray, intermediate between that of lava flows (black) and pelagic sediment (white) and with mottled textures as well.

Figure 5.10 shows two high-resolution images of volcanic deposits, acquired with the same sonar. Smooth lava flows (left) have consistently high reflectivities, with little variation across the width of the picture (approximately one-third of the swathwidth, and covering therefore some angular variations). Some larger volcanic constructions are identifiable in the bottom-right part of the image, as more mottled textures with distinct shadows. Rougher volcanic deposits (Figure 5.10, right) appear

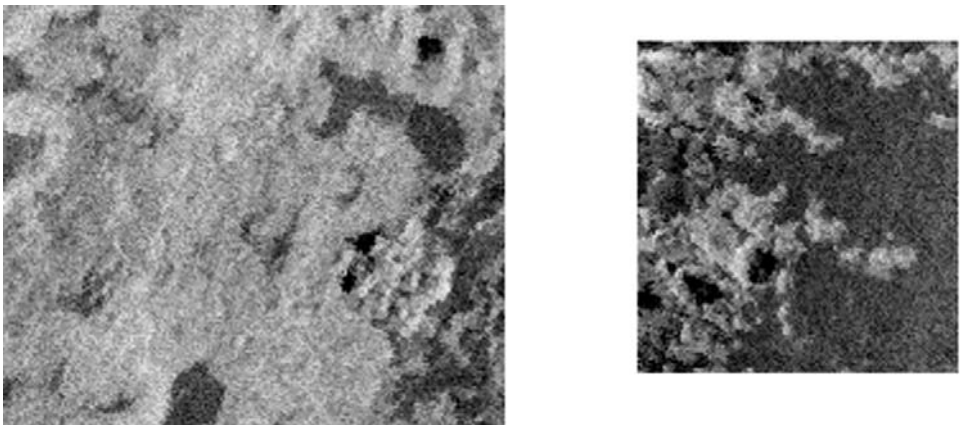

Figure 5.10. Volcanic deposits vary but generally show higher backscatter and (depending on the imaging wavelength) rougher textures. (Left) Smooth lava flows (imaged from bottom right). (Right) Mottled terrain (imaged from top left). Both images were acquired at 30 kHz and processed to 6 m/pixel resolution; they are respectively 1,200 m and 750 m wide.

as bright, mottled patterns in a region mostly covered with darker, smoother sediments. Individual volcanic edifices (this time in the bottom left of the image) can be identified from their slightly rougher textures, but mostly from their shadows, and from the variations in acoustic reflectivity on each side. Indeed, the side facing the sonar is brightest, with symmetric drops on each side of the structure, and the side facing away from the sonar is each time much darker or completely in shadow. In summary, the high reflectivity is typical of volcanic deposits, and the changes in local and general textures indicate what type they are most likely to be. The interpretation needs of course to take into account the imaging angle and the sonar's frequency (i.e., which micro-roughness scale will have the most effect on the backscatter) (cf., Figure 4.24).

Larger accumulations of volcanic material will have different shapes, depending on the type and number of original eruptions, and how they might have been affected by subsequent activity (e.g., tectonics, sedimentation, partial or total collapse). They range in size from a few meters to several kilometers. Although they are all volcanic, they can be classified with the simple scheme adopted by the ICES (International Council for the Exploration of the Sea). Underwater mountains of heights above 1,000 m are considered to be seamounts, those between 500 m and 1,000 m are knolls, and those below 500 m are hills. Imaged with sonar, they will all have similar characteristics: the slopes facing toward the sonar will appear brighter as the angle of incidence increases, and slopes facing away from the sonar will be darker or completely in the shadow. The length of this shadow can be used to infer the relative height of these volcanoes above the seabed, and its shape can be used to derive the approximate morphology of the top of the volcano.

Small point source volcanoes, ranging from a few hundred meters to a kilometer in diameter and up to a few hundred meters high, are the most common volcanic structures on the seabed (Smith and Cann, 1990). Figure 5.11 shows a large point source volcano, several hundreds of meters wide. The direction of ensonification (dashed arrow) and the length of the shadow (amplified by the low grazing angle, as the boundary of the image indicates the end of the 3 km wide swath) show it is as high, with a roughly conical shape and at least two main levels of construction (slight "kinks" in the sides of the shadow). Variations in the acoustic textures show the different levels (marked with different patterns in the interpretation). The central caldera is clearly visible, with its own shadow at the top of the volcano, but its depth cannot be inferred from the slope of the facing wall. Central summit craters are common on all types of ridge volcanoes, and suggest subsidence of the magma in the conduit, or collapse of a high-level magma body close to the base of the volcano. In some cases, parasitic cones on the floor of the craters are evidence of late-stage eruptions. The smooth texture and high reflectivity of the image background shows it is most likely made of sheet flows. Individual volcanic edifices are visible throughout the image, although only a few typical ones have been highlighted in the interpretation (to avoid cluttering). Some form larger constructions, like the composite volcano in the south of the image (large black circle). These types of volcanoes are commonly formed by slow and episodic lava eruptions. Others coalesce to form ridges, known as hummocky ridges and typical of all spreading centers. The clearest one is immediately

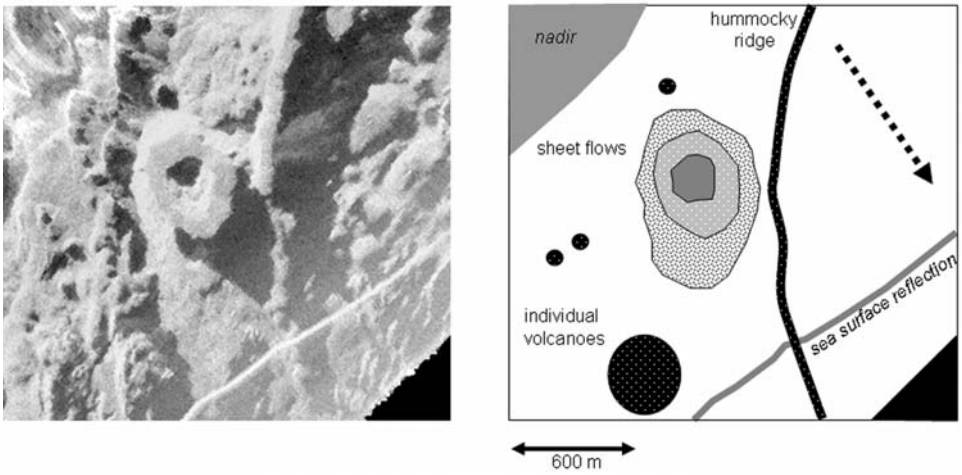

Figure 5.11. Point source volcano, composite volcano, and hummocky ridge on smooth sheet flows, imaged by TOBI on the Mid-Atlantic Ridge. For clarity, only some of the individual volcanoes have been noted. Note how they cluster (bottom left) to form composite edifices. The detailed textures of the main volcano (center) show it is monogenic and flat-topped, with a central caldera. The ensonification direction is from top left to bottom right, as can be inferred by the presence of the nadir (top left) and swath edge (bottom right). The shadows give an idea of the height of the different structures.

right of the point source volcano. Its large shadow gives an indication of how high it might be, although the topographic variations behind the hummocky ridge are not likely to be constant. Bright lobate reflectors farther to the right correspond to the curved fronts of lobate lava flows that have originated on the ridge and flowed down and away from its flanks. The elongate plan form of the hummocky ridge is a function of fissure-controlled eruption. Often, such ridges are formed perpendicular to the spreading direction, and indicate the direction of minimum compressive stress. The predominance of multiple eruptive centers (haystack edifices), several tens of meters in height and diameter, is also a typical indicator of low effusion rates. As a last note, one can remark that the decreasing contrast and absence of any clear shadow at the far range (bottom-right corner of the sidescan image), characteristic of a very low grazing angle and affecting how much of this part of the image, can be interpreted with certainty.

At mid-ocean ridges, variations in the geochemical characteristics of the magmatic supply are narrow enough that the effusion rate is the main control on the shape of the lava flows and the edifices they form. Flat-topped volcanoes (Figure 5.12) can then be interpreted as an indication that the edifice has achieved its maximum height in relation to the depth of its underlying feeder magma chamber (Cann *et al.*, 1992; Magde and Smith, 1995). Once this has happened, and because of the high effusion rates, further lavas that reach the summit will flow horizontally, increasing the volcano's diameter and forming a flat top. This is consistent with the observation of smooth textures on the top of the volcanoes identified in Figure 5.12,

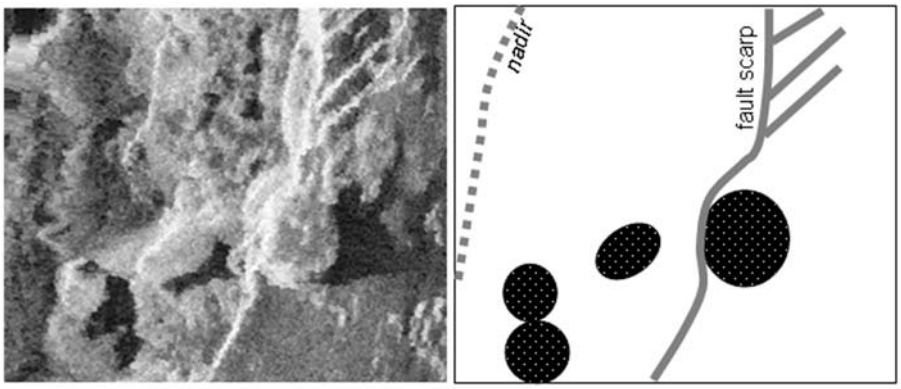

Figure 5.12. Examples of flat-topped volcanoes (1.4 km wide image, ensonified from the left at 30 kHz). Note how shadows give an indication of the heights of these volcanoes around the surrounding seafloor (and how the shadow of the middle volcanoes is truncated by the rising fault scarp).

likely to be sheet flows. This particular sidescan image was also acquired with TOBI, which has a 30 kHz frequency and a final resolution of 6 m/pixel. The main structures visible are the flat-topped volcanoes in the bottom half, with different shapes. Some, and in particular the rightmost one, reveal on closer inspection individual edifices on their tops (most likely parasitic cones, formed during the later stages of eruption). A fault scarp (not noted in the interpretation) is visible close to the nadir. A larger fault system is also visible, closely connected to the rightmost volcano. This important fault scarp is made of several levels, and appears splayed toward the top of the image. This is typical of an edifice controlled by an underlying fissure system. This volcano, because of its size, shows many of the features also visible at a smaller scale on the other flat-topped volcanoes. Its flank facing the sonar has a more speckled appearance, likely to be a scree. Its shadow (away from the sonar) can be used to infer its height above the fault scarps. The terrain immediately to the south is mottled, with intermediate backscatter levels: in this case, it is interpreted as a hummocky volcanic field, covered with sediments.

To show the similarities in interpretation to other high-resolution sonars, Figure 5.13 shows sidescan imagery from SeaMARC I: deep-towed, with an imaging frequency of 11 kHz to 12 kHz, a pixel resolution $\sim$10 m and a swathwidth of 5 km. The far left-hand side of this image is part of another swath, as shown by the changes in the directions of the shadows of the individual volcanic mounds, each part of the separation (Figure 5.14). The absence of shadows does not preclude the recognition of the hummocky volcanic ridge on the left, compared with the one on the right. The latter has a very small, dark, and circular feature surrounded by a bright curvilinear pattern on its side facing the sonar. This is interpreted as a cratered volcano. A similarly bright structure, at far range and with little variations in overall textures, is interpreted as a flat-topped volcano. On a more general scale, the speckled and brighter terrains around the hummocky volcanic ridge are interpreted as sedimented

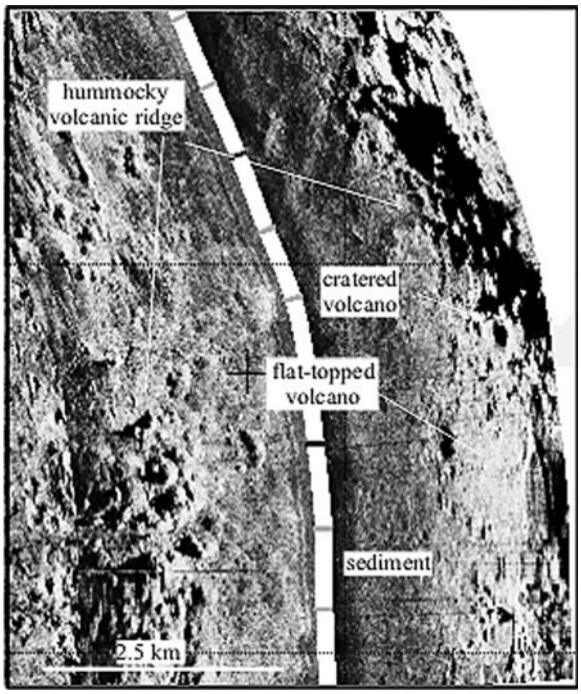

Figure 5.13. SeaMARC I deep-towed sidescan sonar image of hummocky volcanic ridges and terrain on the East Pacific Rise. Note the similarities between this SeaMARC I image of the East Pacific Rise and the previous TOBI images of the Mid-Atlantic Ridge. Both have similar textures, with many small volcanic mounds and a few simple volcanic cones having coalesced to form the hummocky ridges (courtesy of the RIDGE-2000 database).

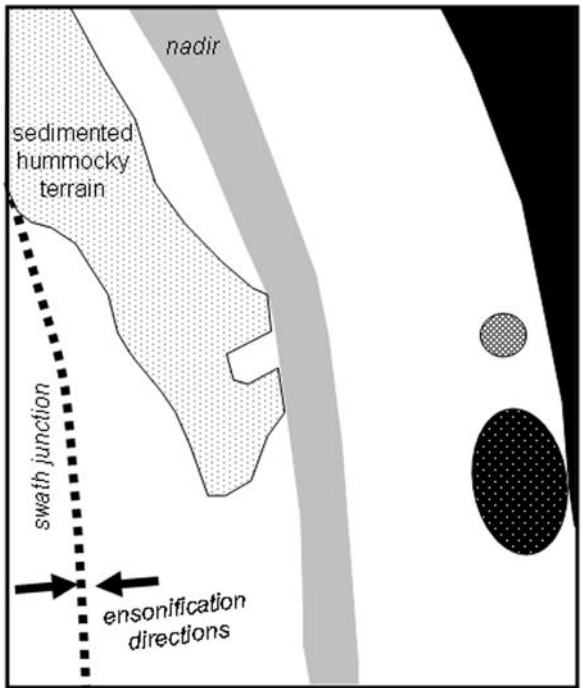

Figure 5.14. Basic interpretation of the previous image. The hummocky volcanic ridges are not presented again, but the exact outlines of the cratered volcano and the flat-topped volcano are shown. The changes in the directions of the shadows each side of the junction between swaths are very visible. The mottled terrain in the top-left quadrant is interpreted as sedimented hummocky terrain (see text for details).

hummocky terrain, whereas the smoother and less reflective background to all these structures is interpreted as sedimented sheet flows (labeled as "sediments" in Figure 5.13).

The combination of volcanic edifices can also form larger structures, such as axial volcanic ridges (AVRs).They are common on slow-spreading and medium-spreading ridges. For example, about 90% of the Mid-Atlantic Ridge axis is characterized by AVRs. They are elongated structures, 10 km to 50 km long, 3 km to 10 km wide, and 50 m to 200 m high. Recently formed, they are the essential unit of volcanic construction of the ocean crust (e.g., Parson *et al.*, 1993a, b). Variations in geochemistry show they are formed from material from the same magmatic supply (i.e., they are cogenetic) but adjacent AVRs differ chemically and are individual systems (e.g., Taylor *et al.*, 1995). AVRs are of variable ages, most often with a cyclic history of volcanism and tectonism, causing them to grow and then degrade (e.g., Murton and Parson, 1993).

Figure 5.15 is a typical example of an axial volcanic ridge. It corresponds to a half-swath of TOBI imagery (i.e., next to 3 km wide, imaged at 30 kHz, and processed to a 6 m resolution). This image is ensonified from the right; the nadir line is quite visible in the right of the image, and varies in width with both the altitude of the sonar and a change in course visible in the upper part of the nadir line. Far-range measurements are more "misty", but still correspond to volcanic terrain. A long fault scarp is visible as a thin white line from the top to the bottom of the image; in some places (middle and bottom), it subdivides into two narrower scarps, separated by small terraces. The AVRs themselves are easily recognizable as a curvilinear combination of distinct volcanic structures. Each has clear shadows, giving indications of its height (although the local slope and, mostly the scarp, will limit the length of the shadows)

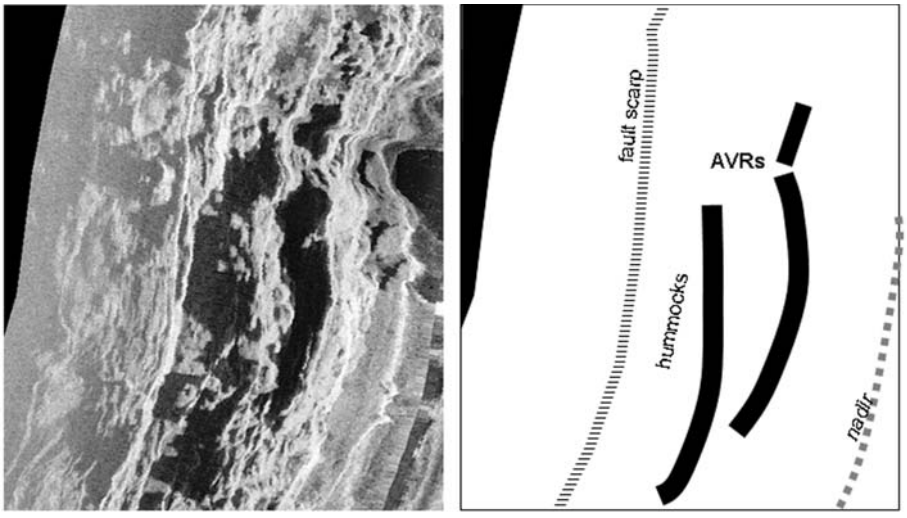

Figure 5.15. This half-swath (3 km wide) of TOBI imagery from the Mid-Atlantic Ridge shows axial volcanic ridges (AVRs) of varying widths and heights (as inferred from the shadows), with hummocks in the background.

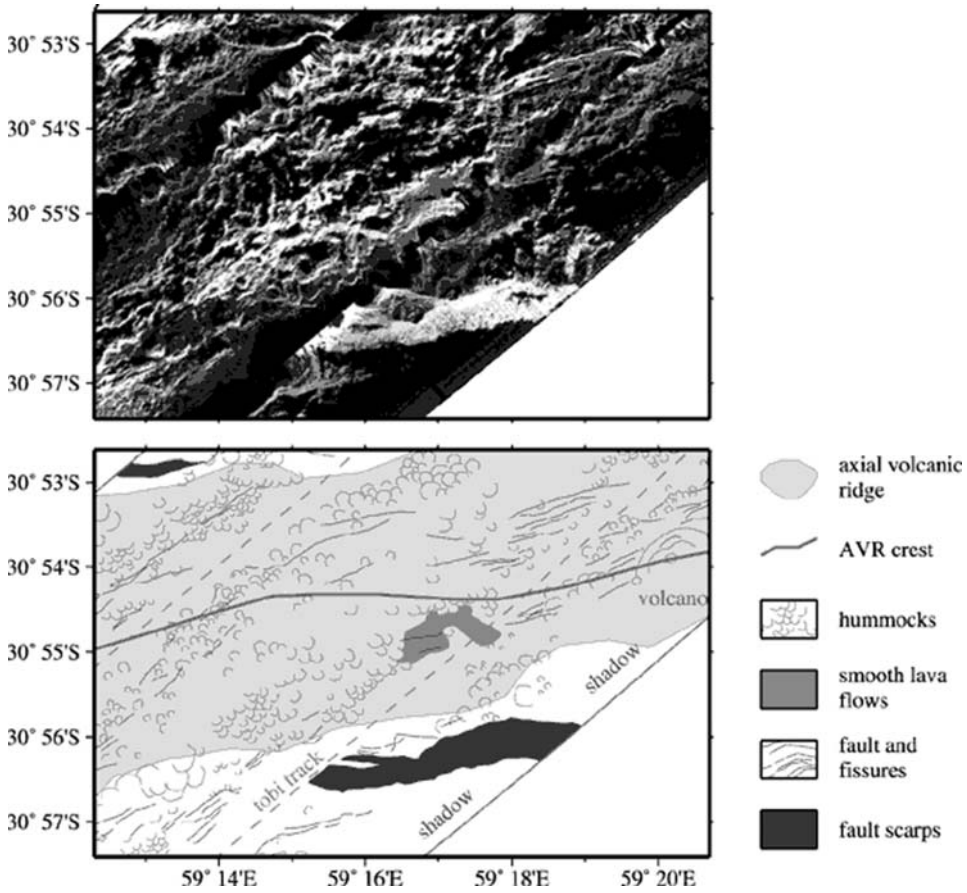

Figure 5.16. TOBI imagery from the very slow–spreading South-West Indian Ridge, showing a partially faulted axial volcanic ridge with hummocks in the background (from Mendel *et al.*, 2003; © American Geophysical Union).

and of its shape (showing the individual structures, especially near the bottom of the leftmost AVR).

As they degrade with age and tectonic activity, AVRs do not always exhibit such clear structures. This will be compounded by the imaging geometry. In Figure 5.15, the sonar was high enough above the seabed and flying in a direction parallel to the axis of each AVR, emphasizing their respective shapes and shadows. Figure 5.16 shows an older AVR, imaged with the same sonar flying at an angle to the axis of the AVR. The interpretation shows there are two tracks, meaning the image has been mosaicked and the imaging angles will also vary around the AVR. Partially faulted, it is even harder to recognize as such, and in this case, only the experience of the interpreter and the analysis of concurrent bathymetry and gravity (Mendel *et al.*, 2003) could lift the ambiguity. This compound problem of structure degrading and

the influence of the imaging geometry needs to be kept in mind when mapping both the existence of AVRs and their actual extent, as they will be difficult to identify and follow fully.

5.4 SEDIMENTED AREAS

As oceanic crust ages, the general decrease in volcanic activity and the different expression of tectonics tend to degrade the structures built at mid-ocean ridges. These structures are slowly covered by a smooth blanket of pelagic sediments, made of the remains of pelagic organisms (by opposition to hemipelagic sediments, found closer to the shores and also containing small amounts of terrigenous material). These sediments also contain a small proportion of products of volcanic origins and, in very limited areas, hydrothermal sediments (see Section 5.5). On sonar images, they will be characterized by very low and uniform backscatter, organized in smooth and poorly contrasted textures. Sedimentation will generally decrease with distance from the axis and be important at segment discontinuities. It will mask the underlying structures, either completely or partially (ponding and draping). Figure 5.17 shows a sedimented area in one of the non-transform discontinuities of the Mid-Atlantic

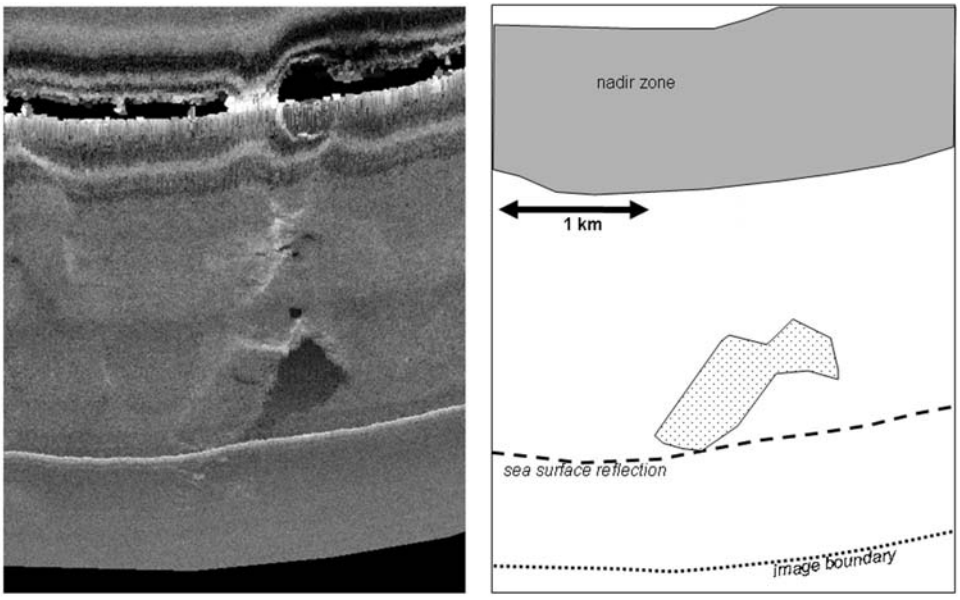

Figure 5.17. A typical example of a fully sedimented area on a mid-ocean ridge (TOBI imagery, 30 kHz, 6 m resolution). Some structures are still visible, the largest of which is highlighted in the interpretation (it is mostly visible because of its height, as seen from its significant shadow). The sediments show a homogeneous backscatter and smooth textures on scales of several kilometers.

Ridge. Over scales of several kilometers, the seabed appears homogeneously smooth. Some structures are hinted at but completely draped, and only the largest one (a relict outcrop still covered with sediments) is still visible, mostly because of its shadow and a small, bright sonar-facing side. The smoothness of the sediments, and the number of structures visible, will depend mostly on the sonar used. A dramatic example is shown in the regional imagery of the abyssal plains around Hawaii in Chapter 6 (''Abyssal basins and the polar seas''). The frequency of the imaging sonar affects its potential depth of penetration (lower frequencies can go deeper), and the angle of imaging has some effect too (closer to vertical gives a better potential penetration than a grazing angle).

5.5 HYDROTHERMAL STRUCTURES

The presence of localized, anomalously hot water had been documented at least for the last half-century, and the first deep-sea hydrothermal vents were identified and documented in 1977. These vents discharge mineral-rich waters heated by the underlying molten rock and expelled through cracks in the young ocean crust (Rona, 1986). The water temperature can reach close to 400°C, compared with a few degrees for the surrounding deep water.[1] Still liquid because of the high pressure at these depths, the water carries many dissolved metal species (iron, manganese, copper, etc.), often giving them the appearance of ''black smokers''. They usually host distinctive chemosynthetic communities (e.g., Van Dover, 2000) and are of great scientific interest because of their biology, and because of the insights they give into the deeper fluid circulation at mid-ocean ridges. Increasing numbers of vents have now been discovered at mid-ocean ridges and other locations over the world.

Hydrothermal vents vary in height between a few meters and a few tens of meters, with small, conical morphologies or tall chimneys, sometimes grouped in clusters. When they are active, the high temperature of the fluids ejected also changes the local acoustic properties of the water column. The metallic mineral particles making up the hydrothermal plumes are small (<1 mm) compared with the wavelengths of imaging sonars (~ 1 cm), but specialized techniques can be used to reconstruct plume geometries by imaging them sideways (i.e., with the sonar looking not at the seabed but at the water column; Rona *et al.*, 2008). Significant portions of the particles discharged by the vents deposit on the seabed nearby, accumulating sulfide deposits and other materials over relatively large distances (up to several hundred meters). By affecting large areas, and by accumulating over time, these deposits will become visible on sidescan sonar imagery (the higher the imaging frequency, the lower the depth of deposits necessary to be detected). Because of their composition, the acoustic

[1] This affects the local speed of sound when the sonar is flying very close to the vents. Anecdotal evidence shows that, very often, the hottest hydrothermal plumes can be detected on raw imagery, particularly for frequencies below ~ 15 kHz. The drastic changes in water temperature, salinity, and chemical content create ''hourglass'' shapes, compressing the swath toward the nadir.

impedance of vents is therefore very distinct from that of basaltic constructs and closer to sediments. The smallest hydrothermal constructs might be at the limit of resolution of the imaging sonar (a few pixels with different backscatter) but they can often be detected by their surrounding deposits and their overall setting (Blondel *et al.*, 1993a).

Figure 5.18 shows one of the early high-resolution sonar images from a hydrothermal field at the Juan de Fuca Ridge (NE Pacific). It was taken with the DSL-120 sonar (120 kHz, 1 m resolution after processing), flying on a straight path along the ridge axis. The valley walls are clearly visible on each side of the nadir, as an elongated, bright, and wide series of fault scarps. The ones on the right are marked with shadows after some of the steps, whereas the ones on the left have a large darker portion before the brighter top of the wall (and the clear fissure in the bottom left). The small-scale, rough textures behind the valley wall are tilted blocks, identified through image analysis (Blondel *et al.*, 1993b) and visual observations. The still rough but darker textures farther north consist in talus on the slope facing toward the axial valley. The latter is relatively flat and acoustically reflective. A narrow fissure, called "The Highway" by submersible pilots because it enables accurate navigation to the hydrothermal field, is clearly visible at the top of the image, as a long and narrow dark stripe. The hydrothermal field has been enlarged in the bottom of Figure 5.18, to show how even narrow hydrothermal chimneys can create significant acoustic shadows (across-track). Some of the largest hydrothermal vents can be recognized as structures a few pixels wide, and the sulfide rubble around each vent has acoustically distinct characteristics, with mottled textures smoother than those of volcanic deposits.

In some instances, vents that have been particularly active for a long time can create substantial mineral deposits, forming mounds up to several tens of meters high and hundreds of meters in diameter. Similar in size to deposits on land, they are also amenable to industrial exploitation. The technical challenges associated with the extraction of mineral ore are now mostly solved, and a few companies have recently (2006–2007) shown it was feasible to mine mineral deposits in the Kermadec Arc and offshore Papua New Guinea. Although these activities are not achieving economic viability now, they might become more common in the future, and associated environmental impact studies will surely make a large use of sidescan sonar measurements.

Figure 5.19 shows one exceptionally large hydrothermal mound on the Mid-Atlantic Ridge. Named TAG, for its discovery during the Trans-Atlantic Geotraverse, this mound is a precipitate of iron and copper sulfides mixed with anhydrite. This interesting edifice has been the subject of considerable research (e.g., Humphris *et al.*, 1995; Kleinrock and Humphris, 1996; and many others). The TOBI imagery (30 kHz, 6 m resolution) shows the typical view of the axial valley wall of a slow-spreading mid-ocean ridge. Regular fault scarps are cutting diagonally across the image, all aligned in the same direction (perpendicular to the direction of spreading). The bottom left of the image shows a typical volcano on top of a scarp, with a round shape and a characteristic shadow. The semi-circular apron of volcanic terrain right of the volcano also has significant shadows, and most likely corresponds

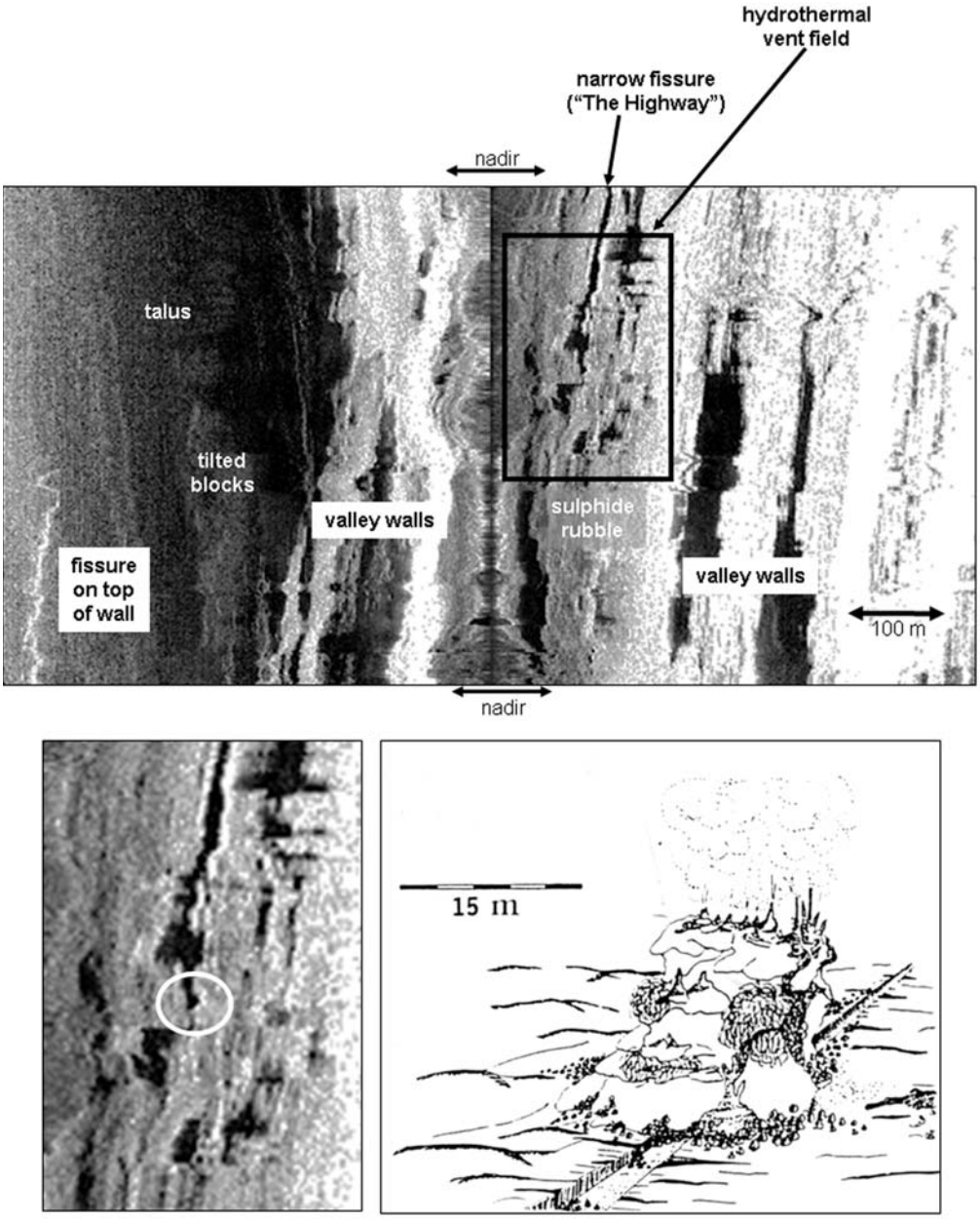

Figure 5.18. (Top) Annotated DSL-120 image of the Hulk hydrothermal site on the Juan de Fuca Ridge, northeast Pacific (from Blondel *et al.*, 1993a). The linear features are fissures and faults, with the long linear axial summit graben lying just to the left of the inset square. (Bottom) Enlargement of the hydrothermal site (a circle highlighting one of the most prominent vents) and drawing of the Hulk vent based on submersible dives and video observations (sketch by V. Robigou, University of Washington).

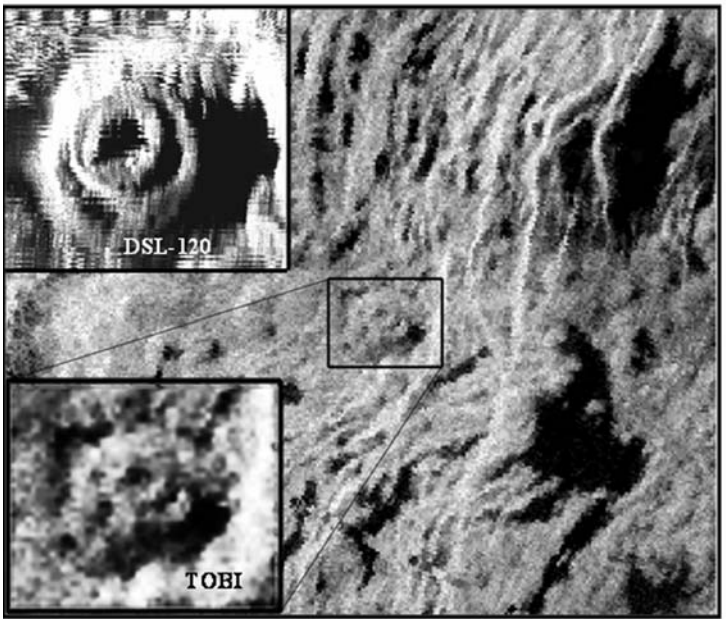

Figure 5.19. TOBI imagery of the TAG hydrothermal mound on the Mid-Atlantic Ridge (from Blondel and Murton, 1997). This 2.5 km square area is ensonified from the left (data courtesy J. Cann, University of Leeds, U.K.). The TAG mound is the button-shaped feature in the center, enlarged in the inset. The top inset shows its high-resolution image with the DSL-120 (data courtesy S. Humphris and M. Kleinrock, Woods Hole Oceanographic Institute, U.S.A.).

to its first stage of construction. The bottom right of the image shows a bright, curvilinear pattern with regular elliptical shapes, whose shadows reveal to be volcanoes; this is most likely an axial volcanic ridge. At first glance, the TAG mound (middle of the image, in a black rectangle) does not look worthy of more attention, although its shadow looks rather small for an edifice of this extent. But closer examination (bottom inset) reveals a more complex structure, with a moat and several individual structures on the top of the mound. Higher resolution mapping with the DSL-120 sonar (120 kHz, 1 m resolution) reveals more details (top inset). The structures on the top can be unambiguously resolved, and several concentric rings (some with additional structures) are now visible. This characteristic shape of the mound comes from periodic variations of hydrothermal activity that have allowed anhydrite to dissolve and reform. Seawater and hot hydrothermal fluids mix throughout the mound structure, escaping with different temperatures and compositions and creating different types of structures (''black'' and ''white smokers'') in the process (Figure 5.20).

5.6 SEAFLOOR STRUCTURES ASSOCIATED WITH SUBDUCTION

Subduction zones have been intensively studied over the last decades, because of their high activity (earthquakes, landslides, eruptions) and because of their proximity to generally densely inhabited coastlines. Most of the information about these regions comes from multibeam bathymetry and 2-D/3-D seismic surveys. These instruments yield wide horizontal coverage and sub-surface penetration. But high-resolution

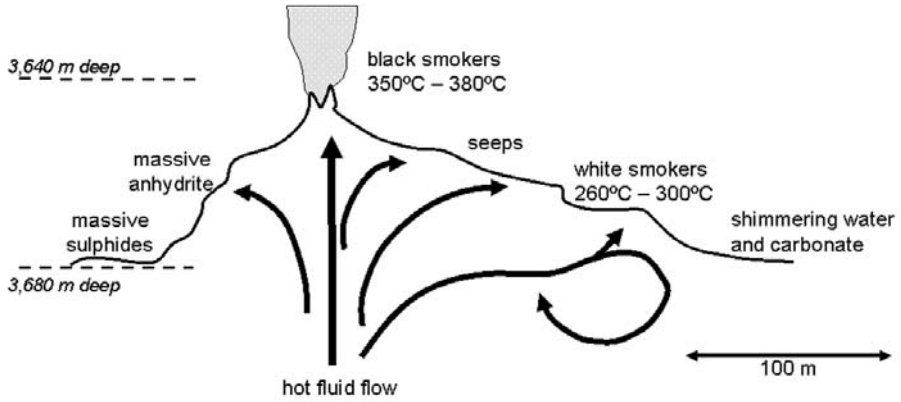

Figure 5.20. Cross-section of the TAG mound, compiled from submersible dives (redrawn from Rona, 1986) and showing the different patterns of fluid circulation and corresponding surface structures.

mapping of surface structures provides detailed insights into how subduction works at the local scale, as well as how it affects (and is affected by) the existing geology (e.g., Faugères *et al.*, 1997; Dominguez *et al.*, 1998; Lewis *et al.*, 1998; Sumner and Westbrook, 2001). This complex interplay of, mostly, tectonic and sedimentary processes gives rise to a host of structures acoustically and superficially similar to their counterparts on mid-ocean ridges (Sections 5.2–5.6) and at continental margins (Chapter 7). Rather than repeating similar images of faults, sediment patches, etc., this section aims at showing the distinctive structures of subduction areas, as they can be identified on sidescan sonar imagery. The interaction between these structures, and their general geophysical interpretation, are presented in more detailed studies like textbooks (e.g., Juteau and Maury, 1999) and reference articles (e.g., Thornburg *et al.*, 1990; Pickering *et al.*, 1995; Lewis *et al.*, 1998; Martínez *et al.*, 2000; Hühnerbach *et al.*, 2005; and Fryer *et al.*, 2003, to cite but a few).

Faults and trench walls will have slightly different acoustic expressions depending on whether they are facing the imaging sonar or not, and also depending on the local geometry of ensonification. Considering the large variations in depths across subduction areas (e.g., Figure 5.3), this explains why long-range sidescan sonars are often preferred. At subduction zones, the fault scarps are usually aligned parallel to the trench axis (Figure 5.21). They are mostly compressional in the overriding plate, and trench-facing and extensional in the under-thrusting plate. In the (very rare) cases where no detailed bathymetry is available, this can therefore be used to locate the junction between the two plates. The deep accumulation of material filling the trench (Figure 5.4) is called an accretionary prism (Leggett, 1982). Its deformation induces fold and thrust structures, which combine with the other structures (Figure 5.21). Taken with the IZANAGI sidescan sonar, this image clearly shows the combination of all these structures over a small distance of a few tens of kilometers at most (Pickering *et al.*, 1995). The deformation front (i.e., the junction between the two plates) is marked by a series of important faults (highlighted in gray in the interpreted

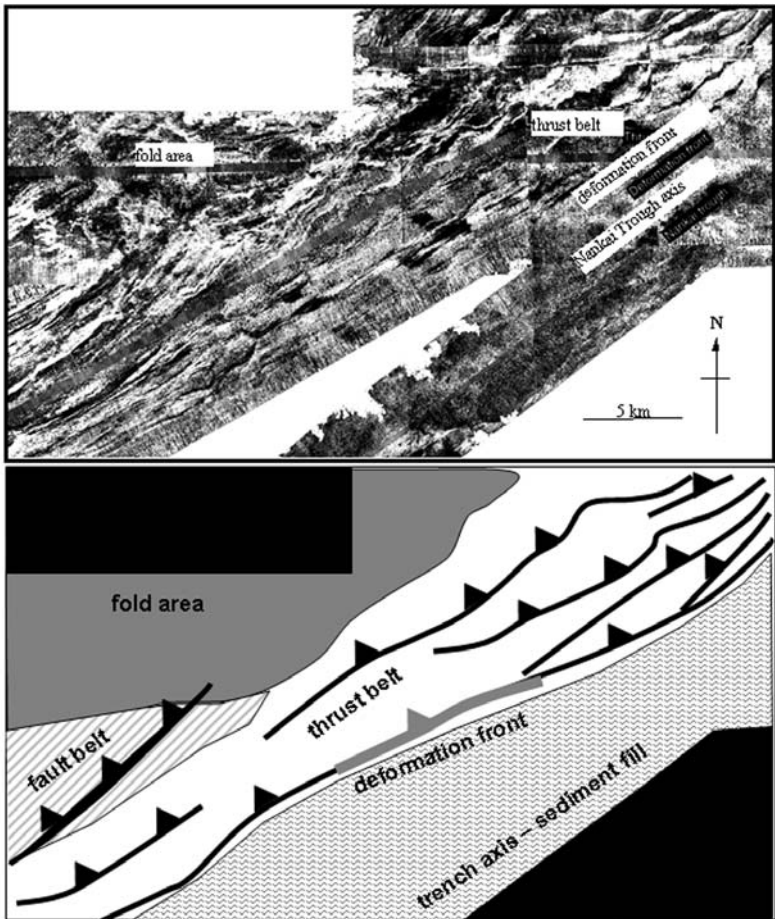

Figure 5.21. (Top) IZANAGI imagery of part of the Nankai Trough (Pickering *et al.*, 1995; © Chapman & Hall). IZANAGI is an interferometric sidescan sonar, shallow-towed (~100 m deep) like HMR-1, that also transmits at 11 kHz to 12 kHz, with a swathwidth varying between 20 km and 1 km depending on the settings. For a 10 km swath, the pixel resolution is 5 m (Tokuyama *et al.*, 1996). (Bottom) Interpretation of the main structures, showing the deformation front (highlighted in gray) of the accretion prism and the faults (black triangles indicate the thrust of each fault).

image). Behind it, the sediment prism is cut by thrusts and folded into a complex pattern of sonar-facing ridges and troughs, and detailed analyses of higher resolution imagery from these structures would reveal their evolution with the subduction of the under-thrusting plate. These folds are likely to result from compression or slumping of the accretionary prism. Finally, the filling of the trench axis shows the smooth textures and low backscatters typical of pelagic sediments (e.g., Figure 5.17).

When the plates converge obliquely, strike–slip faults can develop. They are often associated with complex curvilinear fault systems (e.g., Thornburg *et al.*, 1990). Figure 5.22 shows an example in a portion of GLORIA imagery from the Columbian Trench. The acoustically reflective ridges formed by the folding of the sediments under the oblique compression are characteristic of the formation of "flower structures" (e.g., Woodcock and Fischer, 1986; An and Sammis, 1996). Small basins visible in the central portion of the image, also called tear-apart basins, act as relay zones.

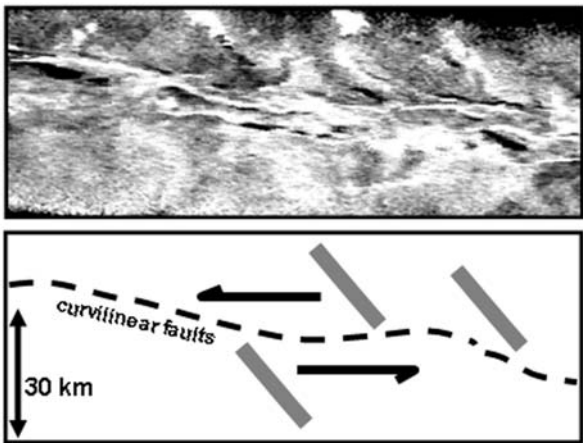

Figure 5.22. GLORIA imagery from the Columbian Trench and its schematic interpretation, showing the curvilinear fabric of a strike–slip zone. The strike–slip direction is shown with the half-arrows, and specific structures on each side of the fault zone are highlighted in gray. GLORIA is another shallow-towed sonar (like IZANAGI and HMR-1), with a 6.5 kHz frequency and a 60 m footprint (sonar image courtesy of Prof. G. Westbrook, University of Birmingham, U.K.).

When close to a continental margin, the trench is supplied sediments by distribution fans, slumps, and occasionally contourite deposits (e.g., Schweller and Klum, 1978). As they belong to margins, these structures will be presented in detail in the appropriate sections of this book (Chapter 7). Because they are usually steeper than on passive continental margins, and with less consolidated sediments, these structures are often associated with strong earthquakes and landslides (also presented in Chapter 7).

Back-arc volcanism can give rise to a large number of large and small edifices. A good example of high-resolution imaging, using the HMR-1 interferometric sonar, is shown at *http://oceanexplorer.noaa.gov/explorations/03fire/logs/anatahan/media/fig4.html* (it is not presented here as it shows the same structures as major volcanic edifices on the Mid-Atlantic Ridge). As volcanic structures move closer to the ridge axis and finally get subducted, they create arcuate deformation fronts, folds, slumps, and slides (e.g., von Huene *et al.*, 2004). Excellent high-resolution TOBI imagery from these different processes can be seen in Hühnerbach *et al.* (2005).

Fluid venting can take place as hydrothermalism, with cold and hot seeps (e.g., Embley *et al.*, 2004; McConachy *et al.*, 2005). When imaged with sidescan sonars, the resulting structures, although geologically distinct, look similar to those presented earlier at mid-ocean ridges (Section 5.5). On a slightly larger scale, gas or fluid seeps might be visible as headless gullies, nearly linear and of limited extents. Co-seismic liquefaction structures have also been documented on high-resolution multibeam imagery (e.g., Collot *et al.*, 2005), as very narrow, acoustically reflective stripes perpendicular to these gullies. More important structures are mud volcanoes (e.g., Brown and Westbrook, 1988; Sumner and Westbrook, 2001). Mud diapirism consists in the buoyancy-driven rise of muddy fluids through the overlaying seabed. Once at the surface, the mud builds volcanoes, domes, and ridges, ranging in size from tens of meters to a few kilometers. Like structures on land (e.g., Shih, 1967), this depends mostly on the viscosity of the mud and the overpressure of the source material. The presence of these structures is facilitated by local tectonics (e.g., faults

or fissures through which the mud can rise more easily and in greater volumes). Examples of mud volcanoes seen with lower resolution sonars like GLORIA were presented in Blondel and Murton (1997). They are, however, better known, and easier to image, at continental margins, and as such will be presented in Chapter 7.

Subducted crust releases water very deep below the seabed, a process known as dehydration. The overlying mantle is predominantly formed of olivine, and it reacts with water to form another mineral called serpentine. Less dense than ocean crust, serpentine tends to flow easily. After finding its way back to the surface, mixed water–serpentine fluids can build up edifices morphologically similar to volcanoes. First documented and explained by Fryer and Fryer (1977) in the Mariana fore-arc, serpentinite volcanoes are generally higher than mud volcanoes and morphologically very similar to volcanic constructs.

Figure 5.23 shows one of the best studied serpentinite structures, known as the Conical Seamount (Fryer *et al.*, 1990). It was surveyed with SeaMARC-II (a precursor to HMR-1, also operated by the University of Hawaii). This shallow-towed sonar transmits at 11 kHz to 12 kHz and covers a swathwidth of usually 10 km. It provides imagery and bathymetry with typical footprint sizes of 120×10 m (along-track vs. across-track). Figure 5.23 shows the sidescan sonar imagery (inverted to show high backscatter with high gray levels) and the co-registered bathymetry (as 100 m contour lines, redrawn from Fryer *et al.*, 1990). This area was surveyed with three mosaicked swaths; the nadir lines are readily visible (linear and dark sub-horizontal lines crossing the entire image) whereas the junction between adjacent swaths is mostly invisible. Contour lines show a nearly circular structure (outlined with a hashed line on the bathymetry), with a base rather different acoustically from the surrounding seabed (lower backscatter, circular structure from swath to swath). The lower flanks show concentric, long-wavelength ridges, particularly on the south-eastern side. Different sinuous flows go down from areas near or at the summit. As demonstrated by Fryer *et al.* (1990) *inter alia*, these sinuous morphologies show they are composed of non-viscous material, covering around 550 km^2 (for a total area of 700 km^2). These flows were initially interpreted to be normal fore-arc sediments mobilized into debris flows by gravitational instability and by infusion of the sediments with fluids venting from a near-surface serpentinite diapir; this implied that the Conical Seamount was a very large mud volcano (Fryer and Fryer, 1987). Dives with the deep-sea submersible *Alvin* showed in fact that the Conical Seamount was an active serpentine mud volcano (Fryer *et al.*, 1990). Visual observations revealed areas of unsedimented (and therefore probably recent) serpentine flow, with numerous clasts of metamorphosed rocks and, at or near the summit, silicate and carbonate chimneys (0.5–1.5 m high) sometimes with serpentinite pedestals <0.5 m high. These structures are too small to be resolved with SeaMARC-II, but they certainly contribute to the overall backscatter by adding to the general roughness. Submersible observations and sampling of this and other serpentinite seamounts in the vicinity (e.g., Oakley *et al.*, 2007) show that, in general, recent or active serpentinite flowing is associated with high acoustic reflectivity, preferentially along one direction, and that variations with sediment cover (i.e., mostly the time since the last venting stage) are good indicators of the different episodes.

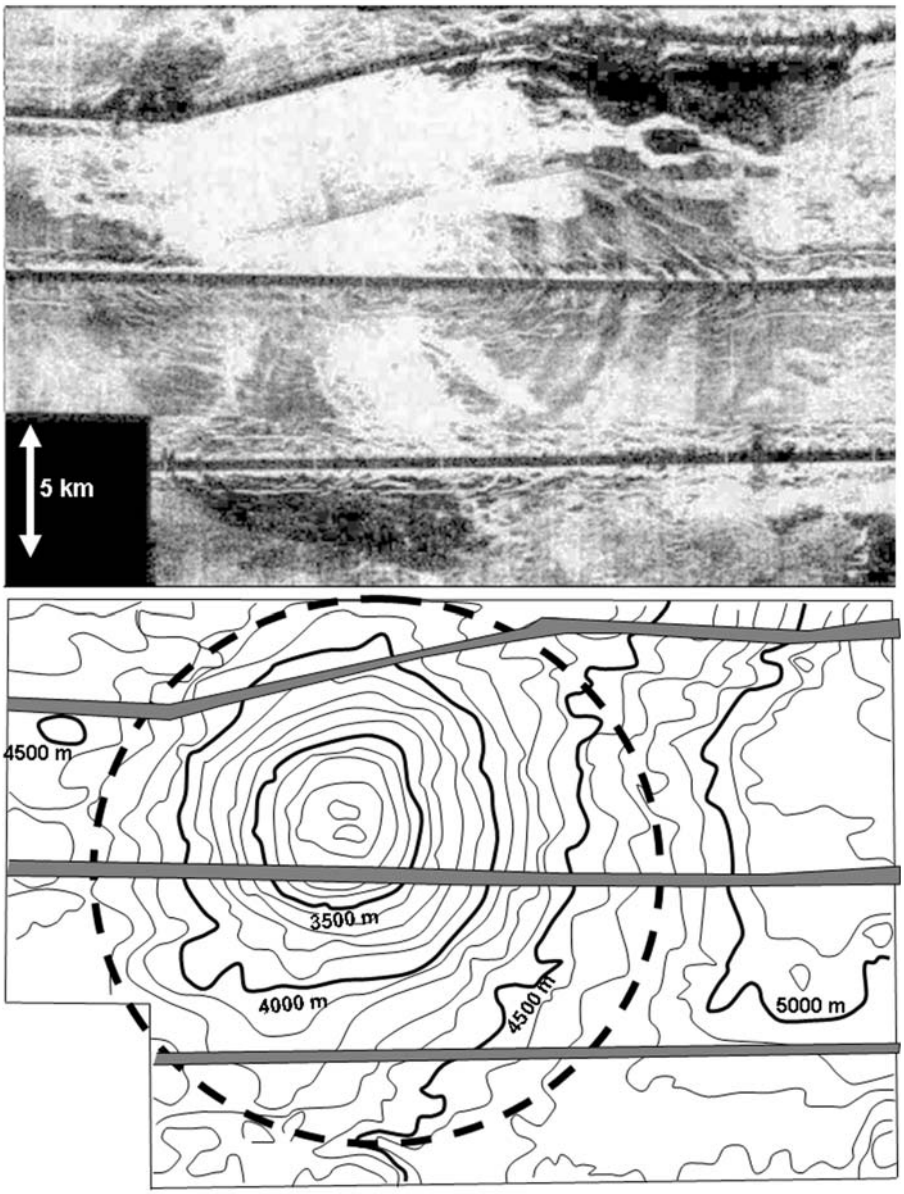

Figure 5.23. SeaMARC-II imagery (top) and bathymetry (bottom) of the Conical Seamount, a well-studied serpentinite structure in the Mariana fore-arc (redrawn from Fryer *et al.*, 1990). The imagery has been inverted to show high backscatter with high gray levels, and the bathymetry has been slightly modified to show the 100 m contour lines (thin) and the 500 m contour lines (thick). The nadir lines from the three swaths forming this mosaic are clearly visible (thick gray lines, horizontally crossing the entire image), and the maximum extent of the visible structure of the seamount has been highlighted as a hashed circle. See text for detailed interpretation.

The Conical Seamount was the first serpentinite structure to be fully documented, benefiting from additional seismic surveys (e.g., Fryer *et al.*, 1990; Oakley *et al.*, 2007) and drilling (Fryer and Pearce, 1992). Structures associated with the growth and deformation of serpentinite seamounts include (Oakley *et al.*, 2007) summit depressions, formed by dewatering/degassing of serpentinite muds and generally deflation and collapse of the volcano; concentric ridges, which modeling and observations show are the surface expression of seamount settling and lateral growth; and mass-wasting debris piles, caused by over-steepening of the flanks. Active convergent margins can accommodate large quantities of fluids and under appropriate tectonic conditions, serpentinite seamounts should exist anywhere in a fore-arc, but this does not seem to be the case (e.g. Fryer *et al.*, 1990; Oakley *et al.*, 2007). One reason could be that the Mariana fore-arc shows extensive recent vertical tectonic deformation, contrary to other fore-arcs. Observation of flow morphologies typical of non-viscous flows, correlated with seamount-type morphologies, active venting (e.g., observable in the overlaying water column chemistry), and the regional prevalence of vertical tectonics would therefore indicate active serpentinite seamounts, if supported by the regional geodynamic setting.

5.7 EXAMPLES OF REGIONAL IMAGERY

The previous sections have shown the main types of structures that can be detected with sidescan sonar imagery and bathymetry of spreading centers and subduction zones, the two end-members of plate tectonics. As much as possible, sonar examples strived to show these structures in isolation, but this was not always possible, as they are often part of a complex history of interlinked volcanic, tectonic, and sometimes hydrothermal processes. Sonar surveys at the regional scale will usually show all these structures together, and the extension from the interpretation of individual features to their geological and geophysical meaning is beyond the scope of this book, particularly as it often uses a body of pre-existing knowledge (other surveys, regional gravity, etc.) and sensors used concurrently during the survey (e.g., magnetometers, heat flow sensors, dredges, etc.). For typical examples of how to integrate sidescan sonar imagery and bathymetry into a general interpretation, readers are invited to look at readily available and well-documented articles like Parson *et al.* (2000), Sauter *et al.* (2004), and Gomez *et al.* (2006) *inter alia*.

Regional coverage of deep seabeds (e.g., at subduction zones and mid-ocean ridges) is easier to achieve with shallow-towed sonars covering a large swath, like IZANAGI or GLORIA. Towed generally 100 m or so below and several kilometers behind the ship, these sonars must obey a compromise between improving the stability (beyond the reach of surface waves, acting on the sonar platform and its towing cable) and maximizing the coverage (i.e., flying as high as possible above the seabed). Typical daily coverage at standard surveying speed was in the region of 20,000 km^2 for GLORIA (now retired) and slightly less for other sonars (e.g., table 2.2 of Blondel and Murton, 1997). But this impressive number comes at a cost: larger swathwidths imply a larger range of imaging angles, not always predictable (cf. Figures 5.1 and

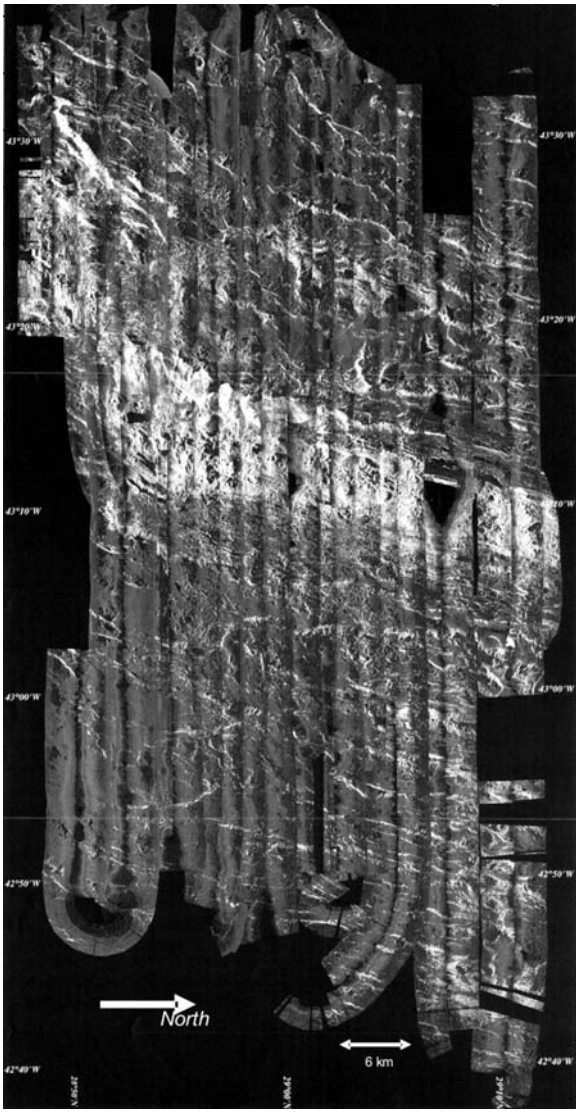

Figure 5.24. Mosaic of TOBI imagery from the Mid-Atlantic Ridge, showing the floor of the median valley (made of young, unsedimented basalt) as a broad band of high backscatter. The narrow, bright lines are fault scarps of different heights and sizes. Note how sedimentation (smoother and darker textures) increases with distance away from the ridge axis (from Escartín *et al.*, 1999; © American Geophysical Union).

5.3) and larger footprints mean lower pixel resolutions (e.g., 60 m for GLORIA). Conversely, high-resolution sonars often need to be towed much closer to the seabed (75 to 300 m, typically), yielding much smaller daily coverages (e.g., $\sim$470 km^2 for TOBI). The range of imaging angles is better controlled by choosing how the sonar is flown (e.g., across or along a mid-ocean ridge). Each approach has its advantages and disadvantages.

Figure 5.24 shows a mosaic of at least a dozen swaths of high-resolution TOBI imagery from the Mid-Atlantic Ridge (from Escartín *et al.*, 1999). The floor of the

median valley (made of young, unsedimented basalt) stands out as a broad band of high backscatter. The narrow, bright lines are fault scarps of different heights and sizes. Sedimentation (smoother and darker textures) increases with distance away from the ridge axis. The clearly asymmetric distributions of volcanic and tectonic structures are clear surface expressions of the actual asymmetric spreading of this portion of the Mid-Atlantic Ridge, already inferred from magnetic profiles (Allerton, 1997 in Escartín *et al.*, 1999). The zone of deformation extends around 10 km to 20 km away from the axis of the ridge, and interpretation of the detailed sidescan sonar imagery in conjunction with other geophysical measurements (Escartín *et al.*, 1999) indicates thermal control by the structures below the spreading center as well as changes in lithospheric thickness, as confirmed by later studies.

Conversely, Figure 5.25 shows a large-coverage sonar mosaic from the Challenger Deep, the deepest trench in the world at ~11 km (not counting the new structure proposed by Fryer *et al.*, 2003 in their article). This series of horizontal swaths (stepped at decreasing depths parallel to the axis of the trench) were acquired with the HMR-1 sonar (12 kHz imaging frequency, swathwidth <25 km). This interferometric sonar acquires both sidescan sonar imagery, gridded here at 16 m/pixel, and phase bathymetry, gridded here at 100 m/pixel (to match across-track variations with increasing depths). This regional mosaic shows clearly asymmetric acoustic patterns, with intense faulting and debris flows close to the trench axis (highlighted in black). A round structure in the south, on the descending plate, is interpreted as a forming mud volcano. Several debris flows are clearly visible in the steepest parts. Their high backscatter suggests they are not covered by sediments and therefore relatively recent. The co-registered phase bathymetry also shows that sediments do not entirely fill grabens before they are subducted (Fryer *et al.*, 2003). This image shows perfectly the difficulty of sonar imaging at subduction trenches, as presented in Blondel and Murton (1997): steep slopes induce high variations in imaging angles (note the systematic variations in reflectivity each side of nadir lines); acoustic footprints vary across-track, more spectacularly on the descending slope facing away from the sonar; and the deepest part of the trench is very difficult to image with accuracy (witness the variations in measured depth of the Challenger Deep, as discussed in Fryer *et al.*, 2003). Finally, although this is not visible on this regional image, structures on the sonar-facing slopes will be imaged at much greater angles than those on the slopes facing away from the sonar, possibly creating artifacts such as foreshortening or displacement (see Chapter 10 for more explanations of these effects).

5.8 CONCLUSIONS

Most structures present on the seabed, or on the bottom of large lakes, will follow the same processes presented here: tectonics, volcanism, or venting of fluids or gases. This chapter aimed at showing representative examples in a variety of settings, imaged with different sonars. The change in resolution from older, lower resolution sonars (like GLORIA) to more recent, generally higher resolution sonars (like TOBI or

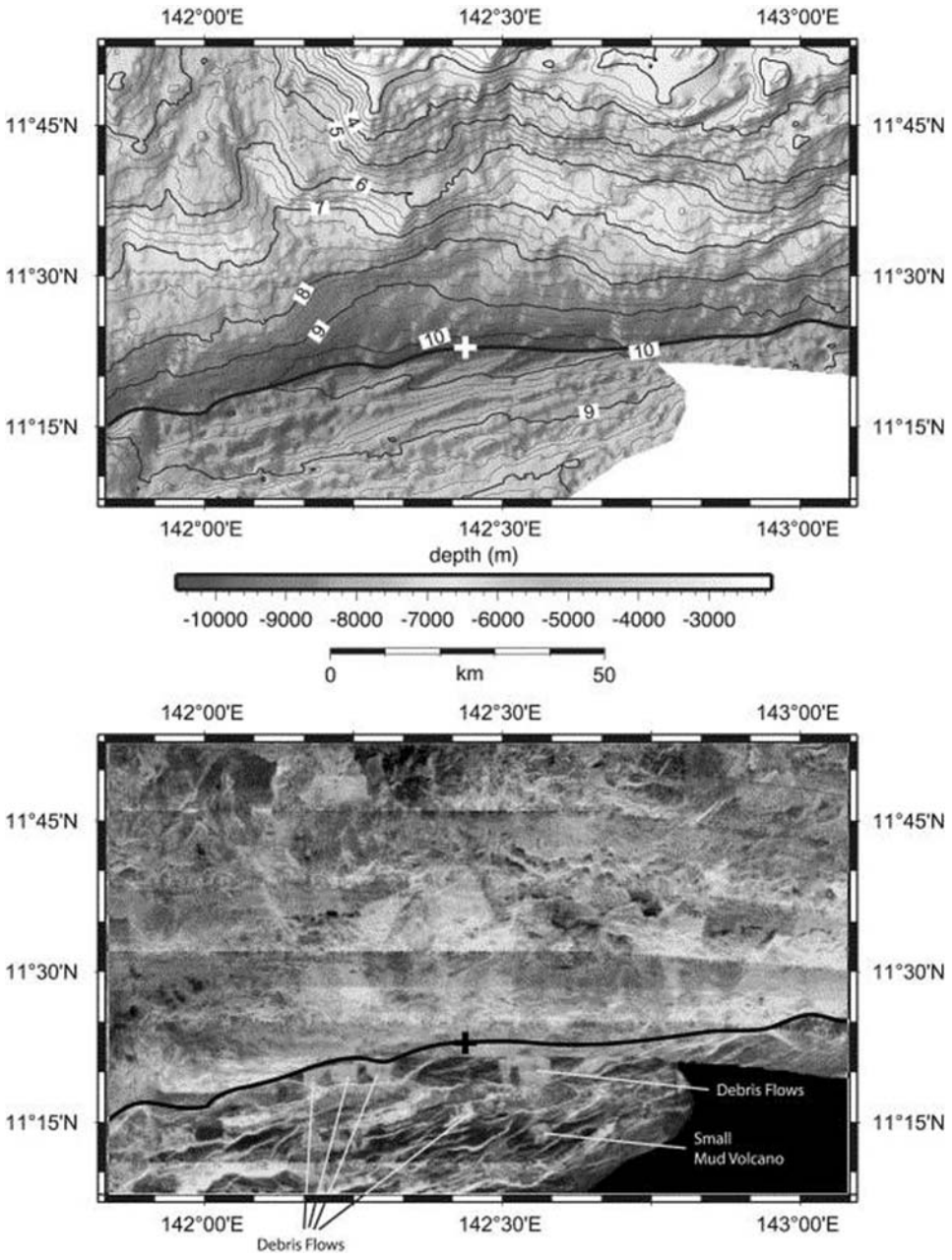

Figure 5.25. (Top) Gray-shaded HMR-1 bathymetry (with 250 m contour lines) showing the location of the Challenger Deep as a white cross and the axis of the subduction trench as a thick line. (Bottom) HMR-1 imagery from the same area (inverted from the original image to show high backscatters as high gray levels), with a series of complex structures explained in the main text (adapted from Fryer *et al.*, 2003; © Elsevier).

DSL-120) is abrupt and spans several orders of magnitude. This makes it difficult for geologists to recognize features which will be common to all sonars. A mud volcano, just identifiable on SeaMARC-II imagery, will be revealed in greater detail by TOBI imagery (because the sonar is flown closer). Similarly, faults and terrain changes seen on DSL-120 imagery will not be resolvable with GLORIA, because they are too subtle or occur at scales too small. This is why, as much as possible, the emphasis has been on high-resolution images of the different structures, processed with a high quality. Their appearance at lower resolution can easily be inferred by "blurring" and smoothing the acoustic images. The often visually stunning sonar images acquired at mid-ocean ridges and subduction zones, which have been the object of a large number of investigations over the last decades, should, however, not mask the fact that they correspond to only small portions of the overall seabed. Most of the World Ocean's seabed is made up by the abyssal plains, which are presented in the next chapter.

5.9 FURTHER READING (*see also* References at end of book)

About mid-ocean ridges

German, C.R.; J. Lin; and L.M. Parson (Eds.) (2004). Mid-ocean ridges: Hydrothermal interactions between the lithosphere and oceans. *AGU Geophys. Monograph Series*, **148**, 311 pp.

Lowell, R.P.; J. Seewald; A. Metaxas; and M. Perfit (Eds.) (2008). Magma to microbe: Modeling hydrothermal processes at oceanic spreading centers. *AGU Geophys. Monograph*, **178**, 300 pp.

About subduction and crust recycling

Juteau, T.; and R. Maury (1999). *The Oceanic Crust: From Accretion to Mantle Recycling*. Springer/Praxis, Heidelberg, Germany/Chichester, U.K., 390 pp.

Larter, R.D.; and P.T. Leat (2003). *Intra-oceanic Subduction Systems*, Spec. Pub. 219. Geological Society, London, 352 pp.

Hühnerbach, V.; D.G. Masson; G. Bohrmann; J.M. Bull; and W. Weinrebe (2005). Deformation and submarine landsliding caused by seamount subduction beneath the Costa Rica continental margin: New insights from high-resolution sidescan sonar data. In *Submarine Slope Systems: Processes and products*, Spec. Pub. 244. Geological Society, London, pp. 195–205.

6

Abyssal basins and the polar seas

6.1 INTRODUCTION

Abyssal plains and basins are traditionally defined as areas of the deep-ocean floor in which the seabed is flat, with a slope of less than 1°, and deeper than 4,500 meters. They were not recognized as distinct physiographic features until the late 1940s, and there have been very few systematic investigations of limited areas. As a result, they are among the least known areas of the Earth's surface. The examples presented in the *Handbook of Seafloor Sonar Imagery* (Blondel and Murton, 1997) came mostly from a single sonar (TOBI, 30 kHz) and from a single world-leading team at the National Oceanography Centre (U.K.). Many new results have been published in the decade since by several research groups around the world and the most representative examples will be presented in this chapter (Sections 6.3 and 6.5).

Abyssal plains and basins have an important economic potential. As a matter of routine, transcontinental cables and pipelines are laid on the deep-sea floor, and their safety and reliability relies on the correct identification of the geological features and seismic activity observed from route surveys. The 1929 Grand Banks earthquake, offshore Canada, led to a devastating tsunami and broke telecommunications between North America and Europe (e.g., Piper *et al.*, 1999). The reliance on knowledge of the seabed, particularly in abyssal regions, has become increasingly critical with the large increase in communication volume and speed requirements of the last decade. In February 2001, for example, the severing of an undersea cable cut Internet access to millions of users in China and, as a consequence, limited online speeds in the entire Asia–Pacific region, particularly in the economic hubs of Hong Kong and Singapore, until the repair could be made three weeks later. Starting in the late 1970s, several research programs have also examined selected areas for the disposal of radioactive waste, and recent studies have looked at the abyssal plains for the disposal of environmentally harmful compounds (such as from the Brent Spar oil rig in 1995). Recent studies (e.g., Müller and Holloway, 1995) have also shown the role of

abyssal plains in the circulation of water masses and the modeling of ocean circulation.

Ocean circulation is of increasing interest now because of its influence on climate change, and the recent debate on the possible slowing down of the Gulf Stream has highlighted the importance of polar regions. Polar seas have always been difficult to access, and even with the decrease in ice cover, seabed mapping in these areas has long been hampered by logistical difficulties. The *Handbook of Seafloor Sonar Imagery*, published in 1997, could not present any worthwhile example of sonar imagery taken in either the Arctic or Antarctic regions. Thanks to the efforts of many teams, this edition can remedy this, and examples in Sections 6.4 and 6.5 show the acoustic variability and richness of the polar environments.

6.2 USING ANCILLARY INFORMATION

6.2.1 Other acoustic tools

We saw in Chapter 5 (“Spreading and subduction”) that the presence of sediments had a significant influence on the visibility of surface structures with sidescan sonars. This is particularly true in abyssal plains, which are by definition very flat and homogeneous. They are mainly filled with sediments, which look relatively similar and uniform on sidescan sonar images. Regions with different backscatter patterns can sometimes be seen, but they are less easily distinguishable and interpretable than terrains in, for example, mid-ocean ridges. Another unknown is the depth of penetration of the acoustic wave, which depends on sonar frequency and the physical properties of the sediments (see Chapter 10, “Anomalies and artefacts”). This penetration effect, known as volume reverberation, is more significant at frequencies of 12 kHz or lower (corresponding to acoustic wavelengths of 12.5 cm and larger). Normark *et al.* (1993) published a famous example of the abyssal plain around Hawaii, in which large volcanic blocks visible on GLORIA imagery (6.5 kHz frequency) do not appear on higher frequency maps of the same area because of the sediment cover.

To account for this possible penetration, and to supplement the interpretation with more details, additional information is required. Sonar surveys of abyssal plains are usually coupled with seismic surveys, which provide sub-surface information. Varied acoustic energy sources can be used: air or water guns, boomers, sparkers, dynamite or other explosives (e.g., Telford *et al.* 1990; Juteau and Maury, 1999). These sources usually transmit at frequencies between 10 Hz and several hundred Hertz. After propagating through the water column, the acoustic wavefronts penetrate the sedimentary layers or the hard rocks below the seabed. They are reflected or refracted by geological discontinuities, and some of the energy returns back toward the surface. They are recorded by receivers towed behind the survey vessel. Mono-channel seismic reflection provides a good resolution for shallow penetration, whereas multi-channel seismic reflection provides a variable resolution, but deeper penetration. Seismic refraction techniques are used to study the deepest

structures, usually with two ships carrying out long seismic profiles, or using one ship and a buoy. The accumulation of close 2-D seismic profiles can be used to create 3-D seismic images of the seabed and sub-seabed, and the industry has now firmly moved into 4-D seismics: 3-D seismic data + time as the extra dimension allowing, for example, the tracking of flow paths and fluid distributions in reservoirs (e.g., Ristow *et al.*, 2002).

But not all surveyors can afford the associated cost and time, nor do all studies necessitate such information. Most if not all sonar platforms have a depth-sounder or sub-surface acoustic profiler, which gives the height of the vehicle above the seafloor. Because it transmits at lower frequencies (typically 3.5 or 7.5 kHz), the depth profiler can penetrate sedimented seafloor, and show the structure of the shallow sub-surface (Figure 6.1). These profiles show time (i.e., position along-track) on the horizontal axis and travel time (i.e., distance to the transducer, or depth) of the echoes on the

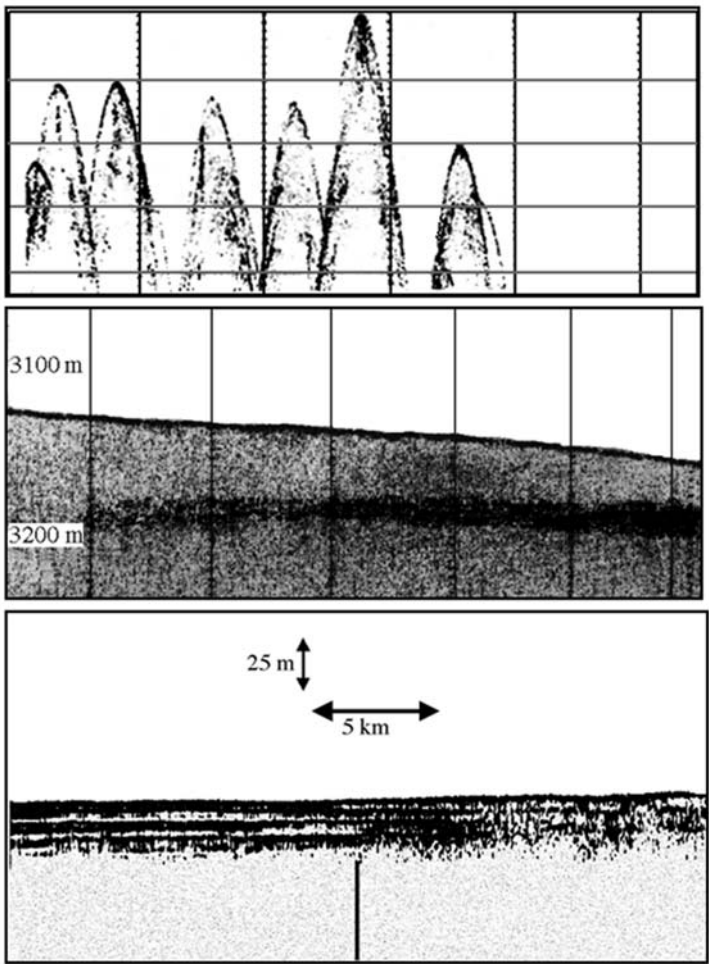

Figure 6.1. Examples of typical 3.5 kHz profiles in different terrains: (top) hyperbolas corresponding to topographic highs and lows; (middle) acoustically transparent seafloor; (bottom) transition between turbidites (left of the vertical bar) and debris flow deposits (right of the vertical bar).

vertical axis. Penetration depths vary according to frequency and the type of terrain. For example, the top profile in Figure 6.1 exhibits steep hyperbolas. Their sharp definition indicates a hard seafloor. The high variations in travel times are characteristic of bathymetric highs and lows. This corresponds to an acoustically hard seafloor (little or no sedimentation), deeply cut by gullies or troughs. As with seismic profiles, travel times exaggerate the apparent depth shown in acoustic profiler records. The middle profile of Figure 6.1 exhibits a continuous and strong first return that gently slopes down to the right. This sharp line lies above a gray sub-stratum in which a horizontal thick black line can be seen. This is an example of an acoustically transparent seafloor (top echo), under which are small objects with varying homogeneities or compositions. The second harder reflector beneath may be the original basement, now completely covered with softer, acoustically transparent sediments. The seafloor shows a small-scale depth variation of a few meters. In conjunction with the sidescan sonar image with which it was acquired, the data are consistent with the interpretation of a debris flow deposit. The lower profile shows a smooth, flat seafloor underlain by two different regions (the transition is indicated by the vertical bar). On the left is a transparent substrate with parallel-layered harder echoes. This corresponds to different sequences of turbidites, emplaced successively. On the right, the echoes are more complex: they change from a sharp or prolonged echo to fuzzy weakly reflective patches. These correspond to mud flow or debris flow deposits. These are just a few simple examples of low-frequency acoustic profiler data. New types of profilers can use several frequencies, to penetrate to different depths and gain different types of information (e.g., Dung and Stepnowski, 2000; Kloser *et al.*, 2001) or the non-linear acoustic interaction of two beams to generate a very thin beam with high penetration (parametric arrays, like the TOPAS sub-bottom profiler). More systematic explanations of the relationship of sub-bottom profiles with sidescan sonar imagery and the local geology, calibrated with coring, dredging, and deep-tow camera surveys, can be found in Pratson and Laine (1989), O'Leary and Dobson (1992), and Masson *et al.* (1992a) *inter alia*.

6.2.2 Non-acoustic remote sensing

Acoustic imaging of the seabed can be supplemented with non-acoustic techniques but, as expected, there is a trade-off between resolution/coverage and proximity to the seabed. Optical images of the seabed are now routinely recorded, using video or still photography, from vehicles close to the seabed. The general type of seafloor can generally be identified, along with its biological coverage (if any), and techniques such as stereophotogrammetry (e.g., Lyons *et al.*, 2002) can provide highly detailed information about its topography and small-scale objects. But the other characteristics of the seabed (e.g., exact grain size, amount of sub-surface bioturbation, sediment contents) remain inaccessible. The conditions under which the images are acquired often cause problems too: inadequate and variable lighting, unaccounted variations in the water column inside the field of view (e.g.. shimmering or turbulence from propellers), high turbidity, etc. Laser-based techniques offer the advantage of

constant, quantifiable illumination and independence from all but the most severe disturbances in the water column. Laser linescan systems (e.g., Raytheon LS-4042) sweep the seafloor with a pencil-thin laser beam, using a mechanism similar to the "push-broom" devices of Earth-orbiting satellites. Use of different filters in analyzing the reflected light yields multispectral capability, at ranges three to four times longer than conventional systems. The emergence of high-repetition solid-state blue–green lasers and fast electronics provide new possibilities, although the operational range remains determined by the red channel (more attenuated in water, cf. Figure 1.1). The differences in polarization of the transmitted and received light can also help in discriminating between objects. But even these new systems still provide coverage around the survey vehicle of the order of meters.

Wider, deeper coverage can be achieved with controlled source electromagnetic (CSEM) remote sensing. It has been developed through the last 15 to 20 years (e.g., Cox *et al.*, 1986) and is now used in marine surveys to image the structure of the seafloor at scales comparable with those of seismic techniques (e.g., Sinha *et al.*, 1990; MacGregor *et al.*, 1998). CSEM techniques use the variation with time of an electromagnetic field from an artificial source, towed at depth behind the ship. Energy variations detected by a receiver far enough from the transmitter follow diffusion paths through the crust, and give details of the resistivity structure (i.e., the structure of the sub-surface down to depths of several kilometers; see MacGregor *et al.*, 1998).

An interesting and unusual approach has used radionuclides to distinguish types of seabeds. Their concentration in sediments depends on size, origin, and mineral composition; it is usually very low, but still measurable with state-of-the-art equipment. According to de Meijer *et al.* (2000), mud shows more radioactivity per unit mass than sand or gravel, whereas sediments originating from granites are more radioactive than the weathering products of basalt. In addition, sediments occasionally also contain radionuclides released by anthropogenic processes (e.g., fertilizer production). Each type of seafloor, sedimentary or not, should therefore exhibit a distinctive radioactive signature. The implementation by de Meijer *et al.* (2000) led to the Multi-Element Detector Dystem for Underwater Sediment Activity (MEDUSA), based around a highly sensitive scintillation crystal encased in a watertight casing. MEDUSA is towed over the bottom at speeds of about 2 m/s (*ca.* 4 knots), and the γ rays emitted by the seabed are measured at 10-second intervals. Radioactivity concentrations are analyzed in real time, using calibration points from a couple of samples taken at the beginning of the survey. The applications presented by de Meijer *et al.* (2000) include the mapping of mud concentrations in a dumping site 20 km northwest of Rotterdam Harbor (for an area of 15×10 km), and a high-resolution sand/mud map of the Hollandsch Diep (for an area of 20×3 km). Radioactive characterization of the different types of seabeds is accurate and relatively fast. However, the method has been tried only in shallow waters (down to 100 m with the GIMS/CS3 system of Noakes *et al.*, 1999), and both technological and scientific developments may be needed for use in deeper waters such as on continental margins, let alone abyssal plains. This approach is also limited as it provides information only for the small portion of seafloor directly below the instrument.

6.2.3 Direct sampling

Most of the techniques of direct sampling have not evolved much since the 19th century, despite improvements in either measurements of the samples or control of their position (through GPS and acoustic transponder technology). Coring is commonly used for sampling soft and water-saturated oceanic sediments. There are many types of coring techniques, but all enable the sampling of a complete cross-section of sediments, down to depths of several meters or hundreds of meters, and its laboratory analysis for different properties, using geoacoustics, X-ray tomography, microscopic analysis, etc. (e.g., Orsi *et al*. cited in Pace *et al*. 1997; Balsam *et al*. 1999). Cores can be very precisely located on the seafloor, and use of video data adds to the final interpretation, in particular by showing how representative it is. The problem is that cores are very localized (a few centimeters or tens of centimeters in diameter), and very time-consuming and expensive to acquire, especially in deeper waters. More superficial measurements can be obtained with freefall instruments. Penetrometers dropping through the water column penetrate the seabed to different depths and at different rates depending on the geometry, mass, and impact velocity of the probe, and on the shearing strength of the sediment. If the physical dimensions and terminal velocity of the probe are fixed, it is possible to infer the shearing strength and certain other properties based on an analysis of the deceleration signature, compared with a database compiled from tests on different types of sediments. This is the approach used by Stoll and Akal (1999) for the XBP (expendable bottom probe). Rosenberger *et al*. (1999) developed a similar instrument, measuring the resistivity of the seafloor. Longer stations on the seafloor are possible with complete instrumentation platforms, which can take more time-demanding measurements of seabed properties. This is, for example, the case of ISSAMS, the In Situ Sediment Geoacoustic Measurement System, developed by Barbagelata *et al*. (1991), which measures compressional and shear speed and compressional attenuation. On a less localized scale, finally, dredges consist in a strong frame attached to a heavy wire and lowered to the seafloor. The dredge is towed directly on the bottom, pulling out anything not strongly attached. There are different types of dredges (e.g., Juteau and Maury, 1999), but even the most adapted dredge might bounce off obstacles (e.g., rocky outcrops) or scrape the seafloor without sampling it. Furthermore the samples collected are mixed and their precise location along the dredge track is impossible to know. Figure 6.2 shows several typical instruments. Note that dredges are potentially the most destructive to the seabed and possible habitats (see Chapter 9).

6.3 ABYSSAL BASINS

6.3.1 Geological background

Study of the abyssal plains started in earnest in the 1970s, with the examination of their potential for the disposal of radioactive waste. With the exception of trenches (see Chapter 5, "Spreading and subduction"), abyssal plains often form the deepest and largest parts of the oceans. Approximately 75 flat areas have been recognized in

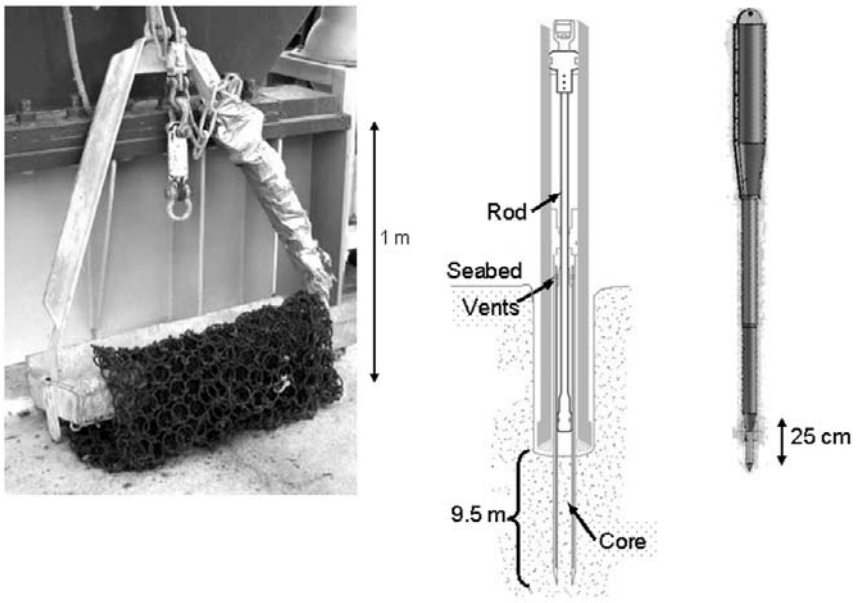

Figure 6.2. Instruments used for direct sampling of the seabed (note the different sizes). (From left to right) A typical dredge; a deep-sea coring system, and a freefall penetrometer (adapted from *http://www.mbari.org/expeditions/EasterMicroplate/gear.htm*, *http://www-odp.tamu.edu/publications/tnotes/tn31/apc/fig_01.htm*, and *http://www.marum.de/Binaries/Binary 16863/CPT_Flyer.pdf*, respectively).

the world as being abyssal plains. In the Atlantic, the largest abyssal plains are located between the base of the continental slopes and the distal parts of the Mid-Atlantic Ridge, and in such topographic highs as the Madeira–Tore rise. Their monotonously flat seabed is produced by the ponding of sediments transported beyond the base of continental slopes (Figure 6.3), which causes an infilling of the deeper areas between abyssal hills. The hills become gradually submerged as the area of the plain extends, although few plains have become so mature as to have no protruding hills left. As a result of the infilling, all depressions in the seabed become flattened and there are few undulations in the seabed of more than a few meters, although small regional slopes may exist. Their surface consists in a smooth blanket of pelagic sediments, made of the remains of pelagic organisms (by opposition to hemipelagic sediments, found closer to the shores and also containing small amounts of terrigenous material), with a small proportion of products of volcanic origins, and, in very limited areas, hydrothermal sediments (see Section 5.5). On sonar images, they will be characterized by very low and uniform backscatter, organized in smooth and poorly contrasted textures. The term of "abyssal plains" is often extended to include abyssal basins. The latter are the product of tectonic and volcanic processes associated with ridge dynamics, subsequently modified by off-axis sedimentation and

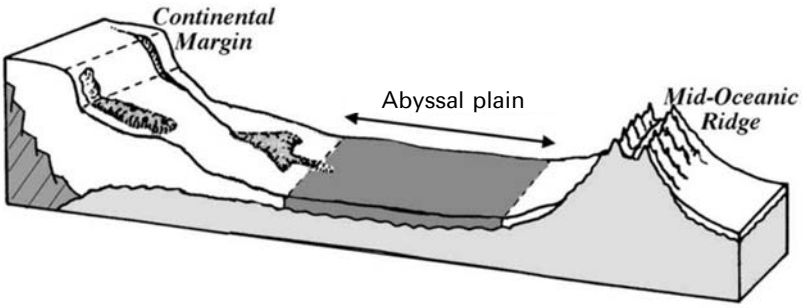

Figure 6.3. Abyssal plains and basins are the flattest areas on the seabed. On sonar images, they will be characterized by very low and uniform backscatter, organized in smooth and poorly contrasted textures.

mass-wasting. They are also associated with important depths and small topographic variations, and cover large areas of the seafloor. Abyssal plains generally disappear at subduction zones (see Section 5.1).

6.3.2 Sediment input

The abyssal plains are covered with sediments, mainly turbidites. Large-scale surveys around the world have shown that hemipelagic sediments usually make up less than 10% to 20% of the sediment input, and that debris flows are a distant third in overall importance (Pilkey, 1987). How are all these sediments transported there? The bulk comes from neighboring continental margins (see Chapter 7, ''Continental margins''). It arrives via point sources (i.e., submarine canyon mouths and fans). Events that provide material from adjacent slopes without canyons tend to be small and infrequent and are only minor sources of sediments. These events are constant through long periods of time.

The first example is a GLORIA image of the Mississippi Fan (Figure 6.4). Every day, the Mississippi River discharges several millions of cubic meters of water heavily laden with sediments. The sediments are transported down the continental slope and deposited along the Mississippi Canyon and, close to the abyssal plain, on the Mississippi Fan. This sidescan image was acquired during the survey of the southern United States Exclusive Economic Zone, using the shallow-towed system GLORIA (6.5 kHz, 60 m pixel size after processing). Regularly spaced survey lines run in a SW–NE direction, and the resulting swaths have been merged into this mosaic. The terrain slopes gently down to the southeast, with water depths varying from 2,250 m to 3,000 m in the area covered by the image. The Mississippi Fan is the dominant morphologic feature of the Gulf of Mexico and appears as a large region of high backscatters extending several hundreds of kilometers. Much of the surface of the fan comprises highly reflective deposits, called depositional lobes. They all seem to have been fed from a single meandering channel system that can be traced across the fan. The largest of these is a mass-wasting deposit on the middle to upper part of the fan. The low-backscatter regions around the edges of the fan are interpreted to be

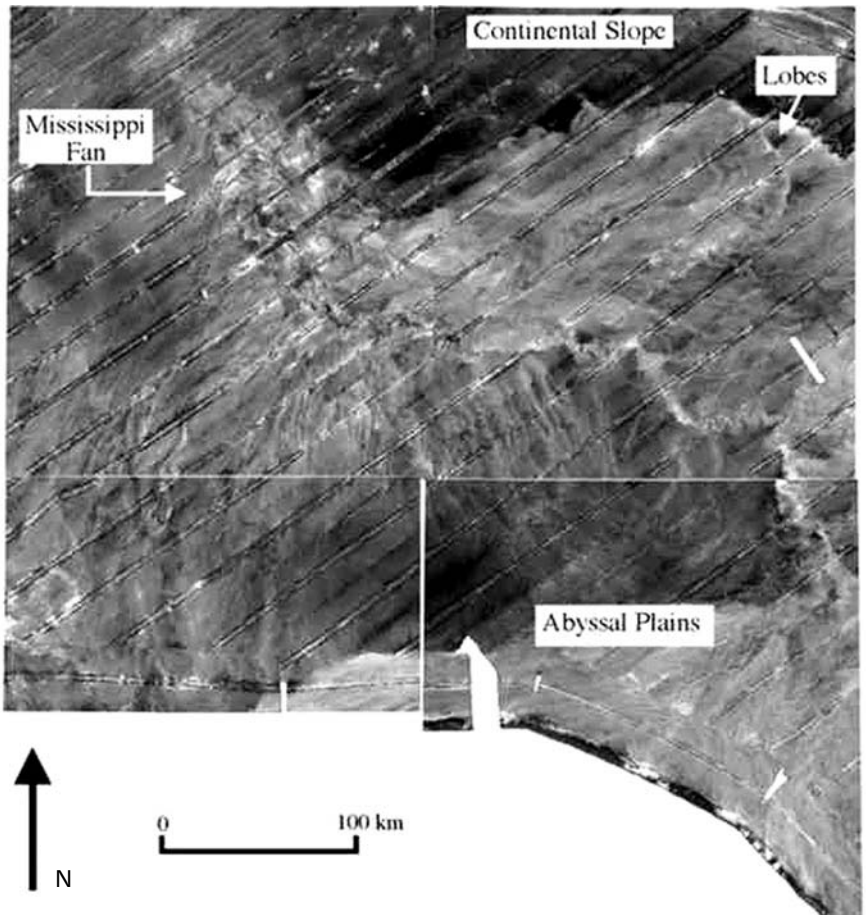

Figure 6.4. GLORIA imagery of the Mississippi Fan, Eastern Gulf of Mexico. Huge flows of sediments (turbidites) are coming from the Mississippi River. They cross the continental slope (see Chapter 7) down to the abyssal plains (courtesy of the United States Geological Survey).

fine-grained hemipelagic deposits. The surface of the fan to the west of the channel has a different acoustic texture than in the east, with radiating linear stripes of undetermined origin (but apparently related to the redistribution of sediments).

Submarine canyons are the other high providers of sediments for the abyssal plains. Connecting with the Mississippi Fan, the De Soto Channel is the highly meandering channel visible in Figure 6.5. This image was also acquired with GLORIA, and actually corresponds to a small subset of Figure 6.4. The channel shows as a bright sinuous line on a darker background, trending to the southeast. The channel is constantly less than a kilometer wide and does not show any interruption apart from the sonar tracks, where its structure is not visible. The De Soto Channel is part of an elevated channel and levee system (levee ridge). The highly reflective debris

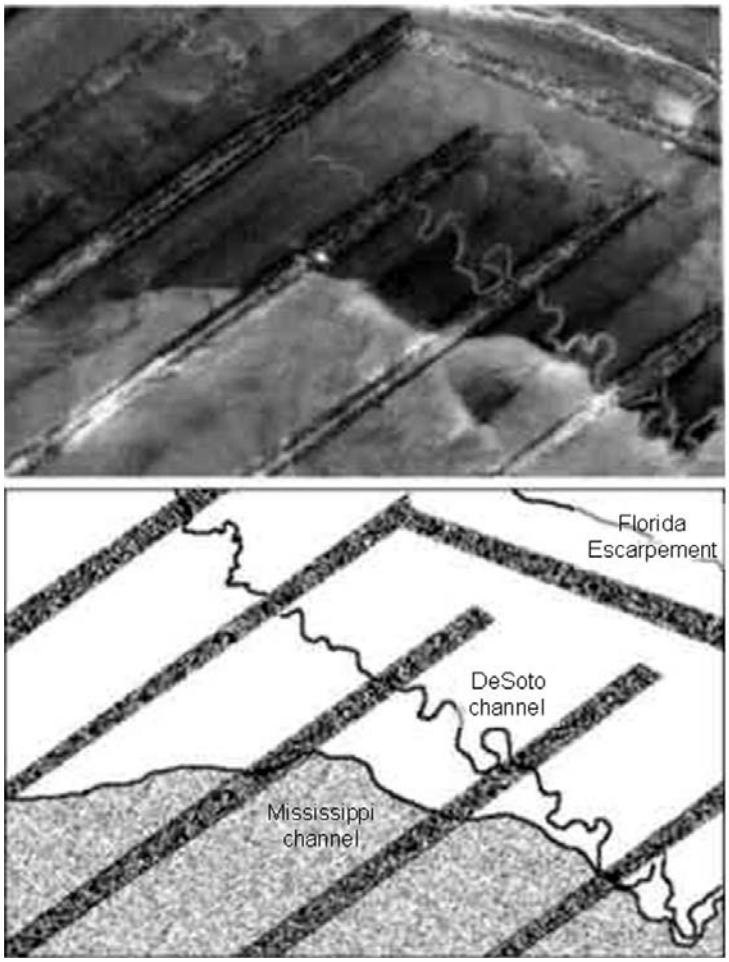

Figure 6.5. GLORIA imagery of the De Soto Channel, Eastern Gulf of Mexico. The schematic interpretation shows the nadir tracks of the survey lines (dark gray pattern), the northern portion of the Mississippi Fan (light gray pattern) and the highly meandering canyon in black. The image covers a ground area of 110×75 km (courtesy of the United States Geological Survey).

flow deposits from the Mississippi Canyon area are dammed by this elevated channel until the flow eventually overtops the levee and buries the channel. The southern extent of this channel and its deposits is masked by the debris flow deposits of the Mississippi Fan. The bright straight line visible in the northeast corner of the image corresponds to the fault scarp of the Florida Escarpment (where the depth goes down from 2,000 to 3,000 m in less than 3 km).

Not all processes of abyssal plain filling occur with this regularity and constancy. Recent discoveries have shown that some major abyssal plain deposits were in fact the product of huge submarine landslides (e.g., Holcomb and Searle, 1991; Hampton *et al.*, 1996; Masson, 1996), triggered by events up to several hundred kilometers away. They can involve enormous amounts of material: volumes as large as 20,000 km^3 and run-out distances in excess of 140 km have been reported (e.g., Hampton *et al.*, 1996). One such example comes from the Storegga Slide complex, offshore Norway. It forms

the largest exposed submarine slide in the world, affecting an area of approximately 95,000 km^2 (Haflidason *et al*., 2004), and the latest slide, around 8,000 years ago involved an area the size of Iceland and created a tsunami whose effects were documented all the way to the British Isles. Figure 6.6 shows high-resolution TOBI imagery from a portion of the slide, acquired at 30 kHz and processed at the 6 m pixel size (Micallef *et al*., 2006). The larger image on the left corresponds to a half-swath, ensonified from upper left to bottom right (facing the slope). The low, mottled backscatter corresponds to the background sediment. Several very bright, localized reflectors with jagged outlines are visible. They correspond to blocks carried downslope by the Storegga landslide. The inset shows a close-up of some of these blocks, imaged at near-range to mid-range. Their sonar-facing slopes are very bright, close to saturation, indicating they are high and made of rougher or acoustically more reflective material. Dimensions of the order of 120 m for the largest blocks are impressive. Some, in particular in the top-left corner of the inset image, have dark areas facing toward the sonar. Most likely, they correspond to local depressions caused by the weight of these blocks on the underlying sediment (the depressions on the other side of the blocks, facing away from the sonar, are generally not visible because they are masked by the higher blocks). Similar structures are visible on sidescan sonar imagery associated with many other landslides around the world, including the El Golfo avalanche, extending 600 km west of the Canaries on to the Madeira Abyssal Plain (Masson, 1996), the Saharan debris flow, with a run-out of 700 km (Gee *et al*., 2001), or the Alika landslide off Hawaii, believed to have caused

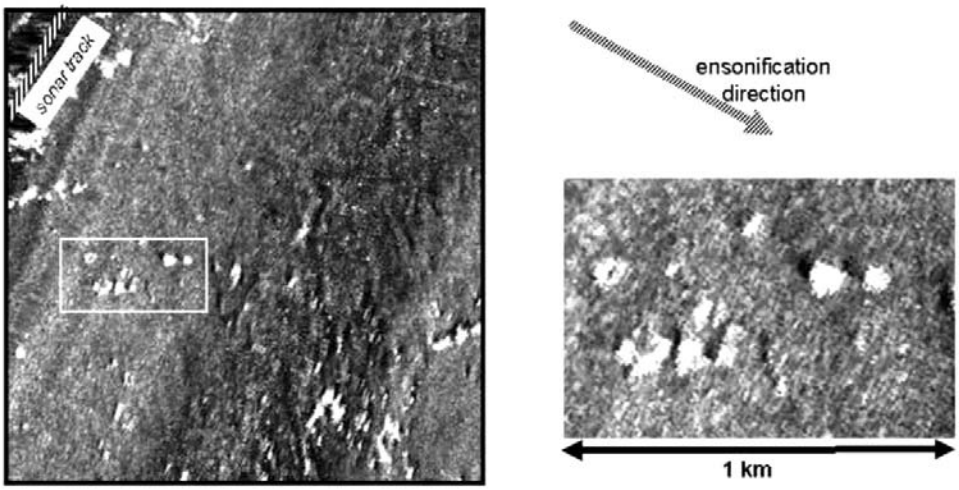

Figure 6.6. High-resolution TOBI imagery from a portion of the Storegga Slide complex (from Micallef *et al*., 2006). The half-swath on the left is approximately 3 km wide, with a 6 m pixel resolution. The slope decreases from SE to NW. The inset (right) shows some large blocks carried down the slope. Their sonar-facing slopes are very bright, hinting they are rather high, and some (top-left corner) have dark areas facing toward the sonar, and most likely to be depressions caused by their weight.

the enormous tsunami that reached a height of 325 m on the neighboring island (Moore and Moore, 1984).

6.3.3 Relict structures

The high input of sediments in the abyssal plains does not always obliterate pre-existing structures. These relict structures may come from previous sediment flows, or from the original basement on which the sediments have accumulated. Figure 6.7 shows a high-resolution TOBI image of sediments which have nearly completely obliterated pre-existing structures. This image is nearly 3 km wide and ensonified from the top. The first structure is visible on the left, because some reliefs have not completely disappeared and, facing the sonar, they appear slightly brighter, with textures a little rougher. The structure can be traced as a sub-vertical ellipse, and very slightly darker sediments are visible on its SW slope. The second structure, on the right of the image, is more compact: its sonar-facing slope is nearly invisible, and it is mostly its near-triangular shape and the small variations in sediment textures that give it away. Again, slightly darker sediments on its SW slope are another hint of the relief. But the small variations in overall gray levels mean that these pre-existing structures are better checked with concurring bathymetry or sub-bottom profiling, if available.

If new sediment flows come in, they will move around the structures, usually creating streamlined halos of coarsely textured rubble, teardrop-shaped or just elliptical depending on the velocity of the flows. These teardrops are elongated down the slope, and aligned along the apparent flow direction. The streamlined structures may be formed by material aggregated to the edges of the block, or by the progressive fragmentation of the block's edges in the flow. Some relict structures could be "rafted

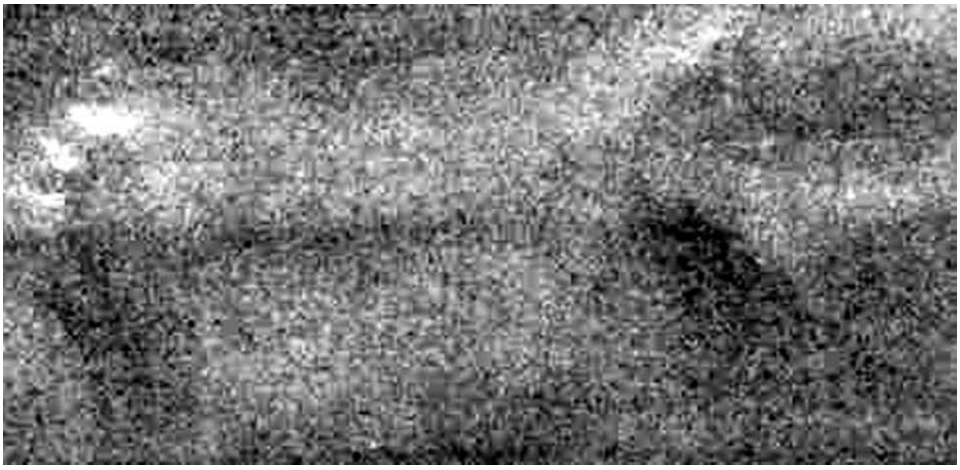

Figure 6.7. This TOBI image (2.9 km wide) was acquired at 30 kHz and ensonified from the top. The draping of sediments over pre-existing structures nearly masks the original relief.

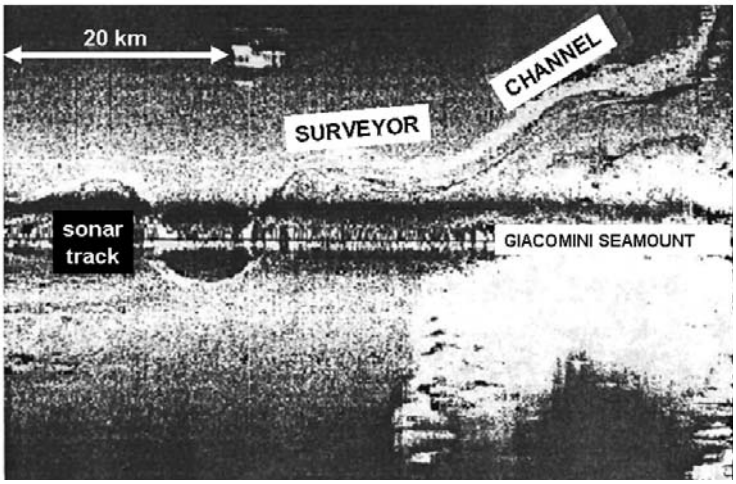

Figure 6.8. This GLORIA image was acquired at 6.5 kHz and despite its low resolution (60 m/pixel) shows how pre-existing structures (in this case the Giacomini Seamount, off Alaska) can affect the path of sediments (here, the Surveyor Channel) (modified from Carlson *et al.*, 1990).

blocks'' (i.e., a coherent sediment block rafted by the flow to its present position). The distinction between the two hypotheses would be made on the dimensions of the block (it should not be much thicker than the flow deposit which transported it) and if possible on additional ground-truthing data such as cores. Figure 6.8 shows a GLORIA image from a sizable sediment flow, moving around a pre-existing seamount. The Surveyor Channel is recognizable as a sinuous flow, similar to a river on land and clearly showing the sonar-facing bank and distinct sediment textures. It veers off from NE/SW to ENE/WSW to move around the Giacomini seamount, with its characteristic shape (sub-circular, bright rough to saturated backscatter textures and central summit leaving a shadow in the SE corner of the image).

The teardrop shape of diverted sediment flows is familiar from terrestrial equivalents: sediments around islands in a rapidly flowing river exhibit a similar shape. So do the yardangs, positive features shaped like inverted boat hulls and formed by high wind erosion of old lava flows. Spectacular analogues of these features are also observed on Mars. The planet is thought to have been at one time submitted to catastrophic flooding, huge rivers carving out large canyons such as Valles Marineris and producing important flows. These flows were deflected by pre-existing structures and created similar teardrop shapes (Figure 6.9).

6.3.4 Sedimentary structures

Sediments are transported down the continental slope to the abyssal plains by gravity, through four possible mechanisms: slides, slumps, debris flows, and turbidity currents (e.g. Bowles *et al.*, 1998 and references therein; Weaver *et al.*, 2000). Slides generally occur higher on the continental shelf, and examples are presented in Chapter 7 (''Continental margins''). Slumps correspond to local sediment failure or shear along a usually curved surface. The downslope motion is rotary such that

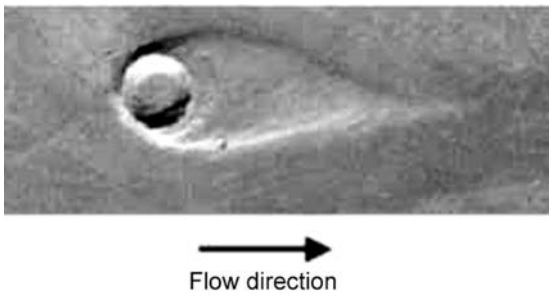

Figure 6.9. Martian analogue of a relict block and a teardrop-shaped deflection of the flows. In this case, the block is an 8 km wide impact crater formed by a meteorite. The flows were created by the intense floods thought to have prevailed on Mars a long time ago. They created a moat about 600 m high. The scale of these features is much higher than on Earth, but their size/height ratio and their morphology are similar to those of terrestrial features (this optical image was taken by the NASA Viking satellite; © NASA-JPL).

as the back of the block slides down the front tips upward. This backward tilting may be so extreme that the top surface of the slump block exhibits a reverse slope and faces uphill. The actual downslope displacement of the sediment mass is relatively small and slumps often keep the sediments as coherent masses (Bowles *et al.*, 1998). Figure 6.10 shows a typical slump, at the edge of the Storegga landslide. This image was acquired with TOBI (30 kHz, 6 m/pixel) and shows a well-defined slump with its characteristic arcuate pattern, made of small concentric ridges and troughs (alternating bright and dark edges on the sonar image, depending on whether the slopes face toward or away from the sonar). The bends show the direction in which the slump occurred. Slumps are not restricted to abyssal plains and basins, and can occur in all areas with sufficient sediment instability (as we shall also see in Chapter 7).

Only debris flows and turbidity currents are capable of transporting sediments for long distances (10 km or more) over gentle slopes (1° or less) to the deep-sea floor (e.g., Pickering *et al.*, 1989; Bowles *et al.*, 1998; Weaver *et al.*, 2000). Debris flows are considered an intermediate step between slides and turbidity currents, a transition that involves extensive dilution of the debris flow material (Bowles *et al.*, 1998 and references therein). Turbidity currents are gravity-driven, bottom-flowing currents laden with suspended sediment (Bowles *et al.*, 1998). Whereas debris flows exhibit a viscous-like behavior, high-density turbidity currents rely on turbulence to maintain sediment in suspension, which explains how they can move downslope at high speeds. Values as high as 100 km/h have been, for example, quoted by Bowles *et al.* (1998) for the 1929 Grand Banks event. Turbidity currents are the main mode of transport of terrigenous sediments from shallow water to deep water, usually via large canyons or canyon systems that incise the margins (see Chapter 7, "Continental margins"). As the flow leaves the canyon, it will spread and, owing to the much smaller slopes, decelerate. The reduced turbulence will deposit the coarsest materials. This reduces further the density of the current, slowing it down again until the next coarsest

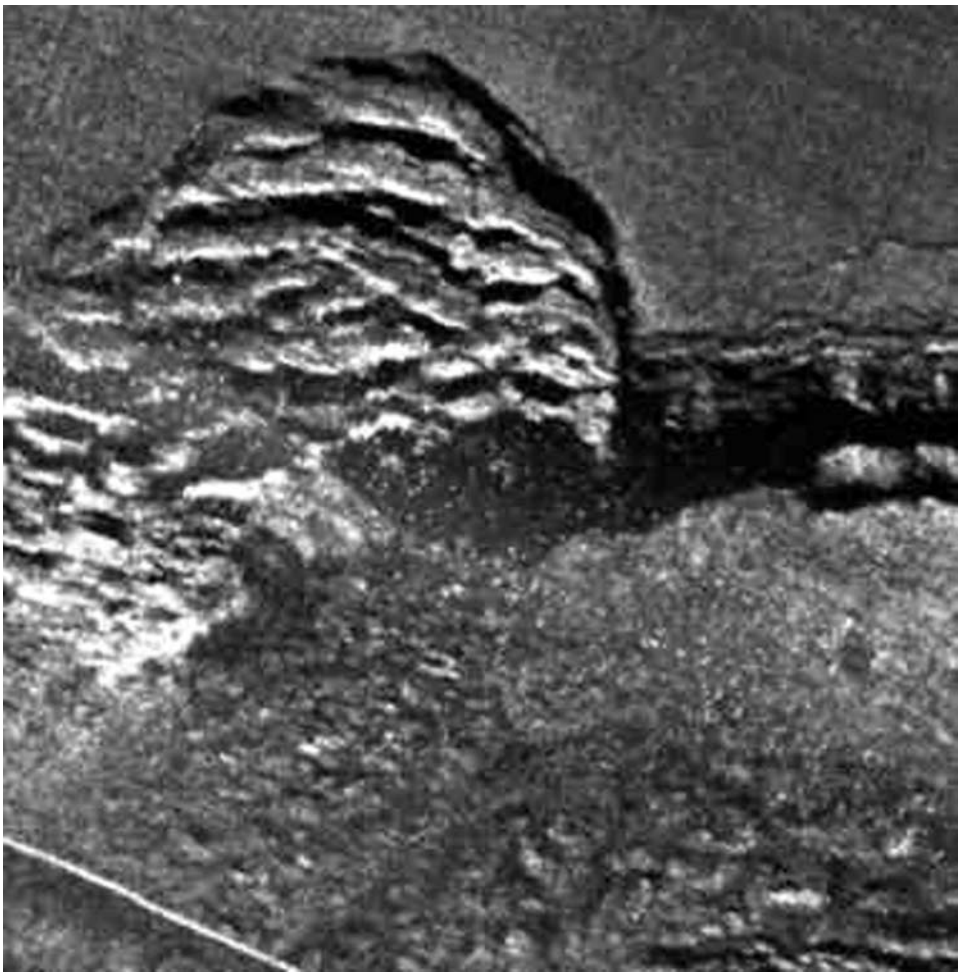

Figure 6.10. High-resolution TOBI imagery from a slump at the edge of the Storegga landslide. The image is approximately 3 km square and ensonified from the NE. The diagonal white line in the SW corner is a sea surface reflection. The main morphological units in this image are easily recognized: undisturbed sediments in the NE, the slump and its characteristic arcuate pattern, and rougher textures close to the deformation area (data from Micallef *et al.*, 2006).

fraction of sediments gets deposited (see details in Bowles *et al.*, 1998). Through several iterations of the same process, the turbidity current will gradually fan out and deposit increasingly less coarse sediments, in thinner layers. These deposits are called turbidites. They are most often graded both along the flow direction (change in coarseness, i.e., brightness and texture) and vertically (with finer materials closer to the top of the sediment layer). A single layer, representing one depositional event, can extend over $100\,km^2$ or more, and be several meters to millimeters thick. The surface of debris flows will vary with composition and mode of deposition, and this

difference will be modified depending on the frequency and resolution of the imaging sonar, as well as its imaging geometry (cf. Figure 5.5). On sidescan sonar, debris flow deposits are brighter and sport an irregularly textured appearance, with no strong linear structures. Sub-bottom profiles show acoustically transparent sediment bodies slightly higher than the background.

In abyssal plains, the pre-existing bathymetry plays an important role in determining flow paths and turbidite thicknesses. The individual turbidity currents produce tongue-shaped turbidites elongated in the direction of the flow. The production of turbidites with other shapes is usually due to material arriving on the plain from several points at the same time, combining to form a single turbidite system, or to the restriction of the flow by topographic contours (the turbidites are then named contourites). Strictly speaking, contourites are sediments deposited or substantially reworked in deep water by the action of bottom currents (Rebesco and Stow, 2001). First observed in the 1960s along the eastern North American continental margin, they are now known to cover large parts of ocean floors and continental margins. Contourites are widespread throughout the deep sea, ranging from those that build up individually distinct bodies (mounded drifts) to those that occur closely interbedded with other deep-water facies. Most typically, they are composed of fine-grained, structureless (highly bioturbated) mud. However, they also show wide variation in grain size, including sandy contourites and gravel lag deposits, as well as in composition and preserved sedimentary structures. When not mixed with other types of deposits (e.g., turbidites or hemipelagites), contourites may be clearly recognized in seismic data according to widely agreed criteria (e.g., Faugères *et al.*, 1999 and the revised criteria of Rebesco and Stow, 2001).

High-resolution imagery will show bands of distinct backscatter intensities, corresponding to fine-scale flow banding along the main directions of sediment transport (Figure 6.11). If they are nearly parallel to the sonar track, these lineations are more difficult to see than if there is a substantial angle. This may be due to the small distances between the different lineations. The distance between two successive lineations will appear larger if it is imaged in an oblique line, and therefore will stand more chances of being visible on the sonar record. Flow banding is generally on a scale of tens to hundreds of meters. Sidescan images show no indication of relief, except rare tiny acoustic shadows at the edges of the bands. This indicates the relief is small, probably less than 1 meter. Flow banding is considered to result from flow streaming of clasts, with variations in clast size between bands affecting the amount of backscatter. Some of the flow lineations are oriented with varying angles, showing buckles reminiscent of structures under compression. These features are pressure ridges. They have been observed in some sidescan images of other submarine sediment slides, and are usually seen in sub-aerial landslides, mud slides, and sedimentary facies (e.g., Price and Cosgrove, 1990). The orientation of the indentations and their wavelengths give details about the direction and strength of the compression they have undergone.

Similar lineations can sometimes be seen in high-resolution imagery from abyssal plains, but with different spatial characteristics: 10 m to 50 m wide, 20 m to 200 m apart. From their context, at the limit between a debris flow and undisturbed

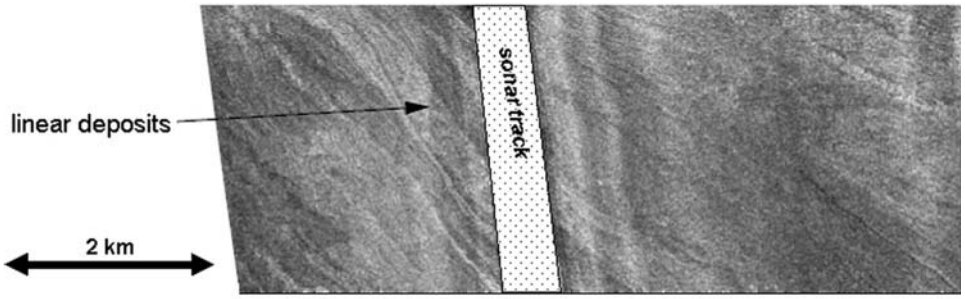

Figure 6.11. High-resolution TOBI imagery of flow-banding oriented obliquely to the sonar. The flow is oriented along the main direction of the lineations. Note how the acoustic appearance of the lineations varies with relative angle to the sonar track (adapted from Gee *et al*., 2001).

sediments, they are interpreted as erosional grooves. They are sometimes associated with erosional scarps (e.g., Piper *et al*., 1999; Gee *et al*., 2001). The reader is directed to Gee *et al*. (2001) for a detailed analysis of sidescan sonar imagery from debris flows and turbidity currents, in the context of the Saharan Debris Flow.

6.4 POLAR SEAS

6.4.1 General setting

The environments of the two poles (Arctic and Antarctic) look rather dissimilar, but they cover similar types of seabeds. In this section, we shall focus on what makes them different from other seabeds around the world. Domack (2000) pointed out the near absence of "glaciated seafloor features" in the *Handbook of Seafloor Sonar Imagery*, and explained that "much of the information [had] only just been published in the open literature". Bibliographic references throughout this section will therefore aim at showing the relative abundance of new articles on this subject. The reader will be pointed toward relevant sections of other chapters when seafloor features, as seen with sidescan sonar, are not significantly distinct from their equivalents in more temperate regions. Very often, the scale of seabed structures and the amounts of sediment cover mean they are best seen with other acoustic instruments than sidescan sonar (namely, multibeam and echo-sounders). The interested reader will find beautiful images in Wille (2002) and in-depth analyses in the authoritative volume on *Glaciated Continental Margins* edited by Davies *et al*. (1997).

Following Jakobsson *et al*. (2003), we define here the Arctic Ocean seabed as the combination of the broad continental shelves of the Barents, Kara, Laptev, East Siberian, and Chukchi Seas, the White Sea, and the narrow continental shelves of the Beaufort Sea and the Arctic continental margins of the Canadian Arctic Archipelago and northern Greenland (Figure 6.12, top, see color section). The Arctic Ocean is almost completely landlocked, with Fram Strait (between Greenland and Svalbard)

being its only connection to the rest of the global ocean. The neighboring landmasses are bordered with continental margins (making up ~70% of the Arctic Ocean). Variable calving from ice sheets and glaciers will affect the amount of sediment input and the areas over which it is deposited. As a brief summary (from Ashley and Smith, 2000), in temperate glacial environments, terrigenous sand and mud are layered periodically and decrease in grain size with distance from the glacier's calving front; in sub-polar glacial marine environments, the biogenic proportion of sediments increases and the terrigenous proportion decreases with distance from the glacier; and in polar glacial marine environments, terrigenous mud is located below the surface ice at the glacier's front and biogenic mud outside. High rates of sediment supply, steep slopes, and large depths at the end of the slopes mean slope instability and debris flows will be more important than at non-polar continental margins (e.g., Martinsen, 2005). The role of ice sheets and glaciers is explained further in Dowdeswell and Siegert (1999) and Gipp (2003); in particular, how variations in sediment input will affect the types of debris deposits at glacial margins. The main types of seafloor structures, as visible on sidescan sonar records, are presented in Chapter 7 (''Continental margins'') and will not be repeated here. Abyssal plains make up ~14% of the Arctic Ocean. They are overlain by thick sedimentary covers (up to 6–14 km beneath the Canada Abyssal Plain) (Jakobsson *et al.*, 2003). Literature and reasoning both show that the surface features of abyssal plains will be identical to those seen in Section 6.3. Spreading ridges include the ultra-slow spreading Gakkel Ridge (Edwards *et al.*, 2001) and a series of spreading segments linking it (through Fram Strait) to the northern extremities of the Mid-Atlantic Ridge. Other ridge systems include the Alpha–Mendeleev Ridge, a long mountain range crossing the Arctic Ocean, the Lomonosov Ridge, and the Northwind and Chukchi systems. Highly detailed sonar maps of the Gakkel Ridge (e.g., Edwards *et al.*, 2001) and the other segments (e.g., Okino *et al.*, 2002) have shown these spreading centers are typical, with the interplay of volcanism and tectonics seen in Chapter 5 (''Spreading and subduction''), although some areas seem to have a thicker sediment cover. In a different (non-spreading) context, the sediment thickness over the Lomonosov Ridge is ~450 m (Kristoffersen *et al.*, 2004). The acoustic expression of these different ridges will therefore be more or less ''muted'' depending on the imaging frequency. Finally, the combination of stronger currents with finer surface sediments will change the surface expression of some features. For example, the teardrop-shaped deposits around isolated outcropping features (similar to Figure 6.9) might instead form two tails, corresponding to current directions and named ''comets''. Some might be several hundreds of meters long and their length/width ratios can be used to infer near-bottom current velocities (e.g., Kuijpers *et al.*, 2007). Similarly, string-like trains of dunes or ripples can be observed in areas of focused, stronger currents (e.g., Kuijpers *et al.*, 2007). Fluid/gas seepage can be seen as pockmarks and mud volcanoes (see Chapter 7, ''Continental margins'' for more explanations and examples), like the Håkon Mosby mud volcano on one of the continental slopes (Beyer *et al.*, 2005), but their setting in polar seas does not induce any noticeable difference.

The southern polar seas are in a very different setting, because of the presence of the ice-covered Antarctic continent (Figure 6.12, bottom, see color section). They are

usually defined as including the Amundsen Sea, the Bellingshausen Sea, part of the Drake Passage, the Ross Sea, a small part of the Scotia Sea, and the Weddell Sea. The Antarctic waters are surrounded by evidence of plate tectonics, such as the Pacific–Antarctic Ridge (e.g., Géli *et al.*, 1997), the Australian–Antarctic Discordance (West *et al.*, 1994), or the Bransfield Strait back-arc basin (e.g., Grácia *et al.*, 1996). The Weddell Sea sports a large series of topographic highs named the Herringbone Relief because of their organization, and interpreted as relict structures from early plate spreading (e.g., Wille, 2002). The Antarctic continental shelf is narrow and much deeper (400–800 m) than the average continental shelf (~200 m) (see Chapter 7, "Continental margins") (e.g., Dowdeswell *et al.*, 2006). It has given rise to large submarine fan complexes such as the Weddell Fan, possibly one of the largest in the world (Anderson *et al.*, 1986). The Antarctic Circumpolar Current is a permanent strong eastward current, likely to affect the deposition of sediments and erosion features. The Antarctic icepack, like the Arctic icepack, varies with seasons (varying by a factor of 5 at least from austral summer to austral winter, depending on the years). The influence of ice, icebergs, and continental glaciers will therefore be a critical factor, as it is in the Arctic. Very large icebergs or larger portions of the ice pack (like the famous "Larsen B ice shelf") will be deep enough to significantly affect the seafloor. This glacial setting and active sedimentary processes led to the development of large sediment mounds on the continental rise during glacial periods, in connection with ice dynamics on the continental shelf (e.g., Amblas *et al.*, 2006). The spacing between originating ice streams influenced the drifting of fine-grained sediments developing into these mounds (Rebesco *et al.*, 1996; Amblas *et al.*, 2006) and large debris flow deposits are evidence of longer term processes, over at least the last 3 million years (e.g., Shipp *et al.*, 2002; Rebesco *et al.*, 2006). Interestingly, similar structures on Mars can be explained with analogue processes (e.g., Lucchitta, 2001) like the teardrop-shaped deposits behind the abyssal outcrops of Figure 6.9. Off the shelf, sets of parallel ridges and grooves 100 km long and 25 km wide overall, named "bundle structures" by Canals *et al.* (2000, 2002), are interpreted as sediments also deposited by these giant ice streams over very long periods. Finally, sediment waves with 4 km to 7 km wavelengths and smaller (1 km wavelength) dunes have also been observed (Rebesco *et al.*, 1996). Because similar structures have been presented in other parts of this book, we will only focus here on those typical of the polar seas.

6.4.2 Ice-related structures

Moving glaciers, either advancing or retreating, will be in direct contact with the seabed. Icebergs, if deep enough, will at some point also be in contact with the seabed, either through their entire course or when the seabed is shallow enough (e.g., on topographic rises). The resulting erosion will create linear "ploughmarks" or furrows, of sizes and depths varying with the size of the originating ice body, from a few meters to a few tens of meters in extreme cases. If old enough, or if the sedimentation rate is high enough, these trenches will be filled with thinner sediments, generally acoustically transparent at the frequencies used. Figure 6.13 shows a typical image acquired during the SCICEX series of Arctic surveys (Kristoffersen *et al.*, 2004). This image

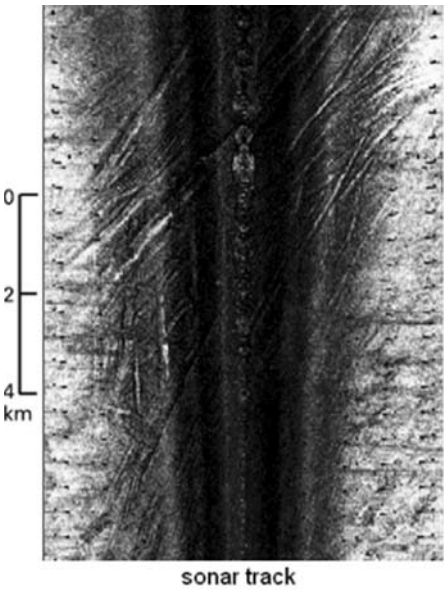

Figure 6.13. Iceberg ploughmarks on the Yermak Plateau, obtained with the SCICEX 12 kHz submarine-mounted sonar (Kristoffersen *et al.*, 2004; © American Geophysical Union).

was acquired with a 12 kHz sonar mounted on a submarine (and therefore relatively close to the seabed). Variations in the width of the sonar track show that the sonar and seabed are getting closer toward the bottom of the image. The total swathwidth is 8 km (from one side of the image to the next), and the area covered shows a large number of sub-parallel linear features, generally trending diagonally. The image is affected by far-range artifacts (black cross-track lines at regular intervals), presumably coming from interference with another instrument (see Chapter 10, "Anomalies and artifacts" for similar examples) and across-track backscatter variations have not been corrected for. The iceberg ploughmarks are nonetheless highly visible and can be followed on each side of the sonar track. They can be used to reconstitute the movements of icebergs, individually or in groups.

Giant ploughmarks (up to 750 m wide) at significant depths (800–1,085 m) in the Arctic have led some researchers (e.g., Kuijpers and Werner, 2007; Kuijpers *et al.*, 2007) to speculate that they were created by extremely large icebergs with commensurate keel depths. These discoveries have obviously important implications for the modeling of ice sheet and sea ice modeling, past, present, and future.

Some surveys (e.g., Lien *et al.*, 1989 in the Antarctic, Kuijpers *et al.*, 2001 in the Arctic) have shown the regional organization of iceberg scours can follow specific patterns (e.g., "washboard patterns") associated with the wobbling motion of grounded, tabular icebergs pushed by the advancing ice shelf. Toward the end of their course, icebergs leave "outrunner blocks", made of sediments carried along the track until the disappearance or significant reduction of the icebergs (their depth having decreased enough that they do not touch the seabed any longer). Figure 6.14 shows typical outrunner blocks, imaged by Kuijpers *et al.* (2001) in the Arctic. Contrary to Figure 6.13, this image has been corrected for slant range (as seen with the regular nadir coverage). A highly reflective structure is visible at nadir on the left, on both sides of the track, and its visibility in the water column argues for a topographic high, most likely a relict outcrop. Diagonal tracks from the top left of the image can be followed for several kilometers. They sometimes cross, or have wobbly outlines (outlined with black arrows) corresponding to different movements of the icebergs (as fully explained in Kuijpers *et al.*, 2001). The tracks are sometimes

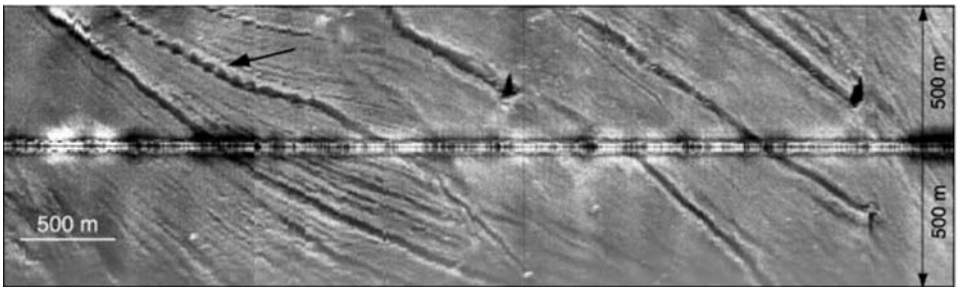

Figure 6.14. Outrunner blocks (adapted from Kuijpers *et al.*, 2001). Iceberg scouring created tracks of varying width with several blocks at their respective ends. Crossing slide paths are observed as well, and the black arrows show the distinct irregular patterns of some tracks (image © Springer-Verlag).

interrupted, and small, brighter deposits at their end correspond to the outrunner blocks. As they move, melting icebergs can leave behind individual rocks (drop stones). Of a scale of a few meters at most, these drop stones are generally not visible on all but the highest resolution sonar images (e.g., Hühnerbach *et al.*, 2008). They would then appear as small, pixel-scale, acoustically bright reflectors with no shadows.

Iceberg scours are important morphological features, and they are known to directly influence marine habitats by modifying the local properties of the seafloor. Gutt (1996) showed, for example, how the regular passing of icebergs can destroy benthic communities with very slow growth typical of polar regions. As the effects of climate change become more evident, the larger number of icebergs is likely to adversely affect some areas, particularly along the ''iceberg alleys'' of the Antarctic (see Figure 6.12 for the location of preferential iceberg paths). The effects on fish (e.g., halibut or flounder) are less easy to quantify, but likely to be as important in areas of glacier retreat (Harney *et al.*, 2005). Similar effects are seen with bottom-trawling in fisheries (presented in Chapter 9, ''Man-made structures'').

By modifying the seabed, sometimes to a significant depth, iceberg ploughmarks can also favor the emergence of underlying gas/fluid, as seen by the author in the Barents Sea (Figure 6.15). This image is a raw image, showing an underlying seabed of glacial till (dark, smooth textures) overlain with rougher deposits (brighter, fine-grained textures). There is a high concentration of pockmarks in this area (see Chapter 7, ''Continental margins'' for more explanations), and most of them are aligned along lines, some of them corresponding to iceberg scouring.

6.4.3 Other typical structures

Recent sonar surveys of the Arctic and Antarctic environments have brought to light interesting images from other types of processes. Not within the scope of this book, but nonetheless very interesting technically and scientifically, the imaging of the underside of sea ice by upward-looking sidescan sonars has greatly progressed over

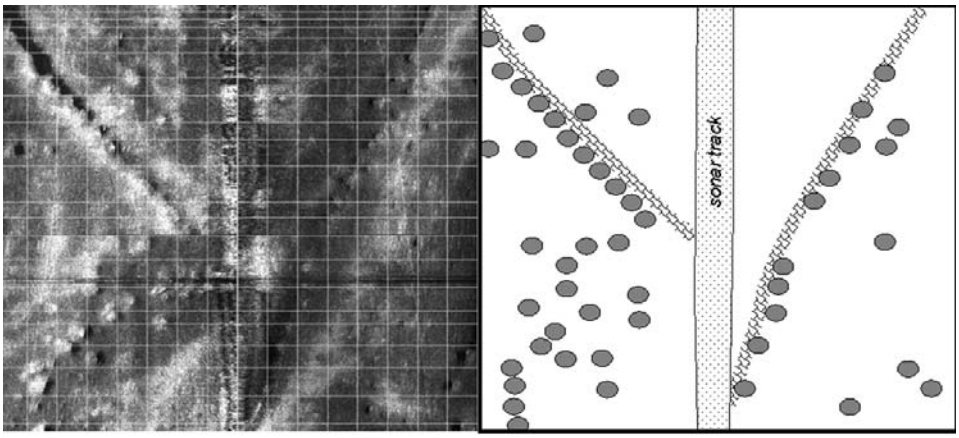

Figure 6.15. (Left) Raw 500 kHz imagery from pockmarks and iceberg furrows in the Barents Sea. The nadir is vertical in the middle of the image, and across-track range is 75 m (on each side of the nadir). (Right) Rough interpretation, showing only the most visible pockmarks (gray ellipses) and furrows (scaled patterns along the diagonals of the image).

the last decade or so (see Wadhams, 2000 and Wadhams and Doble, 2008, for examples). By enabling the mapping of large areas of ice with sonars mounted on autonomous underwater vehicles, these images provide a key tool in understanding sea ice dynamics, its evolution, and its response to climate forcing. Some of these techniques could also be used in more temperate areas such as the Baltic Sea that are regularly covered with ice (e.g., Leppäranta and Myrberg, 2009).

The increasing use of higher resolution sonars and their use in habitat mapping has also revealed the influence that certain animals can have on the seafloor. Gray whales are known to scrape the seabed in their search for small crustaceans and other types of food. These differences are not obviously visible, as they do not perturb the seabed at depth and would only rework the sediments or uproot kelp beds. But in the Arctic, recent sonar images of shallow seabeds have revealed the foraging marks of walrus (Bornhold *et al.*, 2005). Figure 6.16 shows typical examples, with clusters of shallow pits (small dots scattered throughout the images). They are generally much less than 1 m in diameter and 0.3 m deep. Some of these pits can become oblong furrows, as long as 20 m in some cases. Many marine animals, including invertebrates, fish, and seabirds, are capable of creating similar surface disruptions to the seabed (Bornhold *et al.*, 2005) and these intriguing images show what this approach can bring to marine habitat mapping.

6.5 REGIONAL IMAGERY: THE HAWAIIAN ABYSSAL PLAIN

There are not many examples of regional imagery from abyssal plains. Mainly because the abyssal plains have not been much explored with sidescan sonar, the

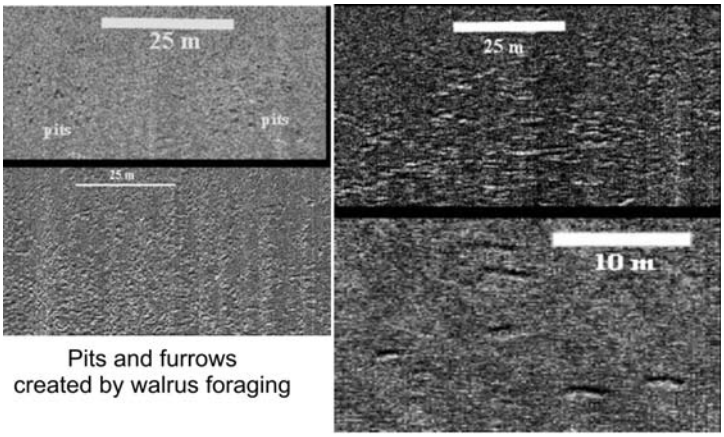

Figure 6.16. Foraging marks from Arctic walrus, imaged with a Klein 5410 sidescan sonar operating at 455 kHz. The underlying seabed (muddy sand) is marked by shallow pits (dots at left, oblong furrows at right). Typical pit densities are 10 to 15 per 100 m^2 (images adapted from Bornhold *et al.*, 2005; © Springer-Verlag).

surveys are usually limited to specific zones, or to a few long swaths covering one large geological object (e.g., the Saharan debris flow). The image presented in this section (Figure 6.17) was acquired by GLORIA during the survey of the U.S. Exclusive Economic Zone around the Hawaiian Islands. It covers the abyssal plains themselves, and the whole slope between the islands of Oahu and Molokai along with their debris avalanches.

The image is a mosaic of several GLORIA swaths oriented SE–NW, and a few additional swaths around the islands of Oahu and Molokai in the southern part of the image. The water depths are rapidly varying from about 1,000 m to 4,500 m in the main part of the slope (southernmost portion of the image), and are then stabilized between 4,500 m and 5,000 m in the rest of the image. These important variations yield large differences in swathwidths between the lines close to the islands, and the lines farther out in the abyssal plain. Each swath was fully processed for radiometric and geometric corrections.

The image can be readily divided into five major parts. The first one, in the southernmost region and close to the islands, exhibits a very bright texture, organized perpendicularly to the islands. The second unit is made up of large reflective blocks on a mottled substrate, and stretches out like a tongue toward the middle of the image. The third and largest unit visible is dark and featureless (apart from the superposed blocks at the limits of the previous unit). The fourth and fifth units are smaller and well-delimited medium to highly reflective patches. Close-up views of these different zones further illustrate their differences (Figure 6.18). In the far north of the image, two very distinctive regions are seen. They have smooth irregular boundaries, and exhibit medium–high to high backscatters and very fine-grained textures, but are nearly homogeneous. No relief is visible, either from variations in backscatter or from clear acoustic shadows. Because its appearance resembles lava

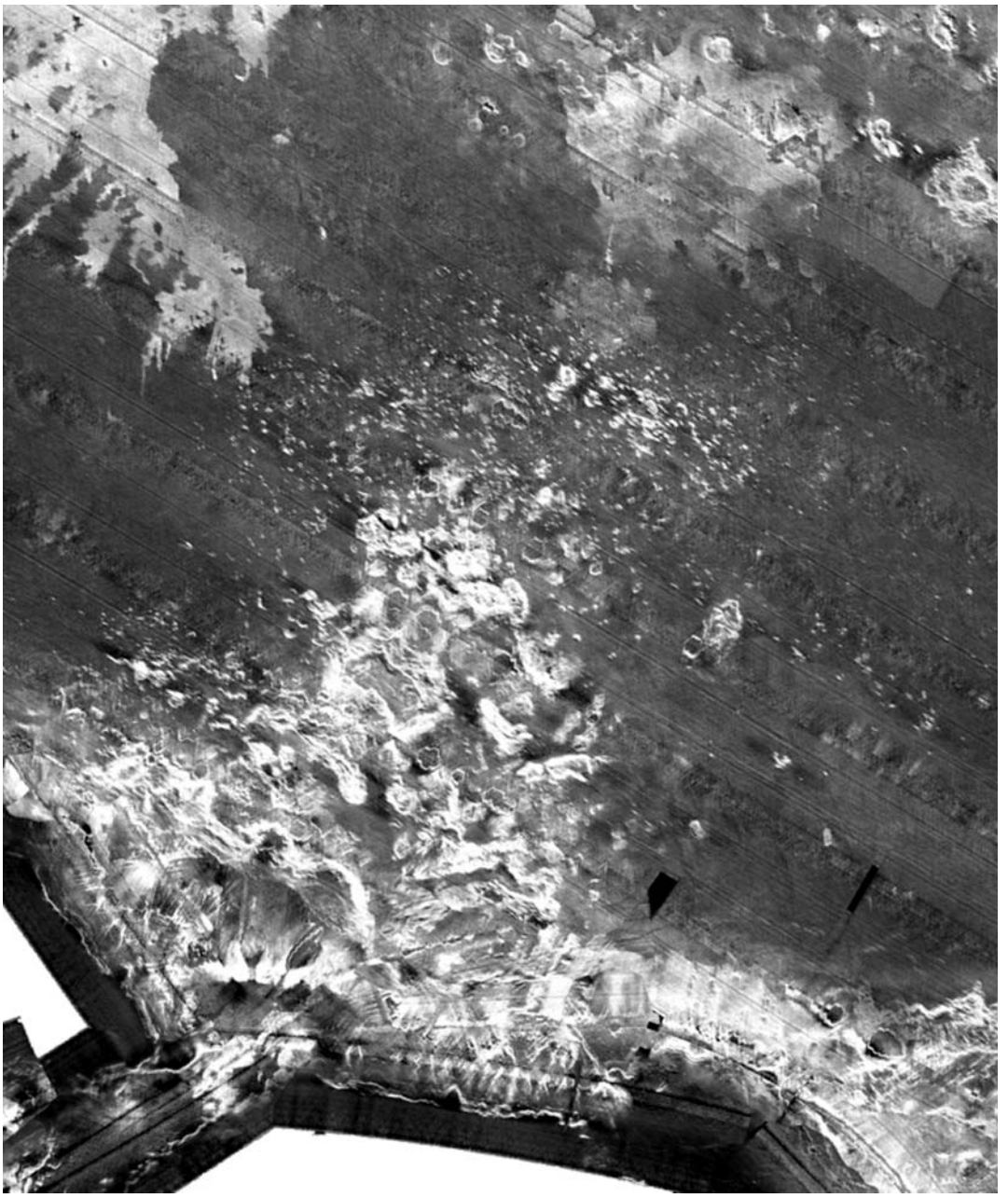

Figure 6.17. GLORIA mosaic of region north of the Hawaiian islands of Oahu and Molokai, showing the important debris avalanches that spilled from the shores down the abyssal plains. The whole image covers an area of 228 km by 274 km, and is oriented with north at the top. It was mosaicked from the fully processed data (50 m/pixel) made available by the U.S. Geological Survey at *http://walrus.wr.usgs.gov/gloria/hwgloria/*

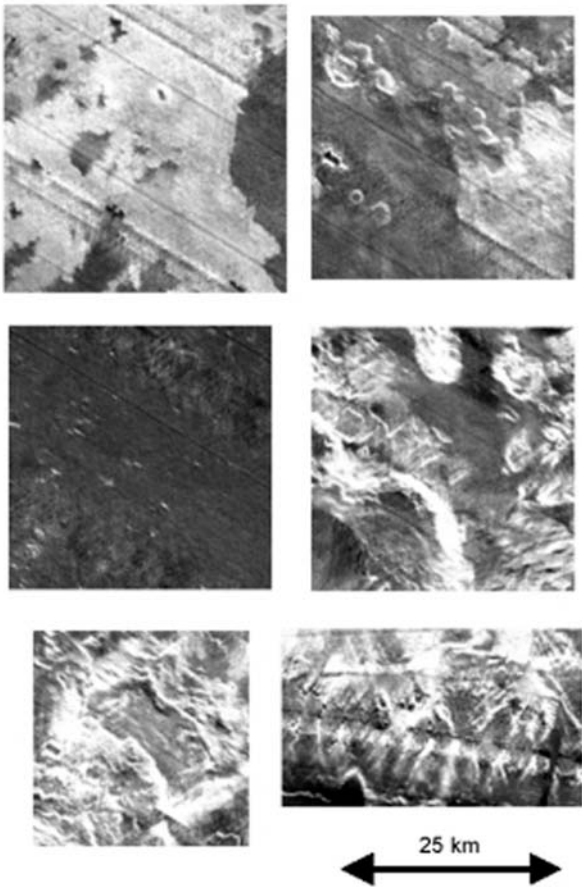

Figure 6.18. Close-up views of the different geological units visible in the regional image of Figure 6.17. (From left to right and top to bottom) Shallow-buried lava flows; more deeply buried lava flows; abyssal plain sediments with small debris blocks; fault scarps at the base of the fault slope and large debris blocks; the flat-topped Tuscaloosa Seamount, and sediment-channeling structures north of Molokai.

flows (see Chapter 5, "Spreading and subduction"), albeit larger than any seen at mid-ocean ridges, this region is interpreted as shallow-buried lava flows (Figure 6.19). A thin layer of sediments is visible on profiler records, but is transparent to GLORIA's acoustic waves (GLORIA's penetration depth is related to its relatively low frequency of 6.5 kHz). The same type of region is visible in the northeast corner of the regional image: same shapes, same texture, and slightly less reflective. This difference is attributed to a thicker sediment layer above the lava flows: the back-scattered waves are more attenuated. This is confirmed by profiler records along the different survey lines. A few rounded blocks are visible in the buried lava flows (Figure 6.18), with a higher backscatter on their slopes facing the sonar. They have dimensions of a few kilometers and belong to the Hawaiian Arc a few tens of kilometers to the north.

Most of the image is made up of a dark, featureless sub-stratum. These are the abyssal plain sediments (Figure 6.18). Around the edges of the tongue-shaped region, they are littered with small debris blocks, with dimensions of a few hundred meters,

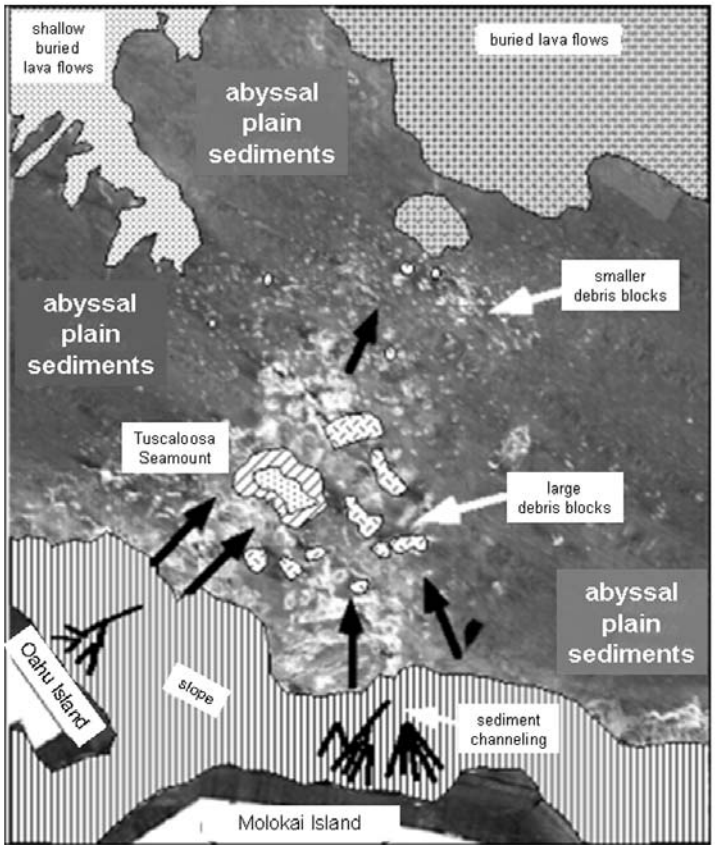

Figure 6.19. Schematic interpretation of regional GLORIA imagery. The black arrows indicate the directions of the two avalanche slides, Nuuanu in the west and Wailau in the east.

some of them at the limit of resolution of GLORIA. Larger debris blocks are seen farther upslope, closer to the two islands (Figure 6.17). These blocks have dimensions of several kilometers, up to 50 km^2 for the largest one. They are highly reflective, with rounded to elongate shapes, and they extend 100 km from the fault scarps at the base of the islands' slopes (Figure 6.18). The blocks are very large at the beginning (some of them have volumes of several cubic kilometers) and then diminish in size with distance from the origins (much like terrestrial landslides). Only the smallest blocks litter the sediments on the seafloor, more than 200 km away from their sources on the islands.

Amid these large blocks, an elliptical patch of darker reflectivity can be noticed (Figure 6.18). It is bounded by highly reflective contours, corresponding to sonar-facing fault scarps, and acoustic shadows in the NE where the slopes are facing away from the sonar. The darker patch itself is quite flat and homogeneous, and forms a large plateau on top of the structure. The whole object seems to have blocked the pathway for the larger blocks coming from the west (Nuuanu Slide). Named Tuscaloosa Seamount, this is actually a detached block from the Nuuanu debris avalanche off Oahu (Figure 6.19). This "seamount" is 30 km long, 17 km wide,

and 1.8 km thick, and it rests 90 km from its source (Normark *et al.*, 1993; Hampton *et al.*, 1996). Some of the blocks in the slide traveled across the 4,600 m deep Hawaii Trough and uphill to 4,300 m deep water, 140 km from their source (Hampton *et al.*, 1996). Other distinct structures include the sediment channels just north of Molokai Island (Figures 6.18 and 6.19). Sediments and debris coming from onshore locations follow the topography and form gullies and canyons. The shapes of these structures are similar to the submarine canyons found on continental margins. They are shown in Chapter 7 (Figures 7.4 and 7.5).

These distinct elements build up a story that can be revealed from the islands' downward slopes. First, several submarine canyons feed sediment down the slope, where it has accumulated to produce a 500 m thick deposit (Moore *et al.*, 1989). The NW canyons are clearly the continuation of sub-aerial canyons, and are thought to have been carved on shore and drowned during the subsidence of the Hawaiian Ridge under the weight of the growing volcanoes. Because the canyon morphology is well developed down to 1,800 m depths, this value is presumed as the amount of subsidence undergone.

The two catastrophic avalanche slides are the Nuuanu Slide in the west and the Wailau Slide in the east. Lying to the north of Oahu Island, the Nuuanu Slide is the largest mapped along the Hawaiian Ridge. It was formed by the collapse of the northern flank of the Koolau Volcano along a volcanic rift zone. Onshore, the line of failure is marked by a line of steep cliffs, the Nuuanu Pali, which are parallel to the coastline. The Nuuanu debris avalanche deposit forms an amalgam with the adjacent Wailau debris avalanche deposit, a similar slope failure deposit originating from the northern flank of the neighboring island of Molokai. Together, they cover around 25,000 km^2 of the seafloor.

The debris avalanche deposit extends for about 230 km from its headwall at the Nuuanu Pali to its toe. It crosses and partially infills the large bathymetric depression known as the Hawaiian Deep, then runs upslope for about 120 km, with a vertical rise of around 300 m (Moore *et al.*, 1989; Jacobs, 1995). Geophysical models, coupled with seismic surveys, make a conservative estimate of a volume of about 5,000 km^3 for the total avalanche, ranking it as one of the largest mass-movement deposits of any type discovered so far on Earth. These slope failures apparently began early in the history of the individual volcanoes, when they were small submarine seamounts. They culminated near the end of sub-aerial shield building and continued long after dormancy. Their importance and possible recurrence emphasize the need for precise charting of the seafloor around major volcanoes, which should help assess the risks associated with massive landslides and tidal waves.

6.6 CONCLUSION

The abyssal plains are the flattest and most extensive regions of the seafloor. They exhibit nearly featureless surfaces and have therefore not been studied extensively with sidescan sonar, as most of the information of interest to geoscientists is obtained using multibeam sonars (for a wider coverage and a higher survey speed) and sub-

bottom profilers or seismic surveys (to penetrate below the thick sediment cover). We saw in this chapter the main structures that were associated with the filling of abyssal plains (sediment channels, debris slides, and debris flows), and those associated with redistribution of sediments in the plains (turbidite flows, flow-banding, and relict structures). A better knowledge of these redistribution patterns is essential for the sometimes envisaged deep-sea disposal of toxic materials. There is no doubt that further sidescan sonar surveys of the abyssal plains will concentrate on these aspects. It is only very recently that high-resolution sonar imagery has revealed the surface expressions of flow-banding and shear in mass-sediment flows (e.g., Masson, 1996; Gee *et al*., 2001) and new insights are being gained from their detailed information. The avalanche slides from the Hawaiian volcanoes of Oahu and Molokai are particularly spectacular examples. These huge structures were recently discovered, as was the evidence that they created major tsunamis at the time. The human and economic implications mean that similar structures are likely to be extensively mapped in the near future, and their potential risks assessed. The same is true of contourites, of increasing interest for oil exploration (e.g., Stow *et al*., 2002).

The second part of this chapter focused on structures typical of the polar seas, both Arctic and Antarctic. The relative lack of images from these regions is easily explained by the difficulty of access, and the logistical challenges associated with any sonar survey. Most of the structures found in polar seas have been covered earlier in this chapter (for the abyssal plains) or, for spreading, subduction, and continental margins, in neighboring chapters (Chapters 5 and 7, respectively). Purely glacigenic structures, such as iceberg ploughmarks, have been presented in detail, and as they can also be observed in more temperate environments, these images might be of interest to researchers not working in the polar seas. The increasingly rapid changes related to the present climate warming mean that sonar surveys near the poles are gaining increasing interest, whether it is to study past climates or modern variations in ecosystems and marine habitats.

A subject we did not touch upon is the anthropogenic influence on abyssal plains. Its manifestations can be summed up as intentional man-made structures (cable lines and pipelines) and unintentional traces (shipwrecks, trawl marks). They are occasional and restricted in space, and typical examples will be presented in Chapter 9 ("Man-made structures"). A topic often associated with abyssal plains has been that of manganese nodules. Long academic, this interest can now be translated into practical applications. Within the broader topic of deep-sea mining, this will also be presented in Chapter 9.

Most structures on the abyssal plains can be explained by what is happening upslope, at continental margins, and this is the subject of Chapter 7.

6.7 FURTHER READING (*see also* References at end of book)

About abyssal plains in general

Weaver, P.P.E.; and J. Thomson (1987). *Geology and Geochemistry of Abyssal Plains*. Blackwell for the Geological Society, Oxford, U.K., 246 pp.

About contourites

Rebesco, M.; and A Camerlenghi (Eds.) (2009). *Contourites*. Elsevier, Amsterdam, 688 pp.

Stow, D.A.V.; C.J. Pudsey; J.A. Howe; J.C. Faugères; and A.R. Viana (Eds.) (2002). *Deep-water Contourites: Modern Drifts and Ancient Series, Seismic and Sedimentary Characteristics*, Memoir 22. Geological Society, London, 472 pp.

About polar seas

Davies T.A.; H. Josenhans; L. Polyak; A. Solheim; M.S. Stoker; and J.A. Stravers (Eds.) (1997). *Glaciated Continental Margins: An Atlas of Acoustic Images*. Chapman & Hall: London, 315 pp.

About landslides and debris flows (submarine or not)

Hampton, M.A.; H.J. Lee; and J. Locat (1996). Submarine landslides. *Reviews of Geophysics*, **34**(1), 33–59.

Jakob, M.; and O. Hungr (2005). *Debris-flow Hazards and Related Phenomena*. Springer/Praxis, Heidelberg, Germany/Chichester, U.K., 739 pp.

7

Continental margins

7.1 INTRODUCTION

Continental margins mark the transition between the oceans and the continents, and are traditionally defined as the region between the upper limit of the tidal range and the base of the continental slope. They extend from the coastal zone (presented in Chapter 8, "Shallow-water environments") to the abyssal plains and basins (presented in Chapter 6, "Abyssal plains and polar seas"), and they are roughly divided into three regions: continental shelf, continental slope, and continental rise (Figure 7.1). Continental margins are the region on Earth where most of the sediments are deposited (as much as 90% of the sediment generated by erosion on land) (McCave, 2002). It is important, however, to recognize the long-term processes that led to their formation: in the past 1 million years, sea level has only been as high as now for less than 5% of the time, and for the past 7,000 years only (e.g.,Thomsen *et al*., 2002). For the most part, continental shelves were developed sub-aerially by fluvial processes at a lower sea level (as much as 130 m lower than now), and their features were smoothed off by wave action during the next sea level rises. For much of the last million years, sediments were fed more directly into the ocean basins, and these variations explain the wide variety of facies observed around the world (see Richards *et al*., 1998 or McCave, 2002 for more complete descriptions).

There are three main types of ocean margins (e.g., McCave, 2002): passive continental margins (such as those around the Atlantic), active continental margins (such as those around the Pacific, near plate subduction regions), and ocean island margins (with very high sediment yields). The geological and morphological differences between types are beyond the scope of this book, which presents the bedforms observable with sidescan sonar, and the reader is referred to Stow and Mayall (2000), Wefer *et al*. (2002), and Mienert and Weaver (2003) *inter alia*. Continental margins are of great importance for biogeochemical cycles because, although they only make up 20% of the ocean's surface, 50% of the global marine production takes place here.

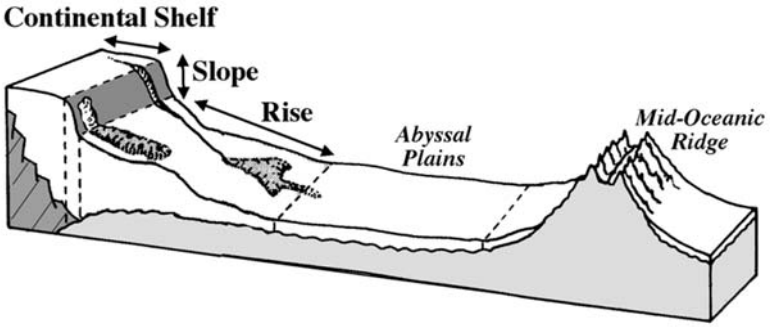

Figure 7.1. Schematic representation (not to scale) of the major physiographic provinces, showing the relatively flat continental shelf and the rapidly descending areas of the continental slope and rise.

Ocean margins influence many aspects of our socio-economic activities and of the world's ecology. The Exclusive Economic Zones of most countries are occupied by continental margins, from which they derive an important portion of their wealth. Hydrocarbon exploitation is concentrated on continental shelves (e.g., in the North Sea or the Gulf of Mexico). The world's largest fish reserves are located in the continental slopes and shelves, and their management often proves politically and economically difficult. Slope failures and the resultant flows are capable of the destruction of marine installations and submarine telecommunications cables, and even of generating tidal waves (tsunamis). Recent environmental studies have also shown the importance of a more complete knowledge of continental margins with the linking of coastal pollution and the offshore dumping of harmful chemical products in poorly known areas that were thought deep and stable enough.

For these reasons, and also because of their higher accessibility, continental margins have become the best and most studied areas on the seafloor. Closest to shore (Figure 7.2), the continental shelf is a relatively flat area (slopes less than 1:1,000, low local relief). Supported by continental crust, it is also remarkably shallow; generally less than 250 m. Depending on the regional geological setting, the shelf will extend from a few kilometers (e.g., near subduction zones) to several hundreds of kilometers (near passive margins) away from the shores. The continental shelves are submitted to the constant input of large quantities of sediments by the rivers, sometimes at large distances from land (e.g., the Indus or the Amazon). The shelves are also affected by pelagic rain. These large volumes of sediments follow the bathymetry gradients down the continental slope (Figure 7.2). This rapidly descending area ranges in depth between approximately 200 m and 2,000 m. The sediments are transported along channels and canyons, far out into the abyssal regions. They also conglomerate to form mounds, structures following the bathymetric contours (contourites), etc. Because of the important slopes, some of the structures may be unstable, and earthquakes or minor sea level changes can trigger their collapse, creating landslides (the larger ones producing tidal waves). The sediments are carried over, down to the continental rise (Figure 7.2). This physiographic province marks

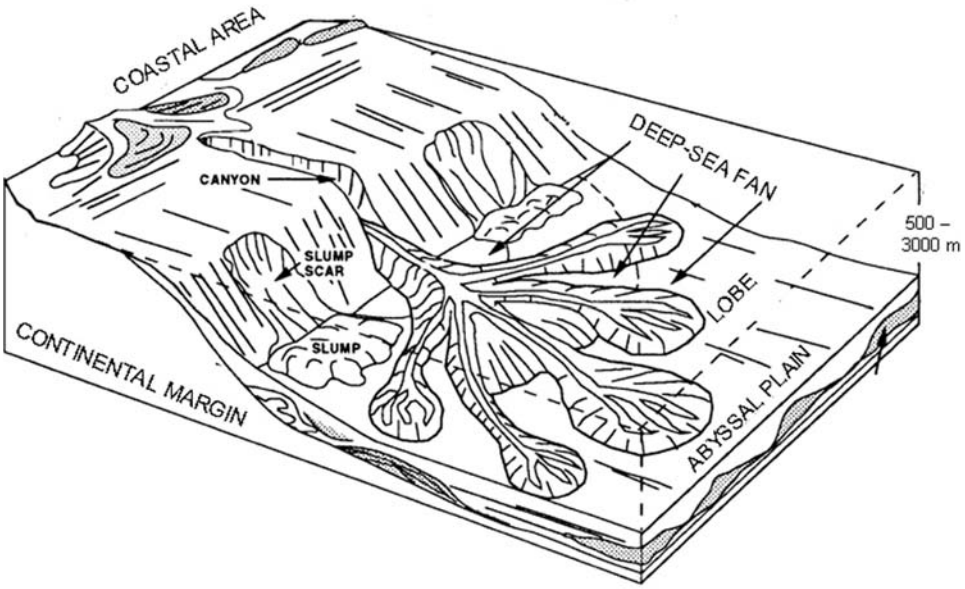

Figure 7.2. The morphology of continental margins varies with the amount of sedimentation and with their geological history, but the main features remain the same. See text for details (sketch adapted from Richards *et al.*, 1998).

the limit between the continental margins and the abyssal plains (see Chapter 6, "Abyssal plains and polar seas"). Deeper than 2,000 m, the continental rise can go down to 6,000 m (such as in the North Atlantic). The more prominent structures visible are the distal fans marking the limits of the canyons and sediment channels. For the sake of simplification, and because they exhibit similar surface structures, we have included in the present chapter the epicontinental marginal seas, such as the North Sea, the Gulf of Maine, and the Gulf of St. Lawrence, and the marginal plateaus. Morphologically similar to continental shelves, the marginal plateaus lie at slightly greater depths and are separated from the shelves by incipient continental slopes. The Blake Plateau in the North Atlantic is a good example. Other marginal plateaus can be found off the coasts of southern Argentina and eastern New Zealand.

7.2 SEDIMENTARY STRUCTURES

7.2.1 Sediment deposition and erosion

Continental margins are submitted to the continuous input of sediments from the continent and of biogenic carbonate deposits. They are deposited in large homogeneous patches, well-stratified and fine-grained, which offer a generally smooth and poorly reflective acoustic appearance. When accumulated on dipping units, unconsolidated sediments may move downslope as distinctly bounded masses ("mass

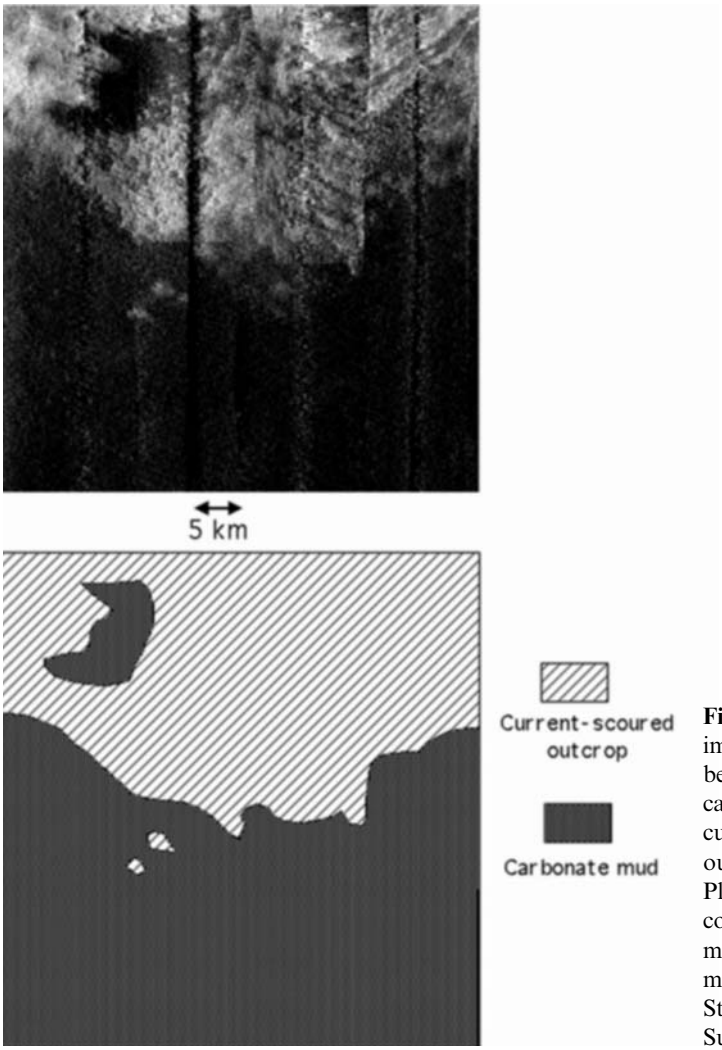

Figure 7.3. GLORIA imagery of the boundary between a patch of carbonate mud and a current-scoured rock outcrop on the Blake Plateau (Eastern U.S.A. continental margin) at a mean depth of 750 meters (courtesy United States Geological Survey).

movement''). These sediments may also be transported by turbidity currents which act as important erosion factors. The interplay of depositional, erosional, and mass movement processes creates complex sedimentary patterns, reflected in the variations of backscattering characteristics in the sonar imagery.

Figure 7.3 shows a perfect example of these different processes. It was collected using GLORIA on the Eastern U.S.A. continental margin, during the survey of the American Exclusive Economic Zone (EEZ-SCAN, 1991). It was acquired in water depths of 750 meters, above the Blake Plateau. The image is a mosaic of several adjacent GLORIA swaths, with a ground resolution of 50 m approximately. The sidescan sonar imagery was radiometrically and geometrically corrected with the

USGS version of WHIPS/PRISM (see Chapter 4). The image is clearly divided into two types of regions: one smooth and very dark, the other brighter and with a mottled texture. In the lower portion of the image, the dark region exhibits a very homogeneous texture, with no visible feature whatsoever. It appears completely flat and uniform, and is interpreted as a patch of sediments (ground-truthing reveals it to be carbonate mud). Conversely, the top portion of the image shows areas of heterogeneous bright backscatter. Some areas are randomly textured, and are outlining blocks. They are interpreted as a rock outcrop. The darker linear narrow channels that cut it at regular intervals and along the same diagonal direction are interpreted as scours created by the turbidity currents and filled by the incoming sediments.The backscatter variations over the outcrop itself are related to its micro-scale roughness; that is, the composition (or induration) of the bedrock and, in this particular case, the presence of corals (evidence from dredging and bottom photographs).

7.2.2 Sediment transport—submarine canyons

A large portion of the accumulated sediment moves downslope, driven by gravity and bottom currents. They are transported through large slides, often called debris slides, or along narrow channels merging into submarine canyons. The processes leading to either one of these two modes are complex and not entirely understood (see Hagen *et al.*, 1994). The major controlling factors are the types of turbidity currents, their importance and velocities, as well as the depth gradients and the geology of the local sub-stratum.

In many areas, the continental slope is cut by canyons. Most of them start on the continental shelf, and act as channels for the transport of sediment down to the abyssal plains. Submarine canyons are created by the erosive action of the sediments suspended in the turbidity currents. They are usually V-shaped and their morphology is reminiscent of river valleys on land. Very large areas extending hundreds of kilometers offshore are covered by different types of sediment flows. They are more reflective acoustically than deposited sediment patches because of their higher micro-scale roughness and their large-scale hummocky topography. The local textural variations are related to the different processes that led to their creation and evolution. A good example of these processes is presented in Figure 7.4. This GLORIA image was collected during the survey of the U.S. Exclusive Economic Zone (EEZ-SCAN, 1991), and covers approximately 200×200 km. It regroups several swaths with a ground resolution of 50 meters. The water depth varies between -250 meters in the upper-left portion of the image, and $-3{,}000$ meters in the lower-right portion. This explains the differences in the swath widths which increase with depth.

On the basis of the textural patterns, the image can be readily decomposed into three large units: the continental shelf (top left) with a dark, nearly homogeneous reflectivity; the continental slope with a medium reflectivity and organized textures going downslope; and the continental rise in the lower right with lighter reflectivities and more random textures. In the continental slope, long ribbons of high backscatter can be seen, nearly parallel to each other. Close-up views show they are closely associated with dark shadows and therefore have a lower relief than their

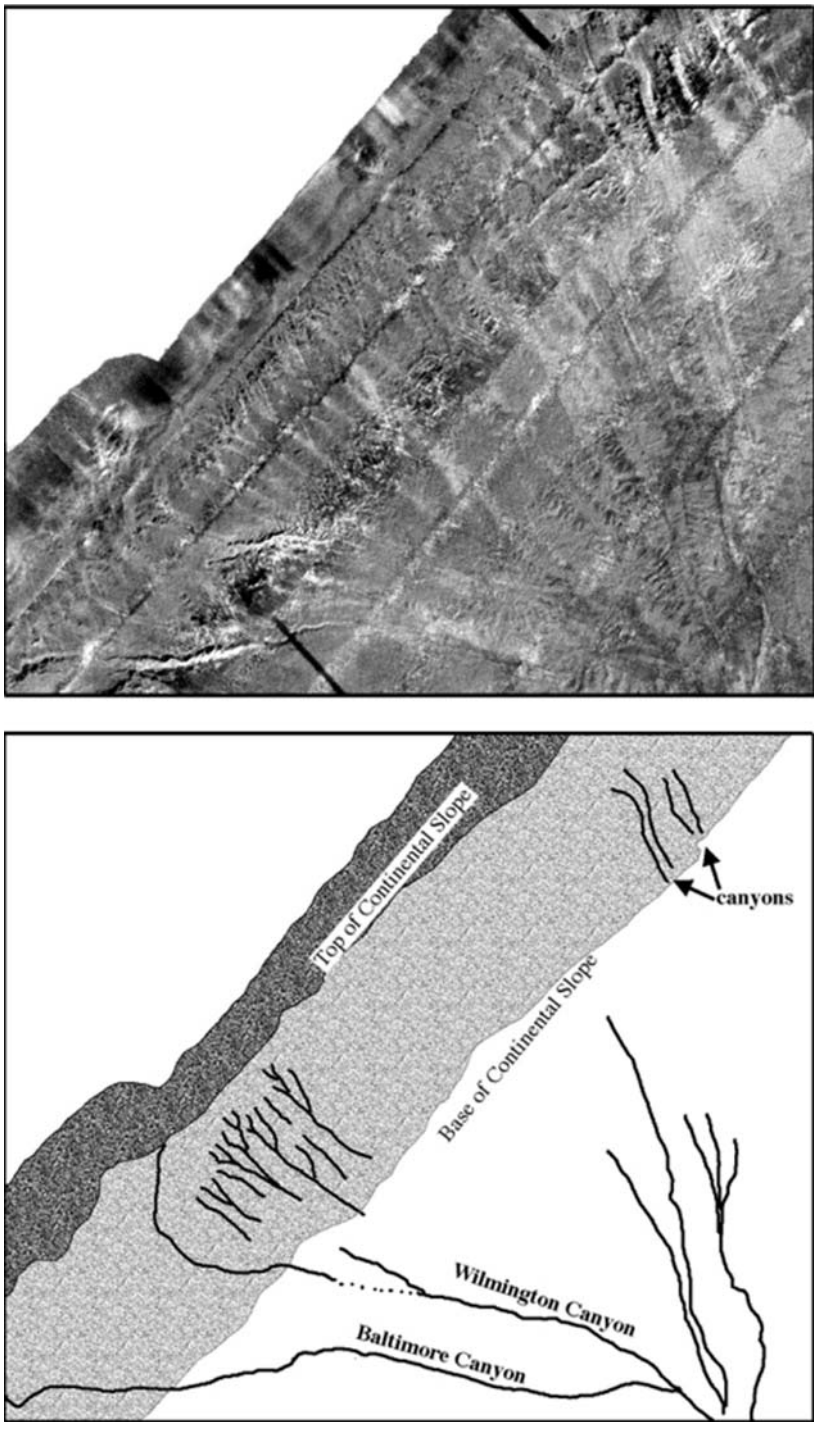

Figure 7.4. Sediments are transported down the continental slope through narrow channels, which merge into canyons. These structures often span tens to hundreds of kilometers (GLORIA imagery, courtesy United States Geological Survey).

surroundings. These channels often merge with other channels, and pour sediments into larger canyons such as the Wilmington and Baltimore Canyons. It is not rare to see canyons extending for tens or even hundreds of kilometers, depending on the local slopes. Their sinuosity will vary according to the bathymetric gradients, the flow of sediments, and the local geology. Large patches of brighter reflectivity are also visible in Figure 7.4 at the base of the continental slope: these are debris flows, shown in better detail in Section 7.2.3.

A closer view at the boundary between the continental shelf and the top of the continental slope shows the dendritic channels along which sediments are transported (Figure 7.5). The continental shelf (upper-left corner) is covered with homogeneously

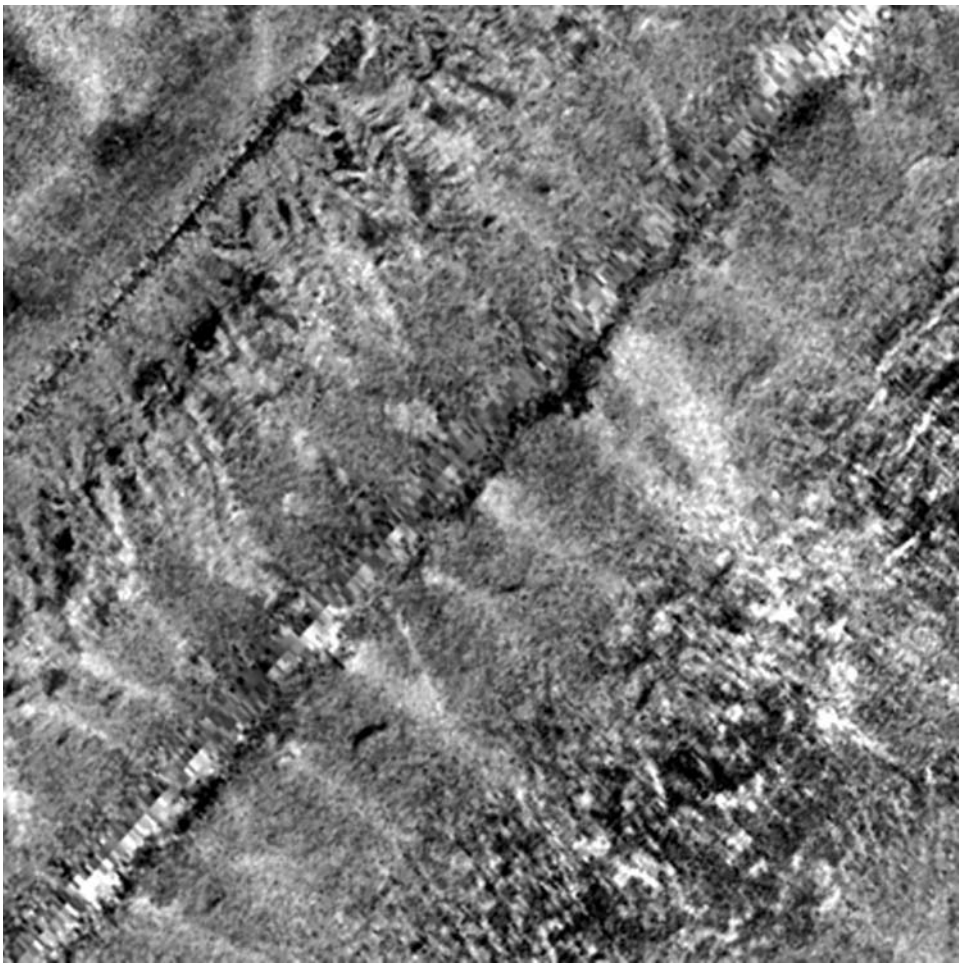

Figure 7.5. Detail of Figure 7.4, showing the dendritic arrangement of sedimentary channels. The image is 35 km wide by 35 km long (GLORIA imagery, courtesy United States Geological Survey).

textured sediments. A trellis-like drainage pattern marks the limit of the slope. In a few hundreds of meters, it organizes itself into cone-like patterns of bright reflectivity, which merge and will later feed the main canyons (in this case, Wilmington Canyon).

Not all submarine canyons look alike. Some die out in the continental slope and some extend far into the continental rise. Some are large, others quite narrow. For example, Baltimore and Wilmington canyons, presented in Figure 7.4, were fed by several channels and in some places are very close morphologically to their surroundings. Conversely, the neighboring Veatch and Hydrographer Canyons extend for nearly 200 km across the Western Atlantic continental rise as tightly sinuous channels with no tributaries (Figures 7.6 and 7.7). The Hydrographer Canyon is even twice narrower than Veatch Canyon. All canyons are conduits for sediments eroded from the slope, but the extents of transport and the modes of delivery have varied, and produced these different morphologies.

The GLORIA imagery presented in Figure 7.6 was acquired during the same survey of the North American EEZ. Water depths vary from 250 meters on the continental shelf (Figure 7.6) to 4,250 meters at the southern extremity of Veatch Canyon. The image is approximately 300 km long by 200 km wide. It results from the mosaicking of many swaths with varying orientations: parallel to the slope in the shallower parts closer to the shelf, and wider swaths going upslope and downslope in the deeper regions. Several geological units are easily distinguished from their backscatters and the orientation of their textures (Figure 7.7). They correspond to sediment slides oriented in the directions of the slopes: Veatch Slide is brighter and has a finer grained texture than Nantucket Slide. A larger unit of dark backscatter is visible in the lower-left portion of the image, with a coarser texture, interpreted as mass-wasting deposits. But the main distinctive features are the two elongated structures crossing diagonally most of the image. They are delimited by parallel bright and dark lines, corresponding to the walls respectively facing toward and away from the imaging sonar (Figure 7.8). These structures are lower than their surroundings and narrow, which along with their context identifies them as canyons. A long linear fault is visible as a dark feature crossing three of the lower-left swaths.

A close-up view of Veatch Canyon shows in greater detail the walls of the V-shaped canyon, as well as the mostly homogeneous surroundings (Figure 7.8). A large sonar artifact is visible in the middle of the image showing the shape of the sonar beam. The first targets apparently correspond to Veatch Canyon itself, which would hint at a problem detecting the first return for at least one ping (see Chapter 9).

When bathymetric gradients are large, and large amounts of sediments are unconsolidated and in precarious locations, or in the presence of seismic activity, some of these submarine canyons can witness spectacular gravity-driven events. Large amounts of sediments are carried away as turbid flows, channeled through the canyons and in some cases creating tsunamis (e.g., Bouma, 2000; Driscoll *et al.*, 2000; Gómez Sichi *et al.*, 2005). These systems are receiving increased attention now, and an example will be presented in Section 7.6 (“Regional imagery”).

In other geological contexts, and when bathymetric gradients in the continental slope are relatively small, submarine canyons can form meanders. These meanders

Figure 7.6. GLORIA imagery of Veatch Canyon. The image is ca. 300 km long and 200 km wide (courtesy United States Geological Survey).

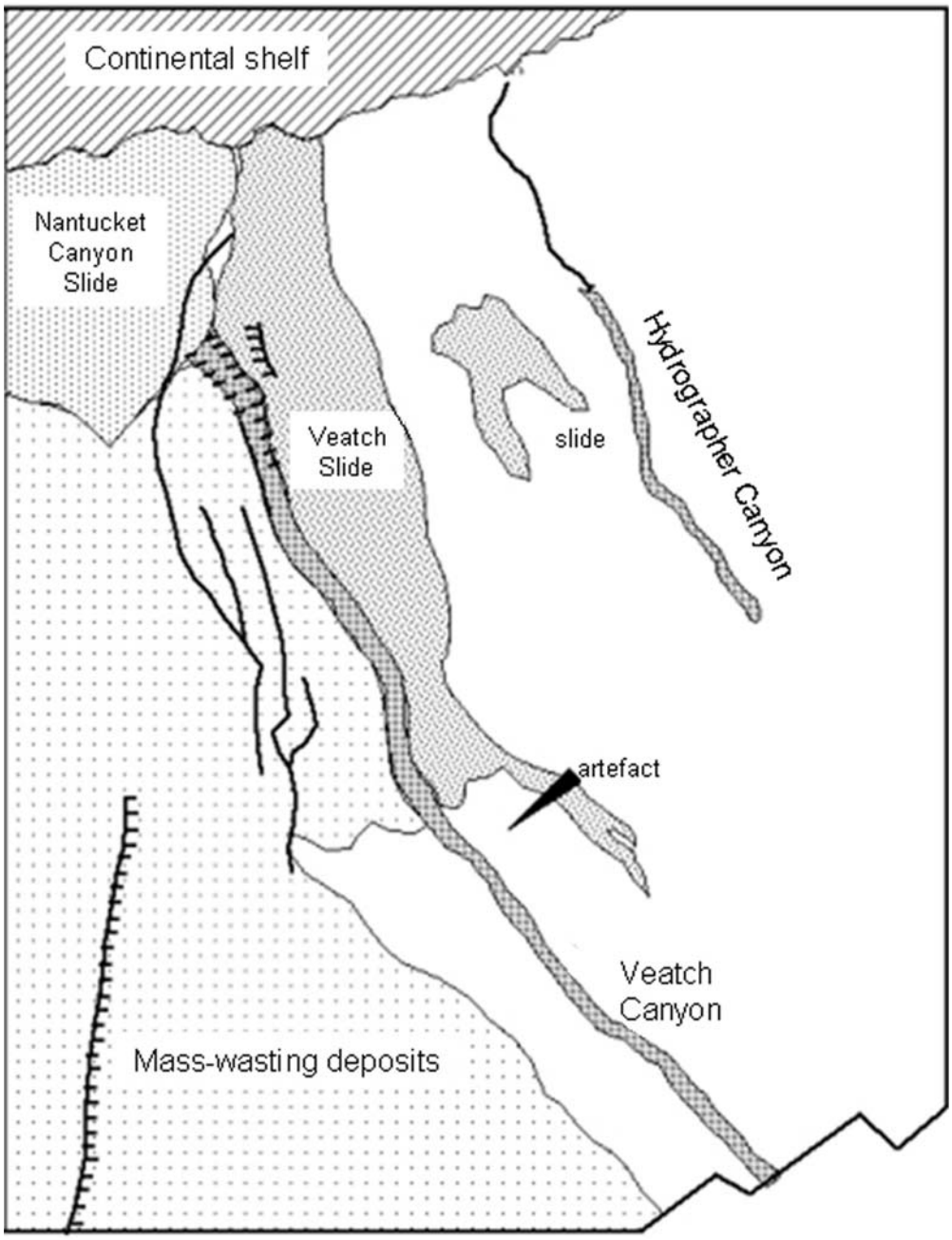

Figure 7.7. Schematic interpretation of the main features visible in Figure 7.6. The two main canyons (Veatch and Hydrographer) are fed with sediments coming from the continental shelf and slope. Very narrow, these canyons extend for several tens of kilometers down to the continental rise.

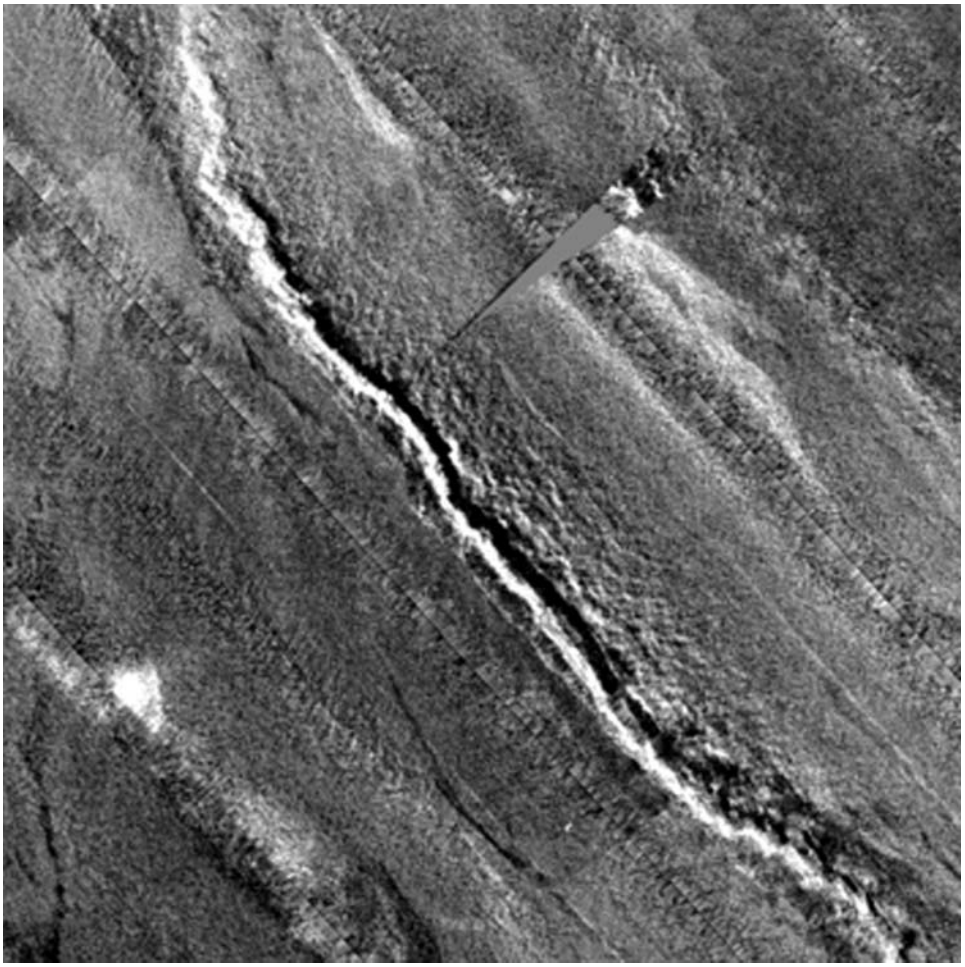

Figure 7.8. Close-up view of Veatch Canyon (GLORIA imagery, courtesy United States Geological Survey).

are comparable with those of land-based rivers such as the Mississippi or the Seine. Meanders are believed to develop as a stream attempts to maintain the optimal channel slope for its sediment load on varying valley slopes (e.g., Hagen *et al.*, 1994; Ritter *et al.*, 1995). Sinuosity in submarine fan channels has been observed on steeper slopes than on land, which may be due to the smaller density difference of turbidity current vs. water compared with water vs. air. Observations and experimental studies show that sinuosity in terrestrial rivers increases with the slope until a threshold is reached, at which point a relatively straight braided channel develops. The abandoned channel segments are called cut-off meanders. Cut-off meanders may also be created by the occasional input of large rapid turbidity currents, which would have difficulty negotiating the tight canyon meanders and would expend their energy

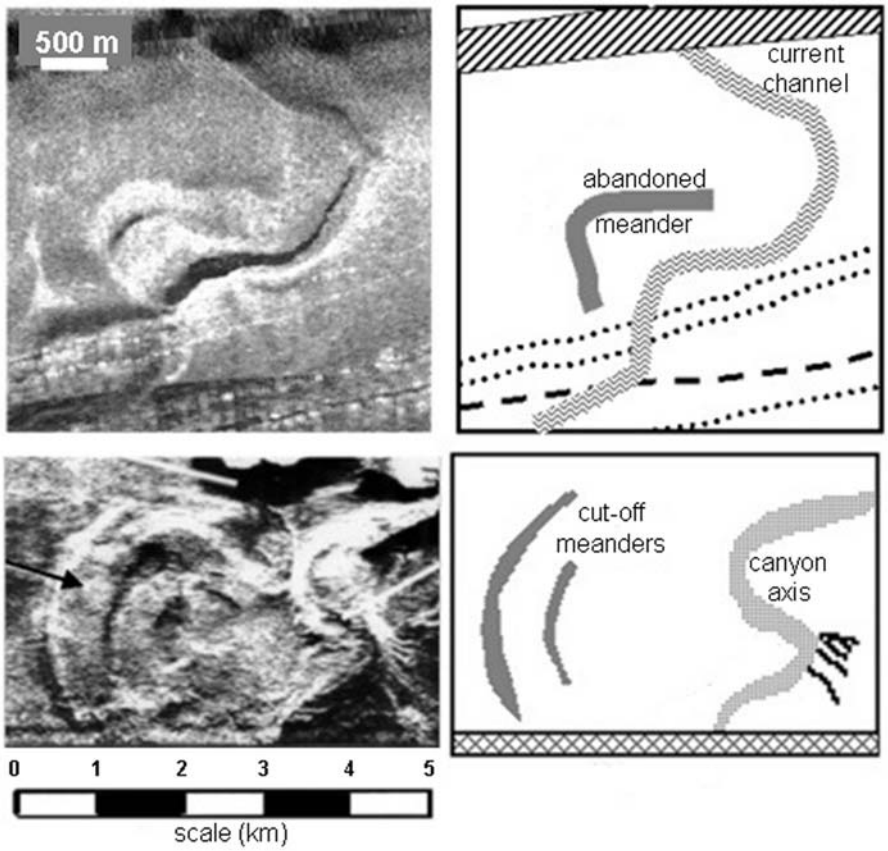

Figure 7.9. (Top) Abandoned meander and currently active channel of the Almeria system imaged with the 30 kHz TOBI sonar (Gómez Sichi *et al*., 2005), with schematic interpretation (the most obvious artifacts have been outlined). (Bottom) A highly meandering canyon and two cut-off meanders imaged with the 12 kHz SeaMARC-II sonar, with schematic interpretation (courtesy Rick Hagen of AWI, Germany and Elsevier Publications).

against the canyon walls (much as springtime rivers coming from glaciers would "jump" over the meanders in a plain and create new river paths).

The images presented in Figure 7.9 were respectively acquired with TOBI (30 kHz) on the continental margin off SE Spain (Gómez Sichi *et al*., 2005) and with SeaMARC-II (12 kHz) on the continental margin off Peru (Hagen *et al*., 1994). Both images correspond to only half-swaths (i.e., the direction of ensonification is constant each time). In each image, the currently active part of the submarine canyon is clearly visible, with the walls facing the sonar being highly reflective. Cut-off meanders on the terraces surrounding the canyon are clearly recognized by the sharp-edged reflections and shadows from the former channel walls, and the high areas in the center of the meander loops. In the SeaMARC-II image, small channels perpendicular to the levees are visible along the southern part of the current canyon axis; they correspond

to crevasse splays where canyon overflow became focused. Note how, despite the difference in imaging frequency (i.e., resolution) and the difference in scale of each image, the structures of both the active channel and the abandoned meander(s) are clearly recognizable.

7.2.3 Mass-wasting, slides, and flows

The continental rise is formed by the processes that transport sediments in a downslope direction. Large sediment accumulations may form at the edge of the continental shelf and the upper continental slope. These accumulations are usually unstable, and can move downslope as slumps, slides, and debris flows, leaving scars on the seafloor and the marks of downslope transportation and deposition of sediments. Factors known to influence these catastrophic events include loading or over-steepening of slopes, under-consolidation of sediments due to rapid sedimentation, earthquakes, gas build-up, and sea level changes (Saxov and Nieuwenhuis, 1982). Mass-movement deposits are often called debris, and correspond to mixed lithologies with hard pebbles and boulders, with sizes up to several tens of meters. They will show up in sidescan sonar images as bright reflective areas (see Figure 7.6) with fine-grained textures.

GLORIA imagery from the Western Atlantic continental rise presents several good examples of debris slides. In particular, Figure 7.10 presents the junction between two slides of different acoustic characters. This image results from the mosaicking of several swaths, and ranges in depths between −4,250 m and −5,000 m. Cape Fear Slide is recognized by its high backscatters and the very fine-grained textures all along the slide. Individual flows are difficult to distinguish because most lack well-defined edges (at least at GLORIA's resolution). Only the two larger ones (upper-left portion of the image) are visible, with medium-bright backscatters. The Cape Fear Slide involved slope failure of an area 37 km long, 10 km to 12 km wide, and up to 80 m thick (EEZ-SCAN, 1991). Debris flows from the scar area can be traced across the continental rise for over 250 km as a bright reflection return. At the NE edge of this image, debris from the Cape Fear Slide flows across earlier debris from the Cape Lookout Slide, indicating that the Cape Fear Slide is more recent. It is also marked by a bright acoustic return across the rise. Within the bright return area, the bottom exhibits a fuzzier texture than the Cape Fear Slide, and sometimes looks more "transparent". This is also characteristic of mass-movement debris as imaged by GLORIA: 3.5 kHz profiles show the "transparent" aspect is related to the deposition of finer sediments on top of an acoustically harder layer.

Mass-movement features include debris tongues or rubble trails that extend from the bases of the larger scarps, and small slides located along the surface of the lower slope ramps. Some of them have a teardrop form similar to land-based features (called "disintegrating soil slips" in California). The image presented in Figure 7.11 has been acquired using SeaMARC-I near the Block Canyon Slide, on the northeastern U.S.A. continental margin (O'Leary and Dobson, 1992). SeaMARC-I was a 30 kHz system with a resolution of 2.5 meters and a swath width of 5 km. This deep-tow sonar was the ancestor of SeaMARC-II but never saw much

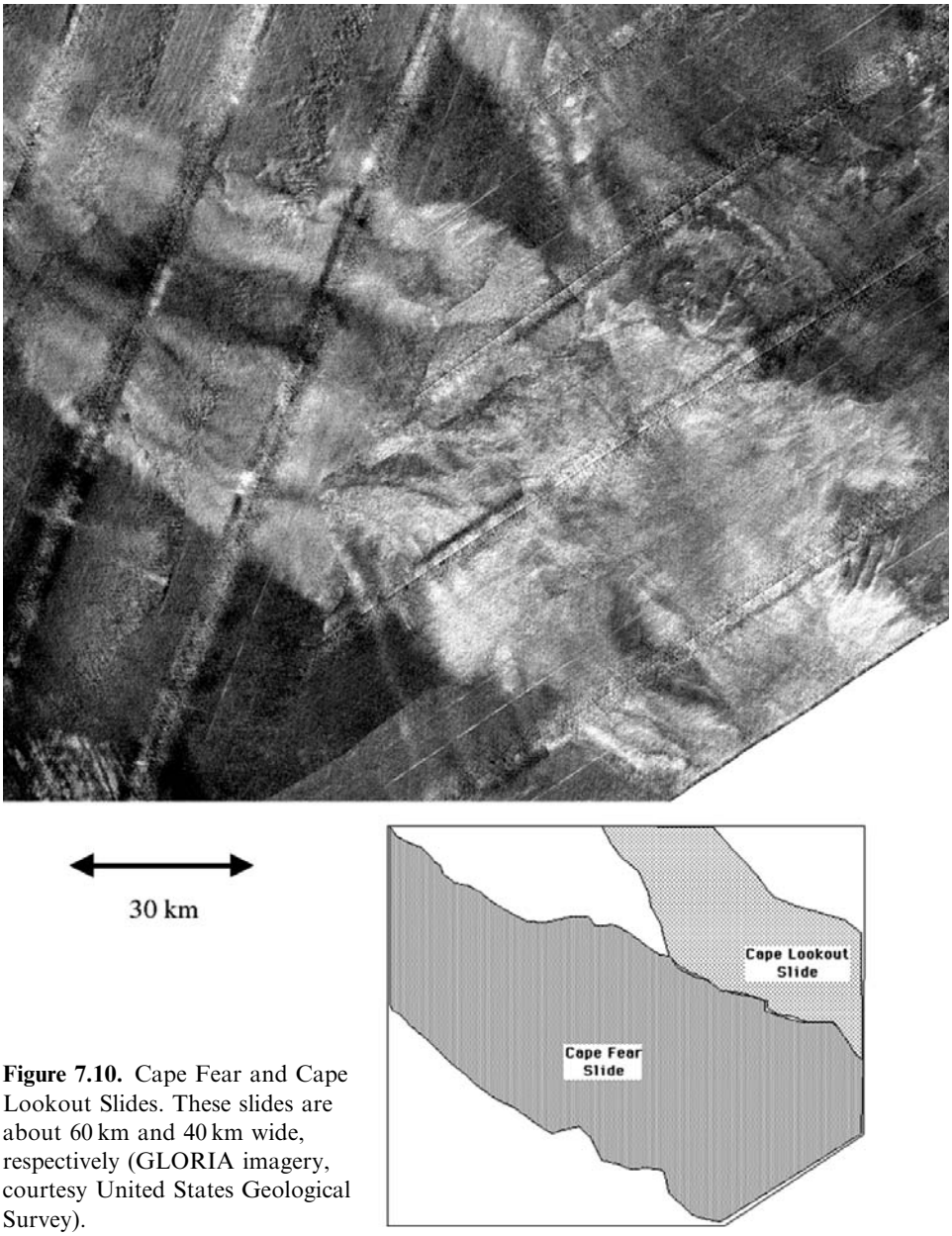

Figure 7.10. Cape Fear and Cape Lookout Slides. These slides are about 60 km and 40 km wide, respectively (GLORIA imagery, courtesy United States Geological Survey).

use. The sonar track is visible as a horizontal black line in the middle of the image. The arcuate head scarp is visible in the upper portion with a bright reflectivity, because it is facing the sonar. Its relief is of the order of 10 meters. The outlines of the slide are brighter than their surrounding, their gray levels apparently not

changing with distance from the sonar track. This can be explained by a higher roughness of the seafloor at the contact between the young slide and its sub-stratum. The slide is 800 m wide and 4,100 m long, going downslope. The toe forms a thin, tapered tail of rubble, with a uniform high backscatter. The presence of teardrop slides in the slopes is often used as evidence of recent slope unstability.

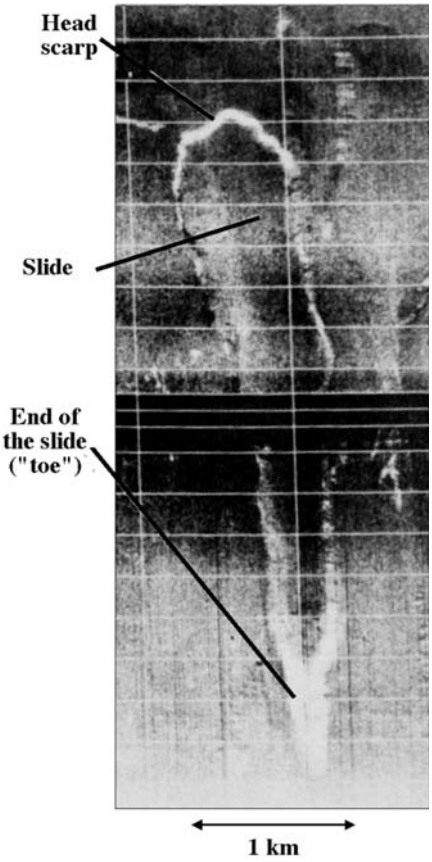

Figure 7.11. Teardrop slide imaged by SeaMARC-I. The image has been inverted so that high backscatters are bright, low backscatters are dark (from O'Leary and Dobson, 1992).

Other types of turbiditic deposits are associated with canyon overflows, when the incoming fluxes of sediments are too large or too rapid to pass through the canyon. Overflows are more likely to happen near meandering canyons. Levees and overbank deposits form low sediment ridges along the banks of the canyons (Figure 7.12). They can be a few hundreds of meters wide, and up to several meters high. They can also form in several episodes, and create terraces (Figure 7.13). These terraces generally extend perpendicular to or even downslope from the canyon. Figure 7.13 presents SeaMARC-II imagery from the continental margin off Peru and Chile. The ensonification direction is constant through the image. The homogeneous area in the middle of the image corresponds to a data gap, when the sonar stopped recording for a short time. The terraces appear as contiguous areas of grainy texture, located on the sides of the canyon axis. One can also note the differences in backscatter as the general slope of the terraces faces away from the sonar (left section of the image) or toward the sonar (right section of the image).

7.2.4 Sediment redistribution

Bottom currents rework and redistribute the deposited sediments and form large, elongated structures in the zones with little or no topographic variations. These structures are sediment waves, similar to sub-aerial sand dunes. They will be recognizable in sidescan sonar imagery from the contrasting acoustic returns between the slopes facing toward and away from the sonar. Depending on the local conditions (speed, direction, and longevity of bottom currents, surrounding topography),

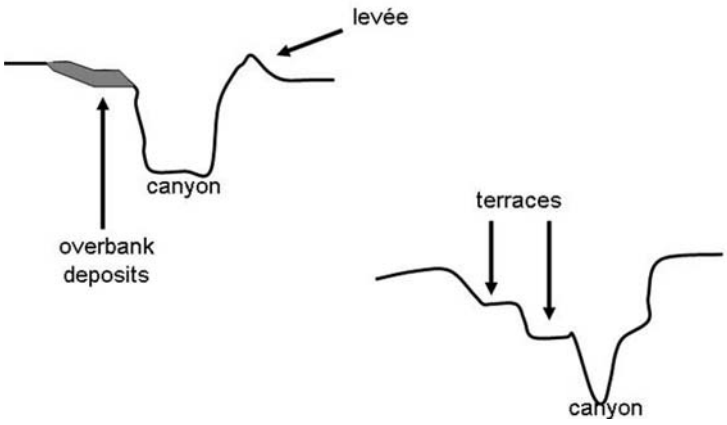

Figure 7.12. Stylized topographic profiles across a submarine canyon, showing different types of erosion and turbidite features.

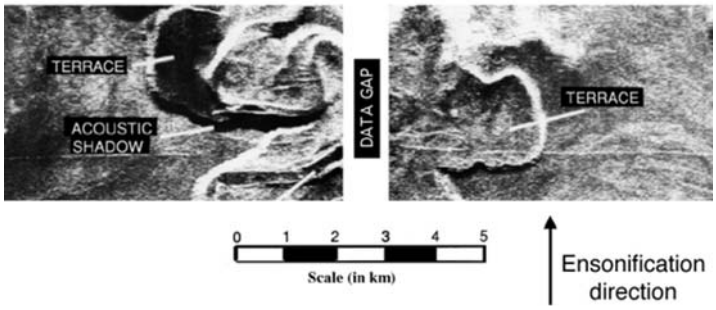

Figure 7.13. Terraces imaged by SeaMARC-II in the southern Pacific (courtesy R. Hagen of AWI, Germany and Elsevier Publications).

sediment waves will have different sizes and shapes. As one example among many, SeaMARC-II imagery from the Peruvian continental margin shows arcuate to linear sediment waves between the canyons (Figure 7.14). These waves vary in orientation and have wavelengths of 400 m to 800 m. Acoustic shadows are small or absent, hinting that the topographic expression of sediment waves is very small. In this case, echo-sounder profiles show it to be less than 5 meters. Individual wave crests can be traced for up to 6 km on the images. In this region, the sediment waves are grouped into distinct wave fields with common orientations and wavelengths.

Sediment waves exist at all scales. The smaller ones are no more than meter-scale ripples, similar to the ones seen in the next chapter (Chapter 8, ''Shallow-water environments''). The larger ones, often called mega-ripples, can extend for several tens of kilometers (Figure 7.15). This image was recorded using GLORIA in water depths of 4,750 m, in the middle of a flat basin with no large variations in topography. The large sediment waves, known as the Lower Rise Hills, are clearly seen from the contrasts between the slopes facing away from and toward the sonar. Closely spaced, they are several tens of kilometers long and up to 5 km wide. These sediment waves are located on the flank of the Hatteras Ridge, and are believed to have been formed by the interaction of contour-following currents, the northeast-flowing Gulf Stream, and the southwest-flowing abyssal Western Boundary Undercurrent.

Figure 7.16 shows a different type of sediment redistribution, with GLORIA imagery of Feni Drift, near Rockall Trough offshore Ireland. Feni Drift is one of the largest and oldest sediment drifts in the North Atlantic (e.g., Unnithan *et al.*, 2000). The image shows only a portion (60×60 km) of the entire drift, 600 km long and 60 km broad overall. The Feni Drift is an elongate, mounded feature adorned by large-scale sediment waves, with amplitudes of 20 m to 60 m, wavelengths of 0.5 km to 4 km, and crest lengths of 2 km to 20 km. It has been investigated by many authors (see Unnithan *et al.*, 2000 for a synthesis), and ancillary information shows the

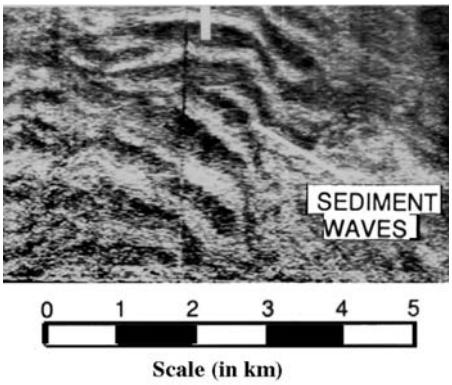

Figure 7.14. SeaMARC-II imagery of arcuate sediment waves, ensonified from the bottom of the image (courtesy R. Hagen of AWI, Germany and Elsevier Publications).

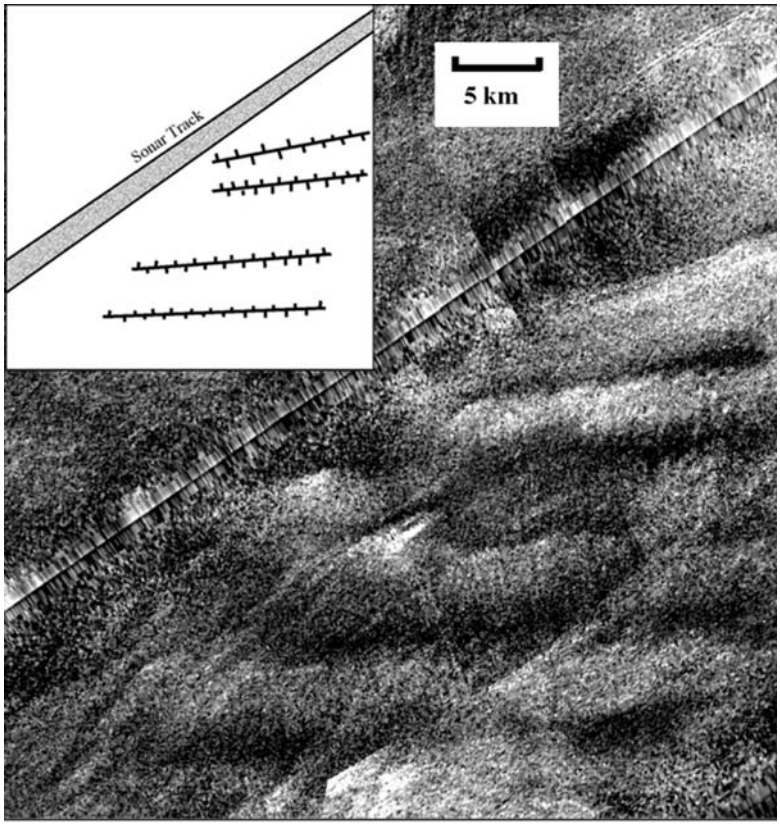

Figure 7.15. Linear sediment waves, imaged by GLORIA in the continental rise off North Carolina, eastern U.S.A. (courtesy United States Geological Survey).

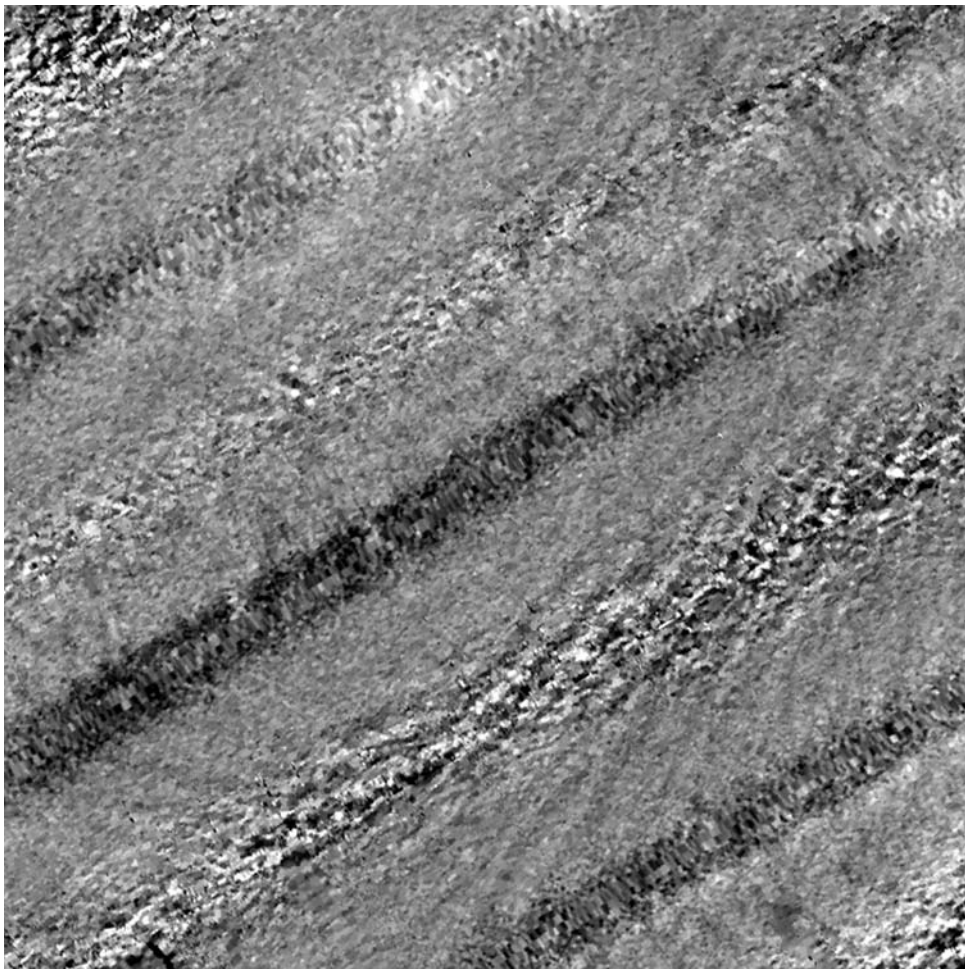

Figure 7.16. GLORIA 6.5 kHz imagery from the Feni Drift, a large Miocene–Recent contourite sediment accumulation (Unnithan *et al*., 2000). The image covers approximately 60×60 km on the ground and includes several diagonal swaths. Because of their physical characteristics (see text for details), the sediment waves are more visible at far range, as diagonal areas with rougher textures (Blondel, 1998).

sediments are mainly calcareous silts, clays, and oozes. They are winnowed by bottom currents and fine-grained, with a low micro-scale roughness. Their acoustic backscatter will therefore be generally low, and sediment waves will be more easily observed for high imaging angles (e.g., at far range). In the case of this image, acquired using GLORIA, this is compounded by the 50 m size of each pixel. The sediment waves visible in Figure 7.16 are diagonal (from bottom left to top right, more or less), with rougher textures than the background sediments, and they are indeed always observed at far range.

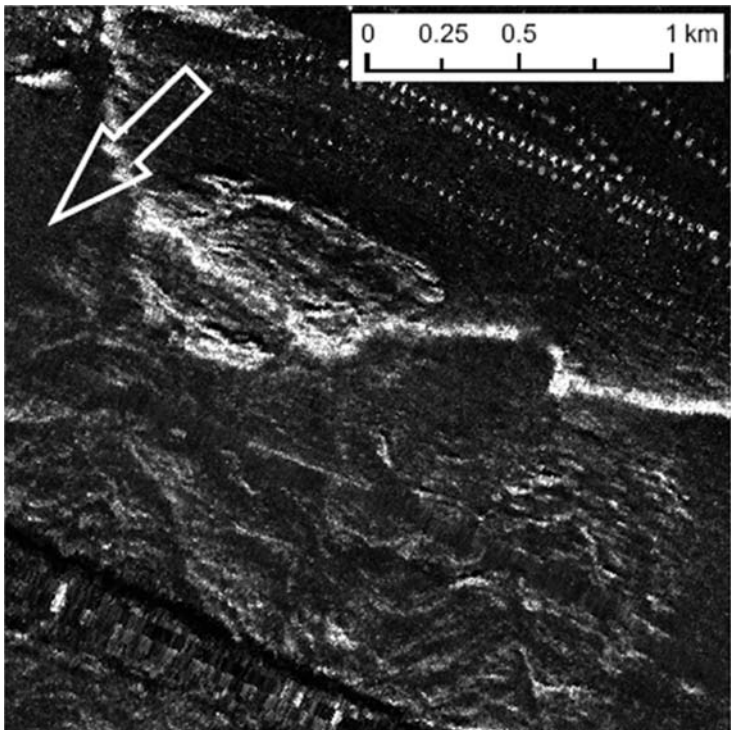

Figure 7.17. Complex lateral spread in the Storegga landslide, imaged with TOBI (30 kHz imaging frequency, 6 m resolution after processing). The arrow shows the direction of the slide (from Micallef *et al.*, 2006).

Sediments deposited along channels can be redistributed through overflow or slumping. Examples of slumping were already seen in Chapter 6 (e.g., Figure 6.10). Lateral spreading corresponds to the extensional movement of sediments over a weak layer, breaking into successive units (creating a series of parallel ridges and troughs). Figure 7.17 shows high-resolution TOBI imagery from a complex lateral spread in the Storegga Slide area, on the Norwegian continental margin. Several swaths have been used to make this image, and their diagonal nadirs are visible, particularly at the bottom left of the image. The image also sports some artifacts (top-right corner), corresponding to cross-talk with other acoustic instruments. The part of the slump facing toward the sonar is much more contrasted than the part facing away, but the structures are still very clear. The slump itself appears as the series of ridges and troughs in the upper half of the image. The degree of disintegration of the blocks increases downslope, as visible from the rougher textures. Their respective geometries and distances can be used to infer the characteristics of the slump when it occurred.

7.3 TECTONIC AND VOLCANIC STRUCTURES

On continental margins, the geological structures that can be directly attributed to tectonism or volcanism are very rarely seen on the surface. They are generally highly

Figure 7.18. Uncorrected MAK-1 record of a fault scarp in the Mediterranean Sea. The image corresponds to a full MAK-1 swath and is 2 km wide (from Beijdorff *et al*., 1994; © UNESCO).

sedimented, and visible only on sub-surface profiler data or on seismic profiles. Nonetheless, some fresh tectonic expressions can be imaged with sidescan sonar. They will appear exactly as their analogues at mid-ocean ridges (see Chapter 5, ''Spreading and subduction''). The slopes facing toward the sonar will be reflective to highly reflective, whereas the slopes facing away from the sonar will be less reflective or completely dark.

The image presented in Figure 7.18 was acquired using the Russian sonar MAK-1 in the Mediterranean Sea, and inverted to show higher backscatter levels as brighter tones. The sonar track is horizontal and in the middle of the image. A single long structure, about 300 m wide, cuts the image diagonally from the lower-left corner to the upper-right corner. This structure shows consistent backscatters, very bright in the upper half of the image, medium dark to medium bright in the lower half, where it is associated with small gullies close to the sonar track. All this argues for an interpretation as a fault scarp, sloping down from the top left to the bottom right. The small circular structures visible in the rightmost part of the image are thought to be pockmarks (i.e., surface manifestations of gas seepage; see Section 7.4.2). Slight along-track variations of backscatter are visible, and are attributed to the lack of appropriate angle-varying gain corrections.

Continental margins are generally far from areas of volcanic productivity, such as mid-oceanic ridges or subduction zones. Very few volcanic structures have been documented in continental margins, and most if not all of them are inactive and highly sedimented. When still intact, these volcanoes look very much like their

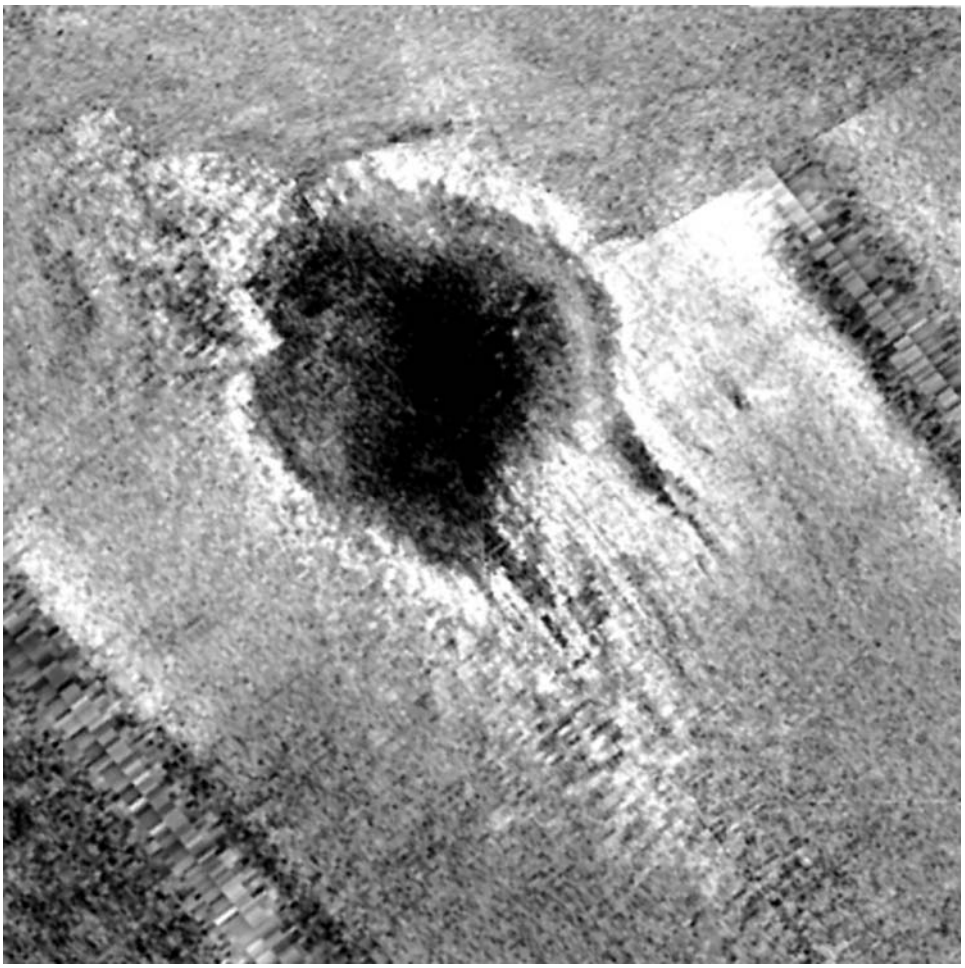

Figure 7.19. GLORIA imagery of Bear Seamount, New England seamount chain. The volcano is nearly circular, 14 km wide, and 1,500 m high (courtesy United States Geological Survey).

counterparts at spreading centers. Their dimensions will be more important, as they need to emerge above the thick sediment layers. Figure 7.19 shows an image of Bear Seamount in the New England seamount chain. The image is made of several swaths (the nadirs of two of them are visible in the bottom-left and top-right corners, respectively). Located off Georges Bank on the eastern U.S.A. continental margin, this slightly sedimented volcano appars as a large circular structure with a diameter of 14 km. The stitching of the two survey lines has been carefully performed, and the seam is barely visible on the median line between the swaths. The noisy areas below the nadir are slightly widening toward the bottom-right corner of the image. This means that the distance between the sonar instrument and the ground is increasing. Because GLORIA is shallow-towed, it can therefore be assumed that the topography

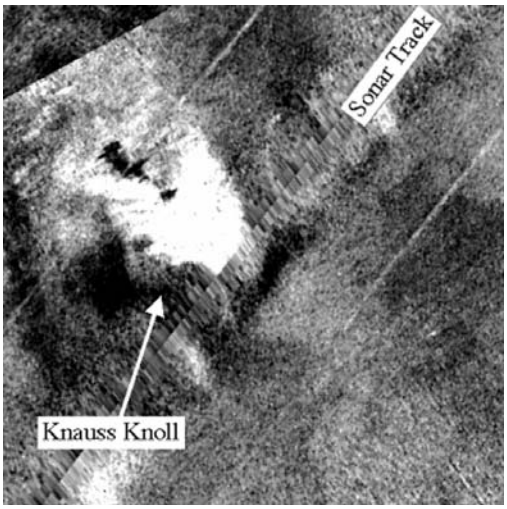

Figure 7.20. Knauss Knoll is a small sediment-covered seamount on the eastern U.S.A. continental margin. Its dimensions are approximately 6 km (along-track) by 10.5 km (across-track) (GLORIA imagery, courtesy United States Geological Survey).

is dipping moderately toward the bottom right. This "educated" guess is confirmed by concurrent bathymetric maps of the area, which show that depths vary between 2,750 m in the NW corner of the image and 3,250 m in the SE corner. The large, circular shape of the seamount is divided into a bright (reflective) half and a dark half, corresponding to the direction of ensonification. The extent of the shadow on the left (several kilometers) indicates that the height of the structure is of the order of a few hundred meters. The reflective area on the right can be separated into a flat semi-circular rim, and a brighter, more homogeneous slope facing directly toward the sonar. Bright textural patterns, associated with debris from the volcano, can be seen all around.

Most seamounts still visible on continental margins have been affected by tectonics and erosion processes. Knauss Knoll (Figure 7.20) is another inactive seamount at the edge of the eastern U.S.A. continental margin. GLORIA imagery reveals an asymmetric shape elongated along-track, with dimensions of 6×10.5 km. The slopes of the seamount close to the sonar track are highly reflective (nearly saturated). A small circular shape on top of the slopes is associated with a small shadow, and is interpreted as the summit crater. The seamount's extremity farther from the sonar track is less reflective. It delimits an embayed slope, indicative of an extensive collapse of the original edifice. Adjacent seafloor sediments overlap the seamount flanks and attenuate the backscatter in the regions that are not directly facing the sonar. They scoured the seafloor and created a small depression (dark backscatter patch SW of the volcano). Analysis of dredge samples gives an age estimate of 100 Ma to 85 Ma. Knaus Knoll is typical of the other seamounts in the New England chain, and, to a certain extent, it is also typical of relict seamounts in continental margins.

7.4 OTHER STRUCTURES

7.4.1 Biological activity—past and present

With the right combination of frequency and ground resolution, sidescan sonar imagery can reveal some manifestations of biological activity. On continental shelves,

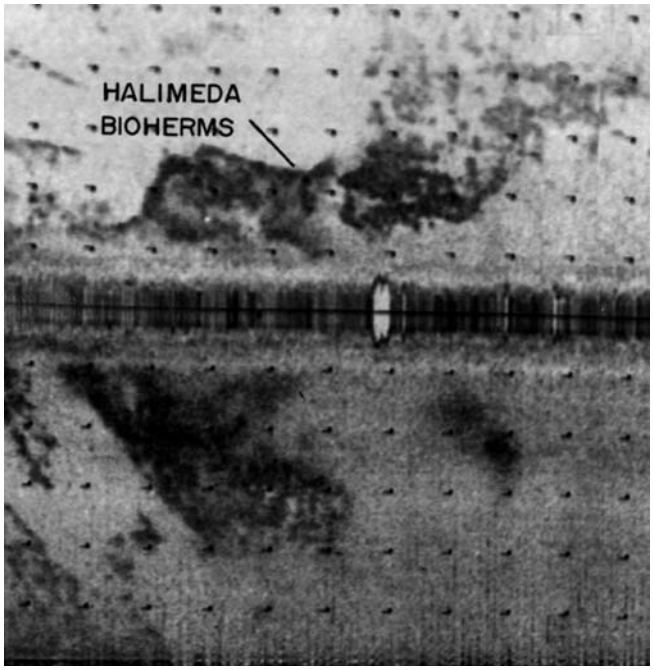

Figure 7.21. Sidescan imagery showing *Halimeda* bioherms on a flat sedimented bottom. The black crosses are spaced evenly every 25 meters. The image comes from a paper record; high backscatters are dark, low backscatters bright (unpublished data, courtesy M. Veerayya and V. Purnachandra Rao, National Institute of Oceanography, India).

slumps of large algae and local accumulations of dead and living plants are the most likely objects to be detected. For example, direct visual observations of *Halimeda* plants on the Indonesian Margin show that living stands of these plants organize themselves into groups with common reliefs of 0.5 m above the seafloor. These structures are quite different from their sedimentary background and will generally present stronger backscatters. Figure 7.21 shows the accumulation of *Halimeda* in a mound (bioherm), on a flat portion of the western Indian continental shelf. This image was acquired using the SMS-960 sidescan sonar (frequency 110 kHz) in water depths close to 90 meters. Backscatters are inverted, and are represented by dark levels when higher. The main part of the seafloor exhibits a medium backscatter, light gray on one side of the swath to dark gray on the other side (due to different calibration settings). This sub-stratum corresponds to a portion of a drowned carbonate platform covered by sediments. The highly reflective patches (dark in Figure 7.21) have unusual shapes. They are formed of several distinct units, are round, and are a few meters wide. These units are interpreted as individual *Halimeda* bioherms, composed of clustered dead and living plants; this was confirmed by coring. Echosounder profiles confirm that these units formed by coalescence of several mounds, 2 m to 14 m high.

Acquired during the same survey, a larger scale image shows the different morphologies of *Halimeda* bioherms (Figure 7.22). Morphologies range from numerous small mounds (a few meters in diameter) through "haystack"-elongated features (several tens of meters wide, several hundreds long) to broad swells in the upper-right

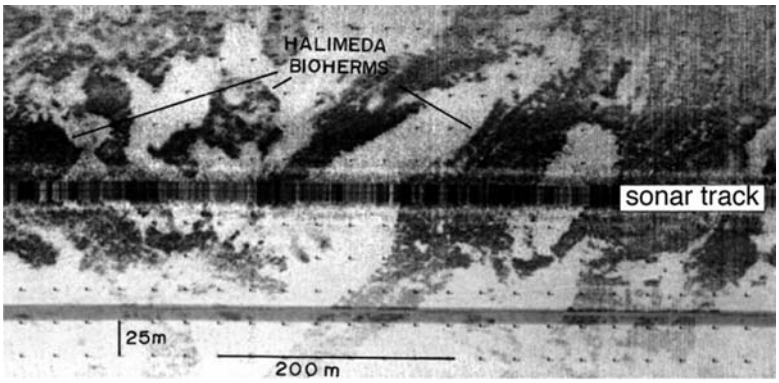

Figure 7.22. Sidescan imagery of massive algal biohermal structures, separated by sediment-covered areas of the Indian continental shelf. High backscatters are dark, low backscatters bright (courtesy V. Purnachandra Rao and M. Veerayya, National Institute of Oceanography, India and Elsevier Publications).

corner of the image. Bioherms on the shelf edge appear more linear (Figure 7.23), whereas bioherms inside the platform generally assume mound-like morphologies. Both types form by biological accumulation, and these shapes are related to the dynamics of *Halimeda* growth and clustering. The lineated aspect of the algal ridges in Figure 7.23 suggests an orientation along the main direction of the bottom currents which bring the necessary nutrients.

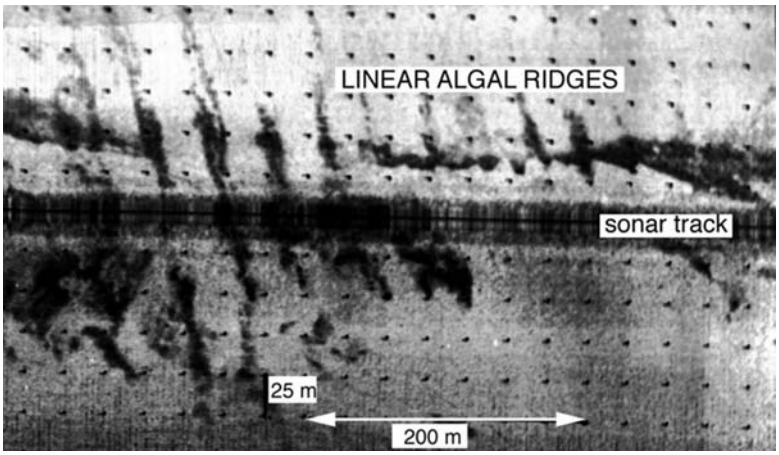

Figure 7.23. Linear algal ridges separated by sediment-covered areas on the carbonate platform off Bombay, western continental shelf of India (M. Veerayya, pers. commun., 1995). The water depth is 90 meters, close to the limit for shallow-water environments (see Chapter 8 for more examples of algae). High backscatters are dark, low backscatters bright (unpublished data, courtesy V. Purnachandra Rao and M. Veerayya, National Institute of Oceanography, India).

Coral reefs are usually associated with warm water, but large research efforts over the last decades have shown the worldwide prevalence of cold-water coral reefs (summed up in a beautiful book by Hovland, 2008). Figure 7.24 shows a series of coral reefs on the Sula Ridge, off Norway (Hühnerbach *et al.*, 2008), acquired with a 100 kHz sonar flying very close to the seabed (ca. 30 m). There are two swaths in this image, with their diagonal nadirs clearly visible. The junction between each swath is also clearly visible, making the interpretation easier. Individual coral reefs are easily recognizable as rounded structures with high backscatters and rough textures, especially when facing toward the sonar. Their acoustic shadows can be used to infer their relative heights and shapes. Smoother areas between the coral reefs, with slightly lower reflectivities, are interpreted as background sediments and coral rubble (from the decay of dead corals). This is confirmed, at least in this case, by video transects all across the ridge (Freiwald, 2002; Freiwald *et al.*, 2002; Hühnerbach *et al.*, 2008). More general information about cold-water coral reefs and their imaging with sonars can be found in Freiwald (2002) and Hovland (2008). Studies by Freiwald *et al.* (2002) interestingly showed that "sharp" backscatter features (in the reefs) indicate living and healthy coral populations. Conversely, smooth backscatter indicates sediment-laden, sponge-overgrown, or mostly dead coral reefs. In the latter case, the seabed near the circular dead reefs is littered with dropstones and/or winnowed moraine boulders. It is therefore not possible to distinguish between these different types by only looking at the first-order (tonal) changes of acoustic backscatter. One must instead use second-order (textural) statistics to try to distinguish between these regions (see Chapter 11, "Computer-assisted interpretation" for more information on the appropriate techniques).

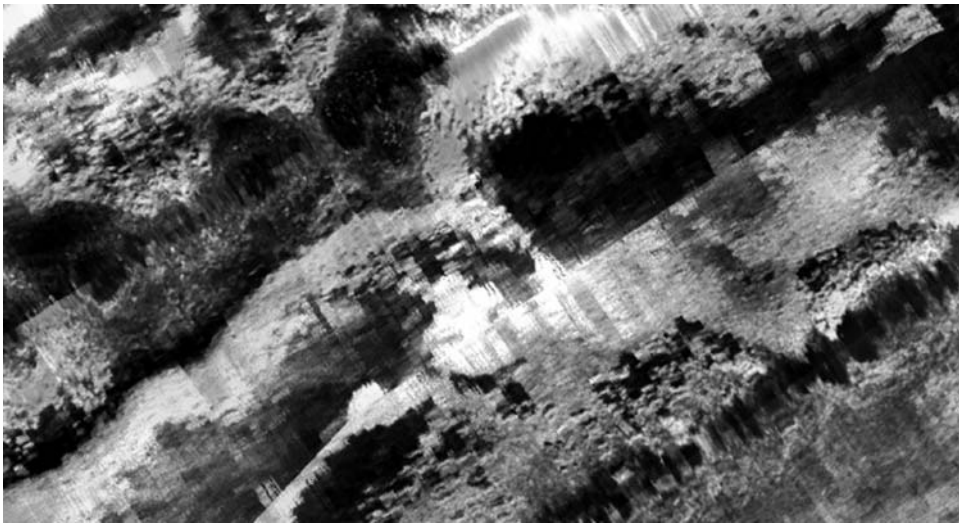

Figure 7.24. Coral reefs imaged at 100 kHz. Image is ca. 430 m wide (from Hühnerbach *et al.*, 2008).

Sidescan sonar provides information about biological activity which supplements efficiently the results from echo-sounder or seismic profiles, coring, and *in situ* observations. It can provide large-scale mapping of biological activity, and repeated surveys can assist in the long-time environmental monitoring of these regions. It can also supply information about paleoclimates. In the case of the *Halimeda* bioherms shown in Figure 7.23, for example, coring shows they date from about 10,000 years BP, and have originated in an arid climate (Rao *et al.*, 1994). Biology-oriented sidescan sonar surveys have significantly progressed in the last decade, along with their multibeam analogues (also using backscatter) (e.g., Kenny *et al.*, 2003; Brown and Blondel, 2008).

7.4.2 Fluid and gas seepage structures

The best visible structures associated with fluid/gas seepage are mud volcanoes. They have been documented in various deep-sea environments all over the world. The most-studied examples are located in the Mediterranean, the Atlantic Margin, and the Black Sea. Other occurrences have been documented in accretionary complexes like the Barbados (where mud volcanoes have been actively formed over at least the last 200,000 years), the Nankai accretionary prism, and the Indonesian arc (see Chapter 5, "Spreading and subduction"). Mud volcanism may also appear in coastal environments, like the Makran region in Pakistan, where active mud volcanoes are found in association with gas seeps onshore and offshore. Their mechanisms of formation are diverse. In the Black Sea, mud volcanoes are formed by the channelized eruption of gas and fluid-saturated clays through thick overlaying sediments (Limonov *et al.*, 1996). Conversely, mud diapirs in the Mediterranean are the result of lateral tectonic compression pushing plastic material upward.

The distinction between mud volcanoes and mud mounds is not purely semantic, as it has important implications on the stage of evolution associated with the structure, but this is considered beyond the scope of this section (see articles by Ivanov *et al.*, 1996; Milkov, 2002; Davies and Stewart, 2005 and many others for better explanations). Mud volcanoes are an important global mechanism for degassing deeply buried sediments (e.g., Dimitrov, 2002), and it has been estimated that several thousands occur globally (e.g., Milkov, 2000). Various architectures connecting extrusive mud volcanic cones to their underlying source layer have been described, and they are summarized in Davies and Stewart (2005). Most of this research has used seismic data, as sidescan sonar images only reveal the surface morphology of the mud volcanoes. Limited as it is, this morphology is still useful for a first guess at the age of the structure, as it evolves from a pioneer cone to, in the end, concentric faults and a downward-tapering cone (Davies and Stewart, 2005).

Mud volcanoes (and mud mounds) appear on sidescan sonar imagery as highly reflective patches of seafloor on a dark background (e.g., Kenyon *et al.*, 1999; Naudts *et al.*, 2008). They generally have a mushroom or cone-like shape, with diameters at their base of a few hundred meters to 3 km, and rise from 20 m to 150 m above the seafloor. The bright patches present irregular boundaries and a backscatter generally much stronger than its surroundings. This stronger backscatter is considered to be

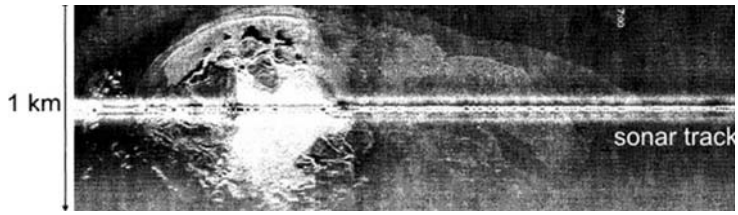

Figure 7.25. Haakon Mosby mud volcano, imaged with the ORETECH sidescan sonar (100 kHz imaging frequency) (reprocessed from Kenyon *et al.*, 1999).

caused by the irregular relief of the crater and cone, and by the presence of mud breccia and rock blasts on the seafloor or at very shallow depths. It seems that mud diapirs are not visible on GLORIA imagery if the pelagic sediment cover is greater than about 2 meters (Fusi and Kenyon, 1996): the highly reflective circular patches can only be interpreted as areas of substantial micro-scale roughness. This indicates that the frequency and the ground resolution (respectively, 6.5 kHz and 50 m for GLORIA) play an important role in the detection or non-detection of the structures associated with mud volcanism. This is why higher resolution sonars, with higher frequencies, are often better for imaging mud volcanoes.

Figure 7.25 shows a single high-resolution swath going through the Haakon Mosby mud volcano offshore Norway (Kenyon *et al.*, 1999). This well-studied mud volcano is very low (a few meters above the surrounding seabed) and overlain with 2 m to 3 m of acoustically transparent sediments (as seen from profiler records). The center of the mud volcano is visible as a complex shape of very high (nearly saturated) backscatter. Immediately left, a series of angular shapes of low backscatter, separated by narrow, dark stripes, are explained by large displaced sedimentary blocks (Kenyon *et al.*, 1999). There is a similar pattern on the other side of the volcano. Radial mud flows, with relatively high backscatter, also spread out from the crater of the mud volcano. The image right of the main structure (1 km in diameter) shows a series of overlapping mud flows, with varying backscatter levels and roughness.

Mud volcanism and the associated structures are very important scientifically, because they provide unique information about the geological processes taking place at larger depths through the study of vented gases and muds. They are also interesting as potential traps for hydrocarbons, and because they create important modifications of the seafloor, which are potential hazards for telecommunication cables and pipelines.

Fluids vented from the seabed are varied in nature. Gamberi *et al.* (1997) found hydrothermal features similar to those found on mid-ocean ridges (see Section 5.5). MacDonald *et al.* (2000) documented, for example, how the seepage of natural oil 600 m deep could be quickly detected at the surface. Asphalt volcanoes and lava-like deposits of solidified asphalt have been discovered by MacDonald *et al.* (2004) in the southern Gulf of Mexico. Hovland *et al.* (2005) explained their occurrence by the interaction of seeping asphalt with supercritical water. The more usual manifestations

of gas seepage are pockmarks. They were first seen on sidescan sonar records in the 1970s, and can be found in the epicontinental seas as well as on continental margins around the world (Hovland and Judd, 1988). Pockmarks are formed in three stages: (1) building up of gas or pore-water pressure in a porous layer of sediments below an impermeable cohesive material (excess pressure is relieved by doming of the seabed); (2) after fracturing of the dome, excess gas pressure is released by eruption, along with the overlying sediments; (3) the fine-grained sediments become suspended in the water and transported elsewhere by currents, while coarser material falls back into or near the newly formed pockmark.

Most pockmarks are approximately circular in plan, but there is a considerable variety in shapes and sizes. Because they are active features, their dimensions are likely to vary over time. They correspond to hollow depressions of the seabed, a few meters deep. Their appearance on sidescan sonar imagery will therefore be sub-circular or elliptical, the slope facing away from the sonar being darker and the slope facing the sonar brighter. This will of course vary according to the angle of incidence and how far the pockmarks are from the sonar.

A sidescan sonar survey of the Eratosthenes Seamount (eastern Mediterranean) shows some circular structures interpreted as pockmarks (Figure 7.26). They are visible on both sides of the sonar track (horizontal line in the middle of the image). These features are characterized by a diameter of some tens to 300 meters, and their relative depth is several meters. These holes are notable by high reflective rims on the side facing the MAK-1 sonar. Many of them have a quite perfect circular shape. The

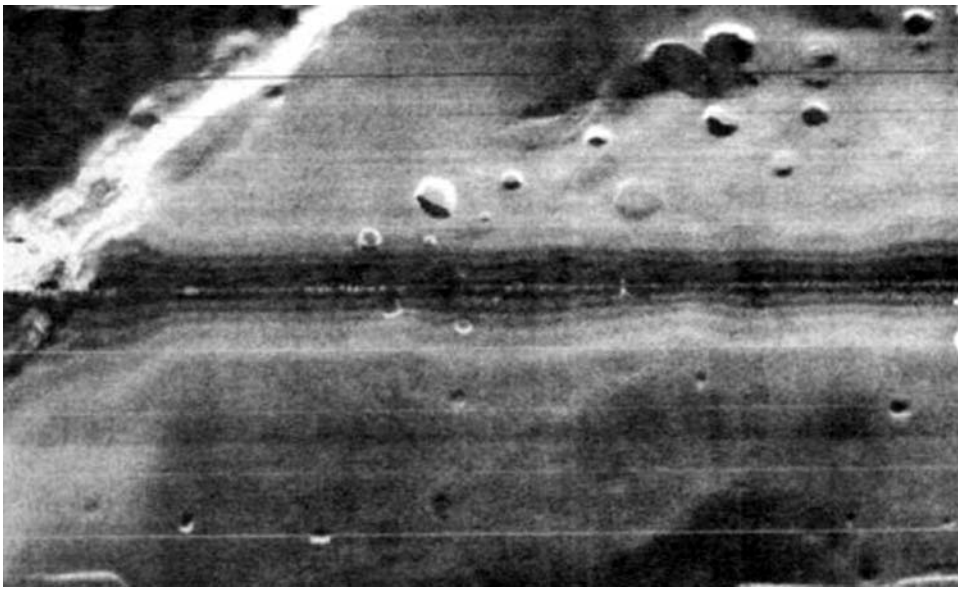

Figure 7.26. Pockmarks on top of Eratosthenes Seamount (eastern Mediterranean), imaged with MAK-1. The image is 3×2 km (from Beijdorff *et al.*, 1994; © UNESCO).

ones north of the sonar track are more elliptical and exhibit a stronger backwall reflection, apparently due to the local slope of the seamount (which goes up northward). The holes could be related to karst, but more likely they originated from shallow gas and/or fluid seeps and represent pockmarks.

A comprehensive study of pockmarks, their dimensions, and their settings was performed by Hovland and Judd (1988). They distinguished several generic varieties:

- *Standard pockmarks and elliptical pockmarks* are the most common (they are shown in Figure 7.26).
- *Composite pockmarks* occur where individual pockmarks merge with one another. In some instances, groups of pockmarks are found clustered together, while in other cases the merging has proceeded to the extent where a single feature with a complex shape is all that is left.
- *Asymmetric pockmarks* on sidescan sonar imagery show a distinct and quite often long tail, and a strong backwall reflection on one side only. This is due to the local slope up to seabed level, one that is long and gentle.
- *Pockmark strings* extend for several hundred meters, and are made up of small pockmarks that are symmetrical, shallow, and 10 m to 15 m in diameter (Figure 6.15 shows a good example). Pockmark strings observed in the Norwegian Trench (North Sea) were attributed to pre-existing iceberg ploughmarks which focused the gas seepages.
- *Elongated pockmarks and troughs* are so elongated that they resemble gullies or troughs. The upper sediment layers are absent and the older sediments exposed.
- *Unit pockmarks* are seabed depressions that are very small (<5 m) and shallow. They are also referred to as "pits" or "pit clusters", and seem to be incipient pockmarks.

Because of their origin (fluid or gas seepage) and of their locations (very often close to hydrocarbon reservoirs), pockmarks generate a considerable interest in offshore industries, in particular those related to gas exploration and exploitation. The direct signs of fluid/gas seepage, when combined with extensive canyon formation and slumping, can be used as indirect evidence of methane gas hydrates in the area (e.g., Gardner *et al.*, 1998; Bouriak *et al.*, 2000). Recent ground-truthing studies have shown that gas leakage is often associated with bacterial mats, but these are at the moment beyond the resolution of most if not all sidescan sonars. This pressing interest in pockmarks is enhanced by the consequences they may have on offshore platforms and the security of drilling exploration. Catastrophic gas escapes can form large, deep pockmarks in very short periods of time. In one occurrence, cited by Hovland and Judd (1988), a crater 600 m across and 30 m deep was formed within a period of 5 days. In another example, the gas blowout at a depth of 240 m reached the surface, and instabilities led to the abandonment of a neighboring drilling platform. Even if these examples are quite extreme, it nonetheless demonstrates the possible consequences of drilling into shallow gas pockets, or what could happen to the stability of platforms in the vicinity of such an event.

7.4.3 Brine pools

Intriguing structures that completely absorb acoustic radiation are seen in varied environments and are known as "brine pools". They manifest themselves as bottom depressions filled with hypersaline water, supporting chemosynthetic communities. They have been particularly well documented in the Mediterranean, but their exact modes of formation are still poorly understood (Westbrook *et al.*, 1995a, b, c). They are thought to result from the rapid dissolution of evaporites (salt deposited by the evaporation of seawater, in this case during the drying of portions of the Mediterranean in the Late Miocene). However, Woodside and Volgin (1996) observed that brine pools can be associated with faults, and recent research in a variety of different settings (MEDINAUT/MEDINETH, 2000) showed that Mediterranean brine pools also display links to mud volcanism. The observation of empty brine pools, evidence of overflow, or variable levels all show these systems are dynamic and more complex than anticipated.

The differences in physical characteristics (salinity, density, temperature) of the hypersaline water and normal seawater create severe acoustic contrasts between the brine pools and their surroundings. Incoming sound waves are reflected and refracted on the different layers that normally constitute the pools. The reflected waves interact with a very smooth interface, and therefore none of their energy is scattered back to the sonar sensor. In the absence of backscattered sound, the pools' surfaces appear uniformly black. Around the edges of the pools, the brine layers are thinner, and constructive and destructive interference from the refracted waves give the edges a locally bright appearance. This can be checked numerically, using the speed of sound in seawater, measured directly or inferred from the Chen–Millero–Li equation (Equation 2.7) and uniform salinity values varying between $\sim$120 psu (MacDonald *et al.*, 1990) and 270 psu (Anschutz *et al.*, 1999) depending on the brine pools observed. In normal conditions, incoming waves will have critical angles of 53°–68° and waves coming out of the brine pool will be totally reflected back in, or with critical angles of 7°, meaning only very restrictive geometries can lead to an actual reflection.

Some dark, echo-free patches were discovered during a survey of eastern Mediterranean mud volcanoes (Figure 7.27), in water depths of 2,050 m and more. When the deep-tow sonar, MAK-1, "flies" at 100 m above the seafloor, the anechoic patch does not present any variation with distance from the sonar track (i.e., the incidence angle). The gray levels are consistently at 1 or 2, compared with gray levels of 20–30 for the surrounding hemipelagic sediments, and gray levels of 100–120 for the neighboring mud volcanoes between which the survey line was run. It is therefore most unlikely that this patch is an outcrop of sediments with different physical properties, as they would still produce some backscattering. The shape is sub-circular, with a diameter of about 260 meters. A few rings of slightly different backscatter intensities are visible around it, presumably where the brine layers are thinner. Larger structures have been discovered, including L'Atalante Basin, a large brine lake several kilometers wide.

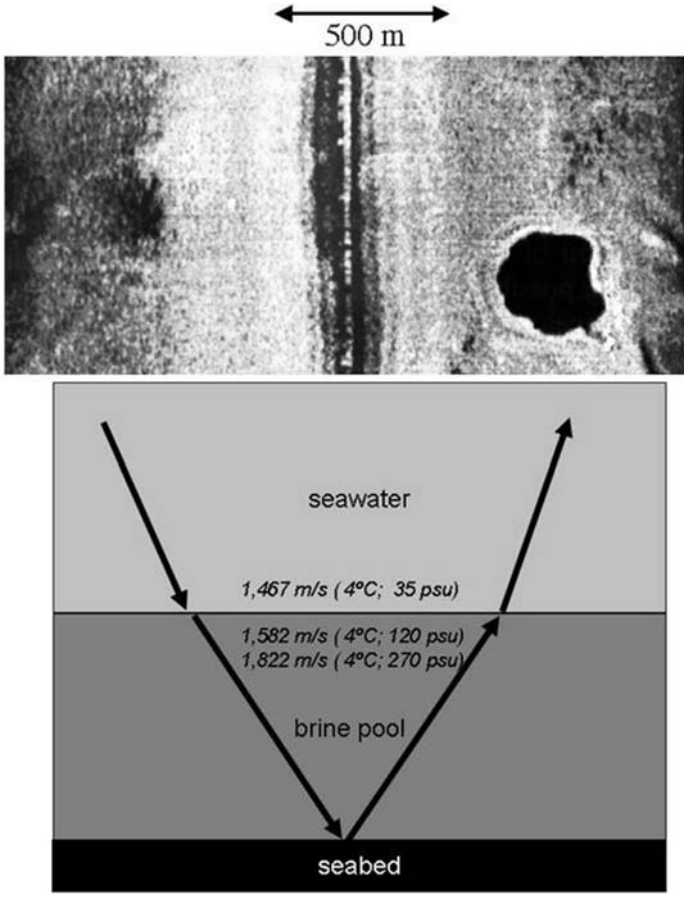

Figure 7.27. (Top) Brine pool imaged using the MAK-1 sidescan sonar (from Woodside and Volgin, 1996; © Elsevier Publications). (Bottom) Acoustic justification. The high differences in salinity will affect the speed of sound (i.e., the angles at which the incident sonar beam will be transmitted into the brine pool and might be reflected back out; see text for typical values). In brine pools, most of the waves will not come out.

7.5 REGIONAL IMAGERY

7.5.1 The Blake Escarpment, North Atlantic

Continental margins have been more extensively surveyed than other regions on the seafloor (e.g., abyssal plains; see Chapter 6). It is difficult to select examples of regional imagery among all the data available, and we have restricted ourselves to only two types of frequency and two types of geological environments. The first example presented was acquired using GLORIA during the survey of the eastern U.S. Exclusive Economic Zone (EEZ SCAN, 1991). Several GLORIA swaths were mosaicked to produce an image of the Blake Escarpment, a spectacular submarine cliff marking the transition between the continental margin and the abyssal plains (Figure 7.28). In fewer than 15 km, the transition is particularly abrupt between the intermediate depths of the Blake Plateau (−2,500 m) and the abyssal depths of the Blake Basin (−4,900 m). The top of the escarpment is visible throughout as a bright

Figure 7.28. GLORIA regional imagery of the Blake Escarpment, on the continental margin east of Florida. The image is 51 km wide and 51 km long, oriented with north at the top. Depths vary abruptly between 2,500 m in the left half of the image and 4,900 m in the right half (courtesy United States Geological Survey).

acoustic reflector, but its base is only visible as the boundary with the homogeneous sediment patches of the Blake Basin.

The Blake Plateau is just west of the Blake Escarpment (Figure 7.29) and is made of sediments with a homogeneous medium-bright backscatter interpreted as large-scale sediment drift deposits. Long, fine lineations are visible close to the escarpment, parallel to it, and extending for several tens of kilometers. They are probably caused by erosion and minor slumping of the deposits. The dark featureless region in the SW of the image is very similar to regions of Figure 7.3 and is confirmed by coring as being a patch of carbonate mud. In the extreme northeast of the image, a very bright zone extends northeastward and is very narrow. This is the steepest part of the escarpment. Only the stronger echoes generated near the top of the escarpment are returned. Submersible dives show that the cliff is near-vertical over much of its extent. The strong bottom currents following the lower contours scoured the seafloor. They created moats, visible as dark linear structures, at the junction with the Blake Basin.

The main portion of the image, in the center, shows that the Blake Escarpment is extensively cut by short dendritic channels merging into canyons. The bands of medium-bright backscatter on top of the escarpment are other indicators of sediment drift deposits, like the ones farther west in the Blake Plateau. They are present all along the escarpment, but are only a few kilometers wide at most. Their narrowness is used in some interpretations to argue for a smaller sediment supply than necessary to

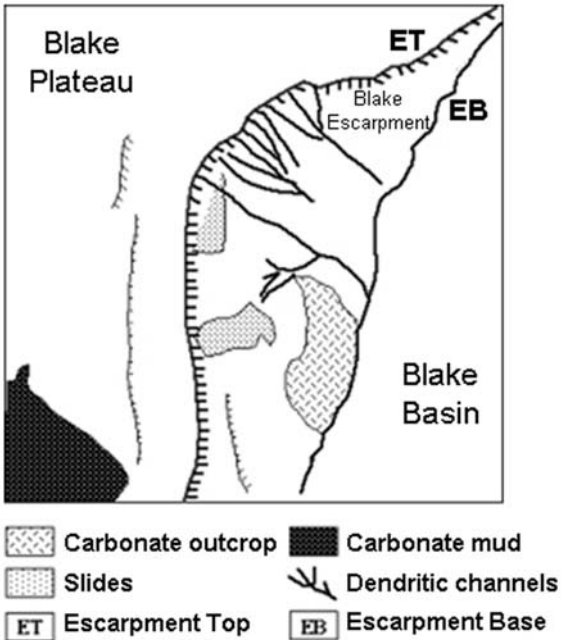

Figure 7.29. Interpretation of the GLORIA image of Figure 7.28.

form the canyons, and for their formation in very shallow waters (in the Early Cretaceous, 100 Ma BP). The larger portions of the Blake Escarpment are also marked by sediment slides, with a more mottled acoustic texture (Figure 7.17b). The southernmost of these slides seems to stop abruptly along a large structure, around which canyons also seem to overlap. This suggests that this structure is fairly old, at least older than the canyons and slides, and resistant to erosion by incoming turbidity flows. Seafloor photographs and samples led to the conclusion this was a large carbonate outcrop.

7.5.2 The Almeria Canyon and Almeria Margin, Mediterranean Sea

Submarine canyons, formed on passive continental margins (such as the eastern U.S.A.), are thought to form by mass-wasting and erosion on the continental slope. They show distinctive patterns similar to fluvial drainage systems. On active margins, submarine canyon systems are more complex, as they are subject to tectonic activity (uplift, subsidence, seismicity) and higher rates of sedimentation. This second example of regional imagery comes from the complex shallow margin south of Almería (Spain), a region with past and present tsunamigenic potential (e.g., Grácia *et al.*, 2001, 2006). It is located in the Alborán Sea (southwest Mediterranean), in the zone of collision between the Eurasian and African plates. The region shown here is seismically active, as shown by recent swarms of shallow earthquakes with magnitudes ranging from $M_w = 4.7$ to $M_w = 5.1$ (Grácia *et al.*, 2001). A sediment

cover of variable thickness has been deposited since the early Miocene, although there is low terrigenous influx at the moment. The Neogene to Quaternary sediment cover is disrupted by active strike–slip faults (e.g., Comas *et al.*, 1992) and by several submarine canyons. The longest submarine canyon is the Almería Canyon, identified by Alonso and Ercilla (2003) as a single-point source turbidite system.

Figure 7.30 shows the entire region south of Almería, at water depths ranging from 80 m (north: the shallowest TOBI deployment at the time) to 1,700 m (south). The image is made of sux adjacent TOBI lines, with the turns from one swath to the other fully processed. The leftmost section in the upper swath corresponds to the insertion of the TOBI platform at the right depth, heading, and speed for imaging, whereas the leftmost section of the lower swath is also cut short, as sonar recording was stopped at the end of the survey and the TOBI platform was hauled back on deck. The main features of Figure 7.30 are the Almería Canyon, extending from the top to the bottom of the image (its actual end is not much farther away, as imaged by Cronin *et al.* (1995) with the comparable MAK-1 sonar); the two banks (Chella and El Sabinal) correspond to two relict volcanoes with old, sedimented coral mounds on top (e.g., Lo Iacono *et al.*, 2008) and the Carboneras Fault, visible as a faint line cutting across the image and offsetting some of the structures. This image is also affected by a few artifacts, such as bright, fuzzy triangular shapes at far range (noise from the shipping lanes nearby, leading to and away from the Gibraltar Strait, and cross-talk with some other acoustic sensors in a few places). Mostly, though, the image is of excellent quality, and its interpretation was bolstered by the concurrent

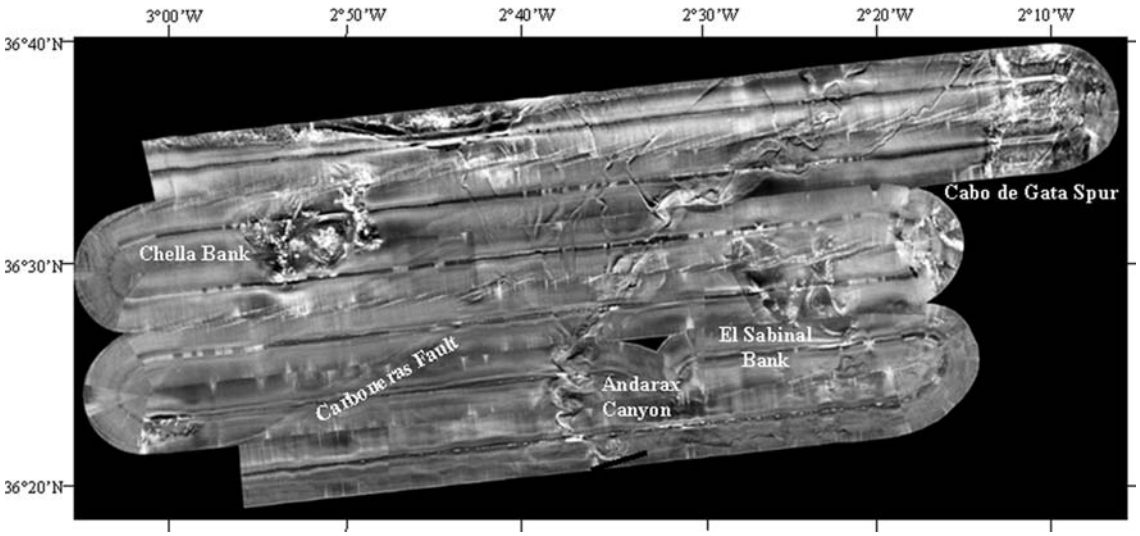

Figure 7.30. Regional imagery from the continental margin south of Almería (Spain). The entire area (ca. 33.3×100 km) has been imaged at high resolution with TOBI (30 kHz, 6 m to 3 m/pixel). Note how the surface expression of the diagonal Carboneras Fault clearly offsets some of the tributaries (northern part of the image) of the Almería Canyon.

Figure 7.31. Extracts from Figure 7.30. (Top left) 3-D view (sonar imagery draped on multibeam bathymetry) of the Carboneras Fault. Although its 2-D expression is subtle, it can be followed across the entire image, on several swaths, and the offset of tributaries to the main turbidite system strengthen its original interpretation as a fault. (Top right) 2-D view of Chella Bank (see Lo Iacono *et al*., 2008 for detailed interpretations). (Bottom) 3-D view (sonar imagery draped on multibeam bathymetry) of one of the meanders in the canyon. Note the deeply incised tributary feeding into it from the northwest, the rougher textures of sediments inside the canyon, and the change in backscatter levels associated with the imaging directions (from the bottom or the top swath).

collection of high-resolution TOPAS sub-bottom profiles and EM-12S multibeam bathymetry (e.g., Gómez Sichi *et al.*, 2005).

The canyon is the main feature visible in this image. Its meandering is apparently controlled by the basin slope and the characteristics of the turbidity currents that form the canyons. Cut-off meanders are visible as thinner loops on the edges of the canyon axis (cf. Figure 7.9, top). Most of the image shows the smoother, darker textures typical of the background sediments, but several structures (other than the canyon) are also visible. They include the end of a slump (northern swath), tributaries to the main submarine canyon offset by the long SW/NE-trending Carboneras Fault (Figure 7.31, top left), and several reliefs with high backscatter variations (interpreted as relict volcanic outcrops, based on their shapes and the pattern of the most reflective areas) (Figure 7.31, top right). Close-up views of some of these distinctive features are better in 3-D, with sidescan sonar imagery draped over multibeam bathymetry, and Figure 7.31 (bottom) shows its potential for parts of the canyon. The strong asymmetry between the left and right banks are clearly visible; the right bank is very steep and with very low reflectivities (as it is imaged from the upper swath, at very high angles), and the left bank is nearly invisible, masked by the strong returns from the canyon floor. The difference between imaging angles is also clearly visible in the deeply incised tributary channel coming from the NW. Near the middle of the image, variations in the reflective textures of one of the corners shows some levees and terraces as the curve of the submarine canyon changes again.

7.6 CONCLUSIONS

The images presented in this chapter aim at presenting the different processes encountered in continental margins. They are focused on the transport of sediments from the coast to the abyssal plains, through channels and slides, and the effects of this transport on the seafloor (e.g., deposits, erosion). Images from wide-swath sonars such as GLORIA are privileged because of the important size of most structures present in the continental slopes. Smaller-scale structures (mainly sedimentary) are very similar to the ones observed in other environments, and only the most unusual or typical ones are described thoroughly. Tectonic and volcanic activity is rare, and only a few occurrences are shown. Rarely published manifestations of biological activity are presented in the chapter, along with some scientifically challenging structures: mud volcanoes, brine pools. Examples of regional imagery were drawn from a passive continental margin, in the eastern U.S.A., and from a large submarine canyon in a tsunamigenic area offshore southern Spain.

Emerged lands are a large provider of sediments to the continental margins, and the shallow-water (mainly coastal) environments are presented in Chapter 8. Although marginal in size, coastal waters are very important in terms of economy, strategy, and environment. They also provide the largest opportunities for sidescan sonar surveys. As the water depths decrease to a few tens of meters at most, the deployment techniques change slightly, and so does the interpretation. Geological or

not, the structures visible near the shores are generally closely related to their sub-aerial equivalents.

7.7 FURTHER READING (*see also* References at end of book)

About continental margins in general:

EEZ-SCAN 87 Scientific Staff (1991). *Atlas of the U.S. Exclusive Economic Zone: Atlantic Continental Margin*, Miscellaneous Investigations Series, Vol. I-2054. U.S. Geological Survey, Reston, VA, 174 pp.

Mienert, J.; and P. Weaver (Eds.) (2003). *European Margin Sediment Dynamics: Sidescan Sonar and Seismic Images*. Springer-Verlag, Berlin, 309 pp.

Wefer G.; D. Billett; D. Hebbeln; B.B. Jørgensen; M. Schlüter; and T.C.E. van Weering (Eds.), *Ocean Margin Systems*. Springer-Verlag, Berlin, 495 pp.

About submarine slides

Hodgson, D.M.; and S.S. Flint (Eds.) (2005). *Submarine Slope Systems: Processes and Products*, Special Publication No. 244. Geological Society, London, 225 pp.

Saxov, S.; and J.K. Nieuwenhuis (1982). *Marine Slides and Other Mass Movements*. Plenum Press, New York.

About brine pools

MEDINAUT/MEDINETH Shipboard Scientific Parties (2000). Linking Mediterranean brine pools and mud volcanism. *EOS Trans. AGU*, **81**(51), 625, 631, 632.

Westbrook, G.K.; and the MEDRIFF Consortium (1995). Three brine lakes discovered in the seafloor of the Eastern Mediterranean. *EOS Trans. AGU*, **76**(33), 313–318.

About pockmarks and seepages

Hovland, M.; and A.G. Judd (1988). *Seabed Pockmarks and Seepages: Impact on Geology, Biology and the Marine Environment*. Graham & Trotman, London, 293 pp.

About the sonar observation of biological activity

Hovland, M. (2008). *Deep-water Coral Reefs: Unique Biodiversity Hotspots*. Springer/Praxis, Heidelberg, Germany/Chichester, U.K., 278 pp.

Rao, V.P.; M. Veerayya; R.R. Nair; P.A. Dupeuble; and M. Lamboy (1994). Late Quaternary *Halimeda* bioherms and aragonitic faecal pellet-dominated sediments on the carbonate platform of the western continental shelf of India. *Marine Geology*, **121**, 293–315.

About mud volcanism

Dimitrov, L.I. (2002). Mud volcanoes the most important pathway for degassing deeply buried sediments. *Earth Sci. Rev.*, **59**, 49–76.

Ivanov, M.K.; A.F. Limonov; and T.C.E. van Weering (1996). Comparative characteristics of the Black Sea and Mediterranean Ridge mud volcanoes. *Marine Geology*, **132**, 253–271.

Milkov, A.V. (2000). Worldwide distribution of submarine mud volcanoes and associated gas hydrates. *Marine Geology*, **167**, 29-42.

8

Shallow-water environments

8.1 INTRODUCTION

Shallow-water environments are even more essential to our everyday life than continental margins (Chapter 7). These environments directly shape and are shaped by our commercial, ecological, and leisure activities. Most of the world's fishing is still drawn from coastal waters, particularly in developing countries, and the pressure on these resources has clearly reached the point of non-sustainable return. As fish stocks dwindle across the world, the pressure on shallow-water environments is amplified by the construction of infrastructure (harbors, dikes, coastal defenses, etc.). Modification of sediment redistribution along shores can now be clearly attributed to specific projects (e.g., along the southern British coastline, where some beaches are more eroded after others have been protected from accelerating erosion). In the past, this had led to the silting of estuaries, or the abandonment or modification of once prospering harbors (e.g., Brugge in Belgium, or antique Greek harbors now lying 5 kilometers inland). The effective monitoring and sustainable management of shallow-water environments and their habitats relies heavily on the mapping of the seabed and water column, and sidescan sonar is the tool of choice, because of its relative cost and higher ease of deployment as well as because of the customer base it has developed among many types of end-users.

But what do we define as shallow-water environments? This has always been a difficult point (e.g., Reading, 1978; Blondel and Murton, 1997). We take here the commonly accepted definition of water-covered areas shallower than 200 meters, reasonably close to the shore, but with a wide range of hydrographic settings. These cover the transition zone between land and sea (i.e., the beginning of the continental shelf), lakes, and rivers. The main processes in shallow water have been shown by many studies to be summed up as erosion processes, deposition processes, and reworking of existing seabeds (e.g., Knebel *et al.*, 1996, 1999; van de Meene *et al.*, 1996). The acoustic aspects of many of these processes have already been shown in

previous chapters, and we shall insist here only on these processes that are most typical of shallow waters.

8.2 SEDIMENTARY STRUCTURES

In shallow waters, the hydrodynamic and geological conditions generally control the pattern of sediment distribution. The decrease of wave energy with water depth often induces a decrease in the grain size and an increase in the mud content of sediments. Figure 8.1 shows two examples from a high-resolution survey of shallow-water bays on the Canadian shelf. Acquired with the Klein 5000 sidescan sonar, operating at 455 kHz and processed to 10 cm to 20 cm/pixel, these images show uniformly homogeneous and low backscatter. (Left) The image shows nearly featureless mud (the diagonal, brighter line corresponds to the water column, with some individual echoes interpreted as fish) (see Section 8.4 for better examples). (Right) The image shows completely featureless sand, with a slightly higher general reflectivity. One must remember, however, that the overall reflectivity of sediments will vary both with the imaging frequency and with the geometry, and that the depth of penetration of the sonar might be an important factor in the interpretation.

The reworking of sediments is the major geomorphological process at play in shallow waters (e.g., van de Meene *et al.*, 1996). Some coastal areas experience semi-diurnal tides with a range of 3 m to 4 m (with higher values in a few places like the Bay of Fundy in Canada or the Bristol Estuary in England), and maximum surface current speeds ranging from 0.6 m/s to 1 m/s. As a result, tidal shelves can exhibit a wide range of bedforms in equilibrium with their hydraulic environment. Distinctive bedforms and sedimentary facies such as straight-crested sandwaves, furrows, gravel waves, and sand ribbons are characteristic of transport by tidal currents (Milkert and Hühnerbach, 1997).

Ripples are the simplest bedforms associated with sediment redistribution. They occur on non-cohesive surfaces (e.g., sands) as undulations, oriented transverse to the main direction of water flow. They can occasionally be found on muddy seafloors. Ripples are conventionally described in terms of their size and shape: wave ripples,

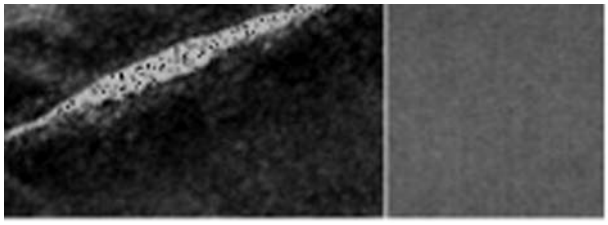

Figure 8.1. Klein 5000 sidescan sonar imagery (455 kHz, 10/20 cm resolution per pixel) from the Canadian coastline. (Left) A 17 m wide patch of nearly featureless mud. The white track corresponds to the nadir, and individual echoes in the water column might be fish. (Right) A 7 m wide patch of totally featureless sand, with a higher acoustic reflectivity.

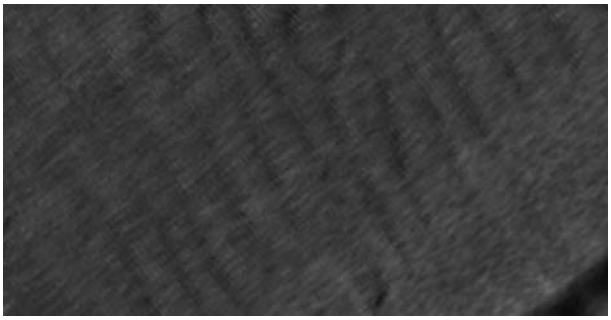

Figure 8.2. Short-wavelength sediment ripples in the tidally influenced west Solent Estuary (England). They were imaged with a Widescan 3050E at 325 kHz and processed to a pixel resolution of 25 cm. The image is nearly 90 m wide overall (from Huvenne *et al.*, 2007).

current ripples (transverse), isolated ripples (incomplete), and combined current/wave ripples (see Reineck and Singh, 1980, for a review and Milkert and Hühnerbach, 1997, for a series of examples).

Figure 8.2 shows typical ripples in the west Solent Estuary, just off Southampton (England).They were acquired with a Widescan sonar, operating at 325 kHz and with a range of 104 m either side. Water depths range from ca. 10 m to 25 m, in a channel 4 km wide approximately. These ripples are tidally influenced and made of material with very low acoustic backscatter. They are regularly spaced, with short wavelengths of around 5 m from crest to crest. Their shadows are too small to estimate their heights with certainty (in this case, they were measured with concurrent multibeam surveying to be around 0.7 m) (Huvenne *et al.*, 2007).

Figure 8.3 shows a larger view of the same region, with gravel waves (brighter, more textured patterns) and a sand ribbon (darker, diagonal ribbon in the center of the image). The gravel waves have higher backscatter levels and more fuzzy textures, related to their heights (1.5 m in this case, also known from multibeam measurements) and to their micro-scale roughness. The sand ribbons have lower backscatter levels, with smoother and more visibly organized textures. One can note the differences in wavelengths and widths of the different waves, as one moves diagonally from top left to bottom right of the image, following the very small slope. These are mostly related to the tides, and the looser sediments might also be reworked by bottom currents.

Figure 8.4 shows another high-resolution image from a survey in the sub-glacial environment of Rose Bay (Nova Scotia, Canada). This is a slightly different environment, with minimal change in bathymetry but strong tidal influence and dynamic variability (e.g., Cameron, 1965). The sediments are organized along large ripples, and there are a few brighter sand ribbons. In this particular survey, the sonar was towed at a regular altitude above the seabed, and the wider nadirs to the bottom left of the image indicate that the end of the brighter patch would actually be slightly deeper than the rest of the image. Figure 8.5 shows a different part of the same survey: the ripple fields are aligned transverse to the direction of the currents, and the ripples show different wavelengths depending on their position within the fields. This image also shows some outcrops at far range. The shadows can be used to infer their heights; they are small enough here that the sediment deposition patterns do not seem to be affected by their presence (see Figure 8.8 for a close-up view).

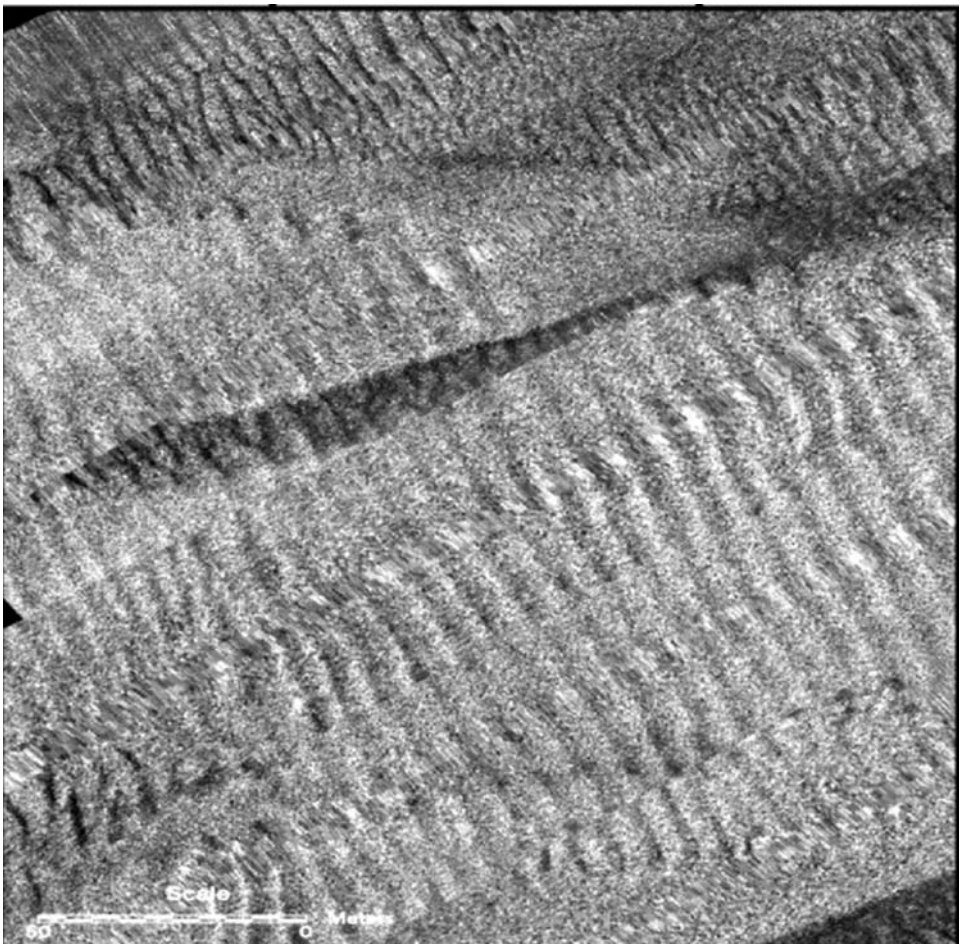

Figure 8.3. Gravel waves and sand ribbons in the same area as Figure 8.2. The scale bar is 50 m across. The sonar imagery comes from the same dataset, with a 25 cm/pixel resolution (from Huvenne *et al.*, 2007).

The reworking of sediments by waves and tidal actions can create interesting interference patterns (e.g., van de Meene *et al.*, 1996; van Lancker and Jacobs, 2000; van Lancker *et al.*, 2004). Crossed dunes have been observed as the effects of interference between at least two formation processes, such as two main seasonal currents. More complex structures can also be observed, depending on the conditions. Hexagonal patterns (50–60 cm in size) have, for example, been observed in a few places around the world, and are currently interpreted as the limit of interaction between two tide regimes and local bottom currents. They are visible on sidescan sonar images in certain conditions (e.g., Garlan, pers. commun., 2006), and in shallow water they can lead to preferential growing of seagrass along the polygonal patterns (e.g. Hühnerbach, pers. commun., 2007).

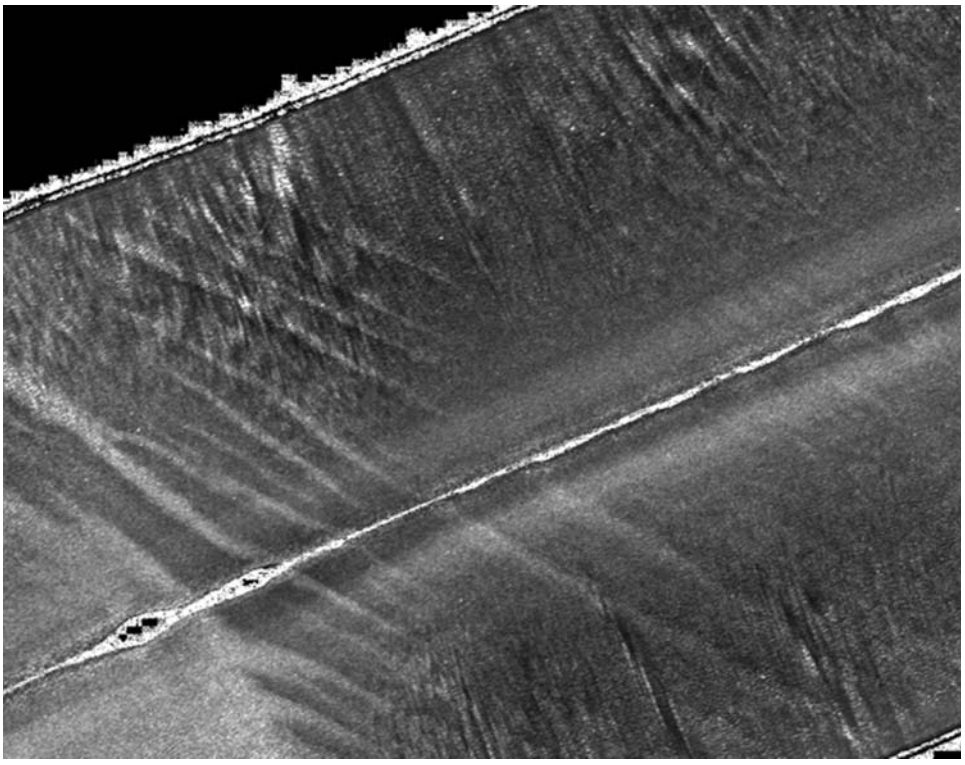

Figure 8.4. Large mud ripples on the Canadian coast, with sand ribbons. The image is 250 m wide and was acquired with a Klein 5500 sidescan sonar operating at 455 kHz. It was processed to 22 cm/pixel resolution (Pouliquen *et al.*, 2002).

The reworking of sediments is also visible in large freshwater bodies. In rivers, sediment waves will tend to follow the downstream currents, and the sediments will be sorted according to the strength of the current, creating different types of deposits. The presence of the river banks and, potentially, of small islands, will be an additional constraint. Figure 8.6 shows a section of sidescan sonar imagery collected in the Colorado River (United States). One can note the different deposition of sediments near the bedrock ledges (the two bright structures on the left of the image), and the differences between deposits after these structures, which in effect constricted the flow of water and the deposition of sediments.

As in continental margins, the presence of fluid/gas seeps can be seen through their surface expressions, as pockmarks or small domes/vents (e.g., Milkert and Hühnerbach, 1997; Hagen and Vogt, 1999, *inter alia*). Figure 8.7 shows a high-resolution sonar image of small depressions on the summit of a larger dome (curved shape spanning both port and starboard swaths). Their shapes are slightly irregular and elongated, and the differences in backscatter are attributed to differences in sediment properties (higher amounts of gas, or higher porosity).

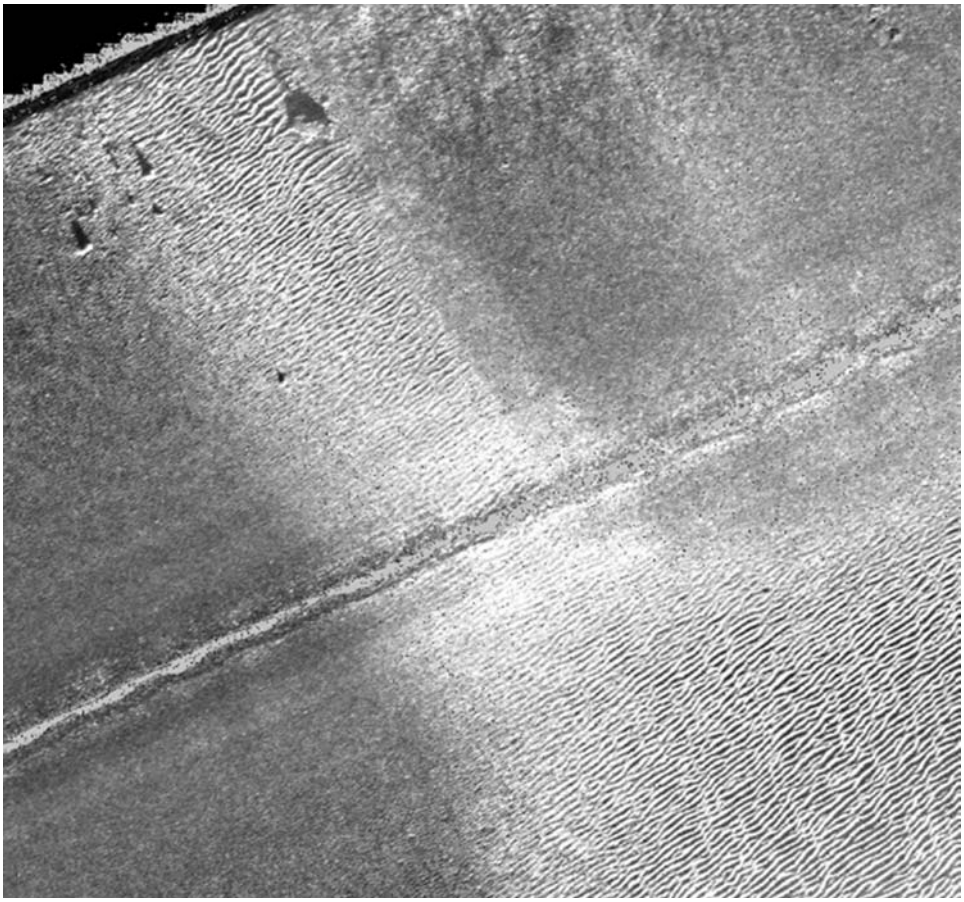

Figure 8.5. Ripple fields with rock outcrops in top-left corner. The image is 250 m wide and was acquired with a Klein 5500 sidescan sonar operating at 455 kHz. It was processed to 22 cm/pixel resolution (Pouliquen *et al.*, 2002).

8.3 ROCK OUTCROPS

In backgrounds of relatively flat sediments, the shapes and distributions of outcropping rocks are easily detected with sidescan sonar. This is due to their distinct acoustic reflectivity as well as the conditions of imaging (small depths, low grazing angles). Figure 8.8 shows a close-up view of the rocky outcrops in Figure 8.5. Because they were imaged at far range, they have long shadows: these can be used to infer their heights and, for the largest ones, their approximate shapes. The brighter rock outcrops on the left are homogeneously bright, with very sharp shadows. They also seem a bit elongated along-track, possibly because of some uncorrected beam spreading (see Chapter 10, "Anomalies and artifacts" for explanations of beam spreading). Based on their morphology, and on the general geological context, they can be

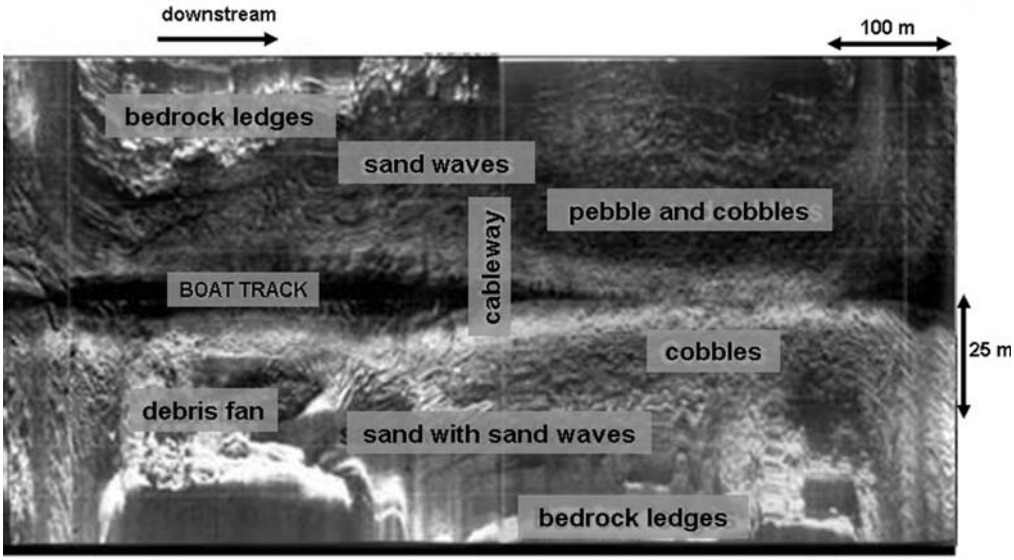

Figure 8.6. Selection of sidescan sonar imagery collected by USGS scientists in the Colorado Canyon (adapted from *http://soundwaves.usgs.gov/1999/07/index.html*). Note the differential reworking of sediments downcurrent and away from the river banks.

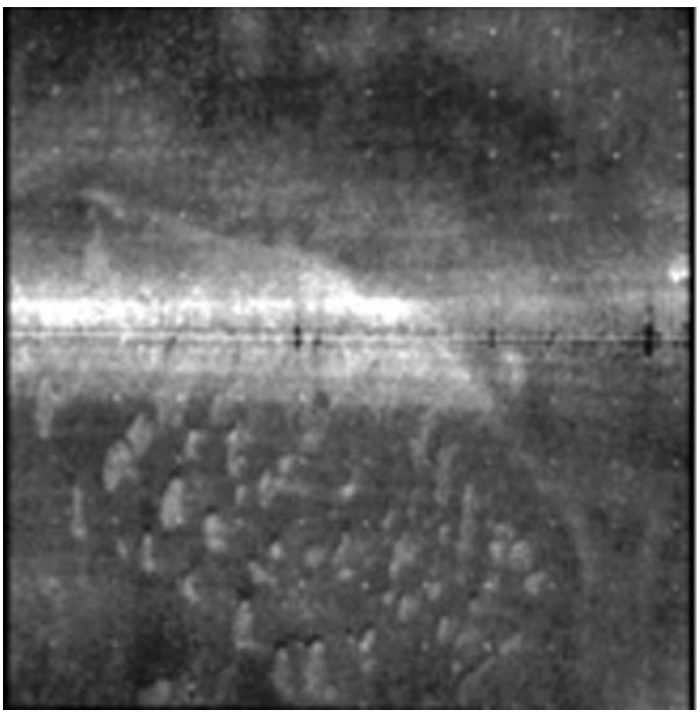

Figure 8.7. Small and shallow depressions, likely to be pockmarks, as observed at the summit of sedimentary domes (from Garlan, 2007). The image is approximately 100 m wide and the horizontal sonar track is clearly visible in the middle (reproduced by permission).

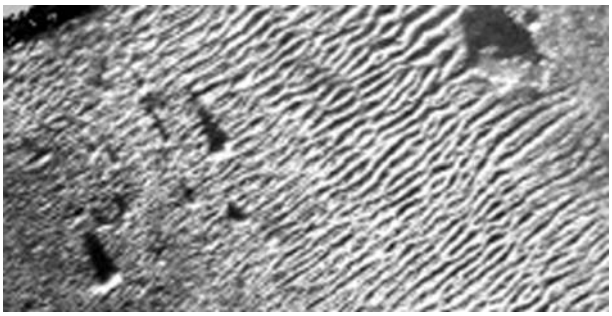

Figure 8.8. Close-up view of the rocky outcrops in Figure 8.5. Shadows give an idea of their shapes and heights. Note the difference between the individual boulders left of the ripple field and the larger outcrop on the right. This image is 50 m wide. It was acquired using a Klein 5500 sidescan sonar operating at 455 kHz. It was processed to 22 cm/pixel resolution (Pouliquen *et al.*, 2002).

interpreted as individual boulders. The outcrop at the top right of Figure 8.8 is different: first, its backscatter levels vary from very bright (on the side facing toward the sonar) to medium (on what is apparently the flat top of the outcrop) and dark (on the side facing away from the sonar). The shadow indicates a more complex shape for its summit. The few pixels with higher intensities on the far side are likely to be individual asperities in what is interpreted as a relict outcrop, with light sedimentation at the top.

Characteristic sedimentary structures form around outcropping structures submitted to bottom currents and flows (see Section 6.3.3). These structures can be classified as crescents, shadows, and moats (e.g., Milkert and Hühnerbach, 1997), and their appearance in shallow water will not be different from what can be seen in abyssal plains or at continental margins. These structures are often very important to assess the local conditions; for example, when dredging (e.g., Wienberg *et al.*, 2004) or installing structures on the seabed such as oil rigs, as high amounts of scouring or sediment transport will show the stresses they will be subjected to. Figure 8.9 shows a 455 kHz image of different types of rocky outcrops, and the sediment reworking around them. The thin ripple field abutting the largest, elongated outcrop stops there, but the bottom currents apparently move around the obstacle, creating small sediment ripples around the left of the outcrop and a small depression (moat). Some of the smaller boulders on the right also affect the deposition of sediments, with halos of different backscatter levels (scour marks).

More compact sediments and buried outcrops can sometimes be exposed by erosion, as the looser sediments on top are moved away by tidal and bottom currents. Figure 8.10 shows hexagonal fracturing on exposed rocks, on scales of 10 m approximately. The exact scale and intensity of this fracturing can be used by sedimentologists to infer the properties of the sub-seafloor, or to monitor changes (e.g., during hydrocarbon recovery; Crampin, 1999).

The extension of acoustic mapping to other in-shore environments such as large lakes has revealed useful information about lacustrine environments, such as the

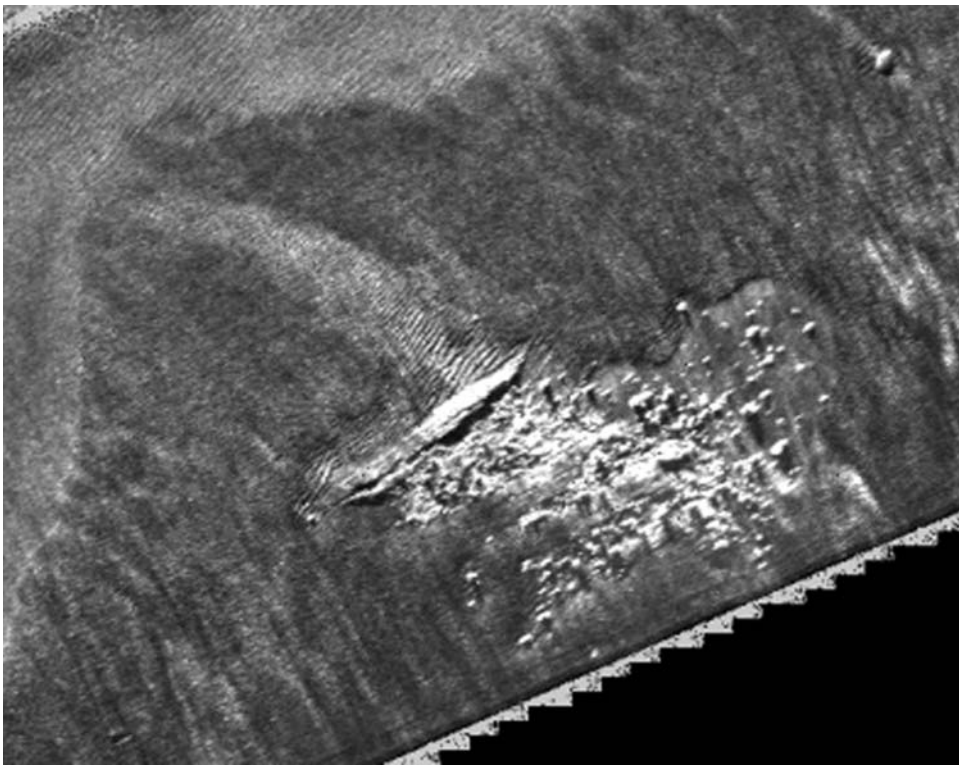

Figure 8.9. Reworking of sediments around a series of outcrops. This image is ca. 200 m wide. It was acquired with a Klein 5500 sidescan sonar operating at 455 kHz and processed to 22 cm/pixel resolution (Pouliquen *et al.*, 2002).

existence of mega-turbidites and other deposits (e.g., Fanetti *et al.*, 2008), structures indicative of mass movement (e.g., Schnellman *et al.*, 2005), or failed moraine dams (e.g., Strasser *et al.*, 2008). Sediment accumulation can sometimes be associated with catastrophic events (e.g., Girardclos *et al.*, 2007; Fanetti *et al.*, 2008). The following two images show outstanding examples of sidescan sonar mapping in a large lake, acquired with the GeoAcoustic GeoSwathPlus interferometric sonar. Operating at 125 kHz, this instrument provides both bathymetry and backscatter level. The 3-D view in Figure 8.11 (see color section) shows a morainic ridge, well below the water line and extending across the Luzern Lake near Gersau, Switzerland. The thin ridge of morainic material is bounded east by steep slopes, west by lower slopes, gullied and with sedimentary deposits extending for several hundred meters. The patterns of erosion and sedimentation on both sides of the ridge can be used to understand its recent and likely evolution.

Figure 8.12 (see color section) corresponds to the southern end of Luzern Lake (Umersee). It shows a complex lake bed. In the top left, a sedimentary apron is the underwater termination of the Isenthal Massif (>1,200 m high) and the alluvial cone

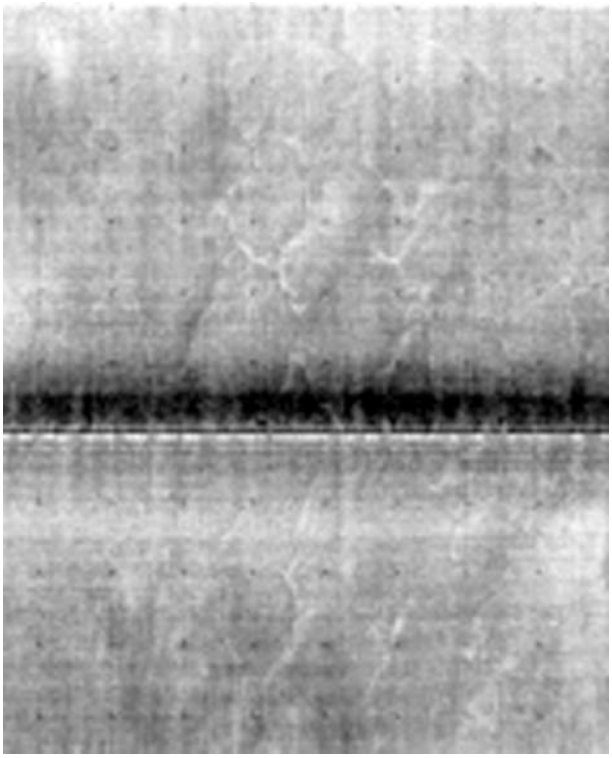

Figure 8.10. Hexagonal fracturing of exposed rocks (from Garlan, 2007). The image is 100 m wide and the horizontal sonar track is clearly visible in the middle. Similar structures are also observed on salt domes in the Persian Gulf (Garlan, per. commun., 2007) (reproduced by permission).

of Isleten (at lake level). At relatively large depths (top half of the image), dune-type structures are prevalent. Their morphologies are very close to those of the ripples and dunes seen earlier in this chapter. Most of the bathymetric variations are visible in the south of the image, where the flat alluvial plain of the Reuss river, dammed all the way to the lake, terminates in the Reuss delta. In the southeast, channels and fan-shaped structures can be seen on the delta front, with some of the structures closer to shore probably influenced by the presence of piers in the nearby harbor and their effect on sediment redeposition. In the middle of the bottom part of the image, one can also see the impact of sand and gravel extraction, with characteristic pits (see Chapter 9, ''Man-made structures'' for more details).

8.4 BIOLOGICAL STRUCTURES

From the first use of sidescan sonar at sea, and in particular long-range sidescan sonars such as GLORIA, unprocessed data often showed systematic echoes in the water column, very small and organized in groups. From their sizes, the strengths of their echoes, and their location away from the seabed, as well as from a very large amount of checking and sampling, we now know these echoes correspond to fish.

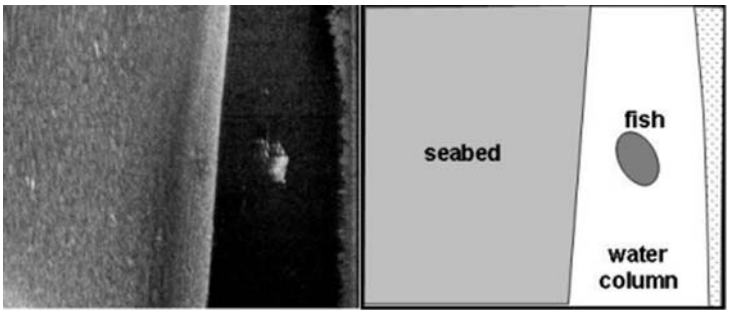

Figure 8.13. High-resolution sidescan sonar image of a school of fish and interpretation. The total range is 30 m (from *http://img.photobucket.com/*)

Figure 8.13 shows a typical image of schools of fish, as taken with a short-range sidescan sonar. This half-swath shows tiny reflectors, only visible in the water column and making up a homogeneous group and interpreted as herring. Unless operators are interested in keeping them, the presence of fish is generally removed (along with all water column data) during processing. However, for the largest species, the acoustic shadows might remain and be difficult to explain without their context. This is one of the reasons why comparing the raw and processed data is always a useful exercise. Less common, Figure 8.14 shows a group of dolphins, visible in both the water column and the range corresponding to seabed returns.

The manifestations of biological activity are also visible directly on the seabed. We saw in Chapter 7 examples of bioherms, algal ridges, and coral reefs in deeper water. With the exponential increase in access to sunlight, and the higher availability of nutrients, biological activity can also be visible as colonization of the seabed by different types of animals. Figure 8.15 shows old oyster beds in a very shallow lake (2–3 m depths). Despite the challenging imaging conditions, most structures are clearly visible, although the across-track distortion increases with range.

Seagrass and algae play an essential role in ecological and sedimentary processes, and there have been many studies to look at their mapping with different sonar instruments, such as echo-sounder (e.g., Kruss *et al.*, 2008 and references therein), sidescan sonar (e.g., Pasqualini *et al.*, 1998), and multibeam sounders (e.g., Komatsu *et al.*, 2003). Acoustically, these structures present a challenging theoretical problem (e.g., Shenderov, 1998; Wilson and Dunton, 2006, 2007). This is compounded by the reality of their imaging (e.g., Bozzano and Siccardi, 1997), where the main problems are their small size, variable gas contents (depending on diurnal cycles as well as type of algae), movements with currents and tides, etc. (e.g., Hermand, 2004). Figure 8.16 shows typical images of *Posidonia oceanica* on the Italian coast, acquired with a dual-frequency EdgeTech sidescan sonar (Blondel and Pouliquen, 2004). These images have not been fully corrected and the water column is still there. The blocks at close range, visible at both frequencies and slightly clearer at 10 kHz, correspond to a Roman shipwreck and its cargo of large amphoras (cluster of individual blocks in the south). The seagrass itself is visible as elongated ribbons, stretching across-track in wavy patterns. At 384 kHz, these ribbons are perfectly visible, and it is possible to map exactly the extent and, to some degree, the health of the *Posidonia*. However, at

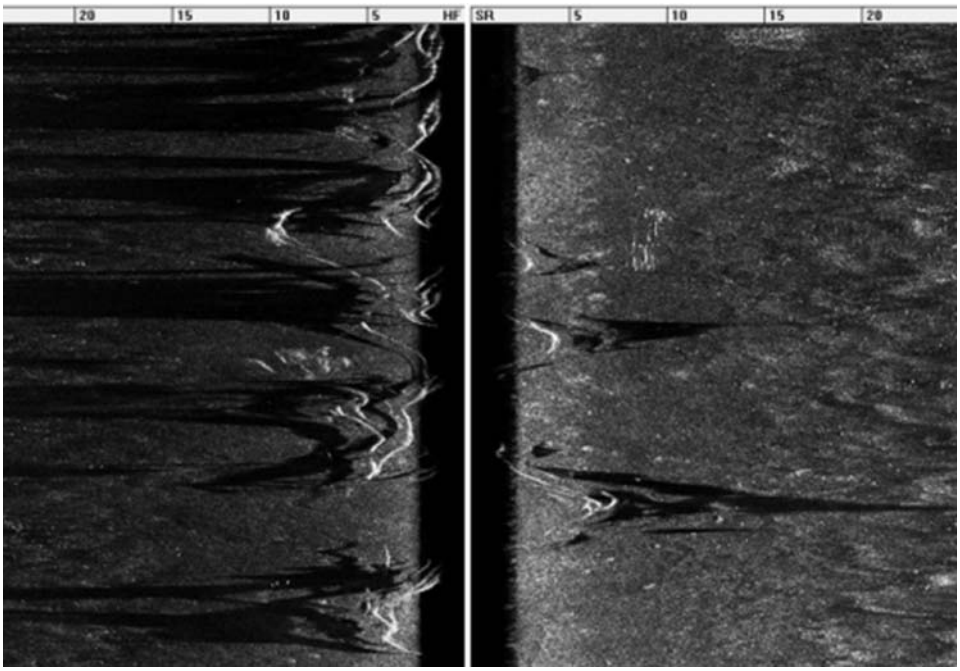

Figure 8.14. EdgeTech 4200 sidescan sonar imaging of a group of dolphins close to the sonar. The imaging frequency is 600 kHz and the total range is 50 m from side to side. Note the dolphins leave strong acoustic shadows over the entire range corresponding to the seabed returns. The parabolic shape and exaggerated apparent size of the dolphins is explained by their movements relative to the towed sonar, and is reminiscent of the exaggerated rendering of the bicycle shown in Figure 4.27 (courtesy of EdgeTech; full-color version available at *http://www.edgetech.com/images25marine.htm*)

100 kHz, these ribbons have disappeared, and only the most reflective ones are still faintly visible at the bottom of the image.

8.5 REGIONAL IMAGERY

Many examples of regional imagery from shallow-water environments have been published, generally as part of environmental and geological studies (e.g., Knebel *et al.*, 1996, 1999; Pasqualini *et al.*, 1998; Brown *et al.*, 2002; van Lancker *et al.*, 2004; Brown and Collier, 2008*, inter alia*). The example presented here (Figure 8.17) comes from an acoustic study of environmental variability and its effects on seafloor classification and object detection systems (Pouliquen *et al.*, 2002). It covers the seabed over most of Rose Bay, Nova Scotia, Canada. It was acquired using a Klein 5500 sidescan sonar, mounted on a towfish. The imaging frequency was 455 kHz. The

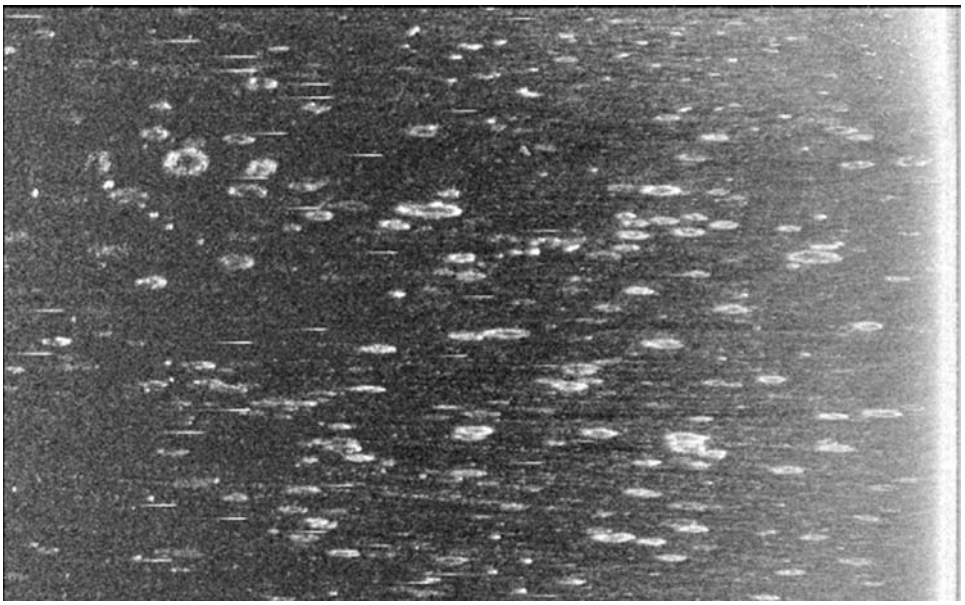

Figure 8.15. High-resolution image of old oyster beds in a shallow lake, acquired with the SwathPlus interferometric, multi-frequency system. The image is 100 m wide and ensonified from the right. Note the across-track distortion of the structures increasing with range, which can be processed using the steps outlined in Chapter 4 (image courtesy SEA Ltd., U.K.).

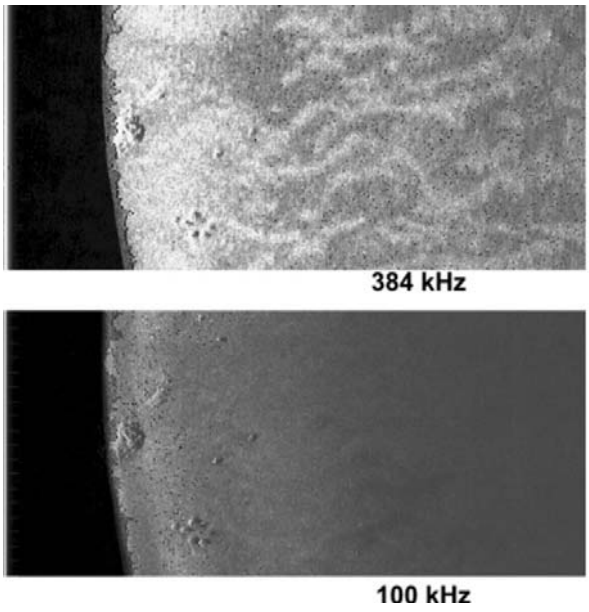

Figure 8.16. Dual-frequency imaging of *Posidonia oceanica* on the Italian coast shows the typical challenge of seagrass mapping using sonars. The top image (acquired at 384 kHz and 57.2 m wide) shows *Posidonia*, 3 cm to 4 cm deep according to divers. The bottom image (co-registered and acquired at 100 kHz) does not show them any more, apart from faint, vague patterns at the bottom of the image. This is explained (in this case) by the relationship between the imaging wavelengths and the diameter/orientation of the algal stipes (adapted from Blondel and Pouliquen, 2004).

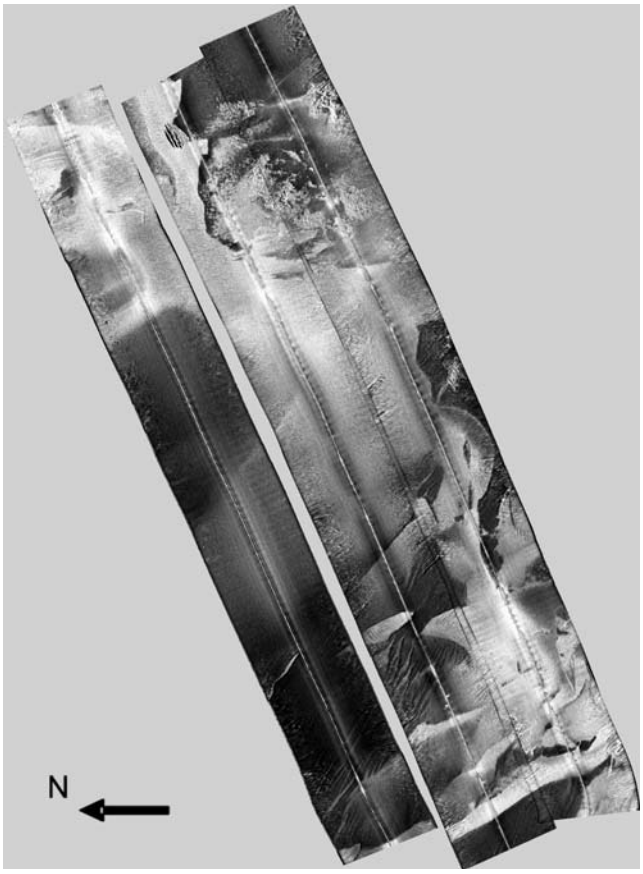

Figure 8.17. High-resolution sonar survey of Rose Bay, Nova Scotia, Canada (Pouliquen *et al.*, 2002). Image size is 1.6 km wide and 1.2 km high. Pixel size is 0.22×0.22 m. The two southern swaths are overlapping and the intersecting pixels have been averaged, preserving the stronger variations of backscatter. See text for details.

along-track resolution is approximately 0.2 m and the across-track resolution varies from 10 cm to 20 cm depending on pulse resolution and tow speed. The sonar recordings have been processed here to a global resolution of 22 cm/pixel The grayscale images do not reflect the absolute acoustic levels, a limitation of most available sidescan sonars, but they provide high resolution and wide coverage, as most of the bay can be covered in only three swaths.

The sidescan sonar imagery was completed with several other acoustic datasets, including echo-sounders and multibeam bathymetry. This allowed the characterization of individual seabed units and the correlation with their sidescan expression. Minimal changes in bathymetry mean there were no particular problems associated with the variations of incidence angles across-track or between swaths. The two southern swaths are overlapping, and their intersection has been averaged. This means that the strongest variations in backscatter (either acoustic shadows or bright reflectors) will be preserved. Most of the fuzzy bright areas in Figure 8.17 correspond to ripples similar in type, size, and wavelength, to those presented in Figure 8.5. Background, muddy areas (lower backscatters, more homogeneous textures) are

crossed by brighter ribbons, generally trending NW/SE. The ripple fields stop near seabed depressions like those in the southeast and slight elevations like the arcuate one in the south (its elevation can be seen at full resolution from the higher backscatter of the slope facing toward the sonar).

8.6 CONCLUSION

The natural structures observed with sidescan sonar in shallow-water environments are not very different from those observed in other environments, apart from the high level of sedimentation and reworking of sediments by tides and currents, and the more visible manifestation of biological activity (i.e., algae). The conditions of sonar data acquisition are rather different in these environments, though, because of the very shallow depths of deployments (a few meters compared with a few hundred meters), the importance of tidal and current corrections, and the limitations brought by other activities (e.g., the need to respect shipping lanes). The small scale at which most features are visible requires the use of higher frequencies. The high number of surveys performed, generally for short times, limited purposes, and limited budgets, also means that the processing of sonar imagery will be less in demand.

In this chapter, we have endeavored to present examples of diverse shallow-water processes and their implications. The distribution of bedforms such as ripples, for example, is a good indicator of the hydrodynamic conditions. Sidescan sonar imagery is an excellent tool for analyzing and monitoring the changes, natural and anthropogenic, undergone by the environment. With the increasing use of coastal and inland areas, and with the possibilities of global warming and its associated sea level changes, such information is a prerequisite to the protection of seafloor and coastal installations. Chapter 9 will therefore present some of the effects of human activity, past and present, on the seabed.

8.7 FURTHER READING (*see also* References at end of book)

Brown, C.J.; and J.S. Collier (2008). Mapping benthic habitat in regions of gradational substrata: An automated approach utilising geophysical, geological, and biological relationships. *Estuarine, Coastal and Shelf Science*, **78**(1), 203–214, doi: 10.1016/j.ecss.2007.11.026).

Garlan T. (2007) Study on marine sandwaves dynamics. *Int. Hydro. Rev.*, **8**(2), 26–37.

Milkert, D.; and V. Hühnerbach (1997). *Coastal environments*. In Ph. Blondel and B.J. Murton (Eds.), *Handbook of Seafloor Sonar Imagery*. Wiley/Praxis, Chichester, U.K., 314 pp.

Reading, H.G. (1978) *Sedimentary Environments and Facies*. Blackwell Scientific, Oxford, U.K., 615 pp.

Reineck, H.-E.; and I.B. Singh (1980). *Depositional Sedimentary Environments*. Springer-Verlag, New York, 551 pp.

9

Man-made structures

9.1 INTRODUCTION

The previous chapters showed the variety of natural features and processes observed underwater with sidescan sonars. But, increasingly, surveys and maps show the presence of man-made structures all over the world. Apart from shipwrecks and a handful of communications cables, human activity has increased over the last half-century to cover all depths with a staggering variety of structures. This chapter will divide them into "planned structures" (Section 9.2) and "accidental structures" (Section 9.3). The former are intentional manifestations, and include pipelines and cables (Section 9.2.1), dump sites (Section 9.2.2), harbors and their approaches (Section 9.2.3), and the exploitation of seabed resources (Section 9.2.4). The latter presents structures that have just come to attention, such as the effects of fishing (Section 9.3.1) or were never intended, like shipwrecks (Section 9.3.2.) and marine pollution (Section 9.3.3). Section 9.4 combines marine waste, although some of it is already presented in Section 9.2.2, and military mines (which, although originally laid with intention, are usually not desired now). Section 9.5 sums up the current state of research on the use of sidescan sonars in underwater archeology, and what the next steps will be. Because of the amount of different structures it shows, this chapter should be of interest to all users of near-shore environments, all developers of underwater sites, and all managers of offshore facilities.

9.2 PLANNED STRUCTURES

9.2.1 Pipelines—cables

Oil exploration has been one of the main drivers behind the mapping of shallow-water and continental margin seabeds, and it is not surprising that the subsequent

exploitation of oil and gas deposits has led to many seabed structures, including pipelines. More than 12,000 producing platforms, 5,000 sub-sea units, 22,000 pipelines of various sizes, lengths, and types and 140 floating production, storage, and off-loading units are built or scheduled in the near future (Esser, 2002). In the North Sea, for example, there are more than 10,000 km of oil and gas pipelines (Esser, 2002). In heavily exploited areas like Lake Maracaibo, in Venezuela, the high density of pipelines makes it difficult to find pristine areas where to lay new pipelines, and the long history of oil production means that the positions (and sometimes the owners) of abandoned pipelines are not known. Sidescan sonar is a tool of choice for detecting and mapping pipelines and their environments (e.g., Esser, 2002; Tian, 2005, 2008). It is usually employed in conjunction with a magnetometer, because of the high magnetization of pipelines and associated structures. This signature varies as a function of the inverse square range, showing the need for sonars to detect (and follow) the pipelines at larger ranges than just below the magnetometer. Regular inspection of pipeline integrity is also conducted using sidescan sonars and video imaging, as it is less invasive and economically costly than employing Molch systems (which travel inside the pipeline and use ultrasonics or magnetic flowmeters) (e.g., Esser, 2002; Hiltscher *et al.*, 2003).

Figure 9.1 shows typical examples of pipelines imaged by sidescan sonars (from Tian, 2005, 2008). In this case, they correspond to medium-size pipelines (diameter <2 m), surveyed in shallow water (<20 m) with the Klein HYDROSCAN sonar system. Figure 9.1 (top left) shows an unprocessed image from a proud pipeline crossing the track of the sonar. It is highly visible on both sides, as a strong, linear and regular discontinuity with high backscatter. Note the variations in apparent width of the pipeline as the sonar moves away from it, and images it at slightly different angles. Figure 9.1 (top middle) shows an unprocessed image from a slightly buried pipeline (indicated with an arrow). Its track is now very faint and difficult to follow, because the penetration depth of the high-frequency sonar used does not penetrate far enough into the sedimentary cover. This is a common problem (e.g., Huvenne *et al.*, 2007) and explains the concurrent use of magnetometers (less affected by sediment layers). Figure 9.1 (top right) shows the end of a pipeline, with a raised valve (clearly visible from its acoustic shadow), and gravel disposed of around the last portion of the pipeline. Figure 9.1 (bottom) shows some of the structures also associated with proud pipelines if they are high enough about the seabed. Mega-ripples and other patterns of sedimentary reworking are visible in this image, and seem to be affected by the pipeline itself (or the portions closer to the seabed). The free-spanning part of the pipeline is associated with acoustic shadows, and at regular points, fishing nets have snagged into the pipeline and been left there. Their bright fuzzy acoustic texture is typical, and can also be found over shipwrecks in fishing areas (e.g., Figure 9.14).

Pipelines are usually sturdy enough to resist fishing activities, but submarine cables are much more sensitive. Messina *et al.* (2001) identify bottom-fishing activities as the greatest danger they face, adding that 95% of all past submarine telephone cable failures have been caused by fishing activities. The current solution is to bury cables during installation, but there are still many cables all over the seabed, at all

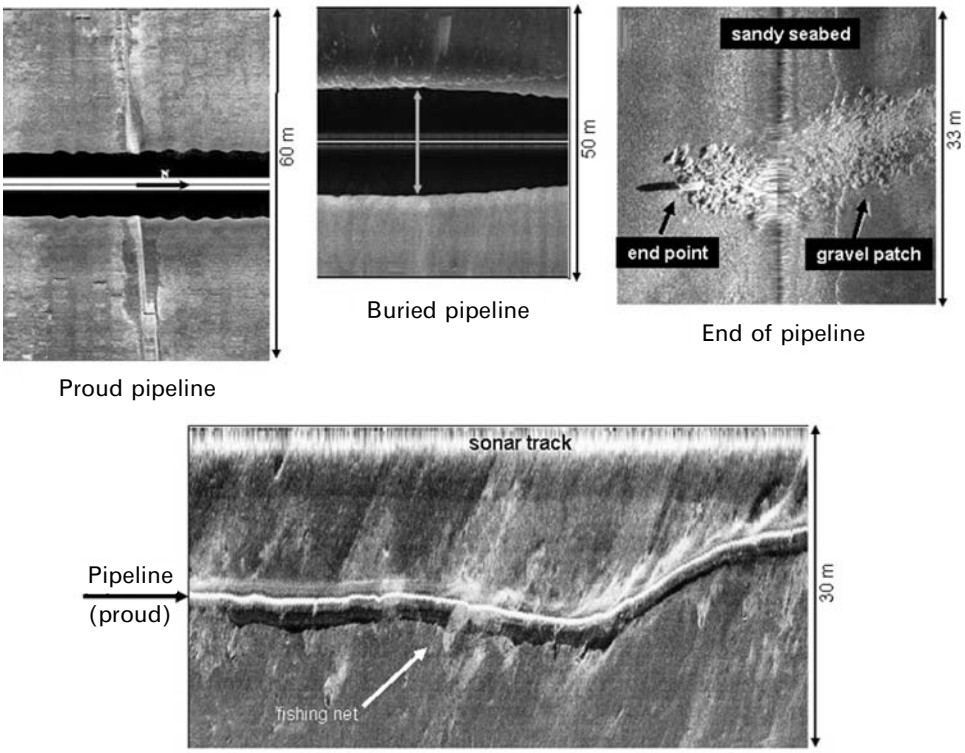

Figure 9.1. High-resolution sonar imagery from different pipelines (from Tian, 2005). Because of their high acoustic reflectivity, proud pipelines are easy to detect, whether imaged across-track (top-left image) or along-track (bottom image). When high enough above the seabed, pipelines are likely to get clogged with fishing nets (fuzzy patterns in the bottom image). Buried pipelines (top-middle image) are more difficult to image, depending on the penetration depth of the imaging sonar in the overlying sediments and the depth of burial. The construction of pipelines often leaves tell-tale debris such as gravel near the endpoints (top-right image).

depths. Recent international legislation has made compulsory the compensation of owners of offshore installations (e.g., cables, pipelines, or seafloor observatories) damaged by activities on the seabed. This puts an added incentive on the mapping of cables, especially if they are located in dangerous places. Figure 9.2 shows, for example, a telephone cable laid on the top of a mud volcano. This image was acquired by the Russian sonar MAK-1 during a survey of mud volcanoes in the Mediterranean Sea (Ivanov *et al.*, 1996). The telephone cable was apparently laid on the seafloor without any preliminary survey; it crosses perturbed mud flows and the top of the Novorossiysk mud volcano. Even with medium-resolution sonars, submarine cables can be detected if the terrain is not too rough, and the concurrent use of magnetometers will also help in their mapping.

Finally, in some areas where pipelines and cables are crossing, they might be protected by covering with stones and ballast, setting the structures in place

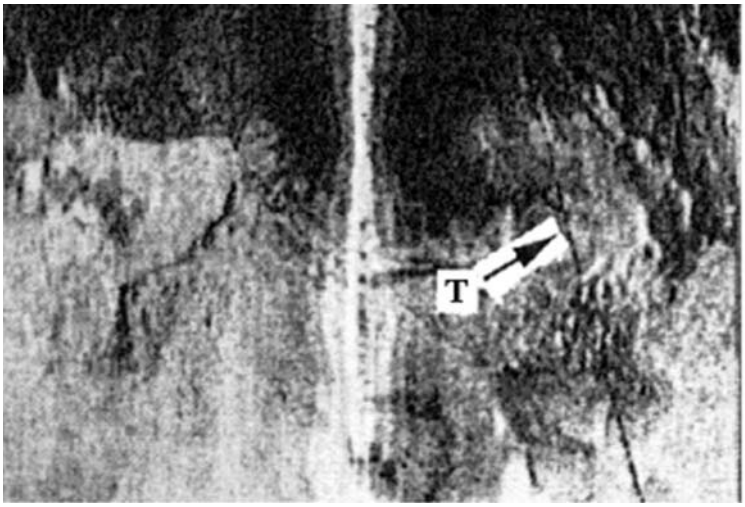

Figure 9.2. Telephone cable (T) on the bottom of the ocean, imaged using the Russian sonar MAK-1. The image is approximately 5 km wide (from Ivanov *et al.*, 1996; © Elsevier Publications).

and preventing either friction (in tidal areas) or uprooting by trawling or anchoring.

9.2.2 Dump sites

Large quantities of material are dumped at sea, in specially designated areas and usually under strict control. This can include loose soil dredged or excavated from elsewhere, at sea or on land, organic material of natural origin, and some sorts of landfill material, etc. The morphology of dump sites will vary depending on how the waste is dumped at sea (Figure 9.3), and there will be acoustic differences due to the dumping process and the nature of the materials being dumped. All objects dumped overboard will fall in a cone, creating elliptical deposits on the seabed. The speed of the dumping vessel relative to the ground will vary, shortening or lengthening the ellipse. Its overall area will depend on the depth below the dumping vessel. Other factors affecting the geometry of the dumpsite are the different currents in the water column, moving objects as they fall to the seabed; bottom currents, affecting the object redistribution with time and sometimes covering them with sediments; and the types of objects (heavier ones will fall closer to the vertical of the ship). The same process can be observed with shipwrecks (see Section 9.3.2). For example, dredged wood waste is normally removed from barges by front-end loaders, leaving clearly defined "strings of pearls" in the sonar imagery as the ship moves on or drifts (Mosher *et al.*, 1997). Excavation material is normally carried to dumping sites in split hull barges and disposal occurs in a few minutes, leaving large acoustically bright "splotches" on the sonar imagery, not too different from those presented in Chapter 10 during Loch Ness studies. Other items, like bundle wire from saw mills, are very reflective and create bright, well-defined targets on the images (e.g., Mosher *et al.*, 1997).

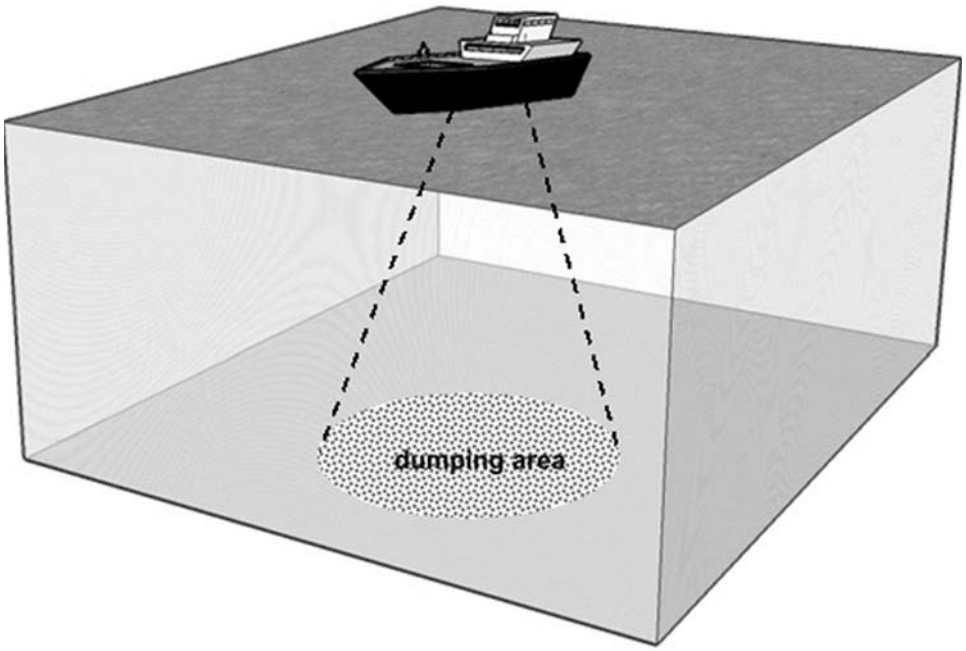

Figure 9.3. The material dumped from a ship will settle into an elliptical area, of dimensions varying with the relative speed of the dumping vessel and any current at depth before the deposition. Individual objects will be separated according to their size (i.e., how easily they could be moved by underwater currents).

Figure 9.4 shows a high-resolution sonar image, 80 m wide, of a dumpsite operated by the Swedish Royal Navy in the Stockholm Archipelago (Moren *et al.*, 2007). On this image, acquired at 380 kHz (I. Karasalo, pers. commun.), the dumpsite appears like a white (i.e., acoustically reflective) "splotch" in the middle of otherwise dark (i.e., low-reflectivity) background sediments. It is ensonified from two directions (black arrows) and the junction between the two swaths (hashed line) passes right through it. Some of the larger objects are clearly visible and a few have created depressions (seen from the minute areas of lower reflectivity at closer range). The portion of dumpsite in the right swath is ensonified from a much higher angle (very close range, nearly at nadir), and this shows in the overall reflectivity of the dumpsite, as well as in the detection of slightly smaller, or buried objects in the top right of the dumpsite. This is a typical dumpsite, and images published elsewhere (e.g., in Mosher *et al.*, 1997; Du Four and van Lancker, 2008) show similar morphologies.

Material (e.g., dredge spoils, sand, gravel) can also be dumped at sea to neutralize erosion; for example, around lighthouses, the pilings of bridges, or other offshore structures (e.g., Wienberg *et al.*, 2004; Wienberg and Bartholomä, 2005; Wienberg and Hebbeln, 2005). The artificial supply of sediments can provoke significant changes in dune fields, with the infill of dune troughs, sometimes to complete burial. In some dynamic places, however, this condition is reversed in a matter of months

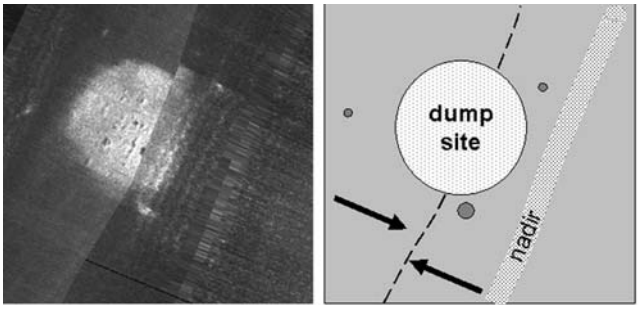

Figure 9.4. Klein sidescan sonar image of a dumpsite in Möja Söderfjärd, Stockholm Archipelago (from Moren *et al*., 2007). It is imaged from both sides by two overlapping swaths (the mosaicking junction is indicated by the hashed line). The image is 80 m wide and pixel resolution is 0.2 m. A few significant targets are visible outside the dumpsite, corresponding to larger objects dumped later (Blondel and Caiti, 2007).

(e.g., Wienberg and Hebbeln, 2005). Scouring can add additional mounds and depressions around the original dumpsites (e.g., Du Four and van Lancker, 2008), again changing the local morphology of the seabed.

9.2.3 Harbor areas

Harbors and estuaries are very busy areas, and this shows on the seabed: all sorts of structures can be found there. Sediment redistribution and evidence of silting (or erosion) of waterways can easily be identified from sidescan sonar, as the surface structures will look very similar to those shown in Chapters 6–8. Dredging of waterways, or extraction of marine aggregates, will lead to dredge pits and beach structures similar to those presented in Section 9.2.4. Structures like docks, jetties, or dams can be imaged with sidescan sonars (e.g., Volovov and Govorov, 1999) and will generally appear as distinct, linear barriers (a bit like fault scarps in Chapter 5). Spoil piles from construction projects will look like other sedimentary deposits, with morphologies close to those of dump sites (Section 9.2.2). Outflow and sewage pipes will look like pipelines (see Section 9.2.1). Their openings will generally be relatively tall structures, standing out of the seabed (some sewage outfall diffusers can be $\sim$3 m above the seafloor). These individual constructions with thin and long shadows will look acoustically a bit like hydrothermal vents (Chapter 5), and their effluents are sometimes detectable as wavy textures centered on the diffusers. Surrounding patterns of sediment accumulation and scouring will vary depending on the local hydrography. Other structures likely to be seen in the sidescan sonar imagery of harbors and estuaries include ballast and concrete blocks (they will look like the rocks seen in Section 8.3); anchor marks (looking like the trawlmarks presented in Section 9.3.1), and in some cases small shipwrecks (like that of Figure 9.10). Sonar imagery can also pick up anchor chains or cables used to moor vessels or buoys (Figure 9.5).

Figure 9.5. A 384 kHz image of a chain used to moor a buoy (bright, wavy line close to nadir). It is visible for a range of 30 m, commensurate with the water depth at the place.

9.2.4 Seabed resources and their exploitation

Sea mining for sand, gravels, diamonds, oil, and gas has been conducted for many years (e.g., Merrill, 2007; Meyer *et al.*, 2008). In the 1980s, the prospect of mining the seabed for manganese nodules attracted considerable and durable scientific interest (e.g., Huggett and Somers, 1988; Weydert, 1990; Scanlon and Masson, 1992; Chakraborty *et al.*, 1997), but this proved economically unviable due to the amount of existing land-based resources and the technological difficulties of sea mining at the time. Meanwhile, sand and gravel dredging have increased worldwide because of growing construction activities, and there is very strong industrial interest in the mining of deep seafloor massive sulfides (SMS), rich in copper, zinc, gold, and silver. Diamond mining in continental margins has been steadily going on for the last 50 years and is now moving at a higher pace (e.g., Stevenson *et al.*, 2002). There is therefore a strong drive to increase the extraction of all sorts of marine resources, at all depths.

The morphology of the different deposits and the techniques of recovery (present and future) are quite varied. Ferromanganese nodules, for example, generally occur as a single layer of potato-size balls on unconsolidated soft sediments, 4,000 m to 5,500 m deep (Meyer *et al.*, 2008). Population densities of 10 kg/m^2 to 25 kg/m^2 are potentially economically recoverable. Precipitating Co-rich crust can create 25 cm thick layers on rock outcrops, 400 m to 3,000 m deep. Whereas the nodules can be recovered with simple collectors, the crusts have to be mechanically stripped. SMS deposits are directly accessible, contrary to their land-based equivalents. Economically attractive concentrations occur in some arc and back-arc basins, where epithermal gold deposits were also recently discovered (Meyer *et al.*, 2008). The International Seabed Authority has been instrumental in developing access to these seabed resources in an environmentally acceptable way (e.g., ISA, 1999). But the methods involved in marine mining, either through mechanical excavation or hydraulic excavation (using high-pressure water), still have a definite environmental impact. Mining for aggregates retains most of the dredged material, whereas precious metal mining results in most of the material being returned to the seabed after processing (e.g., Barrie and Good, 2007). There is less material in undersea mining processes (Merrill, 2007), but it is substantial nonetheless and it definitely affects marine habitats (e.g., Kenny and Rees, 1996; Hitchcock and Bell, 2004; Du Four and van Lancker, 2008), although the timescales of recovery vary widely.

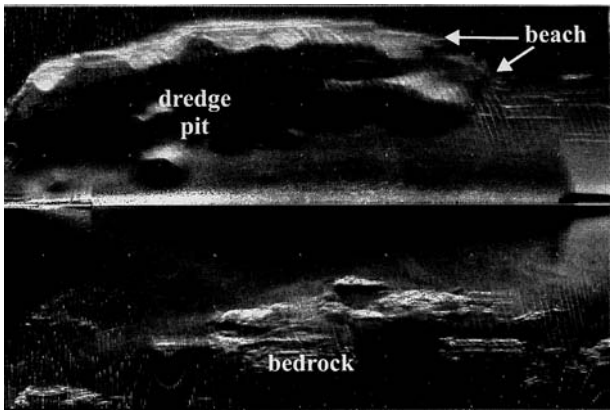

Figure 9.6. Example of seabed change brought about by dredging for marine aggregates next to a beach (reprocessed from Barrie and Good, 2007). This sonar record is 400 m across-track (© 2007 Geological Association of Canada).

Figure 9.6 (reprocessed from Barrie and Good, 2007) shows a typical sonar image from a dredging operation. Each recovery sequence creates dredge pits (in black on the image, as they are depressions in the seabed) and spoils can accumulate over the sides of the dredge pits (arcuate backscatter at far range). During operation, suspended sediments will move with bottom currents and tides, sometimes being redeposited several hundreds of meters away (e.g., Hitchcock and Bell, 2004). Dredge traces tend to erode after a while, although this will vary considerably with the local hydrographic conditions. Kubicki *et al.* (2007) present interesting series of sidescan sonar images of gravel and sand pits, showing their different recovery styles. Gravel pits, for example, do not refill continuously and seem to be dependent on storm events. Sand pits refill faster, as finer sediments are more easily mobilized. As extraction of seabed resources extends to deeper areas, and to other types of deposits (such as placer minerals), it will be interesting to see how similar studies can be used to monitor the extraction processes and their effects on local habitats. Kubicki *et al.* (2007) noted that their study would not have been possible without the synergy of sidescan sonar imagery and multibeam bathymetry, and this is now clearly a role that can filled by interferometric sonars (e.g., placed on ROVs and AUVs).

It should be noted that dredging is not only associated with the extraction of valuable resources. Dunes frequently arise on the seabed of shipping channels (e.g., Wille, 2002; Wienberg and Bartholomä, 2005; Schrottke *et al.*, 2006) and, as they are navigational hazards, they are regularly dredged. Like Du Four and van Lancker (2008), but in a different context, Wienberg and Bartholomä (2005) noted that little is known about the medium-term to long-term effects of these operations, principally because of the lack of adequate monitoring.

9.3 ACCIDENTAL STRUCTURES

9.3.1 Fishing activities

A considerable amount of fishing is done by trawling the seabed to catch fish. This is done by towing a large net over long distances (Figure 9.7). This net can encompass

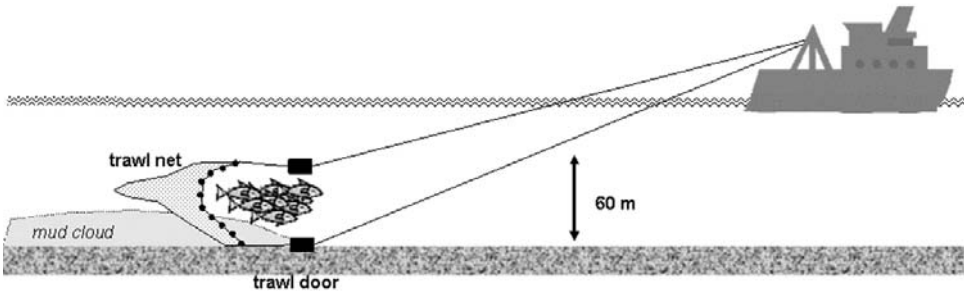

Figure 9.7. A typical trawling operation will tow a trawl net at a long distance behind the ship, laden with weights (~200 kg each) at its opening. It will be weighed down, close to or on the seafloor, with heavy steel doors (up to 5 tonnes each). The typical opening of a net during deployment is around 60 m: it will not only catch fish, but also resuspend bottom sediments in a large cloud behind the net, adding to the overall disturbance.

volumes of 60 m in diameter and several hundreds of meters long. It is weighed down by trawl doors (heavy steel plates, up to 5 tonnes each), which will scour the seabed and anything on or in it. There are different types of trawls, but their effects on the seabed will be the same (e.g., Sanchez *et al.*, 2000). Trawlmarks are visible everywhere around the world, down to several kilometers, and even deep-sea coral reefs are regularly scarred (e.g., Freiwald, 2002; Hovland, 2008). Depletion of fish stock in shallower waters as well as consumer pressure have moved trawling activities to increasing depths. The amount of sediment suspended after the passing of a trawl can be important, and smother existing fauna when redeposited. The trawlmarks themselves rework the seabed at depths of several tens of centimeters. No one knows how long the ecosystem/seafloor takes to recover, and this had led to a ban on bottom trawling in the most ecologically sensitive areas of the seabed (e.g., near most cold-water coral reefs off Norway).

Trawlmarks correspond to rapid and brutal scouring, and their morphology is similar to that of iceberg ploughmarks (see Figures 6.13–6.15 for examples). Trawlmarks will be sharp, narrow, and very long depressions in the seabed, following curvilinear tracks (Figure 9.8). Remobilized sediments in and around the marks can change the overall acoustic response, by increasing the micro-scale roughness and thus the backscatter levels. This can be used to approximately date trawlmarks (e.g., J. Gage, pers. commun.) and assess how fast the seabed and local ecosystems recover. Recent international laws about compensation for damage to seabed installations (e.g., communications cables) mean that fishermen have an incentive to map the seabed before trawling, but also, conversely, that the siting of new instruments on the seafloor needs to follow an assessment of how often the area is or has been trawled (''trawl bumpers'' are expensive and there is not always the option of adding extra obstacles around the equipment to prevent the snagging of trawls or fishing nets).

To encourage more sustainable fishing, aquaculture (e.g., Shang, 1980; Chambers *et al.*, 2002) and the colonization of artificial reefs by fish (O'Leary *et*

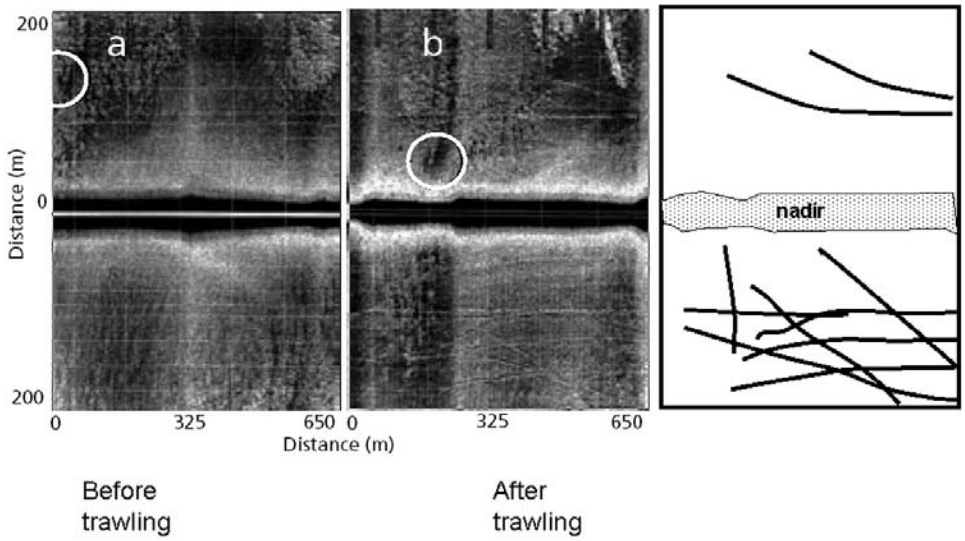

Figure 9.8. Trawling can significantly change the structure of the seabed, as seen in this comparison of the same area (the white circle locates the same patch of seabed, for easier comparison of both "before" and "after" images) (adapted from Løkkeborg, 2005).

al., 2001; Cuevas *et al.*, 2002) have been developed over recent years. The monitoring of fish and habitats is easily done using sidescan sonar, and Figure 9.9 shows an example acquired with a new type of interferometric sonar (SwathPlus, a three-frequency sonar from SEA Ltd., U.K.). On the left side of the image, the sea surface reflection can be traced at relatively close range as a continuous white line. It can also be traced on the right half-swath, where it is combined with the reflections from the top rings of the fish pens (strong reflections too, giving an indication of the diameter

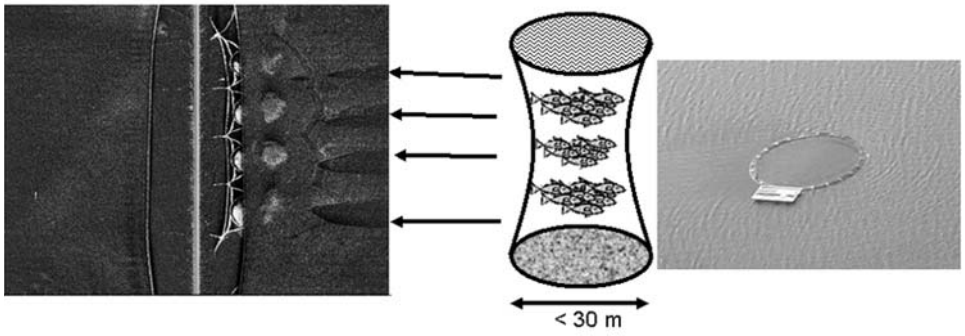

Figure 9.9. Fish pens imaged using the high-resolution interferometric sonar SwathPlus (*http://www.sea.co.uk/swathplus.aspx?nav=products*). (From left to right) Sonar imagery (180 m total swath), a sketch of fish pens, and an aerial picture of a fish pen in the open sea (sonar image © SEA Ltd., U.K.).

of the pens). At further range, one can see more diffuse echoes, in clear groups, corresponding to the fish inside the pens, with acoustic shadows extending over the rest of the range. Note the shape of the shadows is inverted from the shadows of seabed reliefs: instead of starting wide and narrowing with range, they start narrow and widen with range, indicating that the fish are concentrated toward the top half of the pens (which would be logical as they would be closer to light and nutrients).

9.3.2 Shipwrecks

After more than 2,000 years of continuous use of the sea, all around the world, there is a fair number of shipwrecks from all ages, and in all conditions, scattered on the seabed. Because of their frequencies and their low imaging angles, sidescan sonars are ideal tools to detect shipwrecks (and wrecks from other vehicles, from helicopters to planes to submarines). If imaged under the right conditions, sidescan sonars can detect the reflective pixels corresponding to the shipwreck itself and the acoustic shadows projected by the portions of the shipwreck still proud above the seabed. Figure 9.10 shows a typical sonar image of a small shipwreck. It was found during the survey of a large bay in Nova Scotia, Canada (Pouliquen *et al.*, 2002) and overlooked until detailed analysis of the entire mosaic (covering a much larger region). Many shipwrecks (including the *Titanic*) have often been initially detected as simple "blips" on large images of otherwise normal seabed.

But sometimes, the shipwrecks are much harder to detect, either because small patterns of highly reflective pixels do not appear, or because they have degraded beyond easy recognition. Their effects on the seabed, during sinking and after

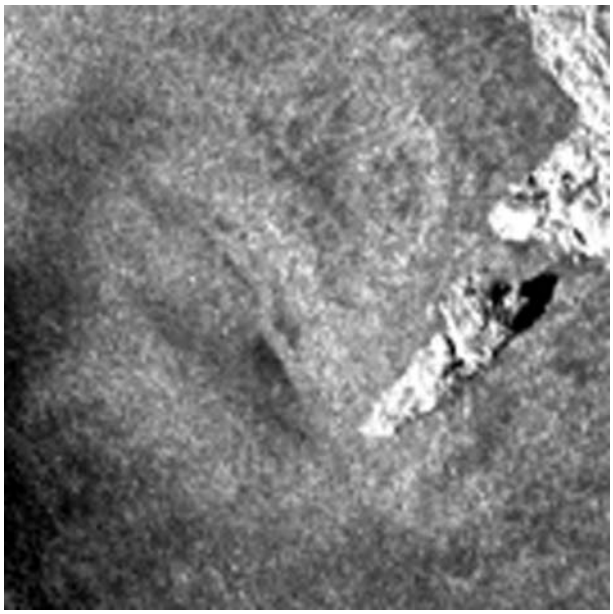

Figure 9.10. Small fishing boat found in a sonar image from a shallow bay in Nova Scotia, Canada. The image is 40 m wide, with a pixel resolution of 20 cm.

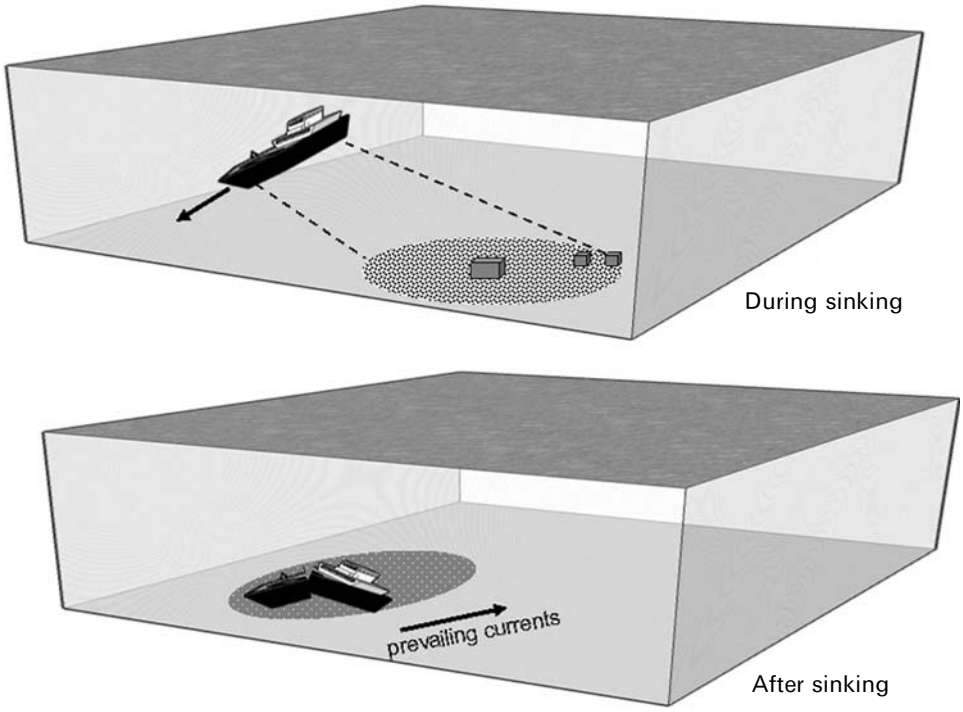

Figure 9.11. Loose objects and cargo on the ship will be scattered along its path when sinking through the water column, pointing to the likely resting place. After sinking, scouring of sediments around the proud parts of the shipwreck can assist its detection or be indirect traces of a possible shipwreck.

sinking, can, however, be more easy to detect (Figure 9.11). Visual exploration of Roman shipwrecks in the Mediterranean has revealed that ships sailing in bad storms often try to jettison their cargo before sinking (R.D. Ballard, pers. commun., 1998), and that detecting and following the trail of cargo and ballast often leads to the shipwreck itself. During sinking, any loose objects or cargo on the ship will scatter along its path through the water column. After sinking, sediment transport will be affected by the presence of the wreck (e.g., Quinn *et al.*, 1997; Quinn, 2006), with scouring similar to that seen around rock outcrops (see Figures 6.8 and 8.9). Long after the ship has been buried or has decayed, the scouring can still be visible as a halo (i.e., an area of enhanced backscatter and rougher textures).

Figure 9.12 shows an example with a Roman shipwreck found on the Italian coast (from Blondel and Pouliquen, 2004). In this image, the wooden shipwreck is not visible, partly because it has heavily decayed and partly because only a small portion is visible (barely) in the upper part of this half-swath, at close range. Instead, coming from the south, one can first detect a cluster of individual targets. These are the dolia, large amphorae used for food and oil transport in Roman times. Divers found that the openings of some of them were facing toward the sonar, adding to the overall

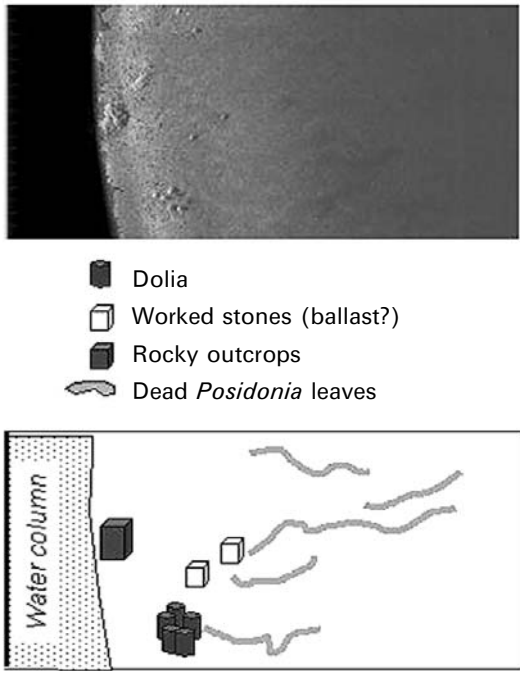

Figure 9.12. A 384 kHz image from a Roman shipwreck near Elba (Italy) (from Blondel and Pouliquen, 2004).

backscatter through internal reflections. They are grouped, indicating that they might have been dumped together, possibly to lighten the ship. Further individual targets are found farther north, looking like small rocks but with sharper reflections, and diver images indicate they were worked stones, most probably used as ballast, as was the custom at the time. So the presence of artifacts on the seabed can be used to infer the direction in which the shipwreck is most likely to be, and ultimately to think about a potential loss scenario, however hypothetical.

A more striking example is shown in Figure 9.13. This sonar image corresponds to the wreck site of M/V *Derbyshire*, a British cargo ship that sank a few decades ago in the Sea of Japan in mysterious circumstances. Over a scale of 1 km^2, the high-frequency sonar image shows ribbons of medium-bright material and many very bright reflectors, with sizes from a few meters to a few tens of meters, over a smooth and dark background. Preliminary investigations (e.g., Parson *et al.*, 1995) identified the background as typical of the sediments in the abyssal plain where the vessel sank. The bright ribbons are mineral ore deposits, coming from the ship cargo and lost during the descent through the water column. Their morphology could be used by experts to model the likely descent path and assess loss scenarios. The bright reflectors are all parts of the ship, scattered over the square kilometer, and subsequent dives with video and optical ground-truthing identified with certainty the position of the stern and bow of the ship (DETR, 1998).

Because of the fascination they exert, and because their investigation can solve many personal and historical enquiries, there are many images of shipwrecks and

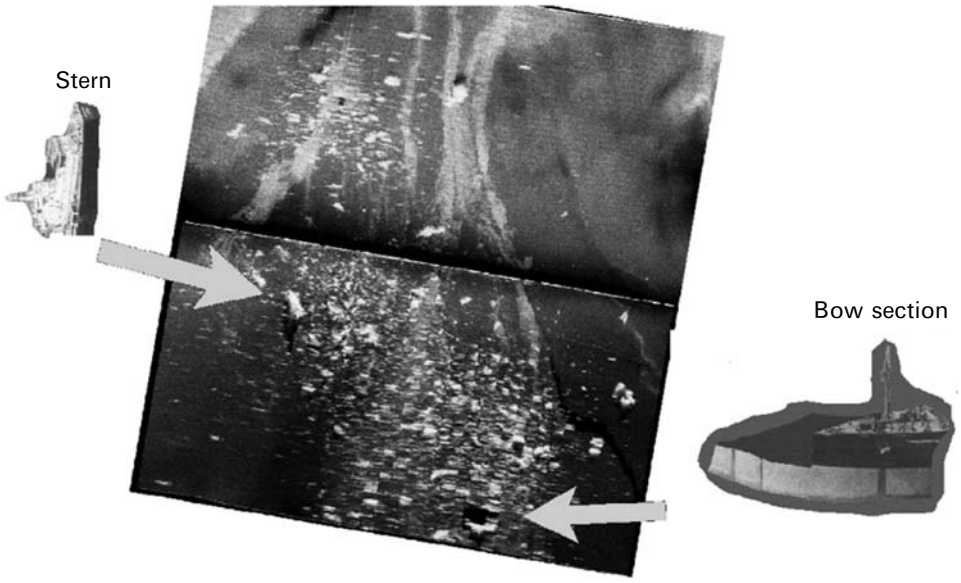

Figure 9.13. High-frequency sonar image of the wreck site of M/V *Derbyshire* in the Sea of Japan (Parson *et al*., 1995; DETR, 1998). The mineral ore carried by the ship is visible as medium-bright ribbons ending at the wreck itself (bright reflectors).

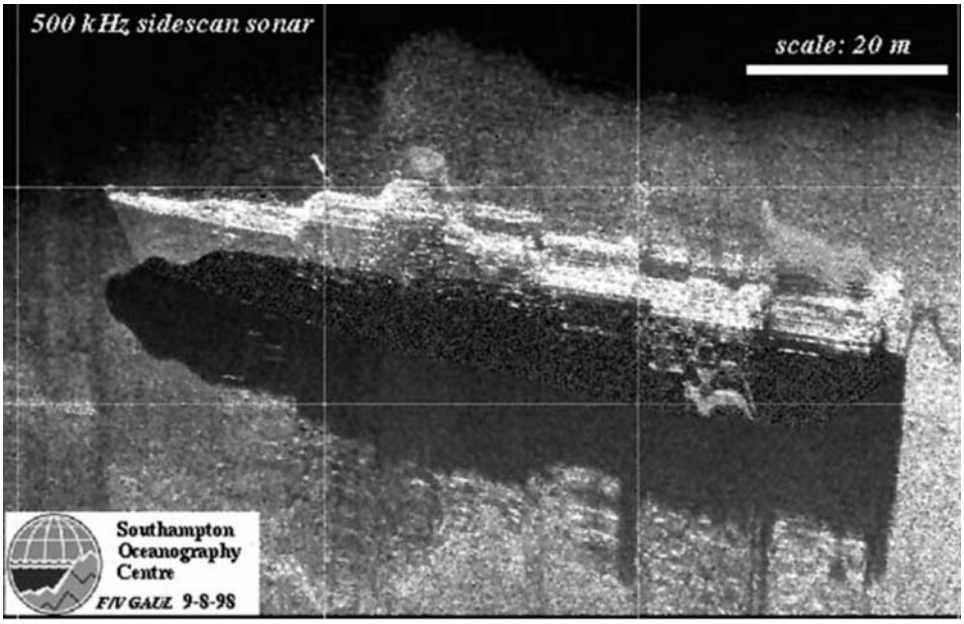

Figure 9.14. Sonar image of a large fishing vessel in the Barents Sea, acquired by the author (then at the Southampton Oceanography Centre, U.K.) and his colleagues.

other sunk vehicles on the seabed. A good selection of famous shipwrecks from around the world is presented in Wille (2002). The last shipwreck presented here is that of a large fishing vessel, F/V *Gaul*, which also sank in mysterious circumstances but this time in the Barents Sea. A full report of the investigation is presented in MAIB (1999), but this image (Figure 9.14) is the raw image acquired at sea by the author and his colleagues of the time. The first pass over the wreck site was done with a lower frequency sonar (~100 kHz) and it showed only a linear white shape, with no resolution and no indication of what it was. The second pass was done after switching to the higher frequency of the sonar (500 kHz). This shows the shipwreck in full, with an intact hull, structures on the bridge, funnels, and even cranes, laying at a slight angle over a sedimented seabed. Fuzzy, bright structures are observable on some of the highest points of the ship, particularly toward the stern: they correspond to fishing nets that got snagged on the cranes and prominent parts of the ship during its 25 years on the seabed. Their mapping was of particular importance as it was used to avoid catching ROVs in the net during the next part of the investigation.

9.3.3 Pollution

The growing use of the oceans increases the risks of accidental pollution, and many catastrophic oil spills of the last 40 years continue to have important repercussions on marine ecosystems and related industries like fishing or tourism. The types of products transported at sea can become suspended in the water column or sink after weathering or mixing with sediments. Heavy oils tend to sink and weather more slowly and can affect sea resources for long periods and at great distances from the release site (e.g., Parthiot *et al.*, 2004). In shallow-water environments, they can get mixed with sediments and deposited, unless weather and currents move them again.

The actual threat to the environment and the best clean-up strategies are hard to assess, because of the difficulty in detecting and mapping chemical pollution. Pools of chemicals on sediments can hardly be seen on video images taken from above (e.g., from an ROV or a towed camera). Especially on coarse-grained sediments, their contours follow the ground, so that the low gradient of the index of optical refraction does not provide sufficient contrast to detect them acoustically and map their extent. We saw in Chapter 7 that sidescan sonars could detect mud volcano deposits, "brine pools", and other structures from their very low backscatters. And the EXCAPI[1] Project has recently shown that sidescan sonar has a definite role to play (Parthiot *et al.*, 2004).

Different types of oil spills were simulated by putting heavy fuel oil in flexible round skirts of varying diameter and thickness with a porous mesh bottom (to avoid air bubbles). These patches were laid on medium-coarse sand in 8.5 m of water, in a test basin open to the sea, and imaged with a series of off-the-shelf sonars, including sidescan sonars. The image presented here (Figure 9.15) was acquired using the Klein 5500-B interferometric sonar, operating at 455 kHz and with a range of 50 m. Because

[1] In French, EXCAPI stands for "EXpérimentation de Capteurs Acoustiques pour repérer le Pétrole Immergé" (loosely translated as "acoustic experiments to detect submerged oil").

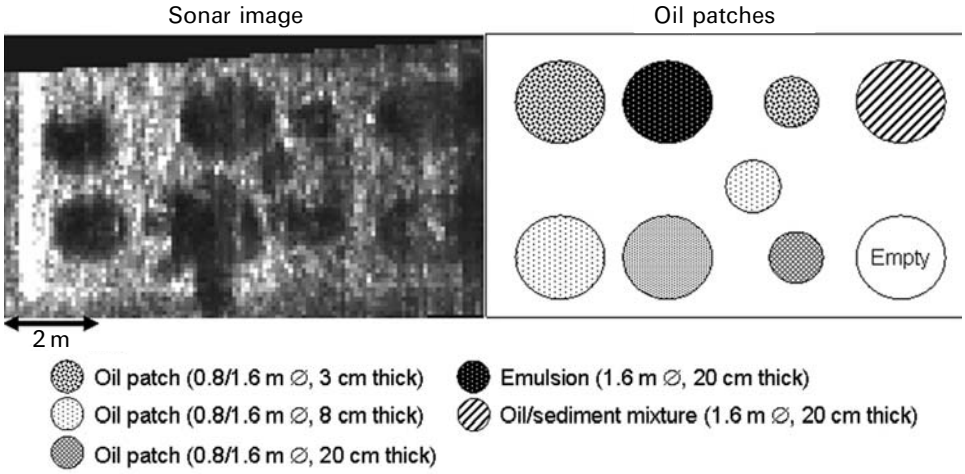

Figure 9.15. Sidescan sonar image of different oil patches in a test tank, from the EXCAPI Project (Parthiot *et al.*, 2004). This high-resolution image was taken with a Klein 5500-B interferometric sonar, with a ground resolution of 3.2 cm (along-track) × 10 cm (across-track). The sonar was 8 m away from the left side of the 5 × 10 m image, ensonified from the left. The sketch on the right shows the original position of oil patches, although some bottom leakage took place and the patches are broader than intended. The EXCAPI experiments showed and quantified the potential of sidescan sonars for oil spill mapping.

this sonar was calibrated, the EXCAPI researchers were able to quantify the acoustic contrast between oil patches and the sedimentary background. Values between 9 dB and 14.4 dB were achieved, meaning sidescan sonars have a fair potential for mapping oil spills. Although oil types could not be distinguished from their sonar backscatter alone, spills as small as 0.3 m were detectable as acoustically absorbent patches. The shapes of the test area do not match exactly the pattern originally laid out, because of some leakage through the porous bottom of the oil containers, but correspond better to what would happen in open water. Bathymetry measurements could not be obtained for the pixels corresponding to the oil patches, and this was seen as a potential way to infer their presence when looking at interferometric bathymetry. Several other tests showed this worked well for other types of reflective seabeds, such as sand, gravel, and rock.

Another conclusion from the EXCAPI Project was that, although sidescan sonar seemed a better tool to detect oil spills and similar products in shallow water or close to the seabed, multibeam sonars would be more efficient in deeper water. Medialdea *et al.* (2008), however, concluded from deep-water studies of the *Prestige* wrecksite that oil spills could not be unambiguously detected with multibeam sonars (although this might have been related to the complex topography of the Galicia Bank). Research in this field is continuing, and a Norwegian firm recently announced a hydrocarbon leak detection device based on a forward-looking multibeam sonar, which detects hydrocarbon escaping from seabed installations and pipelines in zero visibility.

9.4 SEABED WASTE AND MILITARY MINES

9.4.1 Seabed waste

Most natural and artificial waste makes its way to the seabed over time. The intentional dumping of waste at sea, or "ocean dumping", is generally banned worldwide and is regulated by two conventions, the London Dumping Convention (ratified in 1975) and the MARPOL (Marine Pollution) Convention (signed in 1978). The motivation for banning ocean dumping gained momentum when contaminated wastes from sewage-derived micro-organisms were discovered at public beaches and shellfish beds were contaminated with toxic metal (e.g., Edwards, in Blondel and Caiti, 2007). Environmental pressure groups still estimate that the waste currently dumped into the sea weighs as much as all the fish caught in a year. Difficult as these numbers are to measure with accuracy, it is certain, however, that the worldwide prevention of ocean dumping has ensured that little waste now intentionally enters the sea.

But the effects of past dumping are still deeply felt. In the Baltic Sea, for example, existing documentation estimates that 65,000 tons of toxic chemical munitions were dumped after World War II, and this is most likely to be a strong underestimation. Around the British Isles, several sites were used for dumping unused chemical munitions and explosives after each World War (e.g., in the Irish Sea). Some shipwrecks also contain large amounts of toxic and dangerous waste. A sunk freighter at the end of the Thames Estuary, for example, is slowly breaking in two and its explosives are considered a looming menace for nearby harbors and a liquid gas terminal under construction nearby. Munitions dumped in Beaufort's Dyke, a deep submarine trench between Scotland and Ireland, represent more than 1,000,000 tonnes of military waste, according to the British Ministry of Defence. Some of these were dumped short of the Dyke in waters shallower than expected, and hundreds of unstable incendiary bombs wash up on local beaches every winter after strong tides and storms. Information on dumpsites, and particularly toxic dumpsites, is not easily available since, not surprisingly, many dumping operations involving industrial or military hazardous materials were carried out covertly. In areas like the Baltic Sea, monitoring agencies like the Helsinki Commission formally recommended that all waste sites be located and their contents mapped accurately by Baltic nations. Most of this mapping is done with sidescan sonars, because of their ease of use and large coverage.

Other examples of marine waste include residues from industrial activity and also from fishing (e.g., "ghost fishing" is a common problem in some U.S. fishing grounds; Bamford *et al.*, 2008). When mapping marine waste, one should remember the vast diversity of objects and processes leading to their disposal. Although most of the dumpsites, official or not, will tend to look like the one in Figure 9.4, small-scale waste dumping will produce images like the bicycle of Figure 4.27 or the container in Figure 9.16, etc. Wille (2002) documented cars scrapped near the London Docks, and there are many similar instances around the world.

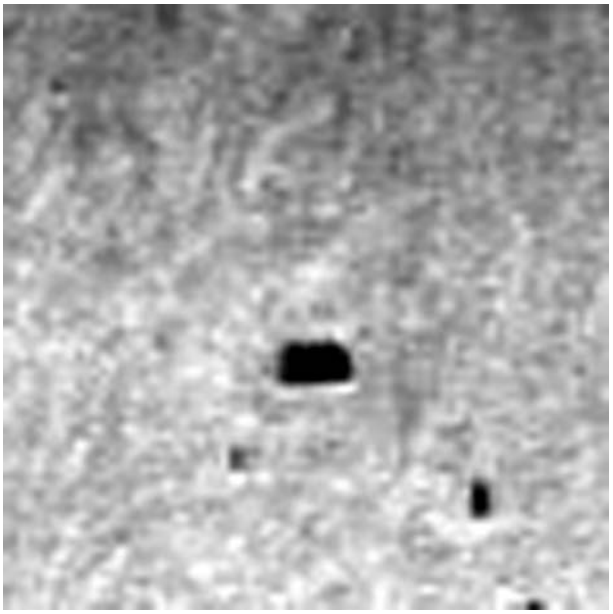

Figure 9.16. A 1.5 m long metal container (middle) and a lobster trap (bottom right), imaged with a high-resolution sonar in shallow water, are individual examples of seabed waste.

In areas with high sedimentation rates, or high reworking rates, marine waste will rapidly get buried. Finding it will then require similar approaches to finding objects with low acoustic signatures such as mines.

9.4.2 Military mines

Sea mines have played a significant role in the majority of naval conflicts since the American Civil War; they can also create major problems even in peacetime (i.e., mines from past conflicts or terrorist actions). Mine monitoring and safe route surveying is becoming an increasing problem for military navies around the world, and the accidental discovery of mines from past conflicts in commercial applications is always unsettling. The sheer importance of research and development work carried out in the field of mine counter-measures (MCM) is a testimony to the significance of the problem. Mines constitute an inexpensive and readily available weapon, easy to deploy and effective against ships and submarines alike. They can be used in either defensive or offensive roles. A country can lay mines in its own harbors and coastal waters in order to deny access to invasion forces, or lay mines in other countries' waters to damage and/or delay shipping by disturbing sea lines of communications. Mines can be cleared by mine-hunting, using dedicated sonar and disposal vehicles or divers, or minesweeping, using towed or remotely controlled vehicles that activate the mines by imitating target signatures. However, before a minefield can be cleared or neutralized, the mines need to be located. Peacetime trials and wartime actions show that active high-resolution sonar is the only tool that can detect mine-like objects

(MLOs) on the seafloor with acceptable success rates and on large areas (e.g., Horwitz *et al*., 1993; Brissette, 1997; Buck, 1997; Kozak, 1997).

The physical compositions of mines and their modes of emplacement can be very varied (e.g., *Janes*, 1995; Brissette, 1997). Moored mines are anchored to the seafloor at a desired depth below the surface. They are more effective in deep waters (greater than 60 m) and are activated by contact (for older models) or by magnetic or acoustic influence. The typical size of a moored mine is $1\,m^3$ to $2\,m^3$ (*Janes*, 1995). Tethered mines are left on or near the seafloor, and detect targets passively before using homing devices to reach them. These mines are predominantly used off the continental shelf in very deep waters and play an important role in antisubmarine warfare (ASW). Ground mines are laid directly on the seafloor, and are predominantly used in shallow waters (e.g., around harbors, rivers, or coastal shipping routes). Ground mines can be composed of materials like glass-reinforced plastic or steel, and their sizes range from cylindrical to multi-faceted. These factors influence the acoustic signature of the mines, and make them generally difficult to detect.

Figure 9.17 shows in high-resolution two types of mines, imaged in a test area with a Klein 500 kHz sidescan sonar. The image on the left covers approximately 10×10 meters on the ground, and was ensonified from the right. The very dark region at the extreme right of the image corresponds to the water column. It varies in width, which may be explained by slight variations in the altitude of the sonar above the seafloor, or by slight changes in the topography of the seafloor itself. This image shows mainly sediments with a mottled texture and varying gray levels. The seafloor

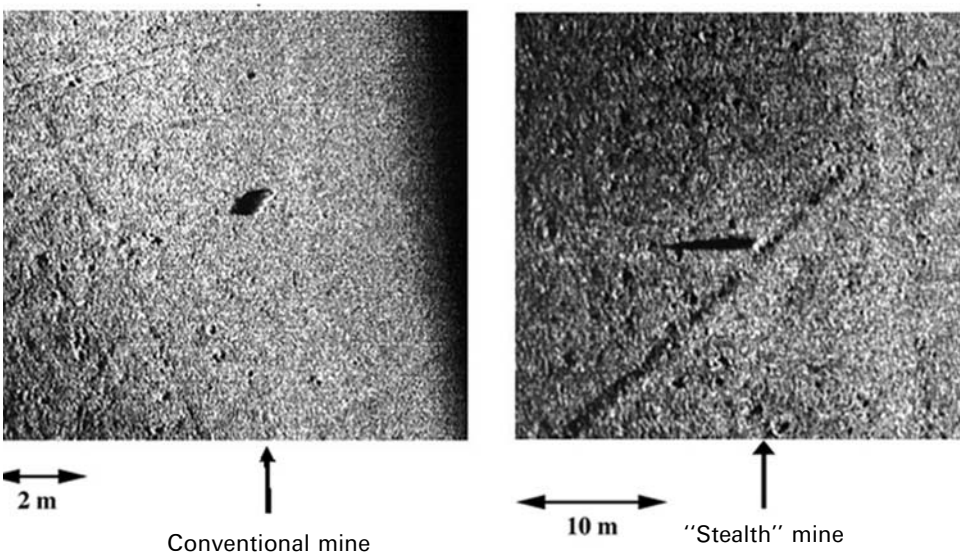

Figure 9.17. 500 kHz images of two mines (from Blondel, 2000). (Left) A conventional mine. (Right) A "stealth" mine with low acoustic signature. Both mines are mainly detected from their shadow, but they could be confused with many other mine-like objects, such as boulders or lobster traps.

is crossed by several quasi-linear tracks, associated with trawlmarks. There are a few boulders and small depressions on the seafloor, and average backscatter levels are significantly high. The mine was imaged at a range of approximately 20 m. Cylindrical in shape, its dimensions are ~1.4 m in length and ~0.5 m in diameter (Kozak, 1997). On the sonar image, its shape is elongated and very thin (one or two very bright pixels at most). It is detected mostly from its shadow and because the conditions of acquisition are "just right" (sonar altitude and imaging angle). The image on the right covers a larger portion of ground. The overall texture of the sediments in the image is very mottled, with a large quantity of small, bright reflectors, interpreted as pockmarks and small rocks. The darker, diagonal linear feature is most probably a trawlmark. The mine was imaged at a range of approximately 25 m, not very different from the previous one. It is ~1 m in diameter at the base and 0.5 m high (Kozak, 1997); it is made of a plastic case and has a conical and low-profile shape, to hamper detection with sonars. Indeed, it is mainly detected from its long shadow. These two images show the difficulty of detecting mines on sidescan sonar imagery, as they are often built to be difficult to detect and their shadows on the seabed could come from many other mine-like objects. This is one of the driving forces behind acoustic characterization efforts (see Sections 11.2 and 11.4).

9.5 SONARS AND UNDERWATER ARCHEOLOGY

Cultural resource managers and licensing agencies around the world are increasingly concerned about submerged prehistoric archeological sites and the possible negative interactions with offshore developments and human activities (Faught and Flemming, 2008). Archeological sites and artifacts are part of our "underwater cultural heritage" (Forrest, 2002) and as such they need to be studied and, if possible, preserved. Most of these sites were submerged after the last ice age, under tens to hundreds of meters of water and, often, layers of sediments. Many sites have been discovered over the last 30 years, usually serendipitously, in shallow-water environments as well as on continental margins.

Archeological sites can be campsites, hunting sites, or gathering sites; they will be discovered through the modification of landscapes or, much more often, by the types and amounts of artifacts found. These sites can consist of large arrays of bones, stone tools, and possibly wood and other organic items preserved under various anaerobic conditions (e.g., Ballard, 2008). Accumulations of artifacts can reach sizable proportions (e.g., in shell middens—some examples on land are known to reach 15 m high). Arrangements of objects like blocks or wooden poles (which can be preserved in anaerobic conditions) can be used to detect anchorage sites or piers (e.g., Coleman and Ballard, 2004). Stone structures up to 300 meters in length have, for example, been identified as fish traps (Dean, unpublished). Individual objects are more difficult to detect (see Section 9.4 for similar examples), and they might also have been dispersed by wave action and movements of sediments in the time since they were deposited. The backscatter from submerged archeological material is still poorly

understood. Quinn *et al.* (2005) conducted a series of controlled sea trials to investigate different types of potential artifacts. Not surprisingly, they confirmed that the pulse length and beam angle govern the resolution of sidescan imagery. More interestingly, they found that both organic (wood/leather) and inorganic (metals, ceramics, glass, and varying aggregate and ballast grades) could be differentiated from their backscatter levels. Stone anchors have been used since before Antiquity (e.g., Evrin *et al.*, 2002) and sidescan surveys have often been able to locate them and identify shipwrecks or assess shipping levels (e.g., Green, 1998). As another example, the distribution of amphoras underwater was also used to map commercial exchanges in Britain during the Iron Age (e.g., Trott and Tomalin, 2003). Moving to larger objects, Quinn *et al.* (2002) showed that the techniques for detection and surveying of modern shipwrecks can also be applied successfully to older, wooden shipwrecks, although their condition varies greatly with local hydrography and how it facilitates (or not) bio-degradation (e.g., Pournou *et al.*, 2001). Sidescan sonar can also be used to reconstruct paleo-landscapes (e.g., Fedje and Josenhans, 2000). One recent example used acoustic imaging to map a paleo-river 9 km long and locate samples dated to 7,500 BC off Gujarat, India (Young, 2002).

In the first exhaustive review of the applications of sonar mapping to underwater archeology, Akay *et al.* (2004) showed that many of the useful techniques include the synergy between different types of instruments (e.g., sidescan sonar and magnetometer) and that new acoustic instruments can improve mapping capabilities. Ballard (2008) showed how these techniques can be adapted to a variety of settings. It was not possible to find for this section sidescan sonar images of sufficient quality showing objects that were not shipwrecks or general seabed maps,[2] but the field of underwater archeology is rapidly expanding and this should be possible soon. To conclude, one should note how Faught and Flemming (2008) showed that open collaboration between the different users of the sea and inland waters can be a good way to advance the field.

9.6 CONCLUSION

This chapter aimed at showing the variety of man-made structures one can now find on the seabed. These structures can be laid intentionally (e.g., cables, pipelines, approved dumpsites) or come as a surprise (e.g. shipwrecks, trawlmarks). By becoming more widespread, they can also become more hazardous. For example, recent international legislation about the breaking of cables by trawling reveals the need for accurate maps of all cables and pipelines on the seabed. Similarly, the development of offshore facilities and increasingly expensive seafloor observatories requires knowledge of routes or areas safe from trawling or excessive erosion. It was not possible to present all variations on generic shapes and types of structures: the difference between concrete blocks, drums, and small cylinders or mines was not worth presenting

[2] A potential stone circle, presented by Milkert and Hühnerbach (1997) in the *Handbook of Seafloor Sonar Imagery*, could not be confirmed without doubt at the time of writing.

through a series of individual images, for example. Other images of man-made structures have not been presented because they are better seen (and more recent) on the websites and commercial brochures of sonar manufacturers (planes, trucks, etc.). And, although sidescan sonars are now increasingly used for search and rescue, images of drowned bodies or recent accidents have not been presented. Finally, we have also looked at the potential of sidescan sonar for underwater archeology, from the reconstruction of now submerged paleo-landscapes to the detection of individual artifacts. The selection of sidescan sonar images presented covers a broad range of subjects, and they all show the pervasive influence of our activities over the entire underwater domain. This chapter should be of interest to all users of near-shore environments, developers of underwater sites. and managers of offshore facilities. Chapter 10 intends to show the limits of sidescan sonar imaging, such as when some of the objects detected are in fact anomalies that need to be corrected or ignored.

9.7 FURTHER READING (*see also* References at end of book)

About the detection of small objects (including mines)

Bell, J. (Ed.) (2007). Detection and classification of underwater targets. *Proc. Inst. of Acoustics*, **29**(6), 267 pp.

About the state of the art in underwater archeology

Ballard, R.D. (Ed.) (2008). *Archaeological Oceanography* Princeton University Press, Princeton, NJ, 283 pp.

10

Anomalies and artifacts

10.1 INTRODUCTION

The previous chapters have shown how sidescan sonar data were acquired, how they were (or should be) processed and interpreted, and examples have been shown at all depths and in all underwater environments so far studied with sidescan sonar. Sidescan sonar imagery, like any data, is rarely devoid of anomalies and artifacts. They may be easy to spot or mistake for real features, and they may be difficult to interpret or remedy. The present chapter aims at showing most sources of errors and artifacts, how they can be avoided during processing, and how to recognize and interpret them when they do occur. This will be demonstrated by drawing both on the most recent theoretical studies on the subject, and on real-world examples from a variety of applications. The reader may also find it profitable to look at a short (but now somewhat dated) publication from EG&G Marine Instruments (Fish and Carr, 1990)[1] which presents sidescan sonar operations in very shallow water, mainly for the detection of man-made structures. The different sections of this chapter follow the acoustic wave from transmission to reception and processing. This includes propagation through the water column, backscattering toward the sonar platform, processing, and final interpretation. All these stages are prone to errors and artifacts; some of them are unavoidable, but all of them should be recognizable.

The presence of anomalies and artifacts is sometimes brushed aside as due to "not having a good enough sonar". But what is a "good sonar"? This is a common question for sonar users who need to quantify the performance of the sidescan sonar they are using, or how to choose between two different sonars. This performance cannot be reduced to just numbers, as it is closely related to the application. One does not choose the same sidescan sonar to look for a small shipwreck in shallow water and to map a submarine canyon all the way down to the abyssal plain. The choice will

[1] There was a new edition in 2001 but it has been listed as unavailable for many years now.

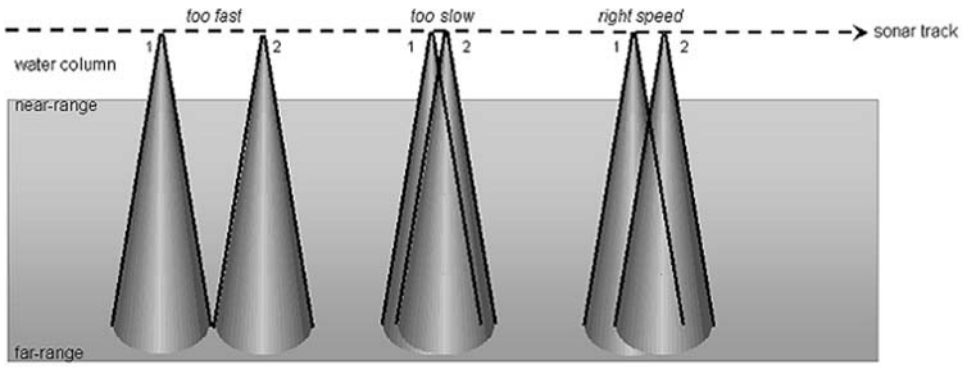

Figure 10.1. Ground coverage (seen from above) as a function of the speed of the survey platform. By adjusting the interval between pings (PRF, pulse repetition frequency), it might be possible to get full bottom coverage, from near range to far range, at most speeds.

be dictated by how close specific parameters match the expected application. Section 2.5 outlined the main parameters. The first one is the footprint size (i.e., the area on the ground that can be resolved by sidescan sonar). It is measured using the across-track Δy and along-track Δx resolutions (given in Equations 2.10 and 2.11, respectively). Nominal resolutions will decrease with range: objects closer to the sonar are usually more noticeable, whereas far-range objects can be smeared by beam spreading (see Section 10.2.2) and are usually fainter. These two resolutions are combined during processing (see Chapter 4, ''Sidescan sonar data processing'') to create square pixels, with constant resolution over the entire map. The second parameter is the range achievable with the sonar. Sounds of different frequency are attenuated differently (we saw in Chapter 2 that for an average depth of 100 m, an acoustic wave would experience an attenuation in water of 0.95 dB/km if transmitted at 10 kHz and 124 dB/km at 500 kHz). The maximum range corresponds to the moment when the incidence angle is sufficiently grazing that the projection of the signal footprint on the seabed can be neglected (its contribution is mainly noise). Finally, complete coverage is desirable: this is done by removing gaps between ensonified areas from successive pings (i.e., by adjusting the speed of the surveying platform relative to water depth and the pulse repetition frequency or PRF; Figure 10.1).

10.2 PROPAGATION ARTIFACTS

10.2.1 Water column variations

Artifacts related to the propagation of acoustic waves in the water column from the platform to the seafloor and back can be attributed to two sources. The first is variations in the structure of the water column itself. These can be density variations, salinity variations, or temperature variations (e.g., Lurton, 2002). They arise from the

stratification of the ocean and can be complicated by horizontal variation and, very frequently, by fluctuations in stratification (i.e., internal waves). The importance of these effects will differ according to the type of sonar used: deep-towed or shallow-towed, short-range or long-range. For deep-tow sonars (e.g., TOBI, DSL-120), the water is almost isothermal and acoustically fairly uniform. Hence the propagation effects are constant and predictable (e.g., Somers, 1993). Shallow-towed sonars will make use of most of the water column (and for long-range sonars like GLORIA, this means being subjected to effects several kilometers down and up to 30 km away). Depending on the depth, a certain number of thermocline layers will modulate the depth and angle at which the acoustic rays propagate. They can give rise to patterns at the far range that are very reminiscent of the linear bedforms associated with a bottom current, and which can only be treated by cutting off the outer portion of the image (Somers, 1993). Shallow-towed sonars in shallow waters (e.g., EG&G-272T) should be less prone to these variations. However, there have been reports of shoal-like structures produced by temperature inversions in summer, with warm layers over cold layers bending the sonar rays up (Fish and Carr, 1990; Tomczak *et al.*, 2002). Other causes of local variations in the properties of the water column can be cold and hot water seeps (anthropogenic or not), and lateral variations in salinity (e.g., near large river estuaries).

Sizable heterogeneities of the water column can be produced by the presence of bubbles. They can be present in the wake of the vessel (or neighboring vessels), or from cavitation caused by the ship's propellers, and they are particularly noticeable during tight turns (especially those now achievable with AUVs) and in agitated water (e.g., during a storm). These bubbles would also be present in the surf zone, for surveys in very shallow water, or when there are strong wind and high waves. These bubbles have lifetimes measurable sometimes in hours. High-frequency systems are quite sensitive to longer lived, very small bubbles. From theoretical and practical studies (e.g., Leighton, 1997; Medwin and Clay, 1998), we know that bubbles will scatter more around their intrinsic resonance frequency f_R, expressed (in Hertz) as:

$$f_R = \frac{3.25}{a}\sqrt{1 + 0.1z} \tag{10.1}$$

where z is the depth of the bubble (in meters); and a its radius (in meters).

In the presence of large numbers of bubbles, sound can be greatly attenuated, or reflected back to the transmitter leading, for example, to the parasite backscattering observed at very close range (i.e., at the beginning of water column returns).

The influence of hydrothermal vents (see Chapter 5, "Spreading and subduction") on the propagation of acoustic beams is a different matter, as their flows are usually enriched with minerals. Interference has been documented in some instances using shallow-towed lower frequency sonars (about 12 kHz), but not, to our knowledge, with higher frequencies. This may be due to the size of the bubbles, their composition, and their acoustic contrast with the surrounding water.

Heterogeneous propagation of sonar beams through the water column can also be affected by biological scattering. Well-dispersed plankton in the deep-scattering layer may affect deep-water shallow-towed sonars such as GLORIA, but is usually

not directly visible on sidescan images. The scattering strength of fish is considerably increased by their possession of a swimbladder full of gas. Depending on sonar frequency, fish can appear as strong discrete targets, the size of which varies with the number and dimensions of the fish involved (see Lurton, 2002 for a detailed yet accessible presentation of the acoustics of fish). And at very high frequencies, marine "snow" might also become a problem as some particulates would have diameters close to the imaging wavelengths (e.g., Kiørboe, 2001).

10.2.2 Beam spreading

Acoustic waves propagating in the ocean are subject to spherical spreading. The principal effect will be the widening of the beamwidth with distance from the sonar, and the subsequent decrease in along-track resolving power (Figure 10.2). In near-nadir regions, two close targets will be resolved by the sonar. At farther ranges, two identical targets at the same distance from each other will be imaged by the same beam, and appear as one single target.

Beam spreading constantly degrades along-track resolution at far ranges. For example, the along-track resolution of GLORIA is 45 m for a pulse repetition frequency of $0.033\,s^{-1}$ (1 ping every 30 s). At a ship speed of 8 knots (14.8 km/h), the along-track resolution is 120 m near the nadir. Because of beam spreading, the along-track resolution increases to 900 m at a 22 km range. Advanced sonar processing techniques (e.g., Masson *et al.*, 1992) use knowledge of the point spread function of the sonar system in use (i.e., the actual pattern of the beam) and constrained

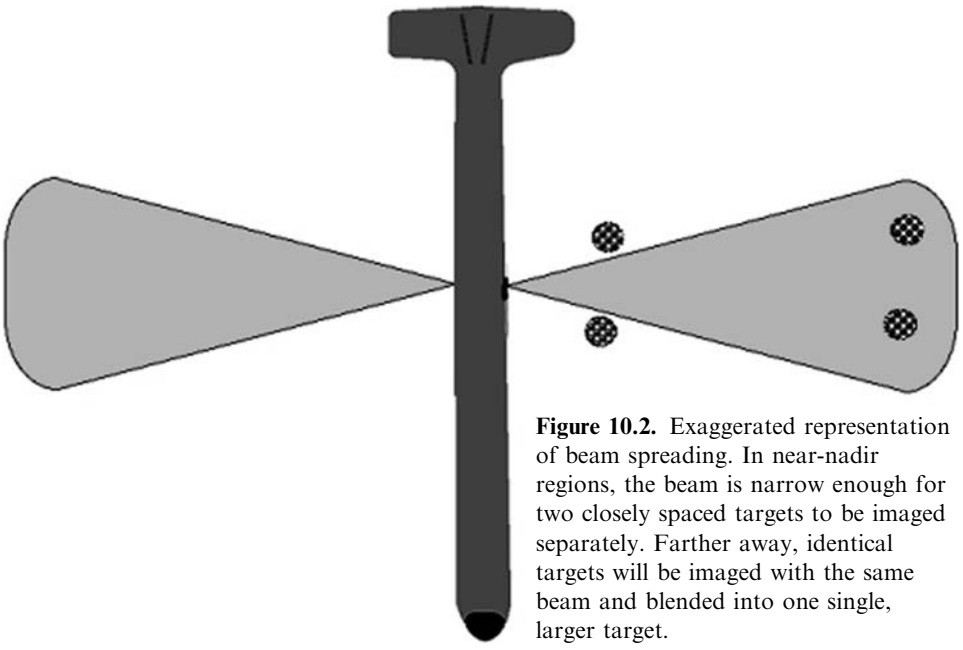

Figure 10.2. Exaggerated representation of beam spreading. In near-nadir regions, the beam is narrow enough for two closely spaced targets to be imaged separately. Farther away, identical targets will be imaged with the same beam and blended into one single, larger target.

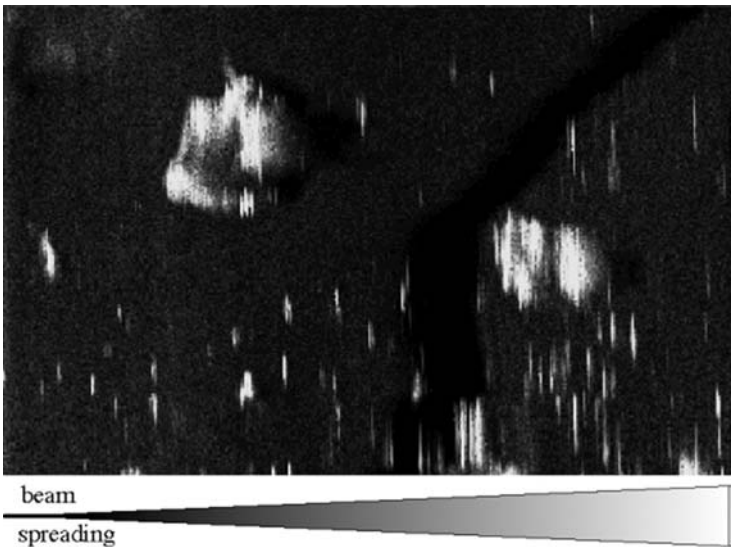

Figure 10.3. High-resolution sidescan sonar image showing the effects at far range of uncorrected beam spreading.

iterative restoration algorithms such as the Jansson–van Cittert method. If beam spreading is important, and corrections are not applied or are incorrectly performed, the discrete targets in the far range will be elongated along-track. They will appear longer than they really are, and individual targets will be erroneously merged (Figure 10.3).

10.2.3 Acoustic noise

Additional noise can come from other sources (e.g., other instruments, cross-talk, interference with other harmonics, etc.) or from natural sources (e.g., rain). Medwin and Clay (1998) showed that, depending on their size, raindrops impacting on the water surface would emit sound at sonar frequencies. This would be louder at 13 kHz to 25 kHz for small raindrops (0.8–1.2 mm diameter) and at 1 kHz to 50 kHz for large raindrops (>2 mm diameter). Experienced users have sometimes identified the presence of rain in sonar records as irregular speckle (e.g., Hühnerbach, pers. commun.). In extreme cases, even whales and dolphins have been known to attempt communication with sonars by transmitting at the same frequency. The resulting structures are usually highly reflective streaks elongated along-track, and stop after a short time (presumably when these animals do not get intelligible answers back from the sonar).

10.3 PHYSICAL (SCATTERING) ARTIFACTS

10.3.1 Sub-surface reflections

Studies of deep-sea sediments show that they often have near-surface sound velocities very close to the sound velocity in the overlying water (a few percent lower). It is

therefore not unnatural to observe volume reverberation. The incident acoustic wave penetrates into the sediments and is backscattered by sub-surface reflectors. Significant deep-sea sediment penetration occurs at frequencies of 12 kHz or lower ($\lambda_{inc} > 12.5$ cm). The depth of acoustic penetration depends on the frequency of the sound and the physical properties of the sediments involved. It can vary between several meters with GLORIA (6.5 kHz) and a few centimeters with DSL-120 (120 kHz).

The buried features scatter more strongly than the sediment interface and are therefore visible in the images. An example was seen in Chapter 6 (Abyssal plains and basins) on GLORIA imagery close to Hawaii (Figures 6.29 and 6.30). Huge fields of lava flows were buried under several meters of sediments, but were still perfectly visible on the image. Additional information (profiler data, optical images) is necessary to demonstrate with certitude the presence of sub-surface penetration. This type of effect is not widespread, but should nonetheless be kept in mind during the interpretation of imagery acquired in sedimentary areas. Sub-surface penetration is known to occur in radar imagery as well, mainly in very dry regions. Elachi *et al.* (1984) were, for example, able to detect fossil fluviatile channels 15 m below the surface of a desert.

Penetration depends on sediment characteristics, the signal transmitted (e.g., Ricker pulses for very high resolution, Chirp pulses for high penetration, and CW pulses for narrow-band, frequency-sensitive applications). High-frequency sonars will look at backscatter mostly from the surface, and low-frequency sonars (with a higher acoustic wavelength) will penetrate deeper into the seabed if it is "porous" enough. The actual "skin depths" for sidescan sonars are hard to quantify, and most evidence so far is anecdotal. *Ad hoc* models of acoustic penetration in the seabed can be created, using informed assumptions about the type of terrain expected (e.g., Mitchell and Somers, 1989; Mitchell, 1999; Guillon and Lurton, 2001) but their use is always limited to the application directly at hand. Unchecked penetration into the seabed means that the echoes from objects in the line of sight (but within the "skin depth") will arrive later, and therefore seem farther away than they actually are (Figure 10.4).

10.3.2 Multipath scattering

The acoustic wave transmitted by a sonar has several possible ways to travel to the target and back to the sonar (Figure 10.5). The first one is directly from the sonar to the target and back in a straight line. This is the recorded backscatter, from which the slant-range and the ground-range are computed. In certain survey geometries, the acoustic energy can be scattered from the target toward the surface of the sea, and a small portion of it will be scattered back to the sonar ("single-surface reflection"). A portion of the incident sonar beam (or its sidelobe) can even scatter toward the surface of the sea, be reflected toward the target, and scattered back to the sea surface and then the sonar ("double-surface reflection"). Following these three paths (and therefore three different slant-ranges), the imagery will display two or three recordings of the same target.

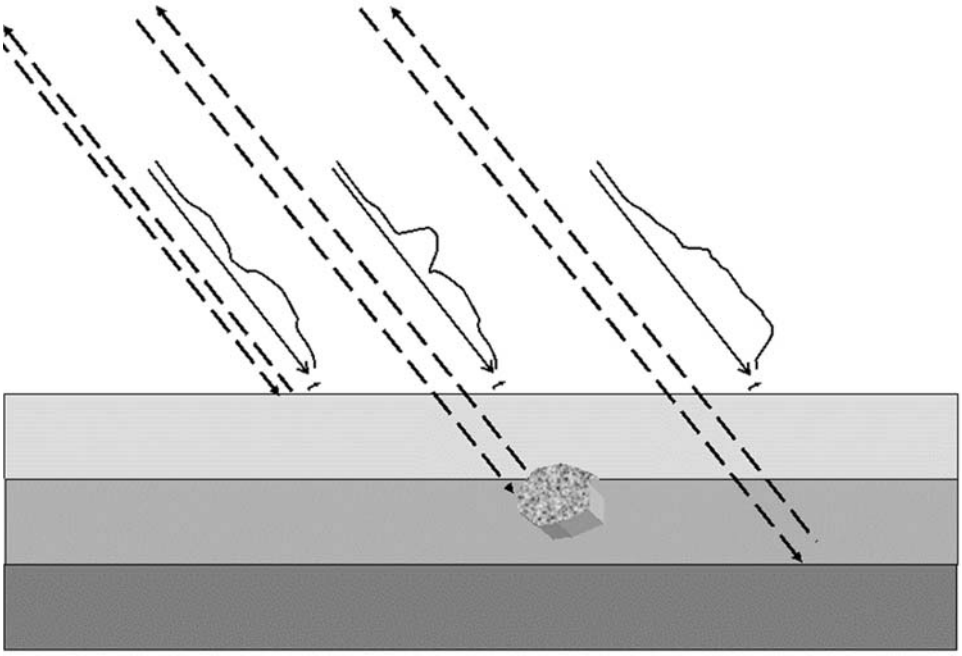

Figure 10.4. Sub-surface penetration can be an important factor in sedimentary terrains. Due to their longer travel times, echoes from buried objects or layers will seem farther across-track than they really are. Interpretation of the resulting images will be complicated by the presence of sub-surface objects and their incorrect positioning.

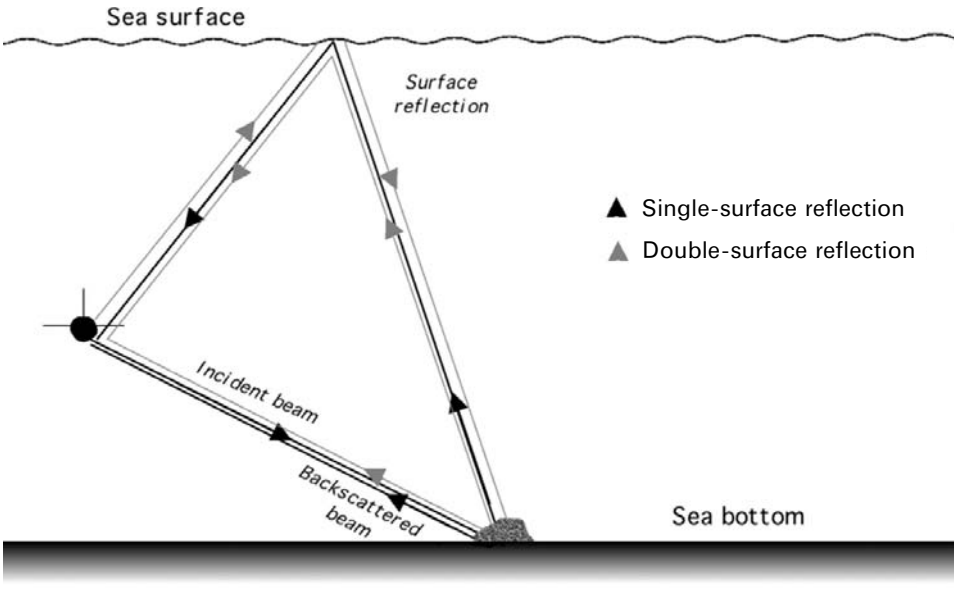

Figure 10.5. Formation of multiples.

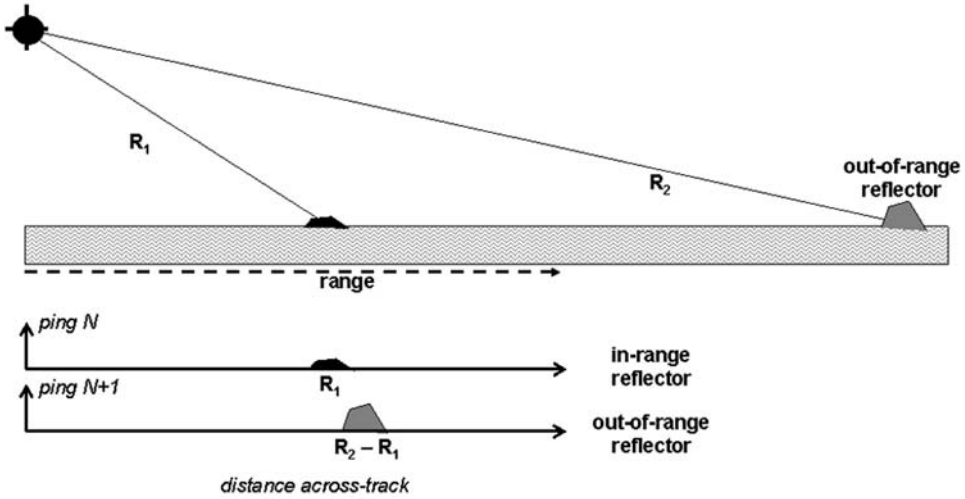

Figure 10.6. Out-of-range targets can be noticed if they are particularly reflective compared with the rest of the seabed. Adapting the pulse repetition frequency (and matching the survey speed) is usually enough to remove these unwanted echoes.

When the water depth is small compared with the ranges involved (i.e., in very shallow water for high-frequency sonars or even in deep water for long-range sonars), the acoustic radiation from the sonar (main lobe and sidelobes) will bounce several times on the seabed and the water surface before being scattered back to the receiver. First reflections from the sea surface are easily identifiable as white lines, at a range corresponding to the water depth (see Section 4.8.4). Multipath interference will be limited in sidescan imagery, because the signal is usually attenuated significantly along the different paths. In some conditions (e.g., in the presence of a strongly contrasted density layer in the water column), residual echoes from previous pings are noticeable (e.g., Tomczak *et al.*, 2002). If targets out of range are still significantly reflective, especially compared with a low-reflectivity seabed, they will also be easier to detect (Figure 10.6). This can happen in harbors with out-of-range reflections from the dock walls (e.g., Fish and Carr, 1990). Multipath interference can also have adverse effects in the processing of phase bathymetry, and the seminal article by Denbigh (1989) shows how it manifests itself during phase unwrapping and how it can be avoided by additional signal processing. Avgerinos (2003) proposed some innovative techniques to improve the processing further

Figure 10.7 shows an example of multiple reflections, acquired by SeaMARC-II in very smooth sea conditions. The meandering channel that occupies most of the image is partially repeated at far range. It is recognized as a multipath reflection because it repeats the first object at farther range and does not fit into the surrounding geological context.

Multiple reflections are also seen on GLORIA images (LeBas and Masson, 1994). They occur mainly in sedimentary areas where the ocean floor is flat and where bottom reflection is strongly specular. In rough and rocky terrains, such as

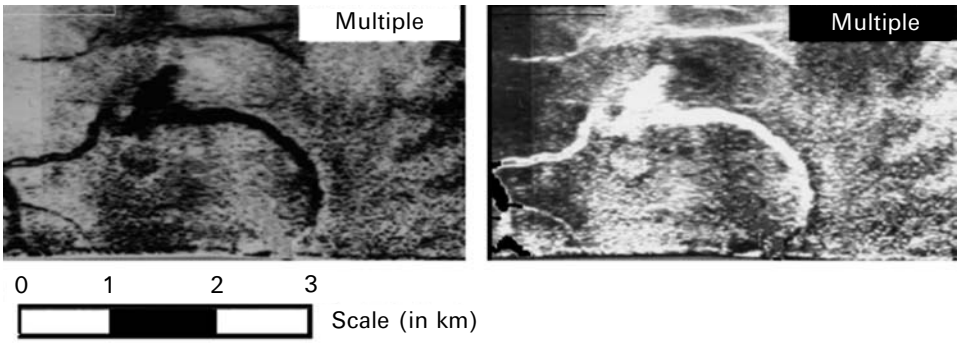

Figure 10.7. Multiple reflections on the seafloor "seen" using SeaMARC-II on the continental shelf off Peru. The original image (left) has been inverted (right) to show gray levels linearly increasing with the amount of backscatter (courtesy R. Hagen of AWI, Germany).

mid-ocean ridges, the dispersal of the specular component, together with the strong backscatter of the terrain, normally masks multiple reflections. On GLORIA imagery, the first multiple reflections usually manifest themselves as a pair of thin bright lines equidistant on either side of the sonar's track. Pairs of higher multiples may appear at greater ranges. In extreme cases, up to five pairs of multiple reflections can be seen. Algorithms for suppression of multiple reflections can be found in articles by Reed and Hussong (1989) and LeBas and Masson (1994).

Another artifact is sometimes observed over flat sedimented seabeds. The sound waves are normally backscattered at the sediment–water interface, but a small proportion penetrates below the seafloor and is scattered by sub-surface reflectors. The two acoustic waves interfere, constructively or destructively, to create interference fringes. Their geometry is similar to that of optical fringes caused by a thin oil film on water or of caustics caused by diffraction of a laser beam. These interference fringes require a transparent sediment layer and a good reflecting layer in close vertical proximity. If the sub-surface layer is too deep, the amplitude differences between the interfering waves are not high enough to create interference patterns. The optimal depth of the second reflector needs to be a whole or a half-multiple of the sonar's wavelength for interference fringes to occur.

Such fringes were first recognized during the survey of the U.S. Exclusive Economic Zone in the NW Bering Sea (Huggett *et al.*, 1992). GLORIA images exhibited strong interference patterns, sub-parallel to the ship's track and 100 m to 2,000 m wide (Figure 10.8). These interference patterns were always sub-parallel to the ship's track, regardless of heading and course changes. If the patterns were related to sub-surface structures, they would be expected to remain similar with varying look-angles. Repeated surveys showed the persistence of these patterns over time, and that they were not related to sea conditions (unlike fringes created by Lloyd's effect, see below). Since then, interference fringes have been observed throughout the world, at quite different frequencies, using SeaMARC-II and TOBI (Figure 10.9). There seem to be no common factors between the geological characters of sediments that

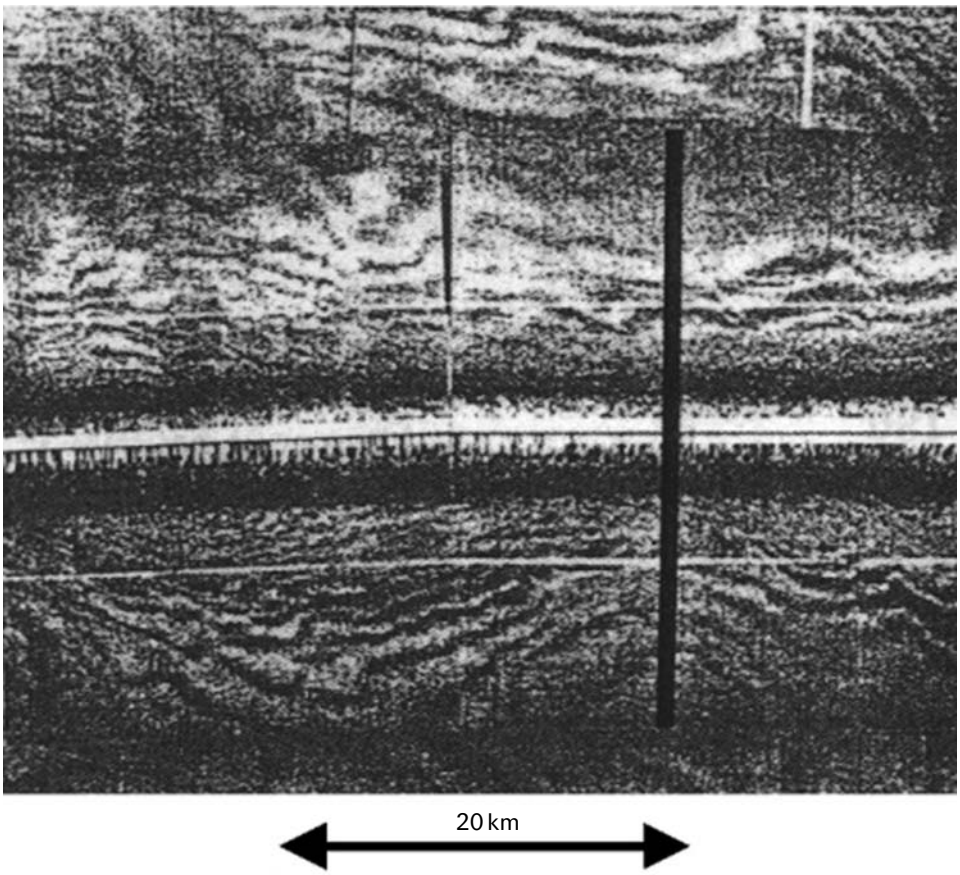

Figure 10.8. Hand-made mosaic of GLORIA paper records from sonar data acquired by the Institute of Oceanographic Sciences, Deacon Laboratory (IOSDL, U.K.) in the Bering Sea, showing interference fringes. The sonar track is the white line in the middle. The high back-scatter bands increase in width with range from the sonar track. Widths vary from 100 m at near range (<5 km) to 2,000 m at far range (22 km).

show interference fringes. The only requirement is that the right acoustic layer lies on a reflective sub-surface layer at a depth appropriate for the frequency of the system.

Interference fringes are not always attributable to rescattering of acoustic waves inside the sediment layers. A local interaction, which sometimes occurs at the surface, is Lloyd's mirror effect, arising from interference between the returning bottom reverberation and its image on the sea surface. To be observed, this effect requires a high degree of coherence in the energy reflected from the sea surface at small grazing angles (i.e., a calm sea, for a start), and a transducer depth which does not exceed a few tens of wavelengths (Somers, 1993). This usually means a hull-mounted or shallow-towed sonar. Otherwise, the fringes are too closely spaced to be resolved. Since the fringes always present themselves as lines parallel to the track, they require

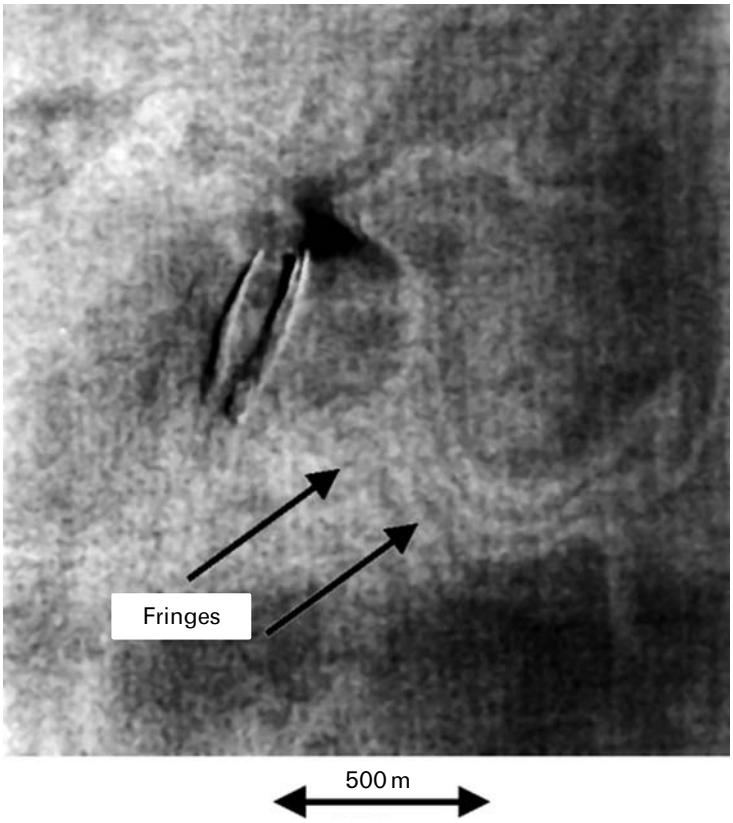

Figure 10.9. Interference fringes "seen" using TOBI in the Madeira Abyssal Plain. They were apparently formed within a first layer of sediments 25 cm thick (courtesy D. Masson, NOC, U.K.).

identical reflection conditions over several pulses, which implies something close to a flat calm sea. This effect has been mainly observed with long-range shallow-towed sonars such as GLORIA. Deep-towed systems cannot generate Lloyd's mirror fringes because the path to the surface is too great. Interference fringes are studied in more detail in Kasatkin (2002), and similar examples to Figures 10.8 and 10.9 are presented from the Sea of Japan and the Barents Sea. Ingham (1975) advises tilting the transducer to produce random interference patterns or, using towed sonars, changing the operating depth to achieve the same effect.

10.3.3 Unexpected features

Interpretation errors may sometimes be related to an incomplete knowledge of the type of local geology. They are, however, generally attributed to unexpected features. Unexpected structures visible on sonar images can include remnants of another type of geological activity, such as old seamounts in abyssal plains. In some cases, they can be attributed to biological activity (schools of fish acting as passive targets, or whales or dolphins transmitting at the sonar's frequency).

Out-of-range returns are another type of unexpected feature. The returns from the acoustic pings sent by the sonar are received at small time intervals. After transmitting each ping, the sonar receives its echoes and stops after a certain time. But the sonar waves are still propagating out into the water column. They may be backscattered and arrive during the receiving time associated with a later ping. These "late echoes" are attenuated so much that they are usually not recorded by the system. However, very reflective targets just out of range will still manage to be recorded and appear on the imagery. These out-of-range returns are very rare, and are generally observed in shallow waters with man-made reflectors such as walls and caissons (Fish and Carr, 1990), or when specific hydrographic conditions are met (e.g., Tomczak *et al.*, 2002).

Unexpected structures are likely to be anthropogenic in nature, as man-made objects can now be found at any depth. Trawlmarks are visible even in the deep abyssal plains. Remnants of other exploration surveys (e.g., drill holes, rig construction remains) can be seen in continental margins. But coastal environments are the most prone to unexpected anthropogenic features. For example, in the last decade, a private company investigated some parts of Loch Ness (Scotland) with sonar. At regular places on the loch's floor, they found large circles of stones. These circles could not be explained as geological structures. Inevitably, rumours about "Nessie's nests" (huge nests where the Loch Ness monster was supposed to live) were rife. The truth was, however, much less romantic. Investigations into the past history of the loch's floor revealed that the last important event was the construction of the Glen Fault Route at the beginning of the century. The large numbers of rocks quarried from the canals linking the lochs together were disposed of by being put on barges and dropped into the lake. These barges opened through the middle, letting the rocks fall to the bottom to form concentric deposits.

Figure 10.10 shows examples of unexpected structures that can be interpreted as anthropogenic, but are purely natural. The "Face on Mars" is a famous image, taken by Viking-1 in the northern latitudes of Mars. In the middle of eroded mesa-like landforms, the optical image shows a huge rock formation, approximately 1.5 km across. The structure resembles a human head, and continues to be called such, despite NASA-JPL's explanations. The rock formation is similar to the other ones nearby, and its strange appearance is explained by the illumination conditions. The Sun was at $\sim 20^{\circ}$ above the horizon, producing long shadows (particularly visible in the south of the structure). These shadows enhanced small topographic variations on the top of the structure, which gave the illusion of "eyes", a "nose", and a "mouth". Pixel-sized speckle (black points) brought about errors during the transmission between Mars and the Earth. Images of the "Face on Mars" taken during later orbits of Viking-1 confirmed the interpretation of the structure as a natural elevated plateau similar to the surrounding mesas. The other image is a TOBI image from the Mid-Atlantic Ridge, north of the Kane Fracture Zone. The image is fully processed for radiometric and geometric distortions. An elongated structure shows up in the middle of the image. It is approximately 500 m long and 200 m wide, and looks very similar to the "Face on Mars". In fact, it corresponds to a seamount, itself part of an axial volcanic ridge (see Chapter 5, "Spreading and subduction"). The ridge is sub-

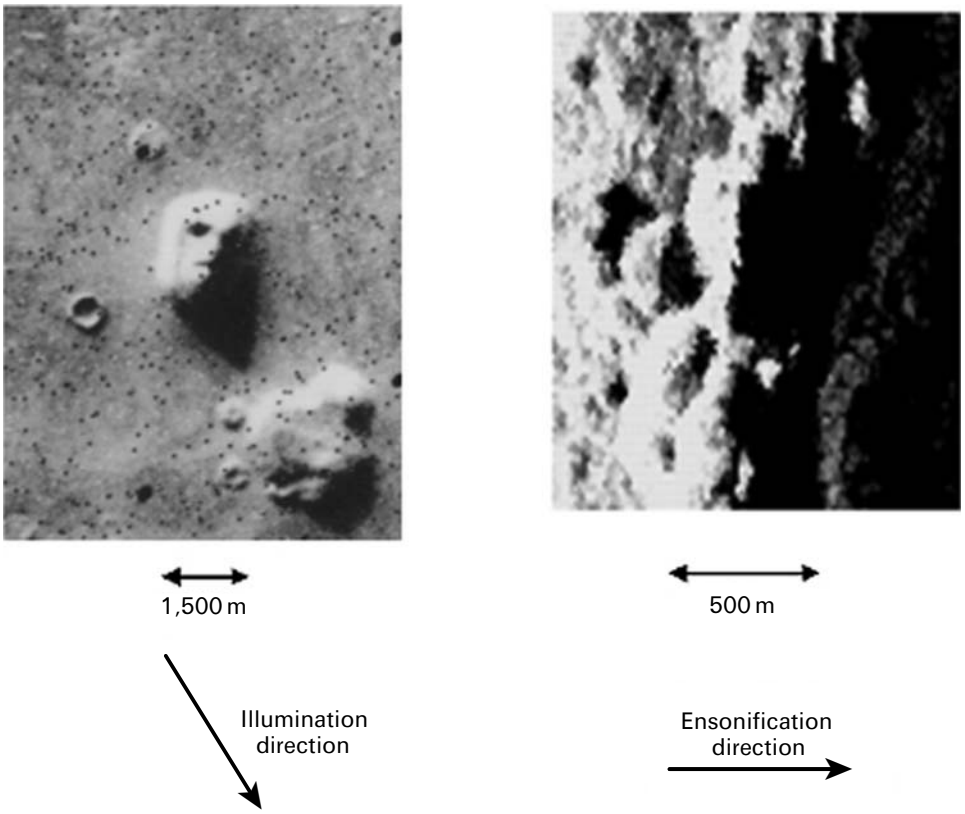

Figure 10.10. (Left) The "Face on Mars" (Viking image P-17384-35A72, © NASA-JPL). (Right) The "Face on the Seafloor" (TOBI imagery). These are two striking examples of artifacts created by the conditions of acquisition and liable to misinterpretation.

parallel to the flight path and ensonified from the left. The high reliefs create important shadows, and small-scale variations in the topography produce small shadows aligned across-track (the "eye", the tip of the "nose", and the "mouth"). A similar structure was seen on Venus during the first Magellan orbit, when the radar imaged at a low angle an elongated seamount with small-scale topography appropriately arranged on the top (the anthropomorphic appearance of the structure also disappeared during the later orbit, when the illumination geometry changed).

10.4 PROCESSING ARTIFACTS

10.4.1 Radiometric artifacts

The first and most frequent cause of systematic radiometric artifacts resides in the acoustic system itself. The sonar cable is a fragile link between the platform and the

recording and processing systems aboard the ship. There are different kinds of cables, depending on the depth and transmit rate requirements: reinforced lightweight cables for shallow operations (e.g., EG&G-272T), armored cables for deep-towed platforms (e.g., TOBI), fiber-optics for high transmission rates (e.g., DSL-120). Lightweight cables have a waterproof coating, but the primary protection, as for most of the other cables, is the conductor insulation itself. The immersed part of the cable (wet cable) is very vulnerable to any unseen obstacle: underwater moorings or fishing gear, and even fish bites. The connections, or terminations, at one end of the cable or the other are likely causes of problems as well. Faulty or broken contacts will cause all manner of radiometric artifacts, from the occasional loss of data to a total blackout of the system. Other sources are related to the platform's design (e.g., cross-talk between badly placed transmitting arrays, or electronic devices with close electromagnetic frequencies interfering with the sonar's electronics). They are usually resolved before operational surveys or are checked before each deployment (e.g., watertight integrity of the electronics).

Another cause of radiometric artifacts is interference from other acoustic sources. Passing ships are discrete sources of acoustic noise, and affect lower frequency, long-range systems particularly. For example, a supertanker radiates enough noise to be very detectable on a GLORIA image at ranges of over 10 kilometers. Higher frequency systems may also be affected when surveying busy shipping routes (as the triangular far-range artifacts of Figure 7.30 showed). The effect of neighboring vessels is often a cross-track band of diffuse noise. It can be suppressed by locally reducing the TVG level close to the nadir (Somers, 1993). A similar phenomenon occurs with icebergs, which are a prolific source of noise and also reflect large amounts of energy. They appear as discrete targets, reinforced by the pronounced surface duct produced by strong surface cooling. Although icebergs do not cast acoustic shadows, they might still be mistaken for objects on the seafloor. The last, and most common, acoustic interference is created by instruments run concurrently, on the survey vessel or on neighboring ships: depth profilers, seismics, etc. They create continuous interference patterns, which are not always easy to remove. The interference can be reduced by increasing the distance between the conflicting instruments, when feasible, or ensuring they operate at different, non-harmonic frequencies.

The type of radiometric artifact common to all sonars is the irregular band of high-backscatter points nearest to the ship's track (Figure 10.11). This band is visible on all the sonar images presented in this book. It is explained by a contribution from near-normal incidence specular and sub-bottom returns, which will only occur within the first few degrees from nadir. Unfortunately, there is no way of directly removing this artifact short of masking it completely. An alternative approach is to create a synthetic backscatter image from swath bathymetry immediately beneath the vehicle's track (Somers, 1993). This approach gives a more continuous image, but is limited to lower resolution sonars like GLORIA.

The across-track attenuation of backscattered waves with increasing distance between the seafloor and the sonar platform is corrected by angle-varying gain (see Chapter 4, ''Sidescan sonar data processing''). Non-systematic variations in

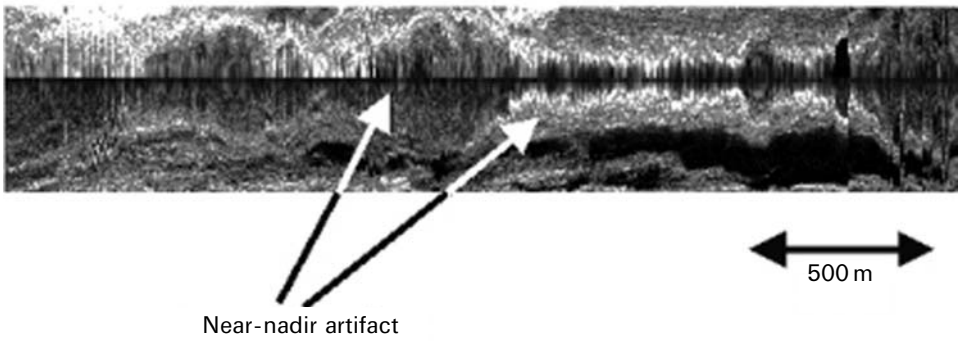

Figure 10.11. Irregular bands of high-backscatter points close to the ship's track are a systematic artifact on all sidescan sonar images.

the beam pattern and the angle of incidence over a uniform seafloor may not be corrected by AVG. Structures imaged in other regions will appear as lower or brighter patches at the same range along the image. Usually they are not difficult to interpret visually, because of continuity with neighboring structures. Problems may arise when employing digital methods that use gray-level statistics (see Chapter 11, "Computer-assisted interpretation"). Correcting algorithms are fortunately available in the literature (e.g., Reed and Hussong, 1989; LeBas *et al.*, 1994; LeBas and Hühnerbach, 1998). To use them effectively, it is important to know what AVG was originally applied to the sidescan sonar data.

Another possible radiometric artifact is the rapid attenuation of the backscattered signal when the sonar platform goes up suddenly (e.g., when hauled back to avoid an obstacle, or if there is a rapid change in seafloor depth). This change is usually too localized and rapid to be corrected with the normal time-varying gain (Figure 10.12), and an appropriate TVG needs to be specifically computed. If the depth change is too great, the sonar receiving times will no longer fit and no additional data will be recorded.

10.4.2 Geometric artifacts

Variations in survey speed

Sidescan sonar data are distorted by variations in the motion of the towfish. Most, if not all, of these variations are accounted for during processing (Chapter 3, "Sidescan sonar data processing"). They are visible if the sonar image has not been fully corrected, or has been badly corrected. The first factor is related to the speed of the survey vessel. Along with the pulse repetition frequency (Chapter 2, "Imagery and bathymetry"), this speed dictates the distance between each swath line. If variations of the ship's speed are not correctly taken into account, the image will be distorted in the along-track direction (Figure 10.13). If the platform speed assumed during processing is higher than the actual value, the swath lines will be positioned too

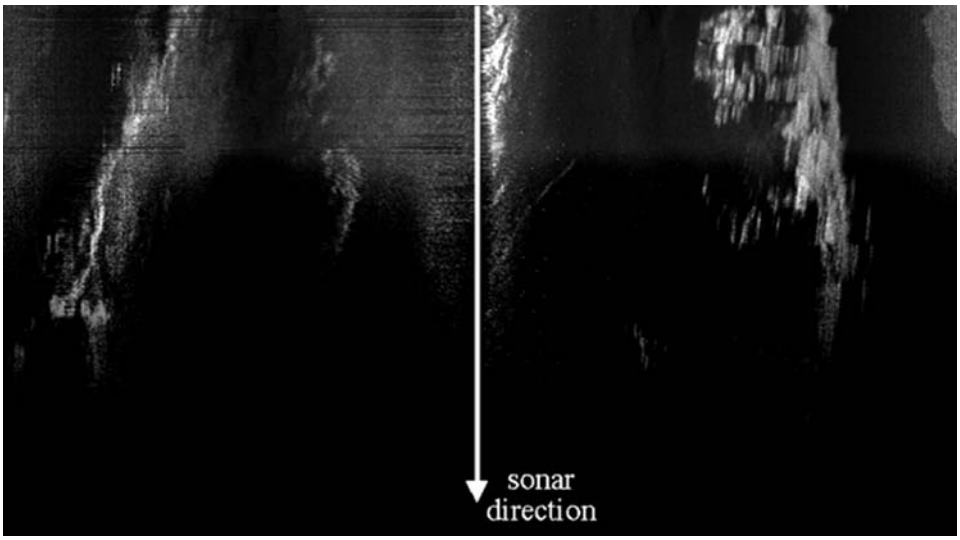

Figure 10.12. Example of sonar imagery acquired when the vehicle is hauled back in a straight line. In less than a kilometer (the length of the image), reflections from the seafloor are attenuated and then disappear. The most reflective and/or higher structures are visible longer.

far away from each other, and the image will be stretched along-track. Conversely, if the platform speed is lower, the swath lines will be positioned too close to each other, and the image will be compressed along-track. In one survey, the speed assumed for processing was 1.5 knot (2.8 km/h). In fact, because of winds and surface currents, the real ship's speed varied between 1.2 knots and 2 knots (2.2 and 3.6 km/h). The survey lines were up to 15 km long, and processed images showed discrepancies as large as 100 m between matching features (such as fault scarps) on adjacent lines. This prompted reprocessing and the reduction of mismatches to a few meters (i.e., close to the limit of resolution of the sonar). It is also important to remember that large variations of the towing speed will cause the sonar platform to pitch either down (when slowing) or up (when accelerating).

Variations in the platform's altitude—heave

Variations in the altitude of the sonar platform are generally accounted for by using a towfish-based altimeter or computing the length of cable out. These methods are not always precise, and some unaccounted fluctuations may occur. If the altimeter's frequency is relatively low (e.g., 3.5 kHz), the signal can penetrate bottom sediments before encountering a reflector hard enough to return the signal. This would cause the altimeter to see the seafloor as deeper than it appears to the sidescan sonar. Conversely, a signal at a higher frequency may be reflected by extremely soft or fluid sediments, or local heterogeneities in the water column. This produces an early return, which shows the seafloor shallower than it really is. In some cases, the

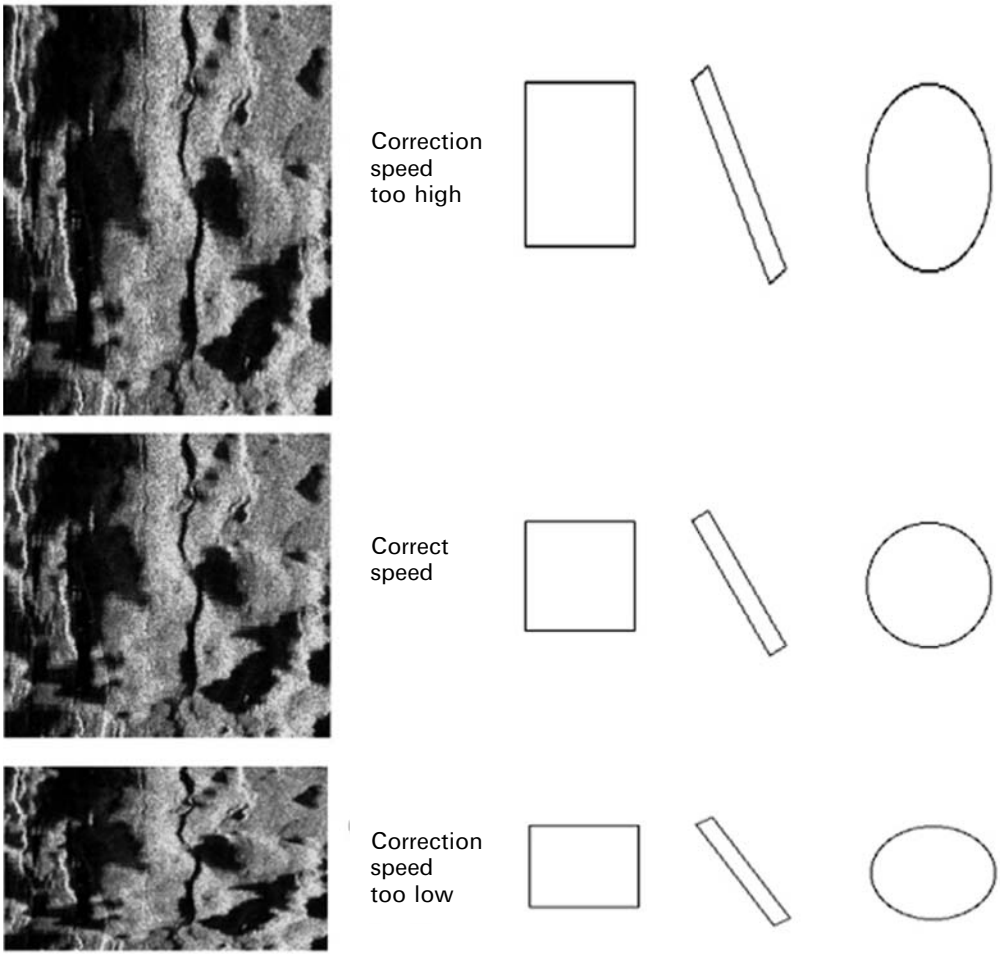

Figure 10.13. Different examples of TOBI imagery, with correct and incorrect speed corrections. The line features at right show the along-track deformation of stylized shapes.

altimeter locks onto these false echoes and gives erroneous depths for an appreciable time (i.e., along-track distance).

The movement of the sonar platform around its nominal altitude above the seafloor is called "heave". If the distance to the seafloor is larger than it should (heave > 0), the sonar will record backscatters from a larger swath than usual (Figure 10.14). But the processing algorithm will assume the swath is the same, and it will place the seafloor reflections closer to the nadir than they really are. Conversely, if the seafloor is closer than it should (heave < 0), the recorded swath will be narrower (Figure 10.15). The processing algorithm will place seafloor structures farther away from the nadir than they should be. Both these processes create across-track distortions of the same amount on each side.

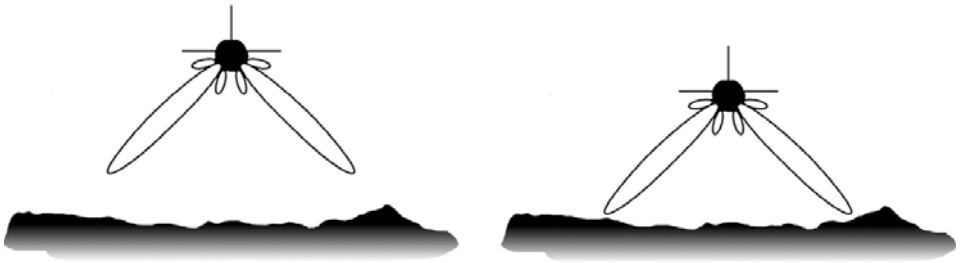

Figure 10.14. When the sonar is at a higher altitude above the bottom the swath width will increase. If the system erroneously records higher altitudes than the real one the image will be compressed across-track. Conversely, if the system records lower altitudes the image will be stretched across-track.

These across-track variations are symmetric and therefore easier to pick up. Figure 10.15 shows a partially processed TOBI image in a mid-oceanic ridge terrain. Aligned along-track, a large axial volcanic ridge is visible in the rightmost portion of the image. Two long white lines span the entire image. They correspond to sea surface reflections and should be nearly parallel to the sonar track. In fact, they show as arcuate features moving away from the nadir. The structures on each side, and particularly the summit line of the volcanic ridge and the fault scarp at the extreme left, are similarly curved. These symmetric variations are as large as 600 meters, and are attributed to unprocessed variations in the platform's altitude above the seafloor.

Unprocessed roll

Roll is the movement of the sonar platform around its longitudinal axis. One transducer will point higher up than intended, and the one on the other side will point lower down (Figure 10.16). Rolling may result in intensity distortions in the area immediately below the towfish because of the rotation of the vertical sidelobes. The transducer pointed up will image structures at a larger range, but the processing system will compress them down to the assumed swath width. Conversely, the transducer pointed down will image at a shorter range than usual, and objects on the seafloor will be stretched by the processing system to accommodate the full swath width. The distortions created by unprocessed roll will therefore occur across-track, and be consistently asymmetric. If two elongated structures are present on the seafloor, the one on the upturned side of the sonar will be positioned closer to the sonar track than it really is, and the one on the downturned side will be positioned farther away from the track.

A sonar towed 100 m above the seafloor, and affected by an unprocessed roll of 10°, will misplace features along-track by 17.6 meters (and more if the height above the seafloor increases). If unprocessed roll decreases to 1° (the limit of resolution of most attitude sensors), the mispositioning will decrease to 1.74 m, much more acceptable for most surveys. Complete mathematical explanations of these variations are given in Anstee (2001) or can be easily rederived from first principles.

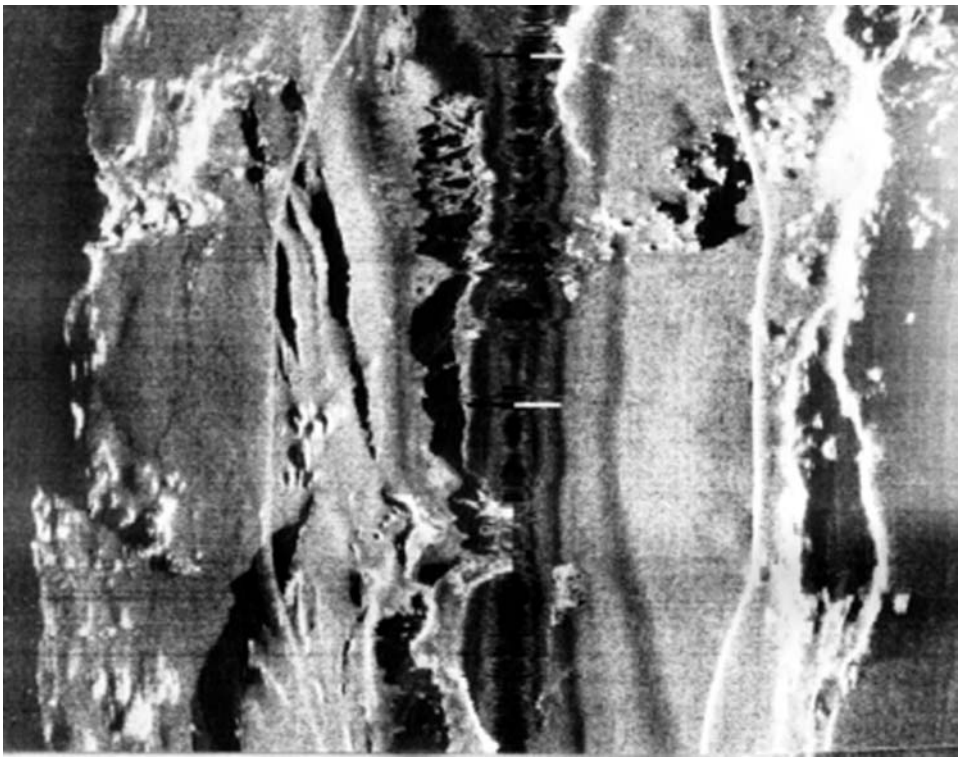

Figure 10.15. Unprocessed variations in the sonar's altitude. This TOBI image is 6 km wide. The sea surface reflections are deviating from straight lines by as much as 600 meters.

Figure 10.16. Unprocessed roll of the sonar platform creates asymmetric across-track distortions of the image.

Unprocessed pitch

Pitch is the orientation of the sonar platform around the horizontal plane (Figure 10.17). When the towfish tilts up (pitch > 0), it scans farther away than intended. The sonar will record a swath line that it will resurvey later. Conversely, when the sonar tilts down (pitch < 0), it will replicate a swath line previously surveyed. Brutal

Figure 10.17. Unprocessed pitch of the sonar platform will replicate previous swath lines (pitch < 0) or anticipate future swath lines (pitch > 0).

and unaccounted changes in pitch will result in structures on the seafloor being suddenly interrupted at all ranges, and resuming after a few swaths (if the pitch goes back to normal). Pitch is usually associated with changes in the towfish's altitude or its speed.

Unprocessed yaw

Yaw corresponds to the side-to-side movement of the sonar platform around its tow path. The swath lines are rotated along the central axis of the platform (Figure 10.18), creating along-track and across-track distortions. The half-swath inside the turn will re-image some features already imaged, but from a different look-angle. The half-swath outside the turn will image some features farther away than intended, and from a different look-angle.

Yaw-like movements in wide swaths can occur when long cable lengths and depressors are used. These movements are referred to as "kiting", and are the result of damaged or improperly attached depressors. Under the effects of bottom currents, or because of problems with the tail fins, the sonar may also exhibit a permanent yaw in one direction ("crabbing").

The variations of altitude, roll, pitch, and yaw are usually simultaneous. The platform's speed, course, and orientation will vary under the influence of underwater currents, changes in the sonar–survey ship geometry induced by wind and sea currents or (in the absence of a depressor weight) caused by movements of the ship communicated to the towfish through the cable. For example, at the end of the survey line, and to start a parallel line in the other direction, the ship will make a 180° turn. If the cable length stays identical, variations in the ship's speed and course will make the cable slacken, the deep-tow sonar will first sink, and then turn. To maintain a constant, safe altitude above the seafloor, the sonar is generally hauled back a little during the turn, which slightly augments the altitude at the beginning of the turn. Both options create variations in altitude, roll (turning more or less in the direction of the turn), pitch (the sonar points upward at varying angles, depending on the speed at which it is hauled back), and yaw (the sonar oscillates quickly around its central axis). State-of-the-art attitude sensors can now measure relative movements with accuracies

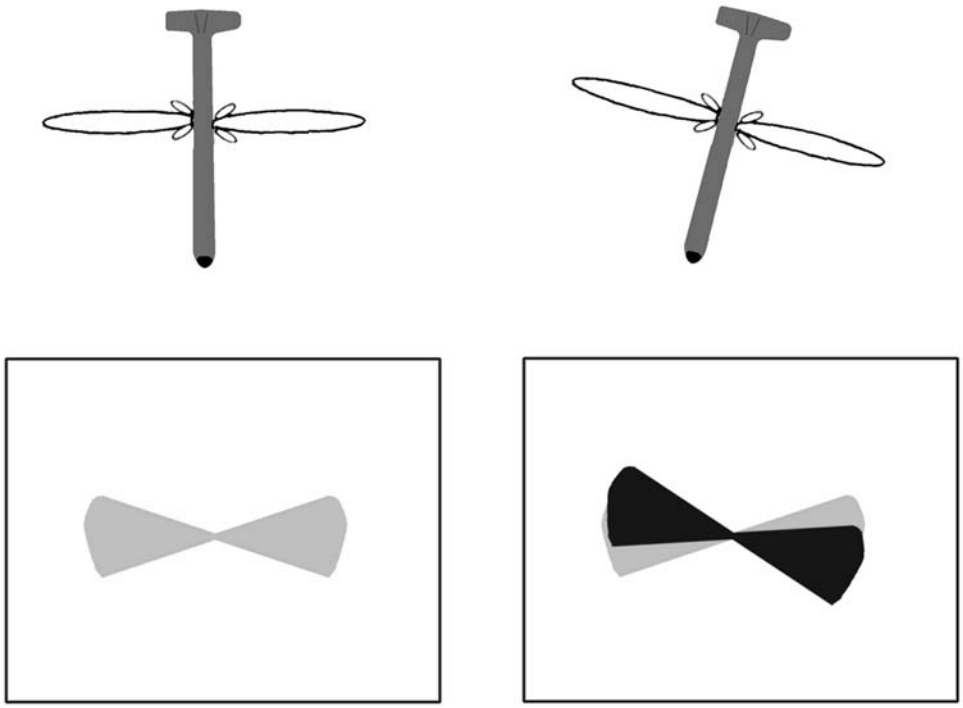

Figure 10.18. Unprocessed yaw of the sonar platform (top) creates asymmetric across-track and along-track distortions of the image (bottom).

smaller than 0.1°, and processing software can correct the images accordingly (see Chapter 4, "Sidescan sonar data processing").

10.4.3 Slant-range correction—layover

Slant-range corrections remap individual pixels from their apparent positions across-track to their true positions (see Section 4.5.1). It assumes a plane seafloor across-track. This can be a problem in areas of high relief, or above regional slopes (Figure 10.19). The first echo to return to the sonar platform will be from point A on the seafloor (i.e., closest to the sonar). This point is higher on the ground than the true nadir, and at some distance from it. Performing a slant-range correction with a flat-bottom assumption will incorrectly assume A is the nadir, and move the central line of the processed image to point B (the real nadir). When the target's echo arrives at the sonar, it is assumed to be at the same depth as the original return. The slant-range correction places it in the image at point D, rather than at its actual location (point C).

For portions of the seafloor sloping up from the nadir of the sidescan fish, the target will appear closer to the nadir than it really is. In particular, topographic features will be positioned systematically closer; they appear to be foreshortened,

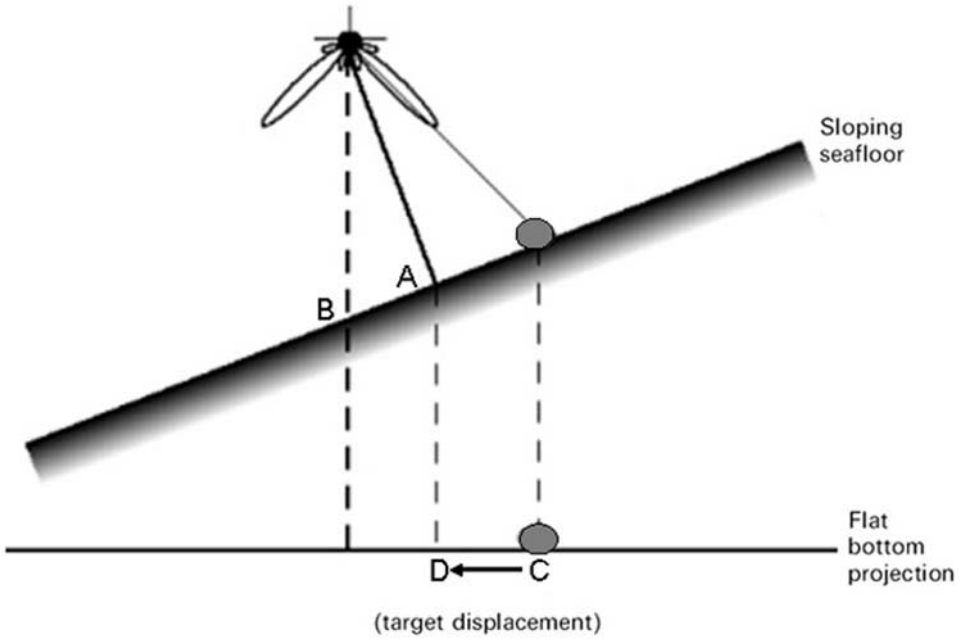

Figure 10.19. Illustration of the layover effect. Structures on the slope facing toward the sonar will appear closer than they really are; structures on the slope facing down from the sonar will appear to be farther away than they are in reality.

or to "lean" toward the nadir. A distant peak would be located before its flanks. This phenomenon is known as "layover". Where the bottom slopes away (down) from the nadir, the target will appear farther away than it really is. These distortions can be important: examples using SeaMARC-II imagery show displacements of up to 1,000 m (for an across-track resolution of 10 m), and an apparent rotation of 20° of fault scarps on slopes (Reed and Hussong, 1989). In mosaics containing parallel tracks with opposite look-angles, features will be displaced in opposite directions.

Correction of layover and foreshortening effects is simple in theory, and lies in determining the actual depth of the target away from the track line. This requires determination of the seafloor slope and the height of the fish above the bottom. Co-registered bathymetry, acquired from phase information or from other sources, is a prerequisite for accurate slant-range correction.

10.4.4 Identifying the origin of artifacts

Image artifacts can be created at different stages in processing if incorrect parameters are chosen, or if some correction stages are omitted. Pre-processing the navigation data (Section 4.2) ensures that the positions of the survey vessel and of the sonar platform with respect to the ship are accurate. Incorrect calculations will show in

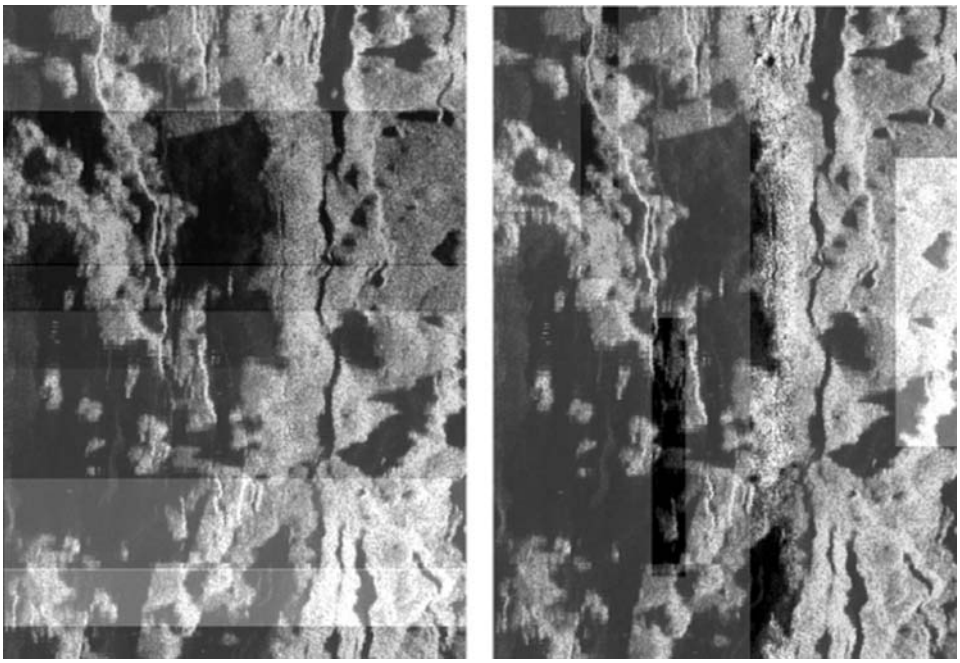

Figure 10.20. Examples of inappropriate time-varying gains (left) and angle-varying gains (right) in TOBI imagery.

mosaics when corresponding structures on adjacent lines are offset or exhibit angles rapidly changing at the intersection of the swaths.

Pre-processing the attitude data (Section 4.2) ensures that outliers and spikes, or long-time offsets with no real significance are removed. If some values subsist, they will create local geometric distortions attributable to the variations in heave, roll, pitch, and yaw (whose effects were shown in Section 10.4.3).

The requantization of individual backscatter values (Section 4.4.1) usually does not create problems. Inappropriate requantization schemes will create flattened radiometric ranges, with small contrasts. Other radiometric corrections include time-varying gain and angle-varying gain. Inappropriate TVG gains will show as series of swaths darker or lighter than adjacent swaths (Figure 10.20). Inappropriate AVG gains will show as darker or lighter patches aligned along-track at definite range intervals.

Radiometric problems leading to across-track striping were explained in Section 4.4. Sometimes, swath lines appear "shifted" across-track. Most of the swath line is black, and the far-range portion shows features which should be at near-range. This is explained by the sonar's altimeter losing the bottom and subsequently timing the backscatter returns inaccurately. One example was visible in Chapter 7 (Continental margins), on Figures 7.7 and 7.8 (Veatch Canyon). The portion at the end of the received beam can be matched back to fit the rest of the canyon (Figure 10.21).

Figure 10.21. Example of an across-track artifact in GLORIA imagery.

10.5 INTERPRETATION OF ARTIFACTS

10.5.1 Output/display artifacts

Often neglected, some artifacts do not come from the original data, but from the way in which they are displayed and presented for interpretation. Up to the beginning of the 1980s, almost all sidescan sonar imagery was made available in near–real time by printing on electro-sensitive paper. This is still the case for small-scale, low-cost surveys and as a backup during other surveys. The thing to remember when looking at paper records is that all radiometric and geometric corrections will not necessarily have been performed. For example, slant-range may be corrected (assuming a flat seafloor, evidently). But anamorphosis would have been calculated using a constant ship speed, supplied by the operator at the time and not always reflecting the actual speed. Structures may be elongated or compressed along-track. This is particularly noticeable when attempting to mosaic paper records of adjacent survey lines: the structures do not always match well, and are sometimes offset by hundreds of meters. Because of the finite size of the paper, geometric corrections taking into account the attitude of the sonar platform are generally not performed; small turns will be projected on the same line, artificially curving linear structures such as fault scarps. There are also risks of saturation or under-saturation, as the dynamic range will differ according to the quality of the printer. When printing for hours at a time, some types of printers will add streaks of artificially uniform data, although the digitally recorded data are fine. Finally, old paper records will not stay constant with time. Some of them will fade, changing the apparent radiometric response of terrains;

others will crumple slightly, mottling the small-scale textures. All these problems seem trivial. They are, however, routinely encountered, and should always be kept in mind when attempting to interpret paper records.

10.5.2 Unexpected features

Interpretation errors may sometimes be related to an incomplete knowledge of the type of local geology. They are, however, generally attributed to unexpected features. Unexpected structures visible on sonar images can include remnants of another type of geological activity, such as old seamounts in abyssal plains. In some cases, they can be attributed to biological activity (e.g., fish, marine mammals). Other examples of unexpected features are related to local hydrographic conditions. Some surveys have, for example, found strange polygonal shapes on the seabed, and optical ground-truthing matches sidescan sonar data to show these structures are real. These shapes were consistently at shallow depths (20–30 m), and analyses revealed they were created at the turn of the tide (T. Garlan, pers. commun., 2007): the incoming tide interferes with waves that are coming back from the shore, and creates these transient patterns. In other cases, the interpreter might be inexperienced or too eager to see a particular feature. The author remembers a survey in which a naval architect, with no prior sonar experience, insisted he could see a Japanese tanker from the 1960s in the data from a calibration run. All the details were there: the length, the width, and the size of what had to be funnels were all matching the technical details of this type of ship. Although the sonar operator was skeptical, a video camera was lowered to this particular spot; it revealed a small outcropping series of old, sedimented lava flows, whose dimensions just happened to coincide with the expected ship.

10.6 CONCLUSION

This chapter is limited in scope and in the number of examples shown. An entire book could be devoted to image anomalies, artifacts, and rare occurrences visible on sidescan sonar imagery. We have tried a more systematic approach and, following the acquisition and processing stages (respectively explained in Chapters 2, 3, and 4), all possible sources of errors and misinterpretations have been reviewed, and their causes and effects explained. Some of these problems are quite commonly encountered (e.g., layover) and some are very rare (e.g., interference fringes). Whenever possible, we have tried to point out possible remedies, either in the operation of the sonar or in the digital processing of the data. Corrections of particular effects specific to certain sonars or operating conditions, and the theoretical background necessary to devise new correction algorithms, are available in the Further reading at the end of the chapter, and in the References at the end of the book.

Hopefully, with the help of the previous chapters, all structures in the sonar images should be interpretable. This interpretation is mostly qualitative; the different structures visible on the seafloor have been shown in their normal context, and can be assigned names and related to their surrounding environment. The progress made in

recent years by computer technology enables the interpreter to go further, to quantify the interpretation, and to detect structures or details that were not readily visible before. These techniques now available for sidescan sonar interpretation are presented in detail in Chapter 11.

10.7 FURTHER READING (*see also* References at end of book)

Capus, C.G.; A.C. Banks; E. Coiras; I. Tena Ruiz; C.J. Smith; and Y.R. Petillot (2008) Data correction for visualisation and classification of sidescan SONAR imagery. *IET Radar Sonar Navig*., **2**(3), 155–169, doi: 10.1049/iet-rsn:20070032.

Cervenka, P.; and C. de Moustier (1993). Sidescan sonar image processing techniques. *IEEE J. Ocean. Eng*., **18**(2), 108–122.

Fish, J.P.; and H.A. Carr (1990). *Sound Underwater Images: A Guide to the Generation and Interpretation of Sidescan Sonar Data*. EG&G Marine Instruments, Cataumet, MA, 189 pp. Available at *http://www.marine-group.com/acoustic.html* (focused on shallow-water surveying of man-made structures).

Fish, J.P.; and H.A. Carr (2001). *Sound Reflections: Advanced Applications of Sdescan Sonar Data*. Lower Cape Publishing, 272 pp. (currently out of print).

Ingham, A.E. (1975). *Sea Surveying*, Volumes 1 and 2. Wiley, New York (rather out of date, but still full of very useful practical advice and a delight to read).

11

Computer-assisted interpretation

11.1 INTRODUCTION

The interpretation of sonar images, and more generally of remote-sensing images, has traditionally been performed visually by trained interpreters. This presents the distinct advantage of using the skill of the interpreter to limits which are often unattainable by computers. But there are also many disadvantages to a purely visual interpretation. First of all, it is subjective: two interpreters with different experience, or different skills, are likely to get different interpretations for some features, depending on their experience of the sonar used or of the environment studied. Visual interpretation is also time-consuming, and a longer amount of time spent on analysis does not ensure higher objectivity. Structural geologists all know that some morphologic trends will be highlighted, unwillingly and unconsciously, when the time spent on interpretation is too long. The other important disadvantage of visual interpretation is that it is qualitative. Objects are outlined, trends and patterns are shown. But their quantitative assessment requires either the interpretation to take place directly on a numeric support (with all the associated problems of screen size and limited range of scales available) or to scan and quantify the interpretation made on physical supports (paper maps, photographs, etc.). The last decade has seen many new useful tools for visualization of data; for example, in 3-D with the ubiquitous Fledermaus software (*http://www.ivs3d.com/*) and the use of immersive environments (based on virtual reality advances) like the ones used in seismic prospecting (e.g., Lin *et al.*, 2000; Shell *et al.*, 2006). Because of their cost and the necessary investment in hardware and software, these systems are still not within the reach of all sonar users, and they will still not replace the need for a full computer-assisted interpretation.

Huge advances have been made in the last two decades in computer technology (hardware), its applications (software), and the underlying concepts (mathematical and physical). Computer-assisted interpretation encompasses the fields of numerical processing, image processing, and information management. It aims at enhancing the

visibility of objects, and relations between objects, that were not accessible previously. In some cases, it can also bring information that was invisible to the human eye for physiological reasons (see Section 11.2.3, ''Texture-oriented analysis''). Most importantly, computer-assisted information brings an objective and quantitative assessment to help the interpreter. The present chapter does not intend to be a complete guide to all aspects of image processing and computer-assisted interpretation. Many excellent books (referenced in Section 11.7, ''Further reading'') have already been published on the subject, and the huge number of articles published each month in technical journals shows it to be an ever-increasing and complex field. Recent advances are also regularly presented at high-quality conferences with underwater acoustics themes; for example, the European Conferences in Underwater Acoustics (ECUA), meetings of the Acoustical Society of America (ASA), the British Institute of Acoustics (IOA), or the Institute of Electrical and Electronics Engineers (IEEE). Rather, this chapter aims at explaining the basics of image processing: what kind of operations can be applied to sonar images, and how they supplement visual interpretation.

Section 11.2 presents what have now become traditional techniques in computer-assisted interpretation. Image statistics are used to enhance the appearance of sonar images prior to interpretation. Contrary to other domains of remote sensing (e.g., satellite imagery), and because of the physics involved, the spectral domain is rarely if ever touched upon during sonar surveys, although Anderson *et al.* (2008) mentions how desirable it would be. The statistical descriptions of sonar images can be used to identify structures or patterns of interest, and Section 11.2 ends with different approaches to mainstream image analysis. Section 11.3 presents the new techniques that are coming of age now, starting with data fusion, geographic information systems, carrying on with neural networks, genetic algorithms, and image compression. The ultimate goal of computer-assisted interpretation is of course the identification and interpretation of all distinctive objects in the sonar images. This is presented in Section 11.4. Voluntarily short, this section offers pointers to some of the leading techniques, which have shown their success with several sonar types and several types of terrains. Artificial intelligence and expert systems are now playing an important role in some neighboring disciplines, such as satellite remote sensing and mountain geoscience (e.g., Bishop and Shroder, 2004). As they are very likely to play an important role in sonar remote sensing in the next decade, their potential for computer-assisted interpretation and the establishment of expert systems is outlined in Section 11.5, along with foreseeable developments.

11.2 TRADITIONAL TECHNIQUES

11.2.1 Image enhancement

To be in a form suitable for computer processing, sonar images are digitized both spatially and in amplitude. The spatial digitization process is called sampling. Because the original sonar images can be too large to visualize and store easily, it

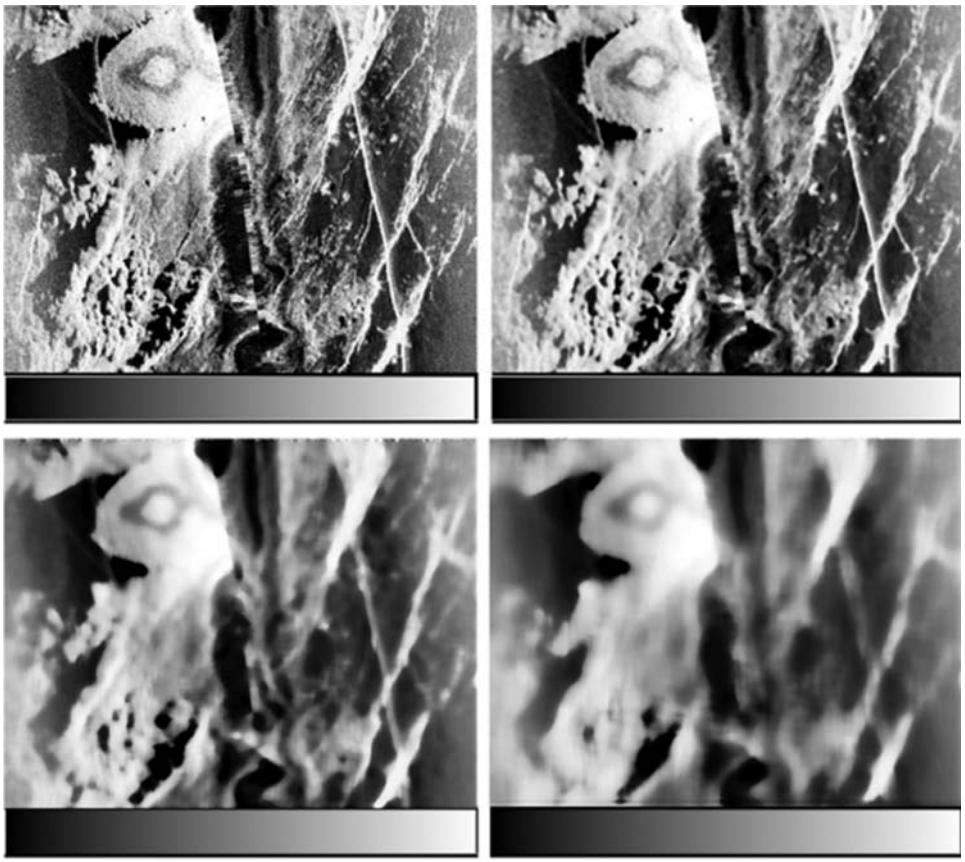

Figure 11.1. Reducing the sampling decreases the resolution and the visibility of small-scale structures. The original TOBI image (top left) has been sub-sampled by a factor of 3 (top right), a factor of 9 (bottom left), and a factor of 12 (bottom right).

may sometimes be useful to reduce the sampling size of the image, therefore decreasing the resolution. For example, a TOBI image originally digitized along 900 columns and 800 lines, with 256 gray levels, will require 703 kilobytes of storage space (Figure 11.1). If the sampling length is decreased by a factor of 3, the image will only require 78 kilobytes (nine times less). By decreasing it again, one can reduce dramatically the space needed for the image. But the original pixel size of 6 meters is similarly degraded to 18 meters and even worse. These effects are shown in Figure 10.1: the original image (top left) has been sub-sampled by a factor of 3 (top right), by a factor of 9 (bottom left), and by a factor of 12 (bottom right). The first sub-sampling does not degrade substantially the visual aspect of the image: all the structures around the flat-topped volcano are still perfectly visible. When the sampling is further decreased (Figure 11.1, bottom-left image), only the larger structures are visible: the seamount and the fault scarps. The smaller details, such as the hummocky mounds, are not

visible. And when the sampling decreases one step further (Figure 11.1, bottom right), only the major faults and the outline of the seamount are recognizable. The degree of discernible detail is strongly dependent on the sampling interval. The latter should therefore be as close as possible to the original footprint of the sonar system.

The digitization of amplitudes is referred to as quantization (see Chapter 4, "Sidescan sonar data processing"). The values are resampled to discrete integer values more adequate for computer handling. Most sonar-processing packages use 16-bit or 8-bit quantization (i.e., integer values between 0 and 65,536 or 0 and 255—$2^8 = 256$ possible values). This is not always the case, and, before, during, or after processing, the values associated with the pixels may be larger or smaller. The reduction in gray-level dynamics (i.e., the number of bits used for the storage of each value) directly leads to a reduction in size of the whole sonar image. The previous TOBI image, stored with 256 gray levels, will use 703 kilobytes. If the dynamic is reduced to 16 gray levels, it will require half as much storage. And if the number of gray levels goes down to 2 ("binarization" of the image), it will require ten times less storage! The gains can be important, but the resolution of the image will be concomitantly degraded (Figure 11.2). The reduction to 64 gray levels still produces an image very close visually to the original. With 16 gray levels, all the small details in the contrasted terrains are lost. And the binarization only produces an outline of the more extreme features in the image: fault scarps facing the sonar beam and shadows.

Although simple, these two examples show the effects on image quality. To be susceptible to a rigorous and exhaustive interpretation, the image displayed and stored should be as close to possible to the original image. Modern storage and computing facilities now allow direct analyses of full-resolution sonar imagery, but the effects of sub-sampling and dynamics reduction should never be underestimated.

The mathematical properties of an image are expressed using different quantities. We saw some of them (e.g., contrast) in Section 4.8. The structures visible in sonar images (e.g., in Figure 11.2) are first distinguished by their varying gray levels. The fault scarps, facing the sonar beam, are bright and homogeneous. The seamount's top is gray and mottled. The terraces between the fault scarps are darker and less mottled, and the shadow regions are homogeneously dark. All these regions present different characteristics. An image with N_r rows and N_c columns can be numerically described by the following statistics:

$$\left.\begin{aligned} \text{mean} = \bar{I} &= \frac{1}{N_r \times N_c} \times \sum_{i=1}^{N_r} \sum_{j=1}^{N_c} I(i,j) \\ \text{variance} = \sigma &= \sqrt{\frac{1}{N_r \times N_c} \times \sum_{i=1}^{N_r} \sum_{j=1}^{N_c} (I(i,j) - \bar{I})^2} \end{aligned}\right\} \tag{11.1}$$

With other statistics like skewness, kurtosis, or energy, these measures are used to describe the whole image or parts thereof, for enhancement or for partitioning. First-

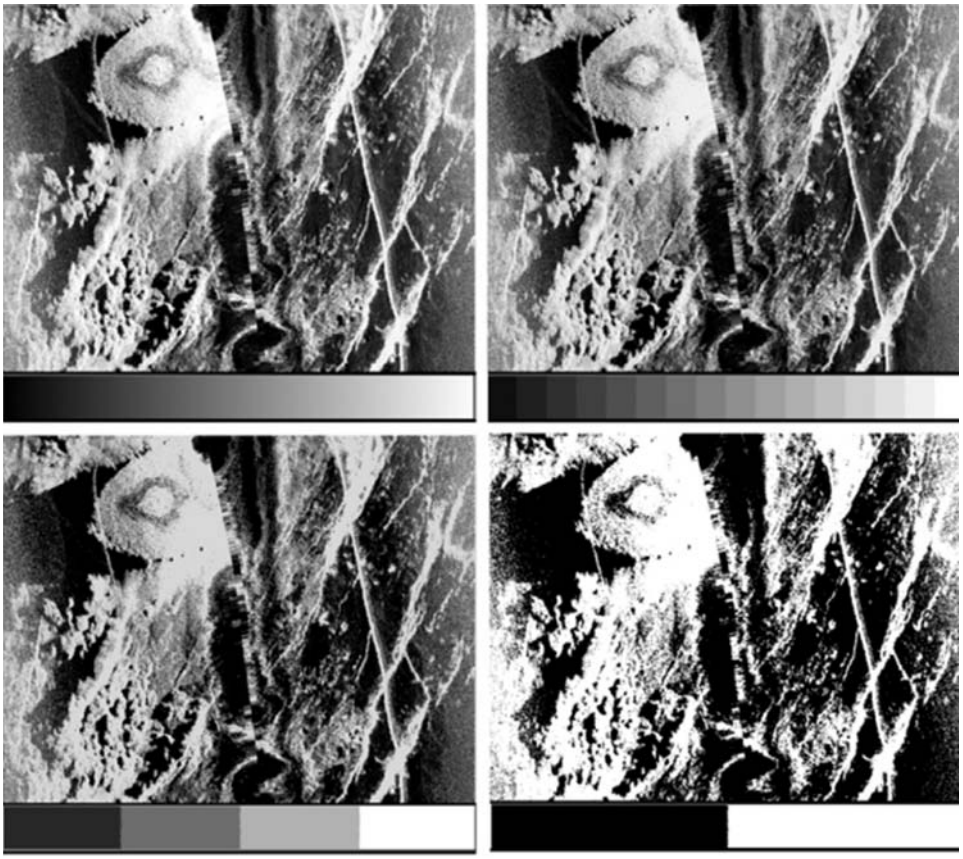

Figure 11.2. The same sonar image, displayed with 256 gray levels (top left), 64 gray levels (top right), 16 gray levels (bottom left), and 2 gray levels (bottom right).

order statistics quantify the global distribution of gray levels in the image. They can be used to distinguish features or regions which are simple enough to be characterized by a few gray levels only (e.g., well-defined fault scarps always facing the sonar). They are not sufficient for more complex features or separate objects sharing the same gray levels.

The objective of image enhancement techniques is not to increase the quality of the sonar image, but rather to increase the visibility of regions of interest. Common operations of histogram manipulation are sliding, stretching, and equalization (Figure 11.3). These techniques are, however, limited, because they aim at transforming the original histogram and making it as uniform as possible. Some applications will require higher detail in homogeneous sedimented regions, whereas others will focus on heterogeneous areas (e.g., volcanic) and not at all on sedimented regions. The interpreter will therefore need to specify which gray level ranges should be enhanced, and which can remain unchanged. This operation is called "direct histogram

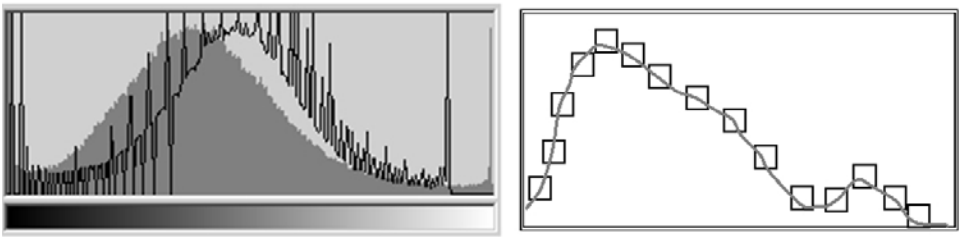

Figure 11.3. Histogram manipulation aims at replacing the current distribution of gray levels (which can emphasize particular levels, or have low contrasts) with either an arbitrary function (left) or a user-specified function (right). The definition of "control points" allows the interpreter to specify which ranges of gray levels need to be enhanced.

specification" and is detailed mathematically in Gonzalez and Wintz (1977). The principal difficulty in applying the histogram specification method to image enhancement lies in being able to construct a meaningful histogram. The first solution is to specify a particular probability density function (i.e., Gaussian, Rayleigh, log-normal, etc.) and then form a "template" histogram by digitizing the given function. The second solution is to specify a histogram of arbitrary shape by forming a string of connected straight line segments, which will be displaced interactively. Because of its flexibility, the direct specification method (also called "piecewise linear stretching") can often yield better results than histogram equalization. Histogram matching applies a predefined set of operations to transform the histogram of an image to resemble the histogram of another image. This process is useful for mosaicking/stenciling (provided the calibrations are similar in both images), and for the detection of changes in the same region (provided the ensonifying geometries are relatively similar).

In some cases, the sonar images may present spurious values due to noise or more systematic problems during acquisition. These values can be removed by smoothing in the spatial or the frequency domain. Smoothing should be attempted with care, as values corresponding to real data (e.g., objects at the limit of resolution of the sonar) may be removed as well. The most simple smoothing method is neighborhood averaging. The value of each pixel in the image is replaced by an average of its neighbors. Depending on the size of the neighborhood, the small-scale details of the image will be more or less filtered. In the case of sonar imagery, a neighborhood of 3×3 pixels is usually sufficient. Mathematically, this corresponds to convolution of the image by a kernel, or filter. Like the image, the kernel is a matrix of values. The convolution of an image I by a kernel J of dimensions $N \times P$ consists in replacing each value $I(i,j)$ of the original image by a new value:

$$\Gamma(i,j) = \sum\sum I(i-k, j-l) \times J(k,l) \tag{11.2}$$

Figure 11.4 shows how smoothing works by considering a spurious pixel (white, gray level 255) in the middle of a uniform region (dark gray, gray level 70). Convolving with a 3×3 smoothing kernel replaces this gray level by the average of its eight neighbors (i.e., 70).

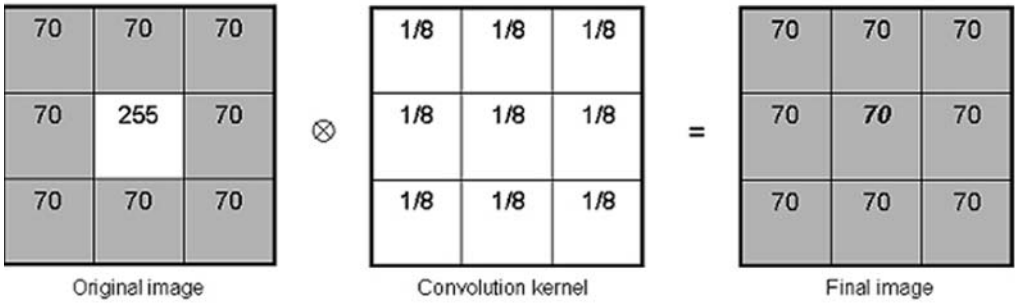

Figure 11.4. Image smoothing works by convolving small portions of the image with an appropriately chosen kernel.

A larger scale application is presented in Figure 11.5 for two sample images. The spurious values are indeed removed by the smoothing, but the image is more "blurry". Depending on the image used and the result desired, other filters can be found in the literature (e.g., Watt and Policarpo, 1998). Another way of smoothing the image would be to take advantage of the frequential properties of spurious values. Sharp transitions contribute heavily to the high-frequency content of its Fourier transform. Smoothing can therefore be achieved by removing or attenuating a specified range of high-frequency components in the Fourier space, and computing the inverse Fourier transform of the image. This method is commonly referred to as "low-pass filtering".

Conversely, the image might sometimes appear too smooth. Sharpening techniques are mainly used to enhance the appearance of edges such as morphologic boundaries. Most commonly used is convolution by a gradient filter. Numerous filters are found in the literature (e.g., Watt and Policarpo, 1998), with varying sizes and coefficients. Sharpening enhances the important transitions between gray levels, and, as such, is liable to enhance small-scale noise and spurious values. This is particularly visible in the image shown in Figure 11.6; small blocks in homogeneous regions (terraces and shadows) become more visible, but their shadows are exaggerated. Since edges and other abrupt changes in gray levels are associated with high spatial frequencies, image sharpening can also be performed in the frequency domain. High-pass filtering of the image's Fourier transform will attenuate the low-frequency components without changing high-frequency information. Computing the inverse Fourier transform should give a sharpened version of the image.

11.2.2 Contour-oriented analyses

The details visible in an image are discernible either as contours (rapid transitions between gray levels) or as textures (the variations of gray levels inside the regions defined by the contours). The contours make up the silhouette of the individual features: spot structures (objects at the limit of resolution of the sonar), line structures (e.g., morphologic boundaries), complete structures (e.g., sedimentation channels, rock outcrops).

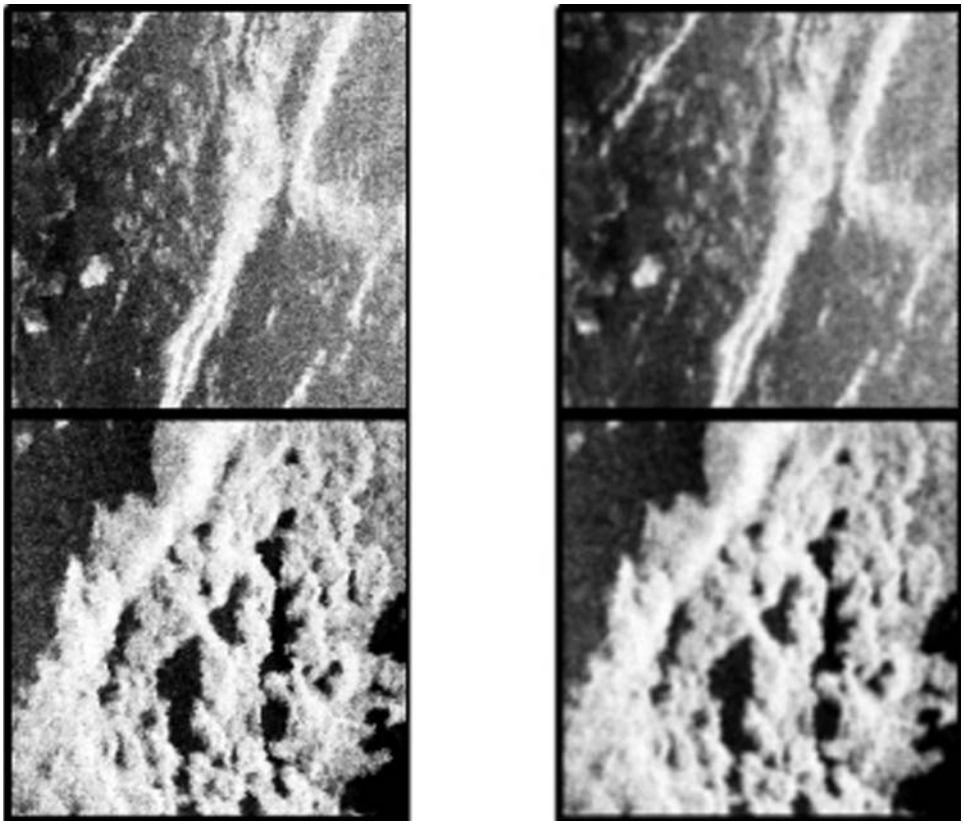

Figure 11.5. Example of smoothing. The original images on the left (top: fault scarps; bottom: hummocky mounds) were imaged with TOBI. Smoothing removes small-scale noise, but loses some details.

An image spot is a relatively small region whose amplitude differs significantly from its neighborhood (Figure 11.7). Its size can vary from just one pixel, if the object detected is at the sonar's limit of resolution (e.g., a piece of man-made debris imaged using DSL-120), to a few pixels (e.g., a small seamount imaged by GLORIA). Spot structures can easily be detected numerically. The easiest method compares the value of each pixel with the average value of the other pixels in a small window around it. If the difference is large enough, the pixel is considered a typical spot structure. More elaborate methods are presented in Watt and Policarpo (1998). One of them consists in smoothing the image with an $N \times N$ low-pass filter, and computing the difference between the value of each pixel in the smoothed image and the mean of its four neighbors (right, left, up, and down) spaced N pixels away. If the difference is large enough, the pixel is labeled a spot. Depending on the geological context and on their size, spot structures may be interpreted differently. There may be spurious values associated with speckle or problems during the acquisition. There may also be

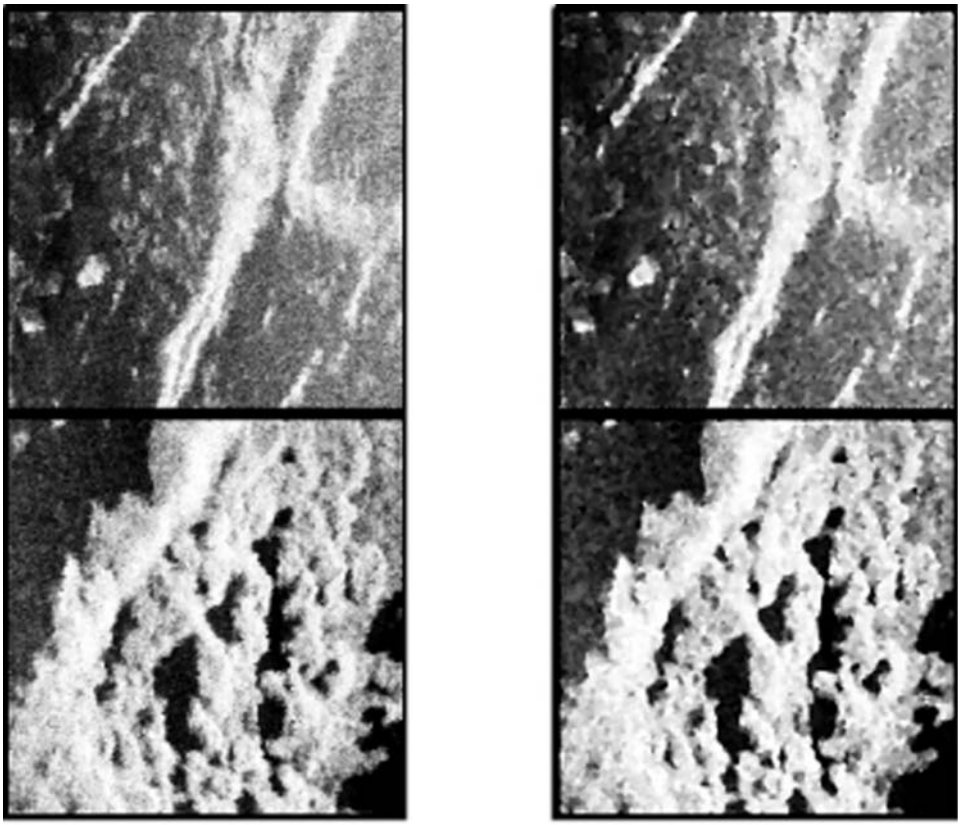

Figure 11.6. Examples of sharpening. The edges and lithologic boundaries are more visible, but noise is added to the image.

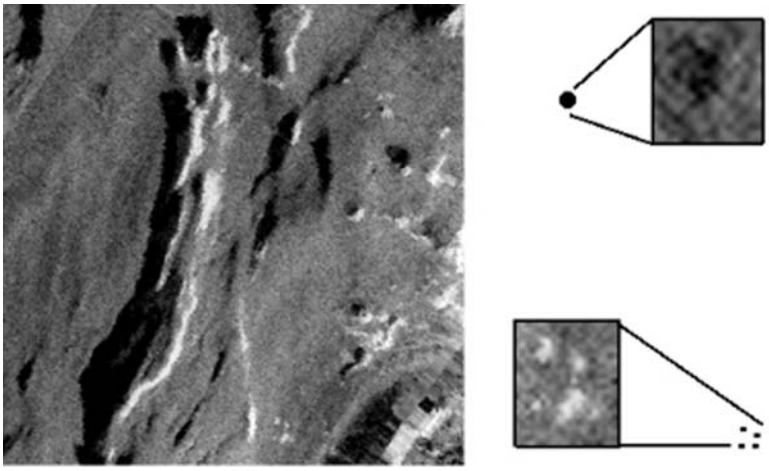

Figure 11.7. Close-up views of spot structures on a high-resolution sonar image. Bright features are facing the sonar beam, dark ones are shadows of objects facing away.

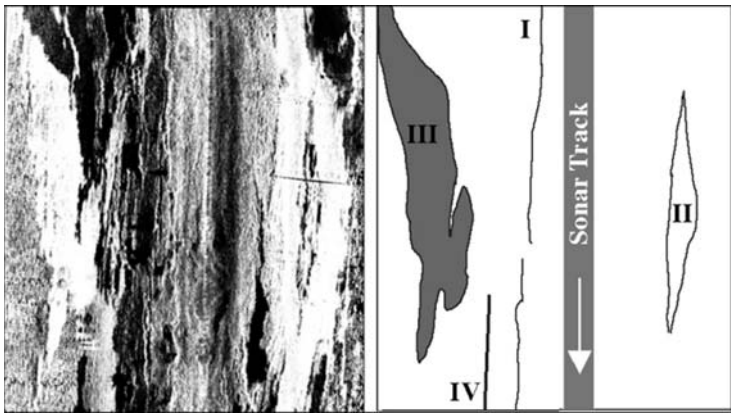

Figure 11.8. The different types of linear structures (contours) are shown in this DSL-120 image: (I) simple line, corresponding to a fissure; (II) closed contour delimiting a lithological region (rock outcrop in the axial wall); (III) unclosed contour, outlining another lithological region; (IV) simple line marking the transition between two regions of differing gray-level ranges.

genuine structures, such as small boulders, hydrothermal edifices, or little seamounts. Statistical analysis of their distribution(s) will help in understanding the local geological processes. For example, small seamounts will be aligned along structural trends and fissures in the Earth's crust (e.g., Lutz and Gutmann, 1995). And boulders spread along a slope and fanning out will show the extent and importance of a submarine landslide.

Individual spots can be organized as line structures, or contours, delimiting regions of rapid changes in gray levels (Figure 11.8). The simplest structures are connected segments, corresponding, for example, to fissures on the seafloor. Closed contours (or unclosed if outside the bounds of the image) will delimit morphological regions (e.g., sediment patches, lava flows). Line detection constitutes a branch of image processing in itself, as no method is always 100% satisfactory and the results always depend on the particular application. The first type of edge detection technique looks at the spectral components of the image. Rapid changes in gray levels occur on short spatial scales (i.e., large spatial frequencies). If these high frequencies can be kept, and the lower frequencies removed or attenuated, the output image should show only the linear structures. In real-world images, the range of spatial frequencies associated with contours will also correspond to small-scale changes inside the regions (local textures), which limits the technique's range.

The second type of technique investigates the spatial content of the image, and looks for large changes in pixel values (first and second derivatives). First derivatives are enhanced by gradient filters (e.g., Sobel, Prewitt, and Kirsch) (Watt and Policarpo, 1998). Each of these filters enhances vertical gradients (i.e., the horizontal lines). The enhancement of contours in other directions is accomplished by rotating the matrices around their central element. Gradient filters enhance particularly well

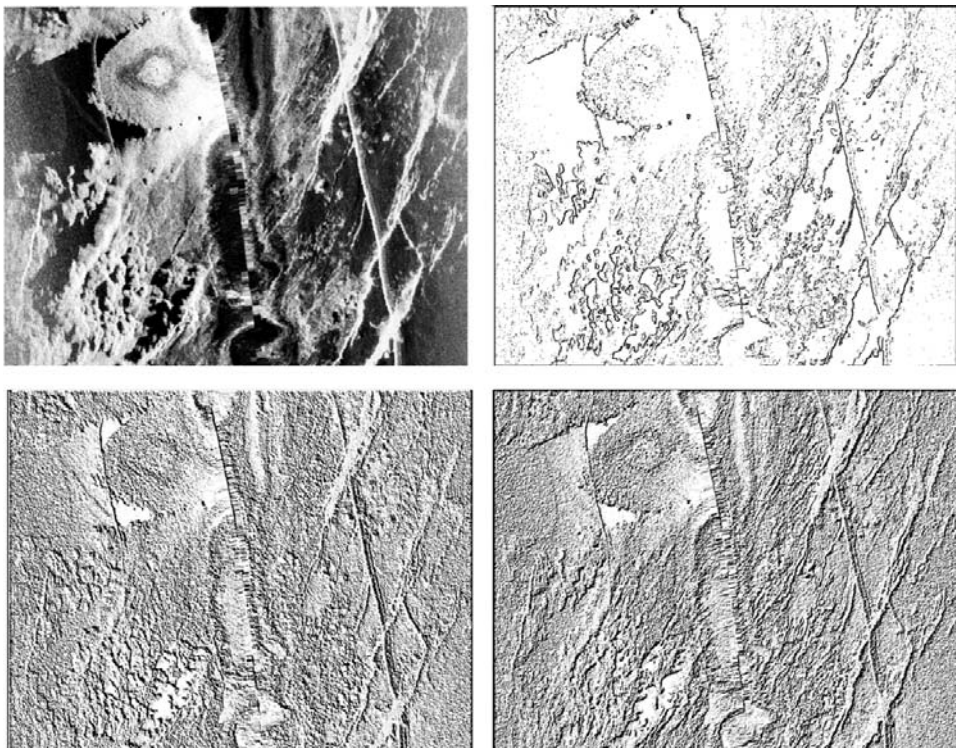

Figure 11.9. (Top) Adaptive filtering of a sonar image. (Bottom) Comparison with individual Kirsch filters oriented in different directions.

the structures perpendicular to the gradient, but attenuate the other structures. To remedy this, it is possible to compute the gradients along all directions at the same time and keep only the maximum ones (adaptive filtering: Blondel *et al.*, 1992). Both approaches are shown in Figure 11.9.

Template matching is used when looking for line structures with pre-established shapes. The Hueckel transform consists in moving a circular window of 40 pixels to 100 pixels across the image (Hueckel, 1971; Pratt, 1978). The line segment separating the moving window into two homogeneous regions is considered to be the local segment of the contour. This transform is not sensitive to noise, but requires many computations and gives erroneous results at angles and intersections (Cocquerez, 1984). The Hough transform is used in satellite remote-sensing applications to find straight lines (e.g., Wang and Howarth, 1989). The fitting of hypothetical lines to curves in coordinate space is replaced by fitting to curves in a parametric space (such as the (ρ, θ) space where ρ is the line length and θ its orientation). This method can be applied to more complex structures than straight-line segments by increasing the number of parameters (which becomes computationally even more heavy). Hough transforms have been applied to detect seamounts in sonar imagery (Keeton, 1994).

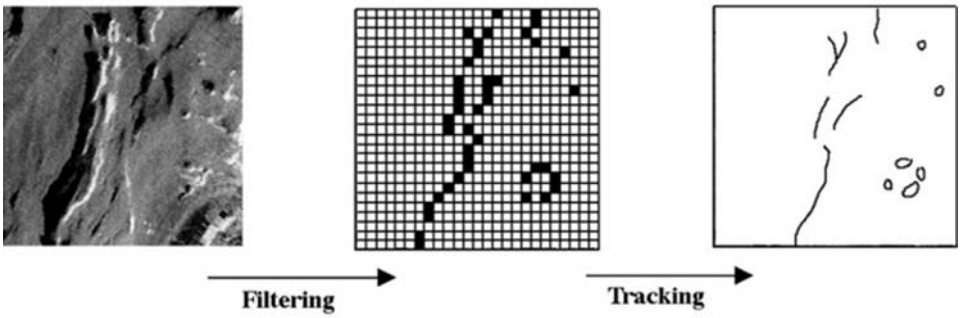

Figure 11.10. Tracking methods aim at transforming the filtered image in an image where the contour lines are properly labeled and quantified.

The last approach to edge detection uses the topological properties of contours. It belongs to the discipline of mathematical morphology (Serra, 1982). The features to detect are compared with simple shapes (disks, segments, etc.), called structuring elements. Mathematical morphology investigates the neighborhood and connectivity relationships of objects, and uses relatively few operations: erosion, dilation, opening, closing, skeletonization. Combined, these operations can help detect contour lines (e.g., Meyer, 1978). However, they are highly susceptible to noise and not applicable to complex structures. As such, they are not widely used for natural images, unless the data have been previously smoothed and filtered.

Once the contour lines have been detected, they can be analyzed qualitatively by eye. But it is possible to fully use the computer power to measure objects (e.g., lengths, sinuosities, directions, etc.) and calculate statistics (Figure 11.10). Different methods have been developed in the last 15 years, for greatly varied applications: anthropometry, character recognition, biomedical imagery, seismic analysis, or mapping of roads in aerial images, and some have been applied to sonar images. They can be divided into two families: ''blind'' methods which use only past information, and heuristic methods which use past information and make assumptions about information to come.

''Blind'' methods assume there is no *a priori* information about the contours. Successive pixels are linked according to logical constraints, without looking for optimal solutions. Three main algorithms have been developed. Generally suited to aerial imagery, the Nevatia–Babu method proceeds in four stages: filtering by 5×5 filters, thinning of contours, search for predecessors and successors of a pixel among its neighbors, and linking of pixels. This technique presents a high signal-to-noise ratio, but loses all the small-scale information. Another method, based on the Hueckel operator presented above, investigates the image statistics. The image is swept line by line, and, each time a contour element is encountered, the contour is followed down to its end. In case of multiple successors to a node, the choice is based on local statistics. The third, and most used, of the ''blind'' methods uses searching patterns. They are pre-established masks superposed on the successive pixels and show where the next successors will be searched. Robinson (1977) proposes 72

possible configurations of 3×3 masks, computationally prohibitive for long structures. A less restrictive searching pattern has also been proposed (Blondel *et al.*, 1992), using the information given by gradient filtering about the likely directions of the structures.

Heuristic contour analysis methods call upon graph theory. Each graph is composed of two sets, one with elements called nodes or summits, the other with ordered series of nodes, called arcs. Searching for a contour line is equivalent to searching the optimal route in the graph. Specific algorithms compare the contour being followed with a reference contour. They orient the searches in one direction or another, depending on a cost function quantifying the differences between the two contours. The definitions of the reference contour and the cost function are the main difficulties in producing good results with these methods. Although a pipeline can be easily modeled mathematically, a submarine canyon is more complex. "Snake-contouring" techniques have also been used with success on complex sonar images (e.g., Reed *et al.*, 2003). These methods are generally computationally demanding, but show definitive improvements upon the earlier applications to sonar images.

The detection and following of contours, associated with the range variation of backscatter, have been used by some to justify the derivation of bathymetry from the imagery alone ("shape from shading"). As seductive as the goal (not needing bathymetry measurements) may be, the practical applications have always left much to desire. Figure 11.11 shows its use in a relatively simple terrain, a portion of the active

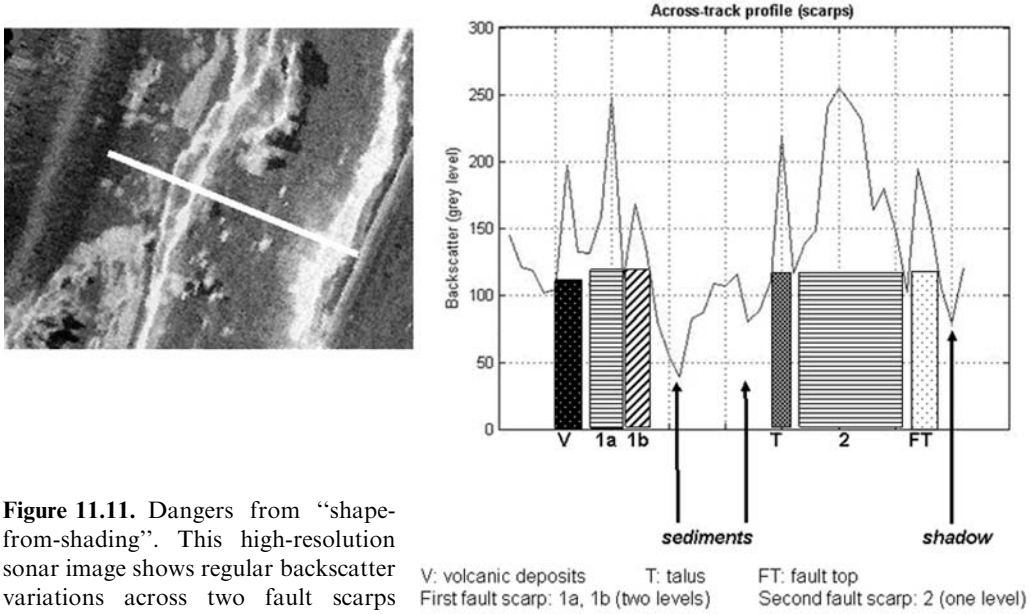

Figure 11.11. Dangers from "shape-from-shading". This high-resolution sonar image shows regular backscatter variations across two fault scarps parallel to the sonar track. The fault scarps are clearly identified from the peaks in backscatter but using cumulated values, or "correcting" them with made-up factors to fit what we think is happening, could give a completely wrong idea. See text for detailed explanations.

segment of a mid-oceanic ridge, imaged at a right angle to the actual bathymetric contours. The topography obligingly increases by steps from left to right. The first scarp is divided into two levels (noted 1a and 1b on the figure): they are sharply defined and, because of the distance to the sonar track, are likely to be relatively steep but not too high. But what about the second fault scarp (2)? Is it much steeper (i.e., reaching higher), or is it more inclined, and not reaching as high? The profile also shows zones of volcanic deposits (V) and talus (T) with similarly high backscatters. An automatic detection technique might mistake them for other scarps and, if cumulating/correcting, add them (wrongly) to the overall topographic trend. Finally, note how the flat sediments vary in backscatter, with lower values below that of the far-range shadows. So-called "shape-from-shading" techniques generally work well with optical imagery (e.g., for the recognition of shapes on a factory line) but are not adapted to sidescan sonar imagery, and the few articles that have been published on the subject have always failed to compare their results with actual bathymetry.

11.2.3 Texture-oriented analyses

Contours enclose areas often characterized by repetitive structures or patterns (Figure 11.12). These repetitions are referred to as textures, and have two main components: statistical (the repetition of a local pattern in a region large in comparison with the pattern's size) and functional or constructional (the decomposition of this pattern in a non-random arrangement of elementary parts with similar dimensions). For example, in Figure 11.12 the sediments exhibit a smooth texture (small variations in gray levels, no discernible spatial organization); the tectonized area shows a more contrasted image, with a preferential (vertical) direction along which the faults and fissures are oriented; and the hummocky mounds have a smaller contrast and the sub-circular structures are not aligned along any preferential direction.

Definitions of texture are quite general and do not lead to simple quantitative measures. Textural measurements can be extracted from the image using various

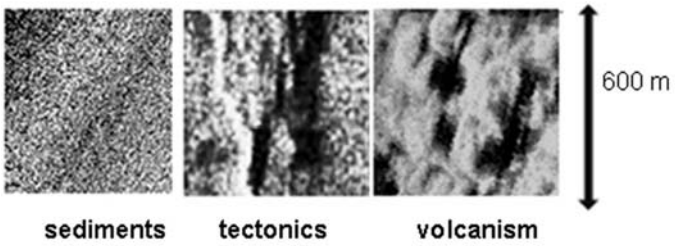

Figure 11.12. Examples of different textures discernible in sonar images (from the TOBI image shown in Figure 11.9). (From left to right) Sediment-covered areas; tectonized area with faults and fissures; volcanic area. All these textures are consistent over fairly large areas (600 m = 100 pixels in this case), but this does not always happen.

techniques:

Structural methods	Auto-regressive models (AR, ARMA, ...) Markov-type models
Statistical methods	*Global* Filtering Auto-correlation *Local* First-order statistics Second-order statistics

Structural methods assume there is an order underlying the local textures and try to model it mathematically. They endeavor to characterize textures in terms of their primitives (basic elements of textures) and the placement rule governing their arrangement within the image. Auto-regressive (AR) models are quite recent. Working in the frequency domain, they assume that each pixel value is a linear combination of its surrounding values, plus some white noise. The number and values of the parameters in the linear combination define the type of AR filters (Max, 1985). Variants are the ARMA (auto-regressive moving average) and CAR (circular auto-regressive, using a circular window) models. Local textures are defined by the AR models they can be associated with. These methods have proven very useful in fields like robotics (e.g., Wang and Howarth, 1989) but they risk being highly sensitive to the noise always present in sonar images. Other models are more mathematical. Markov random fields represent local interactions between neighboring pixel values in terms of Gibbs energy functions (e.g., Nguyen and Cohen, 1993). They have been applied to the recognition of basic geological units in sidescan sonar imagery (Jiang *et al.*, 1993) and are increasingly used in other sonar applications (e.g., Mignotte *et al.*, 2000).

Statistical methods do not assume any order but measure the variations of local or global textures. First-order statistics quantify the global distribution of gray levels in the image. They are a first approach toward texture quantification. Although some geological regions can be coarsely recognized from distinct intervals of gray levels, a natural image cannot be described on the basis of its gray levels alone (e.g., Haralick and Shapiro, 1985; Blondel, 1996). It is more useful to describe the regions by their statistics (i.e., mean, variance, skewness, etc.). Second-order statistics quantify the spatial relationships of gray levels in the image. Experiments on human vision demonstrated the eye could not always distinguish between textures with different second-order statistics, proving the advantage of computer-based methods. The technique most commonly used in remote-sensing studies in general (e.g., glaciology, meteorology, land cover analyses) uses gray-level co-occurrence matrices (GLCMs). GLCMs address the average spatial relationships between pixels of a small region (Haralick *et al.*, 1973). The textural information is described by a set of several matrices $\{P_{\mathbf{D}}(i,j)\}$. Each element $P_{\mathbf{D}}(i,j)$ expresses the relative frequency of occurrence of two points, with respective gray levels i and j, at a distance $\mathbf{D}(d,\theta)$ from one

another. If the image is quantified with NG gray levels, the GLCMs will be $NG \times NG$ arrays. They are computed on finite windows,of dimension $WDSZ \times WDSZ$. In homogeneous regions, the differences between gray levels will be low, and elements close to the diagonal of the GLCMs will therefore have higher values. Less homogeneous regions will yield higher differences between neighboring gray levels, and the resulting GLCMs will therefore have higher values farther away from the diagonal. More detailed discussions of the variations of co-occurrence matrices with images are presented in Haralick *et al.* (1973). Co-occurrence matrices are not easy to interpret directly, and they are more effectively described by statistical measures called indices. More than 25 textural indices are available from the current literature, and their usefulness to different types of sonar imagery has been effectively demonstrated (e.g., Reed and Hussong, 1989; Blondel *et al.*, 1993a; Blondel, 1996; Huvenne *et al.*, 2002; Gómez Sichi *et al.*, 2005; Hühnerbach *et al.*, 2008; Blondel and Gómez Sichi, 2008).

11.3 NEW TECHNIQUES

11.3.1 Data fusion and Geographic Information Systems

Sidescan sonar imagery is greatly enhanced by the presence of bathymetry, if possible co-registered and at a comparable resolution (which is increasingly accessible now with interferometric sonars). Where are the fault scarps and the slopes? Do the local structures observed on the imagery have a bathymetric expression? Are these bright homogeneous terrains bright because they are facing the sonar, because they are extremely rough, or because the radiometric values are saturated? Answers to these questions, and many more, can be found or checked with precise knowledge of the local topography. Bathymetry can also be incorporated into the processing of sonar imagery, by refining the slant-range corrections and adding terrain corrections to the backscatter laws in use (see Chapter 4, "Sidescan sonar data processing"). The combination of bathymetry and sidescan sonar imagery into three-dimensional images also has a definite visual impact, as several of the figures in this book show. Alone or merged into "fly-through" movies, these 3-D presentations help in visualizing the overall environment (e.g., small objects on the seabed or clusters of hydrothermal vents). The increasing accessibility of 3-D visualization software and the budding use of immersive environments (e.g., Shell *et al.*, 2006) make these techniques even more promising.

Other types of information can be useful to constrain interpretation (Table 11.1). Previous surveys, at a larger scale, may have produced geological maps, so that one knows, for example, that the terrain being interpreted is in a sedimentary context and on a continental slope. Additional geophysical data include magnetism (from aerial, surface, or water column data), gravity, or seismics, which provide some insights into larger scale structures. Vertical probes or deep-towed vehicles provide some physical/chemical information about the processes at play in the water column: heavy currents, a large presence of hydrothermally originated particles in suspension in the water, high temperatures in specific spots, etc. Dredges take samples along a linear

Table 11.1. Additional sources of information, other than bathymetry, can help to better constrain interpretation.

Additional sources	*Scale*	*Resulting information*
Geological maps from previous surveys	Large	Geological context at the time of these surveys
Magnetics	Medium	Age of the seafloor and localized heterogeneities
Gravimetry	Medium	Density of the seafloor
Seismics	Medium	Sub-surface structures
Water column data	Small	Presence of active processes such as hydrothermalism or turbidity currents
Dredges	Small	Geochemistry and surface cover (e.g., serpentinization, hydrothermal deposits)
Cores	Fine	In-depth geochemistry at specific points
Profiler data	Fine	Surface sedimentation and very shallow sub-surface structures
Optical data	Fine	Ground-truthing

portion of the seafloor and provide some information about the surface (e.g., the presence of serpentinites or hydrothermal deposits). Vertical cores give point information which is more precise and specific. More systematic information about the sedimentary cover and the eventual presence of shallow sub-surface structures is available from analysis of the profiler data usually recorded simultaneously with sidescan sonar imagery (see Chapter 6, "Abyssal basins and polar seas"). Finally, the most sought-after source of additional information is optical ground-truthing, whether it be from manned submersibles (e.g., *Nautile*), deep-towed platforms (e.g., *Jago*), or more autonomous vehicles (e.g., *JASON* or *ISIS*).

These separate strands of data, with their respective resolutions, can be combined into spatially referenced relational databases, known as geographic information systems (GISs). They are built from spatially referenced features. The geographical element, also called the locational or spatial element, provides the position (x, y, z coordinates, such as latitude, longitude, and depth below sea level). It is associated with a description of the feature, usually called an attribute, or, sometimes, a statistical or non-locational data element. For example, the point location of a core sampling is a geographical element used to provide a reference for a geophysical attribute describing the type of seafloor. Geographic information systems

indiscriminately use point, raster, or vector data. Examples of point data are locations of samples and the associated results (e.g., type of seafloor, biological activity recorded, current measured). Examples of vector data are the vehicle's navigation, bathymetric contours, pipeline routes, etc. Vectors with identical start and end define areas are often referred to as polygons. Examples of polygons are political boundaries such as Exclusive Economic Zones, or zones of homogeneous surface geology. Examples of raster data are images of sonar backscatter such as those presented in this book, bathymetric maps, etc. These different types of representation are usually stacked concurrently and called layers. In a typical GIS application, the first layer would be the sonar imagery (raster), the second layer the bathymetric contours (vector), a third layer the location of cores (point), and a fourth layer the geological interpretation (vectors and polygons). These styles of representation have different advantages, depending on the application. Vector data are feature-based, while rasters are cell-based: vectors therefore represent shapes more accurately. But they sharpen the boundaries, whereas raster images are able to represent gradual transitions between regions. The other main difference is the computer cost of these representations: vector data require less storage space but are more demanding computationally and slower to process than raster data. The number of GIS packages and applications is increasing exponentially, as can be seen in the technical literature (e.g., the *International Journal of Geographic Information Systems*). ARC/INFO has become a *de facto* standard, and major mapping software like ERDAS or processing software like CARIS fully interface with it.

The concept of GIS was still new at the time of the *Handbook of Seafloor Sonar Imagery* and has now come of age thanks to technological advances and increasing user awareness. But GISs are much more than just repositories of information, and they can be used to query relations between datasets, becoming decision support systems (DSSs: see Blondel and Caiti, 2007 for a sonar-related example) (Figure 11.13). CARIS/LOS, for example, can help with the precise definition of exclusive economic zone boundaries and the support of Law of the Sea applications to international bodies. Rhind (1990) and Maguire *et al.* (1991) distinguished six types of problems that could be solved with GIS (Table 11.2). The location question consists in querying the database to determine the types of structures present at a certain place (e.g., what is the structure at this latitude and longitude?). Conversely, the condition question consists in finding the location of specific features (e.g., where are the fault scarps less than 1 km away from the pipeline route?). The trend question consists in monitoring how things have changed over time (e.g., what is the change in sediment distribution in this area of the harbor?). The other problems are more complex and require spatial analysis as well. The routing problem involves computation of the best route (safest, shortest, flattest, etc.) between several points (e.g., what is the safest and shortest route to lay a cable?). The pattern problem involves description and comparison of the distribution of specific structures, in order to understand the underlying processes accounting for their distribution (e.g., is there some common geological setting to all hydrothermal deposits?). The modeling problem consists in simulating the answers to different models (e.g., which areas will be affected by a submarine landslide?).

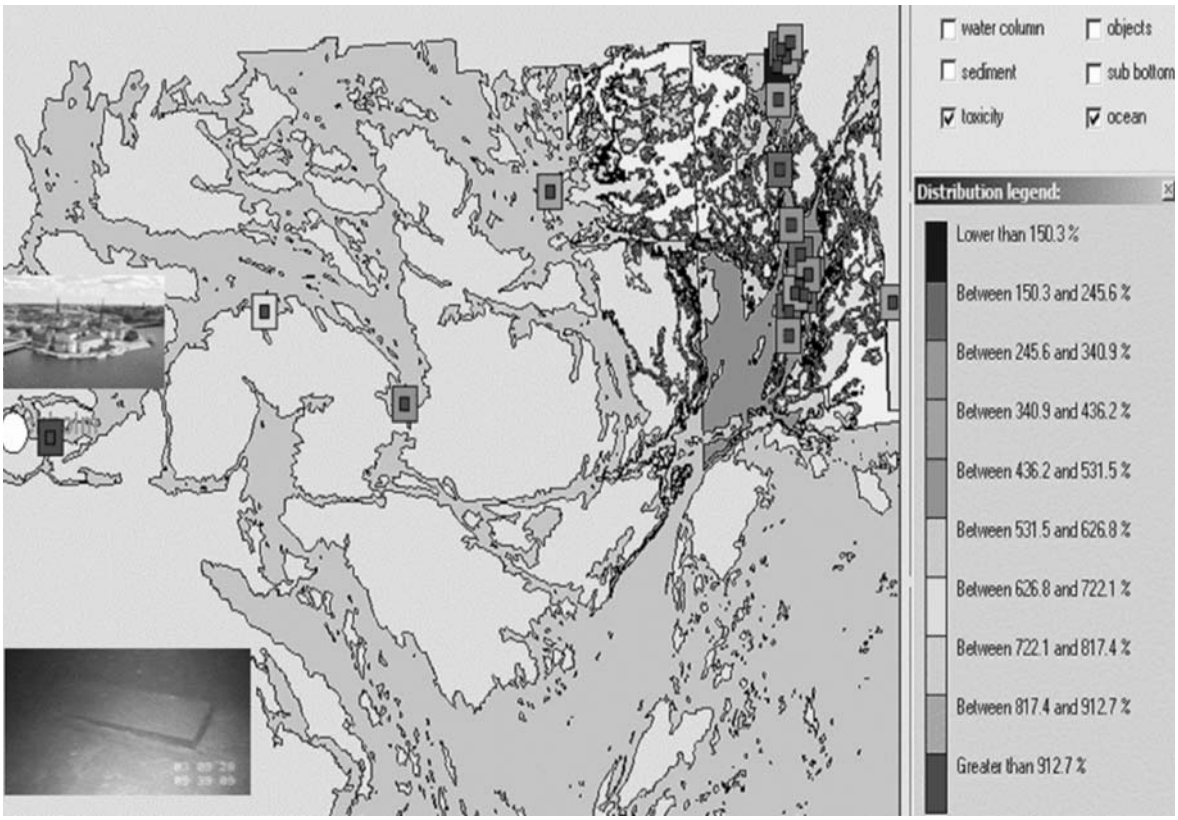

Figure 11.13. Geographic information systems can now be upgraded into decision support systems (DSSs). The European Commission's SITAR project built such a DSS, combining different acoustic datasets with biotoxicology measurements and video ground-truthing to investigate the risk caused by toxic waste dumped at sea (Blondel and Caiti, 2007).

Table 11.2. Geographic information systems can be used to solve many types of problems (after Rhind, 1990 and Maguire *et al.*, 1991).

1	Location	What is at . . .?
2	Condition	Where is it . . .?
3	Trend	What has changed . . .?
4	Routing	Which is the best way . . .?
5	Pattern	What is the pattern . . .?
6	Modeling	What if . . .?

Some of the early applications of GIS to sidescan sonar data included the analysis of small-scale fissuring at fast-spreading mid-ocean ridges (e.g., Wright *et al*., 1995) or the relationship between hydrothermal and other ridge processes (e.g., Blondel, 1996). Many other applications, often much more complex than these early steps, have since been published, and current trends in GIS usage are turning toward fuzzy theory (for imperfectly located or measured data), data mining (to find unexpected relations between datasets), and artificial intelligence.

11.3.2 Neural networks and genetic algorithms

Neural networks are a first example of using artificial intelligence to solve problems related with (generally) the classification of sonar data or the choice of the most appropriate processing parameters. As routine-oriented systems, they get standard data and perform simple, repetitive tasks, modifying them until stable processing is achieved (e.g., Murino and Vernazza, 2001). Neural networks consist in nodes, called neurons, and weighted paths connecting these neurons (Figure 11.14). Each node has an activation level, a function of the activation of the nodes directly connected to it. The number of nodes, the number of layers, and the way they are connected define the types of neural networks. Back-propagation or BP networks (e.g., Stewart *et al*., 1994b) and multi-layer perceptrons (e.g., Michalopolou *et al*., 1995) are used for certain seafloor characterization studies. These neural networks are calibrated (''trained'') with samples of known seafloor types. For each new environment, or each change in the sonar configuration, these neural networks will need to be retrained. They do not have the capability to adapt automatically to new conditions and find new decision rules.

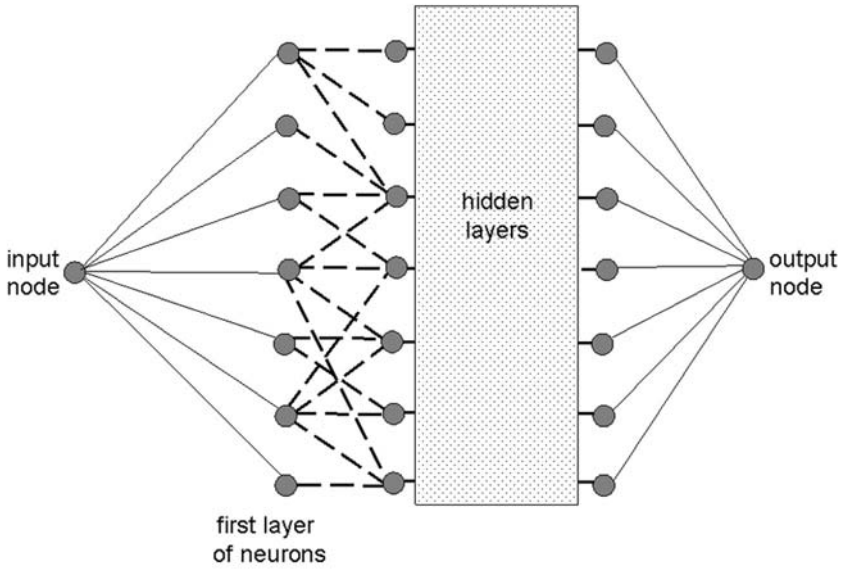

Figure 11.14. Schematic representation of a neural network.

Self-organizing neural networks are based on adaptive resonance theory (ART), intended to emulate the brain functions associated with pattern recognition (e.g., Grossberg, 1976). Its fuzzy-logic extension is known as fuzzy ART (Carpenter *et al.*, 1991), enabling categorization of both binary and analogue feature vectors. The network matches vectors presented in a first layer and a set of category prototypes accumulated in a second layer. The matching process is regulated by an adjustable vigilance parameter. The registration of each new input vector at the first layer initiates a search for the most representative category prototype in the second layer (by winner-take-all choice). If the category prototype of the winning neuron is found to provide an acceptable match to the input (resonance condition), the prototype is refined to incorporate salient features of the input. If the match is unacceptable, the winning neuron is inhibited and a new search initiated among the remaining neurons. The cycle of search and matching is continued until either an acceptable match is obtained or a new category established in the second layer. In such a way, the established categories are buffered against spurious input while allowing the network to maintain the capability of establishing new categories. Neural networks have been used with variable success for acoustic characterization of the seafloor. Mitchell and Spencer (1995) demonstrated the potential of artificial intelligence for the automatic finding of routes for submarine cables or pipelines in complex terrains. Pouliquen *et al.* (2002) showed promising results for seafloor characterization.

Genetic and evolutionary algorithms can also be used for the same purpose (e.g., Avgerinos, 2003; Polheim, 2005). They are stochastic search methods, inspired by the same principles of natural evolution and the Darwinian paradigm of "survival of the fittest". They look at populations of potential solutions and assess how well they fit a certain set of criteria (Figure 11.15). After random initialization of the parameters, at each generation a new set of approximations is created by the process of selecting individuals according to their level of fitness in the problem domain and breeding them together using operators borrowed from natural genetics. This process leads to the emergence of populations of better solutions. Evolutionary algorithms model natural processes, such as selection, recombination, mutation, migration, locality, and neighborhood. They can also be applied in parallel to

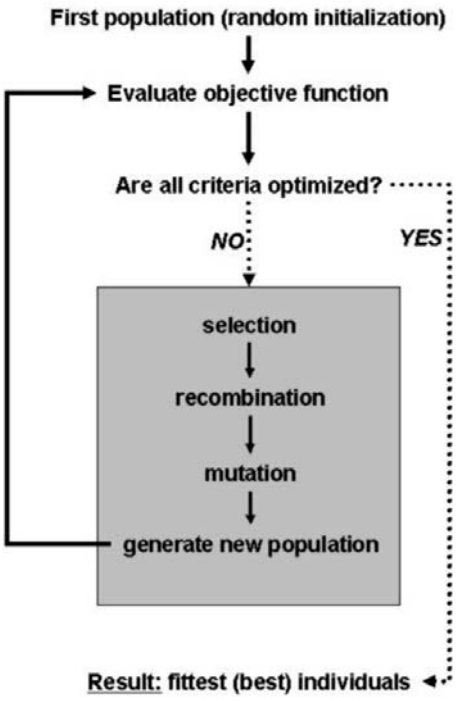

Figure 11.15. General concept of evolutionary algorithms.

different sets, making computations potentially faster, and look concurrently at different solutions.

11.3.3 Image compression

Each sidescan survey produces large amounts of data, including at least imagery, navigation, and attitude. New sonars can routinely collect several tens of gigabytes of data. These data need to be transmitted from the sonar to the recording instrument, through a cable with a finite bandwidth, and thus a finite transmission rate, and the data need to be stored and transferred between computers. To give an example, a final map of TOBI imagery, processed and produced at a scale of 1:100,000 typically corresponds to 660 megabytes (i.e., 6.8×10^8 individual points). This final map results from the processing of raw backscatter recordings, their combination with echo-profiler and bathymetry measurements, and the mosaicking of several swaths (i.e., the storage and—hopefully—archival of raw products and final data), as well as key intermediate steps.

Basic image compression can be attained by restricting the number of bits on which each pixel is stored (i.e., reducing the radiometric range), by sub-sampling or averaging the data (i.e., decreasing its original resolution), or by coding recognizable features (and thus maintaining the original quality). Advanced compression algorithms look at the repetition of values or series of values in the image and code them accordingly: run-length encoding, adaptive Lempel–Ziv compression, cosine–transform (used for webcam communications), etc. These methods do not always take into account the two-dimensional aspect of sonar imagery. Using image classification, objects and regions can be coded more efficiently. For example, fishery applications do not require precise knowledge of the seafloor and a simple definition such as rock/gravel/sand is largely enough. The compressed and coded data can also be used to lighten the burden of a human interpreter looking for specific targets on the seafloor (e.g., in mine detection activities).

11.4 SEABED CHARACTERIZATION

11.4.1 Goals, purposes, limits

The volume of data collected by sidescan sonars increases with their resolution. To ensure efficient utilization of all data, new techniques must be devised to extract more information and supplement the interpreter with reliable quantitative material. The presentation of datasets as mere images is not enough, and these new techniques must support interpretation with quantitative arguments going as far as possible beyond human capabilities. Image classification techniques aim, for example, at recognizing the different morphological units present in an image, and displaying them as an interpreted map, or at identifying specific structures like mine-like objects. The fields of application include hydrography, engineering, environmental surveys, habitat mapping, geology, and mine counter-measures, to cite but a few.

Image classification is an open subject of research, and there is no definitely proven and fault-proof technique. Quantitative measures, or indices, are attached to each point in the image (e.g., local contrast, roughness of local texture). The process of classification relates the indices to corresponding geological interpretations, and organizes in "classes" the multi-dimensional space of the indices. There is no theory of image classification *per se*, as emphasized in the exhaustive review written by Haralick and Shapiro (1985). Classification techniques are basically *ad hoc* and judged on their performance.

Unsupervised classification relinquishes all control of the final classification to the algorithm. The n indices measured at each point will be submitted to clustering algorithms to determine the natural groupings of points in n-dimensional space. Classic clustering algorithms start from an arbitrary partition of n-dimensional space into groups, and rearrange these groups to minimize or maximize certain parameters. Known algorithms include K-Means (e.g., Reed and Hussong, 1989) and simulated annealing (e.g., Selim and Alsultan, 1991; Nguyen and Cohen, 1993). Iterative partition rearrangement schemes such as ISODATA or artificial neural networks (ANNs) have to go through the image many times, which can take excessive computation time. The accuracy of some unsupervised classification schemes depends on the number of regions allowed at the beginning. If the actual number of independent morphologic units is bigger than the starting number of units, the algorithms will produce erroneous results.

Supervised classification techniques use the experience of the interpreter, and/or the reference with calibrated portions of the seafloor, to guide the recognition of units. It is important that all classes are represented, and that the samples used to "train" the algorithms do not represent mixed units. All other sets of n indices will be associated with the classes to which they are most similar. Several classification algorithms are available: for example, minimum-distance classifier, Bayes maximum-likelihood (Duda and Hart, 1973). Measurement space–guided (MSG) clustering is a technique particularly adapted to natural images (Gonzalez and Wintz, 1977; Haralick and Shapiro, 1985), especially in complex and noisy environments such as in the sonar images of mid-oceanic ridges. The MSG technique partitions the measurement space and each pixel in the image can be assigned the label of the cell in the partition ("labeling" process). The regions in the image are then defined as the connected components of the pixels having the same label.

A rapid search through the scientific and technical literature shows many different definitions of the word "classification". These definitions are often blurred by commercial hype, and by the need to communicate between different disciplines (e.g., image processing, marine geology, underwater acoustics) with different vocabularies. These semantic differences can be quite confusing. One usually distinguishes three different stages: segmentation, classification, and characterization. Segmentation comes from the image-processing world, and defines the partition of an image into several regions with different characteristics. The image may come from any source (satellite image, medical image, etc.), and the partitions of the image are not definitely interpreted. They just share the same numerical characteristics, and are generally labeled only by letters or numbers. Classification goes one step further: it

recognizes these different regions as distinct physical entities, even if a physical feature can correspond to several partitions (e.g., "mud = partition 1 & partition 2"), or a partition can correspond to several physical features (e.g., "corals and aggregated pebbles"). Characterization is the next step, where the regions recognized in the images or in the maps correspond to definite characteristics, physical (e.g., particular shear wave attenuation), chemical (e.g., oil slick or metallic object), geological (e.g., fine-grained silt), or biological (e.g., coral mound). For the sake of simplicity, the definition of seabed characterization is adopted here for all these meanings.

11.4.2 Applications

Acoustic ground discrimination systems (AGDSs) can be a basis for comparing, managing, and researching characteristic areas of the seabed (e.g., Blondel and Murton, 1997; Blondel, 2002; Kenny *et al.*, 2003; Anderson *et al.*, 2008). Several solutions are available commercially (e.g., RoxAnn for echo sounders, QTC or GeoTexture for sidescan sonars), or academically (e.g., TexAn). The techniques and systems presented here have been selected because they achieve at least a basic recognition of the type of seafloor surveyed, or because they identify a set of seabed intrinsic characteristics (e.g., grain size, porosity, density) from which the type of seafloor could be recognized. This review does not intend to be exhaustive, and more extensive searches through the literature would find more variants of these approaches, as well as some new techniques still in need of full validation.

The tonal information (i.e., from the backscatter alone) is a combination of too many factors to be unambiguously interpreted (e.g., Blondel 1996; Blondel and Murton 1997). A few studies have endeavored to use tonal information alone, in some cases with co-registered bathymetry and/or with neural networks, but they were limited to geologically simple terrains, or were of very limited accuracy.

QTC-Sideview is an extension of the famous commercial system QTC-View to sidescan sonars (e.g., Preston *et al.*, 2004), and it is now available for a growing list of instruments. It divides sidescan images into classes based on image textures and intensity. Classes typically include material type (sand, gravel, mud, etc.) and features (ripple marks, bedrock, seagrass, etc.). The classes are assembled into a catalog and generate a layer of information to complement bathymetry and other data types. The classification is based on the statistics of the full backscatter signal (similar to the approach used by Pouliquen and Lurton, 1992 for echo-sounder characterization), FFT-derived indices, fractal dimensions, and gray-level co-occurrence matrices (similar to the approach pioneered by Reed and Hussong, 1989 and used in the TexAn system of Blondel, 1996, 2000). Principal component analysis reduces this to three descriptors (Q_1, Q_2, and Q_3), used in iterative clustering of the entire image, and which usually prove enough to recognize the different types of seafloor. Successful use requires calibration of the input sonar. New seabed classes can be recognized during post-processing. QTC-View is also able to recognize subtle differences between sediments, including gas inclusions.

The classification software TexAn (e.g., Blondel, 1996, 2000) quantifies textures with gray-level co-occurrence matrices (GLCMs). GLCMs register, within a moving window of chosen size, the co-occurrence of pixels with all possible combinations of gray levels at a certain spatial position vs. each other (distance and angle). In this way, they quantitatively describe the local image texture, based on second-order statistics. Indices called ''homogeneity'' and ''entropy'' capture most of the textural variability within the data, and are associated with specific physical processes. The entropy describes the amount of local chaos/lack of organization, while the homogeneity parameterizes the amount of local similarities. This technique can be applied to any type of sidescan sonar data: it does not require calibration with each new instrument, and can be used at any stage of processing. After defining on training zones the best processing parameters (gray-level dynamics, window size, etc.) for textural analyses, TexAn clusters the entropy and homogeneity of each and every pixel in the image. The clustering algorithms used so far have included MSG clustering (Blondel, 1996, 2000), fuzzy ART neural networks (Pouliquen *et al.*, 2002), K-Means (Huvenne *et al.*, 2002), and ISODATA (Gómez Sichi *et al.*, 2005; Huvenne *et al.*, 2007). Like RoxAnn or QTC, TexAn can classify seabed types, with accuracies ranging between 60% and 100% (as measured through intensive and extensive comparison with existing ground truth). It can also detect details invisible to the human eye, however trained, because of its physiological limitations (e.g., Blondel, 1996). A typical example is presented in Figure 11.16.

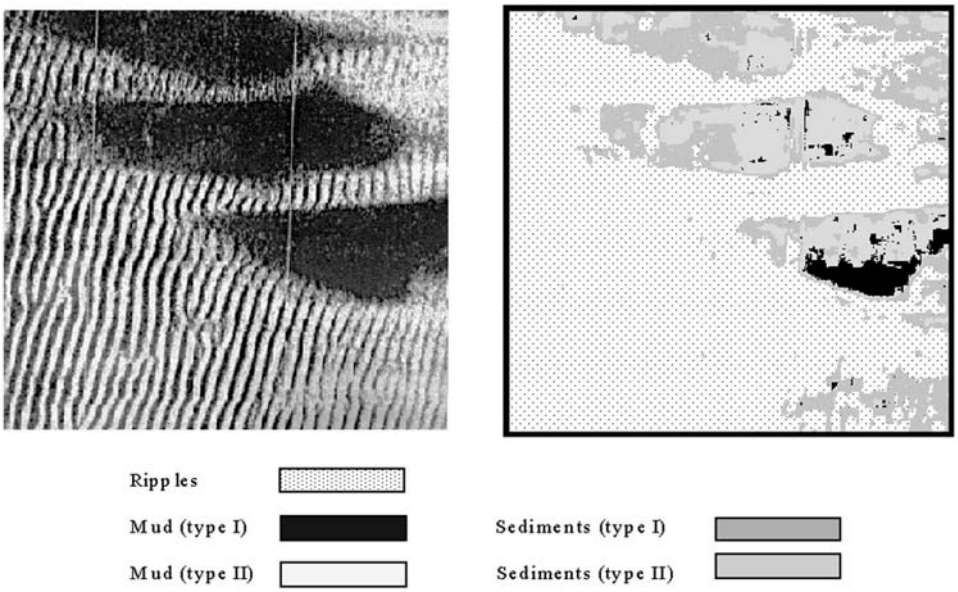

Figure 11.16. Example of seabed classification using TexAn (from Blondel, 2002). The image is ensonified from the right, at an altitude of 6 m above the seafloor, and covers an area approximately 30 m wide.

The performance of any classification technique relies heavily on the quality and amount of data processing performed. In their review of acoustic seabed classification of marine habitats, Anderson *et al.* (2008) identify the ever-present problem of sonar calibration (or lack thereof) as one of the limits to full and accurate classification. One cannot stress enough the progress that could be achieved if all surveying sidescan sonars were properly calibrated, and if the final images were expressing the backscatter in dB and not relative gray levels. Such progress was seen in satellite imagery, where each pixel in the image corresponds to a well-calibrated reflectance, used to refine classification accuracy. More sidescan instruments are now delivering high-resolution bathymetry, or collecting some kind of underway data (chemical, optical, etc.). This new information should also be added to refined or new classification schemes. The current trend toward standardization of the processing techniques (e.g., Blondel and Murton, 1997), the systematic calibration of instruments, and the incorporation of sidescan sonar and other data all promise that this field of research will remain open and active in the next decades.

11.5 ARTIFICIAL INTELLIGENCE—EXPERT SYSTEMS

A new class of computer has emerged in the last decade, with dedicated hardware and/or software that can process equally well numbers and symbols. The best-known of these systems are the expert systems, derived from the rapidly advancing research in artificial intelligence (AI). Artificial intelligence is often assimilated to the reproduction of anthropoid reasoning with a computer. Human intelligence involves both the ability to solve a specific class of problems, and the latent ability to discover solutions for a new class of problems. These two types of capability are still quite distinct in machines. AI-based systems can be divided into three types: routine-oriented, rule-based, and knowledge-based. The former include neural networks (presented in Section 11.3.2).

Systems using the rule-based approach focus on the definition of appropriate rules, sequentially or interactively limiting the set of possible solutions through IF-THEN-ELSE rules (e.g., Moody and Katz, 2004) and their execution in limited specific situations. The input variables can be direct or contextual. These systems are commonly referred to as ''expert systems'', since they codify the rules used by a human expert for a particular task. Expert systems, like decision trees, assume generally some hierarchical view of the problem at hand. There are some limitations to expert systems, as it is difficult to assess the effect on the whole system of adding or changing a few rules. Expert systems are nonetheless used with success in several other domains of industry (e.g., for assessment of hydrocarbon reservoir capacities). And they have shown good potential in mountain geomorphology, outclassing human experts in some cases (e.g., Moody and Katz, 2004).

These systems do not have the ability to really learn independently, or to create new concepts by abstracting from experience or by rearranging pieces of knowledge in novel ways. Knowledge-based systems are concerned with more general problems of the organization of knowledge, and try to enhance cooperation between various

sources of knowledge in a synergistic way. This type of system is often referred to as "knowledge amplifiers".

Applications of artificial intelligence to sonar-related problems have been very few so far. To the best of our knowledge, there are no commercial applications available yet. Prospective applications of AI include terrain recognition and terrain avoidance for deep-sea vehicles, and adaptive processing of incoming sonar data. Although still small, the place of AI in marine science and technology is likely to grow significantly over the next years. The reader is invited to read the excellent and enthusiastic review by Moody and Katz (2004) for a detailed and approachable description of the different uses of artificial intelligence in a domain not too far from sonar surveying applications.

11.6 CONCLUSION

This chapter is intentionally not as detailed as it could be, because it only aims at presenting the basic techniques of computer-assisted interpretation. These techniques have been compiled in a logical order to present how they can intervene at the different stages of interpretation, how they work, and what kind of results they can bring to help the interpreter in his/her task. We saw how the visual appearance of sonar imagery could be enhanced and small defects corrected and how to recognize numerically the structures present in the image. This led to the ever-current research conducted in the fields of image classification, image compression, and the envisaged development of expert systems. Joint analysis of sonar data with other types of information was also presented with the growing use of geographic information systems and decision support systems.

One may wonder why computer-assisted interpretation was not used in the previous chapters, or only on a few occasions. The main reason is that we wanted to show the images themselves, and the thought processes at play behind their interpretation. The second reason is that not all studies require the use of numerical techniques, because of time or budget constraints. But it is indisputable that advanced interpretation of sonar images can only benefit from the techniques outlined in this chapter. The different disciplines constitutive of computer-assisted interpretation are growing rapidly and the next decade should see their rapid development in industrial and academic applications alike.

11.7 FURTHER READING (*see also* References at end of book)

About image processing

Watt, A.; and F. Policarpo (1998). *The Computer Image*. Addison-Wesley, Reading, MA, 784 pp.

About geographical information systems

Maguire, D.J.; M.F. Goodchild; and D.W. Rhind (1991). *Geographical Information Systems, Vol. 1: Principles*. Longman/Wiley, Harlow, U.K., 649 pp.

About artificial intelligence and neural networks

Moody, A.; and D.B. Katz (2004) Artificial intelligence in the study of mountain landscapes. In M.P. Bishop and J.F. Shroder, Jr. (Eds.), *Geographic Information Science and Mountain Geomorphology*. Springer/Praxis, Heidelberg, Germany/Chichester, U.K., pp. 219–251.

Simmons, A.B.; and S.G. Chappell (1988). Artificial intelligence: Definition and practice. *IEEE Journal of Oceanic Engineering*, **13**(2), 14–42.

About the potential of immersive environments for sonar studies

Shell, R.C.; G.C. Bishop; and D.B. Maxwell (2006). Under-ice sonar visualisation. *Linux Journal*. Available at *http://www.linuxjournal.com/article/8299*

12

Conclusion

The Earth is a small planet, and modern communication tools remind us every minute of this simple fact. Browsing through Google Earth or one of its Internet equivalents, we can zoom in on any point in the world, and gather all the information we want about it. But the oceans are still largely hidden from view. We know more about other planets, or asteroids passing in the sky, than we know about the underwater domains just a few kilometers away. Yet, learning about our planet, monitoring its health and its evolution, managing its resources in as sustainable a way as possible cannot happen unless we know what is happening under water. And for this, the only tool is acoustics. Animals developed and have used sonar for a long time: dolphins can detect and identify objects from a few centimeters to a few hundreds of meters in very opaque waters; whales can communicate from one side of the ocean to the other. But we have only just begun to master the construction and use of sonars. Along with the development of computer-aided techniques for processing the signals and interpreting the images, these technologies have greatly advanced our knowledge of the deep seas.

The *Handbook of Seafloor Sonar Imagery*, published in 1997 and now long out of print, started filling the gap in comprehensive reference works about this novel form of remote sensing. There have been many advances in the decade since, and this is why a new book was felt necessary. The *Handbook of Sidescan Sonar* aims at picking up where the *Handbook of Seafloor Sonar Imagery* left off. Since then, we have witnessed the democratization of sonars (some can even be bought on eBay), the emergence of new platforms (e.g., AUVs) and better sonars (e.g., interferometric sonars), advances in our understanding of acoustic scattering at and in the seabed, the quantum leap of computing power, and the increased communication brought by the spread of the Internet (shortly before 1997, I was told by my group manager that it would never catch on). The large number of images and results presented in this book and downloadable from the Internet bears testimony both to the prevalence of this mode of communication and to the healthy dynamism of the sonar community,

both in terms of scientific publication and in terms of general outreach to end-users and the general public.

More than anything else, the last decade has seen tremendous advances in our knowledge of the seabed. In this book, I have intended to provide a general reference covering the entire range of marine seafloor environments. This work is aimed at a range of users: from the professional geologist, environmental scientist, and marine engineer, to the acoustic technician and computer scientist. The intention is not to provide an exhaustive atlas of every marine geological feature, or a "coffee table" book of visually pleasing images, but to illustrate a range of features imaged by different systems and educate the reader in the art and science of sidescan sonar interpretation. This book is divided into three main areas: (1) data acquisition and processing (Chapters 2–4); (2) the different marine environments (Chapters 5–9); and (3) realizing the limits of the data and enhancing interpretation using computer and numerical techniques (Chapters 10–11).

As explained at the beginning of the book, it was not possible to include everybody and everything. A few sonar images will be missing, important works will be unmentioned, complex studies summed up in a few lines. Sometimes this was voluntary, because of the lack of space or because of the lack of consensus on an issue, and sometimes this was because I was unaware of a recent survey or piece of literature. This bears witness to the width and vitality of the field of sonar imaging: it cannot be summed up in a single book, and it is moving fast enough that such a book would never be totally complete. To help compensate for this, I have included a small bibliography (Further reading) at the end of each chapter, with background articles or books for readers wishing to go further.

In conclusion, this book is not a totally exhaustive text on sonar. But, used in conjunction with other textbooks, like the excellent *Introduction to Underwater Acoustics* by Xavier Lurton and other Springer/Praxis books on acoustics, I sincerely believe it will be just as useful to experts as a source of reference as to newcomers seeking an easy introduction to sidescan sonar.

References

(and General bibliography; see also Further reading at chapter ends)

These references do not pretend to exhaustiveness, as there are several thousands of articles dealing with the different subjects covered in this book. Every reasonable effort has been made to acknowledge the owners of copyrighted material.

Akay, T.; R.D. Ballard; and G.F. Bass (Eds.) (2004). *The Application of Recent Advances in Underwater Detection and Survey Techniques to Underwater Archaeology*. Institute of Nautical Archaeology, Bodrum, Turkey, pp. 135–142.

Allen, J.L.R. (1984). Sedimentary structures: Their character and physical basis. *Developments in Sedimentology*, Vol. II. Elsevier, Amsterdam, 663 pp.

Allerton, S. (1997). Evidence for asymmetric accretion at the end of a slow-spreading segment (Abstract). *EOS Trans. AGU*, **78**, F692.

Allerton, S.; B.J. Murton; R.C. Searle; and M. Jones (1995). Extensional faulting and segmentation of the Mid-Atlantic Ridge north of the Kane Fracture Zone (24°00N to 24°40N). *Marine Geophysical Researches*, **17**(1), 37–61.

Allerton, S.; R.C. Searle; and B.J. Murton (1996). Bathymetric segmentation and faulting on the Mid-Atlantic Ridge, 24°00′N to 24°40′N. In C.J. MacLeod, T.A. Tyler, and C.L. Walker (Eds.), *Tectonic, Magmatic, Hydrothermal and Biological Segmentation of Mid-Ocean Ridges*, Spec. Publ. 118. Geological Society, London, pp. 29–48.

Almagor, G.; and G. Wiseman (1991). Analysis of submarine slumping in the continental slope off the southern coast of Israel. *Marine Geotechnology*, **10**(3/4), 303–342.

Alonso, B. and Ercilla, G. (2003). Small turbidite systems in a complex tectonic setting (SW Mediterranean Sea): Morphology and growth patterns. *Marine and Petroleum Geology*, **19**, 1225–1240.

Amblas, D.; R. Urgeles; M. Canals; A.M. Calaft; M. Rebesco; A. Camerlenghi; F. Estrada; M. De Batist; and J.E. Hughes-Clarke (2006). Relationship between continental rise development and palaeo-ice sheet dynamics, Northern Antarctic Peninsula Pacific Margin. *Quat. Sci. Rev.*, **25**, 933–944.

An, L.-J.; and C.G. Sammis (1996). Development of strike-slip faults: Shear experiments in granular materials and clay using a new technique. *Journal of Structural Geology*, **18**(8), 1061–1077.

Anderson, J.B.; R. Wright; and B. Andrews (1986). Weddell Fan and associated abyssal plain, Antarctica: Morphology, sediment processes, and factors influencing sediment supply. *Geo-Marine Letters*, **6**, 121–129.

Anderson, J.T.; D.V. Holliday; R. Kloser; D.G. Reid; and Y. Simard (2008). Acoustic seabed classification: Current practice and future directions. *ICES J. Mar. Sci.*, **65**, 1004–1011, doi: 10.1093/icesjms/fsn061.

Angel, M.V. (1992). Deep abyssal plains: Do they offer a viable option for the disposal of large-bulk low-toxicity wastes? In H.D. Smith (Ed.), *Advances in the Science and Technology of Ocean Management*. Routledge, London, 240 pp.

Anschutz, P.; G. Blanc; F. Chatin; M. Geiller; and M.C. Pierret (1999). Hydrographic changes during 20 years in the brine-filled basins of the Red Sea. *Deep-Sea Research I*, **46**(10), 1779–1792.

Anstee, S. (2001) *Removal of Range-dependent Artifacts from Sidescan Sonar Imagery*, Technical Report DSTO-TN-0354. DSTO Aeronautical and Maritime Research Laboratory, Fisherman's Bend, Victoria, Australia. Available at *http://dspace.dsto.defence.gov.au/dspace/ bitstream/1947/3798/1/DSTO-GD-0089%20PR.pdf*

Arntz, W.E.; and W. Weber (1970). *Cyprina islandica* L. (Mollusca, Bivalvia) als Nahrung für Dorsch und Kliesche in der Kieler Bucht. *Ber. Dt. Wiss. Komm. Meeresforschung*, **21**, 193–209 [in German].

Ashkar, G.P.; and J.W. Modestino (1978). The contour extraction problem with biomedical applications. *Computer Graphics and Image Processing*, **7**, 331–355.

Ashley, G.M.; and N.D. Smith (2000). Marine sedimentation at a calving glacier margin. *Geol. Soc. Am. Bull.*, **112**(5), 657–667.

Avgerinos, E. (2003). Towards evolutionary optimisation for high resolution bathymetry from sidescan sonars. *J. Balkan Geophys. Soc.*, **6**(2), 117–126.

Babb, R. (1989). Feasibility of interferometric swath bathymetry using GLORIA, a long-range sidescan. *IEEE J. Oceanic Engineering*, **14**(4), 299–305.

Ballard, D.H. (1981) Generalizing the Hough transform to detect arbitrary shapes. *IEEE Trans. Pattern Recognition*, **13**, 111–122.

Ballard, R.D. (Ed.) (2008). *Archaeological Oceanography*. Princeton University Press, Princeton, NJ, 283 pp.

Ballard, R.D.; and Moore, J.G. (1977). *Photographic Atlas of the Mid-Atlantic Ridge Rift Valley*. Springer-Verlag, New York, 114 pp.

Ballard, R.D.; and T.H. van Andel (1977). Morphology and tectonics of the inner rift valley at latitude 36°50'N on the Mid-Atlantic Ridge. *Geological Society of America Bulletin*, **88**, 507–530.

Balsam, W.L.; B.C. Deaton; and J.E. Damuth (1999). Evaluating optical lightness as a proxy for carbonate content in marine sediment cores. *Marine Geology*, **161**(2/4), 141–153.

Bamford, H.A.; K. McElwee; and C. Morishige (2008). NOAA addresses the marine debris problem. *Sea Technology*, **49**(9), 10–13.

Bangs, N.L.B.; G.K. Westbrook; J.W. Ladd; and P. Buhl (1990). Seismic velocities from the Barbados Ridge complex: Indicators of high pore pressures in an accretionary complex. *Journal of Geophysical Research*, **95**, 8767–8782.

Banks, S.; T. Sutton; and H. Griffiths (2000). Noise susceptibility of phase unwrapping algorithms for interferometric synthetic aperture sonar. In M.E. Zkharia, P. Chevret, and P. Dubail (Eds.), *Proc. Fifth European Conf. Underwater Acoustics, Lyon, France*, pp. 451–456.

Barbagelata A.; M.D. Richardson; B. Miaschi; E. Muzi; P. Guerrini; L. Troiano; and T. Akal (1991). ISSAMS: An *in situ* sediment geoacoustic measurement system. In J.M. Hovem,

M.D. Richardson, and R.D. Stoll (Eds.), *Shear Waves in Marine Sediments*. Kluwer, Dordrecht, the Netherlands, pp. 305–312.

Barnhardt, W.; B. Andrews; and B. Butman (2005). *High-resolution Geologic Mapping of the Inner Continental Shelf: Nahant to Gloucester, Massachusetts*, USGS Open-File Report 2005-1293. U.S. Geological Survey, Reston, VA, 43 pp.

Barrie, J.; and T.M. Good (2007). Marine mining and habitat. In B.J. Todd and H.G. Greene (Eds.), *Mapping the Seafloor for Habitat Characterization*, SP-47. Geological Association of Canada, St. John's, Newfoundland, Canada, pp. 381–388.

Behrens, E.W. (1988). Geology of a continental slope oil seep, northern Gulf of Mexico. *American Association of Petroleum Geologists Bulletin*, **72**(2), 105–114.

Beijdorff, C.; W. van der Werff; and Yu. Gubanov (1994). Eratosthenes Seamount; MAK-1 sonographs and profiles. In A.F. Limonov, J.M. Woodside, and M.K. Ivanov (Eds.), *Mud Volcanism in the Mediterranean and Black Seas and Shallow Structure of the Eratosthenes Seamount*, UNESCO Reports in Marine Science No. 64. UNESCO, New York, 173 pp.

Belderson, R.H.; N.H. Kenyon; A.H. Stride; and A.R. Stubbs (1972). *Sonographs of the Seafloor*. Elsevier, Amsterdam, 185 pp.

Belderson, R.H.; M.A. Johnson; and N.H. Kenyon (1982). Bedforms. In A.H. Stride (Ed), *Offshore Tidal Sands, Process and Deposits*. Chapman & Hall, London, pp. 27–57.

Bell, J. (Ed.) (2007). Detection and classification of underwater target. *Proc. Inst. of Acoustics*, **29**(6), 267 pp.

Bergersen, D.D. (1991). A synopsis of SeaMARC-II sidescan processing techniques. *Proc. IEEE Oceans '91*, **2**, 921–926.

Bernhard, M. (1989). Sedimentologische Beeinflussung der Oberflächensedimente durch Grundfischerei in der Kieler Bucht, Unveröff. Dipl.-Arbeit, Geol. Inst. Univ. Kiel, Germany, 41 pp. [in German].

Beyer, A.; R. Rathlau; and H.W. Schenke (2005). Multibeam bathymetry of the Håkon Mosby mud volcano. *Mar. Geophys. Res.*, **26**, 61–75.

Bird, J.S.; and G.K. Mullins (2005). Analysis of swath bathymetry sonar accuracy. *IEEE J. Oceanic Engineering*, **30**(2), 372–390.

Bishop, M.P.; and J.F. Shroder, Jr. (Eds.) (2004). *Geographic Information Science and Mountain Geomorphology*. Springer/Praxis, Heidelberg, Germany/Chichester, U.K., 486 pp.

Blackinton, J.G. (1991). Bathymetric resolution, precision and accuracy considerations for swath bathymetry mapping sonar systems. *IEEE Proc.*, 550–556.

Blondel, Ph. (1992). Traitement et interprétation des données radar: Applications à l'étude de la surface de Vénus [Processing and interpretation of radar data: Applications to the study of the surface of Venus] Ph.D. thesis, Univ. Paris-VII Jussieu, France, 327 pp. [in French].

Blondel, Ph. (1996) Segmentation of the Mid-Atlantic Ridge south of the Azores, based on acoustic classification of TOBI data. In C.J. MacLeod, P. Tyler, and C.L. Walker (Eds.), *Tectonic, Magmatic and Biological Segmentation of Mid-ocean Ridges*. Special Pub. No. 118. Geological Society, London, pp. 17–28.

Blondel, Ph. (1998). *Textural Analysis and Geological Characterisation of GLORIA Sidescan Sonar Imagery from the Irish Continental Margin*, SOC Tech. Report No. 23. Southampton Oceanography Centre, Southampton, U.K., 29 pp.

Blondel, Ph. (1999) Textural analysis of sidescan sonar imagery and generic seafloor characterisation. *J. Acoust. Soc. Am.*, **105**(2), 1206.

Blondel, Ph. (2000). Automatic mine detection by textural analysis of COTS sidescan sonar imagery. *International Journal of Remote Sensing*, **21**(16), 3115–3128.

Blondel, Ph. (2002). Seabed classification at continental margins. In: G. Wefer, D. Billett, D. Hebbeln, B.B. Jørgensen, Tj. Van Weering (Eds), *Ocean Margin Systems*. Springer-Verlag, Berlin, pp. 125–141.

Blondel, Ph.; and A. Caiti (Eds.) (2007). *Buried Waste in the Seabed: Acoustic Imaging and Bio-toxicity (Results from the European SITAR Project)*. Springer/Praxis, Heidelberg, Germany/Chichester, U.K., 202 pp.

Blondel, Ph.; and O. Gómez Sichi (2008). Textural analyses of multibeam sonar imagery from Stanton Banks, Northern Ireland continental shelf. *Applied Acoustics* (in press, 2008), doi:10.1016/j.apacoust.2008.07.015.

Blondel, Ph.; and B.J. Murton (1997). *Handbook of Seafloor Sonar Imagery*. Wiley/Praxis, Chichester, U.K.

Blondel, Ph.; and L.M. Parson (1994). *Sonar Processing in the U.K.: A Short Review of Existing Potential and New Developments for the BRIDGE Community*, BRIDGE Report No. 1. Natural Environment Research Council, Swindon, U.K., 27 pp.

Blondel, Ph.; and L.M. Parson (1995). *Sonar Processing in the U.K.*, BRIDGE Report No. 5. Natural Environment Research Council, Swindon, U.K., 14 pp.

Blondel, Ph.; and E. Pouliquen (2004). Acoustic textures and detection of shipwreck cargo: Example of a Roman ship near Elba, Italy. In T. Akay, R.D. Ballard, and G.F. Bass (Eds.), *The Application of Recent Advances in Underwater Detection and Survey Techniques to Underwater Archaeology*. Institute of Nautical Archaelogy, Bodrum, Turkey, pp. 135–142.

Blondel, Ph.; C. Sotin; and Ph. Masson (1992). Adaptive filtering and structure-tracking for statistical analysis of geological features in radar images. *Computers and Geosciences*, **18**(9), 1169–1184.

Blondel, Ph.; J.-C. Sempére; and V. Robigou (1993a). Textural analysis and structure-tracking for geological mapping: Applications to sonar data from Endeavour Segment, Juan de Fuca Ridge. *Proc. OCEANS '93*. IEEE-OES, Victoria, British Columbia, pp. 209–213.

Blondel, Ph.; J.-C. Sempére; V. Robigou; and J.R. Delaney (1993b). High-resolution bathymetry and geology of Endeavour Segment, Juan de Fuca Ridge. *EOS Trans. AGU*, **74**(43), 573.

Booth, J.S.; and D.W. O'Leary (1991) A statistical overview of mass movement characteristics on the North American Atlantic outer continental margin. *Marine Geotechnology*, **10**(1/2), 1–18.

Bornhold, B.D.; C.V. Jay; R. McConnaughey; G. Rathwell; K. Rhynas; and W. Collins (2005). Walrus foraging marks on the seafloor in Bristol Bay, Alaska: A reconnaissance survey. *Geo-Marine Letters*, doi: 10.1007/s00367-004-0205-y.

Bouma, A.H. (2000). Coarse-grained and fine-grained turbidite systems as end member models: Applicability and dangers. *Marine and Petroleum Geology*, **17**, 137–143.

Bouma, A.H.; and H.H. Roberts (Eds.) (1990) Northern Gulf of Mexico continental slope. *Geo-Marine Letters*, **4**, Special Issue.

Bouriak, S.; M. Vanneste; and A. Saoutkine (2000). Inferred gas hydrates and clay diapers near the Storegga Slide on the southern edge of the Vøring Plateau, offshore Norway. *Marine Geology*, **163**, 125–148.

Bowles, F.A.; P.R. Vogt; and W.Y. Jung (1998). Bathymetry (Part I), sedimentary regimes (Part II), and abyssal waste-disposal potential near the conterminous United States. *J. Mar. Sys.*, **14**, 211–239.

Boyle, F.A.; and N.P. Chatiros (1995). A model for acoustic backscatter from muddy sediments. *Journal of the Acoustical Society of America*, **98**(1), 525–530.

Bozzano, R.; and A. Siccardi (1997). A high frequency approach for seabed vegetation characterization. In *Proc. Int. Conf. High Frequency Acoustics in Shallow Water, Lerici, Italy*, pp. 57–64.

Brekhovskikh, L.M.; and Yu. P. Lysanov (1991). *Fundamentals of Ocean Acoustics*, Second Edition. Springer-Verlag, Berlin, 270 pp.

Briggs, K.B.; K.L. Williams; D.R. Jackson; C.D. Jones; A.N. Ivakin; and T.H. Orsi (2002). Fine-scale sedimentary structure: Implications for acoustic remote sensing. *Marine Geology*, **182**(1/2), 141–159.

Brissette, M.B. (1997). The application of multibeam sonars in route survey. Master of Engineering thesis, University of New Brunswick, Canada.

Brown, C.J.; and Ph. Blondel (2008). Developments in the application of multibeam sonar backscatter for seafloor habitat mapping. *Applied Acoustics*, doi:10.1016/j.apacoust. 2008.08.004.

Brown, C.J.; and J.S. Collier (2008). Mapping benthic habitat in regions of gradational substrata: An automated approach utilising geophysical, geological, and biological relationships. *Estuarine, Coastal and Shelf Science*, **78**(1), 203–214, doi: 10.1016/ j.ecss.2007.11.026.

Brown, C.J.; K.M. Cooper; W.J. Meadows; D.S. Limpenny; and H.L. Rees (2002). Small-scale mapping of sea-bed assemblages in the eastern English Channel using sidescan sonar and remote sampling techniques. *Estuarine, Coastal and Shelf Science*, **54**, 263–278.

Brown, K.; and G.K Westbrook (1988). Mud diapirism and subcretion in the Barbados Ridge Accretionary Complex: The role of fluids in accretionary processes. *Tectonics*, **7**, 613–640.

Bruce, M.P. (1992). A processing requirement and resolution capability comparison of sidescan and synthetic-aperture sonars. *IEEE J. Oceanic Engineering*, **17**(1), 106–117.

Buck, C. (1997). Underwater multi-influence signatures. *Sea Technology*, **38**(11), 53–57.

Burdic, W.S. (1984). *Underwater Acoustic System Analysis*. Prentice-Hall, Englewood Cliffs, NJ, 445 pp.

Burrough, P.A. (1986). *Principles of Geographical Information Systems for Land Resources Assessment*. Oxford University Press, Oxford, U.K., 194 pp.

Caiti, A.; R. Chapman; S. Jesus; and J.-P. Hermand (Eds.) (2006) *Experimental Acoustic Inversion Techniques in Shallow-Water*. Springer-Verlag, New York, pp. 155–170.

Cameron, H.L. (1965). Sequential air photo interpretation in coastal change studies. *Atlantic Geology*, **1**(2), 8–13.

Canals, M.; R. Urgeles; and A.M. Calafat (2000). Deep sea-floor evidence of past ice streams off the Antarctic Peninsula. *Geology*, **28**(1), 31–34.

Canals, M.; J.L. Casamor; R. Urgeles; A.M. Calafat; E.W. Domack; J. Baraza; M.L. Farran; and M. De Batist (2002). Seafloor evidence of a subglacial sedimentary system off the northern Antarctic Peninsula. *Geology*, **30**(7), 603–606.

Cande, S.C.; and R.B. Leslie (1986). Late Cenozoic tectonics of the southern Chile Trench. *Journal of Geophysical Research*, **91**(B1), 471–496.

Cande, S.C.; R.B. Leslie; J.C. Parra; and M. Hobart (1987). Interaction between the Chile Ridge and Chile Trench: Geophysical and geothermal evidence. *Journal of Geophysical Research*, **92**(B1), 495–520.

Cann, J.; and C. Walker (1993). Breaking new ground on the ocean floor. *New Scientist*, **140**(1897), 24–29.

Cann, J.; D.K. Smith; M.E. Dougherty; J. Lin; B. Brooks; S. Spencer; C.J. Macleod; E. McAllister; R.A. Pascoe; and J.A. Keeton (1992). Major landslides in the MAR median valley, 25–30°N: Their role in crustal construction and plutonic exposure. *EOS Trans. AGU*, **73**(43), Suppl., 569.

Cann, J.R.; D.K. Blackman; D.K. Smith; E. McAllister; B. Janssen; S. Mello; E. Avgerinos; A.R. Pascoe; and J. Escartin (1997). Corrugated slip surfaces formed at ridge–transform intersections on the Mid-Atlantic Ridge. *Nature*, **385**, 329–332.

Capus, C.G.; A.C. Banks; E. Coiras; I. Tena Ruiz; C.J. Smith; and Y.R. Petillot (2008). Data correction for visualisation and classification of sidescan SONAR imagery. *IET Radar Sonar Navig.*, **2**(3), 155–169, doi: 10.1049/iet-rsn:20070032.

Carbotte, S.M.; R. Arko; D.N. Chayes; W. Haxby; K. Lehnert; S. O'Hara; W.B.F. Ryan; R.A. Weissel; T. Shipley; L. Gahagan *et al.* (2004). New integrated data management system for Ridge2000 and MARGINS Research. *EOS Trans. AGU*, **85**(51), 553, doi: 10.1029/2004EO510002

Carbotte, S.M.; W.B.F. Ryan; S. O'Hara; R. Arko; A. Goodwillie; A. Melkonian; R.A. Weissel; and V.L. Ferrini (2007). Antarctic multibeam bathymetry and geophysical data synthesis: An on-line digital data resource for marine geoscience research in the Southern Ocean. In A.K. Cooper *et al.* (Eds.), *Antarctica: A Keystone in a Changing World—Online Proceedings of the 10th ISAES*. Open-File Report 2007-1047, Short Research Paper 002. U.S. Geological Survey, Reston, VA, 4 pp., doi: 10.3133/of2007-1047.srp002.dd.

Carlson, P.R.; D.M. Mann; Q.J. Huggett; and D. Bishop (1990). *GLORIA Investigation of the Exclusive Economic Zone in the Gulf of Alaska*, Open File Report 90-71. U.S. Geological Survey, Reston, VA, 17 pp.

Carlson, P.R.; H.A. Karl; and B.D. Edwards (1991). Mass sediment failure and transport features revealed by acoustic techniques, Beringian Margin, Bering Sea, Alaska. *Marine Geotechnology*, **10**(1/2), 33–51.

Carlson, P.R.; A.J. Stevenson; T.R. Bruns; D.M. Mann; and Q. Huggett (1996). Sediment pathways in Gulf of Alaska from beach to abyssal plain. In J.V. Gardner, M.E. Field, and D.C. Twichell (Eds.), *Geology of the United States' Seafloor: The View from GLORIA*. Cambridge University Press, Cambridge, U.K., 364 pp.

Carpenter, G.; S. Grossberg; and D. Rosen (1991). Fuzzy ART: Fast stable learning and categorization of analog patterns by an adaptive resonance system. *Neural Networks*, **4**, 759–771.

Caruthers, J.W.; and J.C. Novarini (1993). Estimating geomorphology and setting the scale partition with a composite-roughness scattering model. *IEEE Oceans '93 Proc.*, Vol. III, pp. 220–228.

Cervenka, P.; and C. de Moustier (1993). Sidescan sonar image processing techniques. *IEEE J. Oceanic Engineering*, **18**(2), 108–122.

Cervenka, P.; C. de Moustier; and P.F. Lonsdale (1994). Geometric corrections on sidescan sonar images based on bathymetry: Application with SeaMARC-II and Sea Beam data. *Marine Geophysical Researches*, **16**(5), 365–383.

Chadwick, W.W.; R.W. Embley; and C.G. Fox (1991). Evidence for volcanic eruption on the southern Juan de Fuca ridge between 1981 and 1987. *Nature*, **350**, 416–418, April 4.

Chakraborty, B.; D. Pathak; M. Sudhakar; and Y.S. Raju (1997). Determination of nodule coverage parameters using multibeam normal incidence echo characteristics: A study on the Indian Ocean. *Mar. Geores. Geotech.*, **15**, 33–48.

Chambers, J.; D. Wren; B. Carpenter; C.D. Minchew; and R. Beecham (2002). The development and use of a high frequency horizontal sonar to monitor channel catfish in shallow water commercial aquaculture pond. *J. Acoust. Soc. Am.*, **112**(5), 2432.

Chatillon, J.; M.E. Bouhier; and M.E. Zakharia (1992). Synthetic aperture sonar for seabed imaging: Relative merits of narrow-band and wide-band approaches. *IEEE J. Oceanic Engineering*, **17**(1), 95–105.

Chauhan, O.S.; F. Almeida; and C. Moraes (1992). Regional geomorphology of the continental slope of NW India: Delineation of the signatures of deep-seated structures. *Marine Geodesy*, **15**(4), 283–296.

Chavez, P.S. (1986). Processing techniques for digital sonar images from GLORIA. *Photogrammetric Eng. and Remote Sens.*, **52**(4), 365–388.

Chough, S.K.; and R. Hesse (1985). Contourites from Eirik Ridge, south of Greenland. *Sedimentary Geology*, **41**, 185–199.

Chough, S.K.; and H.J. Lee (1991). Submarine slides in the eastern continental margin, Korea. *Marine Geotechnology*, **10**(1/2), 71–82.

Cita, M.B.; M.K. Ivanov; and J.M. Woodside (Eds) (1996). The Mediterranean Ridge diapiric belt. *Marine Geology*, **132**, Special Issue.

Cloet, R.; S.L. Hurst; C.R. Edwards; P.S. Phillips; and A.J. Duncan (1982). A sideways looking towed depth measuring system. *J. Roy. Inst. Nav.*, **35**, 411–420.

Cobra, D.T. (1991). Estimation of geometric distortions in sidescan images. *Proc. IEEE Oceans '91*, **2**, 927–935.

Cobra, D.T.; A.V. Oppenheim; and J.S. Jaffe (1992). Geometric distortions in side-scan sonar images: A procedure for their estimation and correction. *IEEE Journal of Oceanic Engineering*, **17**(3), 252–268.

Cochonat, P.; L. Droz; C. Geronimi; J. Guillaume; B. Loubrieu; G. Ollier; J.-P. Peyronnet; A. Robin; and R. Tofani (1993). Submarine morphology of the eastern part of the Niger delta (Gulf of Guinea). *C.R. Acad. Sci. Paris, Serie II*, **317**, 1317–1328.

Cochran, J.R.; J.A. Goff; A. Malinverno; D.J. Fornari; C. Keeley; and X. Wang (1993). Morphology of a "superfast" mid-ocean ridge crest and flanks: The East Pacific Rise, 7°–9°S. *Marine Geophysical Researches*, **15**(1), 65–75.

Cocquerez, J. P. (1984). Analyse d'images aériennes: Extraction de primitives rectilignes et anti-parallèles. Ph.D. thesis, Univ. Paris-Sud Orsay, France, 223 pp. [in French].

Coleman, D.F.; and R.D. Ballard (2004). Archaeological oceanography of the Black Sea. In T. Akay, R.D. Ballard, and G.F. Bass (Eds.), *The Application of Recent Advances in Underwater Detection and Survey Techniques to Underwater Archaeology*. Institute of Nautical Archaeology, Bodrum, Turkey, pp. 49–58.

Coles, B.W.; W. Radzelovage; P. Jean-Laurant; and K. Reihani (1998). Processing techniques for multi-spectral laser line scan images. *Proc. IEEE/MTS Oceans '98, Nice, France*, Vol. 3, pp. 1766–1779.

Collot, J.Y.; S. Migeon; G. Spence; Y. Legonidec; B. Marcaillou; J.L. Schneider; F. Michaud; A. Alvarado; J.F. Lebrun; M. Sosson *et al.* (2005). Seafloor margin map helps in understanding subduction earthquakes. *EOS Trans. AGU*, **86**(46), 463, 465.

Comas, M.C.; S.V. García-Dueña; and M.J. Jurado (1992). Neogene tectonic evolution of the Alborán Sea from MCS data. *Geo-Marine Letters*, **12**, 157–164.

Costanza, R.; R. d'Arge; R. de Groot; S. Farber; M. Grasso; B. Hannon; K. Limburg; S. Naeem; R.V. O'Neill; J. Paruelo *et al.* (1997). The value of the world's ecosystem services and natural capital. *Nature*, **387**, 253–260.

Coussot, P.; and M. Meunier (1996). Recognition, classification and mechanical description of debris flows. *Earth Science Reviews*, **40**(3/4), 209–227.

Cox, C.S.; S.C. Constable; A.D. Chave; and S.C. Webb (1986). Controlled-source electromagnetic sounding of the oceanic lithosphere. *Nature*, **320**, 52–54.

Crampin, S. (1999). Calculable fluid-rock interactions. *J. Geol. Soc. London*, **156**, 501–514.

Critchley, M.F.; D.W. Coller; C.R. German; Ph. Blondel; C. Flewellen; L. Parson; I. Rouse; D. Teare; H. Bougault; D. Needham *et al.* (1994). Integration of deep tow sidescan sonar imagery, bathymetry and other data along the Mid-Atlantic Ridge. *EOS Trans. AGU*, **75**(44), November, 579.

Cronin, B.T.; N.H. Kenyon; J. Woodside; T. den Bezemer; A. van der Wal; J. Millington; M.K. Ivanov; and A. Limonov (1995). The Almeria Canyon: A meandering channel system on an active margin, Alborán Sea, Western Mediterranean. In: K.T. Pickering, R.N. Hiscott, N.H. Kenyon, F. Ricci Lucchi, and R.D.A. Smith (Eds.), *Atlas of Deep-water Environments: Architectural Style in Turbidite Systems*. Chapman & Hall, London, pp. 84–88.

Crosby, F.; and Cobb, J.T. (2005). Sonar processing for short range, very-high resolution autonomous underwater vehicle sensors. *OCEANS, 2005: Proceedings of MTS/IEEE*, pp. 398–402, Vol. 1, doi: 10.1109/OCEANS.2005.1639796.

Cuevas, K.J.; M.V. Buchanan; and D. Moss (2002). Utilizing side scan sonar as an artificial reef management tool. *Proc. IEEE Oceans '02*, **1**, 136–140.

Danford, W.W. (1997). *Xsonar/ShowImage: A Complete System for Rapid Sidescan Sonar Processing and Display*, Open-File Report 97-686. U.S. Geological Survey, Reston, VA. Available at *http://onlinepubs.er.usgs.gov/*

Davies, R.J.; and S.A. Stewart (2005). Emplacement of giant mud volcanoes in the south Caspian Basin: 3D seismic reflection imaging of their root zones. *J. Geol. Soc. London*, **162**(1), 1–4.

Davies, T.A., H. Josenhans; L, Polyak; A, Solheim; M,S, Stoker; and J.A. Stravers (Eds) (1997) *Glaciated Continental Margins: An Atlas of Acoustic Images*. Chapman & Hall, London, 315 pp.

de Groot, S.J. (1984). The impact of bottom trawling on benthic fauna of the North Sea. *Ocean Management*, **9**, 177–199.

de Meijer, R.J.; L.B. Venema; and J. Limburg (2000). Synoptical mapping of seafloor sediment. *Sea Technology*, **41**(7), 21–24.

de Moustier, C. (1988). State of the art in swath bathymetry survey systems. *Int. Hydr. Rev.*, **65**(2), 25–54.

Denbigh, P.N. (1989). Swath bathymetry: Principles of operation and an analysis of errors. *IEEE J. Ocean. Engineering*, **14**(4), 289–298.

Deriche, R. (1987). Using Canny's criteria to derive a recursively implemented optimal edge detector. *Intern. Jour. of Computer Vision*, **1**, 167–187.

DETR (1998). *M.V. Derbyshire Surveys: UK/EC Assessors' Report*. U.K. Department of Environment, Transport and Regions, London, March. Also available at *http://www.dft.gov.uk/pgr/shippingports/shipping/safety/mvderbyshire/mvderbyshiresurveysukecasses5012* (last accessed 18 December 2008)

Detrick, R.S.; and S.E. Humphris (1994). Exploration of global oceanic ridge system unfolds. *EOS Trans. AGU*, **75**(29), 325–326.

Dickinson, W.R.; and D.R. Seely (1979). Structure and stratigraphy of forearc regions. *Bulletin of the American Association of Petroleum Geologists*, **63**, 2–31.

Dierckx, P. (1977). An algorithm for least-squares fitting of cubic spline surfaces to functions on a rectilinear mesh over a rectangle. *J. Comp. Applied Math.*, **3**, 113–129.

Dimitrov, L.I. (2002). Mud volcanoes: The most important pathway for degassing deeply buried sediments. *Earth Sci. Rev.*, **59**, 49–76.

Domack, E.W. (2000). Book review: "Handbook of Seafloor Sonar Imagery". *Journal of Quaternary Science*, **15**(6), 659.

Dominguez, S.; S. Lallemand; J. Malavieille; and P. Schnürle (1998). Oblique subduction of the Gagua Ridge beneath the Ryukyu accretionary wedge system: Insights from marine observations and sandbox experiments. *Mar. Geophys. Res.*, **20**, 383–402.

Dorn, W.U.; and F. Werner (1993). The contour-current flow along the southern Iceland–Faeroe Ridge as documented by its bedforms and asymmetrical channel fillings. *Sedimentary Geology*, **82**, 47–59.

Douglas, B.L.; and H. Lee (1993). Motion compensation for improved sidescan sonar imaging. In *Oceans '93*, Vol. I. Institute of Electrical and Electronic Engineers, New York, 491 pp.

Dowdeswell, J.A.; and M.J. Siegert (1999). Ice-sheet numerical modeling and marine geophysical measurements of glacier-derived sedimentation on the Eurasian Arctic continental margins. *Geol. Soc. Am. Bull.*, **111**(7), 1080–1097, doi: 10.1130/0016-7606 (1999)111 < 10808:ISNAM > 2.3.CO;2.

Dowdeswell, J.A.; J. Evans; C.O. Cofaigh; and J.B. Anderson (2006). Morphology and sedimentary processes on the continental slope off Pine Island Bay, Amundsen Sea, West Antarctica. *Geol. Soc. Am. Bull.*, **118**(5/6), 606–619.

Driscoll., N.W.; J.K. Weissel; and J.A. Goff (2000). Potential for large-scale submarine slope failure and tsunami generation along the US mid-Atlantic coast. *Geology*, **28**(5), 407–410.

Duda, R.O.; and P.E. Hart (1973). *Pattern Recognition and Scenes Analysis*. Wiley, New York.

Duda, R.O.; and P.E. Hart (1972). Use of the Hough transformation to detect lines and curves in pictures. *Comm. A.C.M.*, **15**, 11–15.

Du Four, I.; and V. van Lancker (2008). Changes of sedimentological patterns and morphological features due to the disposal of dredge spoil and the regeneration after cessation of the disposal activities. *Marine Geology*, **255**, 15–29.

Dung, T.V.; and A. Stepnowski (2000). Seabottom recognition using multistage fuzzy neural network operating on multi-frequency data. *Acta Acustica*, **86**, 830–837.

Durham, L.S. (1999) 3-D models are making cents. *AAPG Explorer*. Available at *http://aapg.org/explorer/1999/11nov/3dmodeling.cfm*

Dyer, C.M. (2000) Studies of an acoustic sediment discrimination system. MPhil thesis, University of Bath, U.K.

Edwards, A. (2007). Foreword, pp. ix–x. In: Ph. Blondel and A. Caiti (Eds.), *Buried Waste in the Seabed—Acoustic Imaging and Bio-toxicity* (Results from the European SITAR Project). Springer/Praxis, Heidelberg, Germany/Chichester, U.K., 202 pp.

Edwards, M.H.; G.J. Kurras; M. Tolstoy; D.R. Bohnenstiehl; B.J. Coakley; and J.R. Cochran (2001). Evidence of recent volcanic activity on the ultraslow-spreading Gakkel ridge. *Nature*, **409**, 808–812.

EEZ-SCAN 87 Scientific Staff (1991). *Atlas of the U.S. Exclusive Economic Zone: Atlantic Continental Margin*, Miscellaneous Investigations Series I-2054. U.S. Geological Survey, Reston, VA, 174 pp.

Elachi, C.; L.E. Roth; and G.G. Schaber (1984). Spaceborne radar subsurface imaging in hyperarid regions. *IEEE Trans. Geoscience and Remote Sensing*, **GE-22**, 383–388.

Elverhoi, A. (1984). Glacigenic and associated marin sediments in the Weddell Sea, fjords of Spitsbergen and the Barents Sea: A review. *Marine Geology*, **57**, 53–88.

Embley, R.W.; E.T. Baker; W.W. Chadwick, Jr.; J.E. Lupton; J.A. Resing; G.J. Massoth; and K. Nakamura (2004). Explorations of Mariana Arc volcanoes reveal new hydrothermal systems. *EOS Trans. AGU*, **85**(4), 37–40, January 27.

Escartín, J.; P.A. Cowie; R.C. Searle; S. Allerton; N.C. Mitchell; C.J. MacLeod; and A.P. Slootweg (1999). Quantifying tectonic strain and magmatic accretion at a slow spreading ridge segment, Mid-Atlantic Ridge, 29°N. *J. Geophys. Res.*, **104**(B5), 10421–10437.

Esser, D. (2002). METS: The tool for pipeline inspection. *Sea Technology*, **43**(4), 51–52.

Evrin, V.; G. Öke; A.G. Türkmenoglu; and S. Demirci (2002). Stone anchors from the Mediterranean coasts of Anatolia, Turkey: Underwater surveys and archaeometrical investigations. *Int. J. Naut. Archaeo.*, **31**(2), 254–267.

Fanetti, D.; F.S. Anselmetti; E. Chapron; M. Sturm; and L. Vezzoli (2008). Megaturbidite deposits in the Holocene basin fill of Lake Como (Southern Alps, Italy). *Palaeogeography, Palaeoclimatology, Palaeoecology*, **259**, 323–340.

Farre, J.A.; and W.B.F. Ryan (1985). 3-D view of erosional scars on U.S. Mid-Atlantic continental margin. *American Association of Petroleum Geologists Bulletin*, **69**(6), 923–932.

Faugères, J.C.; and D.A.V. Stow (1993). Bottom-current-controlled sedimentation: A synthesis of the contourite problem. *Sedimentary Geology*, **82**, 287–297.

Faugères, J.C., E. Gonthier, C. Bobier, and R. Griboulard (1997). Tectonic control on sedimentary processes in the southern termination of the Barbados Prism. *Mar. Geol.*, **140**, 117–140.

Faugères, J.C.; D.A.V. Stow; P. Imbert; and A. Viana (1999). Seismic features diagnostic of contourite drifts. *Marine Geol.*, **162**, 138.

Faught, M.K.; and N. Flemming (2008). Submerged prehistoric sites: ''Needles in haystacks' for CRMs and industry''. *Sea Technology*, **49**(10), 37–42.

Fedje, D.W.; and H. Josenhans (2000). Drowned forests and archaeology on the continental shelf of British Columbia, Canada. *Geology*, **28**(2), 99–102.

Fischler, M.A.; J.M. Tenebaum; and H.C. Wolf (1981). Detection of roads and linear structures in low resolution aerial imagery using a multisource knowledge integration. *Computer Graphics and Image Processing*, **15**, 201–223.

Fish, J.P.; and H.A. Carr (1990a). *Sound Underwater Images*. Lower Cape Publishing, Orleans, MA, 189 pp.

Fish, J.P.; and H.A. Carr (1990b). *Sound Underwater Images: A Guide to the Generation and Interpretation of Sidescan Snar Data*. EG&G Marine Instruments, Cataumet, MA, 189 pp. Available at *http://www.marine-group.com/acoustic.html*

Fish, J.P.; and H.A. Carr (2001). *Sound Reflections: Advanced Applications of Sidescan Sonar Data*. Lower Cape Publishing, Orleans, MA, 272 pp.

Fitch, T.J. (1972). Plate convergence, transcurrent faults and internal deformation adjacent to southeast Asia and the western Pacific. *Journal of Geophysical Research*, **77**, 4432–4460.

Fleming, B.W. (1976). Sidescan sonar: A practical guide. *Int. Hyd. Rev.*, **LIII**(1), 65–92.

Flewellen, C.; N. Millard; and I. Rouse (1993). TOBI: A vehicle for deep ocean survey. *Electronics and Comm. Eng. J.*, **5**(2), 85–93.

Forrest, C.J.S. (2002). Defining ''underwater cultural heritage''. *Int. J. Naut. Archaeo.*, **31**, 3–11.

Fouquet, Y.; F. Barriga; J.L. Charlou; H. Elderfield; C.R. German; H. Ondréas; L. Parson; J. Radford-Knoery; J. Relvas; A. Ribeiro *et al.* (1998). FLORES diving cruise with the Nautile near the Azores—First dives on the Rainbow Field: Hydrothermal seawater/mantle interaction. *InterRidge News*, **7**(1), 24–28. Available at *http://www.ifremer.fr/flotte/systemes_sm/images/nautile/flores.pdf* (last accessed April 3, 2009).

Fox, C.G.; F.J. Jones; and T.-K. Lau (1990). Constrained iterative deconvolution applied to SeaMARC-I sidescan sonar imagery. *IEEE Journal of Oceanic Engineering*, **15**(1), 24–31.

Frankel, H. (1988). From continental drift to plate tectonics. *Nature*, **335**(6186), 127–130.

Freeman, H. (1961). On the encoding of arbitrary geometric configurations. *IEEE Trans. Elec. Computers*, **EC-10**, 260–268.

Freiwald, A. (1995). R/V Victor Hensen (cruise 24/95): Deep-water coral reef mounds on the Sula-Ridge, Mid-Norwegian Shelf, unpublished cruise report. Univ. Bremen, Bremen, Germany, 13 pp.

Freiwald, A. (2002). Reef-forming cold-water corals. In G. Wefer, D. Billett, D. Hebbeln, B.B. Jørgensen, and Tj. van Weering (Eds), *Ocean Margin Systems*. Springer-Verlag, Berlin, pp. 365–385.

Freiwald, A.; J.B. Wilson; and R. Henrich (1999). Grounding Pleistocene icebergs shape recent deep-water coral reefs. *Sedimentary Geology*, **125**(1/2), April, 1–8, doi: 10.1016/S0037-0738(98)00142-0.

Freiwald, A.; V. Hühnerbach; B. Lindberg; J.B. Wilson; and J. Campbell (2002). The Sula Reef Complex, Norwegian Shelf. *Facies*, **47**, 179–200.

Fryer, P.; and H. Fryer (1977). Origins of non-volcanic seamounts in a forearc environment. In B, Keating, P. Fryer, and R. Batiza (Eds.), *Seamounts, Islands and Atolls*, AGU Monograph Series 43. American Geophysical Union, Washington, D.C., pp. 61–69.

Fryer, P.; and G.J. Fryer (1987). Origins of non-volcanic seamounts in forearc environments. In B.H. Keating, P. Fryer, R. Batiza, and G.W. Boehlert (Eds.), *Seamount Islands and Atolls*, AGU Monograph Series 43. American Geophysical Union, Washington, D.C., pp. 61–69.

Fryer, P.; and J.A. Pearce (1992). Introduction to the scientific results of Leg 125. In P. Fryer, J.A. Pearce, L.B. Stokking *et al.* (Eds.), *Proc. ODP*, Sci. Results 125. Ocean Drilling Program, College Station, TX.

Fryer, P.; K.L. Saboda; L.E. Johnson; M.E. Mackay; G.F. Moore; and P. Stoffers (1990). Conical seamount: SeaMARC-II, ALVIN submersible and seismic-reflection studies. In *Proc. ODP*, Init. Reports 125. Ocean Drilling Program, College Station, TX, pp. 69–80.

Fryer, P.; N. Becker; B. Appelgate; F. Martínez; M. Edwards; and G. Fryer (2003). Why is the Challenger Deep so deep? *Earth and Planetary Science Lett.*, **211**, 259:-260, doi:10.1016/S0012-821X(03)00202-4.

Fusi, N.; and N.H. Kenyon (1996). Distribution of mud diapirism and other geological structures from long-range sidescan sonar (GLORIA) data, in the Eastern Mediterranean Sea. *Marine Geology*, **132**, 21–38.

Galindo-Zaldivar, J.; L. Nieto; and J.M. Woodside (1996). Structural features of mud volcanoes and the fold system of the Mediterranean Ridge, south of Crete. *Marine Geology*, **132**, 95–112.

Gamberi, F.; M. Marani; and C. Savelli (1997). Tectonic, volcanic and hydrothermal features of a submarine portion of the Aeolian arc (Tyrrhenian Sea). *Marine Geology*, **140**, 167–181.

Gardner, J.M.; A.N. Shor; and W.Y. Jung (1998). Acoustic imagery evidence for methane hydrates in the Ulleung Basin. *Mar. Geophys. Res.*, **20**, 495–503.

Gardner, J.V.; and R.B. Kidd (1987). Sedimentary processes on the northwestern Iberian continental margin viewed by long-range side-scan sonar and seismic data. *Journal of Sedimentary Petrology*, **57**(3), 397–407.

Gardner, J.V.; M.E. Field; H. Lee; B.E. Edwards; D.G. Masson; N.H. Kenyon; and R.B. Kidd (1991). Ground-truthing 6.5-kHz sidescan sonographs: What are we really imaging? *J. Geophys. Res.*, **96**(B4), 5955–5974.

Garlan T. (2007). Study on marine sandwaves dynamics. *Int. Hydro. Rev.*, **8**(2), 26–37.

Gee, M.J.R.; D.G. Masson; A.B. Watts; and N.C. Mitchell (2001). Passage of debris flows and turbidity currents through a topographic constriction: Seafloor erosion and deflection of flow pathways. *Sedimentology*, **48**, 1389–1409.

Geen, M.F. (2007). Advances in marine survey products and platforms. *IEEE-Oceans*, 1–6, doi: 10.1109/OCEANSE.2007.4302373.

Géli, L.; H. Bougault; D. Aslanian; A. Briais; L. Dosso; J. Etoubleau; J.P. Le Formal; M. Maia; H. Ondréas; J.L. Olivet; C. Richardson; K. Sayanagi; N. Seama; A. Shah; I. Vlastelic; and M. Yamamoto (1997). Evolution of the Pacific–Antarctic Ridge south of the Udintsev Fracture Zone. *Science*, **278**(5341), 1281–1284.

Gente, P.; J.-M. Auzende; V. Renard; Y. Fouquet; and D. Bideau (1986). Detailed geological mapping by submersible along the East Pacific Rise axial graben near 13°N. *Earth and Planet. Sci. Lett.*, **78**, 224–226.

Gente, P.; R.A. Pockalny; C. Durand; C. Deplus; M. Maia; G. Ceuleneer; C. Mevel; M. Cannat; and C. Laverne (1995). Characteristics and evolution of the segmentation of

the Mid-Atlantic Ridge between 20°N and 24°N during the last 10 million years. *Earth and Planetary Science Letters*, **129**, 55–71, 1995

GeoMapApp. Available at *http://www.geomapapp.org/about.html*

German, C.R.; L.M. Parson; and R.A. Mills (1996). Mid-ocean ridges and hydrothermal activity. In C.P. Summerhayes and S.A. Thorpe (Eds.), *Oceanography: An Illustrated Guide*. Manson, London, 352 pp.

Ginsburg, G.D.; V.A. Soloviev; R.E. Cranston; T.D. Lorenson; and K.A. Kvenvolden (1993). Gas hydrates from the continental slope, offshore Sakhalin Island, Okhotsk Sea. *Geo-Marine Letters*, **13**(1), 41–48.

Gipp M.R. (2003). Subsidence and tectonic controls on glacially influenced continental margins: Examples from the Gulf of Alaska and the western Scotian Shelf and Slope. *Quat. Int.*, **99/100**, 3–27.

Girardclos, S.; O.T. Schmidt; M. Sturm; D. Ariztegui; A. Pugin; and F.S. Anselmetti (2007). The 1996 AD delta collapse and large turbidite in Lake Brienz. *Marine Geology*, **241**, 137–154.

Gomez, O.; A. Briais; D. Sauter; and V. Mendel (2006). Tectonics at the axis of the very slow spreading Southwest Indian Ridge: Insights from TOBI side-scan sonar imagery. *Geochem. Geophys. Geosyst.*, **7**, Q05K12, doi: 10.1029/2005GC000955.

Gómez Sichi, O.; Ph. Blondel; E. Grácia; and J.J. Dañobeitia (2005). Quantitative textural analyses of TOBI sonar imagery along the Almería Canyon (Almería Margin, Alborán Sea, SE Spain). In D.M. Hodgson and S.S. Flint (Eds.), *Submarine Slope Systems: Processes and Products*, Special Pub. No. 244. Geological Society, London, pp. 141–154.

Gonzalez, R.C.; and P. Wintz (1977). *Digital Image Processing*. Addison-Wesley, Reading, MA, 431 pp.

Grácia, E.; M. Canals; M.L. Farràn; M.J. Prieto; J. Sorribas, and the GEBRA Team (1996). Morphostructure and evolution of the Central and Eastern Bransfield Basins (NW Antarctic Peninsula). *Mar. Geophys. Res.*, **128**(2/4), 429–448, doi: 10.1007/BF00286088.

Grácia, E.; Dañobeitia, J.J.; and HITS Cruise Party (2001). High-resolution imaging of tsunamigenic structures in the SW Iberian Margin (Eurasia–Africa convergence): Implications for seismic hazard assessment. *EOS Trans. AGU*, **82**(47), S51B-0610.

Grácia, E.; R. Pallàs; J.I. Soto; M. Comas; X. Moreno; E. Masana; P. Santanach; S. Diez; M. Garcia; J.J. Dañobeitia *et al.* (2006). Active faulting offshore SE Spain (Alboran Sea): Implications for earthquake hazard assessment in the southern Iberian Margin. *Earth Planet. Sci. Lett.*, **241**, 734–749.

Green. J. (Ed.) (1998). *Sri Lanka Department of Archaeology Report on the Joint Sri Lanka–Australia–Netherlands Galle Harbour Project 1996-1997*, Special Publication No. 4. Australian National Centre of Excellence for Maritime Archaeology, Perth.

Gregg, T.K.P.; and J.H. Fink (1995). Quantification of submarine lava-flow morphology through analog experiments. *Geology*, **23**(1), January, 73–76, doi: 10.1130/0091-7613(1995)023<0073:QOSLFM>2.3.CO;2

Grindlay, N.R.; P.J. Fox; and P.R. Vogt (1992). Morphology and tectonics of the Mid-Atlantic Ridge (25°–27.30°S) from Seabeam and magnetic data. *Journal of Geophysical Research*, **97**(B5), 6983–7010.

Grossberg, S. (1976). Adaptive pattern classification and universal recoding, II: Feedback, expectation, olfaction, and illusions. *Biological Cybernetics*, **23**, 187–202.

Guillon, L.; and X. Lurton (2001). Backscattering from buried sediment layers: The equivalent input backscattering strength model. *J. Acoust. Soc. Am.*, **109**(1), January, 122–132.

Gutt, J. (1996). Impact of iceberg scouring on polar benthic habitats. *Marine Ecology Progress Series*, **137**(1): 311.

Haflidason, H.; H.P. Sejrup; A. Nygård; J. Mienert; P. Bryn; R. Lien; C.F. Forsberg; K. Berg; and D. Masson (2004). The Storegga Slide: Architecture, geometry and slide development. *Marine Geology*, **213**, 201–234.

Hagen, R.A.; and P.R. Vogt (1999). Seasonal variability of shallow biogenic gas in Chesapeake Bay. *Marine Geology*, **158**(1/4), 75–88.

Hagen, R.A.; D.D. Bergersen; R. Moberly; and W.T. Coulbourn (1994). Morphology of a large meandering submarine canyon system on the Peru–Chile forearc. *Marine Geology*, **119**, 7–38.

Hambrey, M. (1994). *Glacial Environments*. UCL Press, London, 296 pp.

Hampton, M.A.; H.A. Karl; and N.H. Kenyon (1989). Sea-floor drainage features of Cascadia Basin and the adjacent continental slope, northeast Pacific Ocean. *Marine Geology*, **87**(2/4), 249–272.

Hampton, M.A.; H.J. Lee; and J. Locat (1996). Submarine landslides. *Reviews of Geophysics*, **34**(1), 33–59.

Haralick, R.M. (1979). Statistical and structural approaches to texture. *Proceedings of the IEEE*, **67**(5).

Haralick, R.M.; and L.G. Shapiro (1985). Image segmentation techniques. *Computer Vision, Graphics and Image Processing*, **29**, 100–132.

Haralick, R.M.; K. Shanmugam; and R. Dinstein (1973). Textural features for image classification. *IEEE Trans. Systems, Man, and Cybernetics*, **SMC-3**, 610–621.

Harney, J.N.; G.R. Cochrane; L.L. Etherington; P. Dartnell; N.E. Golden; and H. Chezar (2005). *Geologic Characteristics of Benthic Habitats in Glacier Bay, Southeast Alaska. U.S.*, Open-File Report 2006-1081. U.S. Geological Survey, Reston, VA. Available at *http://pubs.usgs.gov/of/2006/1081/*

Harsdorf, S.; M. Janssen; R. Reuter; B. Wachowicz; and B. Willkomm (1998) Lidar as part of an ROV-based sensor network for the detection of chemical pollutants on the seafloor. *Proceedings IEEE/MTS Oceans '98*.

Hayes, D.E.; and K.A. Kane (1994). Long-lived mid-ocean ridge segmentation of the Pacific–Antarctic Ridge and the Southeast Indian Ridge. *Journal of Geophysical Research*, **99**(B10), 19679–19692.

Hayes, M.P.; and P.T. Gough (1992). Broad-band Synthetic Aperture Sonar. *IEEE J. Oceanic Engineering*, **17**(1), 80–94.

Haymon, R.M.; D.J. Fornari; K.L. von Damm; M.D. Lilley; M.R. Perfit; J.M. Edmond; W.C. Shanks; R.A Lutz; J.M. Grebmeier; S. Carbotte *et al.* (1993). Volcanic eruption of the mid-ocean ridge along the East Pacific Rise crest at 9.45–52°N: Direct submersible observations of seafloor phenomena associated with an eruption event in April, 1991. *Earth and Planetary Science Letters*, **119**(1/2), 85–101.

Hayward, N.; Watts, A.B.; Westbrook, G.K.; and Collier, J.S. (1999). A seismic reflection and GLORIA study of compressional deformation in the Gorringe Bank region, eastern North Atlantic. *Geophysical Journal International*, **138**, 831–850.

Heald, G.J.; and N.G. Pace (1996). An analysis of 1st and 2nd backscatter for seabed classification. *ECUA-1996 Proceedings, Crete*, pp. 649–654.

Hennings, I.; H. Pasenau; and F. Werner (1993). Sea surface signatures related to subaqueous dunes detected by acoustic and radar sensors. *Continental Shelf Research*, **13**(8/9), 1023–1043.

Henrich, R.; A. Freiwald; C. Betzler; B. Bader; P. Schäfer; C. Samtleben; T.C. Brachert; A. Wehrmann; H. Zankl; and D.H.H. Kühlmann (1995). Controls on modern carbonate sedimentation on warm-temperate to arctic coasts, shelves and seamounts in the northern hemisphere: Implications for fossil counterparts. *Facies*, **32**, 71–108.

Henry, P. (1990). Fluid flow in and around a mud volcano field seaward of the Barbados accretionary wedge: Results from Manon Cruise. *Journal of Geophysical Research*, **101**(B9), 20297–20323.

Hermand, J.P. (2004) Acoustic remote sensing of photosynthetic activity in seagrass beds. In L. Seuront and P.G. Strutton (Eds.), *Scaling Methods in Aquatic Ecology, Measurements, Analysis, Simulation*. CRC Press, Boca Raton, FL, pp. 65–96.

Hieke, W.; F. Werner; and H.-W. Schenke (1996). Geomorphological study of an area with mud diapirs south of Crete (Mediterranean Ridge). *Marine Geology*, **132**, 63–93.

Hiltscher, G.; W. Mühlthaler; and J. Smits (2003). *Industrial Pigging Technology: Fundamentals, Components, Applications*. Wiley/VCH, New York, 334 pp.

Hiscott, R.N.; and A.E. Aksu (1994). Submarine debris flows and continental slope evolution in front of Quaternary ice sheets, Baffin Bay, Canadian Arctic. *American Association of Petroleum Geologists Bulletin*, **78**(3), 445–460.

Hitchcock, D.R.; and S. Bell (2004). Physical impacts of marine aggregate dredging on seabed resources in coastal deposits. *J. Coastal Res.*, **20**(1), 101–114.

Hodgson, D.M.; and S.S. Flint (Eds.) (2005). *Submarine Slope Systems: Processes and Products*, Special Pub. No. 244. Geological Society, London, 225 pp.

Holcomb, R.T.; and R.C. Searle (1991). Large landslides from oceanic volcanoes. *Marine Geotechnology*, **10**, 19–32.

Hollister, C.D. (1993). The concept of deep-sea contourites. *Sedimentary Geology*, **82**, 5–11.

Horwitz, A.; G. Graham; and R. Kuwahara (1993). The Canadian Maritime Coastal Defence Vessel (MCDV) and the integrated survey and inspection system. *Proc. IEEE Oceans '93, Victoria, Canada*, pp. 458–462.

Hovland, M. (2008). *Deep-water Coral Reefs: Unique Biodiversity Hotspots*. Springer/Praxis, Heidelberg, Germany/Chichester, U.K., 278 pp.

Hovland, M.; and A.G. Judd (1988). *Seabed Pockmarks and Seepages: Impact on Geology, Biology and the Marine Environment*. Graham & Trotman, London, 293 pp.

Hovland, M.; I.R. MacDonald; H. Rueslåtten; H.K. Johnsen; T. Naehr; and G. Bohrmann (2005). Chapopote asphalt volcano may have been generated by supercritical water. *EOS Trans. AGU*, **86**(42), 397, 402.

Hueckel, M.F. (1971) An operator which locates edges in digitized pictures. *J. of A.C.M.*, **18**, 113–125.

Huggett, Q.J.; and M.L. Somers (1998). Possibilities of using the GLORIA system for manganese nodule assessment. *Mar. Geophys. Res.*, **9**, 255–264.

Huggett, Q.J.; A.K. Cooper; M.L. Somers; and R.A. Stubbs (1992). Interference fringes on GLORIA sidescan sonar images from the Bering Sea and their implications. *Marine Geophysical Researches*, **14**, 47–63.

Hughes Clarke, J.E.; L.A. Mayer; N.C. Mitchell; A. Godin; and G. Costello (1983). Processing and interpretation of 95-kHz backscatter data from shallow-water multibeam sonars. *IEEE Oceans '93 Proc.*, **II**, 437–442.

Hühnerbach, V. (1996). Hierro debris avalanche and the upper part of the Canary Slide: Sidescan sonar imaging and its geological interpretation. Unpublished report, University of Kiel, 69 pp.

Hühnerbach, V.; D.G. Masson; G. Bohrmann; J.M. Bull; and W. Weinrebe (2005). Deformation and submarine landsliding caused by seamount subduction beneath the Costa Rica continental margin: New insights from high-resolution sidescan sonar data. In *Submarine Slope Systems: Processes and Products*, Special Pub. No. 244, Geological Society, London, pp. 195–205.

Hühnerbach, V.; Ph. Blondel; V. Huvenne; and A. Freiwald (2008). Habitat mapping of a cold-water coral reef off Norway, with a comparison of visual and computer-assisted

methods to interpret sidescan sonar data. In B.J. Todd, and H.G. Greene (Eds.), *Mapping the Seafloor for Habitat Characterization*, Special Paper 47. Geological Association of Canada, pp. 297–308.

Humphris, S.E.; P.M. Herzig; D.J. Miller; J.C. Alt; K. Becker; D. Brown; G. Brügmann; H. Chiba; Y. Fouquet; J.B. Gemmell *et al.* (1995). The internal structure of an active sea-floor massive sulphide deposit. *Nature*, **377**, 713–716, doi: 10.1038/377713a0.

Huvenne, V.; Ph. Blondel; and J.-P. Henriet (2002). Sidescan sonar imagery from the Porcupine Seabight and implications from geostatistical analyses. *Marine Geology*, **189**, 323–341.

Huvenne, V.A.I.; V. Hühnerbach; Ph. Blondel; O. Gómez Sichi; and T. LeBas (2007). Detailed mapping of shallow-water environments using image texture analysis on sidescan sonar and multibeam backscatter imagery. *IUCM-2007 Proc., Heraklion, Crete*.

Ingham, A.E. (1975). *Sea Surveying*, Vols. 1 and 2. Wiley, New York.

Inoue, H. (19986). A least-squares smooth fitting for irregularly spaced data: Finite-element approach using the cubic B-spline basis. *Geophysics*, **51**(11), 2051–2066.

Irish, J.L.; and W.J. Lillycrop (1999). Scanning laser mapping of the coastal zone: The SHOALS system. *ISPRS J. Photogrammetry and Remote Sensing*, **54**(2/3), 123–129.

ISA (1999). Deep seabed polymetallic nodule exploration: Development of environmental guidelines. *Proceedings of the International Seabed Authority's Workshop held in Sanya, Hainan Island, People's Republic of China, June 1–5, 1998: ISA/99/02*. International Seabed Authority, Kingston, Jamaica, 289 pp. Available at *http://www.isa.org.jm*

Ivanov, M.K.; A.F. Limonov; and Tj.C.E. van Weering (1996). Comparative characteristics of the Black Sea and Mediterranean Ridge mud volcanoes. *Marine Geology*, **132**, 253–272.

Jacobs, C. (1995). Mass-wasting along the Hawaiian Ridge: Giant debris avalanches. In K.T. Pickering, R.N. Hiscott, N.H. Kenyon, F. Ricci Lucchi, and R.D.A. Smith (Eds.), *Atlas of Deep Water Environments: Architectural Style in Turbidite Systems*. Chapman & Hall, London, 333 pp.

Jakob, M.; and O. Hungr (2005). *Debris-flow Hazards and Related Phenomena*. Springer/Praxis, Heidelberg, Germany/Chichester, U.K., 739 pp.

Jakobsson, M.; A. Grantz; Y. Kristoffersen; and R. Macnab (2003). Physiographic provinces of the Arctic Ocean seafloor. *Geol. Soc. Am. Bull.*, **115**(12), 1443–1455, doi: 10.113/B25216.1.

Janes (1995). *Janes Underwater Warfare Systems*, Seventh Edition. Janes Information Group, Coulsdon, U.K.

Jenkins, C.J.; and J.B. Keene (1992). Submarine slope failures of the southeast Australian continental slope: A thinly sedimented margin. *Deep-Sea Research*, **39A**(2), 121–136.

Jenkins, C.J.; B. Hunt; and M. Lawrence (1991). *GLORIA Super Sidescan Imagery of the Continental Slope East of Sydney: Batemans Bay*, Special Publication No. 27. Hydrographic Society, Monaco, pp. 291–298.

Jiang, M.; W.K. Stewart; and M. Marra (1993). Segmentation of seafloor sidescan imagery using Markov random fields and neural networks. *Proc. IEEE Oceans '93*, **III**, 456–461.

Jin, G.; and D. Tang (1996). Uncertainties of differential phase estimation associated with interferometric sonars. *IEEE J. Oceanic Engineering*, **21**(1), 53–63.

Johnson, D. (1991). Sidescan sonar imagery analysis techniques. *Proc. IEEE Oceans '91*, **2**, 935–941.

Johnson, H.P.; and M. Helferty (1990). The geological interpretation of side-scan sonar. *Rev. of Geophysics*, **28**(4), 357–380.

Jordan, G.F. (1962). Large sand waves in estuaries and in the open sea. *Proc. First Nat. Coastal Shallow Water Res. Conf.*, pp. 232–236.

Juteau, T.; and R. Maury (1999). *The Oceanic Crust: From Accretion to Mantle Recycling*. Springer/Praxis, Heidelberg, Germany/Chichester, U.K.

Kamman, J.W.; and R.L. Huston (1999). Modeling of variable length towed and tethered cable. *J. Guidance, Control and Dynamics*, **22**(4), 602–608.

Karson, J.A. (1992). Tectonics of slow-spreading ridges. *Oceanus*, **34**(4), 51–59.

Karsten, J.A.; J.R. Delaney; J.M. Rhodes; and R.A. Liias (1990). Spatial and temporal evolution of magmatic systems beneath the Endeavour Segment, Juan de Fuca Ridge: Tectonic and petrologic constraints. *Journal of Geophysical Research*, **95**(B12), 19235–19256.

Kasatkin, B.A. (2002). Anomalous phenomena in sound propagation near the sea floor: A review. *Acoust. Phys.*, **48**(4), 379–387.

Kearey, P.; and F.J. Vine (1996). *Global Tectonics*, Second Edition. Blackwell Science, Oxford, U.K., 333 pp.

Keeton, J.A. (1994). The use of image analysis techniques to characterise mid-ocean ridges from multibeam and sidescan sonar data. Ph.D. thesis, Univ. Durham, U.K., 256 pp.

Kenny, A.J.; and H.L. Rees (1996). The effects of marine gravel extraction on the macrobenthos: Results 2 years post-dredging. *Mar. Poll. Bull.*, **32**(8/9), 615–622, doi: 10.1016/0025-326X(96)00024-0.

Kenny, A.J.; I. Cato; M. Desprez; G. Fader; R.T.E. Schuttenhelm; and J. Side (2003). An overview of seabed-mapping technologies in the context of marine habitat classification. *ICES J, Marine Sci.*, **60**(2), 4118.

Kenyon, N.H. (1986). Evidence from bedforms for a strong poleward current along the upper continental slope of NW Europe. *Marine Geology*, **72**, 187–198.

Kenyon, N.H. (1987). Mass-wasting features on the continental slope of northwest Europe. *Marine Geology*, **74**(1/2), 57–77.

Kenyon, N.H. (1970), Sand ribbons of European tidal seas. *Marine Geology*, **9**, 25–39.

Kenyon, N.H.; R.H. Belderson; and A.H. Stride (1978). Channels, canyons and slump folds on the continental slope between south-west Ireland and Spain. *Oceanologica Acta*, **1**, 369–380.

Kenyon, N.H.; M.K. lvanov; and A.M. Akhmetzhanov (Eds.) (1999). *Geological Processes on the Northeast Atlantic Margin*, IOC Technical Series No. 54. UNESCO, New York.

Khandriche, A.; and F. Werner (1995). Freshwater-induced pockmarks in Bay of Eckernförde, Western Baltic. In J.E. Mojski (Ed.), *Prace Panstwowoego Instyitutu Geologicznego CXLXIX: Proceedings of the Third Marine Geological Conference "The Baltic"*, pp. 155–164.

Khandriche, A.; F. Werner; and H. Erlenkeuser, H. (1986). Auswirkungen der Ostwindstürme vom Winter 1978/79 auf die Sedimentation im Schlickbereich der Eckernförder Bucht (Westliche Ostsee). *Meyniana*, **38**, 125–152 [in German].

Kidd, G.D. (1999). Fundamentals of 3-D seismic visualization. *Sea Technology*, **40**(9), 19–23.

Kidd, R.B. (1982). Long-range sidescan sonar study of sediment slides and the effect of slope mass sediment movement on abyssal plain sedimentation. In S. Saxov and J.K.Nieuwenhuis (Eds.), *Marine Slides and Other Mass Movements*. Plenum Press, New York, 353 pp.

Kidd, R.B.; R.W. Simm; and R.C. Searle (1985). Sonar acoustic facies and sediment distribution on an area of the deep ocean floor. *Marine and Petroleum Geology*, **2**(3), 210–221.

King, L.H.; K. Rokoengin; G.B.J. Fader; and T. Gunleikrud (1991). Till tongue stratigraphy. *Geological Society of America Bulletin*, **103**, 637–659.

Kiørboe, T. (2001). Formation and fate of marine snow: Small-scale processes with large-scale implications. *Scientia Marina*, **65**(S2), 57–71, doi: 10.3989/scimar.2001.65s257.

Kirsch, R. (1971). Computer determination of the constituent structures of biological images. *Comp. and Biomed. Res.*, **4**, 315–328.

Kleinrock, M.C. (1991). Overview of sidescan sonar sytems and processing. *IEEE Proc.*, 77–83.

Kleinrock, M.C. (1992). Capabilities of some systems used to survey the deep-sea floor. In R.A. Geyer (Ed.), *CRC Handbook of Geophysical Exploration at Sea: Hard Minerals*. CRC Press, Boca Raton, FL, pp. 36–90.

Kleinrock, M.C.; and S.E. Humphris (1996). Structural control on sea-floor hydrothermal activity at the TAG active mound. *Nature*, **382**(6587), 149–153.

Kleinrock, M.C.; R.N. Hey; and A.E. Theberge, Jr. (1992). Practical geological comparison of some seafloor survey instruments. *Geophys. Res. Lett.*, **19**(13), 1407–1410.

Kloser, R.J.; N.J. Bax; T. Ryan; A. Williams;and B.A. Barker (2001). Remote sensing of seabed types in the Australian South East Fishery; Development and application of normal incident acoustic techniques and associated "ground truthing". *Marine and Freshwater Research*, **52**, 475–489, doi: 10.1071/MF99181.

Knebel, H.J.; R.R. Rendigs; J.H. List; and R.P. Signell (1996). Seafloor environments in Cape Cod Bay, a large coastal embayment. *Marine Geology*, **131**, 11–33.

Knebel, J.J.; R.P. Signell; R.R. Rendigs; L.J. Poppe; and J.H. List (1999). Seafloor environments in the Long Island Sound estuarine system. *Marine Geology*, **155**, 277–318.

Knight, R.J.; and J.R. McLean (Eds.) (1986). Shelf sands and sandstones. *Canadian Society of Petroleum Geologists Memoir*, **II**.

Komatsu, T.; C. Igarashi; K. Tatsukawa; S. Sultana; Y. Matsuoka; and S. Harada (2003). Use of multi-beam sonar to map seagrass beds in Otsuchi Bay on the Sanriku Coast of Japan. *Aquatic Living Res.*, **16**, 223–230.

Kosalos, J.G.; and D. Chayes (1983). SeaMARC: A portable system for ocean bottom imaging and charting. *IEEE Oceans '83 Proc.*, 649–656.

Kozak, G. (1997). Advances in COTS side-scan sonar for MCM applications. In N.G. Pace, E. Pouliquen, O. Bergem, and A.P. Lyons (Eds.), *High-frequency Acoustics in Shallow Water*. NATO, La Spezia, Italy, pp. 299-304.

Kristoffersen, Y.; B. Coakley; W. Jokat; M. Edwards; H. Brekke; and J. Gjengedal (2004). Seabed erosion on the Lomonosov Ridge, central Arctic Ocean: A tale of deep draft icebergs in the Eurasia Basin and the influence of Atlantic water inflow on iceberg motion? *Paleoceanography*, **19**, PA3006, doi: 10.1029/2003PA000985.

Krost, P.; M. Bernhard; F. Werner; and W. Hukriede (1990). Otter trawl tracks in Kiel Bay (Western Baltic) mapped by side-scan sonar. *Meeresforschungen*, **32**, 344–353.

Kruss, A.; Ph. Blondel; J. Tegowski; J. Wiktor; and A. Tatarek (2008). Estimation of macrophytes using single-beam and multibeam echosounding for environmental monitoring of Arctic fjords (Kongsfjord, West Svalbard Island). *J. Acoust. Soc. Am.*, **123**(5), Pt. 2, May, 3213.

Kubicki, A.; F. Manso; and M. Diesing (2007). Morphological evolution of gravel and sand extraction pits, Tromper Wiek, Baltic Sea. *Estuarine, Coastal and Shelf Science*, **71**, 647–656.

Kuijpers, A.; and F. Werner (2007). Extremely deep-draft iceberg scouring in the glacial North Atlantic Ocean. *Geo-Mar. Lett.*, **27**, 383–389.

Kuijpers, A.; T. Nielsen; A. Akhmetzhanov; H. de Haas; N.H. Kenyon; and T.C.E. van Weering (2001). Late Quaternary slope instability on the Faeroe margin: Mass flow features and timing of events. *Geo-Marine Letters*, **20**, 149–159.

Kuijpers, A.; F. Dalhoff; M.P. Brandt; P. Hümbs;T. Schott; and A. Zotova (2007). Giant iceberg plow marks at more than 1 km water depth offshore West Greenland. *Marine Geology*, **246**, 6–64.

Kuijpers, A.; B. Hansen; V. Hühnerbach; B. Larsen; T. Nielsen; and F. Werner (2002). Norwegian Sea overflow through the Faroe–Shetland gateway as documented by its bedforms. *Marine Geology*, **188**, 147–164.

Lagabrielle, Y. (2007). La dorsale est-Pacifique entre 10° et 20°S: Alternance du volcanisme et de la tectonique le long de la zone active axiale. *Géomorphologie: relief, processus, environnement*, **2**. Available at *http://geomorphologie.revues.org/document281.html* (last accessed August 28, 2008) [in French].

Lancaster, P.; and K. Salkaukas (1986). *Curve and Surface Fitting: An Introduction*. Academic Press, London, 286 pp.

Lebart, K.; E. Trucco; and D.M. Lane (2000). Real-time automatic sea-floor change detection from video. *Proceedings IEEE/MTS Oceans 2000*, 337–343.

LeBas, T.P.; and V. Hühnerbach (1998). *PRISM: Processing of Remotely-sensed Imagery for Seafloor Mapping. A Collection of Software for the Processing, Analysis and Enhancement of Sidescan Sonar Imagery*, SOC Technical Report. Southampton Oceanography Centre, Southampton, U.K., 76 pp

LeBas, T.P.; and D.C. Mason (1994). Suppression of multiple reflections in GLORIA sidescan sonar imagery. *Geophysical Research Letters*, **21**(7), 549–552.

LeBas, T.P.; D.C. Mason; and N.C. Millard (1995). TOBI image processing: The state of the art. *IEEE J. Oceanic Engineering*, **20**(1), 85–93.

LeBlanc, L.R.; L. Mayer; M. Rufino; S.G. Schock; and J. King (1992) Marine sediment classification using the chirp sonar. *J. Acoust. Soc. Am.*, **91**(1),107–115.

Legg, C. (1995). *Remote Sensing and Geographic Information Systems: Geological Mapping, Mineral Exploration and Mining*. Wiley/Praxis, Chichester, U.K., 166 pp.

Leggett J (Ed.) (1982). *Trench–Forearc Geology: Sedimentation and Tectonics on Modern and Ancient Active Plate Margins*, Special Pub. No. 10. Geological Society, London, 576 pp.

Leighton, T.G. (1997). *The Acoustic Bubble*. Academic Press, London, 613 pp.

Leppäranta, M.; and K. Myrberg (2009). *Physical Oceanography of the Baltic Sea*. Springer/Praxis, Heidelberg, Germany/Chichester, U.K., 300 pp.

Lewis, K.B.; J-Y. Collot; and S.E. Lallem (1998). The dammed Hikurangi Trough: A channel-fed trench blocked by subducting seamounts and their wake avalanches (New Zealand–France GeodyNZ Project). *Basin Research*, **10**(4),441–468. Available at *http://dx.doi.org/10.1046/j.1365-2117.1998.00080.x*

Li, R. (1992). Correction of pixel locations of sidescan sonar images using bathymetric data acquired separately. *Marine Geodesy*, **15**(2/3), 211–213.

Lien, R.; A. Solheim; A. Elverhøi; and K. Rokoengen (1989). Iceberg scouring and seabed morphology on the eastern Weddell Sea shelf, Antarctica. *Polar Res.*, **7**(1), 43–57, doi: 10.1111/j.1751-8369.1989.tb00603.x

Lillebrand, T.M.; R.W. Kiefer; and J.W. Chipman (2004). *Remote Sensing and Image Interpretation*, Fifth Edition. Wiley, New York, 763 pp.

Limonov, A.F.; J.M. Woodside; and M.K. Ivanov (Eds.) (1994). *Mud Volcanism in the Mediterranean and Black Seas and Shallow Structure of the Eratosthenes Seamount*, Reports in Marine Science No. 64. UNESCO, New York, 173 pp.

Limonov, A.F.; J.M. Woodside; M.B. Cita; and M.K. Ivanov (1996). The Mediterranean Ridge and related mud diapirism: A background. *Marine Geology*, **132**, 7–19.

Lin, C.R.; R.B. Loftin; and H.R. Nelson, Jr. (2000). Interaction with geoscience data in an immersive environment. *IEEE Virtual Reality Proc*, 55–62.

Liu, H.H.; and K.S. Fu (1982). A syntactic pattern recognition approach to seismic discrimination. *Geoexploration*, **20**, 183–196

Lo Iacono, C.; E. Grácia; and J.J. Dañobeitia (2008). Acoustic detection of deep coral mounds. *Sea Technology*, **49**(8), 35–38.

Løkkeborg, S. (2005). *Impacts of Trawling and Scallop Dredging on Benthic Habitats and Communities*, Fisheries Technical Paper No. 472. Food and Agriculture Organization of the United Nations, Rome, 58 pp.

Loncarevic, B.D.; and B.M. Scherzinger (1994). Compensation of ship attitude for multibeam sonar surveys. *Sea Technology*, 10–15.

Lucchitta, B.K. (2001). Antarctic ice streams and outflow channels on Mars. *Geophys. Res. Lett.*, **28**(3), 403–406.

Lurton, X. (2000). Swath bathymetry using phase difference: Theoretical analysis of acoustic measurement precision. *IEEE J. Oceanic Engineering*, **25**(3), 351–363.

Lutz, T.M.; and J.T. Gutmann (1995). An improved method for determining and characterizing alignments of pointlike features and its implications for the Pinacate volcanic field, Sonora, Mexico. *Journal of Geophysical Research*, **100**(B9), 17,659–17,670.

Lyons, A.P.; W.L.J. Fox; T. Hasiotis; and E. Pouliquen (2002). Characterization of the two-dimensional roughness of wave-rippled sea floors using digital photogrammetry. *IEEE Journal of Oceanic Engineering*, **27**(3), July, 515–524.

MacDonald, I.R.; J.F. Reilly, II; N.L. Guinasso, Jr.; J.M. Brooks; R.S. Carney; W.A. Bryant; and T.J. Bright (1990). Chemosynthetic mussels at a brine-filled pockmark in the northern Gulf of Mexico. *Science*, **248**(4959), 1096–1099.

MacDonald, I.R.; D.B. Buthman; W.W. Sager; M.B. Peccini; and N.L. Guinasso, Jr. (2000). Pulsed oil discharge from a mud volcano. *Geology*, **28**(10), 907–910.

MacDonald, I.R.; G. Bohrmann; E. Escobar; F. Abegg; P. Blanchon; V. Blinova; W. Brückmann; M. Drews; A. Eisenhauer; X. Han *et al.* (2004). Asphalt volcanism and chemosynthetic life in the Campeche Knolls, Gulf of Mexico. *Science*, **304**, 999–1002.

MacDonald, K.C. (1982). Mid-ocean ridges: Fine scale tectonic, volcanic and hydrothermal processes within the plate boundary zone. *Annual Review of Earth and Planetary Sciences*, **10**, 155.

MacGregor, L.M.; S. Constable; and M.C. Sinha (1998). The RAMESSES experiment, III: Controlled-source electromagnetic sounding of the Reykjanes Ridge at 57°45′N″. *Geophys. J. Int.*, **135**, 773–789.

Magde, L.S.; and D.K. Smith (1995). Seamount volcanism at the Reykjanes Ridge: Relationship to the Iceland hotspot. *Journal of Geophysical Research*, **100**(B5), 8449–8468.

Maguire, D.J.; M.F. Goodchild; and D.W. Rhind (1991). *Geographical Information Systems, Vol. 1: Principles*. Longman/Wiley, Harlow, U.K., 649 pp.

MAIB (1999). *Report on the Underwater Survey of the Stern Trawler Gaul H.243 and the Supporting Model Experiments, August 1998–January 1999*, Marine Accident Report No. 4/99. Marine Accident Investigation Branch, Southampton, U.K., 79 pp. Available at *http://www.maib.gov.uk/cms_resources/gaul_report_sections_1_to_6.pdf*

Martelli, A. (1976). An application of heuristic search methods to edge and contour detection. *Comm. A.C.M.*, **19**(2), 73–83.

Martelli, A.; and U. Montanari (1972). Optimal smoothing in picture processing: An application to fingerprints. *Inf. Proc.*, **71**, 173–178.

Martinez, F.; P. Fryer; N.A. Baker; and T. Yamazaki (1995). Evolution of back-arc rifting: Mariana Trough, 20°–24°N″. *Journal of Geophysical Research*, **100**(B3), 3807–3827.

Martínez, F.; P. Fryer; and N. Becker (2000). Geophysical characteristics of the southern Mariana Trough, 11°50′N 13°40′N. *J. Geophys. Res.*, **105**(B7), 16591–16607.

Martinsen, O.J. (2005). Deep-water sedimentary systems of Arctic and North Atlantic margins: An introduction. *Norwegian J. Geology*, 261–267.

Mason, D.C.; T.P. LeBas; I. Sewell; and C. Angelikaki (1992). Deblurring of GLORIA sidescan sonar images. *Marine Geophys. Res.*, **14**(2), 125–136.

Masson, D.G. (1994). Late Quaternary turbidity current pathways to the Madeira Abyssal Plain and some constraints on turbidity current mechanisms. *Basin Research*, **6**(1), 17–33.

Masson, D.G. (1996). Catastrophic collapse of the volcanic island of Hierro 15 ka ago and the history of landslides in the Canary Islands. *Geology*, **24**(3), 231–234.

Masson, D.G.; Q.J. Huggett; P.P.E. Weaver; D. Brunsden; and R.B. Kidd (1992a). The Saharan and Canary debris flows offshore Northwest Africa. *Landslide News, Tokyo*, **6**, 9–13.

Masson, D.G.; R.B. Kidd; J.V. Gardner; Q.J. Huggett; and P.P.E. Weaver (1992b). Saharan continental rise: Facies distribution and sediment slides. In C.W. Poag and P.C. de Graciansky (Eds.), *Geologic Evolution of Atlantic Continental Rises*. Van Nostrand Reinhold, New York, 378 pp.

Masson, D.G.; Q.J. Huggett; and D. Brunsden (1993). The surface texture of the Saharan Debris Flow deposit and some speculations on submarine debris flow processes. *Sedimentology*, **40**, 583–598.

Matheron, G. (1970). *La théorie des variables régionalisées et ses applications*, CMM Techn. Rep. Centre de Morphologie Mathématique, Ecole des Mines de Paris, Fontainebleau, France [in French].

Max, J. (1985). *Méthodes et techniques de traitement du signal et applications aux mesures physiques*, Vol. I. Masson, Paris, 354 pp [in French].

McCave, I.N. (1985). Recent shelf clastic sediments. In P.J. Brenchley and B.P.J. Williams (Eds.), *Sedimentology: Recent Developments and Applied Aspects*, Special Pub. No. 18. Geological Society, London, pp. 49–65.

McCave, I.N. (2002). Sedimentary settings on continental margins: An overview. In G. Wefer, D. Billett, D. Hebbeln, B.B. Jørgensen, M. Schlüter, and T.C.E. van Weering (Eds.), *Ocean Margin Systems*. Springer-Verlag, Berlin, pp. 1–14.

McConachy, R.; J. Arculus; C.J. Yeats; R.A. Binns; F.J.A.S. Barriga; B.I.A. McInnes; S. Sestak; R. Sharpe; B. Rakau; and T. Tevi (2005). New hydrothermal activity and alkalic volcanism in the backarc Coriolis Troughs, Vanuatu. *Geology*, **33**(1), 61–64.

Medialdea, T.; L. Somoza; R. León; M. Farrán; G. Ercilla; A. Maestro; D. Casas; E. Llave; F.J. Hernández-Molina; M.C. Fernández-Puga *et al.* (2008). Multibeam backscatter as a tool for sea-floor characterization and identification of oil spills in the Galicia Bank. *Marine Geology*, **249**, 93–107.

MEDINAUT/MEDINETH Shipboard Scientific Parties (2000). Linking Mediterranean brine pools and mud volcanism. *EOS Trans. AGU*, **81**(51), 625, 631, 632.

Medwin, H.; and C.S. Clay (1998). *Fundamentals of Acoustical Oceanography*. Academic Press, London, 712 pp.

Mendel, V.; D. Sauter; C. Rommevaux-Jestin; P. Patriat; F. Lefebvre; and L. M. Parson (2003). Magmato-tectonic cyclicity at the ultra-slow spreading Southwest Indian Ridge: Evidence from variations of axial volcanic ridge morphology and abyssal hills pattern. *Geochem. Geophys. Geosyst.*, **4**(5), 9102, doi: 10.1029/2002GC000417.

Merrill, M.L. (2007). The future is now for deep sea mining. *Marine Technology Reporter*, 22–29, January.

Messina, F.D.; E. Fihn; and J.A. Hill (2001). Enhanced cable burial protection using jet-assisted plowing. *Sea Technology*, **42**(7), 23–30, July.

Meyer, F. (1978). Iterative image transformation for an automatic screening of cervical smears. *Jour. Histochem. Cytochem.*, **27**(1), 128–135.

Meyer, F.M.; P.E. Halbach; P.N. Martens; J.R. Hein; and S. Scott (2008). Deep-sea mining: Integrating geology, oceanography, and engineering. *EOS Trans. AGU*, **89**(39), 365.

Micallef, A.; D.G. Masson;C. Berndt; Ph. Blondel; and D.A.V. Stow (2006). A geomorphological investigation of lateral spreading and translational sliding within the Storegga Slide. *Geophysical Research Abstracts*, **8**, 00352.

Michalopolou, Z.H.; D. Alexandrou; and C. de Moustier (1995). Application of neural and statistical classifiers to the problem of seafloor characterization. *IEEE Journal of Oceanic Engineering*, **20**(3), 190–197.

Mienert, J.; and P. Weaver (Eds.) (2003). *European Margin Sediment Dynamics: Sidescan Sonar and Seismic Images*. Springer-Verlag, Berlin, 309 pp.

Mignotte, M.; C. Collet; P. Pérez; and P. Bouthemy (2000). Markov Random Field and fuzzy logic modeling in sonar imagery: Application to the classification of underwater floor. *Computer Vision and Image Understanding*, **79**, 4–24.

Milkert, D.; and V. Hühnerbach (1997). Coastal environments. In Ph. Blondel and B.J. Murton (Eds.), *Handbook of Seafloor Sonar Imagery*. Wiley/Praxis, Chichester, U.K., 314 pp.

Milkov, A.,V. (2000) Worldwide distribution of submarine mud volcanoes and associated gas hydrates. *Marine Geology*, **167**, 29–42.

Milkov, A.V.; and R. Sassen (2002). Economic geology of offshore gas hydrate accumulations and provinces. *Marine and Petroleum Geology*, **19**, 1–11.

Milliman, J.D.; and W.R. Wright (Eds.) (1987). *The Marine Environment of the U.S. Atlantic Continental Slope and Rise*. Jones & Bartlett, Woods Hole, MA, 275 pp.

Mitchell, N.C. (1991). Improving GLORIA images using Sea Beam data. *J. Geophys. Res.*, **96**(B1), 337–351.

Mitchell, N.C. (1993). A model for attenuation of backscatter due to sediment accumulations and its application to determine sediment thickness with GLORIA sidescan sonar. *J. Geophys. Res.*, **98**, 22477–22493.

Mitchell, N.C. (1999). Penetration depths of sonars and interpreting images of lava flows. *RIDGE Events*, **10**(2), 23–25.

Mitchell, N.C.; and J.E. Hughes-Clarke (1994). Classification of seafloor geology using multibeam sonar data from the Scotian Shelf. *Marine Geology*, **121**, 143–160

Mitchell, N.C.; and M.L. Somers (1989). Quantitative backscatter measurements with a long-range sidescan sonar. *IEEE J. Oceanic Engineering*, **14**(4), 368–374.

Mitchell, N.C.; and J.A. Spencer (1995). An algorithm for finding routes for submarine cables or pipelines over complex bathymetry using graph theory. *Hydrographic Journal*, **78**, 29–32.

Mitchell, N.C.; E. McAllister; C. Flewellen; and C.L. Walker (1994). *Sidescan Sonar: A BRIDGE Workshop, 13/14 July 1993*, BRIDGE Position Paper 4. Natural Environment Research Council, Swindon, U.K.

Montanari, M.; Edwards, J.R.; and Schmidt, H. (2006). Autonomous underwater vehicle-based concurrent detection and classification of buried targets using higher order spectral analysis. *IEEE Journal of Oceanic Engineering*, **31**(1), January, 188–199, doi: 10.1109/JOE.2006.872216.

Moody, A.; and D.B. Katz (2004). Artificial Intelligence in the study of mountain landscapes. In M.P. Bishop and J.F. Shroder, Jr. (Eds.), *Geographic Information Science and Mountain Geomorphology*. Springer/Praxis, Heidelberg, Germany/Chichester, U.K., pp. 219–251.

Moore, J.G.; and G.W. Moore (1984). Deposit from a giant wave on the island of Lanai, Hawaii. *Science*, **226**, 1312–1315.

Moore, J.G.; D.A. Clague; R.T. Holcomb; P.W. Lipman; W.R. Normark; M.E. Torresan (1989). Prodigious submarine landslides on the Hawaiian Ridge. *Journal of Geophysical Research*, **94**(B-12), 17465–17484.

Moore, G.F.; T.H. Shipley; P.L. Stoffa; D.E. Karig; A. Taira;S. Koramoto; H. Tokuyama; and K. Suyehiro (1990). Structure of the Nankai Trough accretionary zone from multichannel seismic reflection data. *Journal of Geophysical Research*, **95**, 8735–8765.

Moren, P.; A. Caiti; M. Zakharia; M.A. Larsen; Ph. Blondel; and J. Dybedal (2007). Acoustic sea trial in the Möja Söderfjärd dumpsite. In Ph. Blondel and A. Caiti (Eds.), *Buried Waste in the Seabed: Acoustic Imaging and Bio-toxicity (Results from the European SITAR project)*. Springer/Praxis, Heidelberg, Germany/Chichester, U.K., pp. 87–102.

Morgan, J.P. (1995). Mid-ocean ridge dynamics: Observations and theory. *Reviews of Geophysics*, **29**(Suppl.), Part 5, 807–822.

Morgan, J.P.; and Y.J. Chen (1993). Dependence of ridge–axis morphology on magma supply and spreading rate. *Nature*, **364**(6439), 706–708.

Mosher, D.C.; R.G. Currie; and D. Sullivan (1997). Monitoring of ocean disposal using side-scan mosaicing. *The Leading Edge*, **6**(11), 1667–1669, doi: 10.1190/1.1437553.

Müller, P.; and G. Holloway (1995). Workshop revisits topographic effects in the oceans. *EOS Trans. AGU*, **76**(30), 300–303.

Murino, V.; and G. Vernazza (2001). Artificial neural networks for image analysis and computer vision (Guest Editorial). *Image and Vision Computing*, **19**, 583–584.

Murton, B.J.; and L.M. Parson (1993). Segmentation, volcanism and deformation of oblique spreading centres: A quantitative study of the Reykjanes Ridge. *Tectonophysics*, **222**(2), 237–257.

Musser, D.D. (1992). GPS/DGPS in Offshore Navigation, Positioning. *Sea Technology*, 61–66.

Naudts, L.; J. Greinert; Y. Artemov; S.E. Beaubien; C. Borowski; and M. De Batist (2008). Anomalous seafloor backscatter patterns in methane venting areas, Dnepr paleo-delta, NW Black Sea. *Marine Geology*, **254**, 253–267.

Needham, H.D.; and C.H. Langmuir (Eds.) (1996). FARA-InterRidge Mid-Atlantic Ridge symposium: Results from 15°N–40°N. *Journal of Conference Abstracts*, **1**(2), 742–888.

Neurauter, T.W.; and H.H. Roberts (1994). Three generations of mud volcanoes on the Louisiana continental slope. *Geo-Marine Letters*, **14**(2/3), 120–125.

Neurauter, T.W.; and W.R. Ryant (1980). Gas hydrates and their association with mud diapir/mud volcanoes on the Louisiana continental slope. In *Offshore Technology Conference, OTC '89 Proceedings*, Vol. 1, pp. 599–607.

Nevatia, R.; and K.R. Babu (1980). Linear features extraction and description. *Computer Graphics and Image Processing*, **13**, 257–269.

Newton, R.S.; and A. Stefanon (1975). Application of sidescan sonar in marine biology. *Marine Biology*, **31**, 287–291.

Newton, R.S.; E. Seibold; and F. Werner (1973). Facies distribution patterns on the Spanish Sahara continental shelf mapped with sidescan sonar. *Meteor Forsch. Ergeb.*, **C15**, 55–77.

Nguyen, H.H.; and P. Cohen (1993). Gibbs random fields, fuzzy clustering, and the unsupervised segmentation of textured images. *CVGIP: Graphical Models and Image Processing*, **55**(1), 1–19.

Niblack, W. (1986). *An Introduction to Digital Image Processing*. Prentice Hall, Englewood Cliffs, NJ, 215 pp.

Nicolas, A. (1995). *The Mid-oceanic Ridges: Mountains below Sea Level*. Springer-Verlag, Berlin, 200 pp.

Nilsson, N.J. (1971). *Problem-solving Methods in Artificial Intelligence*. McGraw-Hill, New York.

Noakes, J.E.; S.E; Noakes; D.K. Dvoracek; and P.B. Bush (1999). Survey and mapping system for surficial marine sediments. *Sea Technology*, **40**(8), 49–54.

Normark, W.R.; J.G. Moore; and M.E. Torresan (1993). Giant volcano-related landslides and the development of the Hawaii Islands. In W.C. Schwab, H.J. Lee, and D.C. Twichell

(Eds.), *Submarine Landslides: Selected Studies in the US Exclusive Economic Zone*, Bulletin 2002. U.S. Geological Survey, Reston, VA, pp. 184–196.

Oakley, A.J.; B. Taylor; P. Fryer; G.F. Moore; A.M. Goodliffe; and J.K. Morgan (2007). Emplacement, growth, and gravitational deformation of serpentinite seamounts on the Mariana forearc. *Geophys. J. Int.*, **170**, 615–634.

Off, T. (1963). Rhythmic linear sand bodies caused by tidal currents. *Bull. Am. Assoc. Petrol. Geol.*, **47**, 324–341.

Ohara, Y.; K. Fujioka; K. Okino; and H.. Fujimoto (2000). Extremely large oceanic core complex in the fast spreading Parece Vela Backarc Basin. *EOS Trans. AGU* (Western Pacific Meeting 2000 on CD-ROM).

Ohara, Y.; T. Yoshida; Y. Kato; and S. Kasuga (2001). Giant megamullion in the Parece Vela backarc basin. *Mar. Geophys. Res.*, **22**, 47–61.

Okino, K.; D. Curewitz; M. Asada; K. Tamaki; P. Vogt; and K. Crane (2002). Preliminary analysis of the Knipovich Ridge segmentation: Influence of focused magmatism and ridge obliquity on an ultraslow spreading system. *Earth Planet. Sci. Letters*, **202**, 275–288.

O'Leary, D.W.; and M.R. Dobson (1992). Southeastern New England continental rise: Origin and history of slide complexes. In C.W. Poag and P.C. de Graciansky (Eds.), *Geologic Evolution of Atlantic Continental Rises*. Van Nostrand Reinhold, New York, 378 pp.

O'Leary, E.; T. Hubbard; and D. O'Leary (2001). *Artificial Reefs Feasibility Study*, Marine Resource Series No. 20. Marine Institute, Dublin, Ireland, 52 pp.

Orsi, T.H.; M.E. Duncan; A.P. Lyons; K.B. Briggs; M.D. Richarson; and A.L. Anderson (1997). High-resolution characterization of seafloor sediments for modeling acoustic backscatter. In: N.G. Pace, E. Pouliquen, O. Bergem, and A.P. Lyons (Eds.), *High-frequency Acoustics in Shallow Water*. SACLANTCEN Publishing, Lerici, Italy, pp. 409–416.

Pace, N.G.; E. Pouliquen; O. Bergem; and A.P. Lyons (Eds.) (1997). *High-Frequency Acoustics in Shallow Water*. SACLANTCEN Publishing, Lerici, Italy.

Palanques, A.; N.H. Kenyon; B. Alonso; and A. Limonov (1995). Erosional and depositional patterns in the Valencia Channel Mouth: An example of a modern channel–lobe transition zone. *Marine Geophysical Researches*, **17**, 503–517.

Parson, L.M.; J.W. Hawkins; and P.M. Hunter (1992). Morphotectonics of the Lau Basin seafloor: Implications for the opening history of backarc basins. *Proceedings of the Ocean Drilling Program*, Initial Report No. 135 (Part 1), pp. 81–82.

Parson, L.M.; B.J. Murton; R.C. Searle; D. Booth; J. Evans; P. Field; J.A. Keeton; A. Laughton; E. Mcallister; N. Millard *et al.* (1993a). En echelon axial volcanic ridges at the Reykjanes Ridge: A life cycle of volcanism and tectonics. *Earth and Planetary Science Letters*, **117**(1/2), 73–87.

Parson, L.M.; P. Patriat; R.C. Searle; and A. Briais (1993b). Segmentation of the Central Indian Ridge between 12°12′S and the Indian Ocean Triple Junction. *Marine Geophysical Researches*, **15**(4), 265–282.

Parson, L.M.; Ph. Blondel; and T.P. LeBas (1995). *Investigation of the Sidescan Data from the M/V Derbyshire Wrecksite: Final Report*, IOSDL Report. Southampton Oceanography Centre, U.K.

Parson, L.; E. Grácia; D. Coller; C. German; and D. Needham (2000). Second-order segmentation: The relationship between volcanism and tectonism at the MAR, 38°N–35°40′N. *Earth Planet. Sci. Lett.*, **178**, 231–251.

Parthiot, F.; E. de Nanteuil; F. Merlin; B. Zerr; Y. Guedes; X. Lurton; J.-M. Augustin; P. Cervenka; J. Marchal; J.P. Sessarego *et al.* (2004). Sonar detection and monitoring of sunken heavy fuel oil on the seafloor. *InterSpill 2004 Conf. Proc., Trondheim, Norway*. Available at *http://www.interspill.com*

Pasqualini, V.; C. Pergent-Martini; P. Clabaut; and G. Pergent (1998). Mapping of *Posidonia oceanica* using aerial photographs and sidescan sonar: Application off the Island of Corsica (France). *Estuarine, Coastal and Shelf Science*, **47**, 359–367.

Paton, K. (1979). Line detection by local methods. *Computer Graphics and Image Processing*, **9**, 316–332.

Pezard, P.A.; R.N. Anderson; W.B.F. Ryan; K. Becker; J.C. Alt; and P. Gente (1992). Accretion, structure and hydrology of intermediate spreading-rate oceanic crusts from drillhole experiments and seafloor observations. *Marine Geophysical Researches*, **14**(2), 93–123.

Phipps Morgan, J. (1991). *Mid-ocean Ridge Dynamics*, IUGG National Report 1987–1990. American Geophysical Union, Washington, D.C., pp. 807–822.

Pickering, K.T.; Hiscott, R.N.; and Hein F.J. (1989) *Deep-marine Environments*. Unwin Hyman, London.

Pickering, K.T.; M.B. Underwood; A. Taira; and J. Ashi (1995a). IZANAGI sidescan sonar and high-resolution multichannel seismic reflection line interpretation of accretionary prism and trench, offshore Japan. In K.T. Pickering, R.N. Hiscott, N.H. Kenyon, F.R. Lucchi, and R.D.A. Smith (Eds.), *Atlas of Deep Water Environments: Architectural Style in Turbidite Systems*. Chapman & Hall, London, pp. 34–49.

Pickering, K.T.; R.N. Hiscott; N.H. Kenyon; F. Ricci Lucchi; and R.D.A. Smith (1995b). *Atlas of Deep Water Environments: Architectural Style in Turbidite Systems*. Chapman & Hall, London, 333 pp.

Pilkey, O.H. (1987). Sedimentology of basin plains. In P.P.E. Weaver and J. Thomson (Eds.), *Geology and Geochemistry of Abyssal Plains*. Blackwell/Geological Society, Oxford, U.K., 246 pp.

Piper, D.J.W.; P. Cochonat; and M.L. Morrison (1999). The sequence of events around the epicentre of the 1929 Grand Banks earthquake: Initiation of debris flows and turbidity current inferred from sidescan sonar. *Sedimentology*, **46**, 79–97.

Poag, C.W.; and P.C. de Graciansky (1992). *Geologic Evolution of Atlantic Continental Rises*. Van Nostrand Reinhold, New York, 400 pp.

Polheim, H. (2005). Evolutionary algorithms: Overview, methods and operators, version 3.7. *Genetic and Evolutionary Algorithm Toolbox for Use with Matlab (GEATbx) On-line Manual*, 97 pp. Available at *http://www.geatbx.com/*

Pouliquen, E. (1992). Identification des fonds marins superficiels à l'aide de signaux d'écho-sondeurs. Ph.D. thesis, Univ. Paris-VII Jussieu, 204 pp. [in French].

Pouliquen, E.; and X. Lurton (1992). Identification of the nature of the seabed using echo sounders. *J. Phys.*, **4**(2/C1), 941–944.

Pouliquen, E.; Ph. Blondel; G. Canepa; and R. Hollett (2002). Multi-sensor analysis of the seabed in shallow-water areas: Overview of the MAPLE-2001 experiment. *Proc. Sixth European Conference on Underwater Acoustics ECUA-2002, Gdansk, Poland*, pp. 167–175.

Pournou, A.; A.M. Jones; and S.T. Moss (2001). Biodeterioration dynamics of marine wreck-site determine the need for their in situ protection. *Int. J. Naut. Archaeo.*, **30**(2), 299–305.

Pratson, L.F.; and E.P. Laine (1989). The relative importance of gravity-induced versus current-controlled sedimentation during the Quaternary along the middle U.S. continental margin revealed by 3.5 kHz echo character. *Marine Geology*, **89**, 87–126.

Pratt, W.K. (2004). *Digital Image Processing*. Wiley-Interscience, New York, 750 pp.

Preston, J.M. (1992). Stability of towfish used as sonar platforms. *IEEE Oceans '92 Proc.*, pp. 888–893.

Preston, J.M.; A.C. Christney; L.S. Beran; and W.T. Collins (2004). Statistical seabed segmentation: From images and echoes to objective clustering. *Proc. Seventh European Conference on Underwater Acoustics (ECUA)*, pp. 813–818.

Prewitt, J.M.S. (1970). Object enhancement and extraction. In B.S. Lipkins and A. Rosenfeld (Eds.), *Picture Processing and Psychopictorics*. Academic Press, New York, pp. 75–150.

Price, N.J.; and J.W. Cosgrove (1990). *Analysis of Geological Structures*. Cambridge University Press, Cambridge, U.K., 502 pp.

Prior, D.B.; and E.H. Doyle (1985). Intra-slope canyon morphology and its modification by rockfall processes, U.S. Atlantic continental margin. *Marine Geology*, **67**(1/2), 177–196.

Quinn, R. (2006). The role of scour in shipwreck site formation processes and the preservation of wreck-associated scour signatures in the sedimentary record: Evidence from seabed and sub-surface data. *Journal of Archaeological Science*, **33**(10), 1419–1432.

Quinn, R.; J.M. Bull; J.K. Dix; and J.R. Adams (1997). The *Mary Rose* site: Geophysical evidence for palaeo-scour marks. *Int. J. Naut. Archaeo.*, **26**(1), 3–16.

Quinn, R.; C. Breen;W. Forsythe; K. Barton; S. Rooney; and D. O'Hara (2002). Integrated geophysical surveys of the French frigate *La Surveillante* (1797), Bantry Bay, Co. Cork, Ireland. *J. Archaeo. Sci.*, **29**, 413–422.

Quinn, R.; M. Dean; M. Lawrence; S. Liscoe; and D. Boland (2005). Backscatter responses and resolution considerations in archaeological side-scan sonar surveys: A control experiment. *J. Archaeo. Sci.*, **32**, 1252–1264.

Rao, V.P.; M. Veerayya; R.R. Nair; P.A. Dupeuble; and M. Lamboy (1994). *Late Quaternary Halimeda* bioherms and aragonitic faecal pellet-dominated sediments on the carbonate platform of the western continental shelf of India. *Marine Geology*, **121**, 293–315.

Reading, H.G. (1978). *Sedimentary Environments and Facies*. Blackwell, Oxford, U.K., 615 pp.

Rebesco, M.; and D. Stow (2001). Seismic expression of contourites and related deposits: A preface. *Marine Geophys. Res.*, **22**, 303–308.

Rebesco, M.; R.D. Later; A. Camerlenghi; and P.F. Barker (1996). Giant sediment drifts on the continental rise west of the Antarctic Peninsula. *Geo-Marine Letters*, **16**, 65–75.

Rebesco, M.; A. Camerlenghi; R. Geletti; and M. Canals (2006). Margin architecture reveals the transition to the modern Antarctic ice sheet ca. 3 Ma. *Geology*, **34**(4), 301–304, doi: 10.1130/G22000.1.

Reed, S.; Y. Petillot; and J. Bell (2003). An automatic approach to the detection and extraction of mine features in sidescan sonar. *IEEE J. Oceanic Engineering*, **28**(1), 90–105.

Reed, T.B.; and D. Hussong (1989). Digital image processing techniques for enhancement and classification of SeaMARC-II side scan sonar imagery. *J. Geophys. Res.*, **94**(B6), 7469–7490.

Reineck, H.-E. (1963). Sedimentgefüge im Bereich der südlichen Nordsee. *Abh. senckenbergische Naturforsch. Ges.*, **505**, 138.

Reineck, H.-E.; and I.B. Singh (1980). *Depositional Sedimentary Environments*. Springer-Verlag, New York, 551 pp.

Rhind, D.W. (1990). Global databases and GIS. In M.J. Foster and P.J. Shand (Eds.), *The Association for Geographic Information Yearbook 1990*. Taylor & Francis, London, pp. 85–91.

Ribe, N.M. (1988). On the dynamics of mid-ocean ridges. *Journal of Geophysical Research*, **93**(B1), 429-436.

Richards, M.; M. Bowman; and H. Reading (1998). Submarine-fan systems, I: Characterization and stratigraphic prediction. *Mar. Petrol. Geology*, **15**, 689–717.

Riesen, W.; and K. Reise (1982). Macrobenthos of the subtidal Wadden Sea revisited after 55 years. *Helgoländer Meeresuntersuchungen*, **35**, 409–423.

Rignot, E.; and R. Chellappa (1992). Segmentation of polarimetric Synthetic Aperture Radar data. *IEEE Transactions on Image Processing*, **1**(3).

Ristow, D.; K. Hinz; J. Hauschild; T. Gindler; A. Berhorst; C. Bönneman (2002). Imaging the subsurface with 2-D and 3-D seismic data. In G. Wefer, D. Billett, D. Hebbeln,

B.B. Jørgensen, and Tj. van Weering (Eds), *Ocean Margin Systems*. Springer-Verlag, Berlin, pp. 33–55.

Ritter, D.F.;, R.G. Kochel; and R. Miller (1995). *Process Geomorphology*, Third Edition. W.C. Brown Publishing, Dubuque, IA, 546 pp.

Roberts, H.H.; C.V. Phipps; and L.L. Effendi (1987). Morphology of large *Halimeda* bioherms, Eastern Java Sea (Indonesia): A side-scan sonar study. *Geo-Marine Letters*, **7**(1), 7–14.

Roberts, L.G. (1965). Machine perception of 3-dimensional solids. In J.T. Tippett *et al*. (Eds.), *Optical and Electro-Optical Information Processing*. MIT Press, Cambridge, MA, pp. 159–167.

Robertson, K.G. (1990). Deep Sea Navigation Techniques. *Marine Geophysical Researches*, **12**, 3–8.

Robinson, G.S. (1977). Edge detection by compass gradient masks. *Computer Graphics and Image Processing*, **6**, 492–501.

Rona, P.A. (1986) Black smokers, massive sulphides and vent biota at the Mid-Atlantic Ridge. *Nature*, **321**, 33–37.

Rona, P.; K. Bemis; D. Jackson; C. Jones; J. Mitsusawa; D. Silver; and D. Palmer (2008). Acoustic imaging, visualizing and quantifying submarine hydrothermal plumes and diffuse flow. In *Mantle to Microbe: Integrated Studies at Oceanic Spreading Centers*, Ridge 2000 Abstract Volume. Ridge-2000, Portland, OR, pp. 54–55. Available at *http://www.ridge2000.org/science/downloads/meetings/reports/spring08.pdf*

Rosenberger, A.; P. Weidelt; C. Spindeldreher; B. Heesemann; and H. Villinger (1999). Design and application of a new free fall in situ resistivity probe for marine deep water sediments. *Marine Geology*, **160**(3/4), 327–337.

Rosenfeld, A.; and M. Thurston (1971). Edge and curve detection for visual scene analysis. *IEEE Trans. Comp*., **C-20**, 562–569.

Rosenfeld, A.; M. Thurston; and Y.H. Lee (1972). Edge and curve detection: Further experiments. *IEEE Trans. Comp*., **C-20**, 677–715.

Rothwell, R.G.; N.H. Kenyon; and B.A. McGregor (1991). Sedimentary features of the south Texas continental slope as revealed by side-scan sonar and high-resolution seismic data. *American Association of Petroleum Geologists Bulletin*, **75**(2), 298–312.

Sanchez, P.; M. Demestre; M. Ramon; and M.J. Kaiser (2000). The impact of otter trawling on mud communities in the northwest Mediterranean. *ICES J. Mar. Sci*., **57**, 1352–1358.

Sanfeliu, A.; and K.S. Fu (1983). A distance measure between attributed relational graphs for pattern recognition. *IEEE Trans. on SMC*, **13**(3), 353–362.

Sauter, D.; V. Mendel; C. Rommevaux-Jestin; L.M. Parson; H. Fujimoto; C. Mével; M. Cannat; and K. Tamaki (2004). Focused magmatism versus amagmatic spreading along the ultra-slow spreading Southwest Indian Ridge: Evidence from TOBI side scan sonar imagery. *Geochem. Geophys. Geosyst*., **5**, Q10K09, doi: 10.1029/2004GC000738.

Saxov, S.; and J.K. Nieuwenhuis (1982). *Marine Slides and Other Mass Movements*. Plenum Press, New York, 1982.

Scanlon, K.M.; and D.G. Masson (1992). Fe–Mn nodule field indicated by GLORIA, north of the Puerto Rico Trench. *Geo-Mar. Lett*., **12**(4), 208–213.

Schacht, R. (1996). Sonographische und sedimentologische Untersuchungen zur Klimaentwicklung in hocharktischen Fjordsystemen. Unpublished thesis, Univ. Kiel., 120 pp. [in German].

Scheirer, D.S.; D.J. Fornari; S.E. Humphris; and S. Lerner (2000). High-resolution seafloor mapping using the DSL-120 sonar system: Quantitative assessment of sidescan and phase-bathymetry data from the Lucky Strike segment of the Mid-Atlantic Ridge. *Marine Geophysical Researches*, **21**, 121–142.

Schnellman, M.; F.S. Anselmetti; D. Giardini; and J.A. McKenzie (2005). Mass movement-induced fold-and-thrust belt structures in unconsolidated sediments in Lake Lucerne (Switzerland). *Sedimentology*, **52**, 271–289.

Schröder, H.G. (1992). *Sedimentoberflächen im östlichen Bodensee-Obersee-Sidescan Untersuchungen im Zusammenhang mit den Auswirkungen der Vorstreckung des Alpenrheins*, Ber. Nr. 43. Internationale Gewässerschutzkommision für den Bodensee, 48 pp. Available at *http://www.igkb.de/* [in German].

Schrottke, K.; M. Becker; A. Bartholoma; B.W. Flemming; and D. Hebbeln (2006). Fluid mud dynamics in the Weser estuary turbidity zone tracked by high-resolution side-scan sonar and parametric sub-bottom profiler. *Geo-Mar. Lett.*, **26**, 185-198.

Schuttenhelm, R.T.E.; G.A. Auffret; D.E. Buckley; R.E. Cranston; C.N. Murray; L.E. Shepard; and A.E. Spijkstra (1989). *Geoscience Investigations of Two North Atlantic Abyssal Plains: The ESOPE International Expedition*, two volumes. Office of Official Publications of the European Communities, Luxembourg, 1293 pp.

Schwarzer, K. (1996). *Auswirkungen der Sandentnahme auf dem Salzsand auf die morphologisch/sedimentologischen Verhältnisse*, Unveröffent. Bericht. Amt für Land- und Wasserwirtschaft, Husum, Germany, 11 pp. [in German].

Schwarzer, K.; K. Ricklefs; W. Schumacher; and R. Atzler (1996). Beobachtungen zur Vorstranddynamik und zum Küstenschutz sowie zum Sturmereignis vom 3./4.11.1995 vor dem Streckelsberg/Usedom. *Meyniana*, **48**, 49–68 [in German].

Schweller, W.J.; and L.D. Klum (1978). Depositional pattern and channelized sedimentation in active eastern Pacific trenches. In D.G. Stanley and G. Keling (Eds,), *Sedimentation in Submarine Canyons, Fans and Trenches*. Dowden, Hutchinson & Ross, Strandsburg, PA, pp. 323–350.

Searle, R.C. (1980). Tectonic pattern of the Azores spreading centre and Triple Junction. *Earth and Planetary Science Letters*, **51**, 415–434.

Searle, R.C.; and A.S. Laughton (1981). Fine-scale sonar study of tectonics and volcanism on the Reykjanes Ridge. *Oceanologica Acta*, **4**, 5–13.

Searle, R.C.; P.J. Schultheiss; P.P.E. Weaver; M. Noel; R.B. Kidd; C.L. Jacobs; and Q.J. Huggett (1985). *Great Meteor East (Distal Madeira Abyssal Plain): Geological Studies of Its Suitability for Disposal of Heat-emitting Radioactive Wastes*, Report No. 193. Institute of Oceanographic Sciences, 162 pp.

Searle, R.C.; T.P. LeBas; N.C. Mitchell; M.L. Somers; L.M. Parson; and Ph. Patriat (1990). GLORIA image processing: The state of the art. *Marine Geophys. Res.*, **12**, 21–39.

Seibold, E.; and W.H. Berger (1993). *The Sea Floor: An Introduction to Marine Geology*, Second Edition. Springer-Verlag, Berlin, 356 pp.

Selim, S.Z.; and K. Alsultan (1991). A simulated annealing algorithm for the clustering problem. *Pattern Recognition*, **24**(10), 1003–1008.

Sempéré, J.-C.; J. Palmer; D.M. Christie; J.P. Morgan; and A.N. Shor (1991). Australian–Antarctic Discordance. *Geology*, **19**(5), 429–432.

Sempéré, J.-C.; and EW9210 Scientific Party (1992). EW-9210 Cruise Report. Unpublished report, 220 pp.

Sempéré, J.-C.; Ph. Blondel; A. Briais; T. Fujiwara; L. Géli; N. Isezaki; J.E. Pariso; L. Parson; Ph. Patriat; and C. Rommevaux (1995). The Mid-Atlantic Ridge between 29°N and 31°30′N in the last 10 Ma. *Earth and Planetary Science Letters*, **130**, 45–55.

Serra, J. (1982). *Mathematical morphology*. Academic Press, New York, 610 pp.

Shang, Y.C. (1980). *Aquaculture Economics: Basic Concepts and Methods of Analysis*. Westview Press, Boulder, CO, 153 pp.

Shapiro, S.D. (1978). Properties for transforms of curves in noisy pictures. *Computer Graphics and Image Processing*, **8**, 219–223.

Sharma, R. (1993). Recommendations for NASA's Space Physics Data System. *EOS Trans. AGU*, **74**(50), 589–590.

Shell, R.C.; G.C. Bishop; and D.B. Maxwell (2006). Under-ice sonar visualisation. *Linux Journal*. Available at *http://www.linuxjournal.com/article/8299*

Shenderov, E.L. (1998). Some physical models for estimating scattering of underwater sound by algae. *J. Acoust. Soc. Am.*, **104**(2), 791–800.

Shih, T.T. (1967). A survey of the active mud volcanoes in Taiwan and a study of their types and the character of the mud. *Pet. Geol. Taiwan*, **6**, 259–311.

Shipp, S.S.; J.S. Wellner; and J.B. Anderson (2002). *Retreat Signature of a Polar Ice Stream: Sub-glacial Geomorphic Features and Sediments from the Ross Sea, Antarctica*, Special Pub. No. 203. Geological Society, London, pp. 277–304, doi: 10.1144/GSL.SP.2002.203.01.15.

Shippey, G. (1997). Simple algorithms for sonar imaging and bathymetry with a linear swept-frequency (Chirp) source. *Int. J. Imaging Syst. Tech.*, **8**, 359–376.

Shokr, M. (1991). Evaluation of second-order texture parameters for sea ice classification from radar images. *Journal of Geophysical Research*, **96**(C6), 10625–10640.

Simaan, M.A. (1998). Texture-based techniques for interpretation of seismic images. *Proceedings Oceans '98*. MTS/Institute of Electrical and Electronic Engineers, Piscataway, NJ.

Simmons, A.B.; and S.G. Chappell (1988). Artificial Intelligence: Definition and practice. *IEEE Journal of Oceanic Engineering*, **13**(2), 14–42.

Sinha, M.C.; P.D. Patel; M.J. Unsworth; T.R.E. Owen; and M.G.R. MacCormack (1990). An active source electromagnetic sounding system for marine use. *Marine Geophys. Res.*, **12**, 59–68.

Sinton, J.M. (1989). *Evolution of Mid Ocean Ridges*, Geophysical Monograph 57, IUGG Vol. 8. American Geophysical Union, Washington, D.C., 77 pp.

Smith, D.K.; and J.R. Cann (1990). Hundreds of small volcanoes on the median valley floor of the Mid-Atlantic Ridge at 24–30°N. *Nature*, **348**(6297), 152–155.

Smith, D.K.; and J.R. Cann (1992). The role of seamount volcanism in crustal construction at the Mid-Atlantic Ridge (24°–30°N). *Journal of Geophysical Research*, **97**(B2), 1645–1658

Smith, D.K.; J.R. Cann; M.E. Dougherty; J. Lin; S. Spencer; C.J. Macleod; J.A. Keeton; E. McAllister; B. Brooks; R. Pascoe *et al.* (1995a). Mid-Atlantic Ridge volcanism from deep-towed side-scan sonar images, 25–29°N. *Journal of Volcanology and Geothermal Research*, **67**, 233–262.

Smith, D.K.; S.E. Humphris; and W.B. Bryan (1995b). A comparison of volcanic edifices at the Reykjanes Ridge and the Mid-Atlantic Ridge at 24–30°N. *Journal of Geophysical Research*, **100**(B11), 22485–22498.

Smith, W.H.F.; and P. Wessel (1990). Gridding with continuous curvature splines in tension. *Geophysics*, **55**(3), 293–305.

Sobel, I. (1978). Neighbourhood coding of binary images for fast contour following and general binary array processing. *Computer Graphics and Image Processing*, **8**, 127–135.

Solheim, A. (1991). *The Depositional Environment of Surging Sub-polar Tidewater Glaciers*. Skrifter Norsk Polarinstitut, Oslo, 194 pp.

Somers, M.L. (1993). Sonar imaging of the seabed: Techniques, performance, applications. In J.M.F. Moura and I.M.G. Lourtie (Eds.), *Acoustic Signal Processing for Ocean Exploration*. Canadian Government, Ottawa, pp. 355–369.

Somers, M.L.; and Q.J. Huggett (19933). From GLORIA to GLORI-B. *Sea Technology*, 64–68.

Somers, M.L.; and A.R. Stubbs (1984). Sidescan sonar. *IEE Proceedings*, **131**(3), Part F, 243–256.

Stefanon, A. (1985). Marine sedimentology through modern acoustical methods, 1: Sidescan sonar. *Bolletino di Oceanologia Teorica ed Applicata*, **3**(1), 3–38.

Stevenson, I.; P. Nicholson; A. Attich; and C. Summers (2002). Ultra-high resolution seabed mapping using an AUV. *Sea Technology*, **43**(8), 40–45.

Stewart, W.K.S. (1990). *Subsea Data Processing Standards*, Workshop Report. RIDGE, Woods Hole, MA. Available at *http://www.ridge2000.org/*

Stewart, W.K.; D. Chu; S. Malik; S. Lerner; and H. Singh (1994a). Quantitative seafloor characterisation using a bathymetric sidescan sonar. *IEEE J. Oceanic Engineering*, **19**(4), 599–610.

Stewart, W.K.; M. Jiang; and M. Marra (1994b). A neural network approach to sidescan imagery classification of a mid-ocean ridge area. *IEEE J. Oceanic Engineering*, **19**(2), 214–224.

Stoker, M.S.; D. Evans and A. Cramp (Eds.) (1998). *Geological Processes on Continental Margins: Sedimentation, Mass-wasting and Stability*, Special Pub. No. 129. Geological Society, London.

Stoll, R.D.; and T. Akal (1999). XBP: Tool for rapid assessment of seabed sediment properties. *Sea Technology*, **40**(2), 47–51.

Stow, D.A.V.; and M. Mayall (2000). Deep-waer sedimentary systems: New models for the 21st Century. *Mar. Petrol. Geology*, **15**, 689–717.

Stow, D.A.V.; C.J. Pudsey; J.A. Howe; J.C. Faugères; and A.R. Viana (Eds.) (2002). *Deep-water Contourites: Modern Drifts and Ancient Series, Seismic and Sedimentary Characteristics*, Memoir 22. Geological Society, London, 472 pp.

Strasser, M.; C. Schindler; and F.S. Anselmetti (2008). Late Pleistocene earthquake-triggered moraine dam failure and outburst of Lake Zurich, Switzerland. *J. Geophys. Res.*, **113**, F02003, doi: 10.1029/2007JF000802.

Stride, A.H. (1970). Shape and size trends for sand waves in a depositional zone of the North Sea. *Geol. Mag.*, 469–477.

Taroudakis, M.I.; and G. Makrakis (Eds.) (2001). *Inverse Problems in Underwater Acoustics*. Springer-Verlag, New York, 216 pp.

Taylor, R.N.; B.J. Murton; and M.F. Thirlwall (1995). Petrogenesis and geochemical variation along the Reykjanes Ridge, 57°N-59°N. *J. Geol. Soc. London*, **152**, 1031–1037.

Tęgowski, J.; and Z. Aubniewski (2000). The use of fractal properties of echo signals for acoustical classification of bottom sediments. *Acta Acustica*, **86**(2), 276–282.

Telford, W.M.; L.P. Geldart; and R.E. Sheriff (1990). *Applied Geophysics*, Second Edition. Cambridge University Press, Cambridge, U.K., 770 pp.

Terwindt, J.H.J. (1971). Lithofacies of inshore estuarine and tidal-inlet deposits. *Geol. Mijnbouw*, **50**, 515–526.

Tharp, M. (1989). *Discovery of the Mid-Ocean Rift System*, Annual Report. Lamont–Doherty Geological Observatory of Columbia University, New York, pp. 20–21.

Thieler, E.R.; A.L. Brill; W.J. Cleary; C.H. Hobbs, III; and R.A. Gammisch (1995). Geology of the Wrightsville Beach, North Carolina shoreface: Implications for the concept of shoreface profile of equilibrium. *Marine Geology*, **126**, 273–287.

Thomsen, L.; T.C.E. van Weering; Ph. Blondel; R. Lampitt; F. Lamy; I.N. McCave; S. McPhail; J. Mienert; R. Neves; L. d'Ozouville *et al.* (2002). Margin building: Regulating processes. In G. Wefer, D. Billett, D. Hebbeln, B.B. Jørgensen, M. Schlüter, and T.C.E. van Weering (Eds.), *Ocean Margin Systems*. Springer-Verlag, Berlin, pp. 195–203.

Thornburg, T.M.; L.D. Kulm; and D.M. Hussong (1990). Submarine-fan development in the southern Chile Trench: A dynamic interplay of tectonics and sedimentation. *Geological Society of America Bulletin*, **102**(12), 1658–1680.

Thorpe, S.A.; A.R. Stubbs; A.J. Hall; and R.J. Turner (1982). Wave-produced bubbles observed by side-scan sonar. *Nature*, **296**, 636–638.

Tian, W.M. (2005). Searching and locating of underwater pipelines. In N.G. Pace and Ph. Blondel (Eds.), *Boundary Influences in High-frequency Shallow-water Acoustics*. University of Bath Press, U.K., pp. 287–294.

Tian, W.M. (2008). Integrated method for the detection and location of underwater pipelines. *App. Acoust.*, **69**, 387–398.

Tokuyama, H.; F. Yamamoto; K. Suyehiro; and A. Taira (1996). IZANAGI ocean floor imaging surveys around Japan. *J. Acoust. Soc. Am.*, **100**(4), 2668.

Tomczak, M.; G.D. Haffner; and E. Fronaes (2002). False-bottom acoustic echo in mid water? A note on how to evaluate and prevent the interference. *IEEE J. Oceanic Engineering*, **27**(4), 870–872.

Tomlinson, J.S.; C.J. Pudsey; R.A. Livermore; R.D. Larter; and P.F. Barker (11992). Long-range sidescan sonar (GLORIA) survey of the Antarctic peninsular Pacific margin. In Y. Yoshida *et al.* (Ed.), *Recent Progress in Antarctic Science*. Terra Scientific Publishing, Tokyo, pp. 423–429.

Trott., K.; and D. Tomalin (2003). The maritime role of the island of Vectis in the British pre-Roman Iron Age. *Int. J. Naut. Archaeo.*, doi: 10.1016/j.ijna.2003.02.002.

TTR cruises. Available at *http://ioc.unesco.org/ttr/cruises.html*

Tucholke, B.E. (1992). Massive submarine rockslide in the rift-valley wall of the Mid-Atlantic Ridge. *Geology*, **20**(2), 129–132.

Tucholke, B.; J. Lin; and M. Kleinrock (1998). Megamullions and mullion structure defining oceanic metamorphic core complexes on the Mid-Atlantic Ridge. *J. Geophys. Res.*, **103**, 9857–9866.

Tunnicliffe, V. (1991). The biology of hydrothermal vents: Ecology and evolution. *Oceanography and Marine Biology Annual Review*, **29**, 319–407.

Turgut, A.; and S.N. Wolf (1998). Inversion of sediment properties from chirp sonar data using an extended Biot–Stoll–Gassmann model. *J. Acoust. Soc. Am.*, **104**(3), 1788,

Twichell, D.C.; and D.G. Roberts (1982). Morphology, distribution and development of submarine canyons on the United States Atlantic continental slope between Hudson and Baltimore Canyons. *Geology*, **10**, 408–412

Ulaby, F.T.; R.K. Moore; and A.K. Fung (1982). Microwave remote sensing: Active and passive. In *Radar Remote Sensing and Surface Scattering and Emission Theory*, Vol. 2. Addison-Wesley, Reading, MA.

Ulrich, J. (1972). Untersuchungen zur Pendelbewegung von Tiderippeln im Heppenser Fahrwasser (Innenjade). *Die Küste*, **23**, 112–121.

Unnithan, V.; P.M. Shannon; K. McGrane; A.W.B. Jacob; P.W. Readman; and R. Keary (2000). *Reconnaissance Survey of the Irish Continental Shelf/Shelf Edge (AIRS '96)*, Mar. Res. Series Pub. 12. Marine Institute, Dublin, Ireland. Also available at *http://www.marine.ie/NR/rdonlyres/1D4DD8D5-1743-4EDF-8C9E-C3E86AB5D6FC/0/r12.pdf*

van de Meene, J.W.H.; J.R. Boersma; and J.H.J. Terwindt (1996). Sedimentary structures of combined flow deposits from the shoreface-connected ridges along the central Dutch coast. *Marine Geology*, **131**, 151–175.

Vanderbrug, G.J. (1976). Line detection in satellite imagery. *IEEE Trans. Geoscience*, **GE-14**, 37–44.

Van Dover, C.L. (1995). Ecology of Mid-Atlantic Ridge hydrothermal vents. In L.M. Parson, C.L. Walker, and D.R. Dixon (Eds.), *Hydrothermal Vents and Processes*. Special Pub. No. 87. Geological Society, London, pp. 257–294.

Van Dover, C.L. (2000). *The Ecology of Deep-sea Hydrothermal Vents*. Princeton University Press, Princeton, NJ, 352 pp.

van Lancker, V.; and P. Jacobs (2000). The dynamical behaviour of shallow-marine dunes. In A. Trentesaux and T. Garlan (Ed.), *Marine Sandwave Dynamics Proc*., 7 pp.

van Lancker, V.; J. Lanckneus; S. Hearn; P. Hoekstra; F. Levoy; J. Miles; G. Moerkerke; O. Monfort; and R. Whitehouse (2004). Coastal and nearshore morphology, bedforms and sediment transport pathways at Teignmouth (UK). *Cont. Shelf Res*., **24**, 1171–1202.

Vickery, K. (1998). Acoustic positioning systems: A practical overview of current systems. In *Proceedings of the 1998 Workshop on Autonomous Underwater Vehicles, Fort*

Vine, F.J.; and D.H. Matthews (1963). Magnetic anomalies over oceanic ridges. *Nature*, **199**, 947–949.

Vogt, P.; and J.M. Gardner (2009). *GOMap: Global Ocean Mapping Project: Examples of Sidescan in Deep Water*. U.S. Naval Research Laboratory, Washington D.C. Available at: *http://mp-www.nrl.navy.mil/marine_physics_branch/gomap.php* (last accessed April 2009).

Volgin, A.V.; and J.M. Woodside (1996). Sidescan sonar images of mud volcanoes from the Mediterranean Ridge: Possible causes of variations in backscatter intensity. *Marine Geology*, **132**, 39–53.

Volovov, V.I.; and A.I. Govorov (1999). Implementation of the acoustical monitoring of underwater engineering structures in bodies of water. *Acoust. Phys*., **45**(2), 158–162.

von Huene, R.; C.R. Ranero; and P. Watts (2004). Tsunamigenic slope failure along the Miidle America Trench in two tectonic settings. *Mar. Geol*., **203**, 303–317.

Voulgaris, G.; and M.B. Collins (1991). Linear features on side-scan sonar images: An algorithm for the correction of angular distortion. *Marine Geology*, **96**(1/2), 187–190.

Wadhams, P. (2000). *Ice in the Ocean*. Taylor & Francis, Philadelphia, PA, 368 pp.

Wadhams, P.; and M. J. Doble (2008). Digital terrain mapping of the underside of sea ice from a small AUV. *Geophys. Res. Lett*., **35**, L01501, doi: 10.1029/2007GL031921.

Wang, J.; and P.J. Howarth (1989). Edge following as graph searching and Hough transform algorithms for lineament detection. *Proc. IGARSS' 89, Vancouver*, pp. 93–96.

Watt, A.; and F. Policarpo (1998). *The Computer Image*. Addison-Wesley, Reading, MA, 784 pp.

Weaver, P.P.E.; and J. Thomson (1987). *Geology and Geochemistry of Abyssal Plains*. Blackwell/Geological Society, Oxford, U.K., 246 pp.

Weaver, P.P.E.; R.G. Rothwell; J. Ebbing; D. Gunn; and P.M. Hunter (1992). Correlation, frequency of emplacement and source directions of megaturbidites on the Madeira Abyssal Plain. *Marine Geology*, **109**(1/2), 1–20.

Weaver, P.P.E.; D.G. Masson; D.E. Gunn; R.B. Kidd; R.G. Rothwell; and D.A. Maddison (1995). Sediment mass wasting in the Canary Basin. In K.T. Pickering, R.N. Hiscott, N.H. Kenyon, F. Ricci Lucchi, and R.D.A. Smith (Eds.), *Atlas of Deep Water Environments: Architectural Style in Turbidite Systems*. Chapman & Hall, London, 333 pp.

Weaver, P.P.E.; R.B. Wynn; N.H. Kenyon; and J. Evans (2000). Continental margin sedimentation, with special reference to the north-east Atlantic margin. *Sedimentology*, **47**(1), 239–256.

Wefer, G.; D. Billett; D. Hebbeln; B.B. Jørgensen; M. Schlüter; and T.C.E. van Weering (Eds.), *Ocean Margin Systems*. Springer-Verlag, Berlin, 495 pp.

Weiland, C.M.; K.C. Macdonald; and N.R. Grindlay (1996). Ridge segmentation and the magnetic structure of the southern Mid-Atlantic Ridge, 26°S and 31°35'S: Implications for magmatic processes at slow spreading centers. *Journal of Geophysical Research*, **101**(B4), 8055–8073.

Welch, T.A. (1984). A technique for high-performance data compression. *IEEE Computer*, **17**(6), 8–19.

Werby, M.F.; G.J. Tango; and G.E. Ioup (1986). Remote seismo-acoustic characterization of shallow ocean bottoms using spatial signal-processing of towed array measurements. *Geophysics*, **51**(7), 1517.

Werner, F. (1977). *Principios de Interpretación del Sonar Lateral y Ejemplos de su Aplicación en la Plataforma Continental Argentina*, Pub. No. 38. Instituto Argentino de Oceanografía, Universidad Nacional del Sur, Bahía Blanca, 36 pp.

Werner, F.; and R.S. Newton (1975). The pattern of large-scale bed forms in the Langeland Belt (Baltic Sea). *Marine Geology*, **19**, 39–62.

Werner, F.; G. Unsöld; B. Koopmann; and A. Stefanon (1980). Field observations and flume experiments on the nature of comet marks. *Sedimentary Geology*, **26**, 233–262.

Werner, F.; G. Hoffmann; M. Bernhard; D. Milkert; and K. Vikgren (1990). Sedimentologische Auswirkungen der Grundfischerei in der Kieler Bucht. *Meyniana*, **42**, 123–151 [in German].

Wessel, P.; and W.H.F. Smith (1991). Free software helps map and display data. *EOS Trans. AGU*, **72**(441), 445–446.

West, B.P.; J.-C. Sempére; D.G. Pyle; J.P. Morgan; and D.M. Christie (1994). Evidence for variable upper mantle temperature and crustal thickness in and near the Australian–Antarctic Discordance. *Earth Planet. Sci. Lett.* **128**(3/4), 135–153.

Westbrook, G.K.; and M.J. Smith (1983). Long decollements and mud volcanoes: Evidence from the Barbados Ridge complex for the role of high pore fluid pressure in the development of an accretionary complex. *Geology*, **11**, 279–283.

Westbrook G.K.; R.F. Woollett; X. Le Pichon; S. Lallemant; N. Chamot-Rooke; J.P. Foucher; F. Harmegnies; E. Suess; A. Bleyer; P. Pavlakis (1995a). Brine lakes and thermal anomalies in the sea floor and bottom water of the western Mediterranean Ridge. In M. Weydert, E. Lipiatou, R. Goni, C. Fragakis, M. Bohle-Carbonell, K.-G. Barthel (Ed.), *Marine Sciences and Technologies: Second MAST Days and Euromar Market, November 7–10*, Project Reports Vol. 1. Office for Official Publications of the European Communities, Luxembourg, 788 pp.

Westbrook, G.K.; and the MEDRIFF Consortium (1995b). Three brine lakes discovered in the seafloor of the Eastern Mediterranean. *EOS Trans. AGU*, **76**(33), 313–318.

Westbrook, G.K.; N. Hardy; and R Heath (1995c). *Structure and Tectonics of the Panama–Nazca Plate Boundary*, Spec. Paper 295. Geological Society of America, New York.

Westervelt, 1963 (in Zakharia and Dybedal, SITAR book 2007 refs.)

Weydert, M.M.P. (1990). Measurements of the acoustic backscatter of selected areas of the deep seafloor and some implications for the assesssment of manganese nodule resources. *J. Acoust. Soc. Am.*, **88**(1), 350–366.

Wienberg, C.; and A. Bartholomä (2005). Acoustic seabed classification in a coastal environment (outer Weser Estuary, German Bight): A new approach to monitor dredging and dredge spoil disposal. *Cont. Shelf Res.*, **25**, 1143–1156.

Wienberg, C.; and D. Hebbeln (2005). Impact of dumped sediments on subaqueous dunes, outer Weser Estuary, German Bight, southeastern North Sea. *Geo-Mar. Lett.*, **25**, 43–53.

Wienberg, C.; J. Dannenberg; and D. Hebbeln (2004). The fate of dumped sediments monitored by a high-resolution multibeam echosounder system, Weser Estuary, German Bight. *Geo-Mar. Lett.*, **24**, 22–31.

Wille, P. (2005). *Sound Images of the Ocean in Research and Monitoring*. Springer-Verlag, Berlin, 471 pp.

Wilson, P.S.; and K.H. Dunton (2006). Seagrass acoustics: Results of an experimental laboratory investigation. *J. Acoust. Soc. Am.*, **119**(5), 3448.

Wilson, P.S.; and K.H. Dunton (2007). Seagrass acoustics: Results of an experimental laboratory investigation. *Proc. Second International Conference "Underwater Acoustic Measurements: Technologies & Results"*, pp. 383–390.

Wingham, D.J.; N.G. Pace; and R.V. Ceen (1986). An experimental study of the penetration of water/sediment interface by parametric array. *J. Acoust. Soc. Am.*, **79**, 363–374.

Wolfe, C.J.; G.M. Purdy; D. Toomey; and S.C. Solomon (1995). Microearthquake characteristics and crustal velocity structure at 29N on the Mid-Atlantic Ridge: The architecture of a slow spreading segment. *Journal of Geophysical Research*, **100**(B12), 24449–24472.

Woodcock, N.H.; and M. Fischer (1986). Strike-slip duplexes. *Journal of Structural Geology*, **7**, 725–735.

Woodside, J.M.; and A.V. Volgin (1996). Brine pools associated with Mediterranean Ridge mud diapirs: An interpretation of echo-free patches in deep-tow sidescan sonar data. *Marine Geology*, **132**, 55–61.

Wright, A.S.C. (1993). Deep-towed sidescan sonars. *IEEE Oceans '93*, **III**, 478–483.

Wright, D.J.; R.M. Haymon; and D.J. Fornari (1995). Crustal fissuring and its relationship to magmatic and hydrothermal processes on the East Pacific Rise crest ($9^{\circ}12'$ to $54'$N). *Journal of Geophysical Research*, **100**(B4), 6097–6120.

Young, E. (2002). Drowned Indian city could be world's oldest. Available at *http://www.newscientist.com* (last accessed January 18, 2002).

Zakharia, M.; and J. Dybedal (2007). The parametric sidescan sonar instrument and synthetic aperture sonar processing. In Ph. Blondel and A. Caiti (Eds.), *Buried Waste in the Seabed: Acoustic Imaging and Bio-toxicity (Results from the European SITAR project)*. Springer/Praxis, Heidelberg, Germany/Chichester, U.K., pp. 13–18.

Zakharia, M.; P. Chevret; and P. Dubail (Eds.) (2000). *Proceedings of the Fifth European Conference on Underwater Acoustics ECUA-2000, Lyon, France*.

Index

Printing: Mercedes-Druck, Berlin
Binding: Stein+Lehmann, Berlin

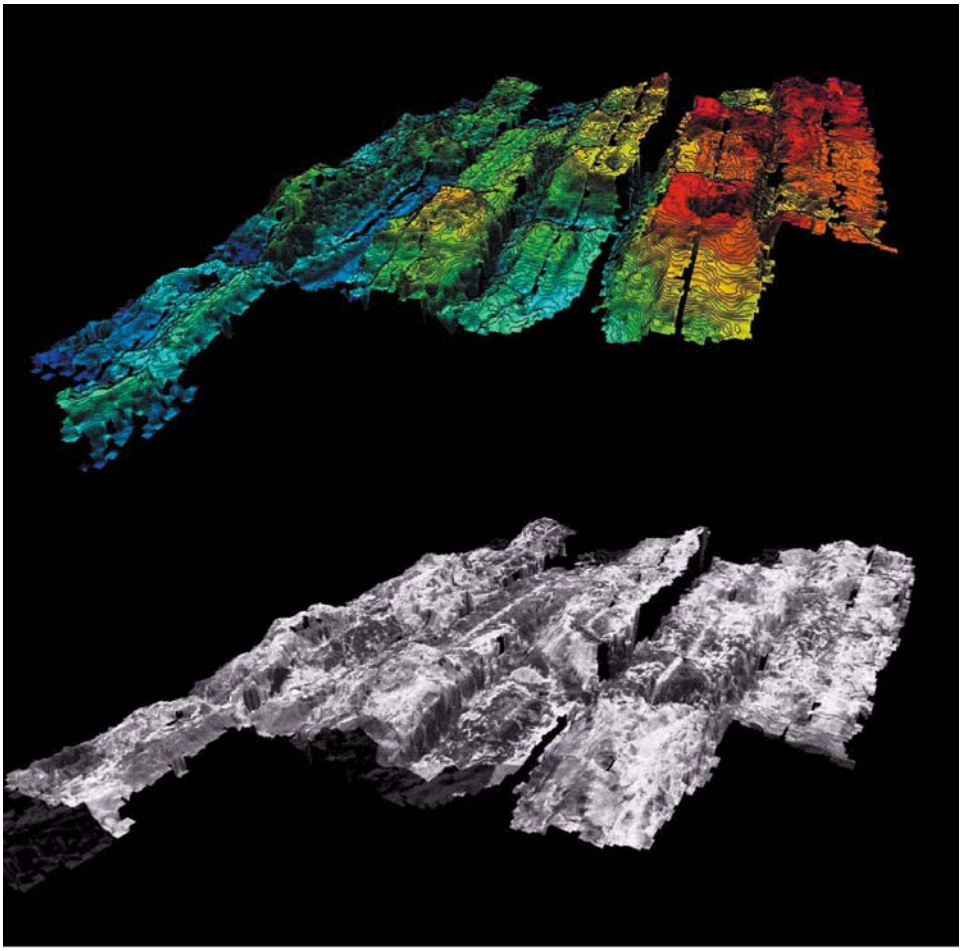

Figure 3.8. The 3-D bathymetry acquired with the swath sonar IMI-30 between the islands of Maui and Hawaii, in perspective (top). Sidescan sonar imagery, acquired with the same sonar and at the same metric resolution, can then be draped over the bathymetry (bottom).

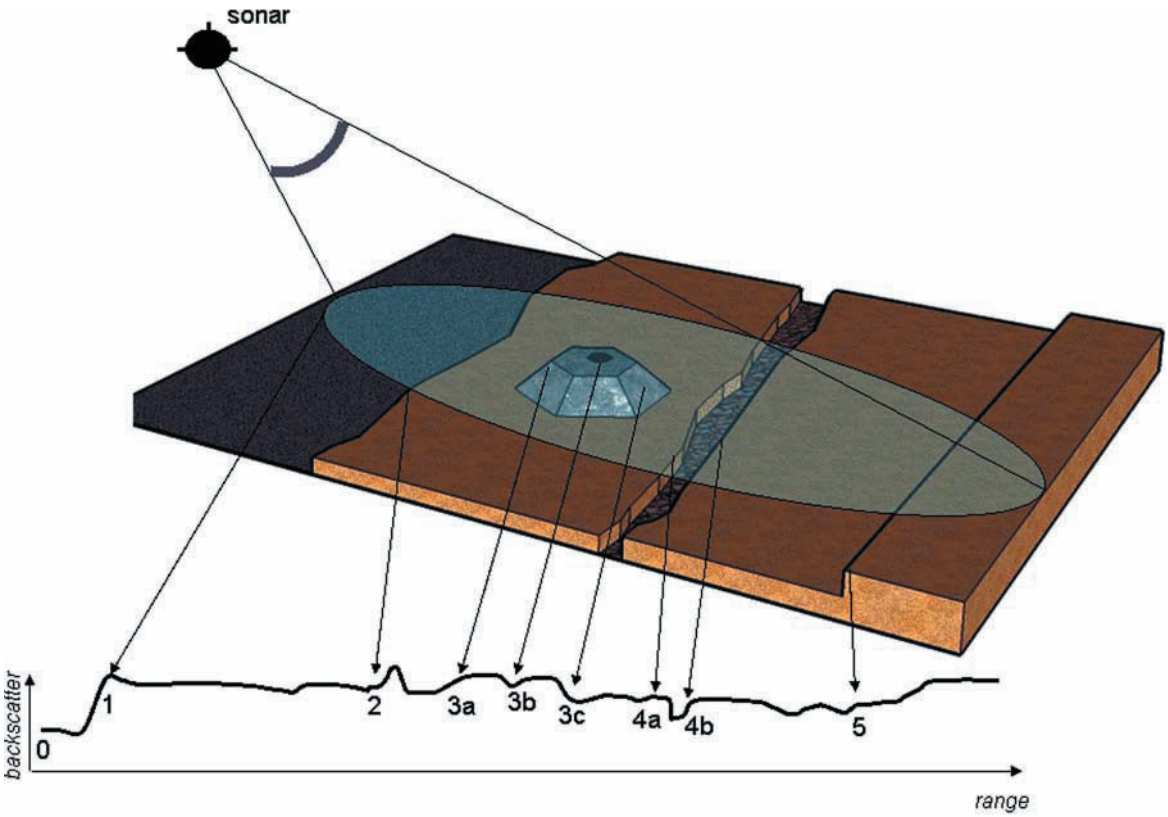

Figure 4.1. Backscatter profiles are measured over the entire area ensonified by the sidescan sonar: (0) background noise and reverberation from the water column; (1) first seabed returns from small rubble; (2) fault scarp and transition to smoother terrain; (3a) volcano slope facing toward the sonar; (3b) dip in the backscatter levels, associated with the caldera at the top of the volcano; (3c) volcano slope, facing away from the sonar; (4a) strong decrease in reflectivity, associated with a fissure on the ground; (4b) return of reflectivity to its previous levels on the other side of the fissure; (5) fault scarp.

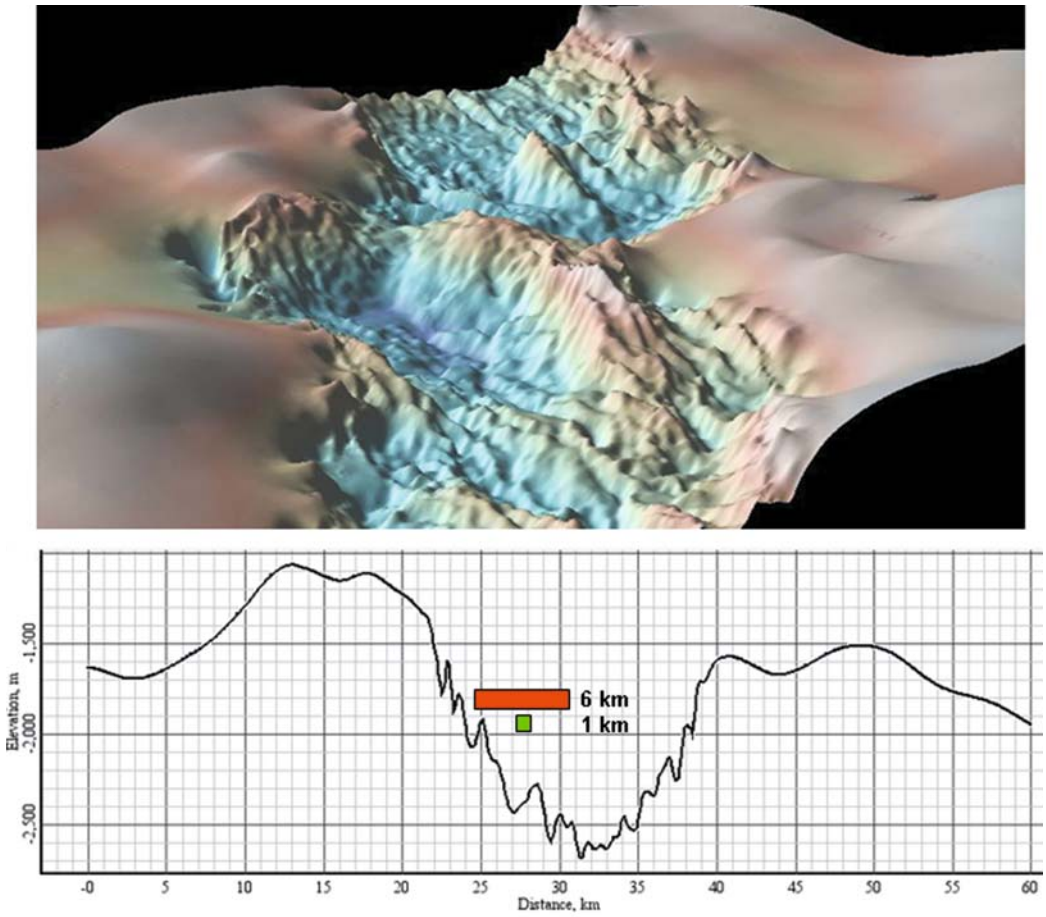

Figure 5.1a. Three-dimensional view of a portion of the slow-spreading Mid-Atlantic Ridge, and bathymetric profile across the ridge. The 60 km length intends to show the depth variations across the swath of a low-resolution sidescan sonar (like GLORIA, with a swath width of 60 km). The swath widths of a medium-resolution sonar like TOBI (6 km) and a high-resolution sonar like DSL-120 (1 km) have been added to show the depth (and imaging angle variations) that can be expected depending on the sonar's height and expected track (i.e., centered on the ridge or on one side). Image and profile were computed using GeoMapApp (*http://www. geomapapp.org/*) and compilation bathymetry from the Ridge 2000 Data Portal (*http://www.marine-geo.org/portals/ridge2000/*) (Carbotte *et al.*, 2004).

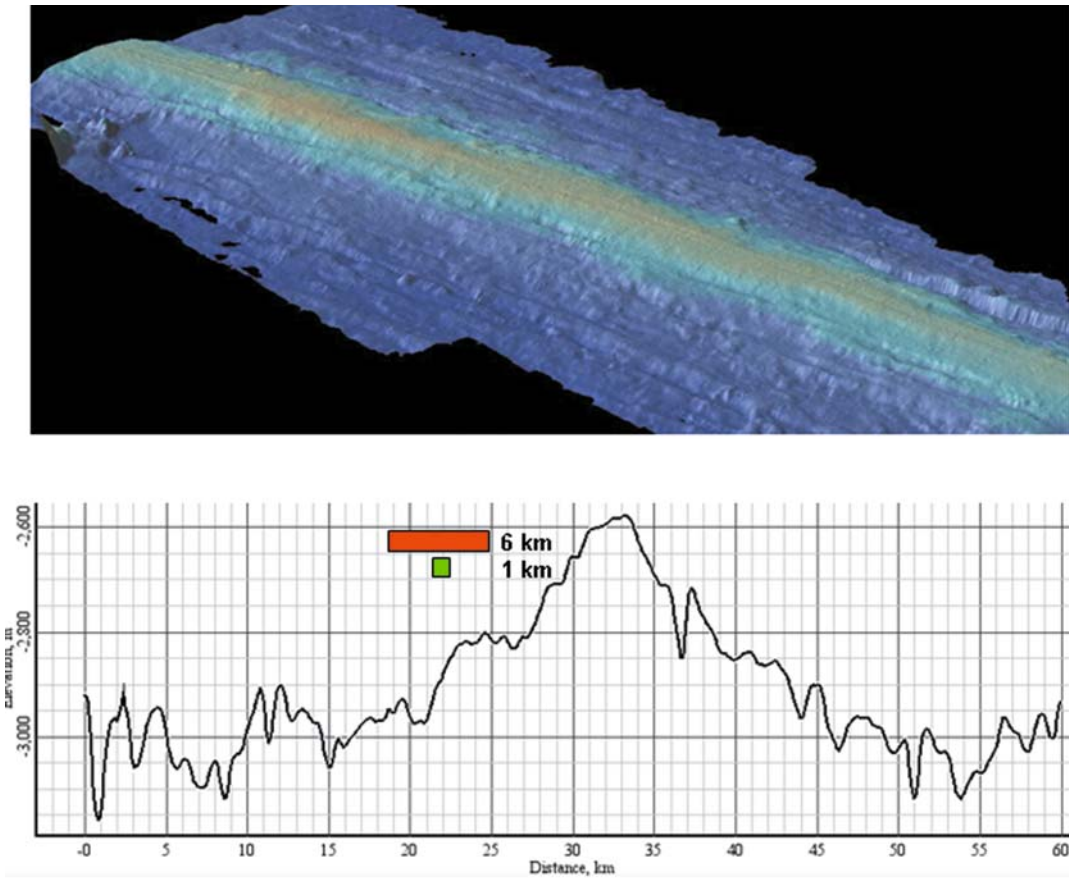

Figure 5.1b. Three-dimensional view of a portion of the fast-spreading East Pacific Rise, and bathymetric profile across the ridge. Explanations and source credits are similar to those of Figure 5.1a.

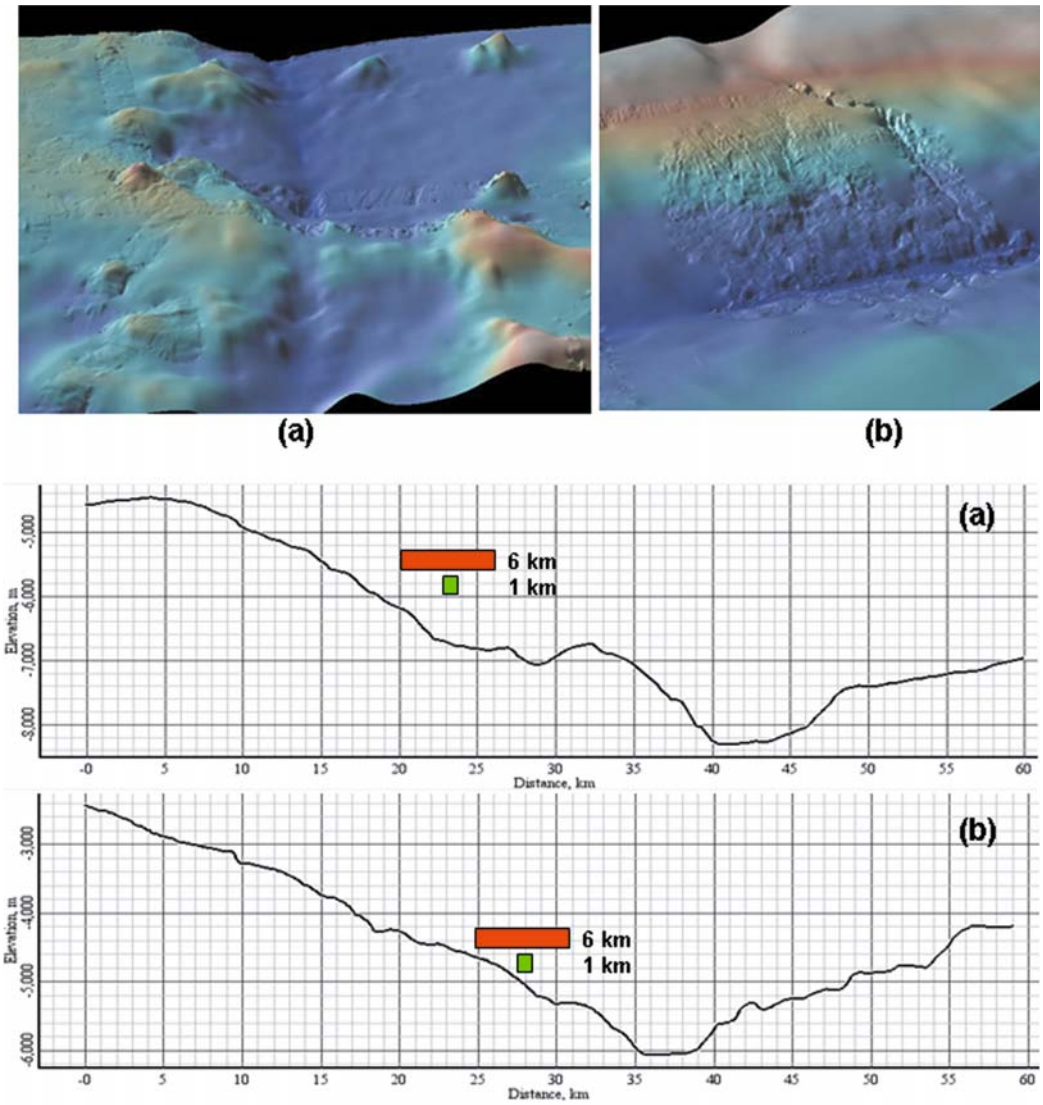

Figure 5.3. Shaded bathymetry and profiles showing two different subduction zones: (a) Mariana Trench; (b) Columbia Trench. Images and profiles were computed using GeoMapApp (*http://www.geomapapp.org/*) and compilation bathymetry from the Ridge 2000 Data Portal (*http://www.marine-geo.org/portals/ridge2000/*) (Carbotte *et al.*, 2004).

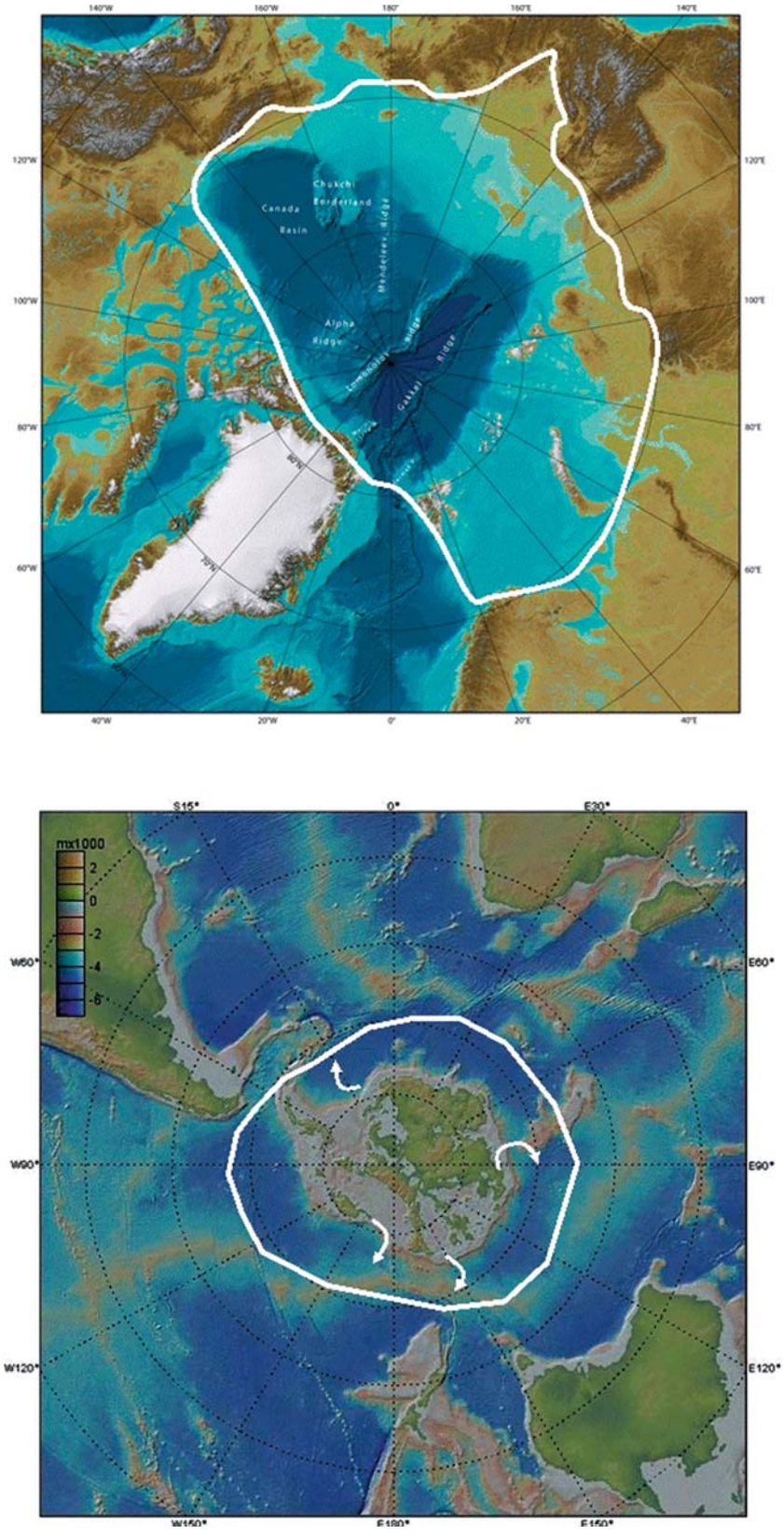

Figure 6.12. General bathymetry of the polar seas. (Top) Arctic polar seas, outlined in white (adapted from Jakobsson *et al.*, 2008). Mostly covered by ice, the Arctic seas encompass a large variety of terrains, including glaciated continental margins and active mid-ocean ridges. (Bottom) Antarctic polar seas (created using GeoMapApp: *http://www.geomapapp.org/*; Carbotte *et al.*, 2007), roughly outlined in white. Arrows show the main paths of iceberg drifts (from Wille, 2002). The areas around the ice-covered Antarctic shelf encompass subduction zones, mid-ocean ridges, and abyssal plains.

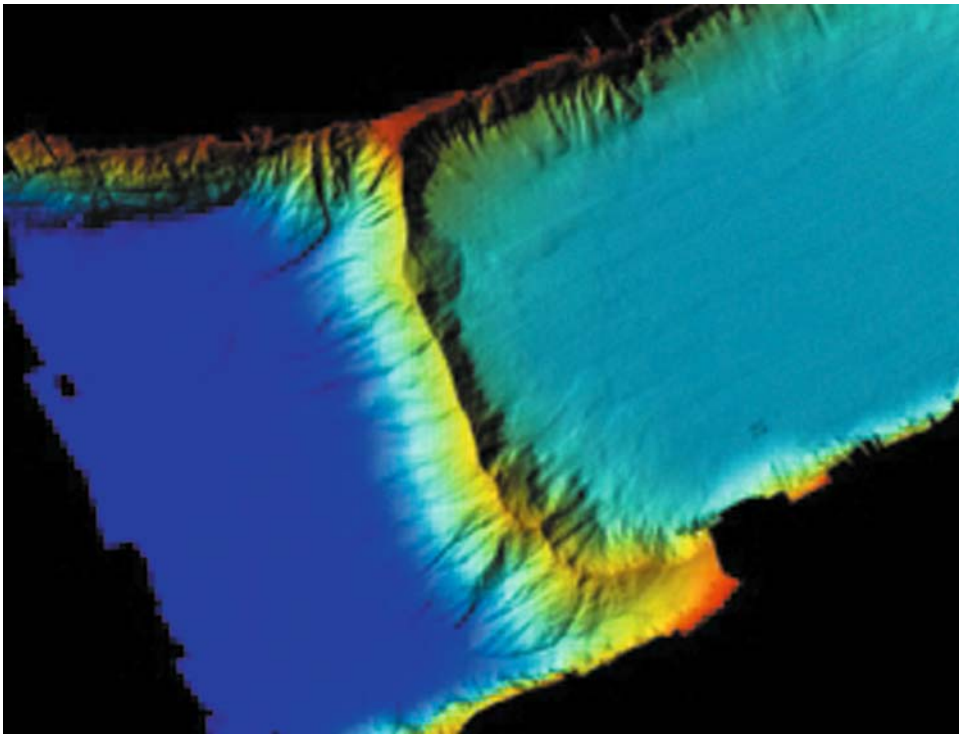

Figure 8.11. GeoSwathPlus interferometric bathymetry from a morainic ridge extending for more than 1 km across the Luzern Lake near Gersau, Switzerland. The bathymetry is color-coded from red (0 m) to deep blue (~200 m) (reproduced by permission from Dr. Flavio Anselmetti, EAWAG, the Swiss Federal Institute of Aquatic Science and Technology).

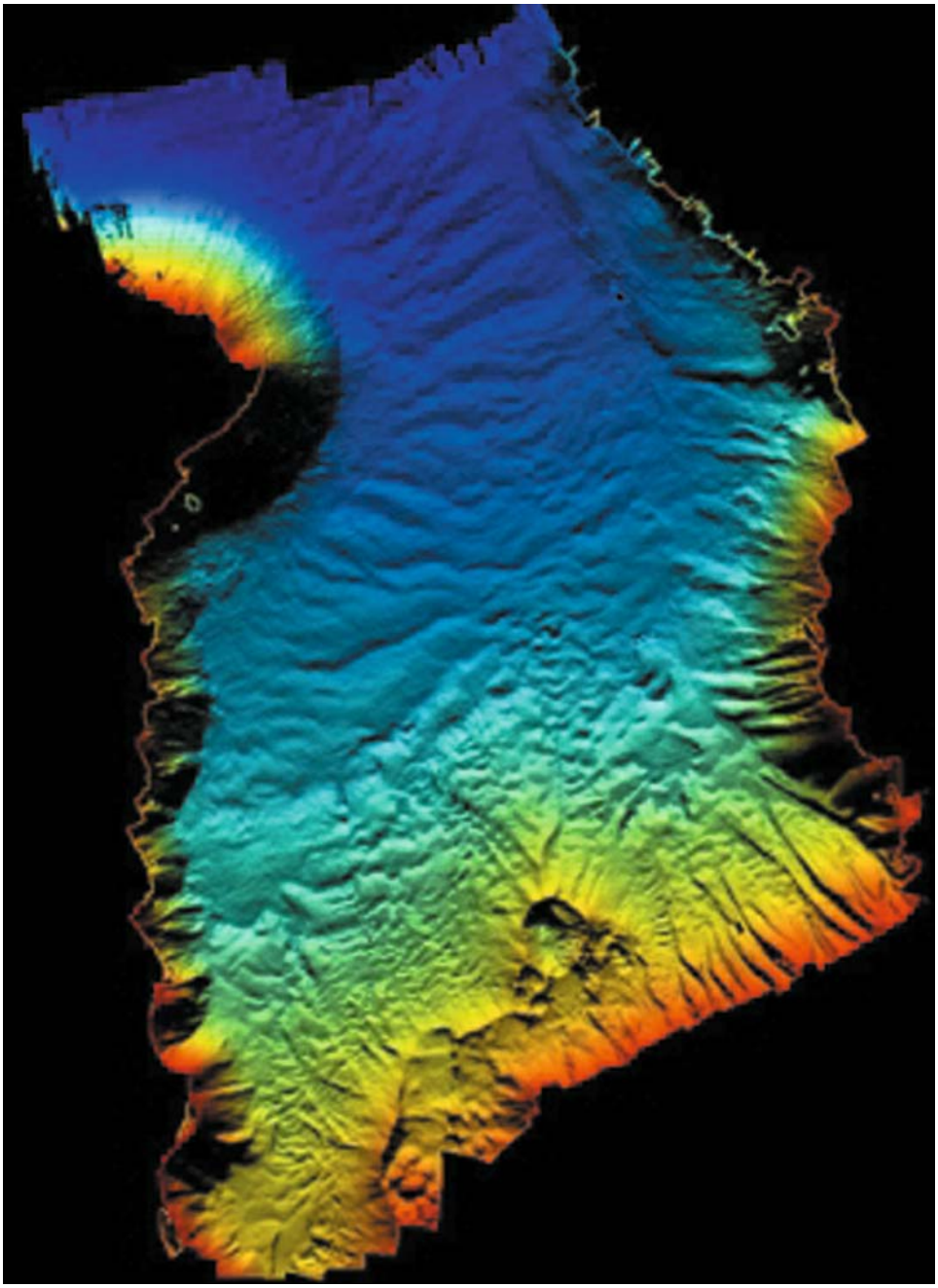

Figure 8.12. GeoSwathPlus interferometric bathymetry from the southern part of the Umersee (Lake Luzern), including the Reuss delta (south) (image width is approximately 2.2 km). The bathymetry is color-coded from red (0 m) to deep blue (~200 m). It shows a wealth of details about the lake bed, including the changes to the Reuss delta from sand and gravel extraction (reproduced by permission from Dr. Flavio Anselmetti, EAWAG, the Swiss Federal Institute of Aquatic Science andTechnology).